Universidad del País Vasco
Euskal Herriko Unibertsitatea

FACULTY OF SCIENCE AND TECHNOLOGY
UNIVERSITY OF THE BASQUE COUNTRY

Departamento de Mineralogía y Petrología

Diseño y desarrollo de pilas de combustible de óxido sólido

Design and development of solid oxide fuels cells

Aritza Wain Martin

Memoria para optar al grado de Doctor por la **UPV/EHU**

Leioa, abril de 2019

Universidad del País Vasco
Euskal Herriko Unibertsitatea

FACULTY OF SCIENCE AND TECHNOLOGY
UNIVERSITY OF THE BASQUE COUNTRY

Departamento de Mineralogía y Petrología

Diseño y desarrollo de pilas de combustible de óxido sólido

Design and development of solid oxide fuels cells

Aritza Wain Martin

Memoria para optar al grado de Doctor por la **UPV/EHU**

Leioa, abril de 2019

"Creo que algún día se empleará el agua como combustible, que el H_2 y el O_2 de los que está formada, usados por separado o de forma conjunta, proporcionarán una fuente inagotable de luz y calor"

Julio Verne, La isla misteriosa (1874)

Agradecimientos

Me gustaría agradecer a las muchas personas que durante estos cuatro años han aportado su tiempo, paciencia y cariño, ayudando a realizar este trabajo.

En primer lugar, agradezco a mi directora, la Prof. Maria Isabel Arriortua, por la confianza y el cariño depositados en mi desde un principio, además de por su continua disponibilidad y ayuda. Doy gracias a mi también director, el Dr. Aitor Larrañaga, su paciencia y aportaciones han sido indispensables para llevár adelante este trabajo. Ha sido un honor haber formado parte de vuestro equipo.

No olvido a la Dra. Aintzane Goñi, del departamento de Inorgánica. Sin la ilusión contagiada a lo largo del Master de Nuevos Materiales y su propuesta para que yo hiciese la tesis, este trabajo tan siquiera habría empezado. Asimismo, agradezco a la Dra. Karmele Vidal haber sido mi mentora a lo largo de los primeros años y haberme acogido en el grupo, siendo una grandísima compañera. Se te ha echado muchísimo de menos desde que te has ido. También me gustaría agradecer a la Dra. Aroa Morán el haber estado siempre disponible para ayudar y colaborar conmigo. Para mi has sido como una hermana mayor de tesis.

Me gustaría mostrar también mi agradecimiento al personal técnico de los Servicios Generales de Investigación, SGIker, que han hecho posible realizar este trabajo. Agradezco al Dr. Sergio Fernández su ayuda y consejos durante todos estos años. Gracias también al Dr. Juan Carlos Raposo por solventar esas dudas relacionadas con las mediciones de ICP-AES.

Agradezco también al Ministerio de Industria y Competitividad, por la concesión de la beca de formación de personal investigador que he disfrutado. Asimismo, doy las gracias al departamento de Mineralogía y Petrología por el interés y ayuda demostrada durante todos estos años.

Asimismo, doy las gracias al personal investigador del Instituto de Ciencia de Materiales de Aragón (ICMA) de la Universidad de Zaragoza, por haberme facilitado los equipamientos y conocimientos para realizar las medidas electroquímicas presentadas en esta memoria. En especial quiero agradecer al Dr. Miguel Laguna su amabilidad y disponibilidad durante el tiempo disfrutado en Zaragoza. Me gustaría incluir también en este agradecimiento a la Dra. Alodia Orera, por permitirme conocer al pequeño Roque y haberme hecho las estancias más agradables; y al Dr. Angel Larrea, por estar siempre pendiente durante las largas horas pasadas en el laboratorio haciendo las medidas electroquímicas.

I would like to thank to the Prof. Peter Raymond Slater and his group from the University of Birmingham, for their good reception and their help in the realization of new electrochemical measurements. The concerts and the breweries were also a great discovery during this stay. I would like to thanks also to Roberto de la Cruz and the BISH gang, the time spent with you all as a big international family it was wonderful. I hope to see you soon.

De forma especial, agradezco al Centro Nacional del Hidrógeno, y sobre todo al grupo de investigación, por su buena acogida. Particularmente me acuerdo del Dr. Roberto Campana y del Dr. Jesús Rodríguez. No solo por sus conocimientos, equipamiento y nivel de implicación, todos ellos enormes, sino porque también a nivel personal, me han aportado muchísimo. Me habéis abierto las puertas a una kuadrilla manchega (Santi, Nata, Giulli, Ester, Mara, Cris y vosotros dos), uno de los grandes descubrimientos de estos cuatro años. Me vienen a la cabeza los partidos de baloncesto y los jamones colectivizados, además de un montón de buenos momentos junto a vosotros. También me gustaría mencionar al Dr. Leandro Rodríguez y a Gema Sevilla, por su acogida durante mis estancias en Puertollano.

Mi más sincera gratitud a los miembros del tribunal por haber aceptado juzgar este trabajo de investigación.

Igualmente, quiero agradecer a mis compañeros de despacho el haberme ayudado y haberme hecho compartir tan buenos momentos a lo largo de estos años. Habéis sido una pequeña familia en ese rincón llamado F3.S1.5. Entre los que ya se han ido, a Fran le deseo que siga con ese espíritu aventurero, retratándolo siempre en esas fantásticas fotos; y a Eder que siga transmitiendo la pasión por la ciencia que tiene con ese humor que tanto me gusta. A Edurne le tengo que agradecer el mantener el laboratorio tan bien como está, además de cuidar de todos nosotros. A Arkaitz el estar siempre disponible para buscar soluciones al papeleo y dudas de Word. Has sido un buenísimo vecino de mesa. A Roberto, por transmitir ese compañerismo, aún teniendo altos niveles de estrés. A Iñigo, por la honradez y lealtad que has tenido desde que empezaste. A Laura, por la valentía que transmites, celebraremos nuestras tesis a la vez!. A Mikel, por dar siempre ánimos y ser tan buen compañero. Eres el siguiente, así que te deseo mucha fuerza en este camino.

A los compañeros de la universidad me gustaría también mencionarlos. A Amaia Iturrondobeitia, Beñat Artetxe, Xabi Lasheras y a Ohiane Arriortua, que, en cierta manera, me animaron a tomar este camino. Karrerakoei, Maider, Esti, Itziar, Oiane, Ohiane, Onin eta bereziki ostegunetako kedadetara zatoztenoi, pila bat animatu didazuelako urte hauetan zehar, Markel, Itsaso, Lucia eta azkenaldian Aitorsa baita. Honelako egunak berreskuratu behar ditugu beste bidai batzuk antolatzeko.

Me gustaría agradecer a la kuadrilla el haberme sufrido durante estos últimos meses de tesis; en especial, a David, el cual me ha ayudado con algunas de las traducciones. A Aitor, Kike, Naranjo, Fran y Tania por las buenas comidas en casa, y a Iñaki, Eneko, Puyol, Ibai, Mofas, Olga, Marti, Julene, Bea, Peña y Jorge por conseguir que olvidara la tesis algunas noches durante la etapa final.

Por último, me gustaría agradecer su apoyo a mi círculo más cercano. A Eli, por siempre ponerme en mi sitio. A Ama, por empujarme continuamente a implicarme más. A Aita, por ilusionarse tanto o más que yo con este trabajo, además de hacer las infografías que aparecen a lo largo de esta memoria y crear los diseños de la portada. A mi hermana Ainara, por estar siempre pendiente de mí. Eres de las personas más fuertes que conozco. A las pequeñas, Oma e Hize, porque además de alegrarme cada vez que las veo, me apetecía mencionarlas aquí. Puede que sea el primer libro en el que aparezcan, pero estoy seguro de que no será el último que las mencione. Y por supuesto a Ibone. Es de las personas que más ha sufrido esta tesis y que más me ha apoyado durante este tiempo. Espero seguir siendo tu compañero en las próximas etapas de nuestra vida.

Resumen

El procesado de componentes para pilas de combustible de óxido sólido (SOFC), es una de las claves más importantes para la comercialización de estos sistemas de generación de energía sostenible. De esta manera, el presente estudio aporta avances en una tecnología de interés para desarrollar la transición hacia un sistema energético seguro, sostenible y competitivo, objetivo que se contempla en el Horizonte 2030, el mayor programa de investigación e innovación de la Unión Europea.

El uso de la síntesis por combustión, permite controlar las propiedades de los materiales de partida, además de conseguirlo de manera económica. Sin embargo, el empleo de este tipo de síntesis presenta como reto su escalabilidad para la producción de materiales para pilas SOFC.

En este trabajo se ha recogido el desarrollo del procesado de pilas SOFC, partiendo desde la síntesis de grandes cantidades de material de partida y finalizando con la fabricación y caracterización de celdas en funcionamiento, lo que ha permitido la identificación y adaptación de las propiedades clave para obtener este tipo de celdas.

Los primeros ensayos se han realizado sintetizando, a gran escala, los componentes $NiO\text{-}(ZrO_2)_{0.92}(Y_2O_3)_{0.08}$ (ánodo), $(ZrO_2)_{0.92}(Y_2O_3)_{0.08}$ (electrolito), $Sm_{0.2}Ce_{0.8}O_{1.9}$ (barrera), $La_{0.6}Sr_{0.4}FeO_3$ (cátodo), $LaNi_{0.6}Fe_{0.4}O_3$ (capa de contacto) y $MnCo_{1.9}Fe_{0.1}O_4$ (capa protectora), que han conformado las celdas de combustible desarrolladas. La caracterización de los materiales de partida, ha tenido en cuenta la reproducibilidad de la síntesis, así como la composición, microestructura, conductividad y coeficientes de expansión térmica.

El estudio de parámetros como la molienda o el espesor de la capa al realizar el procesado de los materiales primarios, ha permitido analizar el efecto del método de deposición en el comportamiento estructural y electroquímico de la celda. La investigación realizada, ha dado lugar a la preparación de celdas simétricas con configuración de soporte electrolito, que han permitido optimizar el desarrollo del sistema final.

Con el fin de mejorar la adherencia entre los componentes, se ha optado por el uso de intercapas entre los materiales que conforman el sistema final mostrado en esta memoria. Los ensayos de larga duración, así como la respuesta electroquímica a 800 ºC, han demostrado una adecuada integridad estructural para los sistemas completos.

Estos prototipos acercarán a la sociedad la comercialización de los sistemas de generación de energía sostenible.

Summary

The processing of the components for solid oxide fuel cells (SOFC) is one of the most important keys for the commercialization of these sustainable energy generation systems. In this way, the present study provides advances in an interesting technology to develop the transition towards a safe, sustainable and competitive energy system, an objective that is contemplated in Horizon 2030, the largest research and innovation program of the European Union.

The use of combustion synthesis allows to control the properties of the starting materials, to achieving it economically. However, the use of this type of synthesis presents as challenge its scalability for the production of SOFCs materials.

In this work, we have collected the development of SOFC processing, starting from the synthesis of large quantities of starting material and has finishing with the manufacture and characterization of the cells in operation, which has allowed the identification and adaptation of the key properties to obtain this type of cells.

The first tests were carried out by synthesizing in large scale the components $NiO\text{-}(ZrO_2)_{0.92}(Y_2O_3)_{0.08}$ (anode), $(ZrO_2)_{0.92}(Y_2O_3)_{0.08}$ (electrolyte), $Sm_{0.2}Ce_{0.8}O_{1.9}$ (barrier), $La_{0.6}Sr_{0.4}FeO_3$ (cathode), $LaNi_{0.6}Fe_{0.4}O_3$ (contact layer) and $MnCo_{1.9}Fe_{0.1}O_4$ (protective layer), which form the developed fuel cells. The starting materials characterization have taken into account the synthesis reproducibility, as well as the composition, microstructure, conductivity and thermal expansion coefficients.

The study of parameters such as milling or layer thickness when manufacturing the starting materials, has allowed to analyze the effect of the deposition method on the structural and electrochemical behavior of the cells. The performed research has led to the preparation of electrolyte supported symmetric cells, which have allowed optimizing the development of the final system.

With the aim to improve the adherence between the components, it has been decided to use interlayers between the materials that make up the final system of this memory. The long-term tests, as well as the electrochemical response at 800 °C, have shown an adequate structural integrity of the systems.

These prototypes will bring the society closer to the commercialization of sustainable energy generation systems.

Índice

Index

LIST OF SYMBOLS AND ABBREVIATIONS

ac	Alternating Current
AEM	Anion Exchange Membrane
AFC	Alkaline Fuel Cell
ASR	Area Specific Resistance
CFCL	Ceramics Fuel Cells Limited
CS	Combustion Synthesis
Dc	Direct Current
DMFC	Direct Methanol Fuel Cell
EDX	Energy Dispersive Data
EIS	Electronic Impedance Spectroscopy
FCs	Fuel Cells
GDC	Ce_2O_3 Doped Gd_2O_3, $Sm_{0.2}Ce_{0.8}O_{1.9}$
HF	High Frequency
ICP-AES	Inductively Coupled Plasma Atomic Emission Spectroscopy
LD	Laser Dispersion
LF	Low Frequency
LNC	$LaNi_{0.6}Co_{0.4}O$
LNF	$LaNi_{0.6}Fe_{0.4}O_3$
LSCM	$La_{1-x}Sr_xGa_{1-y}Mg_yO_{3-\delta}$
LSF	$La_{1-x}Sr_xFeO_3$, $La_{0.6}Fe_{0.4}SrO_3$
LSFC	$La_{1-x}Sr_xFe_{1-y}Fe_yO_{3-\delta}$
LSM	$LaSrMnO_3$
MC	$MnCo_2O_4$
MCF	$MnCo_{1.9}Fe_{0.1}O_4$
MCFC	Molten Carbonate Fuel Cell
MIEC	Mixed Ionic and Electronic Conducting
OCV	Open Circuit Voltage
ORR	Oxygen Reduction Reaction
PAFC	Phosphoric Acid Fuel Cell
PEMFC	Polymer Membrane Fuel Cell
PDF	Powder Diffraction Files

SCS	Solution Combustion Synthesis
SDC	Ce_2O_3 Doped Sm_2O_3
SEM	Scanning Electron Microscope
SOFC	Solid Oxide Fuel Cell
TEC	Thermal Expansion Coefficient
TPB	Three Phase Boundary
XRD	X-Ray Diffraction
XRF	X-Ray Fluorescence
WPS	Wet Powder Spraying
YDC	Ce_2O_3 doped Y_2O_3
YSZ	Yttria Stabilized Zirconia

1. INTRODUCCIÓN

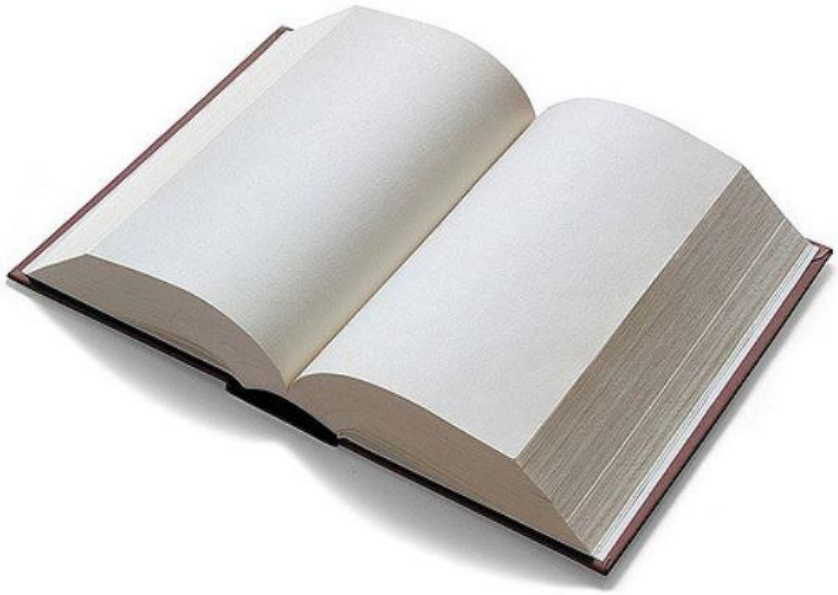

1. INTRODUCTION

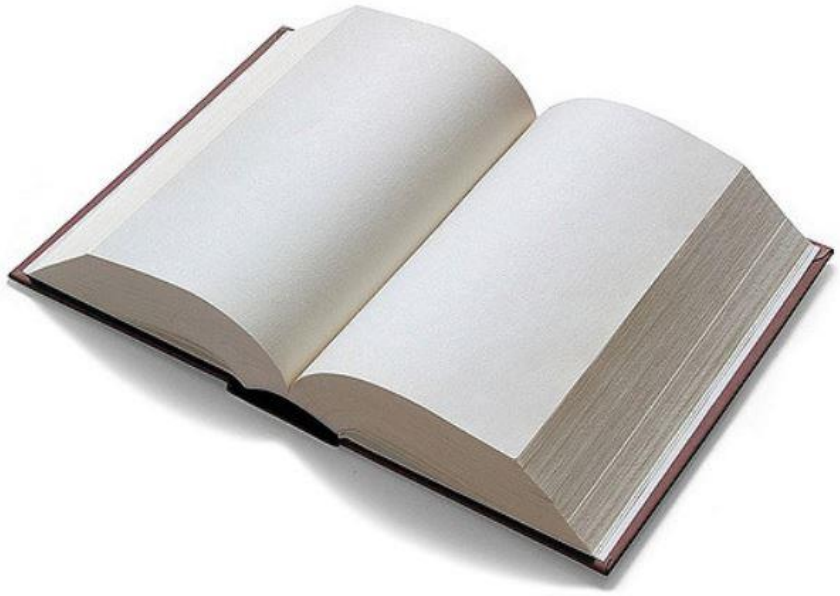

1.1. Contexto energético global

El aumento de nivel de vida, junto con el incremento de población a nivel mundial, hace que se prevea un gran incremento de demanda energética en el futuro. En la Figura 1.1. se muestra cómo el consumo de energía se ha incrementado en un 2.2 % en 10 años. Según la Unión Europea, por ejemplo, en Europa se estima que el uso de energía aumente en un 50% en 2050[1], si no se toman medidas en sostenibilidad energética, esperando un incremento poblacional de tan solo el 3.7%[2]. Por ello, existe una creciente preocupación sobre este tema, teniendo en cuenta que se estima que la población a nivel mundial se incrementará en un 53%, en especial en los continentes de África y Asia[3].

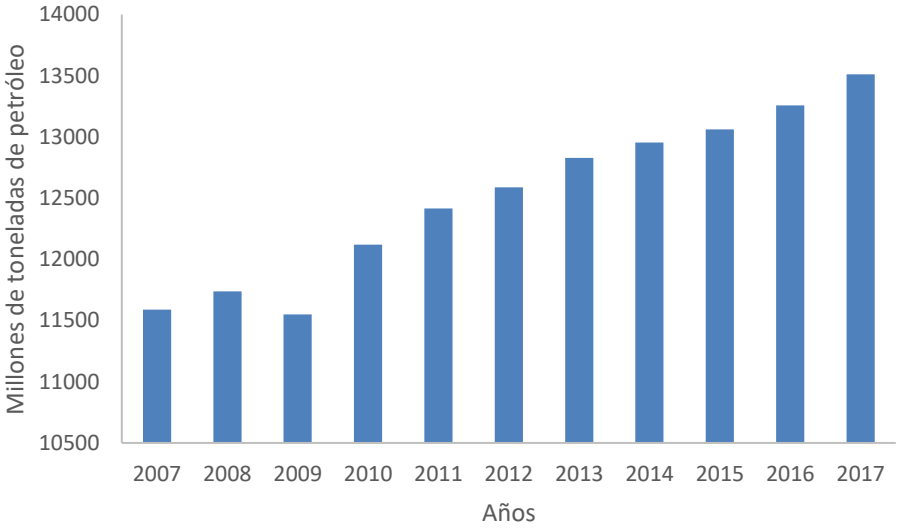

Figura 1.1.- Incremento del consumo de energía a nivel mundial entre los años 2007-2017.

Hoy día, el 80% del suministro mundial de energía proviene de combustibles fósiles, como pueden ser el petróleo, el gas natural y el carbón. Al ritmo de consumo actual, se prevé un agotamiento de las reservas de petróleo en menos de 100 años. Estudios realizados sobre las reservas planetarias de dicho combustible, señalan que es posible que nos encontremos en el "pico de petróleo", tal y como se muestra en la Figura 1.2. El "pico de petróleo" se refiere a un periodo en el que, agotadas el 50% de la dotación de petróleo del planeta, la producción de petróleo disminuye al aumentar sus costos. De esta manera, "el pico de petróleo" representa una edad de oro de energía barata que alimenta nuestro consumo[4]. A medida que se vaya agotando el petróleo, éste aumentará su coste sin sustitutos viables[5]. Las graves consecuencias que puede acarrear una crisis energética como la de 1970, hace que haya un gran interés por parte de las naciones en solucionar esta demanda.

---

1 Košir M., Iglič N., Kunič R., Optimisation of heating, cooling and lighting energy performance of modular buildings in respect to location's climatic specifics, *Renew. Energy.* 129 (**2018**) 527-539.

2 Eurostat (2017), People in the EU - population projections, Bruselas-Eurostat, **2017**.

3 European Environment Agency (2016), Population trends 1950 – 2100: globally and within Europe, **2016**.

4 Campbell, C. Aspo Newsletter n. 100. (**2009**).

5 Barreto R.A., Fossil fuels, alternative energy and economic growth, *Econ. Model*. 75 (**2018**) 196-220.

1.1. Global energy context

The increase of the standard of living, along with the increase of the population to worldwide level, means that a large increase in energy demand is expected in the future. Figure 1.1. shows how the energetic consumption has increased by 2.2% in 10 years. According to the European Union, for example, it is estimated that the use of energy will increase by 50% in 2050[1] in Europe, if no actions are taken regarding sustainable energy, expecting a population increase of only 3.7%[2]. Therefore, there is a growing concern according this issue, taking into account that it is estimated that the worldwide population will increase by a 53%, especially in Africa and Asia[3].

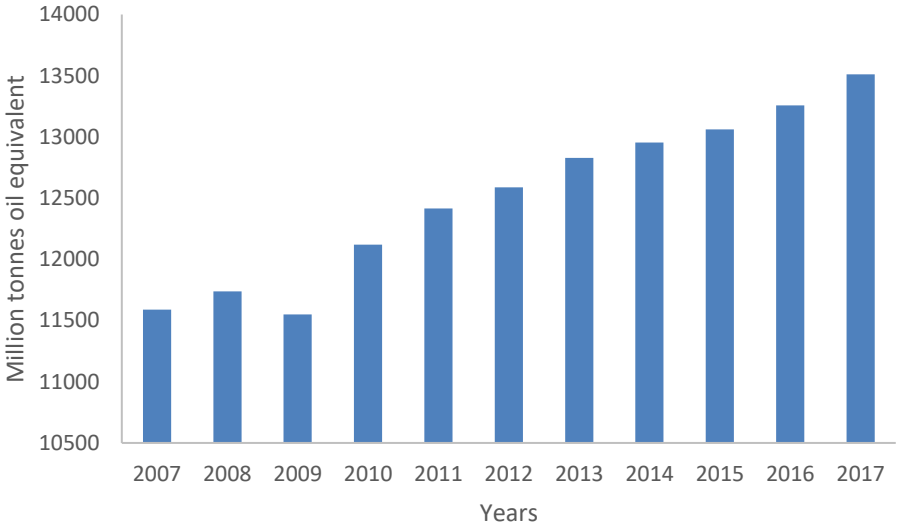

Figure 1.1.- Increase of worldwide energy consumption between 2007-2017.

Today, the 80% of the world energy supply comes from fossil fuels, such as oil, natural gas and coal. At the current consumption rate, a depletion of oil reserves is expected in than 100 years. Studies conducted on planetary oil reserves indicate that it is possible that we are in the "peak of oil". As shown in the Figure 1.2. the "peak of oil" refers to a period in which 50% of the planet´s oil production decreases as its cost increase. In this way, the "peak of oil" represents a golden age of cheap energy that feeds our consumption[4]. As the oil runs out, it will increase its cost without viable substitutes[5]. The serious consequences that can lead to an energy crisis like the one happened in 1970, means that there is a great interest by the nations in solving this demand.

---

1 Košir M., Iglič N., Kunič R., Optimisation of heating, cooling and lighting energy performance of modular buildings in respect to location's climatic specifics, *Renew. Energy.* 129 (**2018**) 527-539.

2 Eurostat (2017), People in the EU - population projections, Bruselas-Eurostat, **2017**.

3 European Environment Agency (2016), Population trends 1950 – 2100: globally and within Europe, **2016**.

4 Campbell, C. Aspo Newsletter n. 100. (**2009**).

5 Barreto R.A., Fossil fuels, alternative energy and economic growth, *Econ. Model*. 75 (**2018**) 196-220.

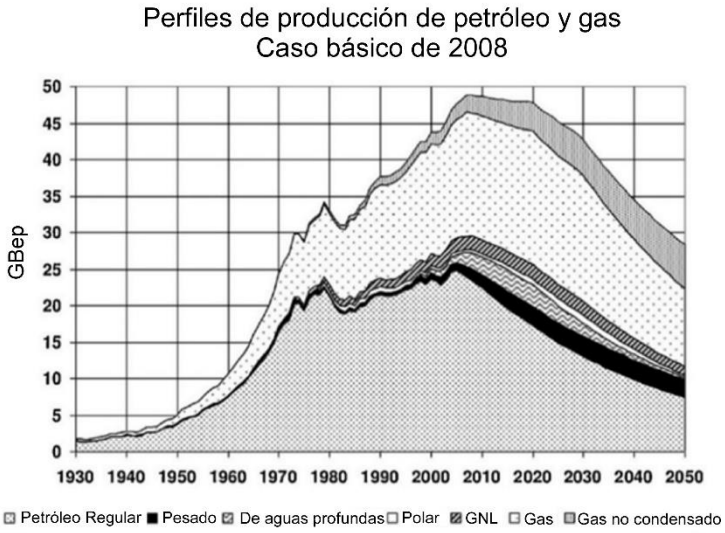

Figura 1.2.- Proyección de la producción de petróleo mostrando el denominado "pico del petróleo.

Para hacer frente a este problema, la energía primaria utilizada para satisfacer las demandas energéticas se seguirá basando, principalmente, en las energías fósiles, aunque se espera un aumento en las energías renovables. Entre las energías alternativas al petróleo, carbón y gas se incluyen: las plantas de energía hidroeléctrica[6], energía solar[7], eólica[8], biomasa[9], las pilas de combustible de hidrógeno[10], la energía de las mareas, la geotérmica y la hidrotermal.

Como ejemplo, tanto Japón como Alemania están reduciendo su demanda de energía nuclear apostando por energías renovables. Aún así, entre las energías fósiles que se espera seguir utilizando, están el gas natural y el carbón, así como la energía nuclear. Por lo tanto, la producción de energía se debe encauzar también a un mayor aprovechamiento de estos combustibles, con una mayor eficiencia y empleando alternativamente dispositivos que no emitan gases nocivos y que mejoren la eficiencia total. En la Figura 1.3. puede apreciarse la previsión, en consumo, de tipos de energía hasta el año 2040[11].

---

6 Apergis N., Chang T., Gupta R., Ziramba E., Hydroelectricity consumption and economic growth nexus: Evidence from a panel of ten largest hydroelectricity consumers, *Renew. Sust. Energ. Rev*. 62 (**2016**) 318-325.

7 Vanaga R., Blumberga A., Freimanis R., Mols T., Blumberga D., Solar facade module for nearly zero energy building, *Energy*. 157 (**2018**) 1025-1034.

8 Bandoc G., Prăvălie R., Patriche C., Degeratu M., Spatial assessment of wind power potential at global scale. A geographical approach, *J. Clean. Prod*. 200 (**2018**) 1065-1086.

9 Bajwa D.S., Peterson T., Sharma N., Shojaeiarani J., Bajwa S.G., A review of densified solid biomass for energy production, *Renew. Sust. Energ. Rev*. 96 (**2018**) 296-305.

10 Stambouli A.B., Fuel cells: The expectations for an environmental-friendly and sustainable source of energy, *Renew. Sust. Energ. Rev*. 15 (**2011**) 4507-4520.

11 BP Energy outlook 2018 edition, Energy economics, bp.com/energyoutlook, **2018**.

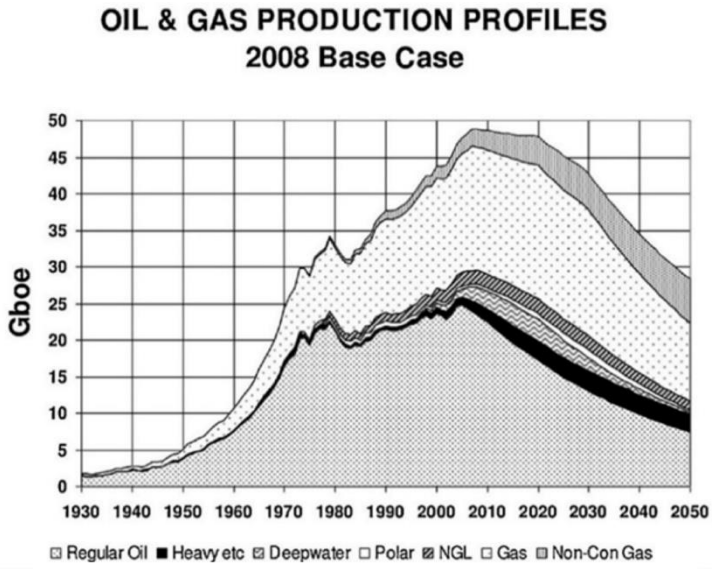

Figure 1.2.- Oil production projection showing the "peak of oil".

To deal with this problem, the primary energy used to meet energy demands will continue to be based, mainly, on fossil fuels, although an increase in renewable energies is expected. Among the alternative energies to oil, coal and gas, are included: hydroelectric power plants[6], solar energy[7], wind[8], biomass[9], hydrogen fuel cells[10], the energy of the tides, the geothermal and hydrothermal.

For example, Japan and Germany are reducing their demand for nuclear energy by investing in renewable energy. Even so, among the fossil energies that are expected to continue using, are natural gas and coal, as well as nuclear energy. Therefore, the production of energy should also be channelled to a greater use of these fuels, with greater efficiency and alternatively using devices that do not emit harmful gases and that improve the total efficiency. In Figure 1.3. the forecast for consumption of energy types can be appreciated up to the year 2040[11].

---

6 Apergis N., Chang T., Gupta R., Ziramba E., Hydroelectricity consumption and economic growth nexus: Evidence from a panel of ten largest hydroelectricity consumers, *Renew. Sust. Energ. Rev*. 62 (**2016**) 318-325.

7 Vanaga R., Blumberga A., Freimanis R., Mols T., Blumberga D., Solar facade module for nearly zero energy building, *Energy*. 157 (**2018**) 1025-1034.

8 Bandoc G., Prăvălie R., Patriche C., Degeratu M., Spatial assessment of wind power potential at global scale. A geographical approach, *J. Clean. Prod*. 200 (**2018**) 1065-1086.

9 Bajwa D.S., Peterson T., Sharma N., Shojaeiarani J., Bajwa S.G., A review of densified solid biomass for energy production, *Renew. Sust. Energ. Rev*. 96 (**2018**) 296-305.

10 Stambouli A.B., Fuel cells: The expectations for an environmental-friendly and sustainable source of energy, *Renew. Sust. Energ. Rev*. 15 (**2011**) 4507-4520.

11 BP Energy outlook 2018 edition, Energy economics, bp.com/energyoutlook, **2018**.

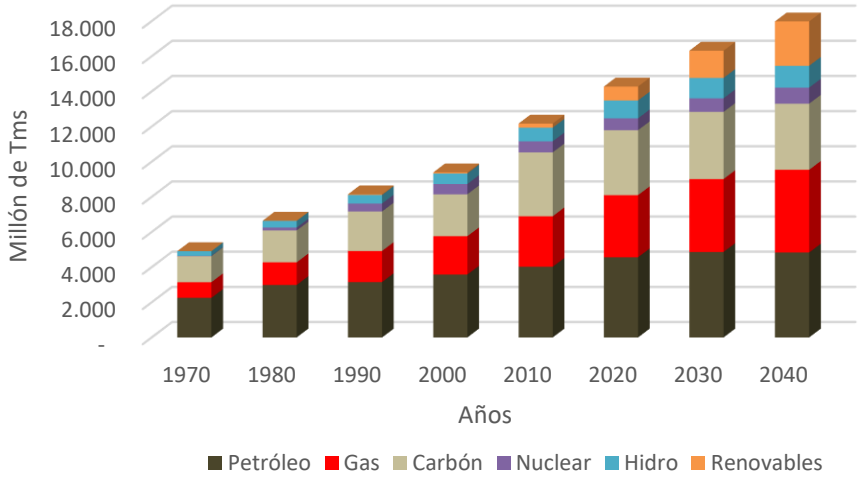

Figura 1.3.- Consumo de energía entre 1970 y prevision para 2040.

A este problema de demanda energética, se suma que, ligado a este incremento del uso de energía, también se prevé un incremento en la emisión de gases de efecto invernadero, siendo el sector energético el responsable del 80% de los gases invernadero[12]. Un gas de invernadero es un gas atmosférico que absorbe y emite radiación dentro del rango infrarrojo. Entre los gases que afectan al efecto invernadero, se encuentran: el vapor de agua, el dióxido de carbono, el metano, los óxidos de nitrógeno, el ozono y los clorofluorocarbonos. El aumento de la concentración de los gases invernadero, ha sido el causante del aumento de la temperatura mundial en el siglo XX y se espera que sean los causantes de un incremento de entre 1-2 °C al finalizar el siglo XXI.

Por otro lado, se espera que las muertes prematuras producidas por los gases de combustibles fósiles se incrementen un 40% para 2040. El aumento de las emisiones de dióxido de carbono (CO_2) es uno de los principales causantes del calentamiento global y el efecto invernadero. Su concentración va ligada al consumo de combustibles fósiles y ha ido creciendo históricamente hasta alcanzar su máximo en la actualidad. En la Figura 1.4. se muestran los datos reales del incremento de las emisiones de CO_2 a la atmosfera a nivel mundial[13]. Tal y como se puede apreciar, solo Europa ha conseguido reducir sus emisiones de CO_2, mientras que África y Asia han intensificado sus emisiones en un 119 y 199 % en los últimos 20 años, respectivamente[14].

---

[12] Borozan D., Decomposing the changes in European final energy consumption, *Energy Strateg. Rev*. 22 (**2018**) 26-36.

[13] http:// www.iea.org/ publications/freepublications/publication/co2-emmisions-from-fuel-combustion-highlights-2014.html. CO_2 emissions from fuel combustion, IEA, **2017**.

[14] Ihobe 2019, Perfil ambiental de Euskadi 2018, Cambio climático, Ed. Ihobe, Sociedad pública de gestión ambiental, Bilbao, **2018**.

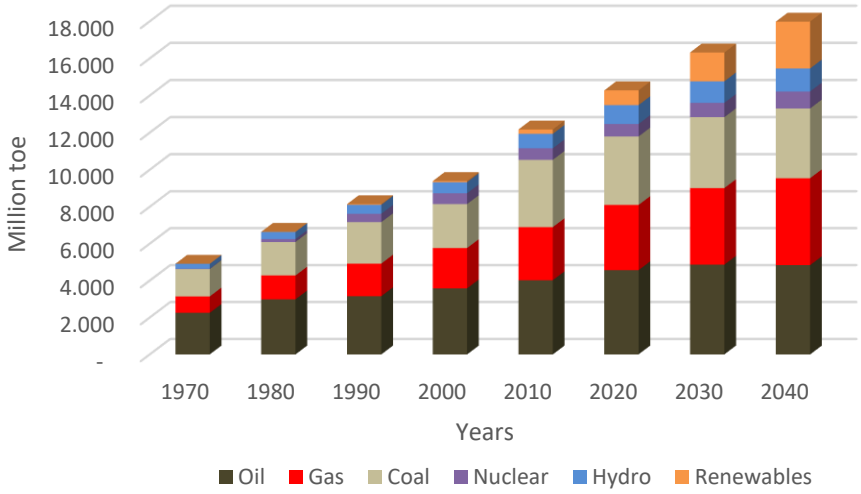

Figure 1.3.- Energy consumption between 1970 and forecast for 2040.

To this problem of energy demand, it is added that, linked to this increase in the use of energy, an increase in the emission of greenhouse gases is also foreseen, since energy consumption is nowadays responsible for the 80 % of greenhouse gases[12]. The greenhouse gas is an atmospheric gas that absorbs and emits radiation within the infrared range. Among the gases that affect the greenhouse effect are water vapour, carbon dioxide, methane, nitrogen oxides, ozone and chlorofluorocarbons. The increase in the concentration of greenhouse gases has been the cause of the increase in global temperature in the twentieth century and is expected to be the cause of an increase of between 1-2 °C at the end of the XXI century.

On the other hand, it is expected that premature deaths caused by fossil fuel gases will increase 40% by 2040. The increase in carbon dioxide (CO_2) emissions is one of the main causes of global warming and the greenhouse effect. Its concentration is linked to the consumption of fossil fuels and has been growing historically until reaching its maximum at present. Figure 1.4. Shows the real data of the increase of CO_2 emissions to the atmosphere worldwide[13]. As can be seen, only Europe has managed to reduce its CO_2 emissions, while Africa and Asia have augmented their emissions by 119 and 199% in the last 20 years, respectively[14].

---

[12] Borozan D., Decomposing the changes in European final energy consumption, *Energy Strateg. Rev*. 22 (**2018**) 26-36.

[13] http:// www.iea.org/ publications/freepublications/publication/co2-emmisions-from-fuel-combustion-highlights-2014.html. CO_2 emissions from fuel combustion, IEA, **2017**.

[14] Ihobe 2019, Perfil ambiental de Euskadi 2018, Cambio climático, Ed. Ihobe, Sociedad pública de gestión ambiental, Bilbao, **2018**.

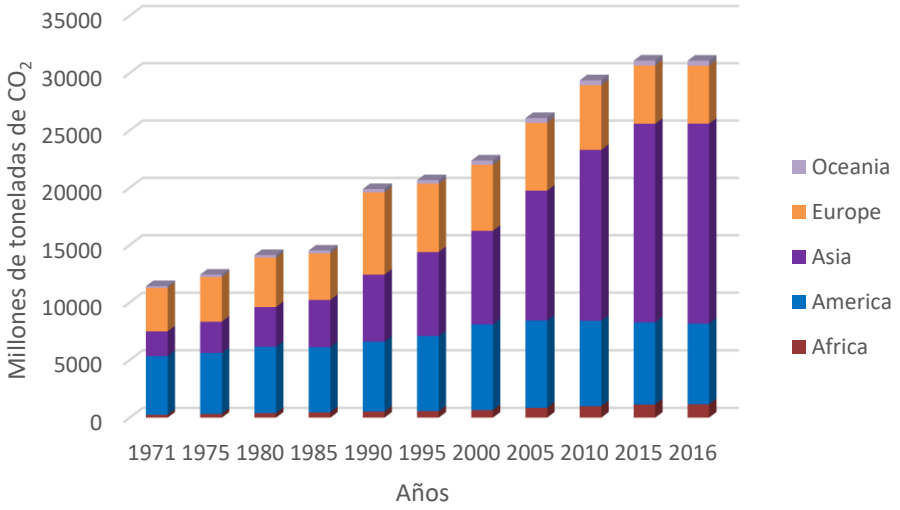

Figura 1.4.- Emisiones de CO_2 acumuladas entre 1971 y 2016.

En este contexto, se ve necesario un cambio de rumbo hacia modelos energéticos más sostenibles, en los cuales el papel de las energías renovables es fundamental. La comunidad europea, tiene como objetivo reducir emisiones de efecto invernadero respecto a 1990, para 2020 y 2030 en un 20% y un 40%, respectivamente, incrementando la proporción del consumo de energía de renovables como mínimo en un 27% y subiendo la eficiencia energética en un 27% para el 2030. Energías renovables como pueden ser la energía eólica y la fotovoltaica, tienen como inconveniente que son energías estacionarias, que han de estar posicionadas en zonas determinadas y dependen de factores climáticos para su efectividad.

Para tener un modelo energético más sostenible, las energías utilizadas tienen que tener como características, el ser energéticamente eficientes, tener la capacidad de minimizar las emisiones de gases contaminantes y tener el menor coste posible. Entre las energías limpias, la tecnología del hidrógeno tiene muchas probabilidades de convertirse en una de las principales alternativas a las energías fósiles utilizadas hoy en día. Dentro de esta tecnología adquieren relevancia las pilas de combustible, las cuales alcanzan notabilidad puesto que son capaces de transformar la energía química del hidrógeno en potencia eléctrica y calor.

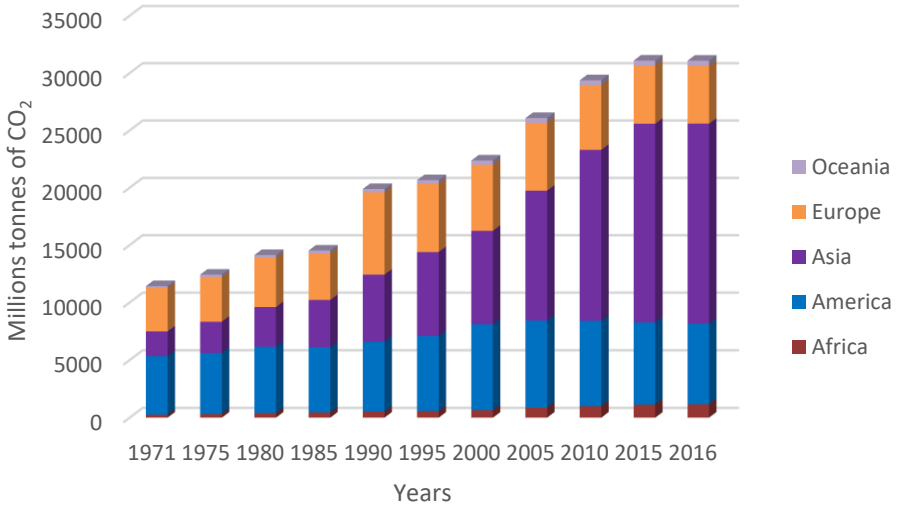

Figure 1.4.- CO_2 emissions accumulated between 1971 and 2016.

In this context, it is necessary a change of direction towards a more sustainable energy models, in which the role of renewable energies is fundamental. The European community, aims to reduce greenhouse gas emissions regarding 1990 by a 20% and a 40% for the 2020 and 2030, respectively, increasing the share of renewable energy consumption by at least 27% and increasing energy efficiency by 27% for the 2030. Renewable energies, such as wind and photovoltaic energy, have the disadvantage that they are stationary energies, which must be positioned in certain areas and depend on climatic factors for their effectiveness.

In order to have a more sustainable energy model, the energies used must have the characteristics of being efficient, have the capacity to minimize emissions of polluting gases and have the lowest possible cost. Among clean energies, hydrogen technology is very likely to become one of the main alternatives to fossil fuels used today. Within this technology, fuel cells become relevant, which acquire relevance since they are capable of transforming the chemical energy of hydrogen into electrical power and heat.

1.2. Tecnología del hidrógeno

El hidrógeno se utilizó comercialmente por primera vez a gran escala a finales del siglo XIX, con el desarrollo de los Zeppelin y los globos de barrera que protegían el Reino Unido durante la Primera y Segunda Guerra Mundial[15]. También se encontraron los primeros problemas causados por el hidrógeno en diferentes materiales, como pueden ser la fragilización del acero, la necesidad de sellos y arandelas especiales o la alta tasa de fuga de los recipientes de almacenamiento.

A principios del siglo XX el empleo del hidrógeno fue impulsado por la industria de los fertilizantes, cuando muchos generadores de energía hidroeléctrica estaban equipados con electrolizadores que producían hidrógeno[16]. También desde principios del siglo XX hasta la década de 1960, el gas de carbón alimentó las redes de suministro de gas urbano en Alemania Oriental y Suecia, utilizándose todavía en ciudades como Estocolmo[17]. Este gas de carbón consiste en hasta un 50% en volumen de hidrógeno, razón por la cual muchas redes de gas natural actuales admiten la adición o la conversión completa al hidrógeno por sus tuberías de acero, las cuales son adecuadas para el transporte de hidrógeno y metano[18].

Actualmente la tecnología del hidrógeno se presenta como una fuente de energía versátil, pudiéndose producir de una gran variedad de fuentes primarias de energía renovables y no renovables[19,20], consiguiendo de esta manera solventar los problemas geopolíticos que existen con las fuentes de energía fósil[21]. El hidrógeno es también uno de los candidatos más importantes para utilizarse como alimentación de energía en combinación con las pilas de combustible, para sus aplicaciones móviles y estacionarias. Igualmente, entre los varios tipos de almacenamiento de energía existentes, como pueden ser las baterías, la energía hidráulica bombeada, el aire comprimido, los volantes o los capacitadores, el hidrógeno se puede emplear como sistema de almacenamiento de energías renovables, produciendo hidrógeno de fuentes como la solar o la eólica y utilizándose, posteriormente, como combustible[22].

---

15 Petrangeli G., Barrage balloons against aircraft threat: A well proven concept revisited, *Nucl. Eng. Des*. 240 (**2010**) 886-890.

16 Fickett A.P., Kaihammer F.R., Water electrolysis, in: Cox K.E., Williamson K.D. (Eds.), Hydrogen - its technology and implications, *Hydrogen production technology*, 1 (**1977**) 3-41.

17 Peebles M.W.H., Evolution of the Gas Industry, *Macmillan*, London/Basingstoke, (**1980**).

18 Steinberger-Wilckens R., Sampson B., Market, Commercialization and deployment-toward appreciating total owner cost of hydrogen energy technologies, 8 (**2019**) 383-403.

19 Khetkorn W., Rastogi R.P., Incharoensakdi A., Lindblad P., Madamwar D., Pandey A., Larroche C., Microalgal hydrogen production – A review, *Bioresour. Technol*. 243 (**2017**) 1194-1206.

20 Serban M., Lewis M., Marshall C., Doctor R., Hydrogen production by direct contact pyrolysis of natural gas, *Energy Fuels*. 17 (**2003**) 705-713.

21 Alstone P., Gershenson D., Kammen D.M., Decentralized energy systems for clean electricity access, *Nat. Clim. Chang*. 5 (**2015**) 305-314.

22 Cabezas M.D., Franco J.I., Fasoli H.J., Optimization of self-regulated hydrogen production from photovoltaic energy, *Int. J. Hydrog. Energy*. (**2018**). https://doi.org/10.1016/j.ijhydene.2018.10.203.

1.2. Hydrogen technology

Hydrogen was commercially used for the first time on a large scale at the end of the 19th century, with the development of the Zeppelin and the barrier balloons that protected the United Kingdom during the First and Second World War[15]. The first problems caused by hydrogen in different materials were also found, such as the embrittlement of steel, the need for special seals and washers or the high leak rate of storage containers.

At the beginning of the 20th century, the use of hydrogen was driven by the fertilizer industry, when many hydroelectric power developments were equipped with hydrogen-producing electrolysers[16]. Also from the beginning of the 20th century until the 1960s, coal gas fed the urban gas supply networks in East Germany and Sweden, still being used today in cities such as Stockholm[17]. This coal gas consists of up to 50% by volume of hydrogen, which is why many today´s natural gas networks admit the addition or a complete conversion to hydrogen because their steel pipes, which are suitable for the transport of hydrogen and methane[18].

Currently, hydrogen technology is a versatile source of energy, since it can be produced from a large variety of primary sources of renewable and non-renewable energy[19,20], managing to solve the geopolitical problems that exist with fossil energy sources[21]. Hydrogen is also one of the most important candidates for it use as power supply in combination with fuel cells, for its mobile and stationary applications. Also, among the various types of existing energy storage, such as batteries, pumped hydraulic power, compressed air, flywheels or capacitors, hydrogen can be used as a renewable energy storage system, producing hydrogen from sources such as solar and wind power, to later be used as fuel[22].

---

[15] Petrangeli G., Barrage balloons against aircraft threat: A well proven concept revisited, *Nucl. Eng. Des*. 240 (**2010**) 886-890.

[16] Fickett A.P., Kaihammer F.R., Water electrolysis, in: Cox K.E., Williamson K.D. (Eds.), Hydrogen - its technology and implications, *Hydrogen production technology*, 1 (**1977**) 3-41.

[17] Peebles M.W.H., Evolution of the Gas Industry, *Macmillan*, London/Basingstoke, (**1980**).

[18] Steinberger-Wilckens R., Sampson B., Market, Commercialization and deployment-toward appreciating total owner cost of hydrogen energy technologies, 8 (**2019**) 383-403.

[19] Khetkorn W., Rastogi R.P., Incharoensakdi A., Lindblad P., Madamwar D., Pandey A., Larroche C., Microalgal hydrogen production – A review, *Bioresour. Technol*. 243 (**2017**) 1194-1206.

[20] Serban M., Lewis M., Marshall C., Doctor R., Hydrogen production by direct contact pyrolysis of natural gas, *Energy Fuels*. 17 (**2003**) 705-713.

[21] Alstone P., Gershenson D., Kammen D.M., Decentralized energy systems for clean electricity access, *Nat. Clim. Chang*. 5 (**2015**) 305-314.

[22] Cabezas M.D., Franco J.I., Fasoli H.J., Optimization of self-regulated hydrogen production from photovoltaic energy, *Int. J. Hydrog. Energy*. (**2018**). https://doi.org/10.1016/j.ijhydene.2018.10.203

Aunque se han realizado grandes avances tecnológicos, la implantación de la economía del hidrógeno no es inmediata, puesto que tiene que dar aún respuesta a importantes retos tecnológicos económicos y sociales. Entre estos retos está la producción de hidrógeno. Los métodos actuales, basados en los combustibles fósiles resultan costosos y los procesos basados en las energías renovables o la nuclear no se encuentran lo suficientemente desarrollados todavía[23], tal y como se puede apreciar en la Figura 1.5. Por otro lado, dar respuesta a una demanda global de hidrógeno conllevaría la necesidad de un sistema de distribución equivalente hoy en día al transporte de la gasolina[24]. El almacenamiento es otro de los retos a franquear, ya que, debido a su baja densidad energética, se requiere de grandes volúmenes de hidrógeno para alimentar procesos de alta demanda energética. Hoy en día, el uso de adsorbentes porosos[25], hidruros metálicos[26] o tanques de alta presión[27] son algunos de los métodos que se investigan para almacenar este compuesto en espacios reducidos. El hidrógeno es un compuesto altamente inflamable y potencialmente explosivo en contacto con el oxígeno de la atmósfera, siendo la seguridad otro reto a superar. Para ello, se deben adoptar normativas de seguridad específicas que no son tan diferentes a las que hoy en día se aplican a la gasolina, el butano o el gas natural. Por último, el precio actual de las pilas de combustible y su fiabilidad a lo largo del tiempo es otra barrera para su aplicación masiva. El elevado precio de fabricación o los problemas de envenenamiento son algunos de los problemas más frecuentes que se suelen encontrar para su implementación.

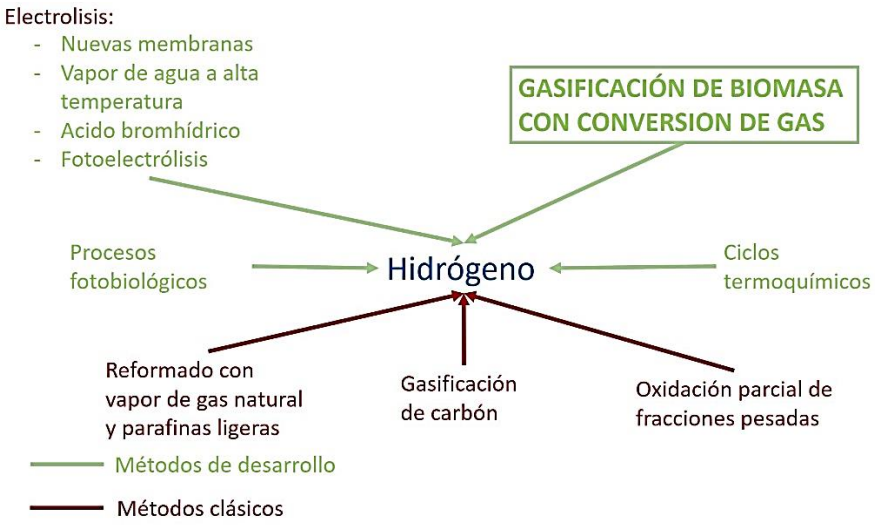

Figura 1.5.- Esquema de las diferentes alternativas para la producción de hidrógeno.

---

[23] Zeng K., Zhang D., Recent progress in alkaline water electrolysis for hydrogen production and applications, *Prog. Energy Combust. Sci*. 36 (**2010**) 307-326.

[24] Wulf C., Zapp P., Assessment of system variations for hydrogen transport by liquid organic hydrogen carriers, *Int. J. Hydrog. Energy*. 43 (**2018**) 11884-11895.

[25] Zhong M.M., Yuan H.K., Huang C., Wang G., Electronic properties of porous graphene and its hydrogen storage potentials, *J. Alloy. Compd*. 766 (**2018**) 104-111.

[26] Bhouri M., Linder M., Bürger I., Metal hydride reactor for dual use: Hydrogen storage and cold production, *Int. J. Hydrog. Energy*. 43 (**2018**) 23357-23371.

[27] Wang C., Huang S., Xu S., Optimization of girth welded joint in a high-pressure hydrogen storage tank based on residual stress considerations, *Int. J. Hydrog. Energy*. 43 (**2018**) 16154-16168.

Although great technological advances have been made, the implementation of the hydrogen economy is not immediate, since it has yet to respond to important economic and social technological challenges. Among these defies, are those of hydrogen production, taking into account that current methods are costly and based on fossil fuels and the processes based on renewable or nuclear energies are not sufficiently developed[23], as can be seen in the Figure 1.5. On the other hand, responding to a global demand for hydrogen would entail the need for a distribution system equivalent to today's gasoline transportation[24]. Storage is another challenge to overcome because, due to its low energy density, large volumes of hydrogen are required to feed high energy demand processes. Nowadays, the use of porous adsorbents[25], metal hydrides[26] or high pressure tanks[27] are some of the methods that are researched to store this compound in small spaces. Hydrogen is a highly flammable and a potentially explosive compound in contact with oxygen in the atmosphere, so another challenge to overcome is safety. To this end, specific safety regulations must be adopted that are not so different from those currently applied to gasoline, butane or natural gas. Finally, the current price of fuel cells and their reliability over time is another barrier to their massive application. The high manufacturing price or the poisoning problems are some of the most frequent problems that are usually found for their implementation.

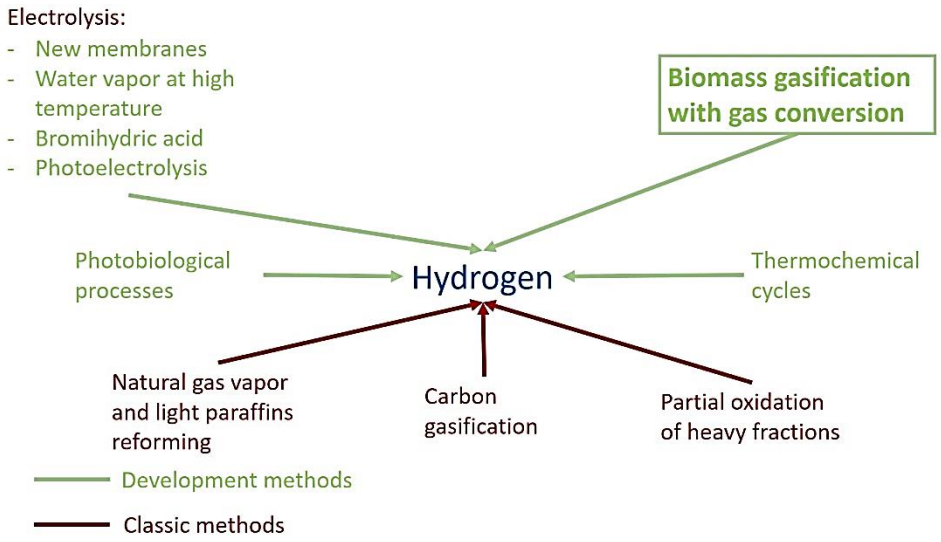

Figure 1.5.- Scheme of different alternatives for hydrogen production.

---

[23] Zeng K., Zhang D., Recent progress in alkaline water electrolysis for hydrogen production and applications, *Prog. Energy Combust. Sci*. 36 (**2010**) 307-326.

[24] Wulf C., Zapp P., Assessment of system variations for hydrogen transport by liquid organic hydrogen carriers, *Int. J. Hydrog. Energy*. 43 (**2018**) 11884-11895.

[25] Zhong M.M., Yuan H.K., Huang C., Wang G., Electronic properties of porous graphene and its hydrogen storage potentials, *J. Alloy. Compd*. 766 (**2018**) 104-111.

[26] Bhouri M., Linder M., Bürger I., Metal hydride reactor for dual use: Hydrogen storage and cold production, *Int. J. Hydrog. Energy*. 43 (**2018**) 23357-23371.

[27] Wang C., Huang S., Xu S., Optimization of girth welded joint in a high-pressure hydrogen storage tank based on residual stress considerations, *Int. J. Hydrog. Energy*. 43 (**2018**) 16154-16168.

1.3. Las Pilas de Combustible

1.3.1. Evolución histórica

El descubrimiento de las pilas de combustible se remonta a 1939, aunque hay bastante controversia sobre quién fue el descubridor del fundamento. Según el departamento de energía de los Estados Unidos, el alemán Cristian Schönbein (1799-1868) realizó los primeros estudios en relación con pilas de combustible, estableciendo los primeros fundamentos de la reacción de electrolisis inversa. En ese mismo año, Sir William Grove (1811-1896) construyó un prototipo de pila de combustible llamado batería de gas[28]. De cualquier modo, son una de las tecnologías de conversión de energía eléctrica más antiguas que existen. Ludwig Mond (1839-1909), con la asistencia de Charles Langer, fue el primero en mejorar la celda de Grove, con el fin de producir energía a partir de combustibles convertidos[29]. Aumentaron, significativamente, la densidad energética además de demostrar que no solo se podía utilizar hidrógeno puro para poner en funcionamiento la pila. Desafortunadamente, estas impurezas envenenaban el catalizador de platino haciendo que el coste de esta tecnología fuese demasiado alto. En 1896, William W. Jacques (1855-1932) desarrolló la primera pila de combustible con uso práctico y, cuatro años después, Walter Nerst (1864-1941) fue el primero en utilizar YSZ como electrolito, además de deducir la ley de termodinámica que rige el principio de funcionamiento de las celdas de combustible.

A principios del siglo XX, la conversión de energía química en energía eléctrica ganó importancia debido al crecimiento del uso de la electricidad. En 1921, Emil Baur (1873-1944) construyó la primera pila de combustible de carbonato fundido (MCFC). Años más tarde, en 1937 también desarrolló la primera pila de combustible de óxido sólido (SOFC)[30]. En 1959 el ingeniero ingles Francis Thomas Bacon (1904-1992), demostró una pila de combustible totalmente operativa. Su trabajo fue suficiente para que fuese adoptado por la NASA, que utilizó pilas de combustible poliméricas (PEMFC) y alcalinas (AFC) en los años 60 como parte de los programas espaciales Apolo y Gemini[31]. Éstas, se emplearon para producir electricidad y calor en las naves espaciales, a la vez que para crear el agua para beber y para la refrigeración de los equipos. En 1973, como consecuencia de la crisis petrolífera, volvió a crecer el interés del uso de estos dispositivos como fuente alternativa al petróleo. Aún así, hubo que esperar hasta la década de 1990 para que las empresas automovilísticas empezaran a desarrollar los primeros prototipos de vehículos comerciales alimentados por pilas de combustible. Hoy en día, las pilas de combustible tienen una amplia gama de aplicaciones, que se dividen en tres grupos principales: (i) transporte, (ii) estacionarias y (iii) portátiles. En la Tabla 1.1. se muestra un cronograma de la historia de las pilas de combustible.

---

[28] Mohammed H., Al-Othman A., Nancarrow P., Tawabeh M., El Haj Assad M., Direct hydrocarbon fuel cells: A promising technology for improving energy efficiency, *Energy*. 172 (**2019**) 207-219.

[29] Guaitolini S.V.M., Fardin F.F., Fuel cells: Hystory (short remind), principles of operation, main features and applications, Advances in Renewable energies and power technologies, *Biomass, fuel cells, geothermal energies, and smart grids*. 2 (**2018**) 123-150.

[30] Andújar J.M., Segura F., Fuel cells: History and updating. A walk along two centuries, *Renew. Sust. Energ. Rev*. 13 (**2009**) 2309-2322.

[31] Sharaf O.Z., Orhan M.F., An overview of fuel cell technology: Fundamentals and applications, *Renew. Sust. Energ. Rev*. 32 (**2014**) 810-853.

1.3. Fuel Cells

1.3.1. Historical evolution

The discovery of fuel cells dates back to 1939, although there is considerable controversy about who was the discoverer of the principle. According to the Department of Energy of the United States, the German Cristian Schönbein (1799-1868) made the first studies in relation to fuel cells, establishing the first foundations of the reverse electrolysis reaction. In the same year, Sir William Grove (1811-1896) built a prototype fuel cell called gas battery[29]. Either way, this devices are one of the oldest energy conversion technologies that exist. Ludwig Mond (1839-1909), with the assistance of Charles Langer, was the first to improve the Grove cell, in order to produce energy from converted fuels[30]. They significantly increased energy density, demonstrating that not only pure hydrogen could be used to power a battery. Unfortunately, these impurities poisoned the platinum catalyst making the cost of this technology too high. In 1896, William W. Jacques (1855-1932) develop the first fuel cell with practical use and four years later Walter Nerst (1864-1941) was the first to use YSZ as an electrolyte, in addition to deducting the law of thermodynamics that governs the operating principle of the fuel cells.

At the beginning of the 20th century, the conversion of chemical energy into electrical energy gained importance due to the growth of the use of electricity. In 1921, Emil Baur (1873-1944) built the first molten carbonate fuel cell (MCFC). Years later, in 1937 he also developed the first solid oxide fuel cell (SOFC)[31]. In 1959 the English engineer Francis Thomas Bacon (1904-1992), demonstrated a fully operational fuel cell. His work was enough to be adopted by NASA, which have use proton exchange membrane fuel cells (PEMFC) and alkaline fuel cells (AFC) in the 1960s as part of the Apollo and Gemini space programs[32], using them to produce electricity in spatial ships, to produce drinking water, cooling equipment's and to generate heat. In 1973, because of the oil crisis, interest in the use of these devices as an alternative source to oil grew again. Even so, it was not until the 1990s that the car companies began to develop the first prototypes of commercial vehicles powered by fuel cells. Today, fuel cells have a wide range of applications, which are divided into three main groups: (i) transport, (ii) stationary and (iii) portable. Table 1.1. shows a chronogram of the history of fuel cells.

---

[28] Mohammed H., Al-Othman A., Nancarrow P., Tawabeh M., El Haj Assad M., Direct hydrocarbon fuel cells: A promising technology for improving energy efficiency, *Energy*. 172 (**2019**) 207-219.

[29] Guaitolini S.V.M., Fardin F.F., Fuel cells: Hystory (short remind), principles of operation, main features and applications, Advances in Renewable energies and power technologies, *Biomass, fuel cells, geothermal energies, and smart grids*. 2 (**2018**) 123-150.

[30] Andújar J.M., Segura F., Fuel cells: History and updating. A walk along two centuries, *Renew. Sust. Energ. Rev*. 13 (**2009**) 2309-2322.

[31] Sharaf O.Z., Orhan M.F., An overview of fuel cell technology: Fundamentals and applications, *Renew. Sust. Energ. Rev*. 32 (**2014**) 810-853.

Tabla 1.1.- Principales sucesos históricos de las pilas de combustible[32].

Año(s)	*Suceso Histórico*
1800	Sir A. Carliste y W. Nicholson describen la electrólisis del agua.
1839	Sir W. Grove inventa la primera pila de combustible (batería de gas) y C. F. Schönbein descubre los primeros fundamentos.
1889	L. Mond y C. Langer desarrollan una matriz para contener el electrolito líquido e introducen catalizadores de platino negro en polvo.
1893	F. W. Ostwald describe el rendimiento teórico de una pila de combustible y determina, experimentalmente, la interconexión de varios componentes de la pila.
1896	W. W. Jacques construye la primera pila de combustible con aplicaciones prácticas.
1900	W. Nerst desarrolla electrolitos sólidos basados en zirconia.
1921	E. Baur construye la primera pila de combustible de carbonato fundido.
1930	E. Baur experimenta con electrolitos de óxido sólido a alta temperatura.
1933-1959	F. T. Bacon desarrolla la tecnología AFC.
1937-1939	E. Baur y H. Preis desarrollan la tecnología SOFC.
1955-1958	T. Grubb y L. Niedrach desarrollan la tecnología PEMFC en General Electric.
1958-1961	G.H.J. Broers y J.A.A. Ketelaar desarrollan la tecnología MCFC.
1960	La NASA utiliza la tecnología AFC de Bacon, en el programa Apolo.
1961	G.V. Elmore y H.A. Tanner desarrollan la tecnología PAFC.
1962-1966	Las PEMFC desarrolladas en General Electric se utilizan en el programa espacial Gemini.
1992	Jet Propulsion Laboratory desarrolla la tecnología DMFC.
1990s	Investigación a nivel mundial de las pilas de combustible enfocado en las PEMFCs.
2000s	Comercialización de las pilas de combustible.

[32] Perry M., Fuller T., A historical perspective of fuel cell technology in the 20th century, *J. Electrochem. Soc.* 149 (**2002**) S59-S67.

Table 1.1.- Main historical events of fuel cells[32].

Year(s)	*Historical events*
1800	Sir A. Carliste and W. Nicholson describe the electrolysis of water.
1839	Sir W. Grove invents the first fuel cell (gas battery) and C. F. Schönbein discovers the first foundations.
1889	L. Mond and C. Langer develop a matrix to contain the liquid electrolyte and introduce powdered black platinum catalysts.
1893	F. W. Ostwald describes the theoretical performance of a fuel cell and experimentally determines the interconnection of several components of the battery.
1896	W. W. Jacques builds the first fuel cell with practical applications.
1900	W. Nerst develops solid zirconia based electrolytes.
1921	E. Baur builds the first melting carbonate fuel cell.
1930	E. Baur experiment with solid oxide fuel cell at high temperatures.
1933-1959	F. T. Bacon develops the AFC technology.
1937-1939	E. Baur y H. Preis expand the SOFC technology.
1955-1958	T. Grubb y L. Niedrach develop PEMFC technology in General Electric.
1958-1961	G.H.J. Broers y J.A.A. Ketelaar expand MCFC technology.
1960	NASA use the Bacon´s AFC technology in Apolo program.
1961	G.V. Elmore y H.A. Tanner develop PAFC technology.
1962-1966	The PEMFC developed at General Electric are used in the Gemini space program.
1992	Jet Propulsion Laboratory develops DMFC technology.
1990s	Global research on fuel cells focused on PEMFCs.
2000s	Marketing on Fuel cells.

[32] Perry M., Fuller T., A historical perspective of fuel cell technology in the 20th century, *J. Electrochem. Soc.* 149 (**2002**) S59-S67.

1.3.2. Principios de operación de las pilas de combustible

En este contexto, la memoria presentada se centra en las pilas de combustible (FCs), las cuales son sistemas que, mediante un sistema electroquímico, convierten la energía química en electricidad y calor, mientras haya un suministro de combustible y agentes oxidantes, sin que medie ningún proceso de combustión. Los principios de operación y sus principales características se resumen en la Tabla 1.2.

Tabla1.2.- Principios de operación de las pilas de combustible y sus características.

Principios de operación	Características
Conversión de energía electroquímica en electricidad.	Alta eficiencia y alta densidad de energía.
Operan de manera continua siempre que haya un suministro de combustible y un agente oxidante.	Largos tiempos de operación.
Disposición de celdas formando “stacks”.	Carácter modular.
Funcionan mejor con hidrógeno.	Se reduce la emisión de gases de efecto invernadero.
Reformado interno de hidrocarburo.	Flexibilidad de combustible.

La estructura básica de una pila de combustible consiste en un electrodo positivo (un cátodo) y un electrodo negativo (un ánodo) conectados electrónicamente por un circuito externo, y separados mediante un material aislante electrónicamente que permite el flujo de iones a través de sí. Tal y como se muestra en la Figura 1.6. en el ánodo el combustible (el hidrógeno) se oxida generando protones (H^+) y electrones (e^-). Los protones migran a través del electrolito hacia el cátodo, mientras que los electrones hacen lo mismo a través del circuito externo, el cual es conductor electrónico. En el cátodo, electrones y protones reaccionan con el gas oxidante produciendo agua y una cantidad importante de energía térmica.

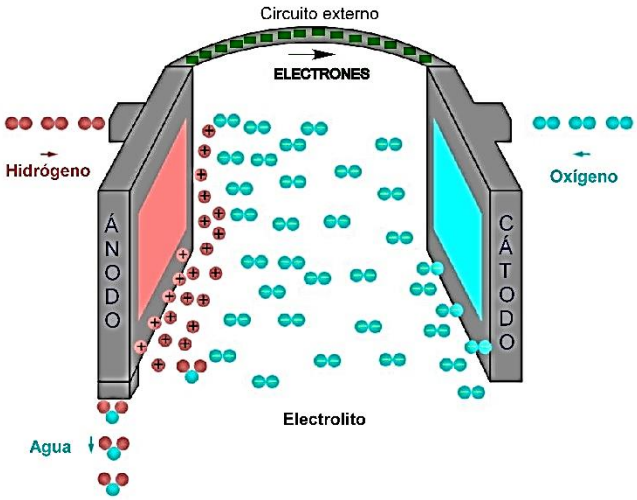

Figura 1.6.- Principio de funcionamiento de una celda de combustible.

1.3.2.- Operation principles of fuel cells

In this context, the presented report focuses on fuel cells (FCs), which are systems that, through an electrochemical system, convert chemical energy into electricity and heat as long as there is a supply of fuel and oxidizing agents, without a combustion process. The operating principles and their main characteristics are summarized in Table 1.2.

Table 1.2.- Operation principles of fuel cells and their characteristics.

Operation principles	Features
Conversion of electrochemical energy into electricity.	High efficiency and energy density.
Fuel cells operate continuously as long as there is a supply of fuel and an oxidizing agent.	Long operational cycles.
Arrangement of cells forming "stacks".	Modularity.
They work better with hydrogen.	Reduced greenhouse-gases.
Internal reforming of hydrocarbons.	Fuel flexibility.

The basic structure of a fuel cell consists of a positive electrode (a cathode) and a negative electrode (an anode) connected electronically by an external circuit, and separated by an electronically insulating material that allows the flow of ions through itself. As shown in Figure 1.6. at the anode the fuel (hydrogen) is oxidized generating protons (H^+) and electrons (e^-). The protons migrate through the electrolyte to the cathode, while the electrons do the same through the external circuit, which is an electronic conductor. At the cathode, electrons and protons react with the oxidizing gas to produce water and a significant amount of thermal energy.

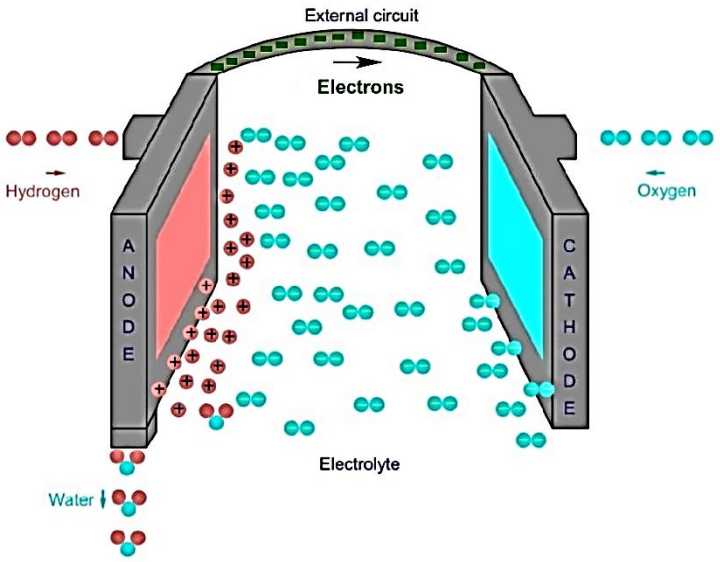

Figure 1.6.- Operating principle of a fuel cell.

La reacción electroquímica global de una celda de combustible, utilizando hidrógeno como combustible y oxígeno como oxidante, produce agua, calor (Q_{heat}) y trabajo eléctrico (W_{ele}), tal y como se describe en la ecuación 1.1:

$$2H_2 + O_2 \rightarrow 2H_2O + W_{ele} + Q_{heat} \qquad (1.1)$$

El trabajo eléctrico de la celda, también está definido como la energía de Gibbs. En una reacción redox, la energía liberada resulta en una diferencia de potencial. El trabajo es el producto de la carga y la diferencia de potencial, como se representa en la ecuación 1.2:

$$W = -\Delta G = q\Delta E = nF\Delta E \qquad (1.2)$$

q es la carga en coulombs, F es la constante de Faraday (96485 J/mol), n es el número de electrones transferidos cuando el combustible se oxida, y ΔE es la diferencia de potencial entre los terminales (el voltaje de la celda).

El potencial eléctrico ideal generado por una celda de combustible, viene dado por la ecuación de Nerst (ecuación 1.3):

$$E = E_0 - \frac{RT}{nF} \cdot ln \frac{P_{H_2O}}{\left(P_{H_2} \cdot P_{O_2}^{1/2}\right)} \qquad (1.3)$$

donde E_0 es el potencial redox estándar, R es la constante de gases (8.31 J/kmol), F es la constante de Faraday, n es el número de electrones involucrados, T la temperatura en K, y P es la presión parcial de cada uno de los gases que participan en la reacción (atm).

Esta expresión permite determinar, en el caso ideal, el máximo voltaje ($E\text{-}E_0$, también conocido como voltaje de circuito abierto, OCV) que puede esperarse cuando una pila de combustible está en funcionamiento. Este potencial, establece el limite o rendimiento máximo que se puede alcanzar con una celda de combustible, aunque en general, nunca se llega a obtener el máximo ideal debido a las diferentes variables que intervienen en el sistema. Se puede determinar la importancia de cada una de estas variables en una celda a partir de las curvas V-I, en las que se evalúa la caída de voltaje para diferentes densidades de corriente. Las caídas de tensión se clasifican en tres grupos:

- En primer lugar, las pérdidas provocadas por la polarización de activación se producen a causa de reacciones electroquímicas que son muy lentas, requiriendo de una energía de activación para que se produzcan. Incluyen la actividad catalítica y la resistencia a las reacciones electroquímicas.

- Por otro lado, están las pérdidas de polarización óhmicas, causadas por las resistencias eléctricas asociadas a los electrodos, el electrolito, los interconectores y las resistencias de contacto en las intercapas.

- Finalmente, se encuentran las pérdidas relacionadas con los procesos de transporte, producidas por las limitaciones en los procesos de adsorción y desorción de los reactivos y productos. Están relacionadas con la densidad de corriente, la actividad de los reactivos y la microestructura de los electrodos e incluyen los procesos de difusión o transporte de gas.

The overall electrochemical reaction of a fuel cell, using hydrogen as a fuel and oxygen as an oxidant, produces water, heat (Q_{heat}) and electrical work (W_{ele}), as described in equation 1.1:

$$2H_2 + O_2 \rightarrow 2H_2O + W_{ele} + Q_{heat} \qquad (1.1)$$

The electrical work of the cell is also defined as the Gibbs energy. In a redox reaction, the released energy results in a potential difference. The work is the product of the charge and the potential difference, as represented in equation 1.2:

$$W = -\Delta G = q\Delta E = nF\Delta E \qquad (1.2)$$

q is the charge in coulomb, F is the Faraday constant (96485 J/mol), n is the number of electrons transferred when the fuel is oxidized, and ΔE is the potential difference between the terminals (the cell voltage).

The ideal electric potential generated by a fuel cell is given by the Nerst equation (equation 1.3):

$$E = E_0 - \frac{RT}{nF} \cdot ln \frac{P_{H_2O}}{\left(P_{H_2} \cdot P_{O_2}^{1/2}\right)} \qquad (1.3)$$

where E_0 is the standard redox potential, R is the gas constant (8.31 J/kmol), F is the Faraday constant, n is the number of electrons involved, T the temperature in K, and P is the partial pressure of each one of the gases that participate in the reaction (atm).

This expression allows determining, in an ideal case, the maximum voltage ($E-E_0$, also known as open circuit voltage, OCV) that can be expected when a fuel cell is in operation. This potential establishes the limit or maximum yield that can be achieved with a fuel cell, although in general, the maximum ideal is never obtained due to different variables that mediate in the system. The importance of each of these variables in a cell can be determined from the V-I curves, in which the voltage drop for different current densities is evaluated. The voltage drops are classified into three groups:

- First of all, the losses caused by the activation polarization occur due to electrochemical reactions that are very slow, requiring an activation energy to happen. They include catalytic activity and resistance to electrochemical reactions.

- On the other hand, there are ohmic polarization losses, caused by electrical resistances associated with the electrodes, the electrolyte, the interconnectors and the contact resistances in the interlayers.

- Finally, there are the losses related to the transport processes, produced by the limitations in the adsorption and desorption processes of the reagents and products. They are related to the current density, the activity of the reagents and the microstructure of the electrodes and include gas diffusion or transport processes.

En la Figura 1.7. se muestra la relación voltaje-intensidad para una celda de combustible en funcionamiento a una temperatura determinada, detallándose las zonas en las que predominan los distintos tipos de pérdidas.

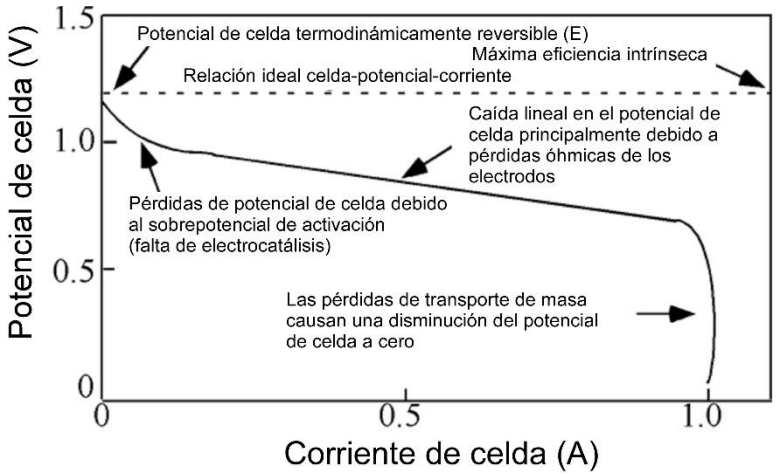

Figura 1.7.- Representación del voltaje de una celda de combustible con la variación de la densidad de corriente (Curva V-I).

1.3.3. Tipos de pilas de combustible

Existe una gran variedad de pilas de combustible, las cuales se suelen clasificar en base al tipo de electrolito que utilizan, se resumen en la Tabla 1.3. Los principales tipos son (i) pilas de combustible alcalinas (AFC), (ii) Pilas de combustible de membrana polimérica (PEMFC), (iii) pilas de combustible de metanol directo (DMFC), (iv) pilas de combustible de carbonato fundido (MCFC), (v) pilas de combustible de ácido fosfórico (PAFC) y (vi) pilas de combustible de óxido sólido (SOFC).

Las pilas de combustible alcalinas (AFC), son pilas que operan entre 100 y 260 ºC, aunque los últimos modelos ya trabajan por debajo de los 70 ºC. Las AFC, funcionan por difusión continua de iones hidroxilos negativos que migran del cátodo al ánodo generando agua. El potasio y el sodio hidróxido son los electrolitos más utilizados, los cuales según el diseño permanecen estáticos o circulan a través del sistema. El ánodo, comúnmente níquel poroso, se alimenta con hidrógeno, mientras que el cátodo, generalmente platino o una matriz de carbono, se alimenta con una atmosfera oxidante. Las AFC han demostrado tener eficiencias superiores al 60%, después de ciclos de 8000 horas, pero aún así su alto coste dificulta su comercialización[33].

[33] Mulder G., Fuel cells – Alkaline fuel cells | Overview, Reference module in chemistry, molecular sciences and chemical engineering, *Encyclopedia of electrochemical power sources*, Ed. Garche J., Dyer C.K., Moseley P.T., Ogumi Z. Rand, D.A.J., Scrosati B. (**2009**) 321-328.

In Figure 1.7. the voltage-intensity relationship for an operational fuel cell at a certain temperature is shown, detailing the areas in which the different types of losses predominate.

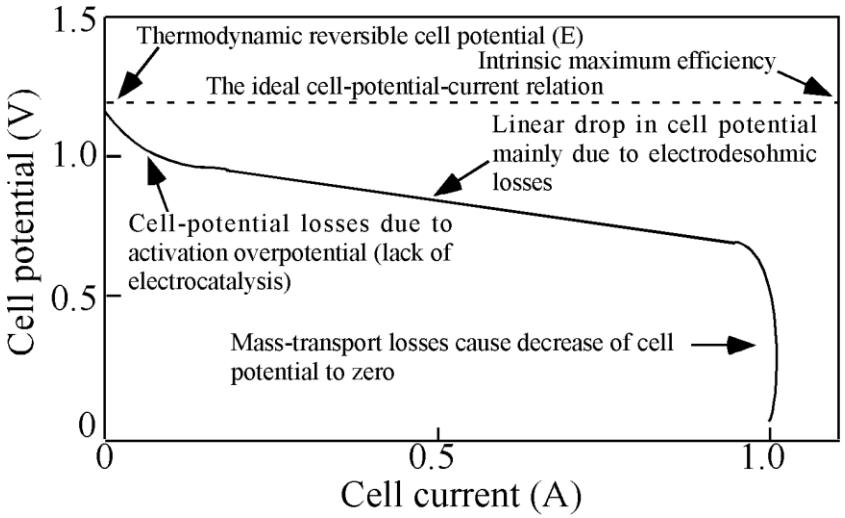

Figure 1.7.- Representation of a fuel cell voltage with the variation of the current density (V-I Curve).

1.3.3. Fuel cell types

There is a wide variety of fuel cells, which are usually classified based on the type of electrolyte they use, summarized in Table 1.3. The main types are (i) alkaline fuel cells (AFM), (ii) polymer membrane fuel cells (PEMFC), (iii) direct methanol fuel cells (DMFC), (iv) molten carbonate fuel cells (MCFC), (v) phosphoric acid fuel cells (PAFC) and (vi) solid oxide fuel cells (SOFC).

The alkaline fuel cells (AFC), are fuel cells that operate between 100 and 260 ºC, although the last models are already working below 70 ºC. The AFC, works by continuous diffusion of negative hydroxyl ions that migrate from the cathode to the anode generating water. Potassium and sodium hydroxide are the most used electrolytes, which according to the design remain static or circulate through the system. The anode, commonly porous nickel, is fed with hydrogen, while the cathode, usually platinum or a carbon matrix, is fed with an oxidizing atmosphere. The AFC have shown efficiencies higher than 60%, after cycles of 8000 hours, but its high cost makes it difficult to comercialize[3].

[33] Mulder G., Fuel cells – Alkaline fuel cells | Overview, Reference module in chemistry, molecular sciences and chemical engineering, *Encyclopedia of electrochemical power sources*, Ed. Garche J., Dyer C.K., Moseley P.T., Ogumi Z. Rand, D.A.J., Scrosati B. (**2009**) 321-328.

Las pilas de combustible de membrana polimérica (PEMFC), utilizan un electrolito de membrana polimérica basada en sulfonatos perfluorados, como el Nafion™, capaz de absorber el agua y favorecer la conducción de protones. Al ser un polímero, las temperaturas de funcionamiento están limitadas por debajo de los 100 ºC, siendo críticas para obtener una alta eficiencia[34]. Los dos electrodos, suelen estar formados por Pt soportado sobre carbón poroso/PTFE, para aumentar el área superficial y limitar el número de catalizadores requeridos, comúnmente Ru[35]. En estas pilas, el hidrógeno se oxida en el ánodo de Pt/Ru y el protón es conducido a través del polímero inmerso en agua que actúa como electrolito. Posteriormente, en el cátodo, los protones de hidrógeno se combinan con el oxígeno formando agua. Las PEMFC son capaces de trabajar a altas densidades de corriente, con una rápida respuesta a demandas de potencia variable. En cuanto a sus aplicaciones, las PEMFC son de las más comercializadas hoy en día, sobre todo en aplicaciones portátiles y de transporte, como puede ser la industria automovilística.

Las pilas de conversión directa de metanol (DMFC), son similares a las PEMFC, con la diferencia de que la membrana polimérica del electrolito tiene que aguantar los 120 ºC para poder utilizar el metanol como combustible. Los retos a superar en este tipo de pilas son el problema denominado "crossover" (paso del reactante anódico al compartimento catódico a través de la membrana) y encontrar un catalizador anódico más activo para la oxidación directa del metanol[36,37]. Siendo viable el transporte de metanol y al trabajar entre 30 y 120ºC, las DMFC representan una opción viable para aplicaciones móviles y portátiles más pequeñas, como podrían ser ordenadores o móviles.

Las pilas de combustible de ácido fosfórico (PAFC) fueron las primeras en comercializarse y se puede decir que son las pilas tecnológicamente más maduras. En este caso el electrolito es el ácido fosfórico contenido en los capilares de una matriz de SiC y las temperaturas de funcionamiento oscilan entre los 150 y los 200 ºC. A bajas temperaturas, el ácido fosfórico es un mal conductor iónico, por lo que el platino que actúa como electrodo, se contamina de carbono monóxido, bajando el rendimiento. Funcionar a temperaturas de 200 ºC, ayuda a reducir al mínimo los problemas a causa del CO en los catalizadores. Entre sus desventajas están su baja eficiencia en torno al 40% y su alto coste económico por el uso de los electrodos de platino[38].

---

[34] Ren H., Chae J., Fuel cells technologies for wireless MEMS, Wireless MEMS networks and applications, *Woodhead Publishing series in electronic and optical materials*, 2 (**2017**) 35-51.

[35] Baroutaji A., Carton J.G., Sajjia M., Olabi A.G., Materials in PEM Fuel Cells, *Reference module in chemistry, molecular sciences and chemical engineering*, Ed. Elsevier, p 1-11, **2016**.

[36] Lee H., Yu J., Kim J., Kim K., Rhee Y., Effects of catalyst loading and oxidant on the performance of direct formic acid fuel cells, *Stud. Surf. Sci. catal.* 159 (**2006**) 589-592.

[37] Chou H., Hwang B., Sun C., Catalysis in fuel cells and hydrogen production, *New and future development in catalysis, Batteries, Hydrogen storage and fuel cells*, 9 (**2013**) 217-270.

[38] Salameh Z., Energy storage, *Renewable energy system design*, 4 (**2014**) 201-298.

The proton exchange membrane fuel cells (PEMFC), use a polymer membrane electrolyte based on perfluorinated sulfonates, such as Nafion^{TM}, capable of absorbing water and promoting the conduction of protons. Being a polymer, operating temperatures are limited below 100° C, being critical to obtain high efficiency[34]. A Pt supported on porous carbon/PTFE usually forms both electrodes, to increase the surface area and limit the number of catalysts required, commonly Ru[35]. In these cells, hydrogen is oxidized at the Pt/Ru anode and the proton is driven through the polymer immersed in water, which acts as an electrolyte. Then, at the cathode, hydrogen protons combine with oxygen to form water. The PEMFCs are capable of working at high current densities, with a rapid response to variable power demands. In terms of their applications, PEMFCs are among the most marketed today, especially in portable and transport applications, such as the automotive industry.

Direct methanol conversion fuel cells (DMFC) are similar to PEMFC, with the difference that the polymer membrane of the electrolyte has to withstand 120 ºC to be able to use methanol as fuel. The challenges to overcome of this type of fuel cells are the problem called "crossover" (passage of the anodic reactant to the cathodic compartment through the membrane) and finding an active anodic catalyst for the direct oxidation of methanol[36,37]. Being the methanol transportation viable and their working temperature between 30 and 120 ºC, DMFCs represent a viable option for smaller mobile and portable applications, such as computers or mobile phones.

The phosphoric acid fuel cells (PAFC) were the first to be commercialized and it can be said that they are the technologically more mature fuel cells. In this case, the electrolyte is phosphoric acid contained in the capillaries of a SiC matrix and the operating temperatures range between 150 and 200 °C. At low temperatures, phosphoric acid is a bad ion conductor, so the platinum which acts as an electrode, is contaminated with carbon monoxide, lowering the yield. Operate at temperatures of 200 °C, helps to minimize the problems caused by the CO in the catalysts. Among its disadvantages are its low efficiency around 40% and its high economic cost due to the use of platinum electrodes[38].

---

[34] Ren H., Chae J., Fuel cells technologies for wireless MEMS, Wireless MEMS networks and applications, *Woodhead Publishing series in electronic and optical materials*, 2 (**2017**) 35-51.

[35] Baroutaji A., Carton J.G., Sajjia M., Olabi A.G., Materials in PEM Fuel Cells, *Reference module in chemistry, molecular sciences and chemical engineering*, Ed. Elsevier, p 1-11, **2016**.

[36] Lee H., Yu J., Kim J., Kim K., Rhee Y., Effects of catalyst loading and oxidant on the performance of direct formic acid fuel cells, *Stud. Surf. Sci. catal.* 159 (**2006**) 589-592.

[37] Chou H., Hwang B., Sun C., Catalysis in fuel cells and hydrogen production, *New and future development in catalysis, Batteries, Hydrogen storage and fuel cells*, 9 (**2013**) 217-270.

[38] Salameh Z., Energy storage, *Renewable energy system design*, 4 (**2014**) 201-298.

Entre las pilas que operan a alta temperatura se encuentran las **pilas de combustible de carbonato fundido (MCFC)**, que utilizan como electrolito una sal de carbonatos alcalinos (Li, Na, K) fundida, retenida en una matriz cerámica porosa (normalmente aluminato de litio, $LiAlO_2$) y operan a temperaturas superiores a 650 ºC. En el ánodo de NiO, se reducen el carbono dióxido y el oxígeno, produciendo iones de carbonato, que migran a través del electrolito fundido, para combinarse con el hidrógeno que se oxida con los metales de Ni. Estos electrodos admiten altas concentraciones de CO y CO_2, permitiendo el uso de combustibles como el gas natural o el biogás. Estas pilas se emplean para aplicaciones estacionarias, por ejemplo, en plantas de energía, teniendo una eficiencia de más del 50%, pudiendo aumentarla aprovechando su calor residual[39].

Las principales características de cada tipo de pila de combustible se resumen en la Tabla 1.3[40]. Las **pilas de combustible de óxido sólido (SOFC)** también operan a altas temperaturas y serán descritas en detalle en el siguiente apartado 1.4.

Tabla 1.3.- Características generales de los distintos tipos de pilas de combustible, clasificadas en función del electrolito.

TIPO DE CELDA	PEMFC	AFC	PAFC
Electrolito	Ácido sulfónico incorporado en una membrana polimérica.	• Disolución acuosa de KOH. • Membrana de intercambio iónico (AEM).	H_3PO_4 líquido en SiC.
Ánodo/ cátodo/ interconector	Pt-carbón. Pt-carbón. Grafito.	Níquel. Ag-carbón. Hilos metálicos.	Pt-carbón. Pt-carbón. Grafito.
Portador de carga	H^+	OH^-	H^+
Temperatura de operación (ºC)	60-80	>0 - 230	160-220
Ventajas	• Estructura compacta. • Arranque rápido. • Baja corrosión.	• Cinética de reducción rápida. • Flexibilidad de catalizador. • Amplio intervalo de temperaturas de operación.	• Buena tolerancia a contaminantes. • Cogeneración de alta eficiencia. • Gestión del agua simple.
Retos	• Catalizadores caros. • Alta sensibilidad a contaminantes.	• Alta sensibilidad a contaminantes. • Baja densidad de energía. • Electrolito altamente corrosivo.	• Arranque lento. • Baja corriente y potencia. • Electrolito corrosivo. • Sistema voluminoso.
Rendimiento eléctrico (%)	40-60	60-70	36-45

[39] Dicks A.L., Fuel cells – Molten carbonate fuel cells | Overview, Reference module in chemistry, molecular sciences and chemical engineering, *Encyclopedia of electrochemical power sources*, (**2009**) 446-453.

[40] Mekhilef S., Saidur R., Safari A., Comparative study of different fuel cell technologies, *Renew. Sust. Energy Rev*. 16 (**2012**) 981-989.

Among the fuel cells that operate at high temperatures are the **molten carbonate fuel cells (MCFC)**, which use a salt of molten alkali carbonates (Li, Na, K) as electrolyte, which is retained in a porous ceramic matrix (usually lithium aluminate, $LiAlO_2$) and operate at temperatures above 650 ºC. At the NiO anode, the carbon dioxide and oxygen are reduced by producing carbonate ions, which migrate through the molten electrolyte, to combine with the hydrogen that is oxidized with the Ni metal. These electrodes admit high concentrations of CO and CO_2, allowing the use of fuels such as natural gas or biogas. These fuel cells are used for stationary applications, for example, in power plants, having an efficiency of more than 50%, being able to increase it taking advantage of its residual heat.

The main features of each type of fuel cell are summarized in the Table 1.3[40]. **Solid oxide fuel cells (SOFC)** that operate at high temperatures, will be further described in detail in the following section 1.4.

Table 1.3.- Main characteristic of different fuel cell types according to the electrolyte.

Fuel cell type	PEMFC	AFC	PAFC
Electrolyte	Sulphonic acid incorporated into a solid membrane.	• KOH water solution. • Anion exchange membrane (AEM).	Liquid H_3PO_4 in SiC.
Anode/ cathode/ interconnect	Pt-carbon. Pt-carbon. Graphite.	Nickel. Ag-carbon. Metallic wires.	Pt-carbon. Pt-carbon. Graphite.
Charge carrier	H^+	OH^-	H^+
Operation temperature (ºC)	60-80	Below zero-230	160-220
Advantages	• Compact structure. • Rapid start-up. • Low corrosion.	• Fast reduction reaction kinetics. • Catalyst flexibility. • Wide range of operation temperature.	• Good tolerance to contaminants. • High-grade heat. • Simple water management.
Challenges	• Expensive catalyst. • High sensitivity to contaminants.	• High sensitivity to contaminants. • Low power density. • Highly corrosive electrolyte leads to sealing issues.	• Slow start-up. • Low power density and electrical efficiencies. • Electrolyte acid loss.
Electrical efficiency (%)	55-65	36-60	65-85

[39] Dicks A.L., Fuel cells – Molten carbonate fuel cells | Overview, Reference module in chemistry, molecular sciences and chemical engineering, *Encyclopedia of electrochemical power sources*, (**2009**) 446-453.

[40] Mekhilef S., Saidur R., Safari A., Comparative study of different fuel cell technologies, *Renew. Sust. Energy Rev*. 16 (**2012**) 981-989.

Tabla 1.3. cont.- Características generales de los distintos tipos de pilas de combustible, clasificadas en función del electrolito.

Tipo de celda	MCFC	DMFC	SOFC
Electrolito	Li_2CO_3, Na_2CO_3, K_2CO_3 líquido en $LiAlO_2$.	Ácido sulfónico incorporado en una membrana polimérica.	Zirconia estabilizada con itria (YSZ).
Ánodo/ cátodo/ interconector	NiCr. Óxido de níquel litiado. Acero inoxidable.	Pt/Ru-carbón. Pt-carbón. Grafito.	Ni-YSZ. LSM. Cerámico/metálico.
Portador de carga	CO_3^{2-}	H^+	O^{2-}
Temperatura de operación (ºC)	600-700	25-110	500-1000
Ventajas	• Flexibilidad de combustibles. • Posibilidad de reformado interno. • Alta tolerancia a contaminantes. • Cogeneración de alta eficiencia.	• Tamaño compacto. • Sistema simple. • Fácil almacenamiento y transporte de combustible.	• Alto rendimiento eléctrico. • Cogeneración de alta eficiencia. • Eliminación de problemas con el electrolito. • Flexibilidad de combustibles.
Retos	• Arranque lento. • Corrosión del electrolito y partes metálicas. • Requiere entrada de CO_2. • Cruce del aire.	• Cinética del ánodo lenta. • Falta de catalizadores para la oxidación directa de CH_3OH. • Cruce del agua y combustible.	• Arranque lento. • Requisitos estrictos para los materiales. • Alto estrés térmico. • Problemas de durabilidad.
Rendimiento eléctrico (%)	55-65	36-60	65-85

Table 1.3.cont.- Main characteristic of different fuel cell types according to electrolyte.

Fuel cell type	MCFC	DMFC	SOFC
Electrolyte	Liquid Li_2CO_3,Na_2CO_3, K_2CO_3 in $LiAlO_2$.	Sulphonic acid incorporated into a solid membrane.	Solid yttria-stabilized zirconia (YSZ).
Anode/ cathode/ interconnect	NiCr. Lithiated NiO. Stainless steel.	Pt/Ru-carbon. Pt-carbon. Graphite.	Ni-YSZ. LSM. Ceramic/metallic.
Charge carrier	CO_3^{2-}	H^+	O^{2-}
Operation temperature (ºC)	600-700	Ambient-110	500-1000
Advantages	• Fuel flexibility. • Possibility of internal reforming. • High tolerance to contaminants. • High-grade heat.	• Compact size. • Simple system. • Easy fuel storage and delivery.	• High electrical efficiencies. • High-grade heat. • Eliminated electrolyte issues. • Fuel flexibility.
Challenges	• Slow start-up. • Electrolyte and metallic parts corrosion. • CO_2 injection requirement. • Air crossover.	• Poor anode kinetics. • Lack of efficient catalysts for direct oxidation of methanol. • Fuel and water crossover.	• Slow start-up. • Strict material requirements. • High thermal stresses. • Sealing and durability issues.
Electrical efficiency (%)	55-65	36-60	65-85

1.4. Pilas de combustible de óxido sólido (SOFC)

El trabajo mostrado en la presente memoria, se centra en las pilas de combustible de óxido sólido (SOFCs). Estas pilas se caracterizan por las altas temperaturas a las que funcionan (600-1000 ºC) y el electrolito sólido que utilizan. Las altas temperaturas a la que trabajan permiten el uso de materiales cerámicos como conductores de iones óxido, además de disminuir las limitaciones cinéticas del cátodo. Cuanto mayor es la temperatura, mayor es la conductividad iónica del electrolito. Las SOFC funcionan con una amplia gama de combustibles y producen una gran cantidad de calor que se puede aprovechar en procesos de cogeneración, alcanzando rendimientos de hasta el 80%.

El esquema básico de su funcionamiento se muestra en la Figura 1.8a. La celda se compone de un electrolito sólido denso situado entre dos electrodos cerámicos porosos. En el cátodo, el oxígeno se reduce a iones óxido que son transportados a través del electrolito hasta el ánodo, donde reaccionan con hidrógeno del combustible, proporcionando electrones al circuito externo. Estos electrones, a su vez, reaccionan con el oxígeno del cátodo volviendo a crear iones óxido. El proceso total se muestra en la Figura 1.8b. Además del hidrógeno, el monóxido de carbono y el metano también pueden ser utilizados como combustible, siendo el producto correspondiente el carbono dióxido.

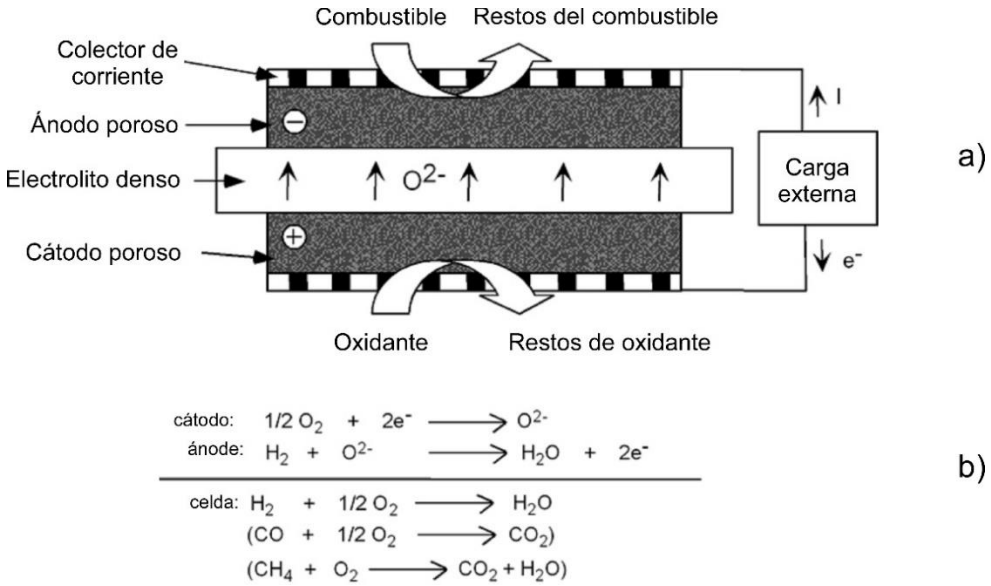

Figura 1.8.- (a) Esquema de una celda de combustible de óxido sólido individual. (b) Proceso químico producido en una celda.

Las altas temperaturas de operación, producen inconvenientes como pueden ser: diferencias en los coeficientes de expansión térmica (TEC) entre los componentes, dificultad en el sellado entre las celdas en el caso de las configuraciones planares y las restricciones en la elección de materiales, lo cual puede dar lugar a complicaciones en los procesos de fabricación, arranques lentos y una aceleración de la degradación.

A causa de sus altas temperaturas de operación, la mayoría de las aplicaciones de las SOFC son estacionarias, aunque también se pueden encontrar aplicaciones portátiles y en el transporte. Aun así, para solventar los problemas de coste y degradación de las pilas SOFC, se realizan importantes esfuerzos en reducir la temperatura de operación a 500-750 ºC, desarrollando materiales más activos a esas temperaturas y mediante el uso de configuraciones que permitan utilizar materiales y procesos de producción de bajo coste.

1.4. Solid oxide fuel cells (SOFC)

This work is focused on solid oxide fuel cells (SOFCs). The high temperatures at which they work (600-1000 ºC) and the solid electrolyte they use characterize these fuel cells. The high temperatures at which they work allow the use of ceramic materials as conductors of oxide ions, in addition to reducing the kinetic limitations of the cathode. The higher the temperature, the greater the ionic conductivity of the electrolyte. SOFCs works with a wide range of fuels and produce a large amount of heat that can be used in cogeneration processes, reaching yields of up to 80%.

The basic scheme of its operation is shown in Figure 1.8a. The cell is composed of a dense solid electrolyte located between two porous ceramic electrodes. At the cathode, the oxygen is reduced to oxide ions that are transported through the electrolyte to the anode, where they react with hydrogen from the fuel, providing electrons to the external circuit. These electrons, in turn, react with the oxygen from the cathode by re-creating oxide ions. The total process is shown in Figure 1.8b. In addition to hydrogen, carbon monoxide and methane can also be used as fuel, being the corresponding product carbon dioxide.

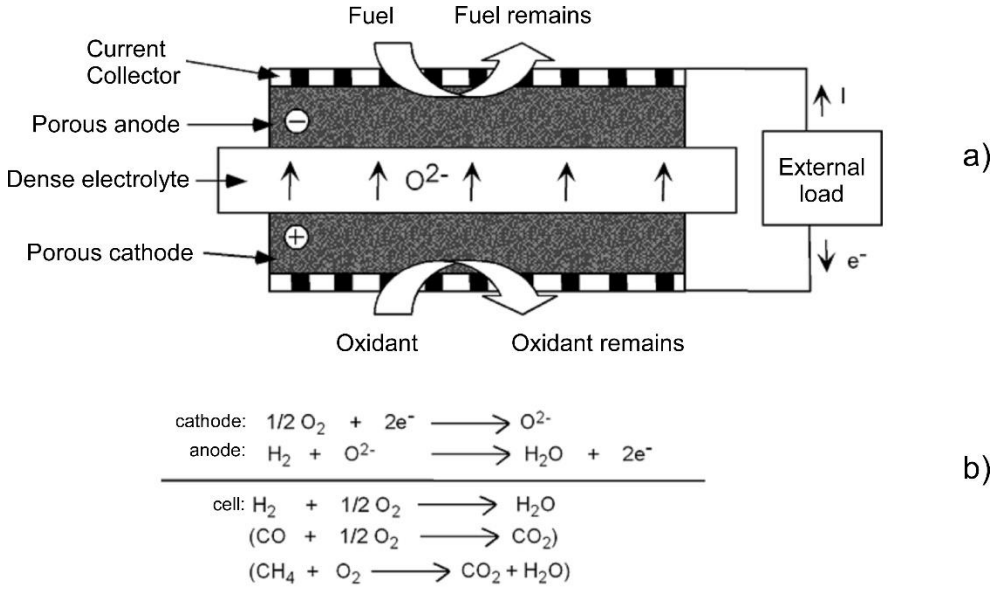

Figure 1.8.- (a) Scheme of an individual solid oxide fuel cell. (b) Chemical process produced in a cell.

The operational high temperatures produce disadvantages such as differences in the thermal expansion coefficients (TEC) between the components, difficulty in the sealing between the cells in the case of planar configurations and restrictions in the choice of materials, which can lead to complications in the manufacturing processes, slow starts and an acceleration of the degradation.

Because of its high operating temperatures, most SOFC applications are stationary, although portable and transport applications can also be found. Even so, to solve the cost and degradation problems of SOFCs, important efforts are made to reduce the operating temperature to 500-750 ºC, developing more active materials at these temperatures and by using configurations that allow the use of materials and low cost production processes.

1.5. Componentes SOFC

Aunque el concepto de operación de las pilas SOFC es bastante simple, la selección de materiales para los componentes individuales representa enormes desafíos. Cada material debe tener las propiedades eléctricas para hacer funcionar la celda y mostrar suficiente estabilidad química y estructural para soportar tanto la fabricación, como el funcionamiento a altas temperaturas. La celda de combustible debe funcionar a altas temperaturas para alcanzar densidades de corriente y potencia de salida suficientemente altas. La reactividad e interdifusión entre los componentes debe de ser lo más baja posible y los TEC tienen que tener valores próximos entre sí, minimizando las tensiones térmicas que pueden provocar grietas y fallos mecánicos. También hay que tener en cuenta los requisitos de la atmósfera correspondiente en la selección de materiales para los componentes.

Electrolito: La función principal del electrolito en cualquier tipo de pila combustible es la de conducir un tipo de ion específico entre los dos electrodos para completar la reacción electroquímica correspondiente. En el caso de las SOFC, el electrolito transporta los iones de oxigeno (O^{2-}) generados en el cátodo, al ánodo. Los requisitos a cumplir por los electrolitos a utilizar en una pila SOFC son los siguientes: (i) tener una elevada conductividad iónica y ser aislante electrónico, para prevenir pérdidas de voltaje por cortocircuito; (ii) tener una compatibilidad química y mecánica con los materiales adyacentes; (iii) ser químicamente estable, tanto en ambientes oxidantes como reductores; (iv) ser denso e impermeable al paso de gases; (v) que sea posible su procesado en forma de películas delgadas con el fin de reducir pérdidas óhmicas y flexibilizar la temperatura de operación; y (vi) que el coste del procesado y los materiales sea favorable[41,42].

Existe una amplia variedad de electrolitos utilizados en las pilas SOFC, entre los cuales destaca la zirconia estabilizada con itria (YSZ, $(ZrO_2)_{1-x}(Y_2O_3)_x$, ($x \approx 0.08$-0.1)), por ser la más utilizada hasta la fecha. El YSZ presenta una estructura tipo fluorita, la cual favorece la migración de iones óxido y facilita la creación de vacantes de oxígeno a temperaturas superiores a 750 ºC. El YSZ se caracteriza por su estabilidad química y mecánica, siendo el más común el estabilizado con un 8% mol de Y_2O_3, por su elevada conductividad[43]. Con esta misma estructura fluorita, se han utilizado otros conductores iónicos, como son los basados en ceria (Ce_2O_3) dopada, que posee una conductividad elevada a temperaturas de operación más bajas (500-700 ºC). Los principales óxidos utilizados como elementos dopantes son el Gd_2O_3, Sm_2O_3 e Y_2O_3 (GDC, SDC e YDC, respectivamente). El GDC y SDC tienen mayor conductividad debido a que los radios iónicos de los iones Sm^{3+} y Gd^{3+}, son más parecidos al del Ce^{4+}.

---

41 Ivers-Tiffée E., Electrolytes | Solid: oxygen ions, Reference module in chemistry, molecular sciences and chemical engineering, *Encyclopedia of electrochemical power sources*, (**2009**) 181-187.

42 Horoz S., Sahin O., Solid oxides, *Comprehensive energy systems*, 2 (**2018**) 593-628.

43 Preux, A. Rolle, R.N. Vannier, Electrolytes and ion conductors for solid oxide fuel cells (SOFCs), Functional materials for sustainable energy applications, *Woodhead publishing series in energy*, (**2012**) 370-401.

1.5. SOFC components

Although the operational concept of SOFC is quite simple, the selection of materials for the individual components represents enormous challenges. Each material must have the electrical properties to operate the cell and have sufficient chemical and structural stability to support the manufacturing and the operation at high temperatures. The fuel cell must operate at high temperatures to achieve sufficiently high current densities and power output. The reactivity and interdifusión between the components must be as low as possible and the TECs have to be as close as possible to each other, minimizing the thermal tensions that can cause cracks and mechanical failures. It is also necessary to keep in mind the requirements of the corresponding atmosphere in the selection of materials for each components.

Electrolyte: The main function of the electrolyte in any type of fuel cell is to drive a specific type of ion between the two electrodes to complete the corresponding electrochemical reaction. In the case of SOFCs, the electrolyte transports the oxygen ions (O^{2-}) generated in the cathode to the anode. The requirements to be fullfilled by the electrolytes to be used in a SOFCs are the following: (i) have a high ionic conductivity and be an electronic insulator, to prevent voltage losses due to short circuits; (ii) have a chemical and mechanical compatibility with the adjacent materials; (iii) be chemically stable, in oxidant and reducing environments; (iv) be dense and impermeable to the gas leakage; (v) be able to be formed in thin films in order to reduce ohmic losses and to make the operating temperature more flexible; and (vi) a favorable cost of materials and processing[41,42].

There is a wide variety of electrolytes used in SOFCs, among which zirconia stabilized with yttria (YSZ, $(ZrO_2)_{1-x}(Y_2O_3)_x$, ($x \approx 0.08$-0.1)), is the most used up to the date. The YSZ has a fluorite structure, which promotes the migration of oxide ions and improves the creation of oxygen vacancies at temperatures above 750 ºC. Its chemical and mechanical stability characterizes the YSZ, being stabilized with 8 mol% of Y_2O_3 the most common composition, due to its high conductivity[43]. With this same fluorite structure, other ionic conductors have been used, such as those based on ceria (Ce_2O_3) doped, which has a high conductivity at lower operating temperatures (500-700 ºC). The main oxides used as doping elements are Gd_2O_3, Sm_2O_3 and Y_2O_3 (GDC, SDC and YDC, respectively). The GDC and SDC have greater conductivity because the ionic radii of Sm^{3+} and Gd^{3+} ions, are more similar to that of Ce^{4+}.

---

41 Ivers-Tiffée E., Electrolytes | Solid: oxygen ions, Reference module in chemistry, molecular sciences and chemical engineering, *Encyclopedia of electrochemical power sources*, (**2009**) 181-187.

42 Horoz S., Sahin O., Solid oxides, *Comprehensive energy systems*, 2 (**2018**) 593-628.

43 Preux, A. Rolle, R.N. Vannier, Electrolytes and ion conductors for solid oxide fuel cells (SOFCs), Functional materials for sustainable energy applications, *Woodhead publishing series in energy*, (**2012**) 370-401.

Además de los óxidos tipo fluorita, hay óxidos con otro tipo de estructuras que exhiben características atractivas como electrolitos SOFC. Dentro de las perovskitas, los compuestos más utilizados como electrolito son los óxidos de galato de lantano, $LaGaO_3$ dopado con Sr y Mg ($La_{1-x}Sr_xGa_{1-y}Mg_yO_{3-\delta}$, LSGM). Su mayor ventaja radica en que presenta mayor conductividad iónica que el YSZ. También muestra una buena compatibilidad con los cátodos de conductividad mixta. Sin embargo, en atmósferas reductoras y, a bajas presiones parciales de oxígeno, el Ga se evapora y los productos formados son incompatibles con el Ni. Su baja estabilidad mecánica y el alto coste del galio son otros aspectos negativos a tener en cuenta en este compuesto[43,44].

Cátodos: Los cátodos desempeñan varias funciones dentro de una SOFC: reducen el oxígeno molecular en iones oxígeno que migran a través del electrolito, transportan especies cargadas al electrolito y distribuyen la corriente eléctrica asociada con la reducción de oxigeno[45]. Los principales requerimientos de los materiales para los cátodos de las SOFC son: (i) alta actividad electrocatalítica para la reducción del oxígeno, (ii) elevada conductividad iónica y electrónica, (iii) estabilidad en atmósferas oxidantes, (iv) estabilidad mecánica, especialmente en las celdas de soporte catódico, y (v) compatibilidad química y térmica con el resto de componentes de la celda. En los electrodos de las pilas SOFC, las reacciones están localmente distribuidas en las interfaces electrodo/electrolito de las partes en contacto con los gases (aire u oxígeno). La reacción del electrodo ocurre únicamente en la zona en la que las especies, gas, electrodo y electrolito, están en contacto. A esta región se la denomina zona frontera de tres fases (three phase boundary, TPB). En la Figura 1.9. se muestran las vías para los procesos de reducción de oxigeno[46]:

- Reacción del oxígeno molecular con la superficie del electrodo.
- Adsorción disociativa de las moléculas de oxígeno y difusión superficial hacia el TPB.
- Reacción en la superficie seguida de la disolución y difusión de los iones de oxígeno hacia el interfaz de cátodo/electrolito; luego, los iones de oxígeno se transportan a través del electrolito hacia el ánodo.

---

[44] Wang L., Li C., Li G., Yang G., Zhang S., Li C., Enhanced sintering behavior of LSGM electrolyte and its performance for solid oxide fuel cells deposited by vacuum cold spray, *J. Eur. Ceram. Soc*. 37 (**2017**) 4751-4761.

[45] Zhuiykov S., Nanostructured semiconductor composites for solid oxide fuel cells (SOFCs), Nanostructured semiconductors, *Woodhead publishing series in electronic and optical materials*, 8 (**2018**) 413-474.

[46] Grenier J.C., Bassat J.M., Mauvy F., Novel cathodes for solid oxide fuel cells, Functional Materials for sustainable energy applications, *Woodhead publishing series in energy*, 13 (**2012**) 402-444.

In addition to fluorite type oxides, there are oxides with other types of structures that exhibit attractive characteristics such as SOFC electrolytes. Among the perovskites, the most commonly used compound as electrolyte are the lanthanum gallate oxides, $LaGaO_3$ doped with Sr and Mg ($La_{1-x}Sr_xGa_{1-y}Mg_yO_{3-\delta}$, LSGM). Its biggest advantage is its greater ionic conductivity than the YSZ. It also shows good compatibility with mixed conductivity cathodes. However, in reducing atmospheres and at low partial pressures of oxygen, Ga evaporates and the formed products are incompatible with Ni. Its low mechanical stability and the high cost of gallium are other negative aspects to keep in mind this compound[43,44].

Cathodes: Cathodes perform several functions within a SOFC: they reduce the molecular oxygen in oxygen ions that migrate through the electrolyte, transport charged species to the electrolyte and distribute the electric current associated with the reduction of oxygen[45]. The main requirements for SOFC cathode materials are: (i) high electrocatalytic activity for oxygen reduction, (ii) high ionic and electronic conductivity, (iii) stability in oxidizing atmospheres, (iv) mechanical stability, especially in the cathode supported cells, and (v) chemical and thermal compatibility with other cell components. In the SOFC electrodes, the reactions are distributed locally at the electrode / electrolyte interfaces of the components in contact with the gases (air or oxygen). The reaction of the electrode occurs in the area in which the species, gas, electrode and electrolyte are in contact. This region is called the three-phase boundary, TPB. In Figure 1.9., the pathways for oxygen reduction processes are shown[46].

- Reaction between the molecular oxygen and the electrode surface.
- Dissociative adsorption of oxygen molecules and surface diffusion towards TPB.
- Surface reaction followed by dissolution and diffusion of oxygen ions towards the cathode/electrolyte interface; then, the oxygen ions are transported through the electrolyte to the anode.

---

[44] Wang L., Li C., Li G., Yang G., Zhang S., Li C., Enhanced sintering behavior of LSGM electrolyte and its performance for solid oxide fuel cells deposited by vacuum cold spray, *J. Eur. Ceram. Soc*. 37 (**2017**) 4751-4761.

[45] Zhuiykov S., Nanostructured semiconductor composites for solid oxide fuel cells (SOFCs), Nanostructured semiconductors, *Woodhead publishing series in electronic and optical materials*, 8 (**2018**) 413-474.

[46] Grenier J.C., Bassat J.M., Mauvy F., Novel cathodes for solid oxide fuel cells, Functional Materials for sustainable energy applications, *Woodhead publishing series in energy*, 13 (**2012**) 402-444.

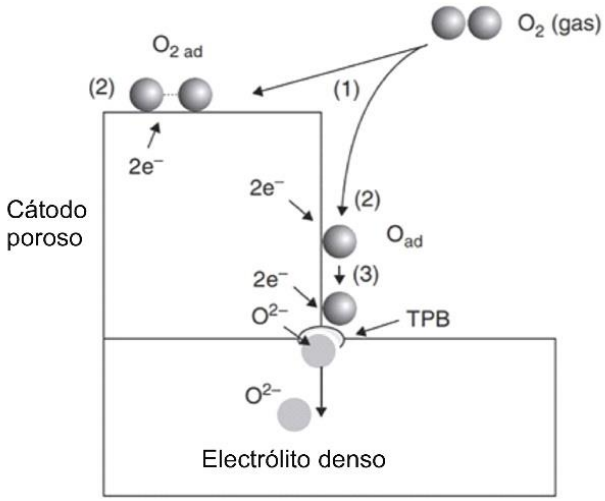

Figura 1.9.- Representación esquemática de las diversas vías de reacción de la reducción electroquímica del oxígeno en el interfaz cátodo/electrolito.

Para obtener altas potencias eléctricas, es necesario que se produzcan altas velocidades de conversión y bajos valores de sobrepotencial. Esto requiere alta actividad electrocatalítica o un alto número de zonas TPB, por lo que el cátodo debe tener una alta concentración de TPB activos, para que las reacciones electroquímicas no estén únicamente limitadas a la región frontera de tres fases electrolito-gas-electrodo, y así, éstas se extiendan a la estructura interna del cátodo. Para ello, una de las opciones es elegir electrodos que tengan conductividad iónica y electrónica intrínseca (mixed ionic and electronic conducting, MIEC). De esta forma, en lugar de multiplicar las líneas de reacción de TPB, el área catalíticamente activa se extiende a toda la superficie del cátodo, tal y como se esquematiza en la Figura 1.10. Asimismo, se espera que las pérdidas de polarización del electrodo se reduzcan considerablemente.

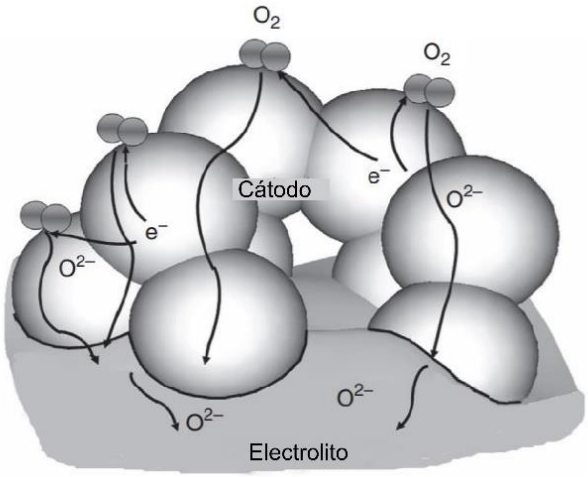

Figura 1.10.- Representación de la reducción de oxígeno en un MIEC.

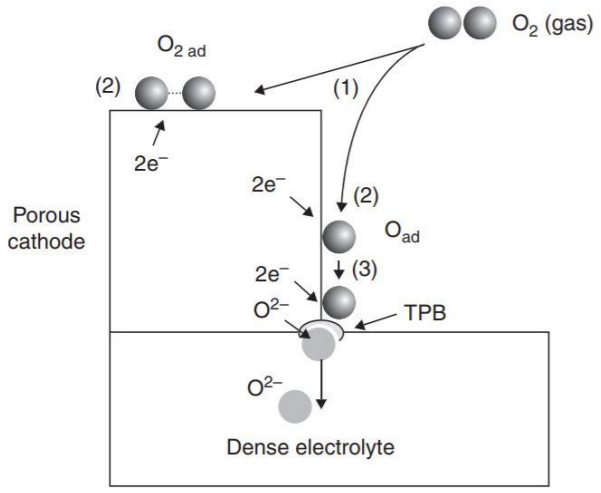

Figure 1.9.- Schematic representation of the reaction pathways of the electrochemical reduction of oxygen at the cathode/electrolyte interface.

In order to obtain high electrical power, a high conversion speeds and low over potential values production are needed. This requires high electrocatalytic activity or a high number of TPB zones, so the cathode must have a high concentration of active TPB, so that the electrochemical reactions are not only limited to the boundary region of three electrolyte-gas-electrode phases, and thus, it extend to the internal structure of the cathode. For this, one of the options is to choose electrodes that have ionic and electronic conductivity (mixed ionic and electronic conducting, MIEC). In this way, instead of multiplying the TPB reaction lines, the catalytically active area is extended to the entire cathode surface, as outlined in Figure 1.10. In addition, it is expected that the polarization losses of the electrode will be considerably reduced.

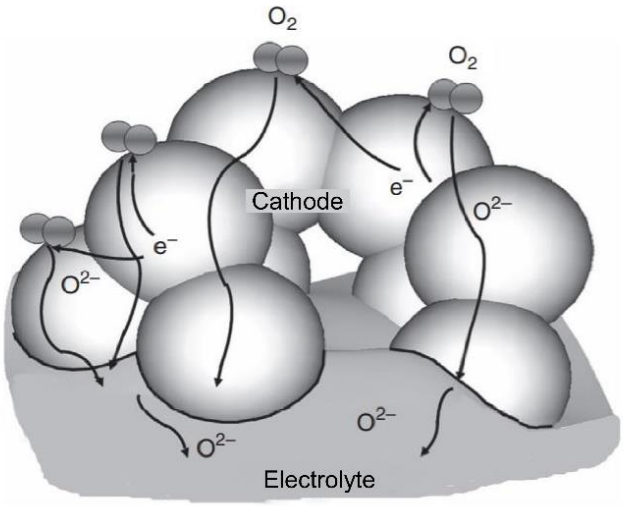

Figure 1.10.- Representation of oxygen reduction in a MIEC.

Uno de los materiales tradicionalmente más empleado en celdas con electrolito YSZ y que opera a temperaturas superiores a 800 ºC es la manganita de lantano ($LaMnO_3$) dopada con estroncio (LSM). El LSM tiene una estructura perovskita (ABO_3) y es un conductor tipo p. El dopaje de $LaMnO_3$ con un catión de valencia más baja aumenta la conductividad electrónica incrementando el contenido del catión Mn^{4+} en el material. Aunque el LSM funciona correctamente a 1000ºC, el que sea poco conductor iónico hace que su resistencia aumente a temperaturas más bajas, limitando las reacciones electroquímicas a la región frontera TPB. La composición de la perovskita también influye en las propiedades químicas del cátodo, afectando a la compatibilidad química del YSZ. Los principales productos de reacción son el $La_2Zr_2O_7$ y el $SrZrO_3$ para composiciones con bajo y alto contenido en estroncio, respectivamente. La formación de ambos compuestos bloquea la reacción de reducción del cátodo. Para prevenir la formación de este tipo de compuesto, el uso de barreras químicas como la ceria dopada con samario ($Ce_{0.8}Sm_{0.2}O_{1.9}$, SDC) entre el cátodo y el electrolito está bastante extendido.

A pesar de que el LSM se ha utilizado extensamente, está generalmente aceptado que el rendimiento electroquímico a temperaturas inferiores a 800 ºC es insuficiente. Una de las alternativas más populares es el uso de los materiales con conducción mixta. Estos materiales se consiguen mezclando compuestos conductores iónicos y electrónicos formando un composite o reemplazando el átomo de la posición B(Mn) de la perovskita por elementos que le confieren una conductividad mixta, como pueden ser el cobalto, el hierro o el níquel. Unos de los candidatos más prometedores para utilizar en temperaturas de operación intermedias son las cobaltitas. Destacan los compuestos de la serie $La_{1-x}Sr_xCoO_{3-\delta}$ (LSC) que presentan alta conductividad electrónica y iónica en un amplio intervalo térmico. En comparación con otros metales de transición (Cr, Mn, Fe, Ni), el cobalto muestra menores sobrepotenciales catódicos. Sin embargo, entre los principales problemas de las cobaltitas se encuentran su alto TEC y su tendencia a reaccionar con el YSZ por encima de los 900 ºC. Otras alternativas para ser utilizadas como cátodo son las $La_{1-x}Sr_xCo_{1-y}Fe_yO_{3-\delta}$ (LSFC), que muestran una menor problemática con los TEC[47].

Los compuestos de óxido de hierro con estructura perovskita (B=Fe) con fórmula general $La_{1-x}Sr_xFeO_3$ (LSF) también son compuestos atractivos en el área de los cátodos[48]. Se ha observado que, para ciertos valores de x, estas fases poseen buenas propiedades catalíticas y conductoras entre 600 y 800 ºC. En comparación con las cobaltitas, esta serie muestra una compatibilidad térmica superior con el YSZ y los electrolitos basados en Ce. En la Figura 1.11. se muestra la resistencia superficial específica, ASR, de varias perovskitas de lantano en el intervalo de temperatura 650-850 ºC, con YSZ como electrolito. Tal y como se puede observar, el comportamiento de las manganitas es inferior al resto, mientras que las perovkitas de hierro muestran una menor resistencia interfacial. El estudio de los compuestos $AFeO_3$[49], determinó que estos compuestos eran ideales para ser utilizados en esta investigación.

---

47 Zhou F., Liu Y., Zhao X., Tang W., Yang S., Zhong S., Wei M., Effects of cerium doping on the performance of LSCF cathodes for intermediate temperature solid oxide fuel cells, *Int. J. Hydrog. Energy*. 43 (**2018**) 18946-18954.

48 Vidal K., Rodríguez-Martínez L.M., Ortega-San-Martin L., Martínez-Amesti A., Nó M.L., Rojo T., Laresgoiti A., Arriortua M.I., The effect of doping in the electrochemical performance of $(Ln_{1-x}M_x)FeO_{3-\delta}$ SOFC cathodes, *J. Power Sources*. 192 (**2009**) 175-179.

49 Ecija-Verdejo A., Óxidos mixtos tipo perovskita $Ln_{0.5}M_{0.5}FeO_{3-\delta}$ (Ln=La, Sm, Nd, Gd; M=Ba, Sr) para su aplicación como catodos en pilas SOFC. Ph.D. tesis doctoral, UPV/EHU, **2012**.

One of the materials most traditionally used YSZ electrolyte cells and operating at temperatures above 800 °C is the lanthanum manganite ($LaMnO_3$) doped with strontium (LSM). The LSM has a perovskite structure (ABO_3) and is a p-type conductor. The doping of $LaMnO_3$ with a lower valence cation increases the electronic conductivity by increasing the Mn^{4+} content in the material. Although the LSM works correctly at 1000ºC, the fact that it is a low ionic conductor causes its resistance to increase at lower temperatures, limiting the electrochemical reactions to the TPB border region. The composition of the perovskite also influences the chemical properties of the cathode, affecting the chemical compatibility of the YSZ. The main reaction products are $La_2Zr_2O_7$ and $SrZrO_3$ for compositions with low and high strontium content, respectively. The formation of both compounds blocks the cathode reduction reaction. To prevent the formation of this type of compound, the use of chemical barriers such as samarium doped ceria ($Ce_{0.8}Sm_{0.2}O_{1.9}$, SDC) between the cathode and the electrolyte is quite widespread.

Although LSM has been widely used, it is generally accepted that electrochemical performance at temperatures below 800 ºC is insufficient. One of the most popular alternatives is the use of materials with mixed driving. These materials are obtained by mixing ionic and electronic conductive compounds forming a composite or replacing the atom of B (Mn) position of the perovskite by elements that give it a mixed conductivity, such as cobalt, iron or nickel. One of the most promising candidates to use at intermediate operating temperatures are cobaltites. The compounds of the series $La_{1-x}Sr_xCoO_{3-\delta}$ (LSC) that exhibit high electronic and ionic conductivity over a wide thermal range stand out. In comparison with other transition metals (Cr, Mn, Fe, Ni), cobalt shows lower cathodic overpotentials. However, among the main problems of cobaltite are its high TEC and its tendency to react with the YSZ above 900 ºC. Another alternative to be used as a cathode are the $La_{1-x}Sr_xCo_{1-y}Fe_yO_{3-\delta}$ (LSFC), which show less problems with the TEC[47].

Iron oxide compounds with perovskite structure (B=Fe) with general formula $La_{1-x}Sr_xFeO_3$ (LSF) are also attractive compounds in the area of cathodes[48]. It has been observed that, for certain values of x, these phases have good catalytic and conductive properties between 600 and 800 ºC. Compared with cobaltites, this series shows superior thermal compatibility with YSZ and Ce-based electrolytes. The area specific resistance, ASR, of several lanthanum perovskites with YSZ as electrolyte in the 650-850 °C temperature range is shown in Figure 1.11. As can be seen, the behavior of the manganites is lower than the rest, while the iron perovkites show a lower interfacial resistance. The study of $AFeO_3$[49] perovskites, determined that LSF compounds were ideal to be used in this research.

---

47 Zhou F., Liu Y., Zhao X., Tang W., Yang S., Zhong S., Wei M., Effects of cerium doping on the performance of LSCF cathodes for intermediate temperature solid oxide fuel cells, *Int. J. Hydrog. Energy*. 43 (**2018**) 18946-18954.

48 Vidal K., Rodríguez-Martínez L.M., Ortega-San-Martin L., Martínez-Amesti A., Nó M.L., Rojo T., Laresgoiti A., Arriortua M.I., The effect of doping in the electrochemical performance of $(Ln_{1-x}M_x)FeO_{3-\delta}$ SOFC cathodes, *J. Power Sources*. 192 (**2009**) 175-179.

49 Ecija-Verdejo A., Óxidos mixtos tipo perovskita $Ln_{0.5}M_{0.5}FeO_{3-\delta}$ (Ln=La, Sm, Nd, Gd; M=Ba, Sr) para su aplicación como catodos en pilas SOFC. Ph.D. thesis work, UPV/EHU, **2012**.

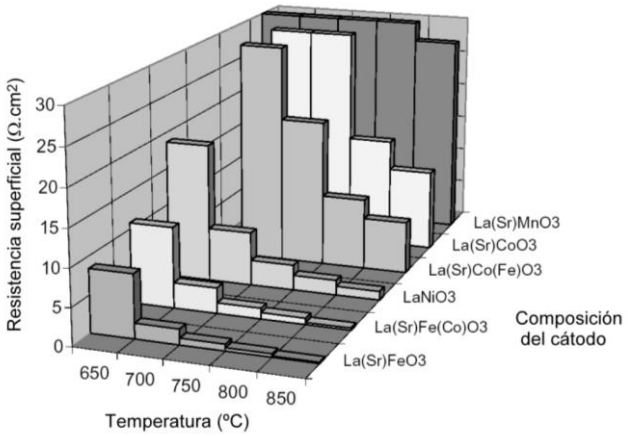

Figura 1.11.- Resistencia superficial de varios cátodos tipo perovskita con el electrolito YSZ.

Intercapa: Uno de los principales problemas de los dispositivos SOFC es la compatibilidad entre las fases que forman las diferentes partes activas de la celda (cátodo-electrolito-ánodo). Estudios previos muestran que los materiales tipo perovskita (LSM, LSF, LSCF) empleados como cátodo, reaccionan con el electrolito dando lugar a las fases $La_2Zr_2O_7$ o $SrZrO_3$, que dan propiedades menos favorables al cátodo y un impacto negativo al rendimiento de la celda[50,51].

Con objeto de solucionar esta problemática, algunos estudios indican que la utilización de una capa de ceria dopada con cationes trivalentes, pertenecientes al grupo de las tierras raras como el Y, Sm, Gd o La, inhibe la formación de dichas fases, evitando la degradación de la celda[52-54].

La intercapa de $Ce_{0.8}Sm_{0.2}O_{1.9}$ (SDC) entre el electrolito de YSZ y el cátodo LSF, actúa como barrera para prevenir la reacción química entre ellos, evitando la formación de fases anteriormente mencionadas[55,56]. Teniendo en cuenta estas características, se ha seleccionado el SDC como barrera protectora entre el cátodo y el YSZ a lo largo del presente estudio.

---

[50] López-Robledo M.J., Laguna-Bercero M.A., Silva J., Orera V.M., Larrea A., Electrochemical performance of intermediate temperature micro-tubular solid oxide fuel cells using porous ceria barrier layers, *Ceram. Int*. 41 (**2015**) 7651-7660.

[51] Yang K., Shen J., Yang K., Hung I.M., Fung K., Wang M., Formation of $La_2Zr_2O_7$ or $SrZrO_3$ on cathode-supported solid oxide fuel cells, *J. Power Sources*. 159 (**2006**) 63-67.

[52] Coddet P., Amany M., Vulliet J., Caillard A., Thomann A., YSZ/GDC bilayer and gradient barrier layers deposited by reactive magnetron sputtering for solid oxide cells, *Surf. Coat. Tech*. 357 (**2019**) 103-113.

[53] Morales M., Miguel-Pérez V., Tarancón A., Slodczyk A., Torrell M., Ballesteros B., Ouweltjes J.P., Bassat J.M., Montinaro D., Morata A., Multi-scale analysis of the diffusion barrier layer of gadolinia-doped ceria in a solid oxide fuel cell operated in a stack for 3000 h, *J. Power Sources*. 344 (**2017**) 141-151.

[54] Wang W.G., Mogensen M., High-performance lanthanum-ferrite-based cathode for SOFC, *Solid State Ion*. 176 (**2005**) 457-462.

[55] Martínez-Amesti A., Larrañaga A., Rodríguez-Martínez L.M., Nó M.L., Pizarro J.L., A. Laresgoiti, Arriortua M.I., Chemical compatibility between YSZ and SDC sintered at different atmospheres for SOFC applications, *J. Power Sources*. 192 (**2009**) 151-157.

[56] Martínez-Amesti A., Larrañaga A., Rodríguez-Martínez L.M., Aguayo A.T., Pizarro J.L., Nó M.L., Laresgoiti A., Arriortua M.I., Reactivity between La(Sr)FeO_3 cathode, doped CeO_2 interlayer and yttria-stabilized zirconia electrolyte for solid oxide fuel cell applications, *J. Power Sources*. 185 (**2008**) 401-410.

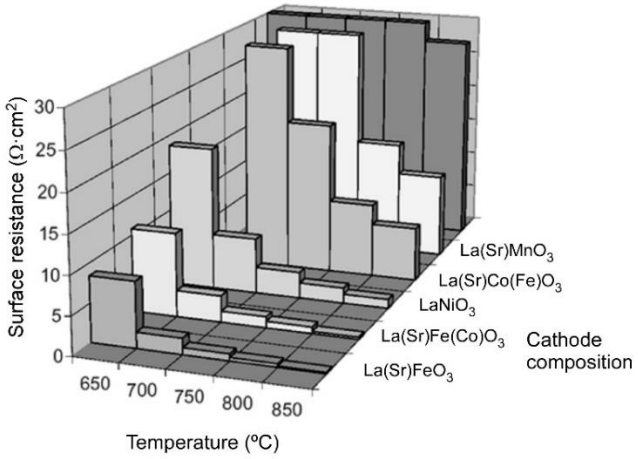

Figure 1.11.- Surface resistance of perovskite type cathodes with YSZ electrolyte.

Interlayer: One of the main problems for SOFC devices is the compatibility between the phases that form the different active parts of the cell (cathode-electrolyte-anode). Previous studies show that perovskite type materials (LSM, LSF, LSCF) used as a cathode, react with the electrolyte, giving rise to the $La_2Zr_2O_7$ or $SrZrO_3$ phases, which give less favorable properties to the cathode and a negative impact on cell performance[50,51].

In order to solve this problem, some studies indicate that the use of a layer of ceria doped with trivalent cations, belonging to the group of rare earths such as Y, Sm, Gd or La, inhibits the formation of these phases, preventing the degradation of the cell[52-54].

The $Ce_{0.8}Sm_{0.2}O_{1.9}$ (SDC) interlayer between the YSZ electrolyte and the LSF cathode, acts as a barrier to prevent the chemical reaction between them, avoiding the formation of the aforementioned phases[55,56]. In view of these features, the SDC has been selected as a protective barrier between the cathode and the YSZ throughout the actual study.

---

[50] López-Robledo M.J., Laguna-Bercero M.A., Silva J., Orera V.M., Larrea A., Electrochemical performance of intermediate temperature micro-tubular solid oxide fuel cells using porous ceria barrier layers, *Ceram. Int*. 41 (**2015**) 7651-7660.

[51] Yang K., Shen J., Yang K., Hung I.M., Fung K., Wang M., Formation of $La_2Zr_2O_7$ or $SrZrO_3$ on cathode-supported solid oxide fuel cells, *J. Power Sources*. 159 (**2006**) 63-67.

[52] Coddet P., Amany M., Vulliet J., Caillard A., Thomann A., YSZ/GDC bilayer and gradient barrier layers deposited by reactive magnetron sputtering for solid oxide cells, *Surf. Coat. Tech*. 357 (**2019**) 103-113.

[53] Morales M., Miguel-Pérez V., Tarancón A., Slodczyk A., Torrell M., Ballesteros B., Ouweltjes J.P., Bassat J.M., Montinaro D., Morata A., Multi-scale analysis of the diffusion barrier layer of gadolinia-doped ceria in a solid oxide fuel cell operated in a stack for 3000 h, *J. Power Sources*. 344 (**2017**) 141-151.

[54] Wang W.G., Mogensen M., High-performance lanthanum-ferrite-based cathode for SOFC, *Solid State Ion*. 176 (**2005**) 457-462.

[55] Martínez-Amesti A., Larrañaga A., Rodríguez-Martínez L.M., Nó M.L., Pizarro J.L., A. Laresgoiti, Arriortua M.I., Chemical compatibility between YSZ and SDC sintered at different atmospheres for SOFC applications, *J. Power Sources*. 192 (**2009**) 151-157.

[56] Martínez-Amesti A., Larrañaga A., Rodríguez-Martínez L.M., Aguayo A.T., Pizarro J.L., Nó M.L., Laresgoiti A., Arriortua M.I., Reactivity between $La(Sr)FeO_3$ cathode, doped CeO_2 interlayer and yttria-stabilized zirconia electrolyte for solid oxide fuel cell applications, *J. Power Sources*. 185 (**2008**) 401-410.

Ánodo: Las funciones más importantes del ánodo son oxidar el combustible y ser capaz de transportar los electrones creados a lo largo de la reacción de oxidación. Al igual que con el cátodo, los principales requisitos para los materiales ánodo son: (i) elevada actividad electrocatalítica, (ii) elevada conductividad iónica y electrónica, (iii) estabilidad en atmósferas reductoras, (iv) coeficientes de expansión térmica semejantes al electrolito y al resto de los componentes de la celda, (v) estructura física adecuada para el transporte de combustible, (vi) estabilidad química y mecánica, especialmente en celdas de soporte anódico, (vii) a ser posible, capacidad de reformar hidrocarburos, y (viii) estabilidad en presencia de compuestos de azufre[57]. El material anódico más citado en la literatura es el cermet Ni-YSZ, que es una mezcla entre un cerámico y un metal. Habitualmente la concentración de Ni es de entre un 40 y un 60% en volumen, para permitir la conexión entre partículas y garantizar la conductividad eléctrica del material. La red cerámica permite adecuar el TEC del ánodo al electrolito y evita la aglomeración de partículas de níquel. Además, permite extender el TPB en todo el volumen del ánodo. Para facilitar la llegada de los gases a la zona electroquímicamente activa, la porosidad típica del ánodo es de cerca del 40%. En general, los ánodos suelen estar formados por un material composite formado por una parte metálica y una cerámica con composición similar al electrolito. Un ejemplo son las celdas de soporte electrolito de CGO y LSGM, que suelen presentar Ni-CGO y Ni LSGM como materiales anódicos, respectivamente[58]. Teniendo en cuenta que en este estudio se ha seleccionado el YSZ como electrolito, se ha empleado el Ni-YSZ como material anódico.

Interconectores: Del mismo modo que un motor de combustión interna se basa en varios cilindros para proporcionar suficiente potencia, las celdas de combustible se pueden emplear en combinación para generar suficiente voltaje y corriente. Esto significa que las celdas deben estar conectadas entre sí, de ahí la necesidad de interconexiones. La interconexión funciona como el contacto eléctrico con el cátodo, lo que garantiza la separación del aire y el combustible dentro de la pila de combustible, protegiéndola de la atmósfera reductora del ánodo. Los requerimientos para los materiales que actúan como interconector son: (i) una alta conductividad eléctrica bajo atmósferas reductoras y oxidantes, (ii) ser impermeable a los gases, (iii) estabilidad química y microestructural a la temperatura de operación de la celda, tanto en atmósferas reductoras como en oxidantes, (iv) compatibilidad térmica y química con los materiales adyacentes, (v) alta resistencia mecánica, (vi) alta conductividad térmica y (vii) elevada densidad[59].

El material tradicional para su uso como interconector en SOFC, a altas temperaturas (~1000 ºC) es la cromita de lantano ($LaCrO_3$). Para empezar, esta cerámica tiene una alta conductividad electrónica en las condiciones de funcionamiento de las SOFC y su conductividad puede ser mejorada considerablemente dopándola con Ca, Mg o Sr. Junto con esto, el dopaje con metales de transición, por ejemplo, $La_{0.8}Sr_{0.2}Cr_{0.97}V_{0.03}O_3$ o $LaCr_{0.78}Mg_{0.05}Al_{0.16}O_3$, puede ajustar el TEC y bajar la temperatura de sinterizado.

---

[57] Tao S.W., Cowin P.I., Lan R., Novel anode materials for solid oxide fuel cells, Functional materials for sustainable energy applications, *Woodhead publishing series in energy*, 14 (**2012**) 445-477.

[58] Wincewicz K.C., Cooper J.S., Taxonomies of SOFC material and manufacturing alternatives, *J. Power Sources*. 140 (**2005**) 280-296.

[59] Xu X., Ceramics in solid oxide fuel cells for energy generation, Advances in ceramic matrix composites, *Woodhead publishing series in composites science and engineering*, 31 (**2018**) 763-788.

Anode: The main functions of the anode are to oxidize the fuel and be able to transport the electrons created throughout the oxidation reaction. As the cathode, the main requirements for anode materials are: (i) high electrocatalytic activity, (ii) high ionic and electronic conductivity, (iii) stability in reducing atmospheres, (iv) similar thermal expansion coefficients to the electrolyte and the rest of the components, (v) a suitable physical structure for transporting fuel, (vi) chemical and mechanical stability, especially in anode supported cells, (vii) if possible, ability to reform hydrocarbons, and (viii) stability in the presence of sulfur compounds[57]. The most used anodic material in the literature is the Ni-YSZ cermet, which is a ceramic and metal mixture. Usually, the Ni concentration is between 40 and 60% by volume, to allow the connection between particles and ensure the electrical conductivity of the material. The ceramic network makes it possible to adapt the TEC of the anode to the electrolyte and prevents the agglomeration of nickel particles. In addition, it allows extending the TPB over the entire anode volume. To facilitate the arrival of gases in the electrochemically active zone, the typical porosity of the anode is about 40%. In general, the anodes are usually formed by a composite material formed by a metal part and a ceramic with a similar composition to the electrolyte. For example, CGO and LSGM electrolyte supported cells usually present Ni-CGO and Ni LSGM as anodic materials, respectively[58]. Considering that YSZ has been selected in this study as electrolyte, Ni-YSZ has been adopted as an anodic material.

Interconnects: In the same way as an internal combustion engine relies on several cylinders to provide enough power, fuel cells can be used in combination to generate enough voltage and current. This means that the cells must be connected amongst each other, hence the need for interconnections. The interconnection works like the electrical contact with the cathode, which guarantees the separation of air and fuel inside the fuel cell, protecting it from the reducing atmosphere of the anode. The requirements for the materials that act as an interconnector are: (i) a high electrical conductivity under reducing and oxidizing atmospheres, (ii) be gas impermeable, (iii) chemical and microstructural stability at operating temperature of the cell, in reducing and oxidant atmospheres, (iv) thermal and chemical compatibility with adjacent materials, (v) high mechanical strength, (vi) high thermal conductivity and (vii) high density[59].

The traditional material for use as an interconnector in SOFC at high temperatures (~ 1000 ºC) is the lanthanum chromite ($LaCrO_3$). To begin with, this ceramic has a high electronic conductivity under the operating conditions of the SOFC and its conductivity can be improved considerably by doping it with Ca, Mg or Sr. Along with this, the doping with transition metals, for example, $La_{0.8}Sr_{0.2}Cr_{0.97}V_{0.03}O_3$ or $LaCr_{0.78}Mg_{0.05}Al_{0.16}O_3$, you can adjust the TEC and lower the sintering temperature.

---

[57] Tao S.W., Cowin P.I., Lan R., Novel anode materials for solid oxide fuel cells, Functional materials for sustainable energy applications, *Woodhead publishing series in energy*, 14 (**2012**) 445-477.

[58] Wincewicz K.C., Cooper J.S., Taxonomies of SOFC material and manufacturing alternatives, *J. Power Sources*. 140 (**2005**) 280-296.

[59] Xu X., Ceramics in solid oxide fuel cells for energy generation, Advances in ceramic matrix composites, *Woodhead publishing series in composites science and engineering*, 31 (**2018**) 763-788.

La reducción de temperaturas de funcionamiento a 600-800 ºC abre la oportunidad de utilizar materiales metálicos en vez de interconectores de $LaCrO_3$, los cuales presentan una serie de ventajas respecto a este material: (i) presentan una mayor resistencia mecánica, (ii) tienen una alta conductividad térmica, (iii) una conductividad electrónica superior, y (iv) métodos de fabricación simples y de bajo coste. Hay que tener en cuenta que la mayoría de estas aleaciones contienen Al y Cr y pueden proporcionar resistencia a la oxidación formando capas protectoras de Al_2O_3 y Cr_2O_3, respectivamente. No obstante, a largos tiempos de operación, las aleaciones basadas en cromo forman una capa excesiva de Cr_2O_3 que empeora la estabilidad de las mismas (por ejemplo, el Ducrolloy, Cr-5Fe-Y_2O_3).

Sin embargo, las aleaciones basadas en Fe-Cr (aceros inoxidables ferríticos) siguen siendo estudiadas, puesto que continúan teniendo un alto contenido en cromo para formar capas protectoras, son magnéticas y presentan una baja concentración en carbono. Los aceros inoxidables están divididos en cuatro grupos: (i) aceros ferríticos, (ii) aceros austeníticos, (iii) aceros martensíticos, y (iv) aceros de endurecimiento por precipitación. De estos, el grupo más utilizado son los aceros inoxidables ferríticos, los cuales, al tener una estructura centrada en el cuerpo, les da un TEC similar a otros materiales SOFC, además de tener un coste menor comparándolo con aceros con mayor contenido en Ni. El Crofer22 APU desarrollado por la compañía Thyssen Krupp ha sido el interconector más extensamente seleccionado para su uso como interconector de SOFC. La velocidad de difusión en los óxidos con estructura espinela suele ser menor que en los óxidos simples y la pasivación de las aleaciones de interconector suele ser una formación de una doble capa superficial. Esta capa, está formada a partir de la oxidación de los sistemas Fe-Cr-Mn, que se da en los sustratos del Crofer 22 APU, y está compuesta por una capa interna de Cr_2O_3 y una capa externa de estructura espinela, M_3O_4 ($M=Mn^{3+/4+}$ y Cr^{6+})[60]. Al mostrar un rendimiento bastante bueno en la tasa de oxidación, la conductividad eléctrica y la evaporación de Cr en condiciones de funcionamiento, se ha optado por utilizar el Crofer 22 APU como interconector para este estudio[61].

[60] Fontana S., Amendola R., Chevalier S., Piccardo P., Caboche G., Viviani M., Molins R., Sennour M., Metallic interconnects for SOFC: Characterisation of corrosion resistance and conductivity evaluation at operating temperature of differently coated alloys, *J. Power Sources*. 171 (**2007**) 652-662.

[61] Jo K.H., Kim J.H., Kim K.M., Lee I., Kim S., Development of a new cost effective Fe–Cr ferritic stainless steel for SOFC interconnect, *Int. J. Hydrog. Energy*. 40 (**2015**) 9523-9529.

The reduction of operating temperatures to 600-800 ºC opens the opportunity to use metallic materials instead of $LaCrO_3$ interconnectors, which present a series of advantages with respect to this material: (i) they present a greater mechanical resistance, (ii) they have a high thermal conductivity, (iii) superior electronic conductivity, and (iv) simple and low cost manufacturing methods. It must be taken into account that most of these alloys contain Al and Cr and can provide resistance to oxidation by forming protective layers of Al_2O_3 and Cr_2O_3, respectively. However, at long operating times, the chromium-based alloys form an excessive layer of Cr_2O_3, which worsens the stability (for example, Ducrolloy, Cr-5Fe-Y_2O_3).

However, alloys based on Cr-Fe (ferritic stainless steels) are still studied, since they still have a high chromium content to form protective layers, they are magnetic and have a low carbon concentration. The stainless steels are divided into four groups: (i) ferritic steels, (ii) austenitic steels, (iii) martensitic steels, and (iv) precipitation hardening steels. Among these, the most commonly used group are ferritic stainless steels, which, having a body centered structure, gives them a similar TEC to other SOFC materials, moreover to having a lower cost compared to Ni content steels[47]. The Crofer22 APU developed by the Thyssen Krupp company has been the most extensively selected interconnector for SOFC interconnector use. The diffusion speed in oxides with spinel structure is usually lower than in simple oxides and the passivation of interconnector alloys is usually a double layer formation. This layer is formed from the oxidation of the Fe-Cr-Mn systems, which occurs in the substrates of the Crofer 22 APU, and is composed of an internal layer of Cr_2O_3 and an external layer of spinel structure, M_3O_4 ($M=Mn^{3+/4+}$ and Cr^{6+})[60]. By showing a good performance in the oxidation rate, the electrical conductivity and the evaporation of Cr under operating conditions, Crofer 22 APU was chosen as interconnector for this study[61].

---

[60] Fontana S., Amendola R., Chevalier S., Piccardo P., Caboche G., Viviani M., Molins R., Sennour M., Metallic interconnects for SOFC: Characterisation of corrosion resistance and conductivity evaluation at operating temperature of differently coated alloys, *J. Power Sources*. 171 (**2007**) 652-662.

[61] Jo K.H., Kim J.H., Kim K.M., Lee I., Kim S., Development of a new cost effective Fe–Cr ferritic stainless steel for SOFC interconnect, *Int. J. Hydrog. Energy*. 40 (**2015**) 9523-9529.

Capa protectora: El uso de capas protectoras entre el cátodo e interconector, puede disminuir la cinética de oxidación y mejorar la adhesión de la capa de óxido sobre los sustratos, además de prevenir la difusión de cromo. Los materiales empleados como capas protectoras deben cumplir los siguientes requisitos: (i) alta conductividad eléctrica, (ii) adecuada compatibilidad química y un TEC similar a los materiales adyacentes, (iii) una baja difusividad de los cationes de cromo, y (iv) estabilidad química y estructural en aire a la temperatura de operación de celdas SOFC[62]. Los materiales empleados como capas protectoras para interconectores se dividen en cuatro grupos principales: (i) óxidos de elementos reactivos (La_2O_3, CeO_2, Nd_2O_3 y Y_2O_3), (ii) óxidos con fórmula general MAlCrYO (M=Co, Mn, Ti, Ni), (iii) perovskitas conductoras, tales como $La_xSr_{1-x}CoO_3$, $La_{1-x}Sr_xCrO_3$ y $La_xSr_{1-x}MnO_3$, y (iv) espinelas conductoras, $(Mn, Co)_3O_4$, Co_3O_4 y $(Cu, Mn)_3O_4$, por ejemplo. Entre todos estos materiales, los óxidos mixtos con estructura espinela son los más utilizados dada su sinterabilidad y su conductividad eléctrica superior, debido a la capa de óxido superficial (Cr_2O_3, $(Mn, Cr)_3O_4$).

Aunque las espinelas $Mn_{1-\delta}Co_{2-\delta}O_4$ (MC) son las más estudiadas, algunos estudios sugieren que la adherencia de estas capas sobre aleaciones tipo Crofer22 puede ser un factor a mejorar para su posterior aplicación en sistemas SOFC. La presencia de cerio como elemento reactivo en la capa protectora, aumenta su adherencia al substrato. Por ejemplo, los estudios realizados sobre la composición $Ce_{0.05}Mn_{1.475}Co_{1.475}O_4$ mostraron una capa de óxido bien adherida al interconector. Además, debido al bajo coste del níquel, también se han estudiado las espinelas $NiMn_2O_4$ y $NiFe_2O_4$ como capas protectoras, obteniéndose una adecuada conductividad sobre el substrato. Asimismo, otros grupos de investigación han estudiado espinelas Mn-Co dopadas con Fe, Ti y/o Cu, logrando mejoras en la densificación del material y una mayor conductividad eléctrica con respecto a la capa $MnCo_2O_4$. Trabajos previos, realizados en el grupo de investigación[62], concluyen que la capa de $MnCo_{1.9}Fe_{0.1}O_4$ (MCF) es más efectiva como barrera para el cromo que la $MnCo_2O_4$ (MC), debido a que la presencia de hierro en la espinela mejora la estabilidad de estos óxidos, mostrando mejores resultados electroquímicos. Es por ello que se ha optado por el uso de MCF como material adecuado para utilizar como capa protectora entre el interconector y la celda.

---

62 Miguel-Pérez V., Martínez-Amesti A., Nó M.L., Larrañaga A., Arriortua M.I., The effect of doping $(Mn,B)_3O_4$ materials as protective layers in different metallic interconnects for solid oxide fuel cells, *J. Power Sources*. 243 (**2013**) 419-430.

Protective layer: The use of protective layers between the cathode and interconnector, can decrease the oxidation kinetics and improve the adhesion of the oxide layer on the substrates, in addition to preventing the diffusion of chromium. The materials used as protective layers must meet the following requirements: (i) high electrical conductivity, (ii) adequate chemical compatibility and TEC similar to adjacent materials, (iii) low diffusivity of chromium cations, and (iv) chemical and structural stability in air at the operating temperature of SOFC cells[62]. The materials used as protective layers for interconnectors are divided into four main groups: (i) oxides of reactive elements (La_2O_3, CeO_2, Nd_2O_3 and Y_2O_3), (ii) oxides with general formula MAlCrYO (M= Co, Mn, Ti, Ni), (iii) conductive perovskites, such as $La_xSr_{1-x}CoO_3$, $La_{1-x}Sr_xCrO_3$ and $La_xSr_{1-x}MnO_3$, and (iv) conductive spinels, $(Mn, Co)_3O_4$, Co_3O_4 and $(Cu, Mn)_3O_4$, for example. Among all these materials, the mixed oxides with spinel structure are the most used due to their sinterability and superior electrical conductivity, due to the surface oxide layer (Cr_2O_3, $(Mn, Cr)_3O_4$).

Although $Mn_{1-\delta}Co_{2-\delta}O_4$ (MC) spinels are the most studied, some studies suggest that the adhesion of these layers on Crofer22 type alloys may be a factor to be improved for their subsequent application in SOFC systems. The presence of cerium as a reactive element in the protective layer increases its adhesion to the substrate. For example, the studies carried out on the composition $Ce_{0.05}Mn_{1.475}Co_{1.475}O_4$ showed an oxide layer well adhered to the interconnector. In addition, due to the nickel low cost, $NiMn_2O_4$ and $NiFe_2O_4$ spinels have also been studied as protective layers, obtaining an adequate conductivity on the substrate. Likewise, other research groups have studied Mn-Co spinels doped with Fe, Ti and / or Cu, obtaining improvements in the densification of the material and a greater electrical conductivity with respect to the $MnCo_2O_4$ layer. Previous work, carried out in the research group[62], concludes that the layer of $MnCo_{1.9}Fe_{0.1}O_4$ (MCF) is more effective as a barrier for chromium than $MnCo_2O_4$ (MC), because the presence of iron in the spinel improves the stability of these oxides showing better electrochemical results. Therefore, the use of MCF has been chosen as a suitable material to be used as protective layer between the interconnector and the cell.

---

[62] Miguel-Pérez V., Martínez-Amesti A., Nó M.L., Larrañaga A., Arriortua M.I., The effect of doping $(Mn,B)_3O_4$ materials as protective layers in different metallic interconnects for solid oxide fuel cells, *J. Power Sources*. 243 (**2013**) 419-430.

Capas de contacto: Uno de los retos en la investigación para pilas SOFC reside en disminuir las altas pérdidas óhmicas que se producen como consecuencia de los problemas de contacto entre el cátodo y el interconector. Además, uno de los principales problemas para la comercialización de las pilas, es la velocidad de degradación para los stacks, en la que el contacto interconector-cátodo juega un papel importante[63]. Por esta razón, se ve necesaria la utilización de una capa de contacto entre el interconector y el cátodo para mejorar el contacto entre dichos componentes, sin reducir la capacidad de la celda y aumentando la conductividad eléctrica interfacial[64]. La mayoría de compuestos que se han evaluado como capas de contacto son materiales de tipo perovskita, dada la posibilidad de excluir metales nobles como la plata o el platino por su coste económico. Entre éstas, perovskitas de fórmula general $LaMO_3$ (M= Co, Cr, Mn, Ni, Fe) han sido de las primeras en evaluarse, pero su baja conductividad y su pobre sinterabilidad no las hacen aptas para su uso en SOFC.

La introducción de elementos alcalinotérreos como pueden ser el Ca, Ba o Sr, mejoran la sinterabilidad y la conductividad de los materiales. Sin embargo, si se introducen estos elementos en exceso, la celda se deteriora rápidamente a causa de la formación de fases como $SrCrO_4$, $CaCrO_4$ o $BaCrO_4$, consecuencia del Cr liberado por el interconector. También se han llevado a cabo estudios de perovskitas con bajo contenido en Sr, con fórmula general $La_{0.8}Sr_{0.2}MO_3$ (M= Co, Cu, Mn, Fe). Estos compuestos han mostrado propiedades de sinterizado, conductividad eléctrica y TEC adecuados, además de una menor formación de fases de Cr. Estos estudios concluyen que: (i) altas cantidades de cobalto aumentan la conductividad y mejoran la compatibilidad del coeficiente de expansión térmica de los materiales de contacto, (ii) grandes cantidades de Mn favorecen la formación de espinelas de Mn-Cr por reacción con el Cr liberado por el interconector, (iii) tienen una menor tendencia a liberar Sr que las perovskitas de Co y (iv) es necesario introducir pequeñas cantidades de cobre para conseguir una alta densificación de las perovskitas.

Cuando se han utilizado las fases $(La,Sr)CoO_3$, $(La,Sr)(Co,Fe)O_3$ y $La(Ni,Fe)O_3$ como capas de contacto sobre diferentes aleaciones ferríticas (Crofer22APU, E-Brite y 430), se ha observado una difusión de cationes (Ni,Fe,Co) de la perovskita hacia la fase con estructura espinela, formada a partir de los metales de transición presentes en la aleación, que proporciona una mayor conductividad eléctrica a la capa de óxido[65]. Además, algunos estudios han puesto de manifiesto que las perovskitas como $La(Ni,Co)O_{3-\delta}$, $La(Ni,Fe)O_{3-\delta}$ y $LaSr(Fe,Co)O_3$ muestran una menor reactividad con la espinela protectora $MnCo_2O_4$[66,67]. Para la construcción de las celdas presentadas en esta memoria, al utilizarse LSF como cátodo y un interconector Crofer22 APU, se ha optado por utilizar la capa de contacto $LaNi_{0.6}Fe_{0.4}O_3$ (LNF) junto con la capa protectora MCF.

---

63 Xin X., Liu L., Liu Y., Zhu Q., Novel perovskite-spinel composite conductive ceramics for SOFC cathode contact layer, *Int. J. Hydrog. Energy*. 43 (**2018**) 23036-23040.

64 Zhu J.H., Ghezel-Ayagh H., Cathode-side electrical contact and contact materials for solid oxide fuel cell stacking: A review, *Int. J. Hydrog. Energy*. 42 (**2017**) 24278-24300.

65 Lacey R., Pramanick A., Lee J.C., Jung J., Jiang B., Edwards D.D., Naum R., Misture S.T., Evaluation of Co and perovskite Cr-blocking thin films on SOFC interconnects, *Solid State Ion*. 181 (**2010**) 1294-1302.

66 Wang F., Yan D., Zhang W., Chi B., Pu J., Jian L., $LaCo_{0.6}Ni_{0.4}O_{3-\delta}$ as cathode contact material for intermediate temperature solid oxide fuel cells, *Int. J. Hydrog. Energy*. 38 (**2013**) 646-651.

67 Morán-Ruiz A., Desarrollo de capas de contacto para su aplicación en SOFC/Development of contact coating for SOFC. Ph.D. thesis work, UPV/EHU, **2015**.

Contact layers: One of the challenges in research for SOFCs lies in reducing the high ohmic losses that occur because of contact problems between the cathode and the interconnector. In addition, one of the main problems for the commercialization of fuel cells is the degradation speed for the stacks, in which the interconnector-cathode contact plays an important role[63]. For this reason, it is necessary to use a contact layer between the interconnector and the cathode to improve the contact between these components, without reducing the capacity of the cell and increasing the interfacial electrical conductivity[64]. The majority of compounds that have been evaluated as contact layers are perovskite-type materials, with the possibility of excluding noble metals as silver or platinum because of their high economic cost. Among these, perovskites of general formula $LaMO_3$ (M= Co, Cr, Mn, Ni, Fe) were among the first to be evaluated, but their low conductivity and poor sinterability do not make them suitable for use in SOFC

The introduction of alkaline earth elements such as Ca, Ba or Sr, improve the sinterability and conductivity of the materials. However, if these elements are introduced in excess, the cell deteriorates rapidly due to the formation of phases such as $SrCrO_4$, $CaCrO_4$ or $BaCrO_4$, consequence of the Cr released by the interconnector. Perovskite studies with low Sr content have also been carried out, with the general formula $La_{0.8}Sr_{0.2}MO_3$ (M= Co, Cu, Mn, Fe). These compounds have shown suitable sintering, electrical conductivity and TEC properties, as well as less Cr phase formation. These studies conclude that: (i) high amounts of cobalt increase the conductivity and improve the compatibility of the thermal expansion coefficients of the contact materials, (ii) large amounts of Mn favor the formation of Mn-Cr spinels with the Cr released by the interconnector, (iii) have a lower tendency to release Sr than the Co perovskites and (iv) is necessary to introduce small amounts of copper to achieve a high densification of the perovskites.

When the $(La, Sr)CoO_3$, $(La, Sr)(Co, Fe)O_3$ and $La(Ni, Fe)O_3$ phases have been used as contact layers on different ferritic alloys (Crofer22APU, E-Brite and 430), a diffusion of B-cations of (Ni, Fe, Co) perovskite has been observed towards the phase with spinel structure, formed from the transition metals present in the alloy, which provides a greater electrical conductivity to the oxide layer[65]. In addition, some studies have shown that perovskites such as $La(Ni, Co)O_{3-\delta}$, $La(Ni, Fe)O_{3-\delta}$ and $LaSr(Fe, Co)O_3$ show a lower reactivity with the protective spinel $MnCo_2O_4$[66,67]. For the construction of the cells of the present memory, when LSF was used as a cathode and a Crofer22 APU as interconnector, it was decided to use the contact layer $LaNi_{0.6}Fe_{0.4}O_3$ (LNF) together with the protective layer MCF.

---

63 Xin X., Liu L., Liu Y., Zhu Q., Novel perovskite-spinel composite conductive ceramics for SOFC cathode contact layer, *Int. J. Hydrog. Energy*. 43 (**2018**) 23036-23040.

64 Zhu J.H., Ghezel-Ayagh H., Cathode-side electrical contact and contact materials for solid oxide fuel cell stacking: A review, I. *J. Hydrog. Energy*. 42 (**2017**) 24278-24300.

65 Lacey R., Pramanick A., Lee J.C., Jung J., Jiang B., Edwards D.D., Naum R., Misture S.T., Evaluation of Co and perovskite Cr-blocking thin films on SOFC interconnects, *Solid State Ion*. 181 (**2010**) 1294-1302.

66 Wang F., Yan D., Zhang W., Chi B., Pu J., Jian L., $LaCo_{0.6}Ni_{0.4}O_{3-\delta}$ as cathode contact material for intermediate temperature solid oxide fuel cells, *Int. J. Hydrog. Energy*. 38 (**2013**) 646-651.

67 Morán-Ruiz A., Desarrollo de capas de contacto para su aplicación en SOFC/Development of contact coating for SOFC. Ph.D. thesis work, UPV/EHU, **2015**.

1.6. Métodos de síntesis

Se han realizado numerosos estudios en los últimos años con objeto de optimizar las condiciones de síntesis de compuestos, estableciendo los métodos de síntesis adecuados en función de la propiedad que se desee priorizar. En la Tabla 1.4. se recogen los procesos de preparación de compuestos más prometedores para este tipo de componentes según los criterios de coste, cualidades del polvo y aspectos ecológicos.

Tabla 1.4.- Comparación de los métodos de síntesis para la preparación de compuestos cerámicos.

Método de síntesis	Descripción	Ventajas	Inconvenientes
Cerámico convencional	Molienda Mezcla Tratamiento térmico de la mezcla precursora	• Fácil de reproducir • Bajo coste • No hay residuos acuosos ni gaseosos • Fácil de transferirse a otras composiciones	• Baja pureza • Baja homogeneidad • Estequiometría imprecisa
Sol-gel	Formación del gel a partir de soluciones de precursores catiónicos y orgánicos	• Polvo fino y homogéneo • Alta superficie activa	• Altas cantidades de compuestos orgánicos • Alto coste
Síntesis por combustión	Formación del gel a partir de nitratos y orgánicos (combustible). Combustión o calcinación/sinterizado	• Polvo fino y homogéneo • Alta área específica • Bajo coste	• Emisión de gases nitrosos • Tratamientos térmicos necesarios
Spray pirolisis	Descomposición térmica de solución acuosa de nitratos en gotas dentro de una cámara de reacción caliente	• Polvo fino y homogéneo	• Equipamiento costoso • Difícil de escalar a nivel de reproducción
Co-precipitación	Co-precipitación de los cationes correspondientes como carbonatos, hidróxidos u oxalatos. Calcinación/sinterización	• Polvo fino y homogéneo • Bajo coste	• Diferente solubilidad de los cationes • Problemas de desechos acuosos • Difícil de transferirse a otras composiciones

En esta investigación se ha optado por utilizar el método de síntesis de combustión, por su simplicidad y coste económico del equipo necesario, además de las propiedades del material obtenido, ideales para su aplicación en técnicas de sprayado.

1.6. Synthesis methods

Numerous studies have been carried out in recent years in order to optimize the conditions for the synthesis of compounds, establishing the appropriate synthesis methods depending on the property to be prioritized. Table 1.4. shows the processes for the preparation of the most promising compounds for this type of components according to the criteria of cost, powder qualities and ecological aspects.

Table 1.4.- Comparison of the synthesis methods for the preparation of ceramic powders.

Synthesis method	Description	Advantages	Inconvenient
Conventional ceramic	Grinding Mixture Heat treatment of the precursor mixture	• Easy reproducibility • Low cost • No aqueous or gaseous residues • Easy to transfer to other compositions	• Low purity • Low homogeneity • Imprecise stoichiometry
Sol-gel	Formation of the gel from cationic and organic precursors	• Fine and homogeneous powder • High active surface	• High quantity of organic compounds • High cost
Combustion synthesis	Formation of the gel from nitrates and organics (fuel). Combustion or calcination/sintering	• Fine and homogeneous powder • High active surface • Low cost equipment	• Emission of nitrous gases • Thermal treatments required
Spray pyrolysis	Thermal decomposition of aqueous solution of nitrates in droplets inside a hot reaction chamber	• Fine and homogeneous powder	• High cost equipment • Difficult to scale at reproduction level
Co-precipitation	Coprecipitation of the corresponding cation such as carbonates, hydroxides or oxalates Calcination/sintering	• Fine and homogeneous powder • Low cost	• Different solubility of cations • Water waste problems • Difficult to transfer to other compositions

In this memory, the combustion synthesis method has been chosen due to the simplicity and economic cost of the equipment, in addition to the properties of the powders that are obtained, ideal for their application in spraying techniques.

1.7. Configuraciones de las SOFC

Una sola celda de combustible estándar suele generar un voltaje de alrededor 0.7 V, por lo que es necesario conectar varias celdas entre sí para crear stacks (apilamientos de celdas) y obtener SOFC con voltajes a niveles más prácticos. Un stack está compuesto por unidades de celdas, interconectores y sellantes, que incluyen materiales metálicos y cerámicos[68]. Al ser todos los componentes sólidos, una celda SOFC se puede configurar de varias formas (tubular, planar, monolítica o dividida en segmentos), como puede observarse en la Figura 1.12.

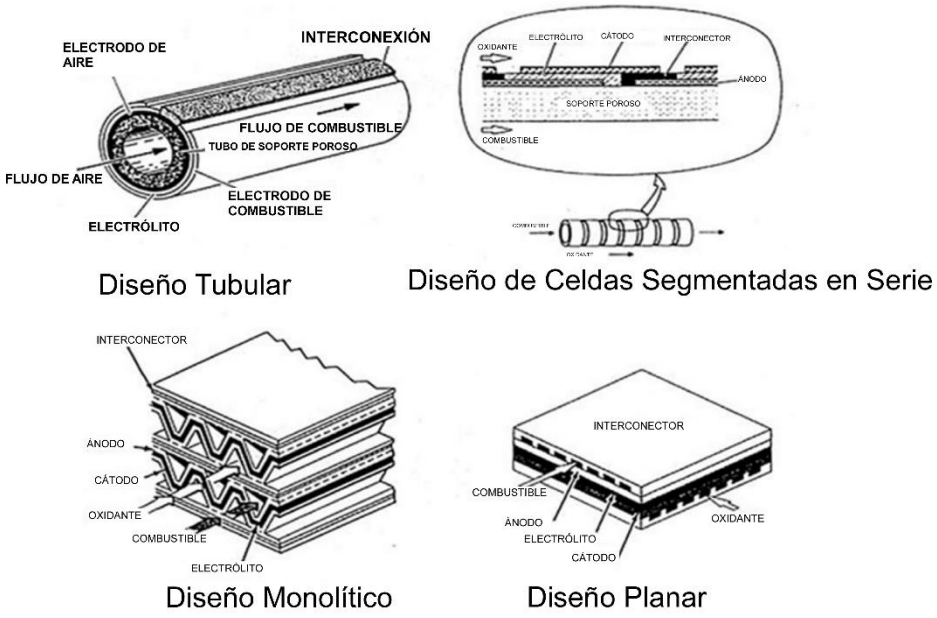

Figura 1.12.- Diseños de stacks SOFC.

Las dos geometrías mayormente utilizadas son la geometría tubular y la planar. Cada configuración tiene diferentes versiones de diseño. Por ejemplo, la geometría tubular puede ser tubular con final cerrado, un microtubo o un tubo aplanado (Figura 1.13.**)**. En el caso de la geometría planar, pueden ser discos circulares, platos rectangulares o con otras formas (Figura 1.14.). En el diseño planar, los electrodos y el electrolito se configuran como elementos planos y delgados, utilizando interconectores acanalados para la circulación de gases. Esta geometría, presenta como ventajas una mayor densidad de potencia; una resistencia eléctrica menor debida a la trayectoria de movimiento que atraviesan los electrones; el fácil montaje de los módulos y el procesado simple, que abarata los costes económicos de procesado; y una alta eficiencia. Sin embargo, debido al TEC cambiante de los componentes a altas temperaturas, el sellado del stack es difícil[69,70].

---

[68] Molla T.T., Kwok K., Frandsen H.L., Efficient modeling of metallic interconnects for thermo-mechanical simulation of SOFC stacks: Homogenized behaviors and effect of contact, *Int. J. Hydrog. Energy*. 41 (**2016**) 6433-6444.

[69] Dong S., Jung W., Rashid K., Kashimoto A., Design and numerical analysis of a planar anode-supported SOFC stack, *Renew. Energy*. 94 (**2016**) 637-650.

[70] Peksen M., A coupled 3D thermofluid–thermomechanical analysis of a planar type production scale SOFC stack, *Int. J. Hydrog. Energy*. 36 (**2011**) 11914-11928.

1.7. SOFC configurations

A standard single fuel cell usually generates a voltage of around 0.7 V, so it is necessary to connect several cells together to create stacks and obtain SOFCs with voltages at more practical levels. A stack is composed of units of cells, interconnectors and sealants, which include metallic and ceramic materials[68]. As all the components are solid, an SOFC cell can be configured in several ways (tubular, planar, monolithic or divided into segments), as can be seen in Figure 1.12.

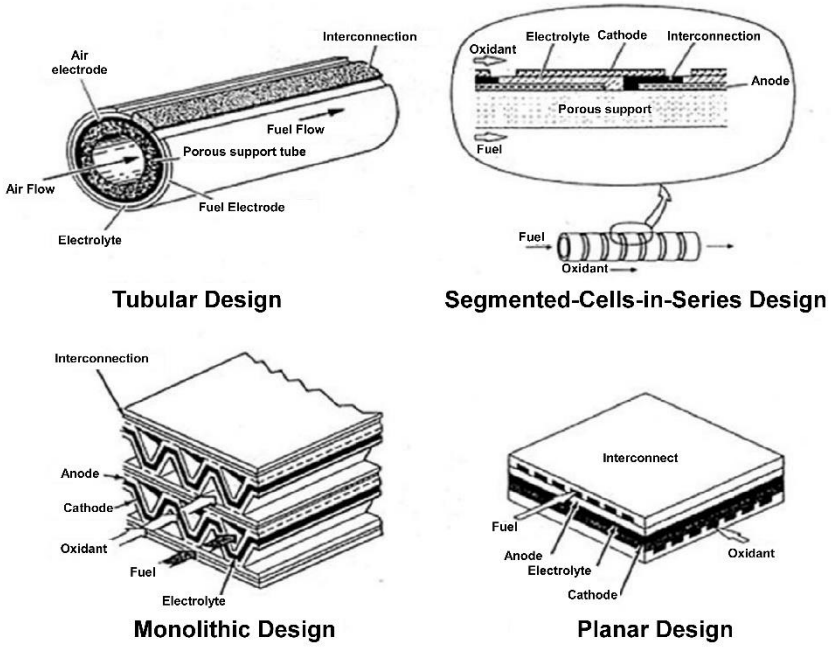

Figure 1.12.- SOFC stack designs.

The two most commonly used geometries are tubular and planar geometry. Each configuration has different design versions. For example, the tubular geometry can be tubular with closed end, a microtube or a flattened tube (Figure 1.13.). In the case of planar geometry, they can be circular disks, rectangular plates or with different shapes (Figure 1.14.). In the planar design, the electrodes and the electrolyte are configured as flat and thin elements, using grooved interconnectors for the circulation of gases. This geometry has as advantages a greater power density; a smaller electrical resistance due to the trajectory of the electrons go through; the easy assembly of the modules and the simple processing, which lowers the economic costs of processing; and high efficiency. However, due to the changing TEC of the components at high temperatures, the sealing of the stack is difficult[69,70].

---

[68] Molla T.T., Kwok K., Frandsen H.L., Efficient modeling of metallic interconnects for thermo-mechanical simulation of SOFC stacks: Homogenized behaviors and effect of contact, *Int. J. Hydrog. Energy*. 41 (**2016**) 6433-6444.

[69] Dong S., Jung W., Rashid K., Kashimoto A., Design and numerical analysis of a planar anode-supported SOFC stack, *Renew. Energy*. 94 (**2016**) 637-650.

[70] Peksen M., A coupled 3D thermofluid–thermomechanical analysis of a planar type production scale SOFC stack, *Int. J. Hydrog. Energy*. 36 (**2011**) 11914-11928.

Figura 1.13.- Configuraciones de celdas tubulares.

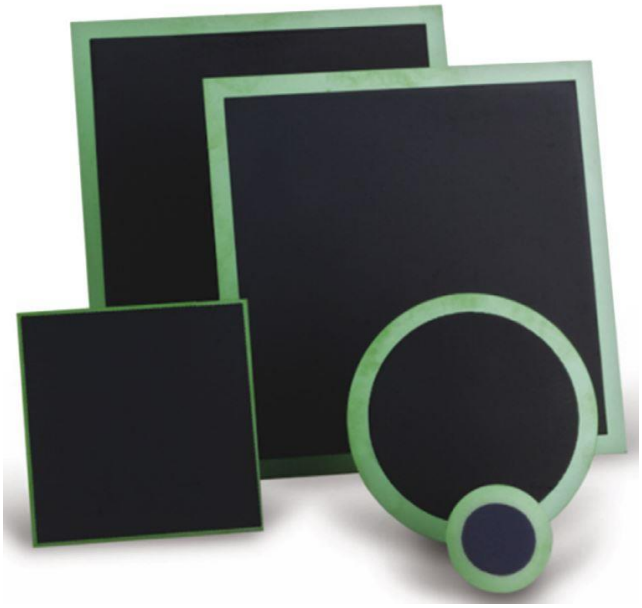

Figura 1.14.- Configuraciones de celdas planares.

En los diseños planares, la configuración de la celda puede clasificarse, según si está soportada sobre sí misma o sobre un soporte externo a la celda. Los soportes externos suelen ser los interconectores o substratos porosos (catódicos o anódicos) quienes dan estabilidad mecánica, permitiendo la creación de celdas más finas. En caso de estar soportada sobre sí misma, la celda puede ser de soporte electródico (ánodo o cátodo) o soporte electrolítico[71]. Para celdas de soporte electrodo, aunque surgen problemas de limitación de masa debido a las gruesas capas de electrodo, pueden proporcionar un rendimiento relativamente alto por el espesor reducido del electrolito. El diseño más popular es el de la celda soportada sobre ánodo. Sin embargo, las celdas soportadas sobre electrolito, tienen estructuras medianamente fuertes y son menos susceptibles a fallos mecánicos. En la Figura 1.15. pueden apreciarse las diferentes celdas planares en función del tipo de soporte.

[71] Mahmud L.S., Muchtar A., Somalu M.R., Challenges in fabricating planar solid oxide fuel cells: A review, *Renew. Sust. Energ. Rev*. 72 (**2017**) 105-116.

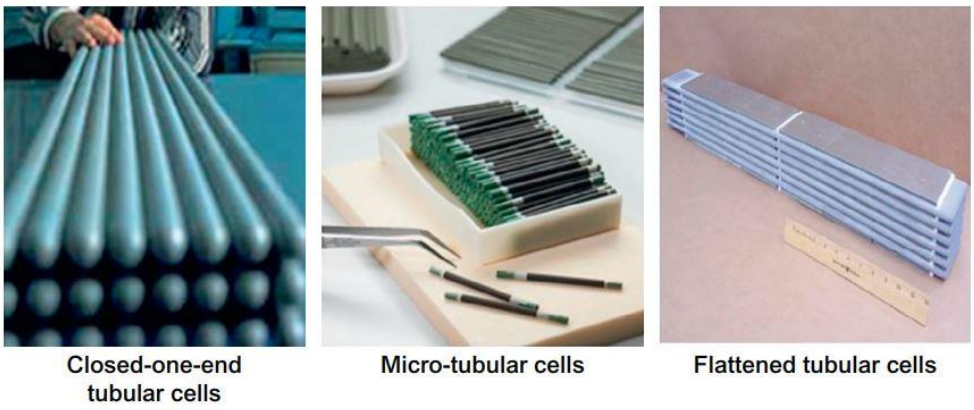

Figure 1.13.- Tubular cell configurations.

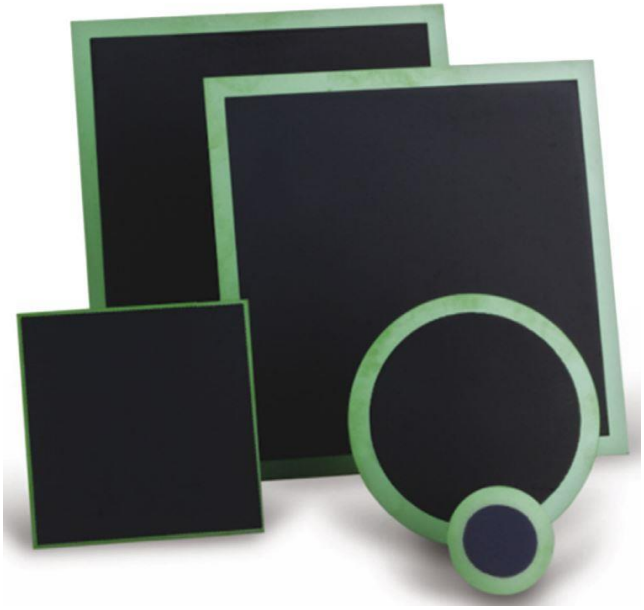

Figure 1.14.- Planar cell configurations.

In planar designs, the cell configuration can be classified according to whether it is supported on itself or on an external support to the cell. The external supports are usually the interconnectors or porous substrates (cathodic or anodic) that give mechanical stability, allowing the creation of finer cells. In case of being supported on itself, the cell can be of electrode supported (anode or cathode) or electrolyte supported[71]. For electrode supported cells, although problems of mass limitation arise due to the thick electrode layers, it can provide a relatively high efficiency due to the reduced thickness of the electrolyte. The most popular design is the anode supported cell. However, the electrolyte supported cells, have strong structures and are less susceptible to mechanical failures. In Figure 1.15. different planar cells can be seen depending on the type of support.

[71] Mahmud L.S., Muchtar A., Somalu M.R., Challenges in fabricating planar solid oxide fuel cells: A review, *Renew. Sust. Energ. Rev*. 72 (**2017**) 105-116.

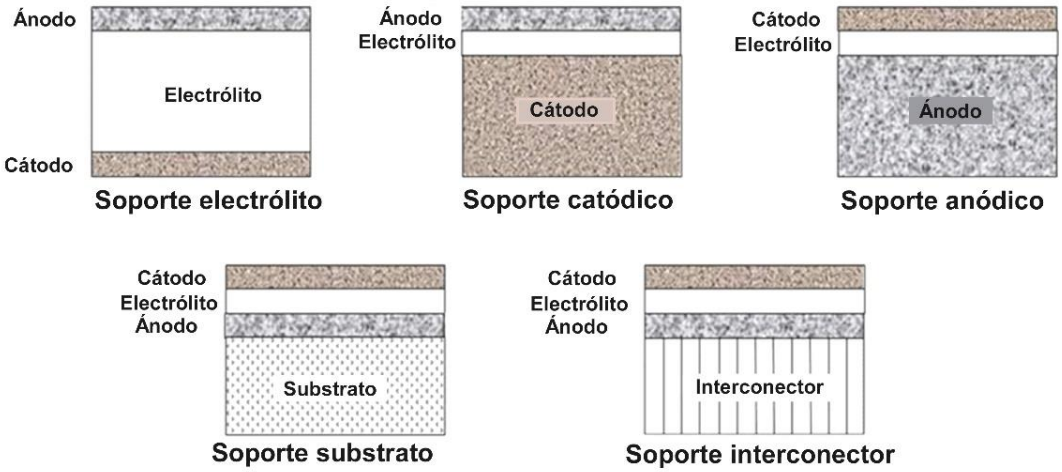

Figura 1.15.- Diferentes configuraciones de celda.

En las celdas tubulares, en cambio, el apilamiento de las mismas garantiza la estanqueidad de los conductos por los que circula el gas, no siendo necesario el empleo de sellantes entre celdas, por lo que es más estable a largos tiempos de operación. Sin embargo, como se ha mencionado anteriormente, es difícil diseñar mallas completas de forma axial y circunferencial porque crea trayectorias de corriente más largas que aumentan las pérdidas óhmicas. En comparación con las planas, las celdas tubulares también disminuyen las densidades de potencia[72,73].

Para la construcción de las celdas presentadas en esta memoria, se ha optado por la configuración planar, por tener un coste económico menor y un procesado mas simple que las configuraciones tubulares.

---

[72] Minh N.Q., Cell and stack design, fabrication and performance, High-temperature solid oxide fuel cells for the 21st century, *Fundamentals, design and applications*, 8 (**2016**) 255-282.

[73] Huang K., Singhal S.C., Cathode-supported tubular solid oxide fuel cell technology: A critical review, *J. Power Sources*. 237 (**2013**) 84-97.

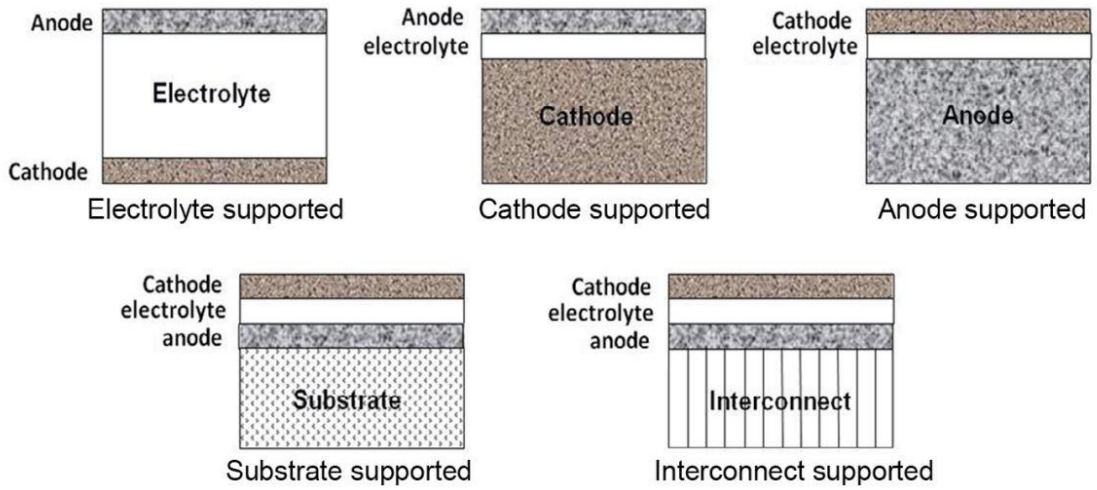

Figure 1.15.- Different SOFC cell configurations.

In tubular cells, on the other hand, the stacking of cells guarantees the tightness of the conduits through which the gas circulates, and the use of sealants between cells is not necessary, which is why it is more stable at long operating times. However, as mentioned above, it is difficult to design complete meshes axially and circumferentially because it creates longer current paths that increase the ohmic losses. In comparison with the flat ones, the power densities also decrease[72,73].

For the construction of the cells of this memory, the flat configuration has been chosen, for his lower economic cost and a simpler processing than the tubular configurations.

---

[72] Minh N.Q., Cell and stack design, fabrication and performance, High-temperature solid oxide fuel cells for the 21st century, *Fundamentals, design and applications*, 8 (**2016**) 255-282.

[73] Huang K., Singhal S.C., Cathode-supported tubular solid oxide fuel cell technology: A critical review, *J. Power Sources*. 237 (**2013**) 84-97.

1.8. Métodos de fabricación para SOFC

Las celdas SOFC se fabrican mayoritariamente por métodos de procesado cerámicos convencionales, como pueden ser el tape casting, el prensado o la serigrafía (screen printing); en conjunción con métodos de recubrimiento como el recubrimiento por spray o el recubrimiento por inmersión (dip coating), más comúnmente utilizados para la fabricación de electrodos.

1.8.1. Métodos convencionales de fabricación de soportes

El **tape casting** es el método de procesado cerámico frecuentemente utilizado para la fabricación de componentes SOFC. El proceso del tape casting consiste en la dispersión de un polvo cerámico en un disolvente, utilizando para ello un dispersante, un "binder" y un plastificante, los cuales se muelen conjuntamente para bajar la viscosidad. Esta mezcla, llamada "slurry", es añadida a una tolva que forma una película, tal y como se muestra en la Figura 1.16. El slurry pasa por debajo de una cuchilla llamada "doctor blade", que la aplana, dejándola como una cinta cerámica precocida. El espesor del slurry se puede controlar ajustando la cuchilla del doctor blade o a través de la viscosidad. A continuación, la cinta se pone a secar, haciendo que el disolvente se evapore. Esta técnica, se utiliza para hacer soportes homogéneos, por lo que es apta para el procesado de ánodos porosos y electrolitos. Su uso permite el cosinterizado de diferentes capas (ánodo y electrolito) a la vez, reduciendo de esta manera el tiempo y el coste económico del procesado[74].

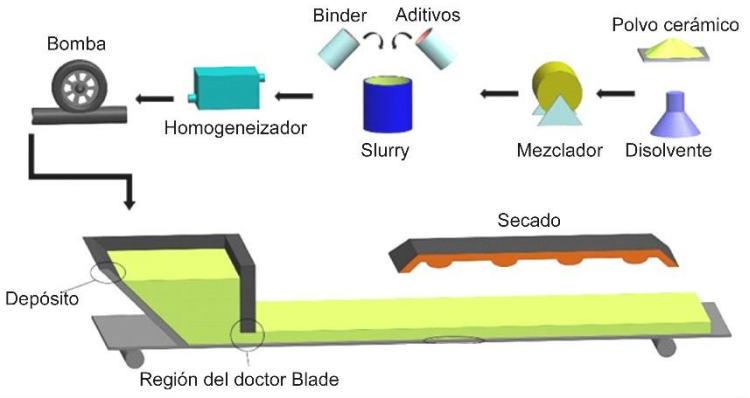

Figura 1.16.- Descripción esquemática del proceso de tape casting.

Como se ha mencionado anteriormente, los ingredientes necesarios para preparar un slurry son: los polvos cerámicos, un disolvente, un dispersante, un binder y un plastificante. Los polvos son los que más adelante formarán el cuerpo cerámico y, en función de sus características se determinará qué cantidades hay que añadir de cada ingrediente[75]. El parámetro más importante a determinar es su área superficial, que suele estar comprendido entre 5 y 10 m^2/g para su uso en tape casting.

---

[74] Jabbari M., Bulatova R., Tok A.I.Y., Bahl C.R.H., Mitsoulis E., Hattel J.H., Ceramic tape casting: A review of current methods and trends with emphasis on rheological behaviour and flow analysis, *Mater. Sci. Eng. B.* 212 (**2016**) 39-61.

[75] Nishihora R.K., Rachadel P.L., Quadri M.G.N., Hotza D., Manufacturing porous ceramic materials by tape casting: A review, *J. Eur. Ceram. Soc.* 38 (**2018**) 988-1001.

1.8. SOFC fabrication methods

The SOFC cells are mainly manufactured by conventional ceramic processing methods, such as tape casting, pressing or screen printing; in conjunction with coating methods such as spray coating or dip coating, most commonly used for the manufacture of electrodes.

1.8.1. Conventional methods for the manufacture of supports

Tape casting is the most frequently used ceramic processing method for the manufacture of SOFC components. The tape casting process consists in the dispersion of a ceramic powder in a solvent, using a dispersant, a binder and a plasticizer, which are ground together to low the viscosity. This mixture, called slurry, is added to a hopper that forms a film, as shown in Figure 1.16. The slurry passes under a blade called "doctor blade", which flattens it, leaving it as a precooked ceramic tape. The thickness of the slurry can be controlled by adjusting the positionof the doctor blade or through the viscosity. Then, the tape is dried, causing the evaporation of the solvent. This technique is used to make homogeneous supports, so it is suitable for the processing of porous anodes and electrolytes. Its use allows the cosinterization of different layers (anode and electrolyte) at the same time, reducing the time and the economic cost of processing[74].

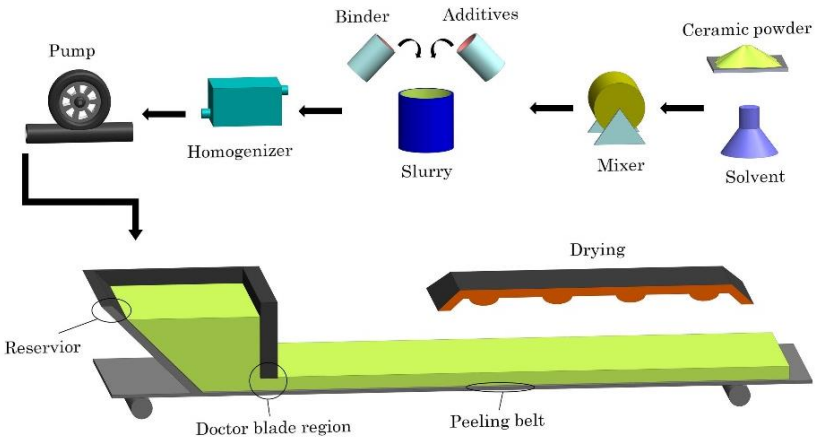

Figure 1.16.- Schematic description of tape casting process.

As already mentioned before, the ingredients needed to prepare a slurry are: ceramic powders, a solvent, a dispersant, a binder and a plasticizer. The powders are the ones that will later form the ceramic body and depending on their characteristics, it will be determined what quantities to add of each ingredient[75]. The most important parameter to determine is its surface area, which are usually between 5 and 10 m^2/g for use in tape casting.

---

[74] Jabbari M., Bulatova R., Tok A.I.Y., Bahl C.R.H., Mitsoulis E., Hattel J.H., Ceramic tape casting: A review of current methods and trends with emphasis on rheological behaviour and flow analysis, *Mater. Sci. Eng. B.* 212 (**2016**) 39-61.

[75] Nishihora R.K., Rachadel P.L., Quadri M.G.N., Hotza D., Manufacturing porous ceramic materials by tape casting: A review, *J. Eur. Ceram. Soc.* 38 (**2018**) 988-1001.

El disolvente es el líquido en el cual los polvos se dispersan homogéneamente. Los disolventes se eligen en función de los compuestos orgánicos que se vayan a utilizar, dado que tiene que ser capaz de disolver el dispersante, el binder y el plastificante a la vez.

Los dispersantes se utilizan para alterar las propiedades de la superficie de los polvos de manera que puedan quedarse suspendidas en el disolvente. Además, el dispersante cubre las partículas cerámicas de manera que asegura su suspensión dentro de la pasta evitando la aglomeración. En suspensiones acuosas, el dispersante ajusta el pH cambiando la carga de la partícula y generando repulsión iónica. En los disolventes orgánicos, se utilizan aditivos poliméricos, como pueden ser el éster de fosfato, el polietilen glicol y el ácido esteárico, que se adsorben en las partículas, separándolas estéricamente entre sí.

Los binders o aglomerantes, mantienen las partículas juntas en sistemas cerámicos una vez están en estado verde, proporcionando integridad mecánica. El aglomerante es el que determina la resistencia mecánica, la flexibilidad, la plasticidad, la durabilidad, la dureza y la capacidad de impresión de la cinta verde. El material aglomerante debe ser soluble en el solvente, capaz de alcanzar una viscosidad razonablemente baja en el sistema y quemarse sin dejar ningún residuo. Los aglutinantes típicos utilizados son el polivinil butiral, el alcohol polivinílico, la metil celulosa, el éster de poliacrilato y el politetrafluoroetileno. El plastificante se utiliza para mejorar el rendimiento del aglutinante en los sistemas cerámicos y se agrega para hacer que las cintas verdes sean más plásticas o flexibles.

El **screen printing** (serigrafia) es uno de los métodos más utilizados para la producción comercial de componentes SOFC planares, especialmente para el procesado de electrolitos y cátodos. Siendo similar al tape casting, el slurry se prepara con polvos cerámicos, disolventes y dispersantes/binder, teniendo en este caso una mayor viscosidad[76,77]. El polvo se mezcla en un disolvente con el aglomerante y se pasa a través de tres rodillos, que tienen como función eliminar los aglomerados duros de partículas en la tinta. Tras esto, un marco de serigrafía con un patrón de malla se coloca sobre el soporte y la pasta se deposita en el borde de la malla. Posteriormente, se utiliza una escobilla de goma para arrastrar la pasta y aplicar presión para que el slurry pase a través de la malla, consiguiendo capas de espesores de entre 10 y 200 µm encima de los soportes. Un esquema del screen printing se presenta en la Figura 1.17.

---

[76] Somalu M.R., Muchtar A., Daud W.R.W., Brandon N.P., Screen-printing inks for the fabrication of solid oxide fuel cell films: A review, *Renew. Sust. Energ. Rev*. 75 (**2017**) 426-439.

[77] Carrijo M.M.M., Lorenz H., Rambo C.R., Greil P., Travitzky N., Fabrication of Ti_3SiC_2-based pastes for screen printing on paper-derived Al_2O_3 substrates, *Ceram. Int*. 44 (**2018**) 8116-8124.

The solvent is the liquid in which the powders disperse homogeneously. The solvents are chosen depending on the organic compounds that are going to be used, since it has to be able to dissolve the dispersant, the binder and the plasticizer at the same time.

The dispersants are used to alter the surface properties of the powders so that they can remain suspended in the solvent. In addition, the dispersant covers the ceramic particles in such a way as to ensure their suspension within the paste avoiding agglomerations. In aqueous suspensions, the dispersant adjusts the pH by changing the charge of the particle and generating ionic repulsion. In organic solvents, polymeric additives are used, such as the phosphate ester, polyethylene glycol and stearic acid, which are adsorbed on the particles separating them sterically.

The binders keep the particles together in the ceramic system once they are in a green state, providing them mechanical integrity. The binder determines the mechanical strength, flexibility, plasticity, durability, hardness and printing capacity of the green belt. The binder material must be soluble in the solvent, capable of reaching a reasonably low viscosity in the system and burning without leaving any residue. Typical binders used are polyvinyl butyral, polyvinyl alcohol, methyl cellulose, polyacrylate ester and polytetrafluoroethylene. The plasticizer is used to improve binder performance in ceramic systems and is added to make green films more plastic or flexible.

Screen printing is one of the most widely used methods for the commercial production of planar SOFC components, especially for the processing of electrolytes and cathodes. Being similar to tape casting, the slurry is prepared with ceramic powders, solvents and dispersants/binder, having in this case a higher viscosity[76,77]. The powder is mixed in a solvent with the binder and passed through three rollers, which have the function of eliminating the hard agglomerates of particles in the ink. After this, a serigraphy frame with a mesh pattern is placed on the support and the paste is deposited on the edge of the mesh. Subsequently, a rubber brush is used to drag the paste and apply pressure so that the slurry passes through the mesh, obtaining layers of thickness between 10 and 200 μm above the supports. A screen printing scheme is presented in Figure 1.17.

[76] Somalu M.R., Muchtar A., Daud W.R.W., Brandon N.P., Screen-printing inks for the fabrication of solid oxide fuel cell films: A review, *Renew. Sust. Energ. Rev*. 75 (**2017**) 426-439.

[77] Carrijo M.M.M., Lorenz H., Rambo C.R., Greil P., Travitzky N., Fabrication of Ti_3SiC_2-based pastes for screen printing on paper-derived Al_2O_3 substrates, *Ceram. Int*. 44 (**2018**) 8116-8124.

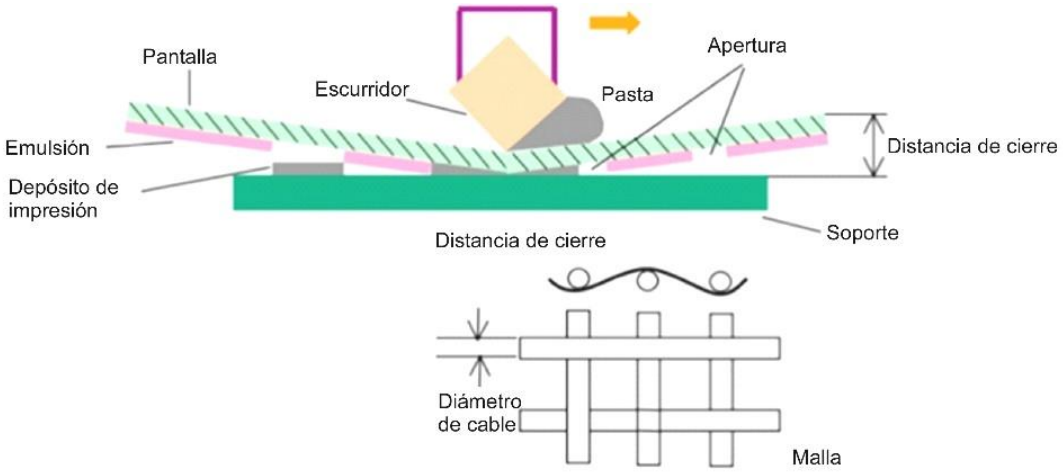

Figura 1.17.- Esquema del proceso de Screen printing.

Mientras que el componente orgánico ha de tener características similares a las anteriormente mencionadas, el disolvente tiene que poseer una baja viscosidad, gozar de poca tendencia a formar burbujas y tener una alta velocidad de evaporación[78,79]. Entre los disolventes que cumplen estas características se encuentran el agua, el etanol, el isopropanol o el tolueno. Entre los compuestos orgánicos frecuentemente utilizados se encuentran el ácido oléico, la glicerina o el polivinil butiral como dispersantes; y el polivinil alcohol, el polietilen glicol o el polivinil butiral como binder. Entre las variables que se pueden cambiar para el control de los parámetros de la capa se encuentran: el número de malla, los tiempos de impresión, las temperaturas y tiempos de sinterización y la reología de las tintas[80-82]. El número de malla varía en función del número de cables y aperturas que componen las mallas (cambiando la distancia lineal entre un cable y el cable adyacente) en una pulgada lineal.

El **gel casting** es un método para fabricar cuerpos cerámicos a través de una polimerización in-situ. La polimerización de monómeros uniformemente distribuidos crea polímeros entrelazados que actúan como un aglutinante que mantiene unidas las partículas cerámicas. El polímero que actúa como aglutinante representa el 2-5% del peso de los sólidos en seco. La adición de más monómeros puede generar la creación de poros interconectados dentro de la estructura cerámica.

---

[78] Pan J., Tonkay G., Quintero A., Screen printing process design of experiments for fine line printing of thick film ceramic substrates, *J. Electron. Manuf.* 9 (**1999**) 203-213.

[79] Phair J.W., Rheological analysis of concentrated zirconia pastes with ethyl cellulose for screen printing SOFC electrolyte films, J. Am. *Ceram. Soc*. 91 (**2008**) 2130-2137.

[80] Piao J., Sun K., Zhang N., Xu S., A study of process parameters of LSM and LSM–YSZ composite cathode films prepared by screen-printing, *J. Power Sources*. 175 (**2008**) 288-295.

[81] Hansch R., Chowdhury M.R.R., Menzler N.H., Screen printing of sol–gel-derived electrolytes for solid oxide fuel cell (SOFC) application, *Ceram. Int*. 35 (**2009**) 803-811.

[82] Zhao L., Huang X., Zhu R., Lu Z., Sun W., Zhang Y., Ge X., Liu Z., Su W., Optimization on technical parameters for fabrication of SDC film by screen-printing used as electrolyte in IT-SOFC, *J. Phys. Chem. Solids*. 69 (**2008**) 2019-2024.

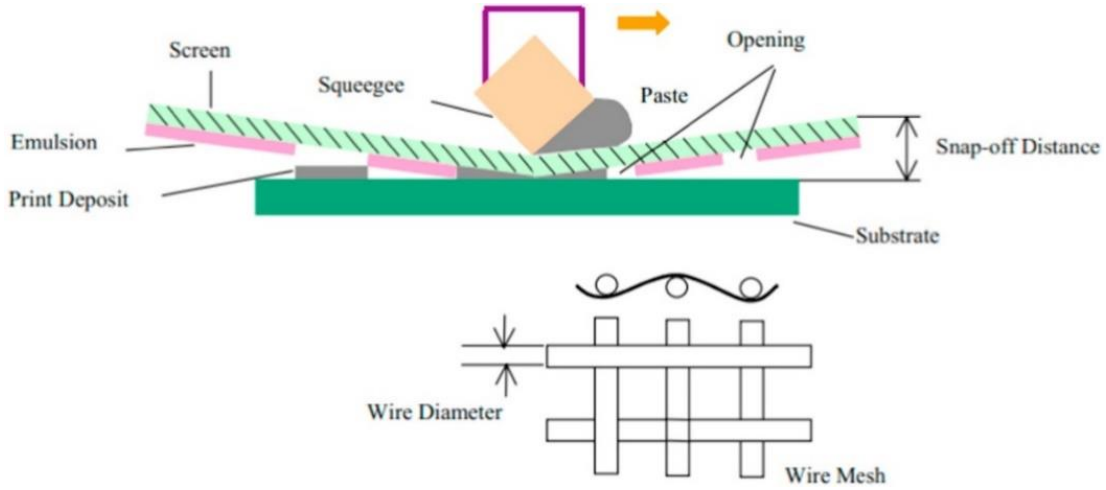

Figure 1.17.- Schematic of the screen printing process.

While the organic component has similar characteristics to those mentioned previously[78,79], the solvent must have a low viscosity, have little tendency to form bubbles and have a high evaporation rate. Among the solvents that meet these characteristics are water, ethanol, isopropanol or toluene. Among the frequently used organic compounds are oleic acid, glycerin or polyvinyl butyral as dispersants; and polyvinyl alcohol, polyethylene glycol or polyvinyl butyral as binder. Between the variables that can be changed for the control of the parameters of the layer are: the mesh number, the printing times, temperatures and sintering times and the rheology of the inks[80-82]. The mesh number varies according to the number of wires and openings that make up the meshes (changing the linear distance between a cable and the adjacent cable) in one linear inch.

Gel casting is a method to manufacture ceramic bodies through an in-situ polymerization. The polymerization of uniformly distributed monomers creates criss-crossed polymers that act as a binder that holds the ceramic particles together. The polymer that acts as a binder represents 2-5% of the weight of the dry solids. The addition of more monomers can generate the creation of interconnected pores within the ceramic structure.

---

[78] Pan J., Tonkay G., Quintero A., Screen printing process design of experiments for fine line printing of thick film ceramic substrates, *J. Electron. Manuf.* 9 (**1999**) 203-213.

[79] Phair J.W., Rheological analysis of concentrated zirconia pastes with ethyl cellulose for screen printing SOFC electrolyte films, J. Am. *Ceram. Soc*. 91 (**2008**) 2130-2137.

[80] Piao J., Sun K., Zhang N., Xu S., A study of process parameters of LSM and LSM–YSZ composite cathode films prepared by screen-printing, *J. Power Sources*. 175 (**2008**) 288-295.

[81] Hansch R., Chowdhury M.R.R., Menzler N.H., Screen printing of sol–gel-derived electrolytes for solid oxide fuel cell (SOFC) application, *Ceram. Int*. 35 (**2009**) 803-811.

[82] Zhao L., Huang X., Zhu R., Lu Z., Sun W., Zhang Y., Ge X., Liu Z., Su W., Optimization on technical parameters for fabrication of SDC film by screen-printing used as electrolyte in IT-SOFC, *J. Phys. Chem. Solids*. 69 (**2008**) 2019-2024.

En la Figura 1.18. se muestra cómo el monómero y el polvo cerámico se mezclan en un solvente para preparar la suspensión. Ésta toma la forma del molde cuando empieza la reacción de polimerización y aparecen los macro-geles. Finalmente, se aplica una cocción y una sinterización a alta temperatura[83].

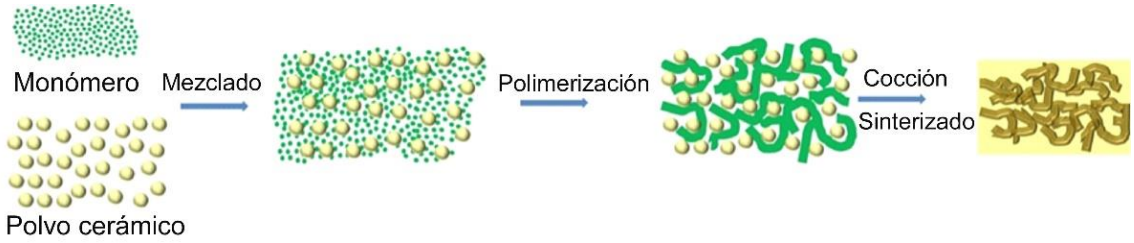

Figura 1.18.- Ilustración esquemática de la preparación de una microestructura macroporosa por gel-casting.

Como se ha mencionado con anterioridad, en función de la concentración del monómero, propiedades como la resistencia a la flexión o la conductividad electrónica pueden controlarse, puesto que están relacionadas con las partículas dispersas. Con esta técnica, las propiedades relacionadas con la porosidad pueden ser fácilmente controladas, como pueden ser la forma, la distribución y el tamaño de los poros, o el grosor y la densidad de las paredes. Además, este método tiene como ventajas su corto tiempo de duración, el bajo coste económico del equipamiento necesario, los altos rendimientos y la buena homogeneidad que produce una alta resistencia a la flexión.

El **prensado** a alta temperatura o a temperatura ambiente es una técnica simple, rápida, de bajo coste y reproducible, que se basa en aplicar presiones isostáticas o axiales durante unos minutos para comprimir los polvos dándoles la forma deseada. Tras aplicar la presión, se requiere de un sinterizado para consolidar la unión entre los polvos cerámicos.

El prensado axial se puede clasificar en prensado húmedo y seco. El prensado seco se ha utilizado extensamente para fabricar substratos para celdas planares, con espesores inferiores a 0.5 mm. Con esta técnica existe la posibilidad de utilizar el coprensado, aplicando presión a diferentes capas a la vez, ahorrando costes y tiempos de producción[84,85]. El prensado húmedo involucra el uso de la adición de un líquido, como puede ser el agua, a la hora de dar forma a los polvos. En la Figura 1.19. se muestra el esquema ilustrativo de la prensa axial.

---

83 Hedayat N., Du Y., Ilkhani H., Review on fabrication techniques for porous electrodes of solid oxide fuel cells by sacrificial template methods, *Renew. Sust. Energ. Rev*. 77 (**2017**) 1221-1239.

84 Liu Q., Dong X., Yang C., Ma S., Chen F., Self-rising synthesis of Ni–SDC cermets as anodes for solid oxide fuel cells, *J. Power Sources*. 195 (**2010**) 1543-1550.

85 Choi H., Cho G.Y., Cha S., Fabrication and characterization of anode supported YSZ/GDC bilayer electrolyte SOFC using dry press process, *Int. J. Precis, Eng, Manuf-Green Technol*. 1 (**2014**) 95-99.

In Figure 1.18. it is shown how the monomer and the ceramic powder are mixed in a solvent to prepare the suspension. This takes the shape of the mold when the polymerization reaction begins and the macro-gels appear. Finally, a high temperature cooking and sintering is applied[83].

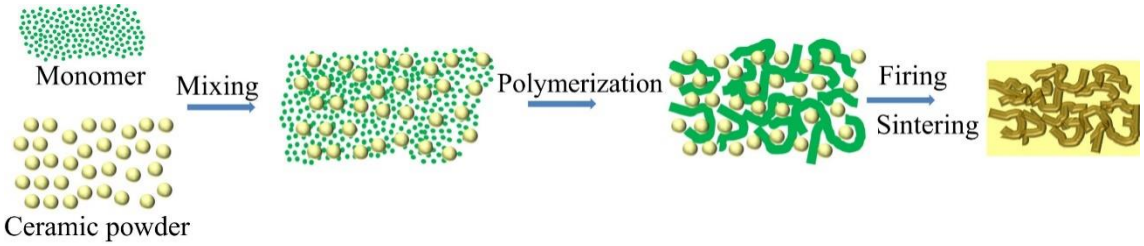

Figure 1.18.- Schematic illustration of preparing a macro-porous microstructure using gel-casting.

As mentioned above, depending on the concentration of the monomer, properties such as flexural strength or electronic conductivity can be controlled, since they are related to the dispersed particles. With this technique, properties related to porosity can be easily controlled, such as the shape, distribution and size of pores, or the thickness and density of the walls. In addition, this method has as advantages its short duration, the low economic cost of the equipment, the high yields and the good homogeneity that produces a high resistance to the flexion.

The **pressing** at high or room temperature is a simple, fast, low cost and reproducible technique, which is based on applying isostatic or axial pressures for a few minutes to compress the powders giving them the desired shape. After applying the pressure, a sintering is required to consolidate the bond between the ceramic powders.

The axial pressing can be classified as wet and dry pressing. The dry pressing has been extensively used to manufacture substrates for planar cells, with thicknesses less than 0.5 mm. With this technique there is the possibility of using co-pressing, applying pressure to different layers at the same time, saving costs and production times[84,85]. Wet pressing involves the use of the addition of a liquid, such as water, when shaping powders. The illustrative diagram of the axial press is shown in Figure 1.19.

---

[83] Hedayat N., Du Y., Ilkhani H., Review on fabrication techniques for porous electrodes of solid oxide fuel cells by sacrificial template methods, *Renew. Sust. Energ. Rev*. 77 (**2017**) 1221-1239.

[84] Liu Q., Dong X., Yang C., Ma S., Chen F., Self-rising synthesis of Ni–SDC cermets as anodes for solid oxide fuel cells, *J. Power Sources*. 195 (**2010**) 1543-1550.

[85] Choi H., Cho G.Y., Cha S., Fabrication and characterization of anode supported YSZ/GDC bilayer electrolyte SOFC using dry press process, *Int. J. Precis, Eng, Manuf-Green Technol*. 1 (**2014**) 95-99.

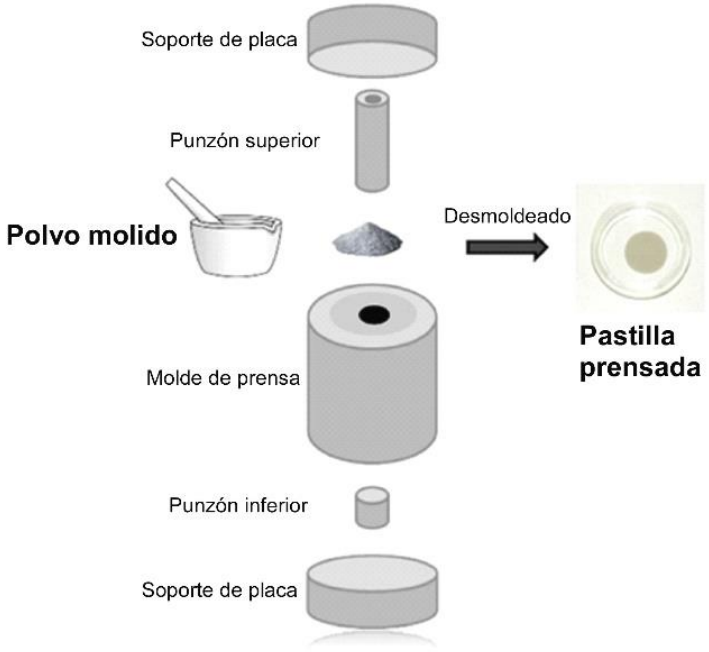

Figura 1.19.- Ilustración esquemática de la prensa axial.

En el prensado isostático, las presiones se aplican desde múltiples direcciones, dando uniformidad y capacidad de forma a la compactación, pudiendo aplicarse en frio o calor[86,87]. También se pueden fabricar soportes con configuración tubular mediante el prensado isostático[88]. La formación de poros se puede controlar en función del tamaño de partícula de los polvos de partida o de la presión.

1.8.2. Métodos de recubrimiento

El **dip-coating** (o revestimiento por inmersión) es una técnica en la que se deposita una capa delgada de manera uniforme utilizando una pasta. Esta pasta, al igual que en el tape casting y el screen printing, está formada por polvos cerámicos, un binder como el butiral de polivinilo, un dispersante como por ejemplo el éster de fosfato, y un disolvente como el etil metil quetona mezclado con isopropanol. Las ventajas principales del dip-coating es su sencillez y bajo coste, junto con la capacidad de controlar el espesor y la suavidad de la capa[89].

---

[86] Chen M., Kim B.H., Xu Q., Ahn B.G., Huang D.P., Fabrication and performance of anode-supported solid oxide fuel cells via slurry spin coating, *J. Membr. Sci*. 360 (**2010**) 461-468.

[87] Monash P., Pugazhenthi G., Saravanan P., Various fabrication methods of porous ceramic supports for membrane applications, *Rev. Chem. Eng*. 29 (**2013**) 357-383.

[88] Mahata T., Nair S.R., Lenka R.K., Sinha P.K., Fabrication of Ni-YSZ anode supported tubular SOFC through iso-pressing and co-firing route, *Int. J. Hydrog. Energy*. 37 (**2012**) 3874-3882.

[89] Jang I., Kim C., Kim S., Yoon H., Fabrication of thin films on an anode support with surface modification for high-efficiency intermediate-temperature solid oxide fuel cells via a dip-coating method, *Electrochim. Acta*. 217 (**2016**) 150-155.

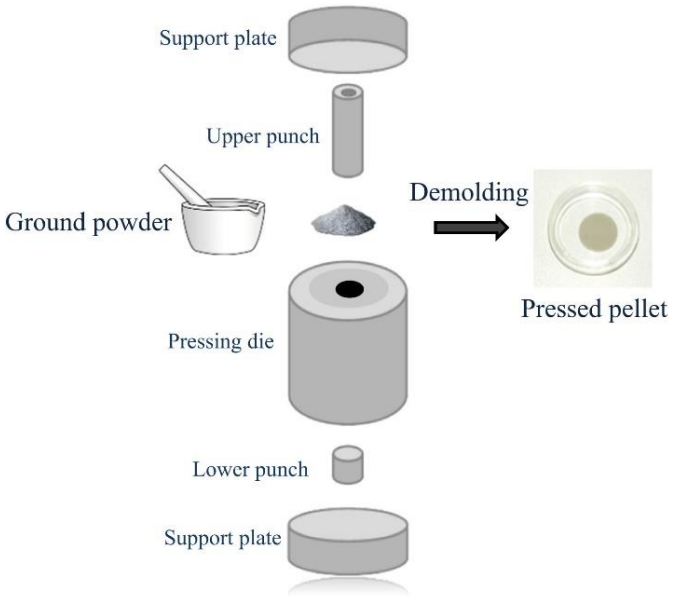

Figure 1.19.- Axial pressing schematic illustration.

In the isostatic pressing, the pressures are applied from multiple directions, giving uniformity and capacity of form to the compaction, being able to apply in cold or heat[86,87]. It is also possible to manufacture supports with a tubular configuration by means of isostatic pressing[88]. The pore formation can be controlled according to the particle size of the starting powders or the pressure.

1.8.2. Coating methods

Dip-coating is a technique in which a thin layer is deposited evenly using a paste. This paste, as in tape casting and screen printing, is made up of ceramic powders, a binder such as polivinyl butyral, a dispersant such as the phosphate ester, and a solvent such as ethyl methyl ketone mixed with isopropanol. The main advantages of dip-coating is its simplicity and low cost, together with the ability to control the thickness and smoothness of the layer[89].

---

[86] Chen M., Kim B.H., Xu Q., Ahn B.G., Huang D.P., Fabrication and performance of anode-supported solid oxide fuel cells via slurry spin coating, *J. Membr. Sci*. 360 (**2010**) 461-468.

[87] Monash P., Pugazhenthi G., Saravanan P., Various fabrication methods of porous ceramic supports for membrane applications, *Rev. Chem. Eng*. 29 (**2013**) 357-383.

[88] Mahata T., Nair S.R., Lenka R.K., Sinha P.K., Fabrication of Ni-YSZ anode supported tubular SOFC through iso-pressing and co-firing route, *Int. J. Hydrog. Energy*. 37 (**2012**) 3874-3882.

[89] Jang I., Kim C., Kim S., Yoon H., Fabrication of thin films on an anode support with surface modification for high-efficiency intermediate-temperature solid oxide fuel cells via a dip-coating method, *Electrochim. Acta*. 217 (**2016**) 150-155.

Los espesores mediante esta técnica varían entre 1 y 100 µm y se pueden controlar ajustando la velocidad a la que se retira el soporte, la viscosidad y la concentración de la pasta[90,91]. Tras secarse la capa puede repetirse el proceso hasta obtener el espesor adecuado. Para no aplicar la capa en zonas indeseadas, se hace uso de máscaras. En la Figura 1.20. está representado un esquema de la técnica.

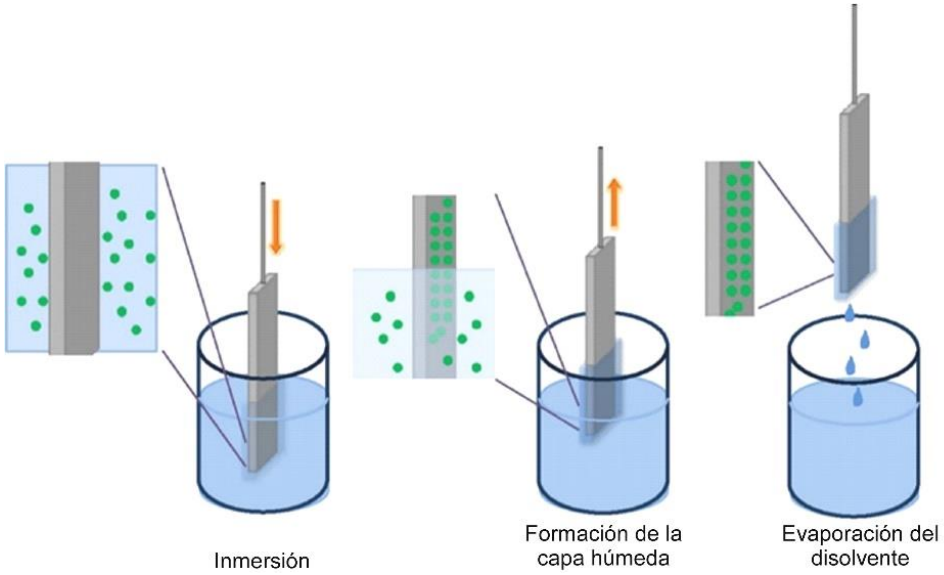

Figura 1.20.- Ilustración esquemática de la técnica dip-coating.

La técnica del **spin-coating** es una técnica en la que se deposita un "slurry" (una pasta) del mismo tipo que en las anteriores técnicas, en un soporte plano. En el soporte se crea una fuerza centrífuga con una rotación que extiende la solución uniformemente sobre el soporte, para posteriormente evaporar el disolvente. La velocidad angular (de entre 300 y 3000 rpm) del soporte giratorio da como resultado una velocidad radial que causa la dispersión de la suspensión, dejando una película delgada sobre el soporte[92]. En la Figura 1.21. se muestra el esquema de esta técnica.

---

90 Torabi A., Etsell T.H., Sarkar P., Dip coating fabrication process for micro-tubular SOFCs, *Solid State Ion*. 192 (**2011**) 372-375.

91 Gamble S., Fabrication-microstructure-performance relationships of reversible solid oxide fuel cell electrodes-review, *Mater. Sci. Technol*. 27 (**2011**) 1485-1497.

92 Jasinski P., Molin S., Gazda M., Petrovsky V., Anderson H.U., Applications of spin coating of polymer precursor and slurry suspensions for solid oxide fuel cell fabrication, *J. Power Sources*. 194 (**2009**) 10-15.

The thicknesses by this technique vary between 1 and 100 μm and can be controlled by adjusting the speed at which the support is removed, the viscosity and the concentration of the paste[90,91]. After drying the layer, the process can be repeated until the appropriate thickness is obtained. To avoid applying the layer in unwanted areas, masks are used. In Figure 1.20. is represented a scheme of the technique.

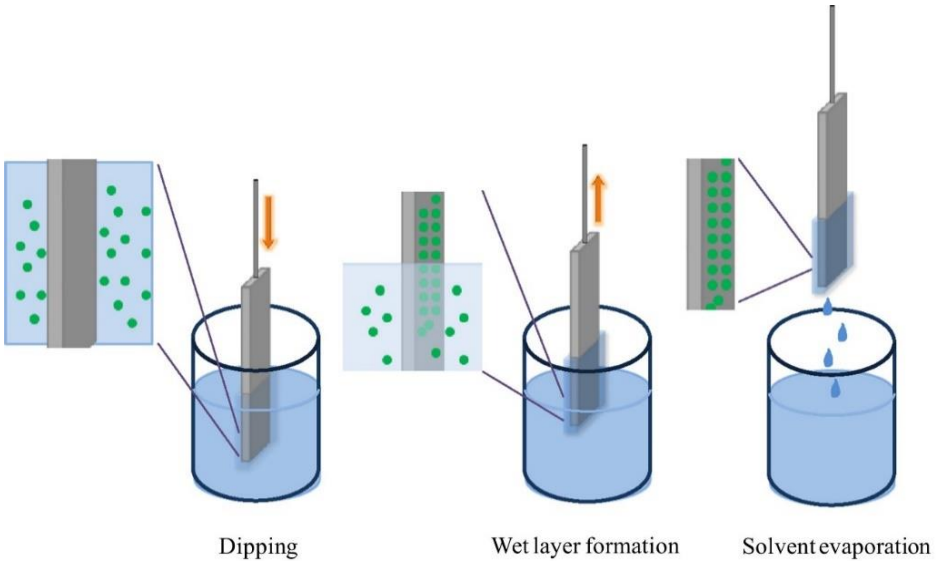

Figure 1.20.- Dip-coating technique schematic illustration.

The **spin-coating** technique is a technique in which a slurry of the same type as in the previous techniques is deposited on a flat support. In the support a centrifugal force is created with a rotation that extends the solution uniformly on the support, to later evaporate the solvent. The angular velocity (between 300 and 3000 rpm) of the rotating support results in a radial velocity that causes the dispersion of the suspension, leaving a thin film on the support[92]. The scheme of this technique is shown in Figure 1.21.

---

90 Torabi A., Etsell T.H., Sarkar P., Dip coating fabrication process for micro-tubular SOFCs, *Solid State Ion*. 192 (**2011**) 372-375.

91 Gamble S., Fabrication-microstructure-performance relationships of reversible solid oxide fuel cell electrodes-review, *Mater. Sci. Technol*. 27 (**2011**) 1485-1497.

92 Jasinski P., Molin S., Gazda M., Petrovsky V., Anderson H.U., Applications of spin coating of polymer precursor and slurry suspensions for solid oxide fuel cell fabrication, *J. Power Sources*. 194 (**2009**) 10-15.

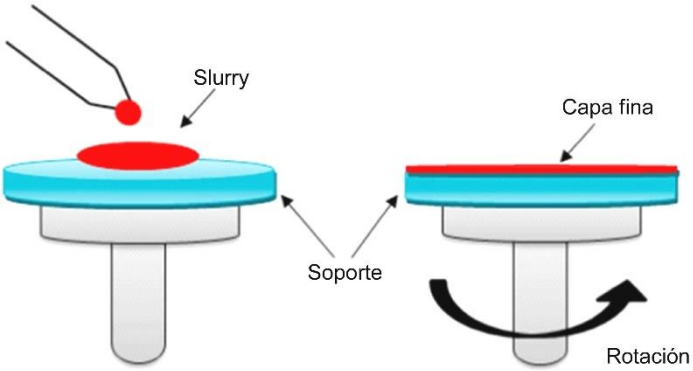

Figura 1.21.- Esquema del proceso spin-coating.

Las capas preparadas mediante la técnica de spin-coating son reproducibles y homogéneas, pudiendo aplicarse en diámetros mayores a 30 cm[93]. El espesor de la capa depende de la velocidad de rotación, la viscosidad y la concentración de la solución preparada[94]. Hay posibilidad de aumentar el espesor aumentando el número de ciclos, añadiendo cada vez más solución. Se trata de una técnica que requiere un equipamiento poco costoso económicamente y que puede comercializarse a gran escala. La microestructura de las capas puede, además, ser modificada cambiando las composiciones de la pasta[95], utilizándose de esta manera para la producción tanto de electrodos porosos como de electrolitos densos[96,97].

La técnica de **spray coating** (recubrimiento por spray) es una técnica simple y económica, con un alto control en la calidad y espesor de las capas depositadas. Extensamente utilizada en aplicaciones industriales, es una técnica considerada apropiada para depositar capas delgadas uniformemente sobre soportes de cualquier forma y tamaño. Esta técnica se ha utilizado para hacer capas de electrolito densas, capas anódicas y catódicas porosas. En la técnica de recubrimiento por spray, la suspensión creada recubre el soporte utilizando una pistola de spray, o en el caso del presente estudio, un aerógrafo. El requisito principal es que las suspensiones estén estables con sus partículas dispersas[98].

---

93 Norrman K., Ghanbari-Siahkali A., Larsen N., Studies of spin-coated polymer films, Annual reports on the progress of chemistry, Section C, *Phys. Chem*. 101 (**2005**) 174-201.

94 Wang J., Lü Z., Chen K., Huang X., Ai N., Hu J., Zhang Y., Su W., Study of slurry spin coating technique parameters for the fabrication of anode-supported YSZ Films for SOFCs, *J. Power Sources*. 164 (**2007**) 17-23.

95 Chen M., Kim B.H., Xu Q., Ahn B.G., Preparation and electrochemical properties of Ni–SDC thin films for IT-SOFC anode, *J. Membr. Sci*. 334 (**2009**) 138-147.

96 Xu X., Xia C., Huang S., Peng D., YSZ thin films deposited by spin-coating for IT-SOFCs, *Ceram. Int*. 31 (**2005**) 1061-1064.

97 Wang J., Lü Z., Huang X., Chen K., Ai N., Hu J., Su W., YSZ films fabricated by a spin smoothing technique and its application in solid oxide fuel cell, *J. Power Sources*. 163 (**2007**) 957-959.

98 Li W., Guan B., Yan J., Zhang N., Zhang X., Liu X., Enhanced surface exchange activity and electrode performance of $(La_{2-2x}Sr_{2x})(Ni_{1-x}Mn_x)O_{4+\delta}$ cathode for intermediate temperature solid oxide fuel cells, *J. Power Sources*. 318 (**2016**) 178-183.

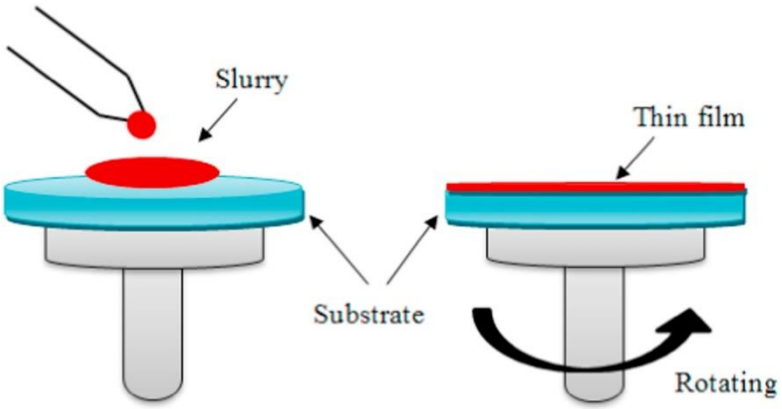

Figure 1.21.- Spin-coating process scheme.

The layers prepared by the spin-coating technique are reproducible and homogeneous and can be applied in diameters greater than 30 cm[93]. The thickness of the layer depends on the speed of rotation, the viscosity and the concentration of the prepared solution[94]. There is the possibility of increasing the thickness increasing the number of cycles, adding more and more solution. It is a technique that requires economically inexpensive equipment that can be commercialized on a large scale. The microstructure of the layers can also be modified by changing the compositions of the paste, thus being used for the production of both porous electrodes[95] and dense electrolytes[96,97].

The **spray coating** technique is a simple and economical technique, with a high control in the quality and thickness of the deposited layers. Widely used in industrial applications, it is considered an appropriate technique to deposit thin layers uniformly on supports of any shape and size. This technique has been used to make dense electrolyte layers or porous anodic and cathodic layers. In spray coating technique, the created suspension covers the support using a spray gun, or in the case of the present study, an airbrush. The main requirement are stable suspensions with their particles dispersed[98].

---

93 Norrman K., Ghanbari-Siahkali A., Larsen N., Studies of spin-coated polymer films, Annual reports on the progress of chemistry, Section C, *Phys. Chem*. 101 (**2005**) 174-201.

94 Wang J., Lü Z., Chen K., Huang X., Ai N., Hu J., Zhang Y., Su W., Study of slurry spin coating technique parameters for the fabrication of anode-supported YSZ Films for SOFCs, *J. Power Sources*. 164 (**2007**) 17-23.

95 Chen M., Kim B.H., Xu Q., Ahn B.G., Preparation and electrochemical properties of Ni–SDC thin films for IT-SOFC anode, *J. Membr. Sci*. 334 (**2009**) 138-147.

96 Xu X., Xia C., Huang S., Peng D., YSZ thin films deposited by spin-coating for IT-SOFCs, *Ceram. Int*. 31 (**2005**) 1061-1064.

97 Wang J., Lü Z., Huang X., Chen K., Ai N., Hu J., Su W., YSZ films fabricated by a spin smoothing technique and its application in solid oxide fuel cell, *J. Power Sources*. 163 (**2007**) 957-959.

98 Li W., Guan B., Yan J., Zhang N., Zhang X., Liu X., Enhanced surface exchange activity and electrode performance of $(La_{2-2x}Sr_{2x})(Ni_{1-x}Mn_x)O_{4+\delta}$ cathode for intermediate temperature solid oxide fuel cells, *J. Power Sources*. 318 (**2016**) 178-183.

La Figura 1.22. muestra la ilustración esquemática del recubrimiento por spray. Entre los parámetros que se pueden ajustar para controlar la reproducibilidad, están: la distancia entre la boquilla y el soporte, la viscosidad de la suspensión, la presión de atomización, la velocidad a la que se deposita o la geometría de la boquilla. En el caso de que la boquilla esté fija, se puede configurar la velocidad del soporte.

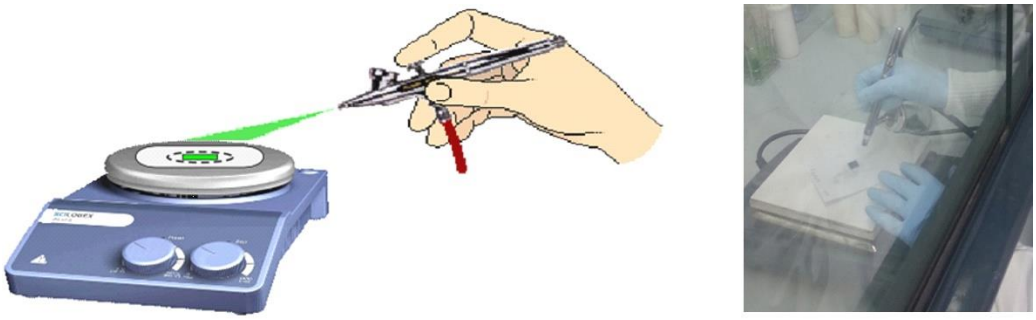

Figura 1.22.- Ilustración y fotografía del método de recubrimiento por spray.

En el presente trabajo, tras múltiples ensayos, se ha optado por utilizar el prensado como técnica de conformación de soportes, por tener previamente la capacidad de modelar los polvos precursores para su procesado mediante esta técnica. Para el recubrimiento de los soportes, a la hora de añadir los demás componentes que configuran las celdas, se ha optado por la técnica de spray coating, puesto que permite el control del espesor de las capas de manera sencilla; además de permitir la porosidad requerida para cada componente.

Figure 1.22. shows the schematic illustration of spray coating. Among the parameters that can be adjusted to control the reproducibility, are: the distance between the nozzle and the support, the viscosity of the suspension, the atomization pressure, the speed at which it is deposited or the geometry of the nozzle. In case the nozzle is fixed, the support speed can be set.

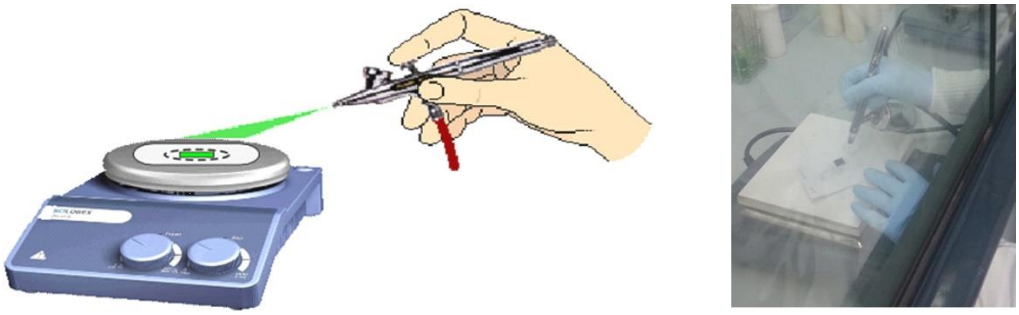

Figure 1.22.- Spray coating method illustration and photograph.

In the present work, after multiple trials, it has been decided to use the pressing technique for modelling the supports, having previously the ability to model the precursor powders for the processing by this technique. For the coating of the supports when adding the other components that make up the cells, the spray coating technique has been chosen, since it allows the control of the thickness of the layers in a simple way, as well as allowing the required porosity for each component.

1.9. Sistemas SOFC

Los sistemas de pilas de combustible de óxido sólido son muy prometedores para la producción económica de electricidad y calor en una variedad de aplicaciones comerciales, de generación industrial y de sistemas eléctricos. Las SOFC tienen el rango de potencial suficiente como para integrarse en un amplio número de aplicaciones, desde dispositivos portátiles de 20 W, hasta plantas de generación de energía de 700 kW. A continuación, se expondrán algunos de los sistemas comerciales o en fase de desarrollo que se pueden encontrar en uso hoy en día.

La empresa australiana CFCL (Ceramics Fuel Cells Limited) comercializa módulos de generación de electricidad con tecnología SOFC, denominados Gennex (Figura 1.23a.). Estos módulos de 1 kW, son capaces de operar todos los días del año, pudiéndose utilizar como generador independiente o para calderas, bombas de calor y sistemas de circulación domésticos. Aunque necesitan 13 h de arranque, su eficiencia está entre un 60 y 85%, sus emisiones a la atmósfera son de CO (<10 ppm) y agua, y tiene un peso de alrededor de 55 kg[99].

La empresa japonesa Osaka Gas Co., tras vender 70.000 unidades de sistemas de pilas de combustible de membrana polimérica, se animó a desarrollar sistemas con tecnología SOFC para uso residencial. Los sistemas Ene-Farm tipo S (Figura 1.23b.), son sistemas con una potencia de salida de hasta 700 W, de los que se espera un uso de más de 80.000 h (más de 10 años), con un ciclo de mantenimiento cada tres años y medio. Tiene una eficiencia de 90% utilizando el ciclo combinado, además de reducir drásticamente las emisiones de CO_2[100].

Para resolver problemas de suministro de energía para la fuerza de equipamiento rápido de los EEUU, Ultra Electronics AMI suministro en 2011 cinco unidades SOFC. Estas unidades, son sistemas portables de menos de 15 kg, capaces de funcionar en temperaturas entre -20 y 50 °C, proveen 300 W de potencia funcionando con propano, butano o gas licuado del petróleo (LPG) como combustible. Además, alcanzan tiempos de funcionamiento más largos que muchas baterías[101].

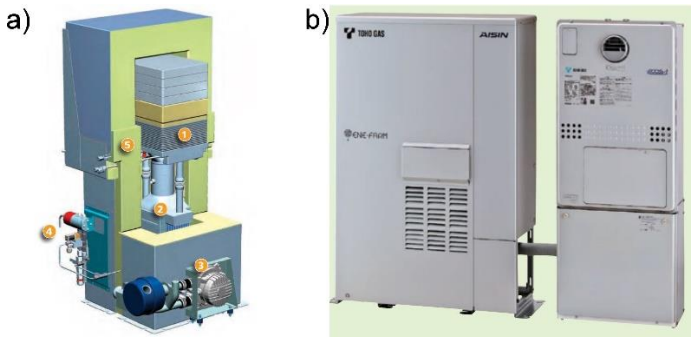

Figura 1.23.- Diferentes sistemas con tecnología SOFC. (a) sistema Gennex y (b) sistema Ene Farm tipo S.

[99] http://www.cfcl.com.au/Gennex/

[100] Japanese group unveils SOFC Ene-Farm residentia cogen unit, *Fuel cells bulletin*. 4 (**2012**) 4.

[101] Ultra Electronics AMI wins SOFC order for Rapid Equipping Force, *Fuel cells bulletin*. 7 (**2011**) 7.

1.9. SOFC systems

Solid oxide fuel cell systems are very promising for the economical production of electricity and heat in a variety of commercial, industrial generation and electrical systems applications. The SOFCs have a sufficient potential range to be integrated in a wide range of applications, from 20 W portable devices to 700 kW power generation plants. Next, some of the commercial or system developments that can be found in use today, will be exposed.

The Australian company CFCL (Ceramics Fuel Cells Limited) sells electricity generation modules with SOFC technology, called Gennex (Figure 1.23a.). These 1 kW modules are capable of operating every day of the year, and can be used as an independent generator or for boilers, heat pumps and domestic circulation systems. Although they need 13 h to start, their efficiency is between 60 and 85%, their emissions to the atmosphere are CO (<10 ppm) and water and has a weight of around 55 kg[99].

The Japanese company Osaka Gas Co., after selling 70,000 units of polymer membrane fuel cell systems, was encouraged to develop systems with SOFC technology for residential use. The Ene-Farm type S systems (Figure 1.23b.), are systems with an output power of up to 700 W and a use of more than 80,000 h (more than 10 years) is expected, with a cycle of maintenance every three and a half years. It has an efficiency of 90% using the combined cycle, reducing the CO_2 emissions[100].

To solve power supply problems for the rapid equipment force of the US, Ultra Electronics AMI supplied in 2011 five SOFC units. These units, are portable systems of less than 15 kg, capable of operating in temperatures between -20 and 50 ° C, providing 300 W of power that work using propane, butane or liquid petroleum gas (LPG) as fuel. In addition, they reach longer operating times than many batteries[101].

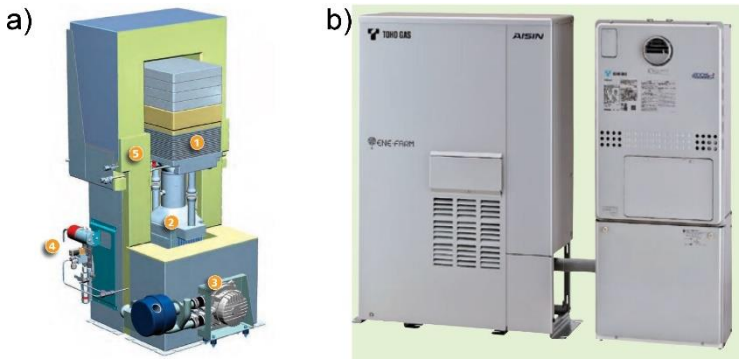

Figure 1.23.- Different SOFC technology systems. (a) Gennex system and (b) Ene-Farm type S system.

[99] http://www.cfcl.com.au/Gennex/

[100] Japanese group unveils SOFC Ene-Farm residentia cogen unit, *Fuel cells bulletin*. 4 (**2012**) 4.

[101] Ultra Electronics AMI wins SOFC order for Rapid Equipping Force, *Fuel cells bulletin*. 7 (**2011**) 7.

En noviembre de 2017, la empresa alemana New Enerday instaló el sistema Powertrailer EN 8000, como generador de energía del sistema de señales a nivel para el paso de trenes. Este sistema portátil, permite suministrar energía a zonas alejadas, independientes de la red eléctrica. En abril de 2018, esta misma empresa, como prueba experimental, puso en funcionamiento el equipo Powerbox en el campo base más al norte del monte Everest, a una altura aproximada de 5300 m (Figura 1.24.). Este equipo, suministró energía durante dos meses a una cabina de infrarrojos, permitiendo a los montañeros calentarse[104].

Figura 1.24.- Sistema Powerbox suministrando energía en un campo base del Everest.

Estos equipos, se encuentran entre los primeros sistemas completos en uso. Aunque todavía se encuentran en fase de desarrollo, se espera que en los próximos años se empiecen a comercializar, de manera más generalizada, al público.

[104] https://www.sunfire.de/en/applications/mobile-energy.

In November 2017, the German company New Enerday installed the Powertrailer EN 8000 system, as a power generator for the passage of trains signal system. This portable system allows energy to be supplied to remote areas, independent of the electricity network. In April 2018, this same company, as an experimental test, put the Powerbox equipment into operation in the north base camp of Mount Everest, at an approximate of 5300 m height (Figure 1.24.). This equipment, supplied power for two months to an infrared cabin, allowing mountaineers to warm up[104].

Figure 1.24.- Powerbox system supplying energy in a Everest base camp.

These devices are among the first complete systems in use. Although they are still in a development phase, it is expected that in the coming years they will begin to commercialize to the public more generally.

[104] https://www.sunfire.de/en/applications/mobile-energy.

1.10 Objetivos

El principal objetivo de este trabajo consiste en el desarrollo y el diseño de una pila de combustible de óxido sólido, teniendo en cuenta todos sus componentes y haciendo uso de materiales previamente sintetizados.

En este aspecto, se plantean retos a los que es necesario dar solución. Entre otros, resulta imprescindible el escalado de la síntesis de todos los compuestos que configuran una celda de combustible. Para ello, es necesaria la caracterización de todos los compuestos a gran escala, para posteriormente, demostrar la reproducibilidad de la síntesis comparando diferentes lotes entre sí. Entre las propiedades a caracterizar, cobran importancia tanto la composición, que se ha analizado mediante espectroscopia de emisión atómica de plasma acoplado por inducción (ICP-AES), la difracción de rayos-X (XRD) para determinar la estructura, así como la morfología, caracterizada mediante el microscopio electrónico de barrido (SEM) y un analizador de tamaños de partícula por dispersión laser (LD). Al mismo tiempo, otras propiedades a examinar han sido el coeficiente de expansión térmica de los compuestos sintetizados y su conductividad iónica y electrónica.

Otro reto a tener en cuenta es el procesado. En primer lugar, la estrategia seguida para abordar este desafío ha consistido en estudiar los polvos sintetizados utilizando una configuración simple, es decir, una configuración simétrica plana. Este estudio, ha permitido optimizar métodos de procesado como la molienda de las pastas de deposición, además de identificar diferentes espesores óptimos para las capas de cada componente. Además, de esta manera se ha podido simular una celda SOFC más real, permitiendo el desarrollo de un sistema, formado por un electrolito, una barrera, un cátodo y una capa de contacto.

Una vez optimizada esta estructura simétrica, con objeto de proceder al procesado de una celda de combustible funcional, se ha procedido a fabricar una celda asimétrica de soporte anódico, en el que se han depositado los mismos componentes estudiados en las anteriores secciones. El estudio de la conformación de estas celdas, ha permitido solventar la problemática surgida a causa de los coeficientes térmicos de expansión (TEC) de los componentes, utilizando para ello composites entre los componentes. Una vez optimizada esta estructura, con objeto de garantizar la funcionalidad de la celda, se han realizado medidas electroquímicas en ellas. Este trabajo finaliza con la aplicación de largos tiempos de operación sobre las celdas, en base a su respuesta electroquímica y su estabilidad a largos tiempos de operación.

1.10. Objectives

The main objective of this work is the development and design of a solid oxide fuel cell, taking into account all its components and making use of previously synthesized materials.

In this aspect, there are challenges that need to be solved. Among other things, it is essential to scale up the synthesis for all the compounds that compose a fuel cell. To do this, it is necessary to make a characterization of all the compounds on a large scale, to subsequently demonstrate the reproducibility of the synthesis by comparing different batches with each other. Among the properties to be characterized, the composition, which have been analysed by inductively coupled plasma- atomic emission spectroscopy (ICP-AES), the X-ray diffraction (XRD) to determine the structure, as well as the morphology, characterized by the scanning electron microscopy (SEM) and the particle size analyser by laser dispersion (LD), are important. At the same time, other properties to examine have been the thermal expansion coefficient of the synthesized compounds and their ionic and electronic conductivity.

Another challenge to take into account is the processing. First, the strategy followed to address this challenge has been to study the synthesized powders using a simple configuration, that is, a planar symmetric configuration. This study has allowed optimizing processing methods such as the grinding of the deposition pastes, in addition to identify different optimum thicknesses for the layers of each component. In addition, in this way it was possible to simulate a more real SOFC cell, allowing the development of a more complete fuel cell, formed by an electrolyte, a barrier, a cathode and a contact layer.

Secondly, once this symmetric structure was optimized, in order to proceed with the processing of a functional fuel cell, a asymmetric cell of anodic support was manufactured, in which the same components studied in the previous sections have been deposited. The study of the conformation of these cells, has allowed solving the problems arising from the thermal expansion coefficient (TEC) of the components, using composites between the components. Once this structure has been optimized, in order to guarantee the functionality of the cell, electrochemical measurements have been made on them. This work ends with the application of long operation times on the cells, based on their electrochemical response and their stability at long operating times.

2. CARACTERIZACIÓN DE LOS MATERIALES DE PARTIDA. ESCALANDO LA SÍNTESIS DE DIFERENTES COMPUESTOS.

Los resultados mostrados en el presente capítulo se han reflejado en una publicación científica indexada: **"Scalable synthetic method for SOFC compounds, Solid State Ionics, 313 (2017) 52-57"**. A su vez se ha optado por añadir como material adicional otros resultados expuestos en comunicaciones a congresos referentes a este capítulo.

Contribuciones a congresos:

- "Materiales para su aplicación en celdas SOFC", XXXV Bienal de la Real Sociedad Española de Química, 2015, A Coruña (España).

- "Celdas de pilas de óxido sólido. Avance en el procesado de materiales", XIV Congreso Nacional de Materiales, 2016, Gijón (España).

- "Scalable synthetic method for IT-SOFCs", 12th European SOFC & SOE Forum, 2016, Lucerna (Suiza).

2. CHARACTERIZATION OF THE STARTING MATERIALS. SCALATING THE SYNTHESIS OF DIFFERENT COMPONENTS.

The results shown in the present chapter have been exposed in an indexed scientific publication: **"Scalable synthetic method for SOFC compounds, Solid State Ionics, 313 (2017) 52-57"**. At the same time it has been chosen to include as additional material other statements exposed in communications to congresses referring to this chapter.

Congress contributions:

- "Materiales para su aplicación en celdas SOFC", XXXV Bienal de la Real Sociedad Española de Química, 2015, A Coruña (Spain).

- "Celdas de pilas de óxido sólido. Avance en el procesado de materiales", XIV Congreso Nacional de Materiales, 2016, Gijón (Spain).

- "Scalable synthetic method for IT-SOFCs", 12th European SOFC & SOE Forum, 2016, Lucerne (Switzerland).

Resumen del capítulo 2

El objetivo inicial planteado ha sido el conformado de una celda de pila de combustible de óxido sólido, por lo cual una de las primeras cuestiones ha sido determinar los materiales de partida y la manera de proceder para conseguirlos. Tras haber revisado las referencias bibliográficas disponibles hasta la fecha, se ha decidido sintetizar los compuestos a utilizar, dado que este procedimiento permite una mayor flexibilidad a la hora de modificar las características de los materiales de partida. La síntesis de los materiales aumenta las alternativas de hacer frente a los problemas que han podido surgir a la hora del procesado de los mismos. Estudios previos han señalado la importancia de las demandas en torno a las síntesis de los materiales para celdas de combustible de óxido sólido. Entre estas demandas, se encuentra que el método de síntesis ha de ser económico, rápido y energéticamente eficiente. Una de las técnicas de síntesis que más se adecúa a estas características es la síntesis por combustión, la cual requiere el uso de un oxidante (generalmente nitratos de metales) y un combustible orgánico (como pueden ser urea, glicina, etc.). La modificación de variables como pueden ser el índice combustible/nitrato o la temperatura a la que se produce la combustión, ha permitido controlar las propiedades de los compuestos finales. Por lo tanto, se ha decidido escoger este método de síntesis y determinar su escalabilidad, teniendo en cuenta las grandes cantidades de material que se han necesitado para llevar adelante la investigación.

Una vez se han establecido los criterios óptimos en la síntesis, se ha procedido con la selección de los materiales para la conformación de las celdas de combustible de óxido sólido. La configuración más simple de una celda de combustible consta de un ánodo, un electrolito y un cátodo. De entre los electrolitos, el compuesto que más extensamente se ha utilizado es la itria estabilizada con zirconio (YSZ). Junto con este electrolito, la literatura existente indica que el ánodo que mejor adherencia y compatibilidad demuestra tener con este electrolito, es el compuesto Ni-YSZ, el cual posee una alta actividad catalítica, una estabilidad mecánica y química apropiada y un coste moderado. Resultados previos obtenidos por el grupo de investigación han demostrado que, de entre los diferentes tipos de cátodos, el compuesto $La_{0.6}Fe_{0.4}SrO_3$ (LSF), es un buen candidato para su conformación dentro de la celda, demostrando un coeficiente de expansión térmico adecuado, junto con una actividad iónica mixta y una alta actividad catalítica para la reducción de oxígeno. Posteriormente, se ha establecido la necesidad del uso de diferentes barreras químicas entre el LSF e YSZ, para evitar la formación de fases no deseadas. Estudios previos realizados han indicado que el uso del material $Sm_{0.2}Ce_{0.8}O_{1.9}$ (SDC) como barrera entre el electrolito y el cátodo, ha sido una opción acertada. Diversas investigaciones han evidenciado que el uso de una capa de contacto compuesta por $LaNi_{0.6}Fe_{0.4}O_3$ (LNF), minimiza las pérdidas óhmicas entre el interconector y el cátodo, por lo que se ha decidido optar por el uso de este compuesto. Finalmente, con el fin de evitar la transferencia de Cr de interconectores formados por aceros inoxidables ferríticos para altas temperaturas, como puede ser el Crofer 22 APU, se ha utilizado una capa protectora como recubrimiento de interconector. Entre las opciones disponibles, se ha optado por utilizar el compuesto $MnCo_{1.9}Fe_{0.1}O_4$ (MCF), con el fin de prevenir la disminución del rendimiento y durabilidad de las pilas de combustible de óxido sólido.

Summary of the chapter 2

The initial objective of the project has been the formation of a solid oxide fuel cell, so one of the first questions has been to determine the starting materials to use and the way to proceed to achieve them. After reviewing the bibliographical references available to date, it has been decided to synthesize the compounds to be used, since this procedure allows greater flexibility when modifying the characteristics of the starting materials. The synthesis of the materials increases the alternatives of dealing with the problems that may have arisen when processing them. Previous studies have pointed out the importance of the demands around the synthesis of materials for solid oxide fuel cells. Among these demands, the synthesis method must be economical, fast and energy efficient. One of the synthetic techniques that best suits these characteristics is the combustion synthesis, which requires the use of an oxidant (usually nitrate metals) and an organic fuel (such as urea, glycine, etc.). The modification of variables such as the fuel/nitrate index or the temperature at which combustion takes place, have allowed to control the properties of the final compounds. Therefore, it has been decided to choose this synthesis method and determine its scalability, taking into account the large amounts of material that have been needed to carry out the research.

Once the optimum criteria have been established in the synthesis, it has been proceeded with the selection of the materials for the conformation of the solid oxide fuel cells. The simplest configuration of a fuel cell consists of an anode, an electrolyte and a cathode. Among the electrolytes, the most widely used compound is zirconium stabilized yttria (YSZ). Along with this electrolyte, the existing literature indicates that the anode with the best adherence and compatibility with this electrolyte is the Ni-YSZ compound, which has a high catalytic activity, a good mechanical and chemical stability and a moderate cost. Previous results obtained by the research group, have shown that among the different types of cathodes, the compound $La_{0.6}Fe_{0.4}SrO_3$ (LSF), is a good candidate for its conformation inside the cell, demonstrating a suitable thermal expansion compatibility, with a mixed ionic activity and a high catalytic activity for the reduction of oxygen. Subsequently, the need for the use of chemical barriers between the compound LSF and YSZ has been established, to avoid the formation of unwanted phases. Previous studies have indicate that the use of the compound $Sm_{0.2}Ce_{0.8}O_{1.9}$ (SDC) as a barrier between the electrolyte and the cathode is an appropriate option. Several studies have shown that the use of a contact layer composed of $LaNi_{0.6}Fe_{0.4}O_3$ (LNF), would minimize the ohmic losses between the interconnector and the cathode, so it has been decided to select the use of this compound. Finally, in order to avoid the transfer of Cr of high temperature ferritic stainless steel interconnects such as the Crofer 22 APU, a protective layer has been used as an interconnector coating. Among the available options, it has been decided to use the compound $MnCo_{1.9}Fe_{0.1}O_4$ (MCF), in order to prevent the decrease in performance and durability of solid oxide fuel cells.

Por último, se ha procedido a una caracterización de los compuestos sintetizados a gran escala por el método de combustión, comprobando su reproducibilidad y la adecuación de los parámetros críticos para su empleo mediante diversas técnicas de conformado. Para ello, la caracterización composicional se ha llevado a cabo a través de ICP-AES y fluorescencia de rayos X (XRF), la caracterización estructural mediante difracción de rayos X; y la microestructural mediante microscopía electrónica de barrido y análisis de tamaños de partícula. Adicionalmente, también se han realizado medidas de coeficiente de expansión térmica y de conductividad eléctrica de los compuestos.

Los resultados alcanzados demuestran que la síntesis es apropiada para obtener grandes cantidades de compuestos de manera fácil y adecuada para su posterior procesado en celdas de pilas de combustible.

Finally, a characterization of the synthesized compounds on a large scale by the combustion method has been proceeded, checking their reproducibility and their suitability and adequacy of the critical parameters for their use for various forming techniques. For this, the compositional characterization has been carried out through ICP-AES and X-ray fluorescence (XRF), the structural characterization by X-ray diffraction; and the microstructural by scanning electron microscopy and particle sizes analysis. Additionally, measurements of the thermal expansion coefficients and electrical conductivity of the compounds have also been made.

The results obtained shown synthetic procedures to get large quantities of compounds easily and adequately for further processing in fuel cell cells.

Scalable synthetic method for SOFCs compounds

Solid State Ionics 313 (2017) 52-57.

2.1. Introduction

New kind of necessities arises from the development of technologies used in synthesis of SOFC materials. These necessities are originated from the demands for appropriate industrial production procedure of SOFC materials, and the respective final products. Therefore, Combustion Synthesis (CS) is an important method for advanced SOFC component fabrication, because is economical, fast and energy efficient method[1].

CS methods can be classified into three categories, on the basis of the physical nature of reaction mixture itself: (i) flame synthesis or gas phase combustion, (ii) heterogeneous condensed phase combustion synthesis and (iii) solution combustion synthesis (SCS)[2]. Focusing in the SCS route, it consists of using an oxidizer (generally metal nitrates) and a suitable organic fuel (urea, citric acid, glycine, etc.)[3]. In this sense, SCS represents an exothermic method, which can provide enough energy to evaporate volatile impurities as well as, for the complete calcination of the products, producing, by a single step, pure nanostructured and homogeneous oxide powders with appropriate microstructural properties[4,5].

The major parameters such as fuel mixture and fuel/oxidizer ratio can play a significant role on phase formation of different compounds[6]. The choice of organic fuel (usually glycine, urea, sucrose, citric acid or alanine) is important because different fuels have different properties such as decomposition temperature, heat of combustion and reducing valence[7]. In general, a good fuel should react non violently, producing non toxic gases, an reacting as a complexant for metal cations[8].

---

1 Kumar A., Cross A., Manukyan K., Bhosale R.R., van den Broeke L.J.P., Miller J.T., Mukasyan A.S., Wolf E.E., Combustion synthesis of copper–nickel catalysts for hydrogen production from ethanol, *Chem. Eng. J*. 278 (**2015**) 46-54.

2 Wilberforce T., Alaswad A., Palumbo A., Dassisti M., Olabi A.G., Advances in stationary and portable fuel cell applications, *Int. J. Hydrog. Energ*. 41 (**2016**) 16509-16522.

3 Kumar A., Mukasyan A.S., Wolf E.E., Combustion synthesis of Ni, Fe and Cu multi-component catalysts for hydrogen production from ethanol reforming, *App. Catal. A-Gen*. 401 (**2011**) 20-28.

4 Vidal K., Morán-Ruiz A., Larrañaga A., Porras-Vázquez J.M., Slater P.R., Arriortua M.I., Characterization of $LaNi_{0.6}Fe_{0.4}O_3$ perovskite synthesized by glycine-nitrate combustion method, *Solid State Ion*. 269 (**2015**) 24-29.

5 González-Cortés S.L., Imbert F.E., Fundamentals, properties and applications of solid catalysts prepared by solution combustion synthesis (SCS), *App. Catal. A- Gen*. 452 (**2013**) 117-131.

6 Rasouli S., Moeen S.J., Combustion synthesis of Co-doped zinc oxide nanoparticles using mixture of citric acid–glycine fuels, *J. Alloy. Compd*. 509 (**2011**) 1915-1919.

7 Singh S., Singh D., $LaSrFeO_4$ nanopowders synthesized by different combustion methods: Effect of fuel/particle size, *Ceram. Int*. 42 (**2016**) 15725-15731.

8 Hajarpour S., Gheisari K., Raouf A.H., Characterization of nanocrystalline $Mg_{0.6}Zn_{0.4}Fe_2O_4$ soft ferrites synthesized by glycine-nitrate combustion process, *J. Magn. Magn. Mater*. 329 (**2013**) 165-169.

As consequence, glycine was selected as the fuel since it is more cost-effective, has demonstrate that can be conveniently employed to prepare ceramic powders and its combustion heat (-3.24 kcal·g^{-1}) is greater than that of urea (-2.98 kcal·g^{-1}) or citric acid (-2.76 kcal·g^{-1}), being more stronger complexing agent and forming stable gels in nitrate solution[8-11]. The advantages of the glycine nitrate combustion process are relatively low cost, fast heating rates, short reaction times, high composition homogeneity and high energy efficiency[12].

The commonly used materials for fuel cell devices are porous cermets of metallic NiO-$(ZrO_2)_{0.92}$ $(Y_2O_3)_{0.08}$ (NiO-YSZ) as an anode and dense $(ZrO_2)_{0.92}$ $(Y_2O_3)_{0.08}$ (YSZ) layers as electrolyte[13,14]. According to other authors and to our previous studies, $La_{0.6}Sr_{0.4}FeO_3$ (LSF40) has demonstrated to be a practical cathode using $Sm_{0.2}Ce_{0.8}O_{1.9}$ (SDC) as barrier between cathode and electrolyte, avoiding poorly conducting secondary phases which increases contact resistance of the system[15,16].

Earlier studies have concluded that the use of $LaNi_{0.6}Fe_{0.4}O_3$ (LNF60) cathode contact layers improves electrons transfer through the contact interface from interconnect to active cathode layer[17]. In addition, $MnCo_{1.9}Fe_{0.1}O_4$ (MCF10) can be used as an interconnect protective coating to avoid the Cr poisoning to the cathode[18].

---

[9] Boobalan K., Varun A., Vijayaraghavan R., Chidambaram K., Mudali U.K., Facile, scalable synthesis of nanocrystalline calcium zirconate by the solution combustion method, *Ceram. Int*. 40 (**2014**) 5781-5786.

[10] da Silva C.A., Ribeiro N.F.P., Souza M.M.V.M., Effect of the fuel type on the synthesis of yttria stabilized zirconia by combustion method, *Ceram. Int*. 35 (**2009**) 3441-3446.

[11] Lenka R.K., Mahata T., Sinha P.K., Tyagi A.K., Combustion synthesis of gadolinia-doped ceria using glycine and urea fuels, *J. Alloy Compd*. 466 (**2008**) 326-329.

[12] Tuichai W., Thongbai P., Amornkitbamrung V., Yamwong T., Maensiri S., $Na_{0.5}Bi_{0.5}Cu_3Ti_4O_{12}$ nanocrystalline powders prepared by a glycine–nitrate process: Preparation, characterization, and their dielectric properties, *Microelectron. Eng*. 126 (**2014**) 118-123.

[13] Monzón H., Laguna-Bercero M.A., Larrea A., Arias B.I., Várez A., Levenfeld B., Design of industrially scalable microtubular solid oxide fuel cells based on an extruded support, *Int. J. Hydrog. Energy*. 39 (**2014**) 5470-5476.

[14] Wang Z., Huang X., Lv Z., Zhang Y., Wei B., Zhu X., Wang Z., Liu Z., Preparation and performance of solid oxide fuel cells with YSZ/SDC bilayer electrolyte, *Ceram. Int*. 41 (**2015**) 4410-4415.

[15] Arregui A., Rodriguez-Martinez L.M., Modena S., Bertoldi M., van Herle J., Sglavo V.M., Stability of ferritic perovskite cathodes in anode-supported solid oxide fuel cells under different processing and operation parameters, *Electrochim. Acta*. 58 (**2011**) 312-321.

[16] Shimura K., Nishino H., Kakinuma K., Brito M.E., Uchida H., Effect of samaria-doped ceria (SDC) interlayer on the performance of $La_{0.6}Sr_{0.4}Co_{0.2}Fe_{0.8}O_{3-\delta}$/SDC composite oxygen electrode for reversible solid oxide fuel cells, *Electrochim. Acta*. 225 (**2017**) 114-120.

[17] Morán-Ruiz A., Vidal K., Laguna-Bercero M.Á., Larrañaga A., Arriortua M.I., Effects of using $(La_{0.8}Sr_{0.2})_{0.95}Fe_{0.6}Mn_{0.3}Co_{0.1}O_3$ (LSFMC), $LaNi_{0.6}Fe_{0.4}O_{3-\delta}$ (LNF) and $LaNi_{0.6}Co_{0.4}O_{3-\delta}$ (LNC) as contact materials on solid oxide fuel cells, *J. Power Sources.* 248 (**2014**) 1067-1076.

[18] Miguel-Pérez V., Martínez-Amesti A., Nó M.L., Larrañaga A., Arriortua M.I., The effect of doping $(Mn,B)_3O_4$ materials as protective layers in different metallic interconnects for solid oxide fuel cells, *J. Power Sources*. 243 (**2013**) 419-430.

The present work presents the adaptation of an existing lab-scale cell components production method to an industrially ready and easily scalable method using glycine-nitrate combustion synthesis. After the synthesis optimization, up to 12 g of sample have been obtained in each batch. The synthesized components were: anodes, electrolytes, interlayers, cathodes, contact layers and interconnect protective coatings. Therefore, results of a complete characterization study have been reported including compositional identification of phases, crystal structure, electrical and ionic conductivity, thermal expansion and morphological structure, showing a good reproducibility in all the cases.

2.2. Experimental

2.2.1. Powder preparation

All the SOFC component powders were prepared by a glycine nitrate process (GNP), as shown in the supplementary material (Figure 2.S1.). Stoichiometric amounts of the corresponding metal nitrates, which were chosen because their low price under 2.90 € per gram, were dissolved in deionized water (see Table 2.1.), to yield 36 g of the final oxide powders.

Table 2.1.-Summary of used starting materials.

COMPOUND	STARTING MATERIALS*
$La_{0.6}Sr_{0.4}FeO_3$ (LSF40)	$La(NO_3)_3{\cdot}6H_2O$ (>99%), $Sr(NO_3)_2$ (>99%) and $Fe(NO_3)_2{\cdot}9H_2O$ (>98%)
$LaNi_{0.6}Fe_{0.4}O_3$ (LNF60)	$La(NO_3)_3{\cdot}6H_2O$ (>99%), $Ni(NO_3)_2{\cdot}6H_2O$ (>98.5%) and $Fe(NO_3)_2{\cdot}9H_2O$ (>98%)
$MnCo_{1.9}Fe_{0.1}O_4$ (MCF10)	$Mn(NO_3)_2{\cdot}xH_2O$ (>98%), $Co(NO_3)_2{\cdot}6H_2O$ (>98%) and $Fe(NO_3)_3{\cdot}9H_2O$ (>98%)
$Sm_{0.2}Ce_{0.8}O_{1.9}$ (SDC)	$Sm(NO_3)_3{\cdot}6H_2O$ (>99.9%) and $Ce(NO_3)_3{\cdot}6H_2O$ (>99%)
$Ni_{0.3}O$-$(ZrO_2)_{0.92}(Y_2O_3)_{0.08}$ (NiO-YSZ)	$Y(NO_3)_3{\cdot}6H_2O$ (>99.9%), $ZrO(NO_3)_2{\cdot}xH_2O$ (>99%) and $Ni(NO_3)_2{\cdot}6H_2O$ (>98.5%)
$(ZrO_2)_{0.92}(Y_2O_3)_{0.08}$ (YSZ)	$Y(NO_3)_3{\cdot}6H_2O$ (>99.9%) and $ZrO(NO_3)_2{\cdot}xH_2O$ (>99%)

* All the starting materials used were from Sigma-Aldrich. See Figure 2.S2. (supplementary material) for more information.

For all compositions glycine was then added into the nitrate aqueous solution (glycine-nitrate stoichiometric solution) while stirring. The resulting viscous liquid was auto-ignited by heating up to approximately 455 ºC. The obtained powders were calcined between 600 and 800 °C for 5 h to remove carbon residues. In the case of LSF40, LNF60 and MCF10, the resulting powders were pelletized and calcined in air at 950 °C for 8 h, which after several test, demonstrated to be the most economical treatment conditions to obtain pure samples.

2.2.2 Characterization techniques

Compositional analysis was performed for all the prepared samples to confirm that the expected elemental composition was achieved. The metal contents of Mn, Co, Fe, Sr, Ni and La, were determined by inductively coupled plasma atomic emission spectroscopy (ICP-AES) on a Horiba Yobin Yvon Activa spectrophotometer. Because their difficulty to dissolve, the analysis of Sm, Ce, Zr and Y contents were carried out with X-ray fluorescence (XRF) on a Fischercope X-ray XDAL.

Room-temperature X-ray diffraction (XRD) data were recorded using an integration time of 10 s/0.026 ° step in the 5<2σ<70 ° range with a Philips X´Pert-PRO X-ray diffractometer equipped with a secondary beam graphite monochromated and Cu-Kα radiation.

The morphologies of the powder samples were observed using a scanning electron microscope (JEOL JSM-7000F). Secondary electron images were taken at 20 kV and $1.1 \cdot 10^{-11}$ A, using a working distance of 8 mm. Particle size distribution of the powders was carried out using a Mastersizer particle size analyzer (Malvern Instruments). All the measurements were done using isopropanol as dispersion medium and using ultrasounds to break up the agglomerates that are formed.

To measure bulk conductivity and thermal expansion coefficient (TEC), pellets of the powders were sintered between 1050 and 1350 °C, and then, cutted in 1×3×7 mm bars. The bulk density of each sample was calculated by measuring the mass and the dimensions of the bars. The samples had a density of around 75% of the theoretical (X-ray) density.

DC conductivity measurements were performed in air by the four-point DC method using a VSP potentiostat controlled by PC using Lab Windows/CVI field point system.

Electrical contacts were made using Pt wires and Pt paste placed over whole end faces ensuring a homogeneous current flow. Voltage contacts were made as small as possible to avoid any disturbance of the contacts on the current flow. Measurements were performed from 450 °C to 950 °C. The conductivity (σ) was determined from a set of V–I values by taking $\sigma = 1/\rho = L / A \times dI / dV$, where L is the distance between voltage contacts and A is the sample cross section. Finally, TEC measurements were carried out from room temperature to 950 °C in air with a heating rate of 5 °C/min by using a Unitherm Model dilatometer.

2.3. Results and discussion

2.3.1. Elemental composition

In order to be able to study the reproducibility of large-scale synthesis of used compounds, three different synthesis have been perform for each compound, labeling as batch the 12 grams of product gained in each synthesis. The nominal composition of the samples and the results from the ICP-AES analysis are shown in Table 2.2.

Table 2.2.- Summary ICP results for LSF (La, Sr, Fe), LNF (La, Ni, Fe) and MCF (Mn, Co, Fe).

	Sr	La	Fe	Ni	Mn	Co
LSF40 (Batch 1)	0.41(1)	0.58(2)	1.02(3)	---	---	---
LSF40 (Batch 2)	0.40(1)	0.58(2)	1.01(3)	---	---	---
LSF40 (Batch 3)	0.41(1)	0.58(2)	1.02(3)	---	---	---
LNF60 (Batch 1)	---	0.98(9)	0.41(6)	0.61(8)	---	---
LNF60 (Batch 2)	---	0.97(9)	0.41(6)	0.60(8)	---	---
LNF60 (Batch 3)	---	1.02(9)	0.45(6)	0.65(8)	---	---
MCF10 (Batch 1)	---	---	0.10(1)	---	0.99(4)	1.86(5)
MCF10 (Batch 2)	---	---	0.10(1)	---	1.02(4)	1.90(5)
MCF10 (Batch 3)	---	---	0.10(1)	---	0.98(4)	1.93(5)

Within the experimental errors for all the samples, the experimental compositional values match the nominal composition.

Because the difficulties to dissolve SDC, NiO-YSZ and YSZ samples, the compositional measurements of these samples has been performed by XRF technique. The results are shown in the Table 2.3.

Table 2.3.- Summary XRF results for SDC (Sm, Ce), NiO-YSZ (Ni, Y, Zr) and YSZ (Y, Zr).

	Zr	Y	Ni	Sm	Ce
SDC (Batch 1)	---	---	---	0.8(1)	0.3(2)
SDC (Batch 2)	---	---	---	0.8(1)	0.3(2)
SDC (Batch 3)	---	---	---	0.8(1)	0.3(2)
NiO-YSZ (Batch 1)	0.8(3)	0.2(1)	0.3(4)	---	---
NiO-YSZ (Batch 2)	0.8(3)	0.2(1)	0.3(4)	---	---
NiO-YSZ (Batch 3)	0.8(3)	0.2(1)	0.3(4)	---	---
YSZ (Batch 1)	0.8(9)	0.2(3)	---	---	---
YSZ (Batch 2)	0.8(9)	0.2(3)	---	---	---
YSZ (Batch 3)	0.8(9)	0.2(3)	---	---	---

The results obtained by XRF analysis (Table 2.3.) were close to the nominal values for all the studied samples. In all the cases, the difference between the relative amounts of the elements in different batches was not significant. Thus, the synthesis procedure shows an adequate chemical reproducibility.

2.3.2. Structural study

The purity of the samples was studied by X-ray diffraction. All the materials (LSF40, LNF60, MCF10, SDC, NiO-YSZ and YSZ) prepared through the glycine nitrate (GN) combustion route present the desired final phases. For the LNF compound, the appearance of extra shoulders in the experimental profile indicates a possible phase segregation to give two perovskite phases with different Ni/Fe ratio. In the NiO-YSZ case, the diffractogram present peaks relative to the phases of NiO and YSZ (cubic structure), which evidences that the materials did not react at these temperatures.

The signal identification for all XRD patterns is in good agreement with the Power Diffraction File database (PDF)[19]. All the synthesis are reproducible and pure as can be observed in Figure 2.1. for different batches. The corresponding Rietvield refinements result and diffraction patterns are displayed as supplementary material (Figure 2.S3.)

[19] ICCD, "Powder Diffraction File-Inorganic and Organic", Pennsylvania, USA, **1995**.

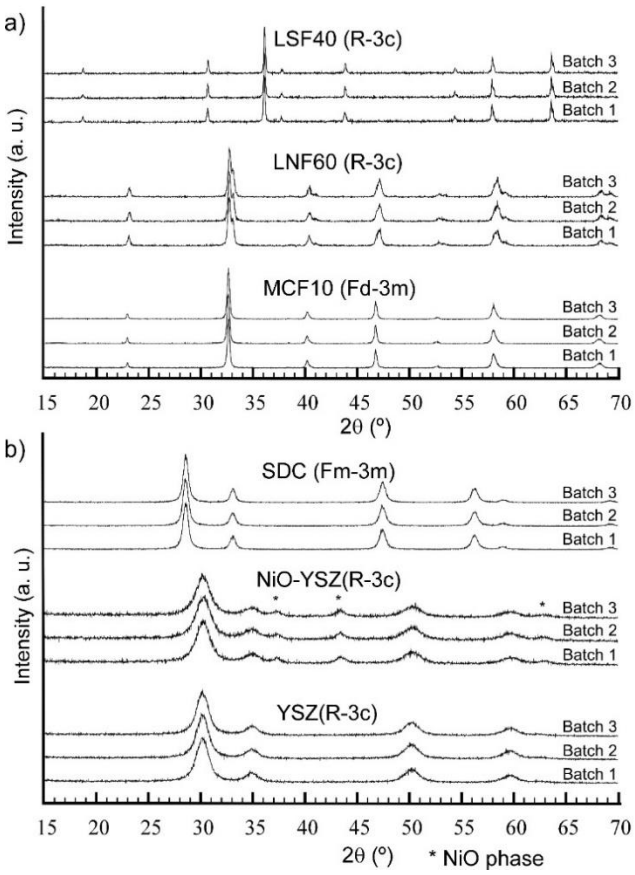

Figure 2.1.- X-ray diffraction patterns measured of (a) LSF40, LNF60, MCF10, (b) SDC, NiO-YSZ and YSZ**.**

The used synthetic temperatures indicate an absence of reactivity or decomposition of the starting materials under SOFC operating conditions (800ºC).

In order to obtain information about the crystal size of the synthesized powders, the Scherrer formula has been used (Table 2.4.). The Scherrer equation relates the width of a powder diffraction peak to the average dimensions of crystallites in a polycrystalline powder (the used instrumental contribution is of 0.1 and the shape factor of 0.9).

Table 2.4.- Crystallite sizes of the synthesized compounds.

Batch	Compound (h,k,l)	Crystallite size (nm)	FWHM	Compound (h,k,l)	Crystallite size (nm)	FWHM
1	YSZ (1,1,1)	6(2)	1.52	LSF40 (1,0,4)	46(2)	0.28
2		6(2)	1.53		45(2)	0.28
3		6(2)	1.55		45(2)	0.28
1	SDC (1,1,1)	15(1)	0.65	LNF60 (1,0,4)	16(1)	0.60
2		15(1)	0.64		17(1)	0.59
3		14(1)	0.67		16(1)	0.60
1	NiO-YSZ (1,1,1)	5(1)	1.70	MCF10 (3,1,1)	182(5)	0.14
2		5(1)	1.70		186(5)	0.14
3		5(1)	1.70		189(5)	0.14
1	NiO (2,2,0)	10(1)	1.00			
2		11(1)	0.87			
3		10(1)	0.99			

As it can be seen, crystallite sizes are homogeneous between different batches of the same compound, showing crystal grown reproducibility.

2.3.3. Microstructure

Figure 2.2. represents the SEM images for all the synthesized powders. In the case of LSF40, LNF60, MCF10 and SDC, well-necked morphologies of the powders synthesized by the combustion method and sintered at 950 °C are shown (a, b, c and d, respectively), which are composed of nanosized particles and agglomerations of grains of small number of micrometers.

The micrographs of the obtained samples of NiO-YSZ and YSZ are shown in Figure 2.2. (e and f, respectively). Nano-sized particles are obtained, morphologically homogeneous and uniformly porous. In these cases, because of a large amount of the outcoming gases as-prepared samples are rather voluminous and very fragile. The particles are bound together into agglomerates of different shapes and sizes of a few micrometers.

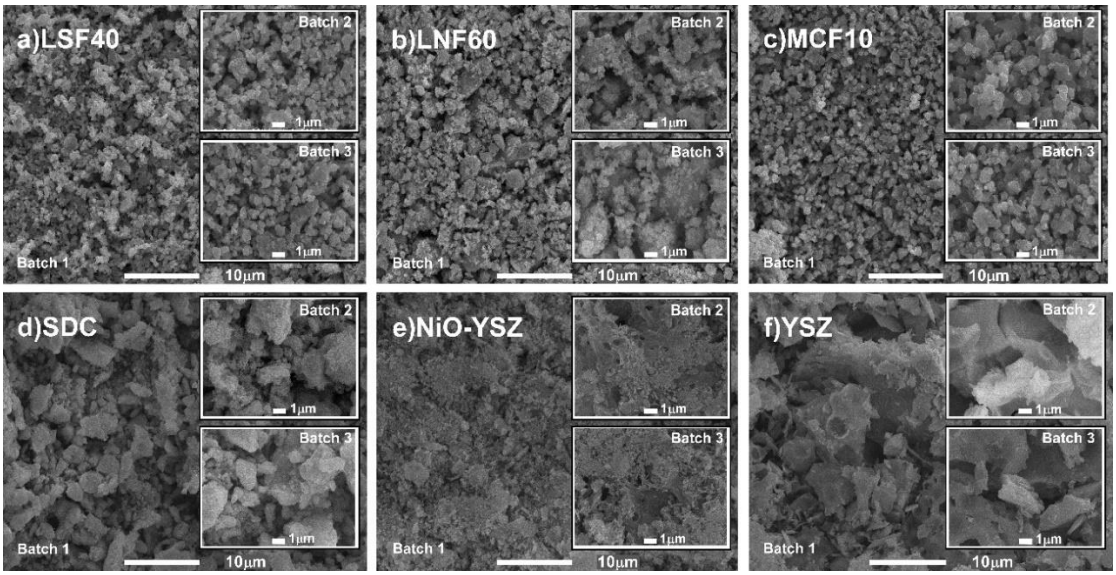

Figure 2.2.- SEM micrographs of the powder samples of a) LSF40, b) LNF60, c) MCF10, d) SDC, e) NiO-YSZ and f) YSZ.

In all the cases, the agglomerates formed during the combustion reaction are usually soft and easy to break due to the higher escaping gases for these samples. In addition, comparing the same compound between different batches, it can be shown that the particle sizes and shapes are homogeneous. In addition, they are very microstructurally suitable starting materials to be used in the manufacture of SOFCs.

Particle size distribution of these materials has been measured for their manufacturing in SOFCs since this parameter influences the rheological properties for their deposition by wet colloidal spraying, after a ball milling with isopropanol.

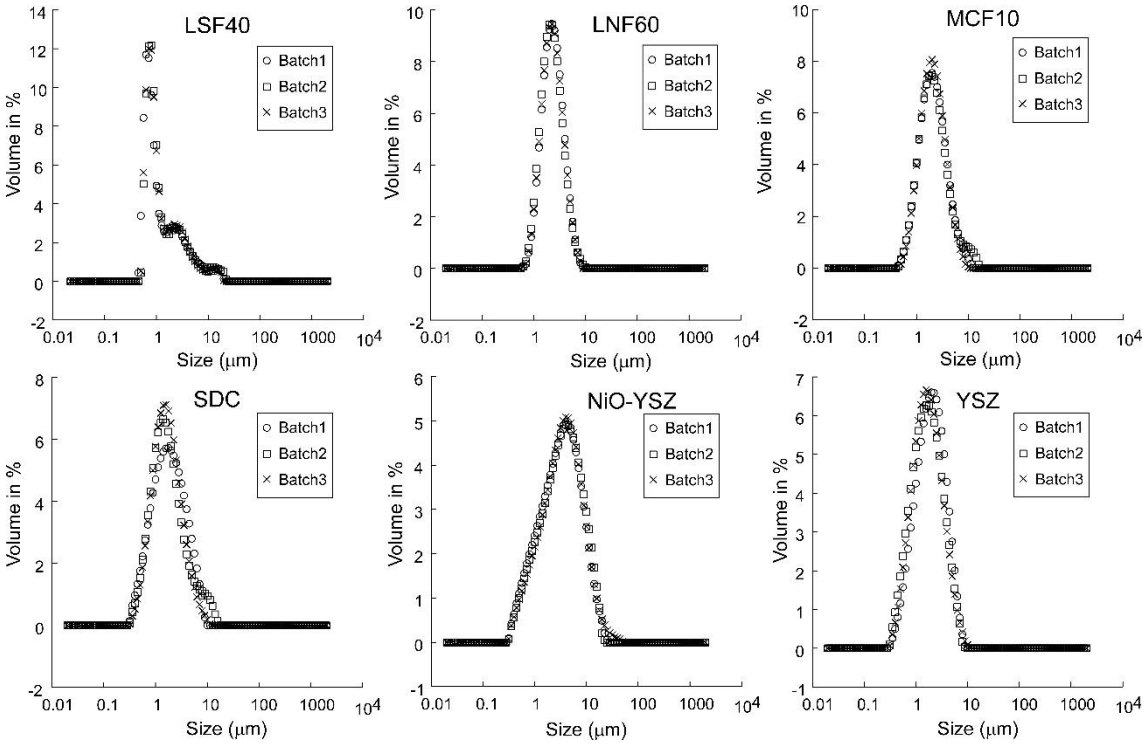

Figure 2.3.- Particle size distribution curves for LSF40, LNF60 MCF10, SDC, NiO-YSZ and YSZ powders.

As it is shown in Figure 2.3., the aggregate sizes are homogeneous between different batches demonstrating that the synthesis is reproducible concerning the final processing sizes. Table 2.5. summarizes the details.

Table 2.5.- Summary results of powders particle size distribution tests.

Compound	d(0.5μm)	Compound	d(0.5μm)
LSF40 (Batch 1)	0.903	SDC (Batch 1)	1.506
LSF40 (Batch 2)	0.902	SDC (Batch 2)	1.495
LSF40 (Batch 3)	0.960	SDC (Batch 3)	1.665
LNF60 (Batch 1)	2.161	NiO-YSZ (Batch 1)	3.293
LNF60 (Batch 2)	2.025	NiO-YSZ (Batch 2)	3.262
LNF60 (Batch 3)	2.063	NiO-YSZ (Batch 3)	3.260
MCF10 (Batch 1)	1.905	YSZ (Batch 1)	1.551
MCF10 (Batch 2)	1.913	YSZ (Batch 2)	1.371
MCF10 (Batch 3)	1.914	YSZ (Batch 3)	1.828

2.3.4. Electrical conductivity

The electronic conductivity of LSF40 and Ni-YSZ, can be described by the thermally activated small polaron mechanism[25,26] which is generally expressed as (Eq 2.1):

$$\sigma = A/T \cdot \exp((-Ea)/kT) \qquad \text{(Eq 2.1)}$$

in which E_a is the activation energy for small polaron hopping conduction, k is the Boltzmann constant, T is the absolute temperature and A is a pre-exponential factor independent of the temperature.

In the case of LSF40, the conductivity increases with increasing temperature up to a maximum and then decreases due to the lattice oxygen loss, implying a small semiconductor behavior. The electrical conductivity of MCF10 increases with increasing temperature. For the Ni-YSZ and LNF60 material, however, the conductivity decreases continuously with increasing temperature, implying a metallic behavior in the measured temperature range.

For comparison, electrical conductivities at different temperatures and activation energies for the oxygen ion transport of the different compounds have been represented in the table 2.6.

Table 2.6.- Electrical conductivity values at different temperatures and activation energy.

Compound	**NiO-YSZ**	**LSF40**	**LNF60**	**MCF10**
σ(600 °C)(S/cm^{-1})	670	89	93	126
σ(700 °C)(S/cm^{-1})	617	74	87	168
σ(800 °C)(S/cm^{-1})	573	63	82	184
Ea(eV)	---	0.03	0.02	0.28

The conductivity values obtained for the compounds are not comparable with the literature conductivity data[22], because these results are obtained on samples prepared using different chemical routes and/or calcined at different temperatures from ours.

---

[25] Pan X., Wang Z., He B., Wang S., Wu X., Xia C., Effect of Co doping on the electrochemical properties of $Sr_2Fe_{1.5}Mo_{0.5}O_6$ electrode for solid oxide fuel cell, Int. J. Hydrog. Energy. 38 (**2013**) 4108-4115.

[26] Lubini M., Chinarro E., Moreno B., de Sousa V.C., Alves A.K., Bergmann C.P., Electrical properties of $La_{0.6}Sr_{0.4}Co_{1-y}Fe_yO_3$ (y = 0.2–1.0) fibers obtained by electrospinning, *J. Phys. Chem. C*. 120 (**2016**) 64-69.

[22] Osinkin D.A., Bronin D.I., Beresnev S.M., Bogdanovich N.M., Zhuravlev V.D., Vdovin G.K., Demyanenko T.A., Thermal expansion, gas permeability, and conductivity of Ni-YSZ anodes produced by different techniques, *J. Solid State Electr*. 18 (**2013**) 149-156.

2.3.5. Thermal expansion study

Thermal expansion coefficients are an important parameter for SOFCs. High temperature fuel cell stacks must meet the critical requirement that all layers have to retain good electrical contact, although large temperature changes occur at assembly and operating temperatures. In an ideal case, all materials would have the same thermal expansion coefficient (TEC), but in real configurations, differences will emerge that can cause thermo-mechanical stress. A further problem can occur because of the differences in the TECs of the different materials which result to a different change in thickness of the various layers and reduction of the system lifetime[23].

Figure 2.4. represents dilatometric curves of samples recorded between 200 to 950 °C in air that are almost linearly dependent on temperature. The value of the average lineal thermal expansion coeffients (TEC) of the compounds obtained over the temperature range of 200-800 ºC are shown in Table 2.7.

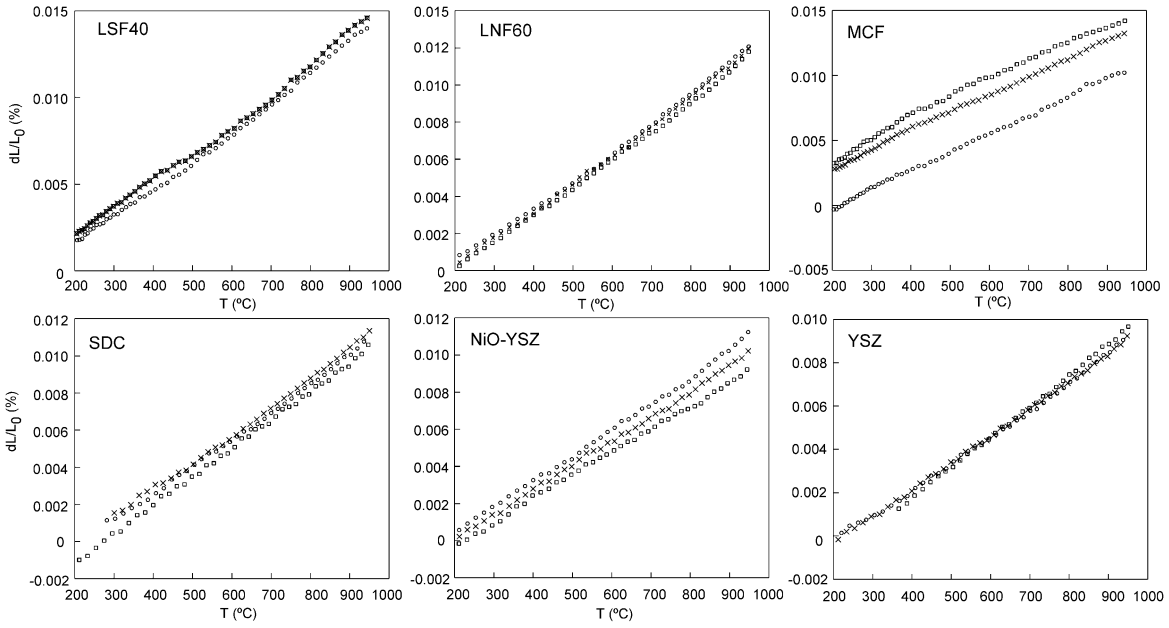

Figure 2.4.- Thermal expansion behavior of components prepared by the combustion method.

[23] Blum L., An Analysis of Contact Problems in Solid Oxide Fuel Cell Stacks Arising from Differences in Thermal Expansion Coefficients, Electrochim. Acta. 223 (2017) 100-108.

Table 2.7.- Average TEC values of the obtained materials.

Component	Average TEC (200-800 ºC) (1.10^{-6} ºC^{-1})
Crofer 22APU	11.8 [20]
MCF10	14.6(1)
LNF60	14.8(3)
LSF40	15.8(3)
SDC	14.4(2)
YSZ	13.1(2)
NiO-YSZ	13.3(2)

The change in the thermal expansion coefficient between the different components is show in Figure 2.5.

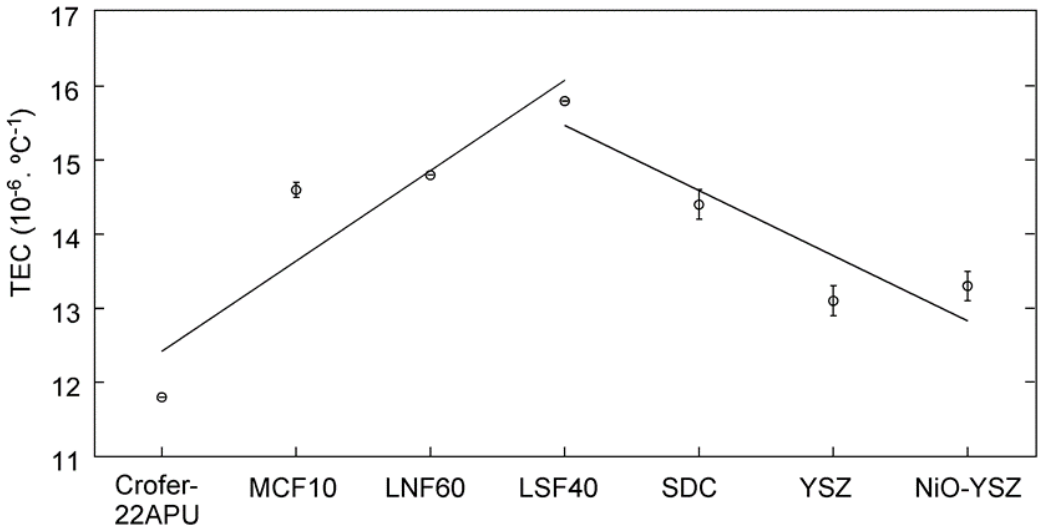

Figure 2.5.- TEC values obtained over the temperature range of 200-800 ºC for all the components.

As can be observed, the introduction of the corresponding layers between the electrolyte and cathode, and between the cathode and interconnector, minimizes the difference between their TEC values giving rise to similar values that are indicative of thermal compatibility, a factor that prevents failure due to stresses in SOFCs at high temperatures caused by thermal mismatches.

2.4. Conclusions

Six different fuel cell compounds have been synthesized in big amounts by glycine-nitrate method with stoichiometric fuel/oxidizer ratio, obtaining high quality materials whose microstructural properties can be modified.

The achieved compounds have similar microstructures which limits the long time degradation for those kinds of multilayer systems.

The synthetic times are short, demonstrating to be compositionally and morphologically reproducible in different batches. Therefore, it can be concluded that the glycine-nitrate process, with an optimal G/N ratio of 1.0, is an appropriate technique for preparing big quantities of different compounds for SOFC fabrication.

2.5. Supplementary material

The results presented in this section are informative scheme figures and preliminary data presented previously in congresses.

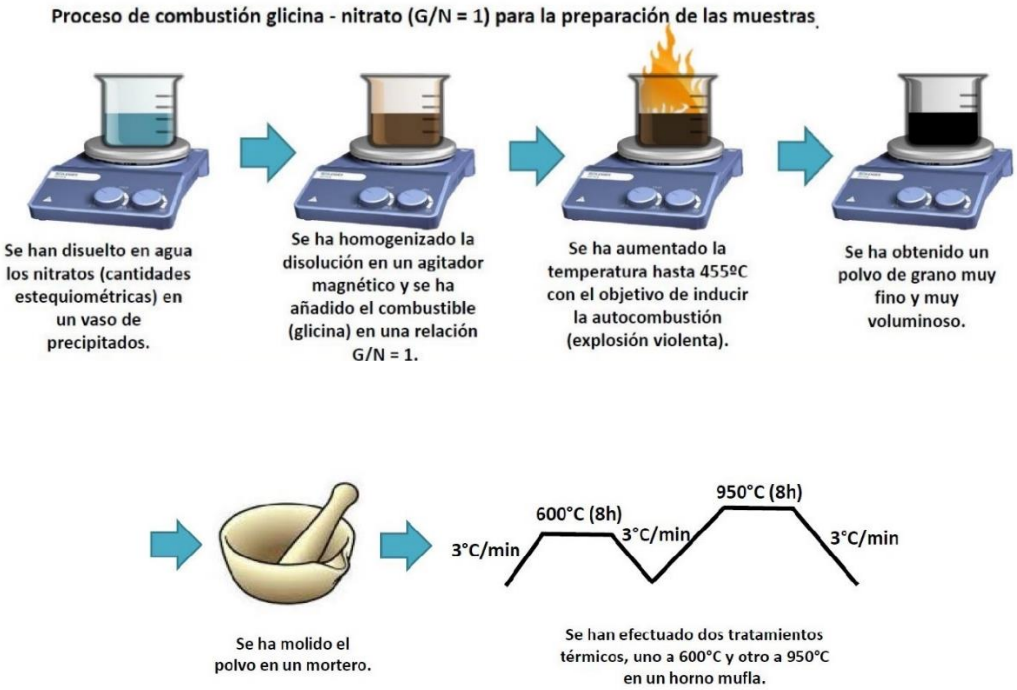

Figure 2.S1.- Scheme of Glycine-Nitrate combustion process. (XXXV Reunión bienal RESQ, page 205)

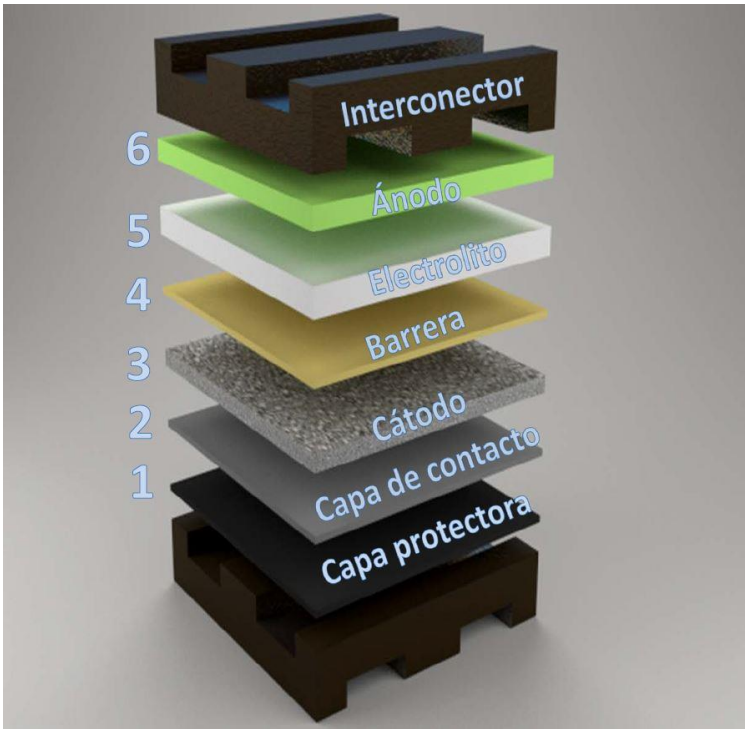

Figure 2.S2.- Scheme of the order in the cell of the synthesized compounds. (XXXV Reunión bienal RESQ, page 205.)

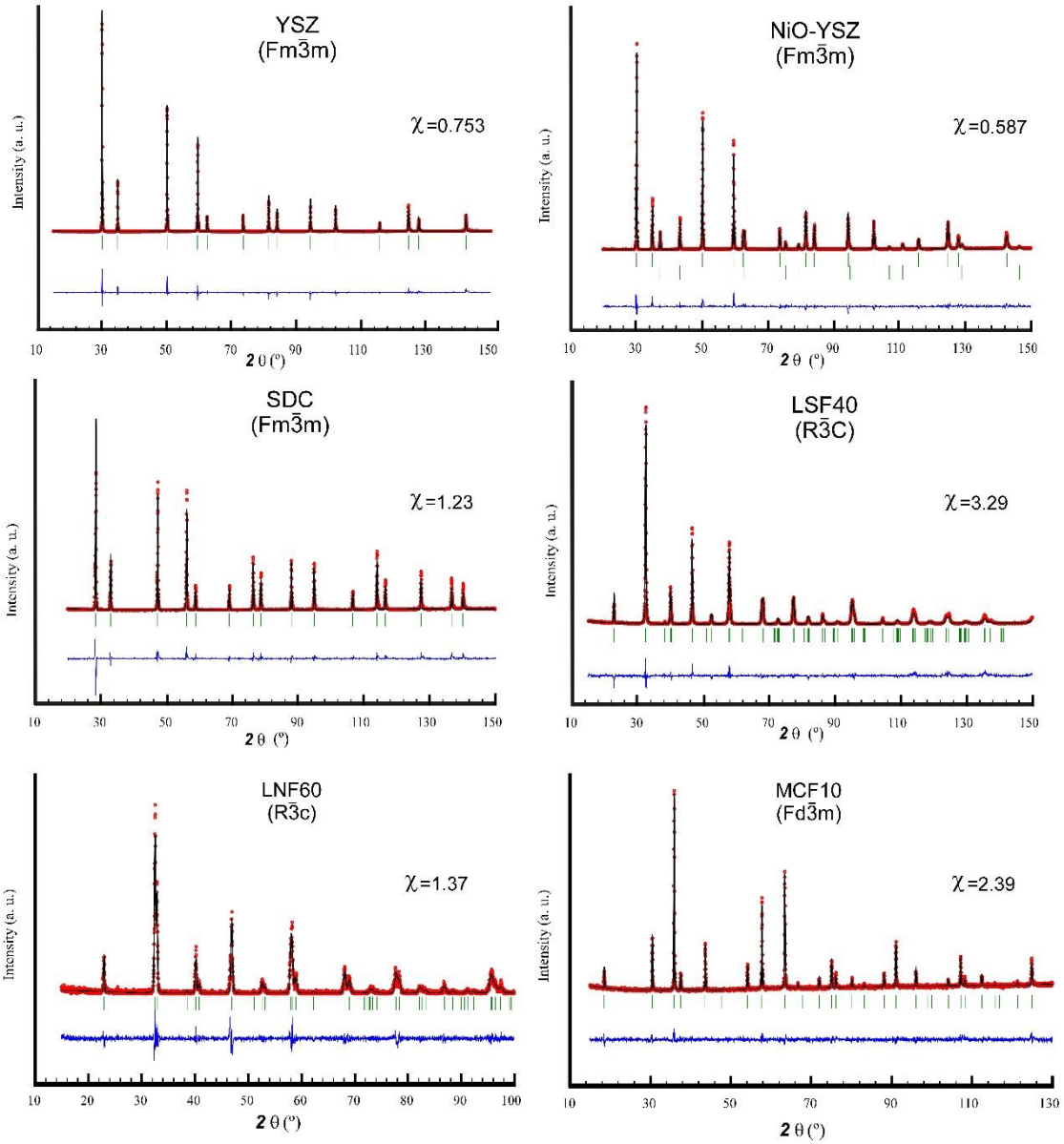

Phase	Space group	a(Å)/c(Å)	V(Å^3)
NiO-$Zr_{0.8}Y_{0.2}O_{1.9}$	Fm-3m	4.179(2)	72.959(1)
NiO-$Zr_{0.8}Y_{0.2}O_{1.9}$	Fm-3m	5.142(1)	135.95(2)
$Zr_{0.8}Y_{0.2}O_{1.9}$	Fm-3m	5.146(1)	136.27(1)
$Sm_{0.2}Ce_{0.8}O_{1.9}$	Fm-3m	5.432(1)	160.26(4)
$La_{0.4}Sr_{0.6}FeO_3$	R-3c	5.527(1)/13.451(2)	355.83(9)
$LaNi_{0.6}Fe_{0.4}O_3$	R-3c	5.513(1)/13.399(5)	352.76(9)
$MnCo_{1.9}Fe_{0.1}O_4$	Fd-3m	8.232(1)	557.80(7)

Figure 2.S3.- X-ray diffraction pattern refinements and Rietveld refinement results of the six analyzed compounds (NiO-YSZ, YSZ, SDC, LSF, LNF, MCF). (XIV Congreso Nacional de Materiales, page 209)

3. FABRICACIÓN DE CELDAS SIMÉTRICAS DE SOPORTE ELECTROLITO POR LA TÉCNICA DE SPRAY

La investigación realizada y mostrada a lo largo de este capítulo ha dado como resultado la publicación del artículo científico **"SOFC cathodic layers using wet powder spraying technique with self synthesized nanopowders, International Journal of Hydrogen Energy, 44 (2019) 7555-7563"** en una revista indexada por la Journal Citation Reports y la difusión de resultados en los siguientes congresos:

- "Electrochemical and degradation behavior study of different SOFC compounds", The Energy & Materials Research Conference- EMR2017, 2017, Lisboa (Portugal).

- "Procesado y caracterización de celdas de soporte electrolito de Pilas de Combustible de Oxido Solido (SOFC)", I Jornada de Jóvenes Investigadores de Cerámica y Vidrio en el ICMA, 2018, Zaragoza (España).

3. FABRICATION OF ELECTROLYTE SUPPORTED SYMMETRIC CELLS BY SPRAYING TECHNIQUE

The studies carried out throughout this chapter have resulted in the **"SOFC cathodic layers using wet powder spraying technique with self synthesized nanopowders, International Journal of Hydrogen Energy, 44 (2019) 7555-7563"** scientific article in a indexed review by Journal Citation Reports and in the congress contributions presented below:

- "Electrochemical and degradation behavior study of different SOFC compounds", The Energy & Materials Research Conference- EMR2017, 2017, Lisbon (Portugal).

- "Procesado y caracterización de celdas de soporte electrolito de Pilas de Combustible de Oxido Solido (SOFC)", I Jornada de Jóvenes Investigadores de Cerámica y Vidrio en el ICMA, 2018, Zaragoza (Spain).

Resumen del capítulo 3

Como se ha indicado, el objetivo final del trabajo se centra en fabricar una pila de combustible de óxido sólido. Tras los resultados que se han mostrado en el capítulo anterior, se ha conseguido el acceso a grandes cantidades de todos los materiales que componen una celda, consiguiendo la escalabilidad de la síntesis mediante el método de combustión. Además, mediante la caracterización de los materiales de partida, se ha determinado que los materiales son aptos para su posterior procesado en soportes y capas.

El propósito de la investigación plasmada en el presente capítulo, ha sido el procesado simple de los polvos sintetizados, empezando por la configuración más básica de una celda de combustible, siendo ésta una configuración plana, simétrica y de soporte electrolito. Uno de los principales problemas en el procesado de las pilas de combustible es el costo y la complejidad de las técnicas. Por ello, como técnica de fabricación de soportes electrolitos, se ha optado por la técnica de prensado uniaxial; y para la deposición de las capas de la parte catódica, la deposición por spray de polvos húmedos. Estas dos técnicas se caracterizan por su simplicidad y su bajo coste.

En el presente apartado se ha prestado especial atención a la estabilidad interfacial de las capas, evaluando la influencia que puede tener el espesor de las mismas y la molienda de las pastas en la adherencia y la electroquímica de las capas. Tras haber concluido la optimización de las capas, se ha procedido al análisis de una celda simétrica con todas las capas (barrera, cátodo y capa de contacto), con el fin de asegurar las propiedades electroquímicas necesarias de la celda completa en funcionamiento.

El análisis de las variables en el procesado de celdas ha permitido una aproximación inicial a la última etapa del presente trabajo.

Summary of the chapter 3

As indicated previously, the main objective of this work is to manufacture a solid oxide fuel cell. After the results obtained in the previous chapter, access to large quantities of the materials that conforms the fuel cell have been obtained, achieving the scalability of the synthesis through the combustion method. Furthermore, by characterizing the starting materials, it has been determined that the powders are suitable for their additional processing in supports and layers.

The purpose of this chapter has been the simple processing of the synthesized powders, starting with the most basic configuration of a fuel cell, being a flat, symmetric and electrolyte supported configuration. One of the main problems in fuel cell processing is the cost and complexity of the techniques. Therefore, as a manufacturing technique for electrolyte supports, the uniaxial pressing technique; and for the cathodic side layer deposition, wet powder spraying method has been chosen. Both techniques are characterized by their simplicity and low cost.

In this study, special attention has been paid to the interfacial stability of the layers, evaluating the influence that the thickness of the layers and ball milling of the pastes can have in the adhesion and electrochemistry of the layers. After having concluded the optimization of the layers, we proceeded to the analysis of a symmetric cell with all the layers (barrier, cathode and contact layer), in order to assume the necessary electrochemical properties of an entire cell in operation.

The study analysis of these variables in the cell processing has been an approximation to what has been intended to do in the next chapter, where it has been planned to manufacture an asymmetric fuel cell with all the components.

SOFC cathodic layers using wet powder spraying technique with self synthesized nanopowders

International Journal of Hydrogen Energy 44 **(2019)** 7555-7563.

3.1. Introduction

The two main configurations of SOFCs are tubular and planar[1,2]. Among the different configurations, this study is focused in planar SOFCs, which have a much simpler manufacturing process and lower fabrication cost than those of their tubular counterparts[3,4]. Regarding planar configuration, two types are preferred: electrode (mainly at anode) supported cells and electrolyte supported cells[5,6]. Although electrolyte supported cells may exhibit higher ohmic losses, they are more robust and have demonstrated much better stability during the reduction-oxidation processes and thermal cycles[7].

The main drawbacks for the industrial implementation of SOFCs are their manufacturing cost and high degradation rate[8,9]. The aim is to replace the expensive and complex processing for the cell manufacturing with cheaper, simpler and industrially scalable techniques. Within these techniques, spray coating is a cost effective deposition method for electrode layers, showing good quality and thickness control. In particular, this method present a highly reproducible process for covering planar surfaces[10].

---

1 Gil V., Gurauskis J., Campana R., Merino R.I., Larrea A., Orera V.M., Anode-supported microtubular cells fabricated with gadolinia-doped ceria nanopowders, *J. Power Sources*. 196 (**2011**) 1184-1190.

2 Duan N., Yan D., Chi B., Pu J., Jian L., High performance anode-supported tubular solid oxide fuel cells fabricated by a novel slurry-casting method, *Sci Rep*. 5 (**2015**) 8174.

3 Yan D., Liang L., Yang J., Zhang T., Pu J., Chi B., Li J., Performance degradation and analysis of 10-cell anode-supported SOFC stack with external manifold structure, *Energy*. 125 (**2017**) 663-670.

4 Myung J., Ko H.J., Park H., Hwan M., Hyun S.. Fabrication and characterization of planar-type SOFC unit cells using the tape-casting/lamination/co-firing method, *Int. J. Hydrog. Energy*. 37 (**2012**) 498-504.

5 Shy S.S., Hsieh Y.D., Huang C.M., Chan Y.H., Comparison of electrochemical impedance measurements between pressurized anode-supported and electrolyte-supported planar solid oxide fuel cells, *J. Electrochem. Soc.* 162 (**2015**) F172-F177.

6 Lin Q., Lin J., Liu T., Xia C., Chen C., Solid oxide fuel cells supported on cathodes with large straight open pores and catalyst-decorated surfaces, *Solid State Ion*. 323 (**2018**) 130-135.

7 Preininger M., Subotić V., Stoeckl B., Schauperl R., Reichholf D., Megel S., Kusnezoff M., Hochenauer C., Electrochemical characterization of a CFY-stack with planar electrolyte-supported solid oxide cells in rSOC operation, *Int. J. Hydrog. Energy*. 43 (**2018**) 12398-12412.

8 Scataglini R., Wei M., Mayyas A., Chan S.H., Lipman T., Santarelli M., A Direct manufacturing cost model for solid-oxide fuel cell stacks, *Fuel Cells*. 17 (**2017**) 825-842.

9 Lee S., Lee K., Jang Y., Bae J., Fabrication of solid oxide fuel cells (SOFCs) by solvent-controlled co-tape casting technique, *Int. J. Hydrog. Energy*. 42 (**2017**) 1648-1660.

10 Liu P., Luo Z., Kong J., Yang X., Liu Q., Xu H., $Ba_{0.5}Sr_{0.5}Co_{0.8}Fe_{0.2}O_3$-delta-based dual-gradient cathodes for solid oxide fuel cells, *Ceram. Int*. 44 (**2018**) 4516-9.

In the development of a planar SOFC stack, each repeating unit is composed of an anode, electrolyte, cathode and interconnect[11,12]. Among the typical material choices, yttria stabilized zirconia (YSZ) is the most commonly used electrolyte for SOFCs because of its low cost, high ionic transference number in oxidizing and reducing atmospheres, and good chemical and mechanical properties[13]. The mechanical properties of the YSZ allow it to withstand the residual stresses from cell fabrication processes as well as the stresses from the operational conditions.

Samarium doped ceria (SDC) or gadolinium doped ceria (GDC) can also be used as electrolytes[1415], or as a protective barrier between the YSZ electrolyte and commonly used cathode materials, preventing the formation of poorly conducting secondary phases, such as $La_2Zr_2O_7$ or $SrZrO_3$, which are deterious for as cathode performance[16,17]. Iron containing perovskites such as $La_{0.6}Sr_{0.4}FeO_3$ (LSF) or $La_{0.6}Sr_{0.4}Co_{0.2}Fe_{0.8}O_3$ (LSCF) are good candidates as SOFC cathodes showing high mixed conductivity and good catalytic activity for the oxygen reduction reaction (ORR)[18,19]. The use of cathode contact layers such as $LaNi_{0.6}Fe_{0.4}O_3$ (LNF) and $LaNi_{0.6}Co_{0.4}O_3$ (LNC) have been demonstrated to improve the electrons transfer through the contact interface from interconnect to the cathode layer.

In addition, it means that the ORR in the triple phase of the cathode has more electrons from the interconnector, greatly increasing the performance of the cell[20].

---

[11] Zhu J.H., Ghezel-Ayagh H., Cathode-side electrical contact and contact materials for solid oxide fuel cell stacking: A review, *Int. J. Hydrog. Energy*. 42 (**2017**) 24278-24300.

[12] Li X., Shi W., Han M., Optimization of interconnect flow channels width in a planar solid oxide fuel cell, *Int. J. Hydrogen Energy*. 43 (**2018**) 21524-21534.

[13] Setevich C.F., Mogni L.V., Caneiro A., Prado F.D., Optimum cathode configuration for IT-SOFC using $La_{0.4}Ba_{0.6}CoO_{3-\delta}$ and $Ce_{0.9}Gd_{0.1}O_{1.95}$, *Int. J. Hydrogen Energy*. 37 (**2012**) 14895-14901.

[14] Sun H., Rainwater B.H., Xiong X., Chen Y., Wei T., Zhang Q., Yang Z., Li C., Liu M., Interfacial effects on electrical conductivity in ultrafine-grained $Sm_{0.2}Ce_{0.8}O_{2-\delta}$ electrolytes fabricated by a two-step sintering process, *Int. J. Hydrog. Energy*. 42 (**2017**) 11823-11829.

[15] Sar J., Dessemond L., Djurado E., Electrochemical properties of graded and homogeneous $Ce_{0.9}Gd_{0.1}O_{2-\delta}$–$La_{0.6}Sr_{0.4}Co_{0.2}Fe_{0.8}O_{3-\delta}$ composite electrodes for intermediate-temperature solid oxide fuel cells, *Int. J. Hydrog. Energy*. 41 (**2016**) 17037-17043.

[16] Martínez-Amesti A., Larrañaga A., Rodríguez-Martínez L.M., Nó M.L., Pizarro J.L., Laresgoiti A., Arriortua M.I., Chemical compatibility between YSZ and SDC sintered at different atmospheres for SOFC applications, *J. Power Sources*. 192 (**2009**) 151-157.

[17] De Vero J.C., Develos-Bagarinao K., Ishiyama T., Kishimoto H., Yamaji K., Horita T., Yokokawa H., Effect of $SrZrO_3$ formation at LSCF-cathode/GDC-interlayer interfaces on the electrochemical properties of solid oxide fuel cells, *ECS Trans*. (USA). 75 (**2017**) 75-81.

[18] Vidal K., Rodríguez-Martínez L.M., Ortega-San-Martin L., Martínez-Amesti A., Nó M.L., Rojo T., Laresgoiti A., Arriortua M.I., The effect of doping in the electrochemical performance of $(Ln_{1-x}M_x)FeO_{3-\delta}$ SOFC cathodes, *J. Power Sources*. 192 (**2009**) 175-179.

[19] Wu X., Tian Y., Zhou X., Kong X., Zhang J., Zuo W., Ye X., High performance yttria-stabilized zirconia based intermediate temperature solid oxide fuel cells with double nano layer composite cathode, *Int. J. Hydrog. Energy*, 42 (**2017**) 1093-1102.

[20] Xin X., Liu L., Liu Y., Zhu Q., Novel perovskite-spinel composite conductive ceramics for SOFC cathode contact layer, *Int. J. Hydrog. Energy*. 43 (**2018**) 23036-23040.

In this research, the deposition of the cathode side components (SDC as protective layer, LSF as cathode and LNF as contact layer) by wet powder spraying (WPS) deposition has been studied with the aim of optimizing the fabrication process using self-made materials, using a cheap, simple and scalable technique. Furthermore, special attention has been paid to the influence of the ball milling process and the layer thickness in determining the morphology and stability of the layers. The cells were characterized by X-ray diffraction (XRD) Scanning Electron Microscopy (SEM) with Energy Dispersive X-ray Spectroscopy (EDX). Electrochemical impedance spectroscopy (EIS) measurements were performed in a button cell test rig (NorECs) and a Zanher Zennium workstation, in air at 700 and 800 °C.

3.2. Experimental

3.2.1. Synthesis and cell fabrication

All the SOFC component powders were prepared by a glycine nitrate (GN) process. Stoichiometric amounts of the corresponding metal nitrates were dissolved in deionized water. For all compositions, glycine was then added into the nitrate aqueous solution (Glycine-nitrate 1:1) under continuous stirring. The resulting viscous liquid was auto-ignited by heating up to approximately 455 °C and the obtained powders were calcined around 600 °C for 5 h to remove carbon residues. In the case of LSF and LNF, the resulting powders were pelletized and calcined in air at 950 °C for 8 h to obtain pure single phase samples. The properties (composition, morphologies, TEC and conductivities) of the primary materials used in the present study could be consulted in previous[21].

Various configurations of the symmetrical systems were performed and investigated in this paper, which are described in Table 3.1. During the first experiments, four cells made out of cathodic and barrier layers, were created with different thicknesses and using inks ball milled at 270 rpm speed. In the second set of samples, with the aim of studying the effect of the ball milling speed in the layers, the cathode powders were ball milled at different speeds maintaining the thicknesses constant. Finally, taking into account previous results, symmetric systems were fabricated adding LNF contact layers (see Supplementary material: Figure 3.S1).

[21] Wain-Martin A., Morán-Ruiz A., Vidal K., Larrañaga A., Laguna-Bercero M.A., Arriortua M.I., Scalable synthetic method for SOFC compounds, *Solid State Ion*. 313 (**2017**) 52-57.

Table 3.1.- Details of the investigated samples.

Sample name	Composition	Layer thickness	Ball milling speed(rpm) for 24 h
T1	SDC-LSF	1 µm SDC and 1 µm LSF	270
T3	SDC-LSF	3 µm SDC and 3 µm LSF	270
T10	SDC-LSF	10 µm SDC and 10 µm LSF	270
T30	SDC-LSF	3 µm SDC and 30 µm LSF	270
EFFECT OF BALL MILLING			
T3BM130	SDC-LSF	3 µm SDC and 3 µm LSF	130
T10BM130	SDC-LSF	10 µm SDC and 10 µm LSF	130
T3BM270	SDC-LSF	3 µm SDC and 3 µm LSF	270
T10BM270	SDC-LSF	10 µm SDC and 10 µm LSF	270
COMPLETE SYSTEM			
MCT3	SDC-LSF-LNF	3 µm SDC, 3 µm LSF and 3 µm LNF	270
MCT10	SDC-LSF-LNF	3 µm SDC, 10 µm LSF and 10 µm LNF	270

To prepare the YSZ supports by uniaxial pressing, with 13 mm of diameter and 300 µm of thickness, the synthesized powders were ball milled with zirconia balls in zirconia cylinders for 24 h using 2-propanol as solvent. After being pressed, the supports were sintered at 1425 °C for 2h. For the deposition of the layers, the starting powders were ground through wet ball milling, by adding the appropriate amount of solvent (2-propanol) and dispersant, for 24 h. The deposition was carried out at room temperature, using an airbrush (Iwata eclipse HP-BCS) operated at an angle of 90 ° with respect to the supporting plane. The distance between the nozzle and the support was varied between 2 and 10 cm. SDC, LSF and LNF layers were sintered separately at a temperature of 1150, 950 and 950 °C, respectively, for 2 h (see Supplementary material: Figure 3.S2). The schematic structure of the electrolyte-supported system is shown in Figure 3.1.

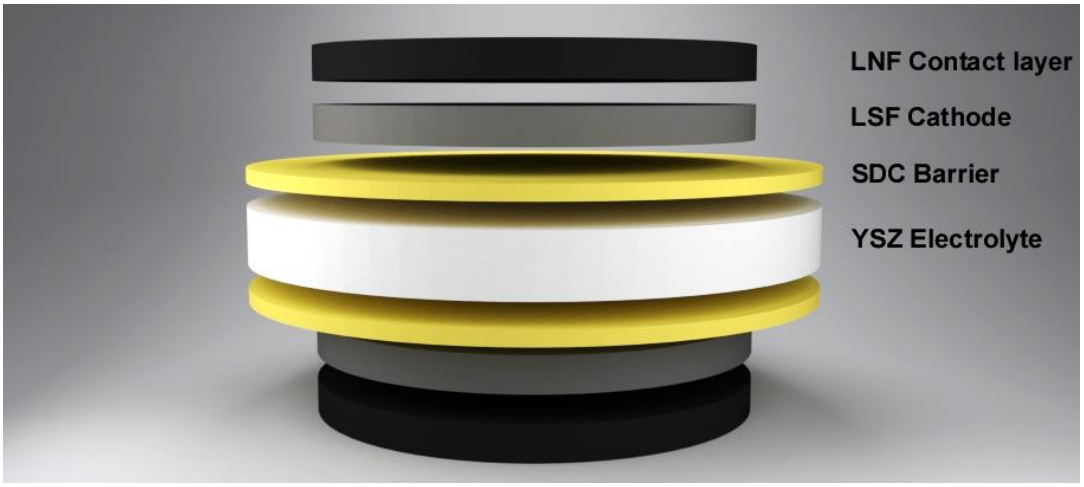

Figure 3.1.- Schematic for an electrolyte supported SOFC design.

3.2.2. Morphological characterization

Room-temperature X-ray diffraction (XRD) data were recorded using an integration time of 10 s/0.026 ° step in the 5 < 2θ < 70 ° range with a Philips X'Pert-PRO X-ray diffractometer equipped with a secondary beam graphite monochromator and Cu-Kα radiation. Full-profile Rietveld refinements were performed using the FullProf program to confirm the structural parameters of the identified phases[22].

Cross sections of the samples were analyzed using SEM/EDX system (JEOL JSM-7000F). Composition analysis was performed using back-scattered electrons (BSE) at 20 kV accelerating voltage and $5x10^{-9}$ A of current. Moreover, EDX mapping was carried out using 70 ms/pixel. The data processing was performed using Oxford INCA software. The characteristic emission lines used for the analysis were L_α for La and Ce, K_α for Ni and Fe, and $L\beta_1$ for Sr.

3.2.3. Electrochemical measurements

Symmetric systems were used to study the electrochemical performance of the compounds using electrochemical impedance spectroscopy (EIS). The layers, with a geometrical area of 0.51cm^2, were deposited onto both sides of the electrolyte. Impedance measurements of symmetric systems were performed in air at 700 and 800 °C. Samples were painted with Au paste to improve current collection and mounted on a button-cell test rig (model Probostat from NorEcs, Norway) for electrochemical testing.

A Zanher Zennium workstation (ZAHNER-elektrik GmbH & Co. KG, Germany) was used to obtain the electrochemical measurements. The frequency was varied between $5{\cdot}10^5$ and 0.01 Hz with an alternating (AC) signal amplitude of 10 mV, at temperatures of 700 and 800 °C. Data were analyzed with the ZPlot 3.5b software, using the equivalent circuit depicted in Figure 3.2., where L is an inductance, R_s, R_H and R_L are resistances and CPE_H-CPE_L are constant phase elements.

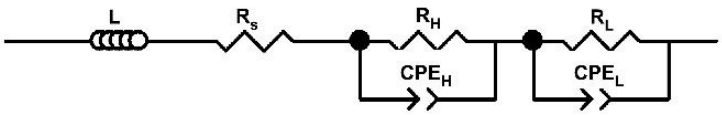

Figure 3.2.- Equivalent circuit used to analyse impedance data.

[22] Rodríguez-Carvajal J., FULLPROF rietveld pattern matching analysis of powder patterns, Grenoble, (**2011**).

The capacitance and relaxation frequency of each contribution have been calculated according to Eq.1 and 2, respectively[23].

$$C = (R^{1-n}Q)^{1/n} \qquad (1)$$

$$f_0 = \frac{(RQ)^{-1/n}}{2\pi} \qquad (2)$$

The ASR was calculated from the ASR =$R_p \cdot S/2$ formula, where S is the surface area of the sample and Rp is the polarization resistance (the sum of the resistance given by the semicircles at high and low frequencies in the niquist plots). Then, all is divided by 2 to take into account the symmetrical geometry of the half systems.

3.3. Results and discussion

3.3.1. Initial structural study of the compounds

The purity of the samples was analysed by X-Ray diffraction. All the materials (YSZ, SDC and LSF) prepared through the GN combustion route show the desired final phases. The signal identification for all XRD patterns was in good agreement with the Powder Diffraction File database (PDF). All the samples were pure as can be observed in Figure 3.3. for different batches. For the LNF compound, the appearance of extra shoulders in the experimental profile indicated a possible phase segregation to give two perovskite phase with different Ni/Fe ratio, as confirmed by Rietveld fitting analysis.

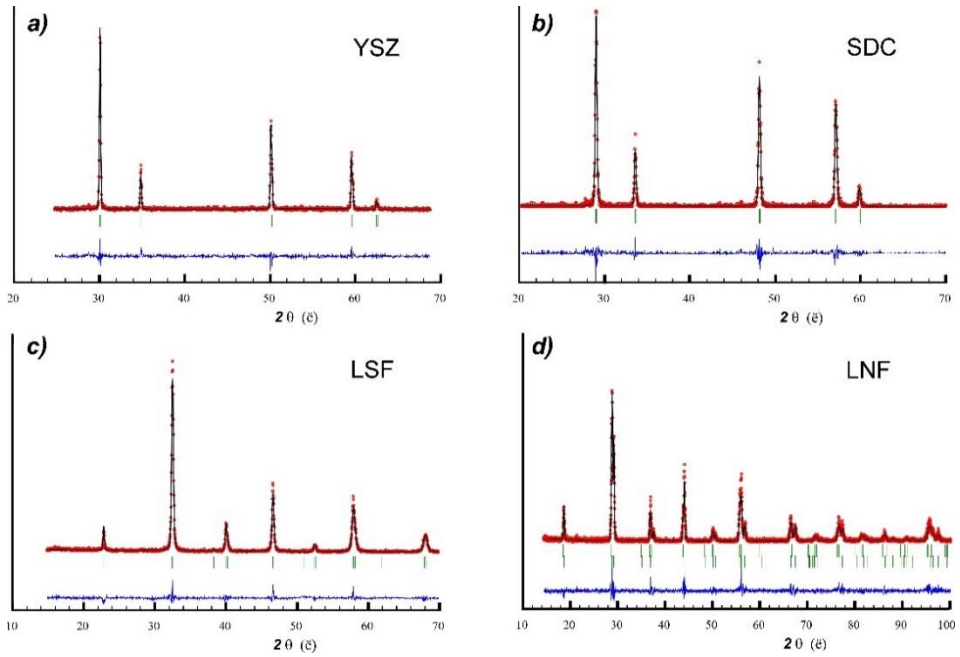

Figure 3.3.- X- ray diffraction pattern refinements results obtained for a) YSZ, b) SDC, c) LSF and d) LNF.

---

[23] Rieu M., Sayers R., Laguna-Bercero M.A., Skinner S.J., Lenormand P., Ansart F., Investigation of graded La_2NiO_4 delta cathodes to improve SOFC electrochemical performance, *J. Electrochem. Soc*. 157 (**2010**) B477-B480.

Figure 3.4. shows the micrographs of the electrolytes supports sintered at 1425 °C for 2 h in air. The heating rate from room temperature to 1425 °C was 3 °C/min and an alumina plate was placed on top to add weight to ensure the production of a flat electrolyte support without bending and/or cracking. After sintering, the diameter of the electrolytes was reduced from 13 to 9 mm (30% of contraction). As can be seen in the micrographs, although there were 1µm pores, it is possible that those pores were not connected, giving the required density to avoid the gas leakage through the electrolyte. No pinhole or cracks were observed, indicating a good sintering with grains of about 0.5-2.5 µm.

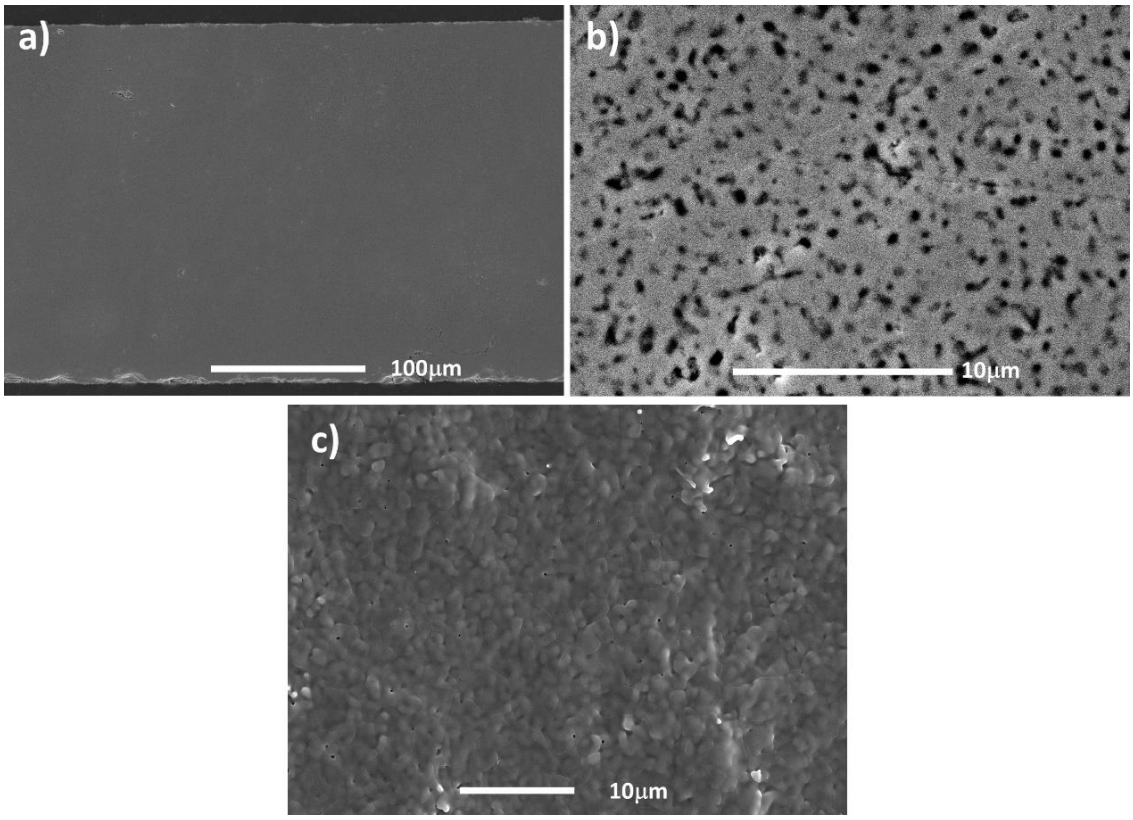

Figure 3.4.- SEM cross-sectional images of a) YSZ electrolyte support, b) higher magnification image and c) surface view.

3.3.2. Influence on the layer thickness on the microstructure

In order to determine the effect of the cathode thickness on the interface stability, a series of symmetrical systems were prepared with different cathode thicknesses. Figure 3.5. shows the typical cross-section micrographs of the systems a) T1 b) T3 c) T10 and d) T30. The study indicated that the microstructure of the layers were similar, with similar grain size, pore size and overall porosity. One can notice that in the case of sample T1 (Figure 3.5a.), the interface was not uniform, probably due to an insufficient amount of deposited material to cover the entire surface. In the other cases, although the layers were uniform, in the case of the sample T30 (Figure 3.5d.) the increase of cathode thickness seemed to detrimentally affect the layer quality, as poor adhesion between the SDC and LSF layers were observed with the appearance of cracks leading to delaminations.

As previously reported, the thickness of the layer had an influence on the residual stress distribution, resulting in a poor adhesion between layers[24]. On the other hand, T3 and T10 samples, presented good adhesion and continuous contact between the interfaces.

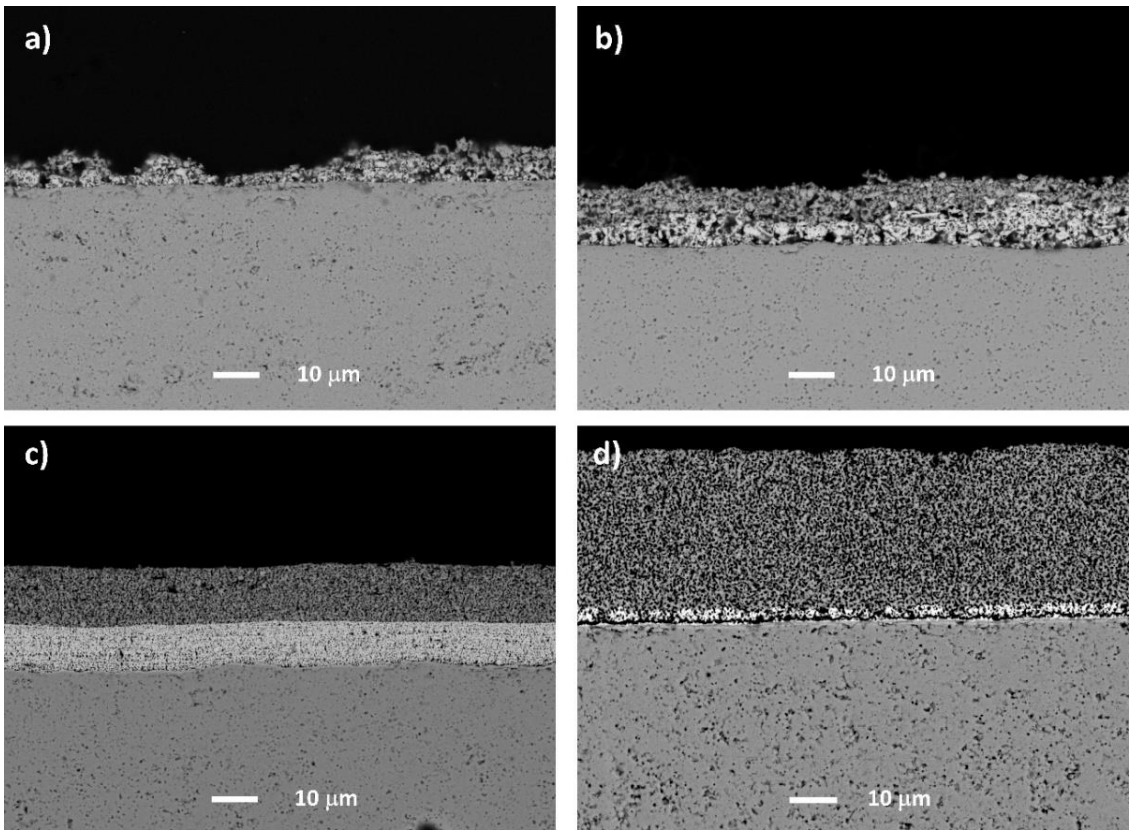

Figure 3.5.- SEM secondary electron cross-sectional images of YSZ-SDC-LSF with the thicknesses of samples a) T1, b) T3, c) T10 and d) T30.

Taking into account the obtained results, we concluded that the layers with better microstructure are the ones with 3 and 10 μm thickness.

3.3.3. Influence of the ball milling effect

With the aim of studying the influence of the ball milling process on the microstructure, different ball milling speeds have been used to prepare the inks. In the Figure 3.6., the micrographs taken from the cross-section of the systems are shown. Obvious morphological differences between the two different treatments were observed. As can be seen, the systems deposited with previously ball milled ink at 270 rpm for 24 hours, T3BM270 and T10BM270, presented more homogeneous layers, better contact and less fissures. In contrast, the results for the T3BM130 and T10BM130 samples show that, the powders were agglomerated and had bigger particle sizes, with broad size distribution, which leads to coarsening at high temperatures.

[24] Su S., Zhang W., Wu J., Zhou C., Effect of component thickness and anode composition on the residual stress of micro-tubular solid oxide fuel cell, *Int. J. Electrochem. Sci*. 12 (**2017**) 9121-9130.

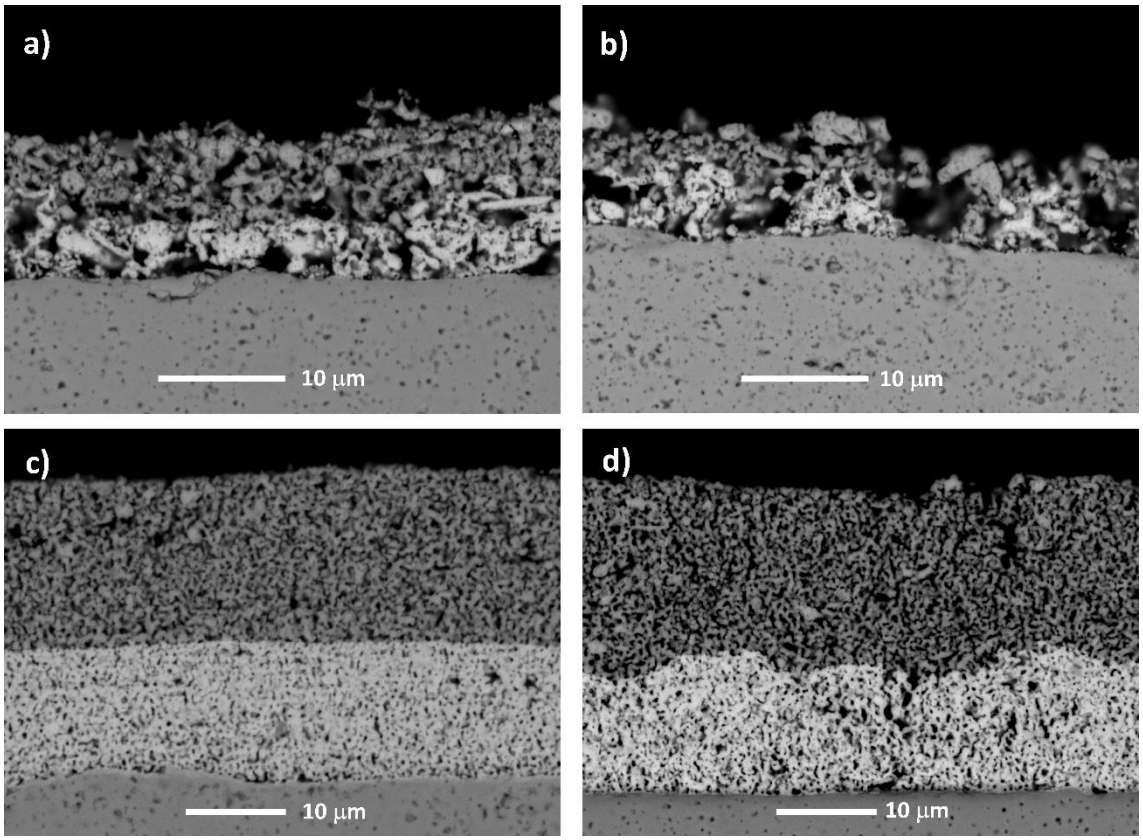

Figure 3.6.- SEM cross-section images of YSZ-SDC-LSF cells with different thicknesses and ball milling processes. The samples are a) T3BM270, b) T3BM130, c) T10BM270 and d) T10BM130.

The particle sizes results are presented in Table 3.2. As can be seen in the table, although there was no significant change on the LSF powders rate of microstructural refinement, in the case of SDC there was significant particle size decrease with increasing ball milling speed. This decrease in size may be the cause of the enhanced microstructure of T3BM270 and T10BM270 samples.

Table 3.2.- The particle size milled at different speeds.

Compound	d(μm)	Before ball milling	Milling speed 130rpm	Milling speed 270rpm
SDC	d_{10}	0.691	0.414	0.109
	d_{50}	1.506	1.032	0.572
	d_{90}	3.582	2.083	2.824
LSF	d_{10}	0.598	0.069	0.069
	d_{50}	0.903	0.136	0.137
	d_{90}	4.213	0.595	0.607

3.3.4. Evaluation of a multi-layered symmetric cell

Taking into account the studies detailed above, SDC, LSF and LNF layers have been deposited onto the electrolyte support. The thickness of the SDC layer was also reduced by taking into account the fact that it has to be thin to minimize the additional contribution to the ohmic resistance of the system, and that an overly thick buffer layer can cause delamination in the cathode[25,26]. To show the characterization of each layer and determine any segregation of elements, EDX micrographs were examined (Figure 3.7.). The identified elements were, Ni from LNF in green, Sr from LSF in red and Ce from SDC in blue. From Figure 3.7., it can be seen that there has been no diffusion between layers and that the adherence between the layers was good. Thus, by taking into account the systematic previous studies, it has been possible to avoid the creation of cracks and delaminations that could be seen in the other systems (see Supplementary material: Figure 3.S3 and Figure 3.S4).

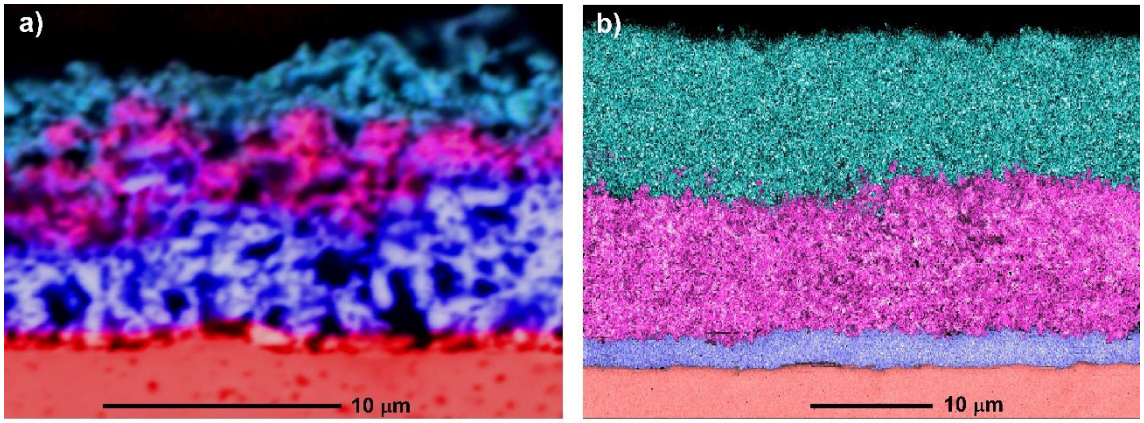

Figure 3.7.- EDX mapping of the cross section of the samples a) MCT3 and b) MCT10 after being optimized.

Figure 3.8. shows the typical electrochemical impedance spectra measured at 700 and 800 °C for the MCT3 and MCT10 samples. The high frequency intercept of the impedance arcs with the x axis corresponds to the ohmic resistance (R_s), which is generally attributed to the electrolyte and the contact resistance[27]. In the present case, R_s were in different ranges due to the electrolyte thickness variability. The Nyquist plots at both temperatures were composed of two semicircles at high frequency (HF) and low frequency (LF) range, which corresponds to R_H and R_L electrode polarization resistances, respectively. The total cathode polarization resistance (R_p) is the sum of both (R_H and R_L). All the results from the simulations are listed in Table 3.3.

---

[25] Kim Y., Kim-Lohsoontorn P., Bae J., Effect of unsintered gadolinium-doped ceria buffer layer on performance of metal-supported solid oxide fuel cells using unsintered barium strontium cobalt ferrite cathode, *J. Power Sources*. 195 (**2010**) 6420-6427.

[26] Endler-Schuck C., Weber A., Ivers-Tiffee E., Guntow U., Ernst J., Ruska J., Nanoscale Gd-doped CeO2 buffer layer for a high performance solid oxide fuel cell, *J. Fuel Cell Sci. Technol*. 8 (**2011**) 041001.

[27] Ecija A., Vidal K., Larrañaga A., Martínez-Amesti A., Ortega-San-Martín, L. Arriortua M.I., Structure and properties of perovskites for SOFC cathodes as a function of the A-site cation size disorder, *Solid State Ion*. 235 (**2013**) 14-21.

Table 3.3. Resistances, capacitances and relaxation frequencies obtained by modelling impedance diagrams of the cells after being optimized.

T (°C)	*Name*		*Contribution no. 1*		
		R_s (Ω cm^2)	R_H (Ω cm^2)	C_H (F cm^{-2})	F_H (kHz)
800	MCT3	1.31	0.13	$1.18x10^{-4}$	10.1
	MCT10	1.52	0.07	$2.41x10^{-4}$	9.62
700	MCT3	2.48	1.88	$2.68x10^{-7}$	315
	MCT10	3.10	0.96	$9.36x10^{-6}$	17.7

T (°C)	*Name*	*Contribution no. 2*			**ASR** (Ω cm^2)
		R_L (Ω cm^2)	C_L (F cm^{-2})	F_L (kHz)	
800	MCT3	0.53	$1.93x10^{-3}$	0.16	0.66
	MCT10	0.43	$2.71x10^{-3}$	0.14	0.50
700	MCT3	5.65	$1.39\ x10^{-3}$	0.02	7.53
	MCT10	4.31	$2.75\ x10^{-3}$	0.01	5.26

For MIEC perovskite electrodes, the HF arc is usually associated with charge transfer processes and the LF arc is usually attributed to oxygen reduction reaction at the cathode surface (adsorption and/or diffusion)[28]. This is consistent with the results listed in table 3.3., and also with previous LSF systems reported in the literature[29-31]. As expected, the total polarization resistances of the systems decrease when increasing the operating temperature, from 7.53 to 0.66 Ω cm^2 and from 5.26 to 0.66 Ω cm^2, for MCT3 and MCT10 samples, respectively. This decrease is a consequence of the higher oxygen diffusion and surface exchange kinetics of the LSF cathode and LNF contact layer, at higher temperatures. It is also evident that increasing the thickness of the cathode layers from 3 to 10 μm reduces the polarization resistance associated to both charge transfer and surface processes. In any case, these systems have adequate polarization resistances, 0.50 and 0.66 Ω cm^2 at 800 °C for MCT10 and MCT3 samples, respectively, as shown in Figure 3.8 in the impedance spectra of the systems.

[28] Adler S., Factors governing oxygen reduction in solid oxide fuel cell cathodes, *Chem. Rev*. 104 (**2004**) 4791-4843.

[29] Li M., Wang Y., Wang Y., Chen F., Xia C., Bismuth doped lanthanum ferrite perovskites as novel cathodes for intermediate-temperature solid oxide fuel cells, *ACS Appl. Mater. Interfaces*. 6 (**2014**) 11286-11294.

[30] Martínez-Amesti A., Larrañaga A., Rodríguez-Martínez L.M., Aguayo A.T., Pizarro J.L., Nó M.L., Laresgoiti A., Arriortua M.I., Reactivity between La(Sr)FeO_3 cathode, doped CeO_2 interlayer and yttria-stabilized zirconia electrolyte for solid oxide fuel cell applications, *J. Power Sources*. 185 (**2008**) 401-410.

[31] Kuengas R., Yu A.S., Levine J., Vohs J.M., Gorte R.J., An investigation of oxygen reduction kinetics in LSF electrodes s, *J. Electrochem. Soc*. 160 (**2013**) F205-F211.

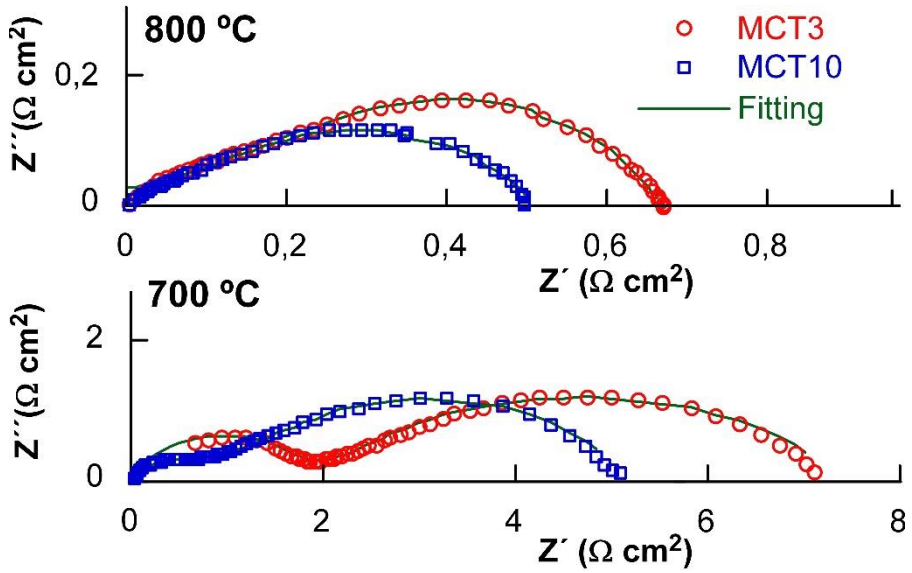

Figure 3.8.- Impedance spectra of YSZ-SDC-LSF-LNF systems at 700 and 800 °C.

3.4. Conclusions

Uniform and well-adhered coatings of LSF, SDC and LNF have been deposited by wet powder spraying onto an YSZ electrolyte support, with self-synthesized materials. The microstructure of the system has been shown to be unstable at thicknesses greater than 10 µm due to stresses caused by different TECs, while layers below 3 µm thickness lacked homogeneity.

The best results have been obtained with the inks ball milled at 270 rpm, avoiding the appearance of coarsening in the layers after sintering. In addition, reducing the thickness of the SDC layer, together with the use of an LNF layer, has produced systems with satisfactory electrochemistry.

To evaluate the systems, electrochemical impedance spectroscopy was performed, and a decrease in ASR was achieved with the thicker cathode layer (sample MCT10). The lowest polarization resistances of 0.5 Ω cm^2 at 800 °C corresponds to a symmetrical system consisting of a 3 µm SDC layer, 10 µm LSF layer and 10 µm LNF layer, with the ink used having been milled at a speed of 270 rpm.

Thus the results show that, despite being a very simple and cheap process, the wet powder spraying technique is an effective method for the deposition of the fuel cell layers, through suitable control of the layer thickness and ink milling regimes employed.

3.5. Supplementary material

Schematic figures and cross section micrographs of different cells.

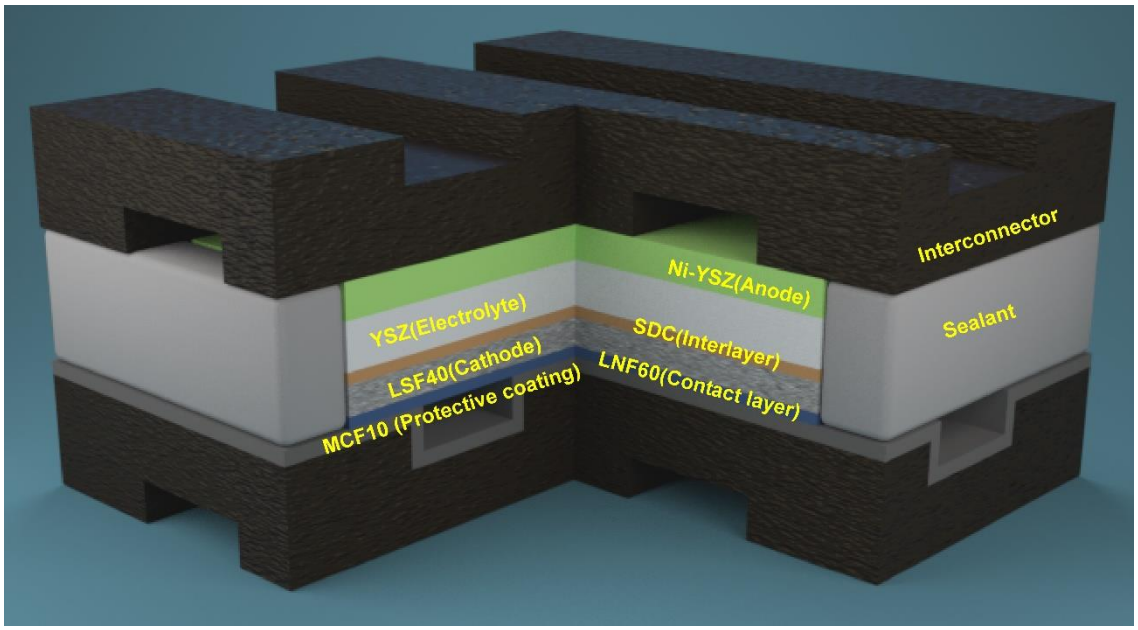

Figure 3.S1.- Technical sketch of a fuel cell stack. (12th European SOFC & SOE Forum 2016, page 213).

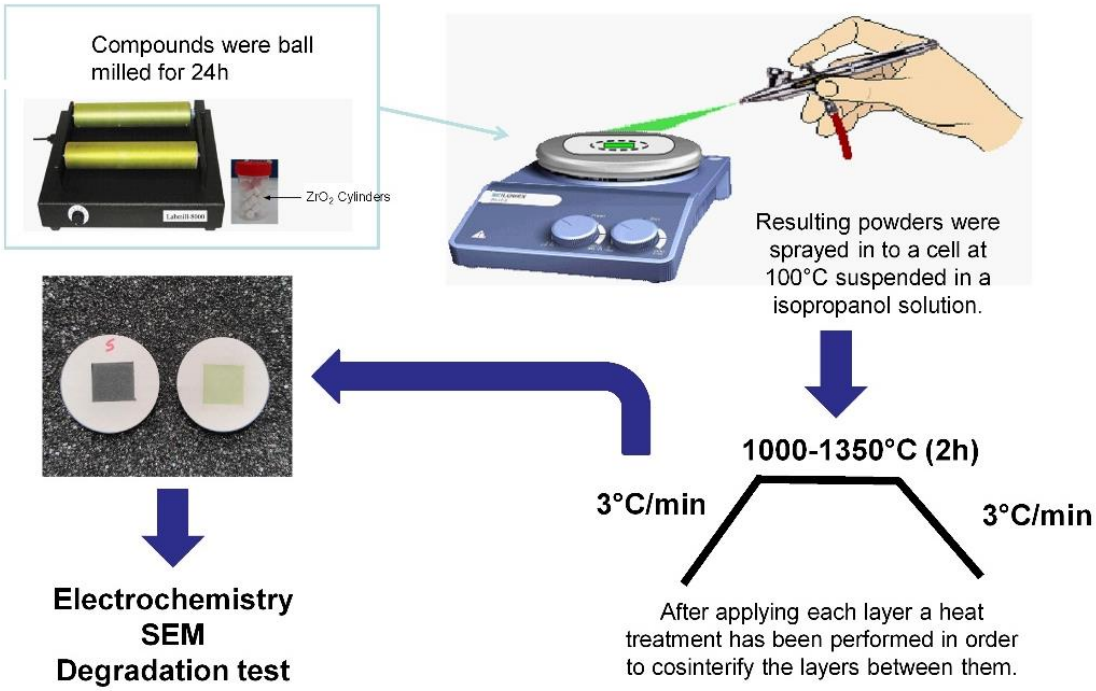

Figure 3.S2.- Deposition process scheme. (I Jornada de Jóvenes Investigadores de Cerámica y Vidrio, page 219).

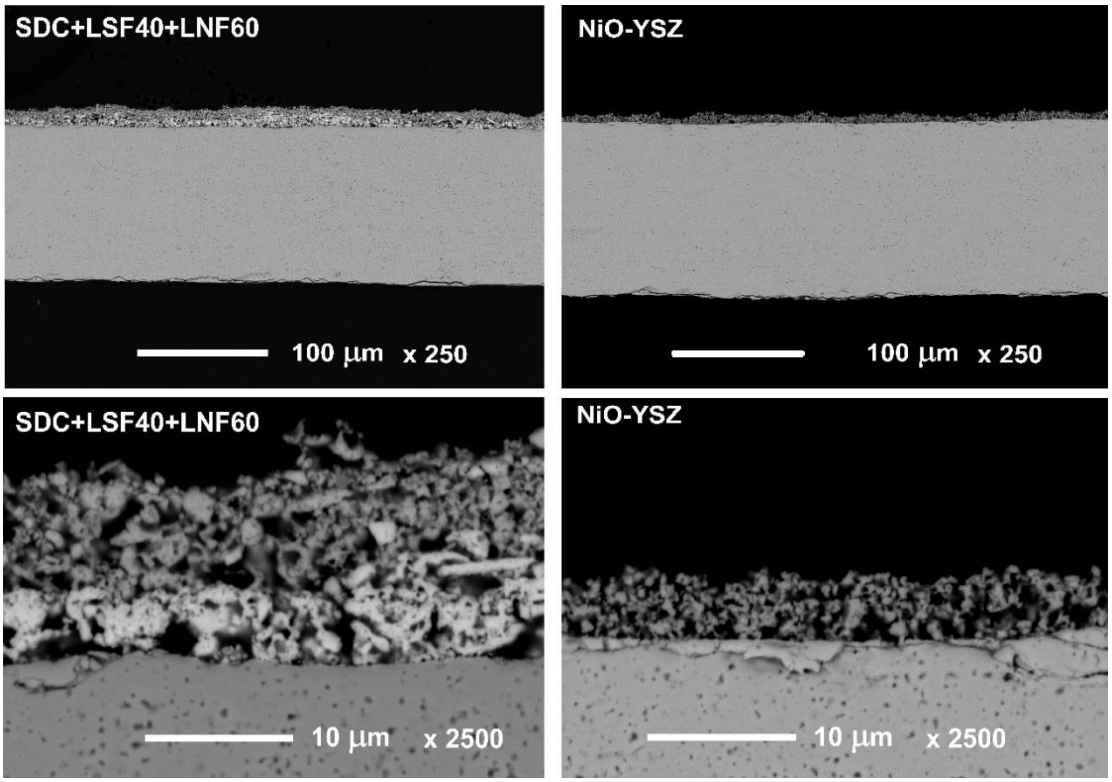

Figure 3.S3.- SEM cross-section images of YSZ-SDC-LSF-LNF and Ni-YSZ cells with 3 µm thickness layers. (The Energy and Materials Research conference 2017, page 217).

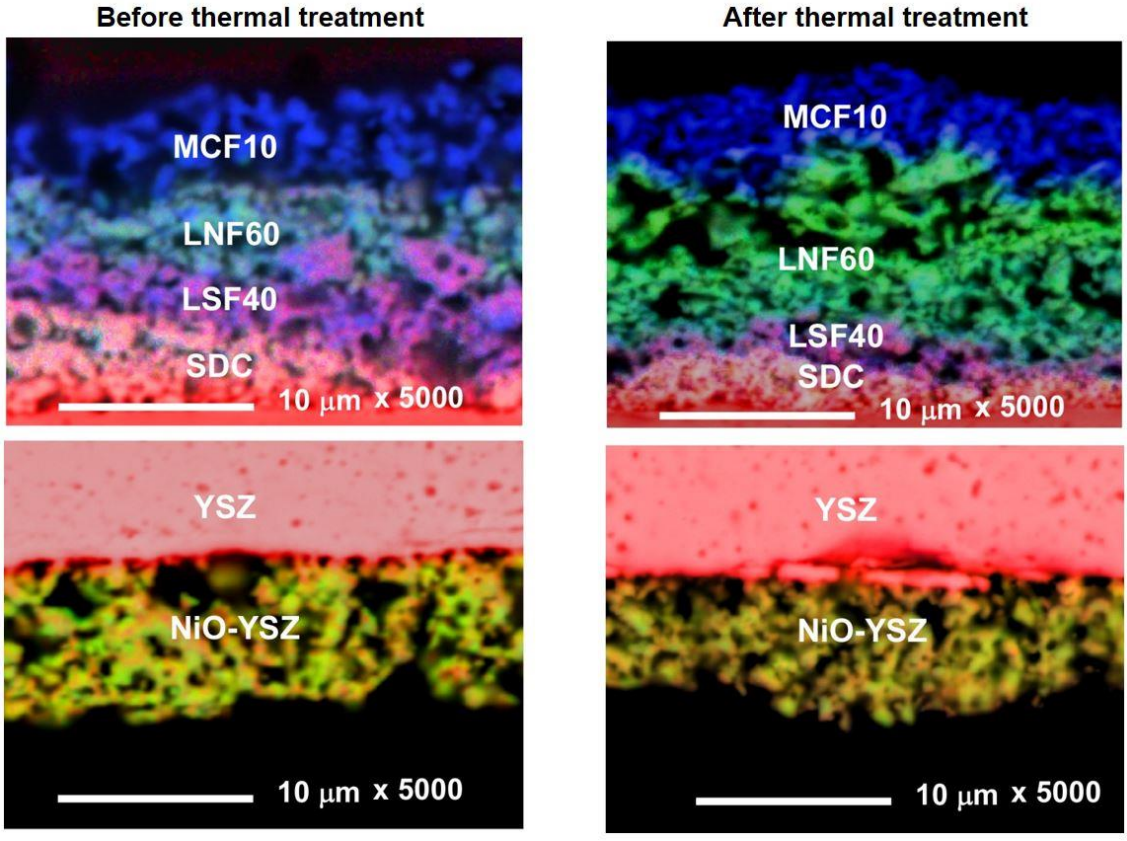

Figure 3.S4.- EDX mapping of the cross section of the first attempts before and after a 200 h thermal treatment. (The Energy and Materials Research conference 2017, page 217).

4. FABRICACIÓN DE UNA CELDA DE COMBUSTIBLE DE ÓXIDO SOLIDO EN SOPORTE ANÓDICO

La investigación realizada, que se presenta en este capítulo, ha quedado reflejada en el artículo **"SOFC cell fabrication procedure with self made nanopowders, International journal of hydrogen energy, XX (2019)XX-XX"** y en la comunicación del congreso:

- "Development of a SOFC cell with self-made nanopowders", 13th European SOFC & SOE Forum, 2018, Lucerna (Suiza).

4. FABRICATION OF ANODE SUPPORTED SOLID OXIDE FUEL CELL

The studies carried out throughout this chapter have resulted in the **"SOFC cell fabrication procedure with self made nanopowders, International journal of hydrogen energy, XX (2019) XX-XX"** scientific article and the communication in the following congres:

- "Development of a SOFC cell with self-made nanopowders", 13th European SOFC & SOE Forum, 2018, Lucerne (Switzerland).

Resumen del capítulo 4

En el capítulo anterior, se ha estudiado el efecto de la molienda en las pastas y del espesor de las capas de la celda. En la última parte del capítulo, se muestra una optimización de la celda simétrica teniendo en cuenta las variables estudiadas, obteniéndose resultados satisfactorios.

En este capítulo, se han recogido los resultados presentados en el apartado previo y se ha avanzado a un sistema complejo, adecuándolo para su utilización en stacks. Para ello, desde un sistema simétrico de soporte electrolito, se ha desarrollado como configuración final, un sistema asimétrico de soporte anódico. También, se ha aumentado el diámetro de las celdas de 1 a 4 cm^2, consiguiendo incrementar sustancialmente la superficie activa de las mismas. A la hora de fabricar los soportes, se ha tenido en cuenta el espesor de los mismos y la influencia de la porosidad del electrodo anódico.

Con el fin de reducir los costes del procesado y la energía, se ha optado por emplear el cosinterizado para el procesado del electrolito y el ánodo. Para la fabricación de las capas, se ha seguido utilizando la técnica de sprayado. Al sustituir el soporte, se han optimizado los coeficientes de expansión térmica de los diferentes componentes, empleando para ello intercapas de mezclas de los materiales base, reduciendo, de esta manera, las tensiones generadas por la diferencia en los coeficientes térmicos de expansión. Con respecto a las medidas electroquímicas del sistema final, se han adecuado los flujos de gases y el sellado de las celdas, aplicando para ello un cemento de altas temperatura. De esta manera, la caracterización electroquímica, se ha realizado mediante medidas de espectroscopia de impedancias y curvas de potencial. Con el fin de estudiar la degradación de la celda, se han empleado largos tiempos a alta temperatura aplicando un potencial.

En paralelo, se han sometido a las celdas a largos períodos de tiempo, 1500h, a 800 ºC, (temperatura de funcionamiento de una pila SOFC convencional), para poder estudiar la posible segregación de fases. Asimismo, la adherencia y la microestructura de las capas se han estudiado mediante microscopia electrónica de barrido y mapas EDX.

Summary of the chapter 4

In the previous chapter, the effect of the ball milling on the pastes and the thickness on the cell layers were studied. In the last part of the chapter, an optimization of the symmetric cell has been done taking into account the studied variables, obtaining satisfactory results.

In the current chapter, the knowledge acquired in the previous studies has been used in order to develop a more complex system has been made, adapting it for real stacks. In this sense, from a symmetric electrolyte support system, the configuration has been developed to an asymmetric anodic support system. The diameter of the cells has also been increased from 1 to 4 cm^2, getting to increase the active surface area of the cell. As a part of manufacturing the supports, the thickness of the layers and the influence of the porosity of the anodic electrode have been taken into account.

In order to reduce the processing costs and the needed energy, it has been chosen to use the cosinterization to prepare the electrolyte with the anode. For the creation of layers, the technique of wet powder spraying has been used. With the change of the support, the thermal expansion coefficients of the different components have also been adapted. To solve this, interlayers of the components mixtures have been used, reducing the stresses generated by the thermal shocks. For the electrochemical measurements of the anode supported cell, which has taken care to adapt the gas flows and the sealing of the measured cells, using a high temperature cement for it. In this way, to perform the electrochemical characterization, impedance spectroscopy and potential curves have been used. With the aim to study the degradation, the cells have been left measuring for long periods of time.

In parallel, the cells have been placed for a long time (1500h) in a muffle furnace at 800 ° C, which is the operating temperature of a conventional SOFC cell, to study the phase segregation. The adhesion and morphology of the different layers has been studied using Scanning Electron Microscopy and EDX maps.

SOFC cell fabrication procedure with self made nanopowders

International journal of hydrogen energy, XXX **(2019)** XXX-YYY

4.1. Introduction

Some of the main limitations of the economic potential of solid oxide fuel cells are their manufacturing costs and short operation life, which are an obstacle for their industrial implementation[1,2]. Accordingly, researchers have attempted to reduce their fabrication cost employing the co-firing method, which saves expensive production steps and improves the adherence between the different layers[2,3]. Moreover, the expensive and complex processing steps for anode-supported electrolyte tapes could be replaced by cheaper, simpler and continuous techniques. Among the deposition methods of composite layers, spray-coating is a relatively cost-effective process. Originally used for preparing porous ceramic layers, has high potential to control the quality and thickness of cell layers. In the simplest way, this method is performed with no handling, presenting a highly reproducible process as well as it is suitable for planar surfaces and appropriate for producing dense layers[4,5].

One of the main problem in the cell performance is the Thermal Expansion Coefficient (TEC) mismatch between the different layer compounds, that leads to delaminations and cracks in the layers during the thermal cycling. To overcome this problem, the TEC could be adjusted by two methods: by doping ions with different ionic radius; or adding other materials with similar TEC, doing in some cases a mixture between the two materials, resulting in excellent matching[6,7].

---

1 Kupecki J., Kluczowski R., Papurello D., Lanzini A., Kawalec M., Krauz M., Santarelli M., Characterization of a circular 80 mm anode supported solid oxide fuel cell (AS-SOFC) with anode support produced using high-pressure injection molding (HPIM), *Int. J. Hydrog. Energy*. (**2018**) doi.org/10.1016/j.ijhydene.2018.02.143

2 Ananyev M.V., Farlenkov A.S., Eremin V.A., Kurumchin E.K., Degradation kinetics of LSM–YSZ cathode materials for SOFC, *Int. J. Hydrog. Energy*. 43 (**2018**) 951-959.

3 Nguyen X.V., Chang C.T., Jung G.B., Chan S.H., Huang W.C.W., Hsiao K.J., Lee W.T.,. Chang S.W, Kao I.C., Effect of sintering temperature and applied load on anode-supported electrodes for SOFC application, *Energies*. 9 (**2016**) 701.

4 Carpanese M.P., Barbucci A., Canu G., Viviani M., $BaCe_{0.85}Y_{0.15}O_{2.925}$ dense layer by wet powder spraying as electrolyte for SOFC/SOEC applications, *Solid State Ion*. 269 (**2015**) 80-85.

5 Morales M., Navarro M.E., Capdevila X.G., Roa J.J., Segarra M., Processing of graded anode-supported micro-tubular SOFCs based on samaria-doped ceria via gel-casting and spray-coating, *Ceram. Int*. 38 (**2012**) 3713-3722.

6 Li N., Wei B., Lü Z., Huang X., Su W., $GdBaCo_2O_{5+\delta}$–$Sm_{0.2}Ce_{0.8}O_{1.9}$ composite cathodes for intermediate temperature SOFCs, *J. Alloy. Compd*. 509 (**2011**) 3651-3655.

7 Patro P.K., Delahaye T., Bouyer E., Development of $Pr_{0.58}Sr_{0.4}Fe_{0.8}Co_{0.2}O_{3-\delta}$–GDC composite cathode for solid oxide fuel cell (SOFC) application, *Solid State Ion*. 181 (**2010**) 1378-1386.

Taking into account the importance of TEC in the deterioration of properties of the cell during the life-time, the analysis of a long-term test could be interesting. Usually, degradation affects not only the electrochemical characteristics of the studied materials, but also the microstructure.

The most common used materials in SOFC´s are nickel- yttria stabilized zirconia (Ni-YSZ) cermets as anode[8,9], yttria stabilized zirconia (YSZ) as electrolyte[10,11] and (La,Sr)MnO_3 (LSM), (La,Sr)FeO_3 (i.e. LSF), or (La,Sr)(Co,Fe)O_3 (i.e. LSCF) as cathode[12-14]. Currently, ceria based materials ($Ce_{0.8}Gd_{0.2}O_{1.9}$ (GDC) and $Ce_{0.8}Sm_{0.2}O_{1.9}$ (SDC)) can be used as reaction barrier layer between the electrolyte and the cathode, with the objective of preventing the formation of poorly conducting secondary phases, such as $La_2Zr_2O_7$ or $SrZrO_3$ phases[15,16]. The use of cathode contact layers such as $LaNi_{0.6}Fe_{0.4}O_3$ (LNF) and $LaNi_{0.6}Co_{0.4}O_3$ (LNC) have demonstrated to provide and maintain stable electrical conduction paths between the interconnect and the cathode layer, minimizing the interfacial ohmic resistance and stack power losses[17].

---

[8] Song B., Ruiz-Trejo E., Bertei A., Brandon N.P., Quantification of the degradation of Ni-YSZ anodes upon redox cycling, *J. Power Sources*. 374 (**2018**) 61-68.

[9] Nagasawa T., Hanamura K., Prediction of overpotential and effective thickness of Ni/YSZ anode for solid oxide fuel cell by improved species territory adsorption model, *J. Power Sources*. 353 (**2017**) 115-122.

[10] Fernández-González R., Molina T., Savvin S., Moreno R., Makradi A., Núñez P., Fabrication and electrical characterization of several YSZ tapes for SOFC applications, *Ceram. Int.* 40 (**2014**) 14253-14259.

[11] Yan K., Kishimoto H., Develos-Bagarinao K., Yamaji K., Horita T., Yokokawa H., Chemical compatibility of doped yttrium chromite and ceria composite materials with YSZ electrolyte, *Solid State Ion*. 288 (**2016**) 88-93.

[12] Zhu J.H., Ghezel-Ayagh H., Cathode-side electrical contact and contact materials for solid oxide fuel cell stacking: A review, *Int. J. Hydrog. Energy*. 42 (**2017**) 24278-24300.

[13] López-Robledo M.J., Laguna-Bercero M.A., Larrea A., Orera V.M., Reversible operation of microtubular solid oxide cells using $La_{0.6}Sr_{0.4}Co_{0.2}Fe_{0.8}O_{3-\delta}$-$Ce_{0.9}Gd_{0.1}O_{2-\delta}$ oxygen electrodes, *J. Power Sources*. 378 (**2018**) 184-189.

[14] Vidal K., Larrañaga A., Morán-Ruiz A., Aguayo A.T., Laguna-Bercero M.A., Yeste M.P., Calvino J.J., Arriortua M.I., Effect of synthesis conditions on electrical and catalytical properties of perovskites with high value of A-site cation size mismatch, *Int. J. Hydrog. Energy*. 41 (**2016**) 19810-19818.

[15] Martínez-Amesti A., Larrañaga A., Rodríguez-Martínez L.M., Nó M.L., Pizarro J.L., Laresgoiti A., Arriortua M.I., Chemical compatibility between YSZ and SDC sintered at different atmospheres for SOFC applications, *J. Power Sources*. 192 (**2009**) 151-157.

[16] Coddet P., Vulliet J., Richard C., Caillard A., Thomann A., Characteristics and properties of a magnetron sputtered gadolinia-doped ceria barrier layer for solid oxide electrochemical cells, *Surf. Coat. Technol*. 339 (**2018)** 57-64.

[17] Morán-Ruiz A., Vidal K., Laguna-Bercero M.A., Larrañaga A., Arriortua M.I., Effects of using $(La_{0.8}Sr_{0.2})_{0.95}Fe_{0.6}Mn_{0.3}Co_{0.1}O_3$ (LSFMC), $LaNi_{0.6}Fe_{0.4}O_{3-\delta}$ (LNF) and $LaNi_{0.6}Co_{0.4}O_{3-\delta}$ (LNC) as contact materials on solid oxide fuel cells, *J. Power Sources*. 248 (**2014**) 1067-1076.

The current work describes the fabrication process with previously self synthesized components[18] (Ni-YSZ, YSZ, SDC, LSF and LNF) which were developed and applied for the creation of a fuel cell. In some cases, to overcome the TEC mismatch between layers, composite layers have been added (between the SDC and the LSF; and the LSF and LNF) doing mixtures. The anode support was carried out via uniaxial pressing and the deposition of thin layers of electrolyte, barrier, cathode and contact layer was made by manual spray coating. The microstructure was characterized by Scanning Electron Microscopy (SEM) and Energy Dispersive X-ray Spectroscopy (EDX). The electrochemical response of this assembly was studied using current-voltage (I-V), current-power (I-P) curves and electrochemical impedance spectroscopy (EIS). An investigation of the degradation phenomena has been done, in order to observe the presence of element diffusion between the different layers.

4.2. Experimental

4.2.1. Synthesis and performance of the cells

The synthesis procedure for NiO-YSZ, YSZ, SDC, LSF and LNF components has been described in details elsewhere[28]. The simultaneous sinterization of the supporting anode and electrolyte was carried out producing the anode by uniaxial pressing and depositing a thin dense YSZ electrolyte layer on top of green anode supports (20 µm), using manual spray coating. The anode was made with NiO/YSZ ratio of 63 wt % /37 wt %, a 18 mm diameter, thickness of 800 µm and a porosity of 40 % using starch as pore former. The anode pellets were pre-sintered in air at 600 °C for 2 h, before being used as supports for YSZ spraying. This thermal treatment was adequate to provide a mechanical resistance without causing a significant shrinkage. The NiO-YSZ/YSZ tapes were co-fired in air at 1425 °C for 2 h. For the deposition of YSZ and the remaining layers, the starting powders were grinded through wet ball milling, by adding the appropriate amount of solvent (2-propanol), at 270 rpm for 24 h. The deposition was carried out at room temperature, through an airbrush (Iwata eclipse HP-BCS) operated at an angle of 90 ° respect to the supporting plane. The distance between the nozzle and the support was ranged between 2 and 10 cm.

Three cells were performed and investigated in this paper, which are described in Table 4.1. The first cell was made out of anode support and YSZ layer. In the second cell, SDC, SDC-LSF composite, and LSF cathode layers were added. Finally, taking into account previous results, LSF-LNF composite and LNF contact layer were added to the previous cell. The deposition of the layers was carried out in the same way as YSZ, with the different that they were sintered separately at a temperature of 1150 °C for 2 h. The schematic structure of the anode supported cells is shown in Figure 4.1 (see Supplementary material: Figure 4.S1).

[18] Wain-Martin A., Morán-Ruiz A., Vidal K., Larrañaga A., Laguna-Bercero M.A., Arriortua M.I., Scalable synthetic method for SOFC compounds, *Solid State Ion*. 313 (**2017**) 52-57.

Table 4.1.- Details of the investigated samples.

Sample name	Layer	Thickness
Cell 1	Ni-YSZ	800 µm
	YSZ	20 µm
Cell 2	Ni- YSZ	800 µm
	YSZ	20 µm
	SDC	5 µm
	SDC-LSF	15 µm
	LSF	45 µm
Cell 3	Ni- YSZ	800 µm
	YSZ	20 µm
	SDC	5 µm
	SDC/LSF	15 µm
	LSF	45 µm
	LSF/LNF	15 µm
	LNF	15 µm

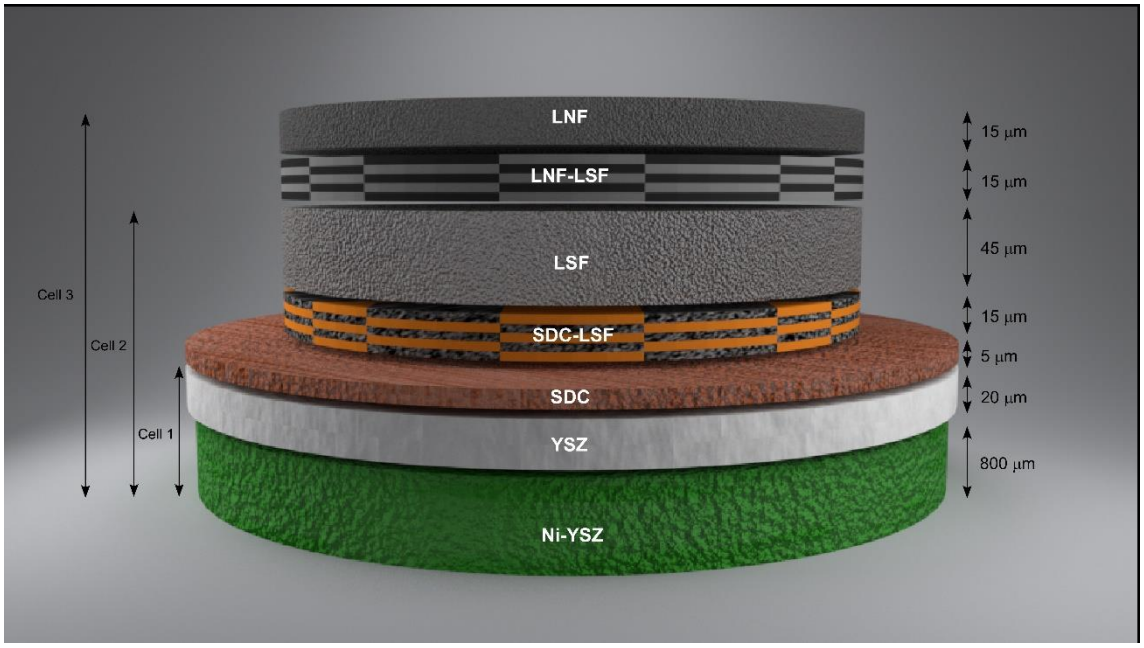

Figure 4.1.- Schematic for an anode supported SOFC design.

4.2.2. Morphological characterization

Cross sections of the samples were analyzed using SEM/EDX system. Composition analysis was performed using back-scattered electrons (BSE) at 20 kV accelerating voltage and $5x10^{-9}$ A current. For EDX point analysis live time was set to 100 s. EDX system calibration was performed measuring the beam current on pure element standards, allowing quantitative elemental analyses. Moreover, EDX mapping was carried out using 13762.56 s (70 ms/pixel) as live time. The data processing was performed using Oxford INCA software. The characteristic emission lines used for the analysis were L_α for La and Ce, K_α for Ni and Fe, and $L_{\beta 1}$ for Sr.

4.2.3. Electrochemical measurements

For the electrochemical test, the samples were painted with Pt paste to improve current collection and mounted on a button-cell test rig (model Probostat from NorECs, Norway) attached by a spring loaded mechanism. Omegabond 700 high temperature cement was introduced to achieve sealing between the two compartments and a thermal treatment at 80 °C for 24 h under air was followed to ensure efficient sealing. The electrochemical measurements were obtained using a multichannel Potentiostat/Galvanostat VMP3 (Biologic) using 100% of H_2 humidified at 3% as reactant gas in the anodic compartment and air in the cathodic one at 750, 800 and 865 °C. Data were analysed with the ZPlot 3.5b software, using the equivalent circuit explained in the previous chapter.

4.3. Results and discussion

4.3.1. Anode-electrolite cell configuration

Figure 4.2. shows the SEM micrographs of the surface and cross-section morphology of the anode supported electrolyte cells. It can be seen from the images that the YSZ layer is well sintered, with closed pores and enough dense electrolyte to avoid fuel leakage. The contact between them is also correct after the measurement, as can be seen in Figure 4.2b. These results reveal that spray coating is an effective and simple method to make a dense electrolyte layer.

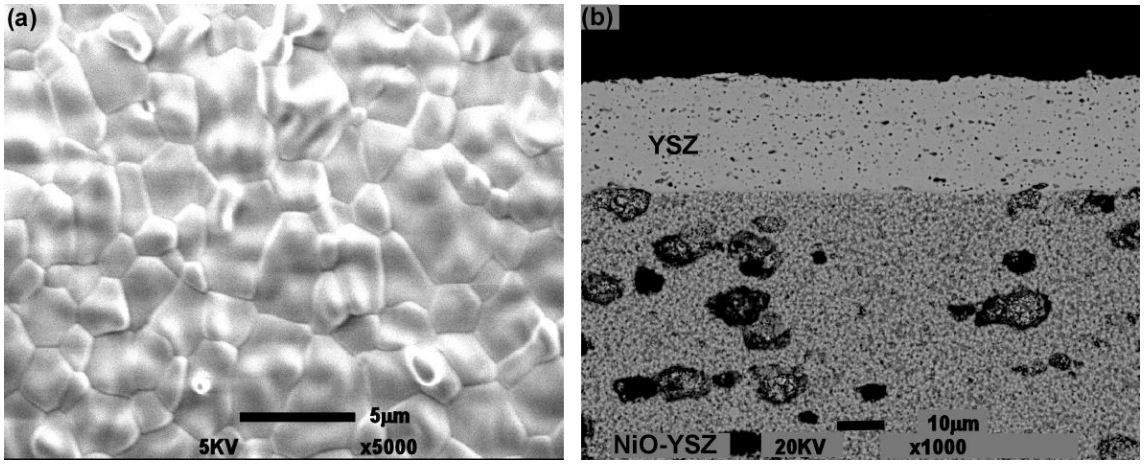

Figure 4.2.- Micrographs of (a) the surface and (b) cross section morphology of the electrolyte layer.

For the electrochemical characterization, in sample cell 1 platinum paste was used as cathode. The current–voltage and current–power characteristics of the cell (1 cm^2 effective area) at various operating temperatures (750, 800 and 865 °C) are given in Figure 4.3.a. The obtained open circuit voltage (OCV) in cell 1 was 0.912 V at 865 °C, proving that the YSZ electrolyte layer was dense enough without gas cross over, and that the performance of the sealing components was excellent. Figure 4.3a. shows that the maximum measurement power densities of the cell 1 reach 123 $mW \cdot cm^{-2}$ and 40 $mW \cdot cm^{-2}$ at 865 and 800 °C, respectively. Figure 4.3b., shows the electrochemical impedance spectra (EIS) of the cell 1 and the fit results obtained using the Zview software are collected in the Table 4.2.

The first intercept on the real axis in the high frequency region represents the ohmic resistance (R_s), which involves the ohmic resistance associated with of the electrodes, interfaces and the electrolyte. In the case of cell 1, can be though that the bigger contributor to the R_s was the YSZ electrolyte. On the other hand, the obtained high total resistance values, could be due to the contribution of a bad contact between the platinum and the electrolyte, caused by a low relation between the TECs of the components.

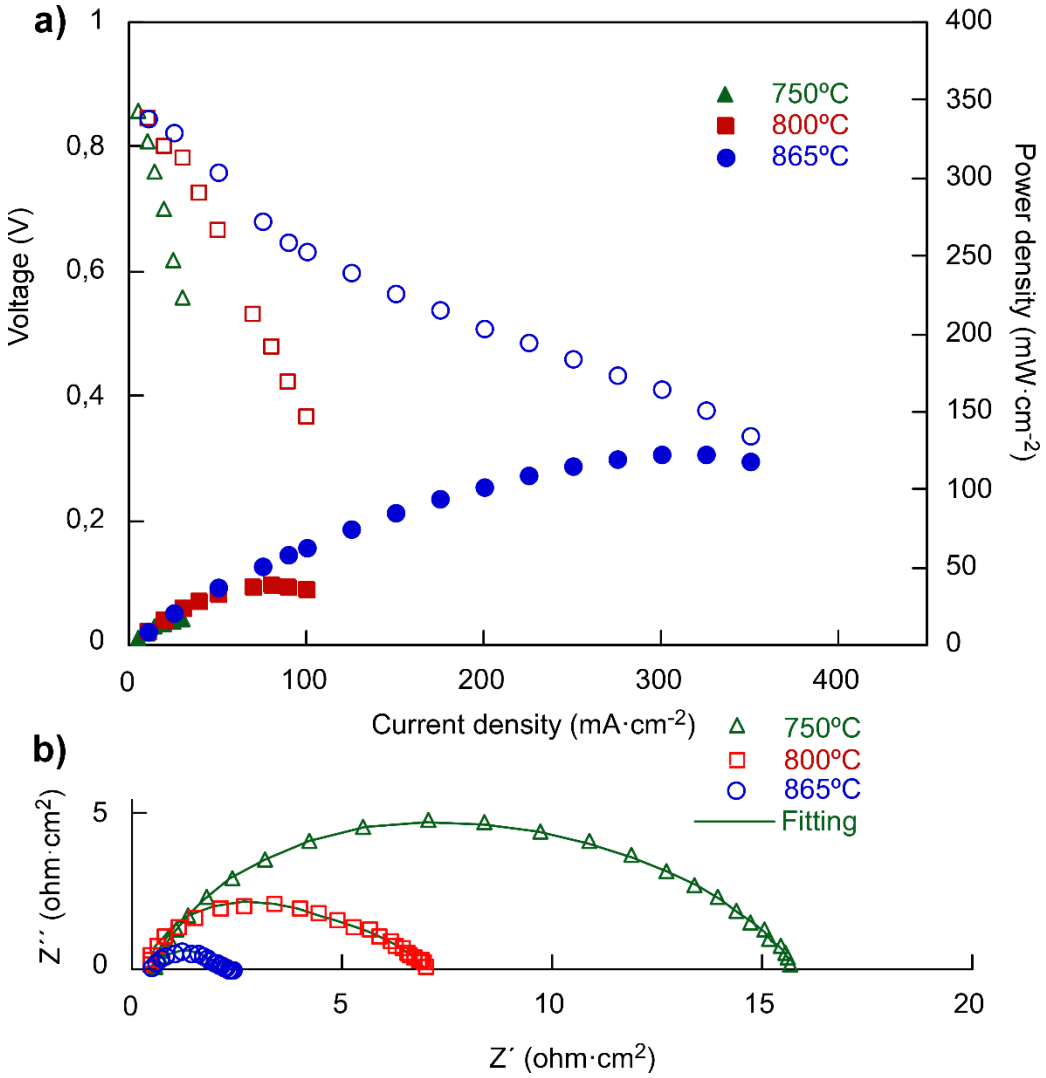

Figure 4.3.- a) (I-V) and (I-P) curves and b) electrochemical impedance spectra of the sample Cell 1 at 750, 800 and 865 °C, using Pt paste as electrode.

Table 4.2.- Polarization resistance of the cell 1 obtained from the fits to EIS.

T (°C)	R_s (Ωcm²)	R_H (Ωcm²)	C_H (Fcm^{-2})	F_H (Hz)
750	0.363	5.487	$1.9 \cdot 10^{-5}$	1472
800	0.330	3.542	$1.2 \cdot 10^{-5}$	3800
865	0.217	1.617	$4.8 \cdot 10^{-5}$	2017

Table 4.2. cont.- Polarization resistance of the cell 1 obtained from the fits to EIS.

T (°C)	R_L (Ωcm^2)	C_L (Fcm^{-2})	f_L (Hz)	R_p (Ωcm^2)	R_{Total} (Ωcm^2)
750	10.0	$3.9 \cdot 10^{-5}$	410	15.5	15.860
800	3.12	$1.1 \cdot 10^{-4}$	480	6.66	6.992
865	1.34	$7.6 \cdot 10^{-5}$	1560	2.96	3.172

4.3.2. Anode-electrolite-cathode cell configuration

Once the tightness of the electrolyte was tested, the function of the cathode in the cell arrangement was determined. To avoid the differences between the TECs, a LSF/SDC composite layer was deposited between SDC and LSF layers to improve the contact between them (see Supplementary material: Figure 4.S2). Shown in Figure 4.4., are the SEM micrographs and an EDX mapping of the cathode side using 15 µm thickness SDC-LSF composite layer. As can be seen, no cracking or delamination in the LSF layer and a good adherence with LSF and SDC layers are observed. The electrodes shows the typical porous microstructure and the layers are continuous. The EDX mapping (shown in Figure 4.4c.) indicated no significant inter diffusion of elements at the interfaces.

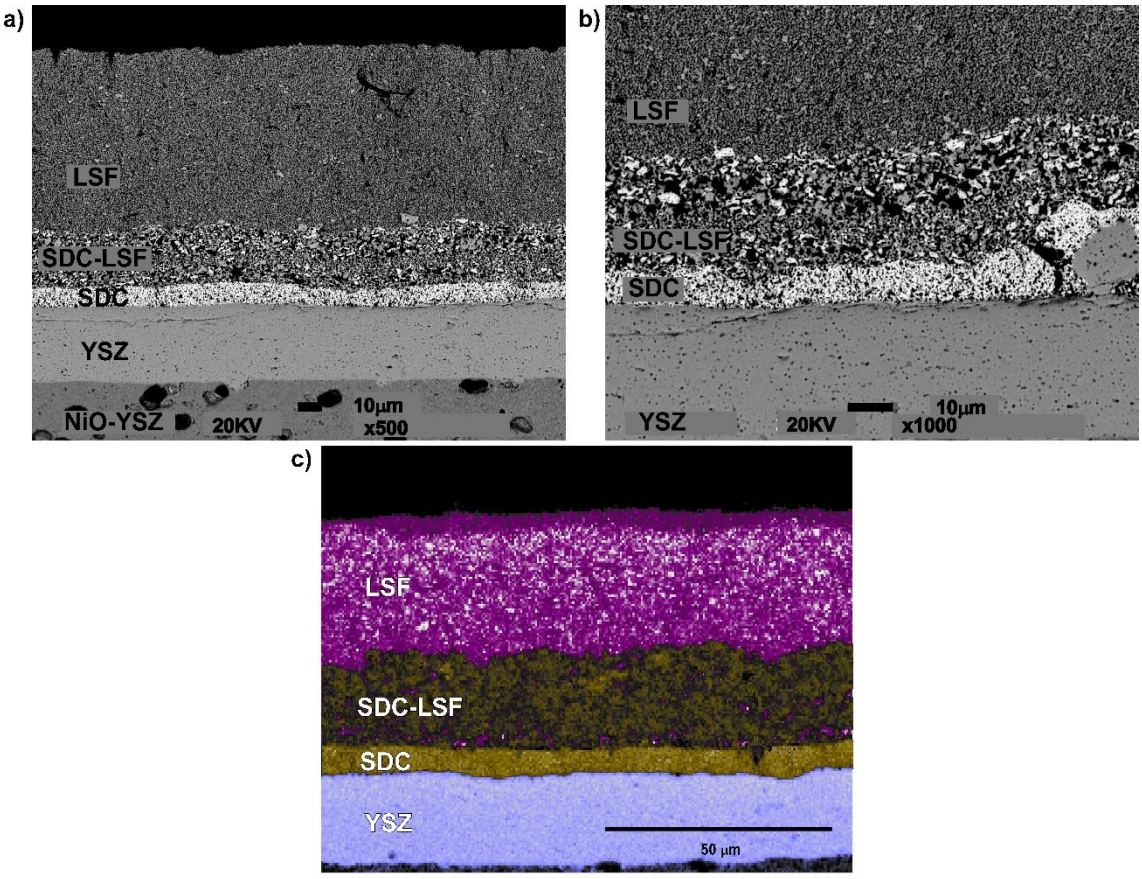

Figure 4.4.- SEM images of the cathode side (a) low magnification image, (b) higher magnification image and (c) EDX mapping.

The obtained open circuit voltage (OCV) in cell 2 reach 1.066 V at 865 °C. Figure 4.5a. shows the typical current–voltage and current–power curves, measured at 750, 800 and 865 °C for the sample cell 2. However, the maximum measurement power densities of the cell 2 using LSF as cathode can reach 190 $mW \cdot cm^{-2}$ and 130 $mW \cdot cm^{-2}$ at 865 and 800°C, respectively. Furthermore, the EIS for the sample cell 2, measured at 750, 800 and 865 °C, are presented in Figure 4.5b. and the obtained fit result are collected in Table 4.3. As might be seen, the use of LSF as cathode improved the OCV, the power density and the conductivity with respect to the cell 1. The LSF is a mixed ionic and electronic conductor (MIEC), which extends the triple phase boundary zone to the entire oxygen electrode, greatly decreasing the polarization resistance[19]. This feature, with a better adhesion between the cathode and the electrolyte, results in better electrochemical result than with the exclusive use of platinum as electrode

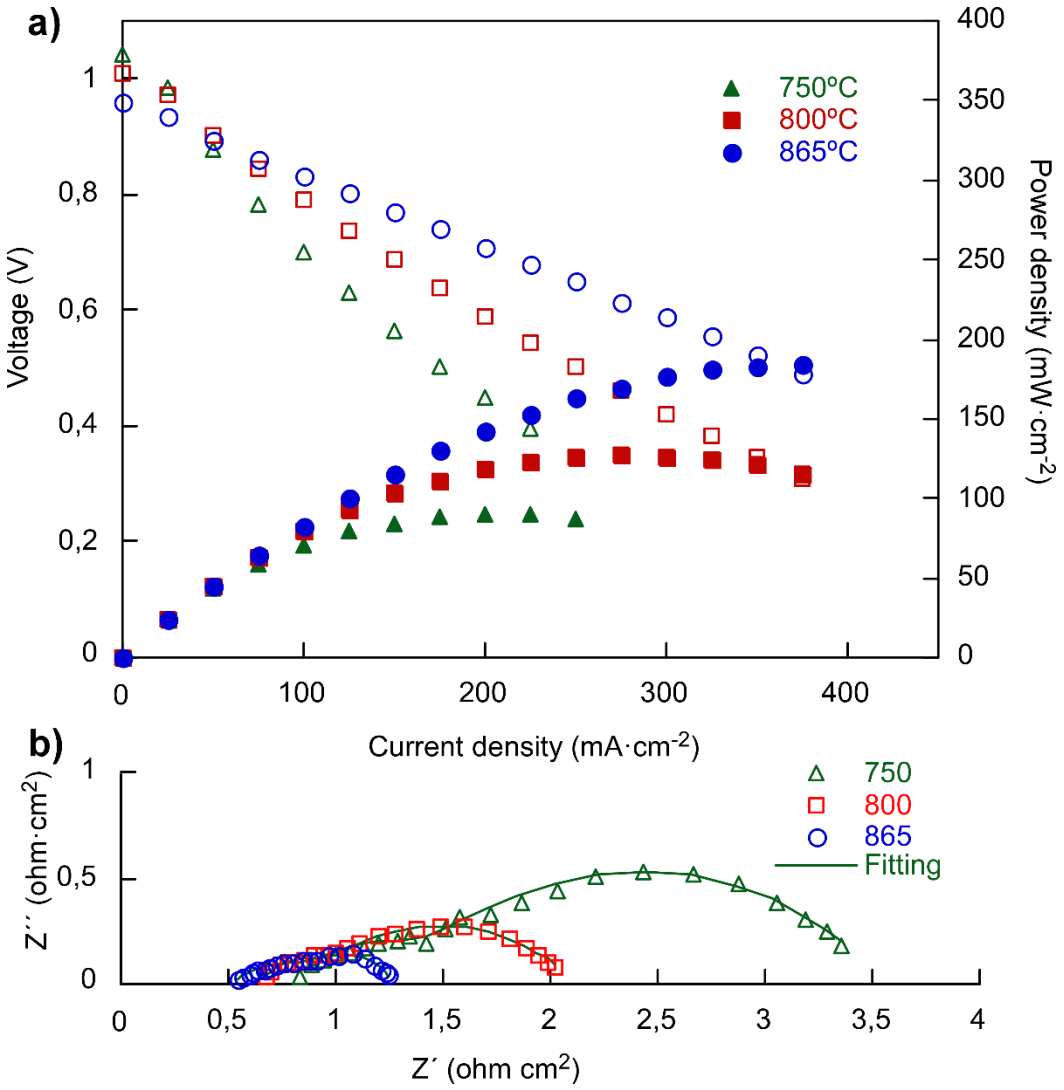

Figure 4.5.- a) (I-V) and (I-P) curves and b) electrochemical impedance spectra of the sample Cell 2 at 750, 800 and 865 °C, using Pt paste as electrode.

[19] Fan H., Zhang Y., Han M., Infiltration of $La_{0.6}Sr_{0.4}FeO_3$-delta nanoparticles into YSZ scaffold for solid oxide fuel cell and solid oxide electrolysis cell, *J. Alloys Compounds*. 723 (**2017**) 620-626.

Table 4.3.- Impedance spectra of cell 3 at 750, 800 and 865 °C.

T (°C)	R_S (Ωcm^2)	R_H (Ωcm^2)	C_H (Fcm^{-2})	f_H (Hz)
750	0.819	0.447	$2.9 \cdot 10^{-4}$	1237
800	0.550	0.458	$5.1 \cdot 10^{-4}$	683
865	0.517	0.407	$4.3 \cdot 10^{-3}$	90

T (°C)	R_L (Ωcm^2)	C_L (Fcm^{-2})	f_L (Hz)	R_p (Ωcm^2)	R_{Total} (Ωcm^2)
750	2.33	$4.1 \cdot 10^{-2}$	1.68	2.78	3.599
800	1.10	$6.2 \cdot 10^{-2}$	2.34	1.56	2.104
865	0.34	$4.4 \cdot 10^{-1}$	1.04	0.75	1.270

To evaluate the stability of the cell for a long time, the performance was tested, and EIS measurements were recorded dependence of time at 800 °C as shown in Figure 4.6. Markedly, the voltage increased gradually with time, which values increased from 0.74 V to 0.81 for 72 h long term testing at 800 °C. This increase is due the cathode activation. There is a decrease in the R_p induced by the cathodic current passage, which as well known, produces enhancement in the performance of cathodes[20,21] (Table 4.4.).

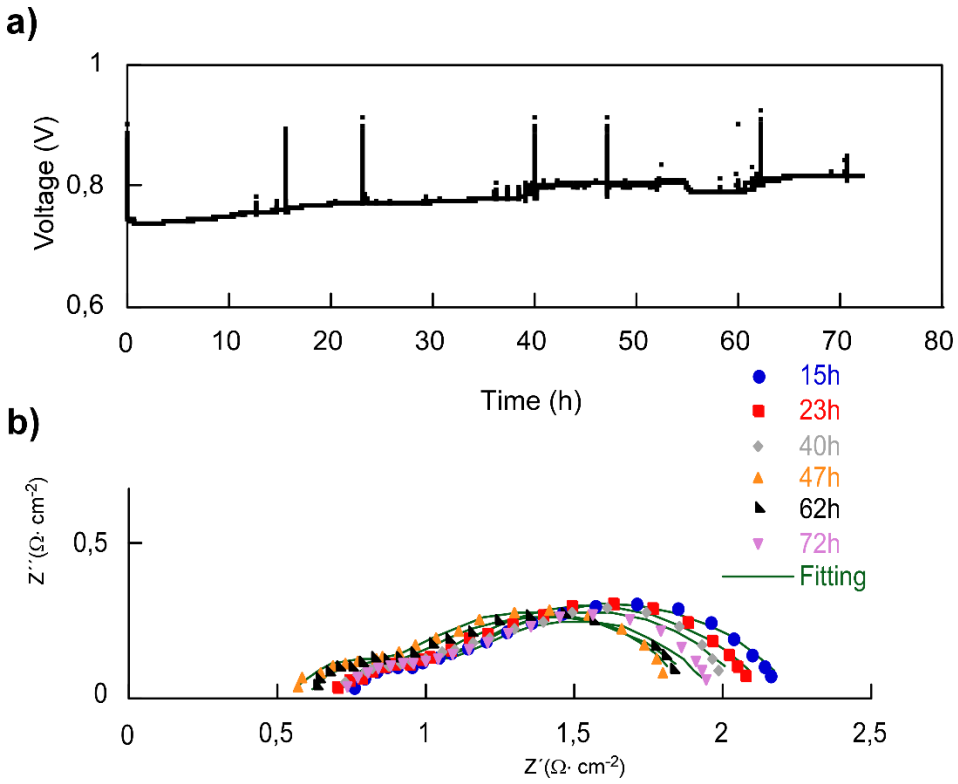

Figure 4.6.- Long-term study of the cell 2. Cell voltage vs operating time. In the inlet are the EIS measurements at different times.

[20] Laguna-Bercero M.A., Ferriz A., Larrea A., Correas L., Orera V.M., Long-term stability studies of anode-supported microtubular solid oxide fuel cells, *Fuel Cells*. 13 (**2013**) 1116-1122.

[21] Jiang S., Zhen Y., Zhang S., Interaction between Fe-Cr metallic interconnect and (La, Sr)MnO_3/YSZ composite cathode of solid oxide fuel cells, *J. Electrochem. Soc*. 153 (**2006**) A1511-A1517.

Table 4.4.- Polarization resistance of the cell 2 obtained from the fits to EIS.

Time (h)	R_s (Ωcm^2)	R_H (Ωcm^2)	C_H (Fcm^{-2})	F_H (Hz)
15	0.730	0.361	$6.4*10^{-4}$	684
23	0.684	0.316	$6.3*10^{-4}$	801
40	0.682	0.417	$6.5*10^{-4}$	583
47	0.538	0.337	$8.5*10^{-4}$	558
62	0.601	0.294	$8.0*10^{-4}$	679
72	0.703	0.354	$6.2*10^{-4}$	729

Time (h)	R_L (Ωcm^2)	C_L (Fcm^{-2})	f_L (Hz)	R_p (Ωcm^2)	R_{Total} (Ωcm^2)
15	1.201	$5.9*10^{-2}$	2.23	1.56	2.29
23	1.159	$6.2*10^{-2}$	2.20	1.475	2.15
40	0.970	$7.9*10^{-2}$	2.07	1.39	2.07
47	1.017	$7.5*10^{-2}$	2.08	1.35	2.02
62	1.028	$7.0*10^{-2}$	2.21	1.32	1.92
72	0.929	$8.2*10^{-2}$	2.08	1.28	1.99

4.3.3. Complete cell configuration

Taking into account the studies detailed above, LSF/LNF composite and LNF layers have been deposited onto the cathode in order to determine the effect of the contact layer into the cell. In the Figure 4.7., the micrographs and the EDX maps taken from the cross-section of the cell 3 sample after 40h of operation are shown. As can be seen, the layers have remained continuous, retaining their adhesion despite having increased in thickness. In addition, the added layers presented an adequate porosity for their use as contact layer. The compositional analysis and elemental mapping obtained by EDX/SEM of the sample cell 3, show a uniform distribution in each layer and no significant inter diffusion of elements between the different layers.

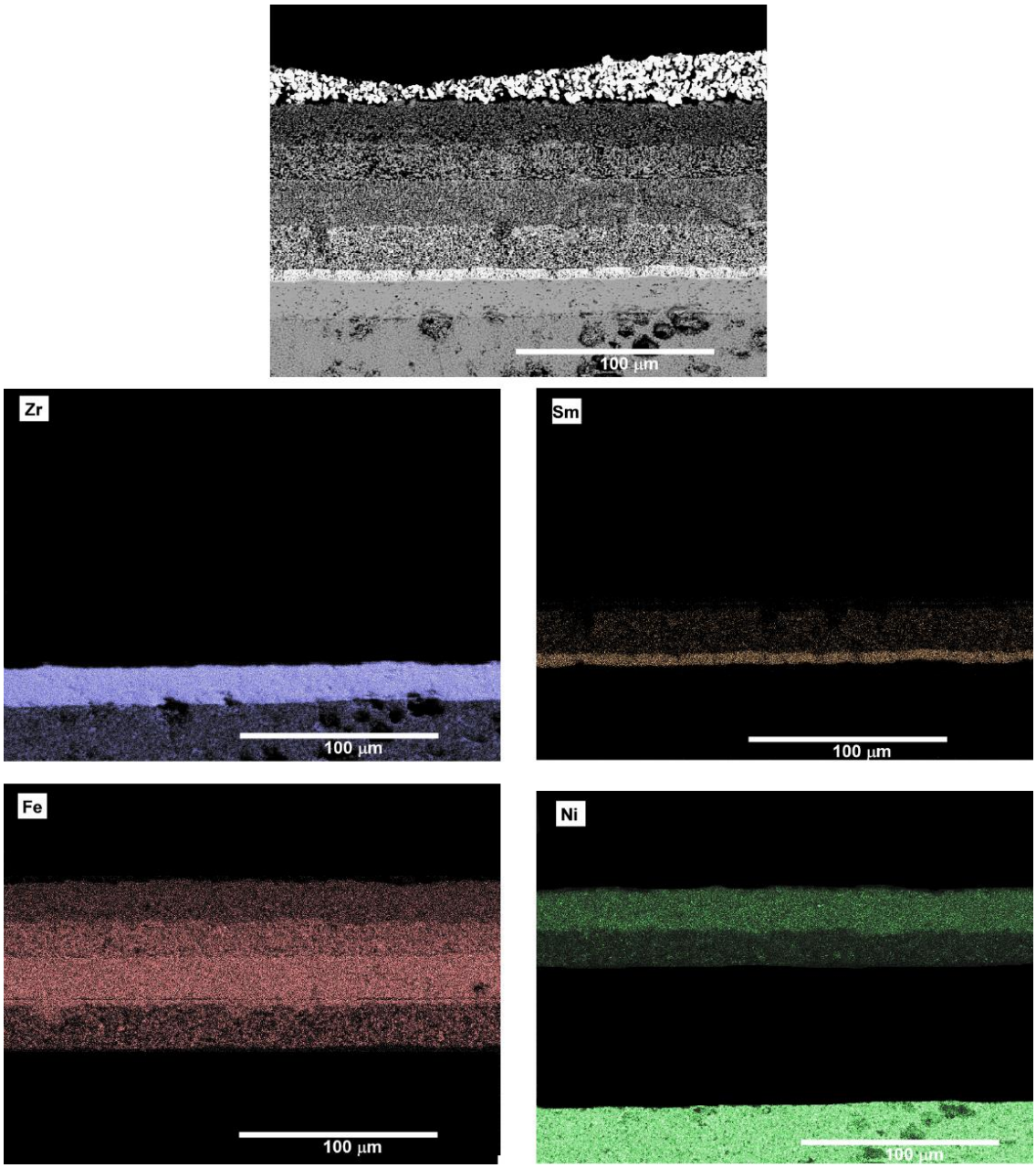

Figure 4.7.- Cross section of the sample cell 3 after being in operation for 40 h and EDX mapping of the selected zone.

The current-voltage characteristic and the corresponding power densities are expressed in Figure 4.8a., measured at 750, 800 and 865ºC. As can be seen from this figure, the cell with LSF/LNF composite and LNF layers delivered a better power output than cell 2, reaching power densities of 175, 222 and 272 mW cm^{-2} at 750, 800 and 865 °C, respectively. With the addition of LSF/LNF and LNF layers, the cell offered a better electro-performance than those without these layers, improving the cell instead of negatively affecting it. Niquist EIS plots of cell 3 are shown in Figure 4.8b. As in the previous cell, the total polarization resistances of the cell 3, determined from the arc length of the impedance spectra, decrease with increasing the operating temperatures, from 0.743 Ωcm^2 measured at 750 °C to 0.589 Ωcm^2 measured at 865 °C, which is lower than the cell 2 at the same temperatures, as can be seen in Table 4.5.

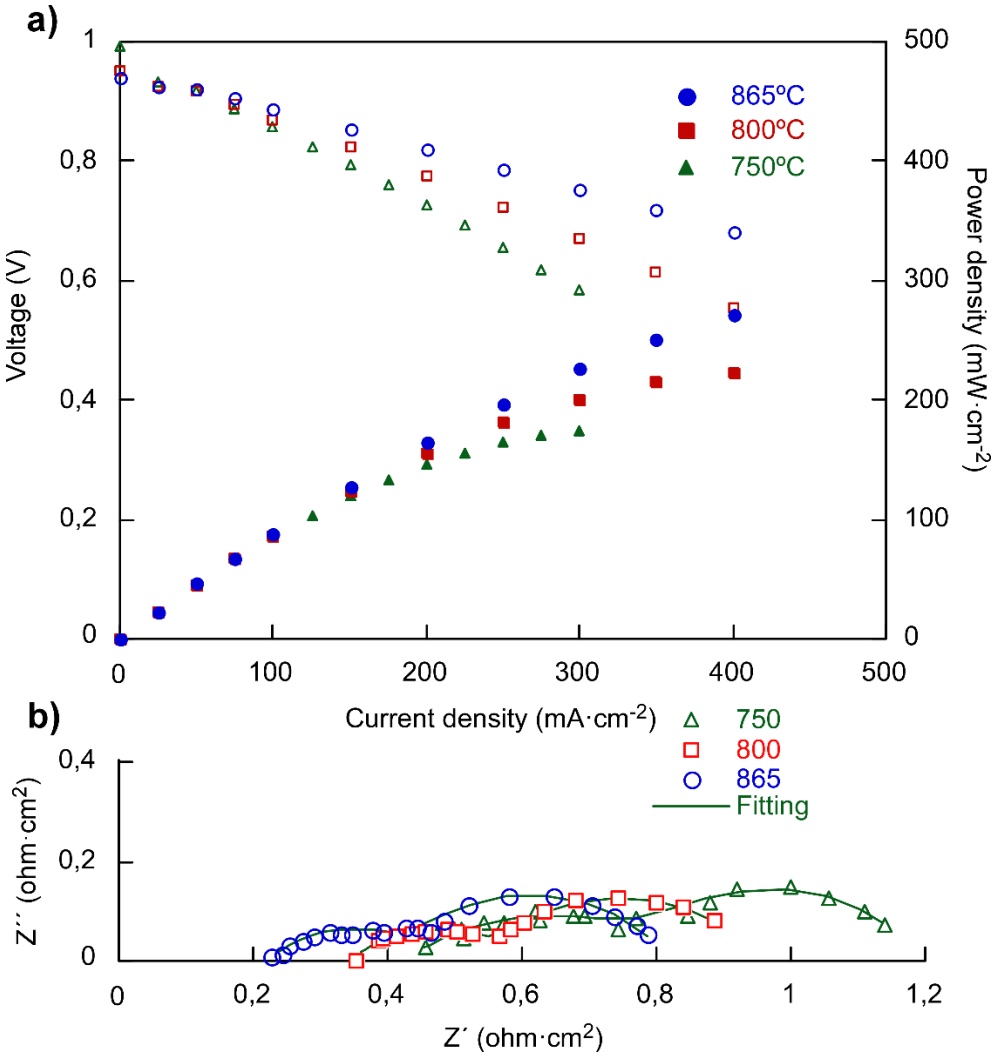

Figure 4.8.- a) (I-V) and (I-P) curves and b) electrochemical impedance spectra of the sample Cell 2 at 750, 800 and 865 °C, using Pt paste as electrode.

Table 4.5. Impedance spectra of cell 3 at 750, 800 and 865 °C.

T (°C)	R_s (Ωcm^2)	R_H (Ωcm^2)	C_H (Fcm^{-2})	f_H (Hz)
750	0,423	0,449	$4.1*10^{-3}$	87
800	0,348	0,225	$3.1*10^{-3}$	231
865	0,226	0,211	$5.0*10^{-3}$	151

T (°C)	R_L (Ωcm^2)	C_L (Fcm^{-2})	f_L (Hz)	R_p (Ωcm^2)	R_{Total} (Ωcm^2)
750	0.295	1.093	0.493	0.743	1.167
800	0.368	0.838	0.516	0.593	0.941
865	0.377	0.717	0.587	0.589	0.814

The long term stability voltage of the cell 3 tested under current load is shown in Figure 4.9. for a total period of 40h. In this figure, the initial voltage was 896 mV and this value decreased to 870 mV after 40 h, a decrease of 0,03 %. Niquist plots obtained by EIS taken at different period of time, shown an increase of polarization resistance with increasing the operating time of the cell, as can be seen in the data of the Table 4.6.

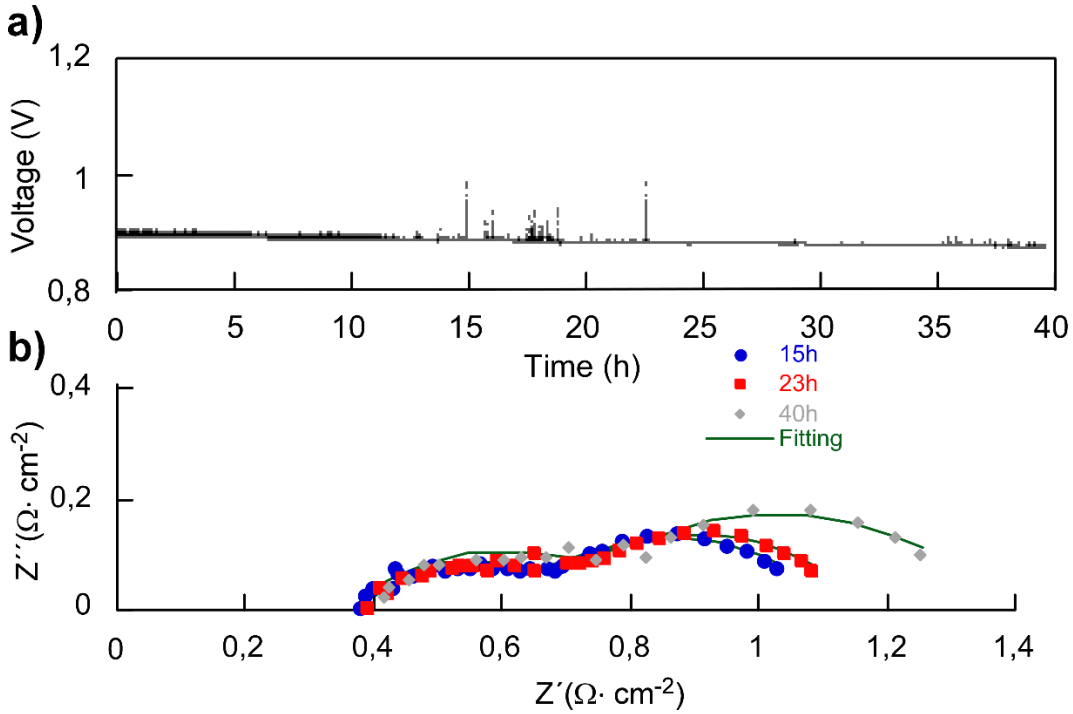

Figure 4.9.- Long-term study of the cell 3. Cell voltage vs operating time. In the inlet are the EIS measurements at different times.

Table 4.6.- Polarization resistance of the cell 3 obtained from the fits to EIS.

Time (h)	R_s (Ωcm^2)	R_H (Ωcm^2)	C_H (Fcm^{-2})	f_H (Hz)
15	0.368	0.265	$2.0*10^{-3}$	376
23	0.381	0.282	$1.4*10^{-3}$	410
40	0.394	0.364	$2.0*10^{-3}$	284

Time (h)	R_L (Ωcm^2)	C_L (Fcm^{-2})	f_L (Hz)	R_p (Ωcm^2)	R_{Total} (Ωcm^2)
15	0.487	0.467	0.700	0.752	1.11
23	0.502	0.373	0.851	0.784	1.16
40	0.543	0.380	0.772	0.906	1.30

4.4. Conclusions

Uniform and well-adhered coatings have been deposited by wet powder spraying onto an Ni-YSZ anode support, with self-synthesized materials. The simultaneous production of supporting anode and electrolyte have been achieved satisfactorily by sintering the two compounds together. Manual spray coating has demonstrated to be an adequate technique in order to create dense or porous layers, depending on the requirements of cell components.

The incorporation of SDC/LSF layer between the SDC barrier and LSF cathode; and the LSF/LNF layer between the cathode and LNF layer, has proved to give an adequate contact, avoiding delamination and cracks of the adjacent layers. To evaluate the cathode side of the cell, electrochemical impedance spectroscopy and current-voltage (I-V) and current-power (I-P) curves were performed, observing the improvement with the addition of the LSF and LNF layers. The long term stability voltage study has shown an increasing voltage with time in the case of the sample cell 2, and an adequate stability in the sample cell 3.

With this study, all the variables that affect the synthesized materials are stablished, being in a situation of moving to an escalation and an industrial manufacturing stage (see Supplementary material: Figure 4.S3).

4.5. Supplementary material

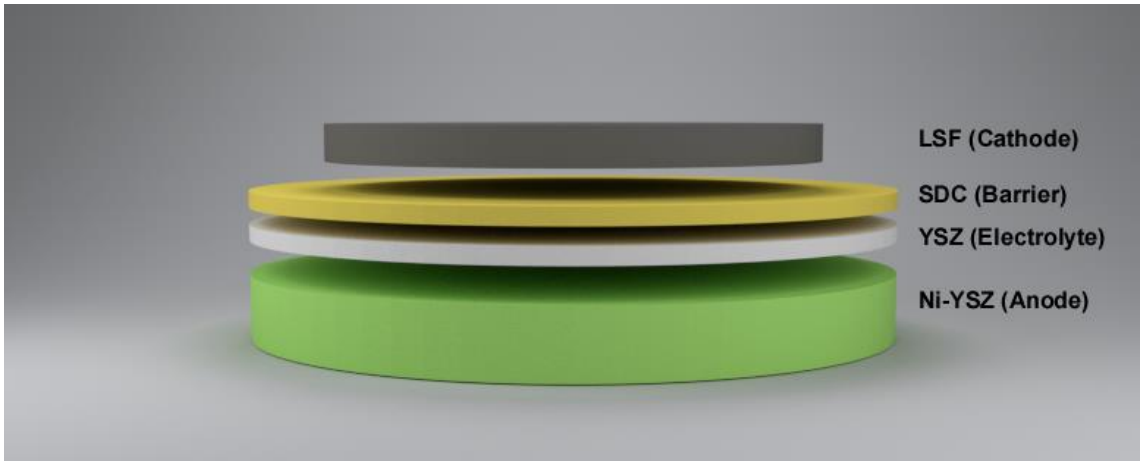

Figure 4.S1.- Schematic for the Cell 2 design. (13th European SOFC & SOE Forum 2018, page 221.)

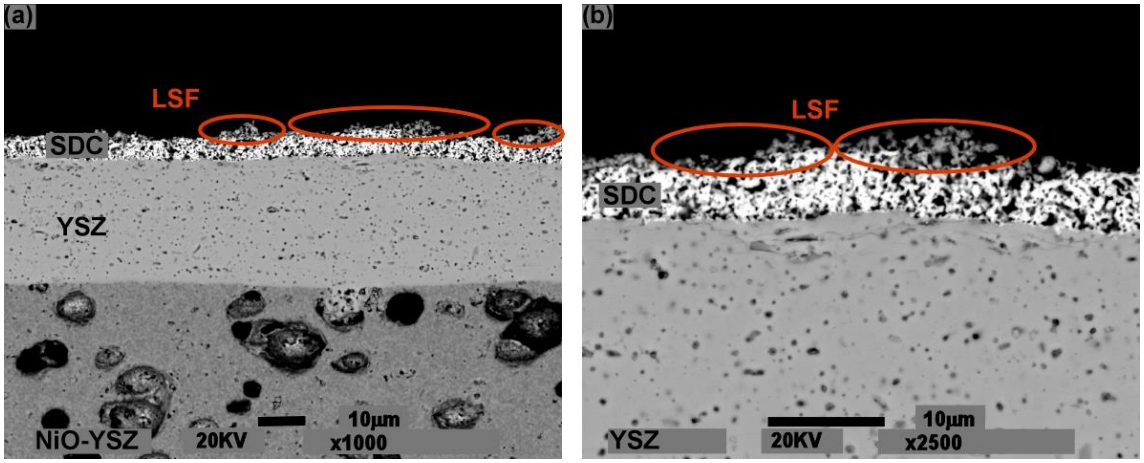

Figure 4.S2.- SEM images of the cathode side without using interlayers (a) low magnification image, (b) higher magnification image. (13th European SOFC & SOE Forum 2018, page 221.)

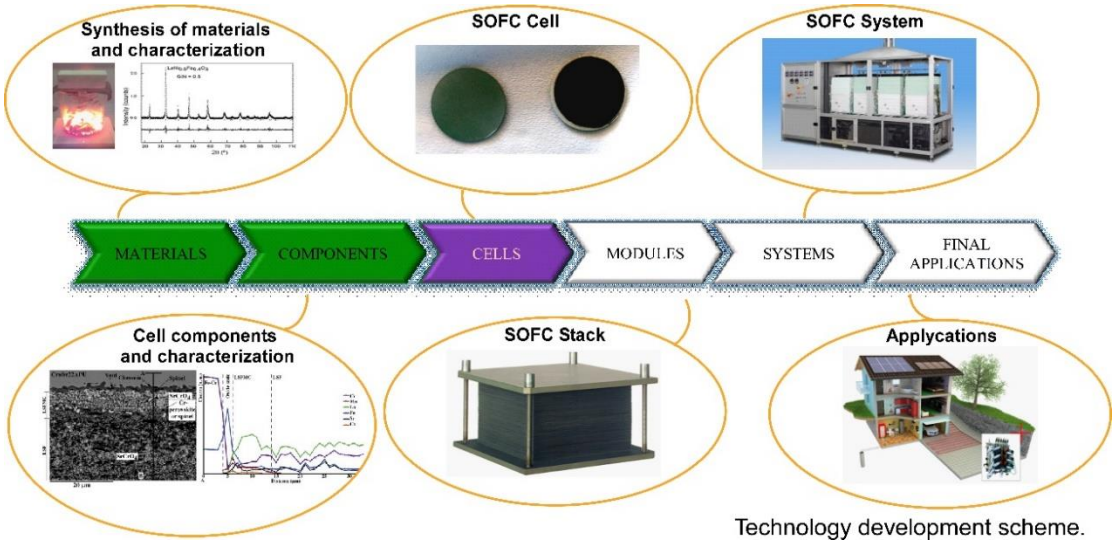

Figure 4.S3.- Solid oxide fuel cell technology development scheme. (13th European SOFC & SOE Forum 2018, page 221).

5. Conclusiones

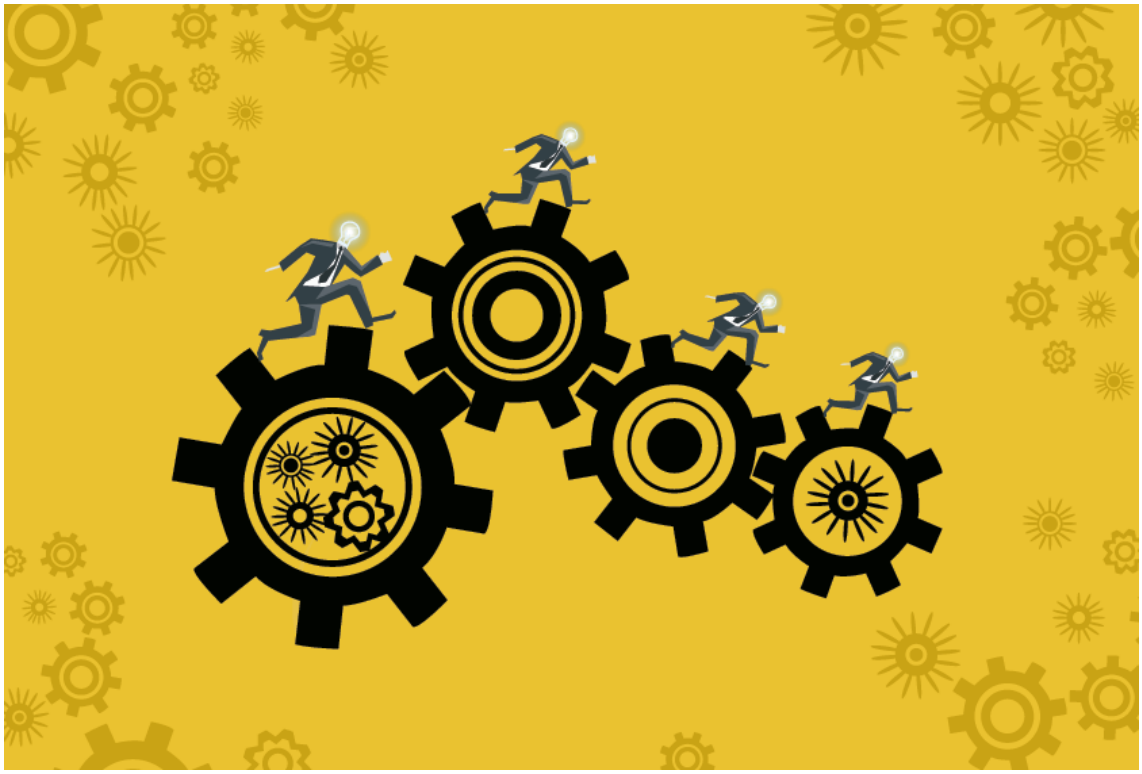

5. Conclusions

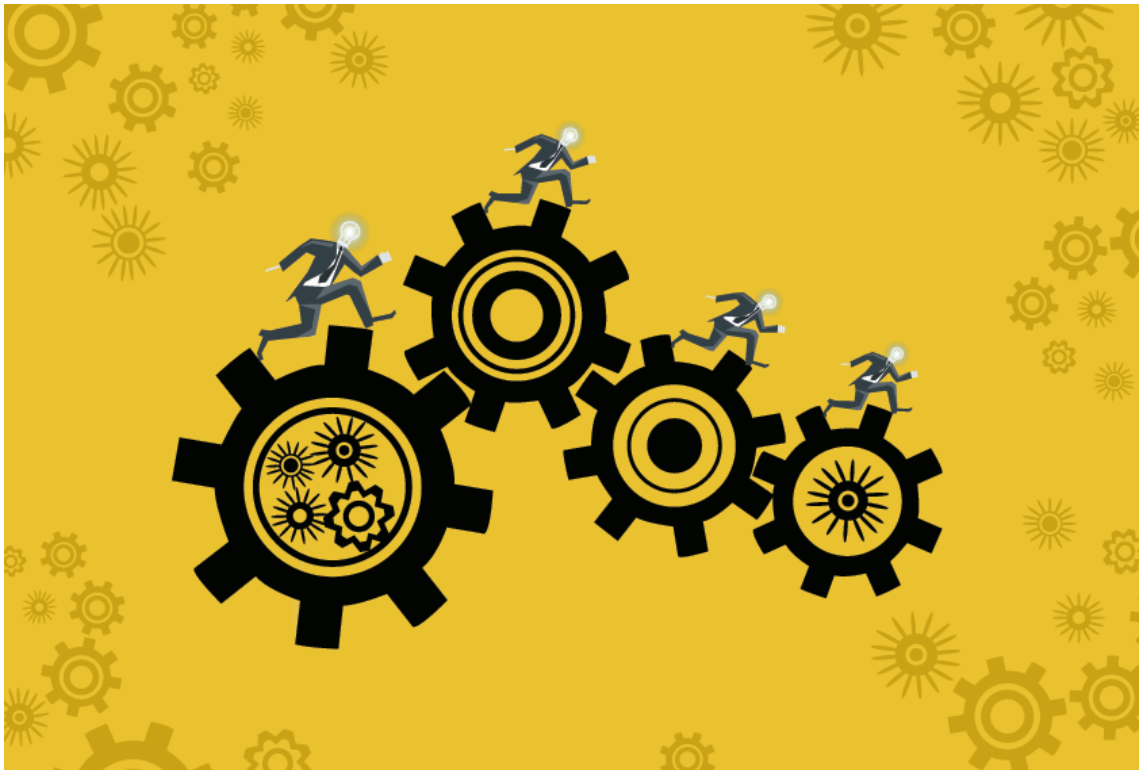

Las conclusiones principales a las que ha conducido el diseño y desarrollo de los sistemas de pilas de combustible de óxido sólido se detallan a continuación:

1. La síntesis por combustión glicina/nitrato ha demostrado ser escalable y reproducible para la síntesis de todas las partes activas de celdas de combustible de óxido sólido (NiO-YSZ, YSZ, SDC, LSF, LNF y MCF).

2. Las partículas de los materiales obtenidos forman aglomerados fáciles de romper y de tamaño micrométrico. Los tamaños de partícula obtenidos en todos los casos son homogéneos y adecuados para su posterior procesado en las celdas SOFC.

3. El procesado por prensado ha permitido la obtención de soportes electrolíticos densos y soportes anódicos porosos. Además, se ha logrado de manera satisfactoria, un cosinterizado entre el electrolito y el soporte anódico. La técnica de recubrimiento por spray, ha permitido controlar la microestructura en cuanto al espesor y porosidad, obteniéndose en todos los casos capas homogéneas y bien adheridas entre sí.

4. La idoneidad de las capas depende del espesor de las mismas y de la molienda de las tintas empleadas en la deposición. En soporte electrolíticos, las capas con un espesor superior a 10 µm han mostrado ser inestables, en contraposición los espesores inferiores a 3 µm generan capas inhomogéneas. La velocidad de molienda adecuada de los materiales sintetizados para el recubrimiento por spray se ha optimizado a 270 rpm.

5. Las intercapas, con un 50% en peso de cada componente, y desarrolladas a partir de la técnica de recubrimiento por spray, han aportado a la estructura de los sistemas completos, la integridad mecánica y térmica necesarias para su ensamblaje, mejorando así la electroquímica de los sistemas.

6. La estructura multicapa del sistema final, compuesta por soporte anódico con electrolito, barrera, cátodo y capa de contacto, integrando intercapas, ha presentado la mejor respuesta de salida en condiciones de operación. A su vez, los sistemas completos, funcionando a largos tiempos han demostrado tener estabilidad electroquímica y mecánica.

7. Se puede concluir que los prototipos finales fabricados se corresponden a un sistema prometedor para su empleo en sistemas de tecnología SOFC con mejores prestaciones en cuanto a durabilidad y desarrollo tecnológico.

From the development and subsequent study of the cells, the following conclusions can be drawn:

1. Glycine nitrate combustion synthesis has been shown scalable and reproducible for the synthesis of all active parts of solid oxide fuel cells (NiO-YSZ, YSZ, SDC, LSF, LNF and MCF).

2. The obtained materials particles form easy to break and micrometric sized agglomerates. The obtained particle sizes are in all the cases homogeneous and suitable for further processing in the SOFC.

3. The pressing processing method has allowed obtaining dense electrolytic and porous anodic supports. In addition, a cosinterization between the electrolyte and the anodic support has been carried out satisfactorily. The use of spray coating technique has allowed controlling the microstructure in terms of thickness and porosity, obtaining in all the cases homogeneous and well-adhered layers.

4. The suitability of the layers depends on the thickness of the layers and the grinding of the used inks in the deposition. In electrolytic support, the layers with a thickness greater than 10 µm have been shown to be unstable, in contrast to layers with thicknesses below 3 µm, which generate inhomogeneous layers. The aproppiate milling speed of the synthesized materials for spray coating has been optimized to 270 rpm.

5. The interlayers, 50% by weight of each component, and developed from spray coating technique; have been contributed to the structure of the complete systems, the mechanical and thermal integrity necessary for their assembly, thus improving the electrochemistry of the systems.

6. The multilayer structure of the final system, composed of anodic support with electrolyte, barrier, cathode and contact layer, integrating interlayers, has presented the best output response under operating conditions. In turn, complete systems, operating at long times have shown electrochemical and mechanical stability.

7. It can be concluded that the manufactured final prototypes correspond to a promising system for use in SOFC technology systems with better performance in terms of durability and technology development.

6. Bibliography

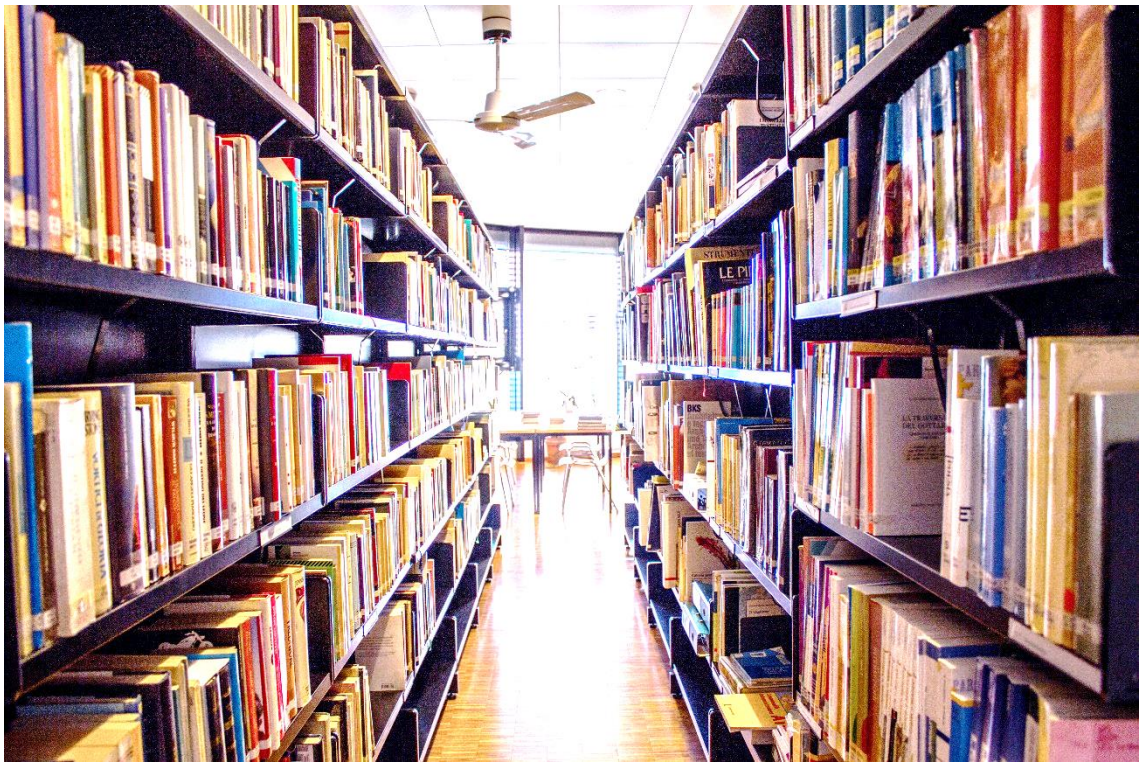

Adler S., Factors governing oxygen reduction in solid oxide fuel cell cathodes, *Chem. Rev*. 104 (**2004**) 4791-4843.

Amorós. J.L. "El Cristal. Morfología, Estructura y Propiedades Físicas". Ed. Atlas, p. 1-33, 201-217, **1990**.

Ananyev M.V., Farlenkov A.S., Eremin V.A., Kurumchin E.K., Degradation kinetics of LSM–YSZ cathode materials for SOFC, *Int. J. Hydrog. Energy*. 43 (**2018**) 951-959.

Andújar J.M., Segura F., Fuel cells: History and updating. A walk along two centuries, *Renew. Sust. Energ. Rev*. 13 (**2009**) 2309-2322.

Alstone P., Gershenson D., Kammen D.M., Decentralized energy systems for clean electricity access, *Nat. Clim. Chang*. 5 (**2015**) 305-314.

Apergis N., Chang T., Gupta R., Ziramba E., Hydroelectricity consumption and economic growth nexus: Evidence from a panel of ten largest hydroelectricity consumers, *Renew. Sust. Energ. Rev*. 62 (**2016**) 318-325.

Arregui A., Rodriguez-Martinez L.M., Modena S., Bertoldi M., van Herle J., Sglavo V.M., Stability of ferritic perovskite cathodes in anode-supported solid oxide fuel cells under different processing and operation parameters, *Electrochim. Acta*. 58 (**2011**) 312-321.

Bahteeva J.A., Leonidov I.A., Patrakeev M.V., Mitberg E.B., Kozhevnokov V.L., Poeppelmeier K.R., High-temperature ion transport in $La_{1-x}Sr_xFeO_{3-\delta}$. *J. Solid State Electr*. 8 (**2004**) 578-584.

Bajwa D.S., Peterson T., Sharma N., Shojaeiarani J., Bajwa S.G., A review of densified solid biomass for energy production, *Renew. Sust. Energ. Rev*. 96 (**2018**) 296-305.

Bandoc G., Prăvălie R., Patriche C., Degeratu M., Spatial assessment of wind power potential at global scale. A geographical approach, *J. Clean. Prod*. 200 (**2018**) 1065-1086.

Baroutaji A., Carton J.G., Sajjia M., Olabi A.G., Materials in PEM Fuel Cells, *Reference module in chemistry, molecular sciences and chemical engineering*, Ed. Elsevier Inc., p 1-11, **2016**.

Barreto R.A., Fossil fuels, alternative energy and economic growth, *Econ. Model*. 75 (**2018**) 196-220.

Bhouri M., Linder M., Bürger I., Metal hydride reactor for dual use: Hydrogen storage and cold production, *Int. J. Hydrog. Energy*. 43 (**2018**) 23357-23371.

Blum L., An Analysis of contact problems in solid oxide fuel cell stacks arising from differences in thermal expansion coefficients, *Electrochim. Acta*. 223 (2017) 100-108.

Boobalan K., Varun A., Vijayaraghavan R., Chidambaram K., Mudali U.K., Facile, scalable synthesis of nanocrystalline calcium zirconate by the solution combustion method, *Ceram. Int*. 40 (**2014**) 5781-5786.

Borozan D., Decomposing the changes in European final energy consumption, *Energy Strateg. Rev*. 22 (**2018**) 26-36.

BP Energy outlook 2018 edition, Energy economics, bp.com/energyoutlook, **2018**.

Chou H., Hwang B., Sun C., Catalysis in fuel cells and hydrogen production, *New and future development in catalysis, Batteries, Hydrogen storage and fuel cells*, 9 (**2013**) 217-270.

Cabezas M.D., Franco J.I., Fasoli H.J., Optimization of self-regulated hydrogen production from photovoltaic energy, *Int. J. Hydrog. Energy*. (**2018**). https://doi.org/10.1016/j.ijhydene.2018.10.203.

Campbell, C. Aspo Newsletter n. 100. (**2009**).

Carpanese M.P., Barbucci A., Canu G., Viviani M., $BaCe_{0.8}5Y_{0.15}O_{2.925}$ dense layer by wet powder spraying as electrolyte for SOFC/SOEC applications, *Solid State Ion*. 269 (**2015**) 80-85.

Carrijo M.M.M., Lorenz H., Rambo C.R., Greil P., Travitzky N., Fabrication of Ti_3SiC_2-based pastes for screen printing on paper-derived Al_2O_3 substrates, *Ceram. Int*. 44 (**2018**) 8116-8124.

Carter S., Seluck A., Charter R.J., Kajda J., Kilner J.A., Steele B.C.H. Oxygen transport in selected nonstoichiometric perovskite-structure oxides. *Solid State Ion.* 53-56 (**1992**) 597-605.

Chen M., Kim B.H., Xu Q., Ahn B.G., Preparation and electrochemical properties of Ni–SDC thin films for IT-SOFC anode, *J. Membr. Sci*. 334 (**2009**) 138-147.

Chen M., Kim B.H., Xu Q., Ahn B.G., Huang D.P., Fabrication and performance of anode-supported solid oxide fuel cells via slurry spin coating, *J. Membr. Sci*. 360 (**2010**) 461-468.

Choi H., Cho G.Y., Cha S., Fabrication and characterization of anode supported YSZ/GDC bilayer electrolyte SOFC using dry press process, *Int. J. Precis, Eng, Manuf-Green Technol*. 1 (**2014**) 95-99.

Coddet P., Amany M., Vulliet J., Caillard A., Thomann A., YSZ/GDC bilayer and gradient barrier layers deposited by reactive magnetron sputtering for solid oxide cells, *Surf. Coat. Tech*. 357 (**2019**) 103-113.

Coddet P., Vulliet J., Richard C., Caillard A., Thomann A., Characteristics and properties of a magnetron sputtered gadolinia-doped ceria barrier layer for solid oxide electrochemical cells, *Surf. Coat. Technol*. 339 (**2018)** 57-64.

da Silva C.A., Ribeiro N.F.P., Souza M.M.V.M., Effect of the fuel type on the synthesis of yttria stabilized zirconia by combustion method, *Ceram. Int*. 35 (**2009**) 3441-3446.

de Haart L.G.J., Peters R., Fuel Cells – Solid oxide fuel cells | Internal and External Reformation, Reference module in chemistry, molecular sciences and chemical engineering, *Encyclopedia of electrochemical power sources*, (***2009***) 88-98.

De Marco V., Iannaci A., Rashid S., Sglavo V.M., Effect of anode thickness and Cu content on consolidation and performance of planar copper-based anode-supported SOFC, *Int. J. Hydrog. Energy*. 42 (**2017**) 12543-12550.

De Vero J.C., Develos-Bagarinao K., Ishiyama T., Kishimoto H., Yamaji K., Horita T., Yokokawa H., Effect of $SrZrO_3$ formation at LSCF-cathode/GDC-interlayer interfaces on the electrochemical properties of solid oxide fuel cells, *ECS Trans*. (USA). 75 (**2017**) 75-81.

Dicks A.L., Fuel cells – Molten carbonate fuel cells | Overview, Reference module in chemistry, molecular sciences and chemical engineering, *Encyclopedia of electrochemical power sources*, Ed. Elsevier Inc, p 446-453, **2009**.

Dong S., Jung W., Rashid K., Kashimoto A., Design and numerical analysis of a planar anode-supported SOFC stack, *Renew. Energy*. 94 (**2016**) 637-650.

Duan N., Yan D., Chi B., Pu J., Jian L., High performance anode-supported tubular solid oxide fuel cells fabricated by a novel slurry-casting method, *Sci. Rep*. 5 (**2015**) 8174.

Dunlap M., Adaskaveg J.E., Introduction to the scanning electron microscope, Cambridge, Edited by Facility for advanced instrumentation, U.C. Davis, p. 3-33, **1997**.

Ecija A., Vidal K., Larrañaga A., Martínez-Amesti A., Ortega-San-Martín, L. Arriortua M.I., Structure and properties of perovskites for SOFC cathodes as a function of the A-site cation size disorder, *Solid State Ion*. 235 (**2013**) 14-21.

Ecija-Verdejo A., Óxidos mixtos tipo perovskita $Ln_{0.5}M_{0.5}FeO_{3-\delta}$ (Ln=La, Sm, Nd, Gd; M=Ba, Sr) para su aplicación como cátodos en pilas SOFC. Ph.D. thesis work, UPV/EHU, **2012**.

Endler-Schuck C., Weber A., Ivers-Tiffee E., Guntow U., Ernst J., Ruska J., Nanoscale Gd-doped CeO_2 buffer layer for a high performance solid oxide fuel cell, *J. Fuel Cell Sci. Technol*. 8 (**2011**) 041001.

European Environment Agency (2016), Population trends 1950 – 2100: globally and within Europe, **2016**.

Eurostat (2017), People in the EU - population projections, Bruselas-Eurostat, **2017**.

Fan H., Zhang Y., Han M., Infiltration of $La_{0.6}Sr_{0.4}FeO_3$-delta nanoparticles into YSZ scaffold for solid oxide fuel cell and solid oxide electrolysis cell, *J. Alloys Compounds*. 723 (**2017**) 620-626.

Fernandes M.D., Andrade S.T.D., Bistritzki V.N., Fonseca R.M., Zacarias L.G., Gonçalves H.N.C., de Castro A.F., Domingues R.Z., Matencio T., SOFC-APU systems for aircraft: A review, *Int. J. Hydrogen Energy*. 43 (**2018**) 16311-16333.

Fernández-González R., Molina T., Savvin S., Moreno R., Makradi A., Núñez P., Fabrication and electrical characterization of several YSZ tapes for SOFC applications, *Ceram. Int*. 40 (**2014**) 14253-14259.

Fickett A.P., Kaihammer F.R., Water electrolysis, in: Cox K.E., Williamson K.D. (Eds.), Hydrogen - its technology and implications, *Hydrogen production technology*, 1 (**1977**) 3-41.

Fontana S., Amendola R., Chevalier S., Piccardo P., Caboche G., Viviani M., Molins R., Sennour M., Metallic interconnects for SOFC: Characterization of corrosion resistance and conductivity evaluation at operating temperature of differently coated alloys, *J. Power Sources*. 171 (**2007**) 652-662.

Gamble S., Fabrication-microstructure-performance relationships of reversible solid oxide fuel cell electrodes-review, *Mater. Sci. Technol*. 27 (**2011**) 1485-1497.

Gil V., Gurauskis J., Campana R., Merino R.I., Larrea A., Orera V.M., Anode-supported microtubular cells fabricated with gadolinia-doped ceria nanopowders, *J. Power Sources*. 196 (**2011**) 1184-1190.

González-Cortés S.L., Imbert F.E., Fundamentals, properties and applications of solid catalysts prepared by solution combustion synthesis (SCS), *App. Catal. A- Gen*. 452 (**2013**) 117-131.

Grenier J.C., Bassat J.M., Mauvy F., Novel cathodes for solid oxide fuel cells, Functional Materials for sustainable energy applications, *Woodhead publishing series in energy*, 13 (**2012**) 402-444.

Guaitolini S.V.M., Fardin F.F., Fuel cells: History (short remind), principles of operation, main features and applications, Advances in Renewable energies and power technologies, *Biomass, fuel cells, geothermal energies, and smart grids*. 2 (**2018**) 123-150.

Hahn Th., "International tables for crystallography, Volume A: Space-group symmetry", D. Reidel Publishing Company, Boston, USA, **1983**.

Hajarpour S., Gheisari K., Raouf A.H., Characterization of nanocrystalline $Mg_{0.6}Zn_{0.4}Fe_2O_4$ soft ferrites synthesized by glycine-nitrate combustion process, *J. Magn. Magn. Mater*. 329 (**2013**) 165-169.

Hansch R., Chowdhury M.R.R., Menzler N.H., Screen printing of sol–gel-derived electrolytes for solid oxide fuel cell (SOFC) application, *Ceram. Int*. 35 (**2009**) 803-811.

Hedayat N., Du Y., Ilkhani H., Review on fabrication techniques for porous electrodes of solid oxide fuel cells by sacrificial template methods, *Renew. Sust. Energ. Rev*. 77 (**2017**) 1221-1239.

Hernandez L., Gonzalez C., *Introducción al análisis instrumental*, Editorial Ariel, S.A., Barcelona, **2002**.

Horoz S., Sahin O., Solid oxides, *Comprehensive energy systems*, 2 (**2018**) 593-628.

Hosseini S.E., Wahid M.A., Hydrogen production from renewable and sustainable energy resources: Promising green energy carrier for clean development, *Renew. Sust. Energ. Rev*. 57 (**2016**) 850-866.

http:// www.iea.org/ publications/freepublications/publication/co2-emmisions-from-fuel-combustion-highlights-2014.html. CO_2 emissions from fuel combustion, IEA, **2017**.

http://www.xtal.iqfr.csic.es/Cristalografia/parte_02.html.

Huang K., Singhal S.C., Cathode-supported tubular solid oxide fuel cell technology: A critical review, *J. Power Sources*. 237 (**2013**) 84-97.

ICCD, "Powder Diffraction File-Inorganic and Organic", Pennsylvania, USA, **1995.**

Ivers-Tiffée E., Electrolytes | Solid: oxygen ions, Reference module in chemistry, molecular sciences and chemical engineering, *Encyclopedia of electrochemical power sources*, (**2009**) 181-187.

Jabbari M., Bulatova R., Tok A.I.Y., Bahl C.R.H., Mitsoulis E., Hattel J.H., Ceramic tape casting: A review of current methods and trends with emphasis on rheological behavior and flow analysis, *Mater. Sci. Eng. B.* 212 (**2016**) 39-61.

Jamil S.M., Othman M.H.D., Rahman M.A., Jaafar J., Ismail A.F., Anode supported micro-tubular SOFC fabricated with mixed particle size electrolyte via phase-inversion technique, *Int. J. Hydrog. Energy*. 42 (**2017**) 9188-9201.

Jang I., Kim C., Kim S., Yoon H., Fabrication of thin films on an anode support with surface modification for high-efficiency intermediate-temperature solid oxide fuel cells via a dip-coating method, *Electrochim. Acta*. 217 (**2016**) 150-155.

Jasinski P., Molin S., Gazda M., Petrovsky V., Anderson H.U., Applications of spin coating of polymer precursor and slurry suspensions for solid oxide fuel cell fabrication, *J. Power Sources*. 194 (**2009**) 10-15.

Jiang S., Zhen Y., Zhang S., Interaction between Fe-Cr metallic interconnect and (La, Sr)MnO_3/YSZ composite cathode of solid oxide fuel cells, *J. Electrochem. Soc*. 153 (**2006**) A1511-A1517.

Jo K.H., Kim J.H., Kim K.M., Lee I., Kim S., Development of a new cost effective Fe–Cr ferritic stainless steel for SOFC interconnect, *Int. J. Hydrog. Energy*. 40 (**2015**) 9523-9529.

Khetkorn W., Rastogi R.P., Incharoensakdi A., Lindblad P., Madamwar D., Pandey A., Larroche C., Microalgal hydrogen production – A review, *Bioresour. Technol*. 243 (**2017**) 1194-1206.

Kim Y., Kim-Lohsoontorn P., Bae J., Effect of unsintered gadolinium-doped ceria buffer layer on performance of metal-supported solid oxide fuel cells using unsintered barium strontium cobalt ferrite cathode, *J. Power Sources*. 195 (**2010**) 6420-6427.

Klein C., Hurlbut J.C.S., *"Manual de Mineralogía"*, 4ª Ed., Ed. Reverté S.A., Barcelona, **1996**.

Košir M., Iglič N., Kunič R., Optimization of heating, cooling and lighting energy performance of modular buildings in respect to location's climatic specifics, *Renew. Energy*. 129 (**2018**) 527-539.

Kuengas R., Yu A.S., Levine J., Vohs J.M., Gorte R.J., An investigation of oxygen reduction kinetics in LSF electrodes, *J. Electrochem. Soc*. 160 (**2013**) F205-F211.

Kumar A., Cross A., Manukyan K., Bhosale R.R., van den Broeke L.J.P., Miller J.T., Mukasyan A.S., Wolf E.E., Combustion synthesis of copper–nickel catalysts for hydrogen production from ethanol, *Chem. Eng. J*. 278 (**2015**) 46-54.

Kumar A., Mukasyan A.S., Wolf E.E., Combustion synthesis of Ni, Fe and Cu multi-component catalysts for hydrogen production from ethanol reforming, *App. Catal. A-Gen*. 401 (**2011**) 20-28.

Kupecki J., Kluczowski R., Papurello D., Lanzini A., Kawalec M., Krauz M., Santarelli M., Characterization of a circular 80 mm anode supported solid oxide fuel cell (AS-SOFC) with anode support produced using high-pressure injection molding (HPIM), *Int. J. Hydrog. Energy*. (**2018**) In Press, doi.org/10.1016/j.ijhydene.2018.02.143.

Lacey R., Pramanick A., Lee J.C., Jung J., Jiang B., Edwards D.D., Naum R., Mixture S.T., Evaluation of Co and perovskite Cr-blocking thin films on SOFC interconnects, *Solid State Ion*. 181 (**2010**) 1294-1302.

Laguna-Bercero M.A., Ferriz A., Larrea A., Correas L., Orera V.M., Long-term stability studies of anode-supported microtubular solid oxide fuel cells, *Fuel Cells*. 13 (**2013**) 1116-1122.

Lee H., Yu J., Kim J., Kim K., Rhee Y., Effects of catalyst loading and oxidant on the performance of direct formic acid fuel cells, *Stud. Surf. Sci. catal.* 159 (**2006**) 589-592.

Lee S., Lee K., Jang Y., Bae J., Fabrication of solid oxide fuel cells (SOFCs) by solvent-controlled co-tape casting technique, *Int. J. Hydrog. Energy*. 42 (**2017**) 1648-1660.

Lenka R.K., Mahata T., Sinha P.K., Tyagi A.K., Combustion synthesis of gadolinia-doped ceria using glycine and urea fuels, *J. Alloy Compd*. 466 (**2008**) 326-329.

Li M., Wang Y., Wang Y., Chen F., Xia C., Bismuth doped lanthanum ferrite perovskites as novel cathodes for intermediate-temperature solid oxide fuel cells, *ACS Appl. Mater. Interfaces*. 6 (**2014**) 11286-11294.

Li N., Wei B., Lü Z., Huang X., Su W., $GdBaCo_2O_{5+\delta}$–$Sm_{0.2}Ce_{0.8}O_{1.9}$ composite cathodes for intermediate temperature SOFCs, *J. Alloy. Compd*. 509 (**2011**) 3651-3655.

Lin Q., Lin J., Liu T., Xia C., Chen C., Solid oxide fuel cells supported on cathodes with large straight open pores and catalyst-decorated surfaces, *Solid State Ion*. 323 (**2018**) 130-135.

Liu P., Luo Z., Kong J., Yang X., Liu Q., Xu H., $Ba_{0.5}Sr_{0.5}Co_{0.8}Fe_{0.2}O_3$-delta-based dual-gradient cathodes for solid oxide fuel cells, *Ceram. Int*. 44 (**2018**) 4516-9.

Liu Q., Dong X., Yang C., Ma S., Chen F., Self-rising synthesis of Ni–SDC cermets as anodes for solid oxide fuel cells, *J. Power Sources*. 195 (**2010**) 1543-1550.

Li W., Guan B., Yan J., Zhang N., Zhang X., Liu X., Enhanced surface exchange activity and electrode performance of $(La_{2-2x}Sr_{2x})(Ni_{1-x}Mn_x)O_{4+\delta}$ cathode for intermediate temperature solid oxide fuel cells, *J. Power Sources*. 318 (**2016**) 178-183.

Li X., Shi W., Han M., Optimization of interconnect flow channels width in a planar solid oxide fuel cell, *Int. J. Hydrogen Energy*. 43 (**2018**) 21524-21534.

López-Robledo M.J., Laguna-Bercero M.A., Larrea A., Orera V.M., Reversible operation of microtubular solid oxide cells using $La_{0.6}Sr_{0.4}Co_{0.2}Fe_{0.8}O_{3-\delta}$-$Ce_{0.9}Gd_{0.1}O_{2-\delta}$ oxygen electrodes, *J. Power Sources*. 378 (**2018**) 184-189.

López-Robledo M.J., Laguna-Bercero M.A., Silva J., Orera V.M., Larrea A., Electrochemical performance of intermediate temperature micro-tubular solid oxide fuel cells using porous ceria barrier layers, *Ceram. Int*. 41 (**2015**) 7651-7660.

Lubini M., Chinarro E., Moreno B., de Sousa V.C., Alves A.K., Bergmann C.P., Electrical properties of $La_{0.6}Sr_{0.4}Co_{1-y}Fe_yO_3$ (y = 0.2–1.0) fibers obtained by electrospinning, *J. Phys. Chem. C*. 120 (**2016**) 64-69.

Macdonald, J.R. "Impedance Spectroscopy". John Wiley & Sons. New York. USA. 1987.

Mahata T., Nair S.R., Lenka R.K., Sinha P.K., Fabrication of Ni-YSZ anode supported tubular SOFC through iso-pressing and co-firing route, *Int. J. Hydrog. Energy*. 37 (**2012**) 3874-3882.

Mahmud L.S., Muchtar A., Somalu M.R., Challenges in fabricating planar solid oxide fuel cells: A review, *Renew. Sust. Energ. Rev*. 72 (**2017**) 105-116.

Martínez-Amesti A., Larrañaga A., Rodríguez-Martínez L.M., Aguayo A.T., Pizarro J.L., Nó M.L., Laresgoiti A., Arriortua M.I., Reactivity between La(Sr)FeO_3 cathode, doped CeO_2 interlayer and yttria-stabilized zirconia electrolyte for solid oxide fuel cell applications, *J. Power Sources*. 185 (**2008**) 401-410.

Martínez-Amesti A., Larrañaga A., Rodríguez-Martínez L.M., Nó M.L., Pizarro J.L., A. Laresgoiti, Arriortua M.I., Chemical compatibility between YSZ and SDC sintered at different atmospheres for SOFC applications, *J. Power Sources*. 192 (**2009**) 151-157.

Medisetti S., Ahn J., Patil S., Goel A., Bangaru Y., Sabhahit G.V., Babu G.U.B., Lee J., Dasari H.P., Synthesis of GDC electrolyte material for IT-SOFCs using glucose & fructose and its characterization, *Nano-Struct. Nano-Objects*. 11 (**2017**) 7-12.

Mekhilef S., Saidur R., Safari A., Comparative study of different fuel cell technologies, *Renew. Sust. Energy Rev*. 16 (**2012**) 981-989.

Miguel-Pérez V., Martínez-Amesti A., Nó M.L., Larrañaga A., Arriortua M.I., The effect of doping $(Mn,B)_3O_4$ materials as protective layers in different metallic interconnects for solid oxide fuel cells, *J. Power Sources*. 243 (**2013**) 419-430.

Miller J.C., Miller J.N., *Statistics for Analytical Chemistry*, Ellis Horwood, 2ª Ed., London, **1988**.

Minh N.Q., Cell and stack design, fabrication and performance, High-temperature solid oxide fuel cells for the 21st century, *Fundamentals, design and applications*, 8 (**2016**) 255-282.

Mohammed H., Al-Othman A., Nancarrow P., Tawabeh M., El Haj Assad M., Direct hydrocarbon fuel cells: A promising technology for improving energy efficiency, *Energy*. 172 (**2019**) 207-219.

Mohan S.V., Bhaskar Y.V., Sarma P.N., Biohydrogen production from chemical wastewater treatment in biofilm configured reactor operated in periodic discontinuous batch mode by selectively enriched anaerobic mixed consortia, *Water Res*. 41 (**2007**) 2652-2664.

Mohsin M., Rasheed A.K., Saidur R., Economic viability and production capacity of wind generated renewable hydrogen, *Int. J. Hydrog. Energy*. 43 (**2018**) 2621-2630.

Monash P., Pugazhenthi G., Saravanan P., Various fabrication methods of porous ceramic supports for membrane applications, *Rev. Chem. Eng*. 29 (**2013**) 357-383.

Montero X., Tietz F., Sebold D., Buchkremer H.P., Ringuede A., Cassir M., Laresgoiti A., Villarreal I., $MnCo_{1.9}Fe_{0.1}O_4$ spinel protection layer on commercial ferritic steels for interconnect applications in solid oxide fuel cells, *J. Power Sources.* 184 (**2008**) 172-179.

Monzón H., Laguna-Bercero M.A., Larrea A., Arias B.I., Várez A., Levenfeld B., Design of industrially scalable microtubular solid oxide fuel cells based on an extruded support, *Int. J. Hydrog. Energy*. 39 (**2014**) 5470-5476.

Molla T.T., Kwok K., Frandsen H.L., Efficient modeling of metallic interconnects for thermo-mechanical simulation of SOFC stacks: Homogenized behaviors and effect of contact, *Int. J. Hydrog. Energy*. 41 (**2016**) 6433-6444.

Morales M., Miguel-Pérez V., Tarancón A., Slodczyk A., Torrell M., Ballesteros B., Ouweltjes J.P., Bassat J.M., Montinaro D., Morata A., Multi-scale analysis of the diffusion barrier layer of gadolinia-doped ceria in a solid oxide fuel cell operated in a stack for 3000 h, *J. Power Sources*. 344 (**2017**) 141-151.

Morales M., Navarro M.E., Capdevila X.G., Roa J.J., Segarra M., Processing of graded anode-supported micro-tubular SOFCs based on samaria-doped ceria via gel-casting and spray-coating, *Ceram. Int*. 38 (**2012**) 3713-3722.

Morán-Ruiz A., Desarrollo de capas de contacto para su aplicación en SOFC/Development of contact coating for SOFC. Ph.D. thesis work, UPV/EHU, **2015**.

Morán-Ruiz A., Vidal K., Laguna-Bercero M.Á., Larrañaga A., Arriortua M.I., Effects of using $(La_{0.8}Sr_{0.2})_{0.95}Fe_{0.6}Mn_{0.3}Co_{0.1}O_3$ (LSFMC), $LaNi_{0.6}Fe_{0.4}O_{3-\delta}$ (LNF) and $LaNi_{0.6}Co_{0.4}O_{3-\delta}$ (LNC) as contact materials on solid oxide fuel cells, *J. Power Sources.* 248 (**2014**) 1067-1076.

Mulder G., Fuel cells – Alkaline fuel cells | Overview, Reference module in chemistry, molecular sciences and chemical engineering, *Encyclopedia of electrochemical power sources*, (**2009**) 321-328.

Myung J., Ko H.J., Park H., Hwan M., Hyun S. Fabrication and characterization of planar-type SOFC unit cells using the tape-casting/lamination/co-firing method, *Int. J. Hydrog. Energy*. 37 (**2012**) 498-504.

Nagasawa T., Hanamura K., Prediction of overpotential and effective thickness of Ni/YSZ anode for solid oxide fuel cell by improved species territory adsorption model, *J. Power Sources*. 353 (**2017**) 115-122.

Nguyen X.V., Chang C.T., Jung G.B., Chan S.H., Huang W.C.W., Hsiao K.J., Lee W.T.,. Chang S.W, Kao I.C., Effect of sintering temperature and applied load on anode-supported electrodes for SOFC application, *Energies*. 9 (**2016**) 701.

Nishihora R.K., Rachadel P.L., Quadri M.G.N., Hotza D., Manufacturing porous ceramic materials by tape casting: A review, *J. Eur. Ceram. Soc.* 38 (**2018**) 988-1001.

Norrman K., Ghanbari-Siahkali A., Larsen N., Studies of spin-coated polymer films, Annual reports on the progress of chemistry, Section C, *Phys. Chem*. 101 (**2005**) 174-201.

Osinkin D.A., Bronin D.I., Beresnev S.M., Bogdanovich N.M., Zhuravlev V.D., Vdovin G.K., Demyanenko T.A., Thermal expansion, gas permeability, and conductivity of Ni-YSZ anodes produced by different techniques, *J. Solid State Electr*. 18 (**2013**) 149-156.

Pan J., Tonkay G., Quintero A., Screen printing process design of experiments for fine line printing of thick film ceramic substrates, *J. Electron. Manuf*. 9 (**1999**) 203-213.

Pan X., Wang Z., He B., Wang S., Wu X., Xia C., Effect of Co doping on the electrochemical properties of $Sr_2Fe_{1.5}Mo_{0.5}O_6$ electrode for solid oxide fuel cell, *Int. J. Hydrog. Energ*y. 38 (**2013**) 4108-4115.

PANalytical, Almelo B.V., Versión 1.0, The Netherlands, **2003**.

Patcharavorachot Y., Arpornwichanop A., Chuachuensuk A., Electrochemical study of a planar solid oxide fuel cell: Role of support structures, *J. Power Sources*. 177 (**2008**) 254-261.

Patro P.K., Delahaye T., Bouyer E., Development of $Pr_{0.58}Sr_{0.4}Fe_{0.8}Co_{0.2}O_{3-\delta}$–GDC composite cathode for solid oxide fuel cell (SOFC) application, *Solid State Ion*. 181 (**2010**) 1378-1386.

Peebles M.W.H., Evolution of the Gas Industry, *Macmillan*, London/Basingstoke, (**1980**).

Peksen M., A coupled 3D thermofluid–thermomechanical analysis of a planar type production scale SOFC stack, *Int. J. Hydrog. Energy*. 36 (**2011**) 11914-11928.

Perry M., Fuller T., A historical perspective of fuel cell technology in the 20th century, *J. Electrochem. Soc.* 149 (**2002**) S59-S67.

Petrangeli G., Barrage balloons against aircraft threat: A well proven concept revisited, *Nucl. Eng. Des*. 240 (**2010**) 886-890.

Phair J.W., Rheological analysis of concentrated zirconia pastes with ethyl cellulose for screen printing SOFC electrolyte films, *J. Am. Ceram. Soc*. 91 (**2008**) 2130-2137.

Piao J., Sun K., Zhang N., Xu S., A study of process parameters of LSM and LSM–YSZ composite cathode films prepared by screen-printing, *J. Power Sources*. 175 (**2008**) 288-295.

Preininger M., Subotić V., Stoeckl B., Schauperl R., Reichholf D., Megel S., Kusnezoff M., Hochenauer C., Electrochemical characterization of a CFY-stack with planar electrolyte-supported solid oxide cells in rSOC operation, *Int. J. Hydrog. Energy*. 43 (**2018**) 12398-12412.

Preux, A. Rolle, R.N. Vannier, Electrolytes and ion conductors for solid oxide fuel cells (SOFCs), Functional materials for sustainable energy applications, *Woodhead publishing series in energy*, (**2012**) 370-401.

Rasouli S., Moeen S.J., Combustion synthesis of Co-doped zinc oxide nanoparticles using mixture of citric acid–glycine fuels, *J. Alloy. Compd*. 509 (**2011**) 1915-1919.

Ren H., Chae J., Fuel cells technologies for wireless MEMS, Wireless MEMS networks and applications, *Woodhead Publishing series in electronic and optical materials*, 2 (**2017**) 35-51.

Rietveld H.M. Line profiles of neutron powder diffraction peaks for structure refinement. *Acta Cryst.* 22 (**1967**) 151-152.

Rietveld H.M. A profile refinement method for nuclear and magnetic structure. *J. Appl. Cryst.* 2 (**1969**) 65-71.

Rieu M., Sayers R., Laguna-Bercero M.A., Skinner S.J., Lenormand P., Ansart F., Investigation of graded La_2NiO_4 delta cathodes to improve SOFC electrochemical performance, *J. Electrochem. Soc*. 157 (**2010**) B477-B480.

Robards A.W., Wilson A.J. Procedures in electron microscopy, John Wiley & Sons, Chichester, UK, **1993**.

Rodríguez-Carvajal J., Fullprof program: Rietveld pattern matching analysis of powder patterns, Grenoble, **2011**.

Sar J., Dessemond L., Djurado E., Electrochemical properties of graded and homogeneous $Ce_{0.9}Gd_{0.1}O_{2-\delta}$–$La_{0.6}Sr_{0.4}Co_{0.2}Fe_{0.8}O_{3-\delta}$ composite electrodes for intermediate-temperature solid oxide fuel cells, *Int. J. Hydrog. Energy*. 41 (**2016**) 17037-17043.

Salameh Z., Energy storage, *Renewable energy system design*, 4 (**2014**) 201-298.

Scataglini R., Wei M., Mayyas A., Chan S.H., Lipman T., Santarelli M., A Direct manufacturing cost model for solid-oxide fuel cell stacks, *Fuel Cells*. 17 (**2017**) 825-842.

Schmidtchen U., Fuels – Safety | Hydrogen: Transportation, Reference module in chemistry, molecular sciences and chemical engineering, *Encyclopedia of electrochemical power sources*, (**2009**) 528-532.

Serban M., Lewis M., Marshall C., Doctor R., Hydrogen production by direct contact pyrolysis of natural gas, *Energy Fuels*. 17 (**2003**) 705-713.

Setevich C.F., Mogni L.V., Caneiro A., Prado F.D., Optimum cathode configuration for IT-SOFC using $La_{0.4}Ba_{0.6}CoO_{3-\delta}$ and $Ce_{0.9}Gd_{0.1}O_{1.95}$, *Int. J. Hydrogen Energy*. 37 (**2012**) 14895-14901.

Sharaf O.Z., Orhan M.F., An overview of fuel cell technology: Fundamentals and applications, *Renew. Sust. Energ. Rev*. 32 (**2014**) 810-853.

Shimura K., Nishino H., Kakinuma K., Brito M.E., Uchida H., Effect of samaria-doped ceria (SDC) interlayer on the performance of $La_{0.6}Sr_{0.4}Co_{0.2}Fe_{0.8}O_{3-\delta}$/SDC composite oxygen electrode for reversible solid oxide fuel cells, *Electrochim. Acta*. 225 (**2017**) 114-120.

Shy S.S., Hsieh Y.D., Huang C.M., Chan Y.H., Comparison of electrochemical impedance measurements between pressurized anode-supported and electrolyte-supported planar solid oxide fuel cells, *J. Electrochem. Soc.* 162 (**2015**) F172-F177.

Singh S., Singh D., $LaSrFeO_4$ nanopowders synthesized by different combustion methods: Effect of fuel/particle size, *Ceram. Int*. 42 (**2016**) 15725-15731.

Somalu M.R., Muchtar A., Daud W.R.W., Brandon N.P., Screen-printing inks for the fabrication of solid oxide fuel cell films: A review, *Renew. Sust. Energ. Rev*. 75 (**2017**) 426-439.

Song B., Ruiz-Trejo E., Bertei A., Brandon N.P., Quantification of the degradation of Ni-YSZ anodes upon redox cycling, *J. Power Sources*. 374 (**2018**) 61-68.

Stambouli A.B., Fuel cells: The expectations for an environmental-friendly and sustainable source of energy, *Renew. Sust. Energ. Rev*. 15 (**2011**) 4507-4520.

Steinberger-Wilckens R., Sampson B., Market, Commercialization and deployment-toward appreciating total owner cost of hydrogen energy technologies, *Hydrogen production and practical applications in energy generation.* Ed. Academic press, 8 (**2019**) 383-403.

Stodolny M.K., Boukamp B.A., Blank D.H.A., van Berkel F.P.F., Impact of Cr-poisoning on the conductivity of different $LaNi_{0.6}Fe_{0.4}O_3$ cathode microstructures, *Solid State Ion*. 225 (**2012**) 136-140.

Su S., Zhang W., Wu J., Zhou C., Effect of component thickness and anode composition on the residual stress of micro-tubular solid oxide fuel cell, *Int. J. Electrochem. Sci*. 12 (**2017**) 9121-9130.

Sun H., Rainwater B.H., Xiong X., Chen Y., Wei T., Zhang Q., Yang Z., Li C., Liu M., Interfacial effects on electrical conductivity in ultrafine-grained $Sm_{0.2}Ce_{0.8}O_{2-\delta}$ electrolytes fabricated by a two-step sintering process, *Int. J. Hydrog. Energy*. 42 (**2017**) 11823-11829.

Tao S.W., Cowin P.I., Lan R., Novel anode materials for solid oxide fuel cells, Functional materials for sustainable energy applications, *Woodhead publishing series in energy*, 14 (**2012**) 445-477.

Tatko M., Mosiałek M., Dudek M., Nowak P., Kędra A., Bielańska E., Composite cathode materials $Sm_{0.5}Sr_{0.5}CoO_3$–$La_{0.6}Sr_{0.4}FeO_3$ for solid oxide fuel cells, *Solid State Ion*. 271 (**2015**) 103-108.

"The Fuel Cell Review". *Institute of Physics Publishing*, United Kingdom, **2005**.

Torabi A., Etsell T.H., Sarkar P., Dip coating fabrication process for micro-tubular SOFCs, *Solid State Ion*. 192 (**2011**) 372-375.

Tuichai W., Thongbai P., Amornkitbamrung V., Yamwong T., Maensiri S., $Na_{0.5}Bi_{0.5}Cu_3Ti_4O_{12}$ nanocrystalline powders prepared by a glycine–nitrate process: Preparation, characterization, and their dielectric properties, *Microelectron. Eng*. 126 (**2014**) 118-123.

Ultra Electronics AMI wins SOFC order for Rapid Equipping Force, Fuel Cells Bulletin. (**2011**) 7.

Vanaga R., Blumberga A., Freimanis R., Mols T., Blumberga D., Solar facade module for nearly zero energy building, *Energy*. 157 (**2018**) 1025-1034.

Vidal K., Larrañaga A., Morán-Ruiz A., Aguayo A.T., Laguna-Bercero M.A., Yeste M.P., Calvino J.J., Arriortua M.I., Effect of synthesis conditions on electrical and catalytical properties of perovskites with high value of A-site cation size mismatch, *Int. J. Hydrog. Energ*y. 41 (**2016**) 19810-19818.

Vidal K., Morán-Ruiz A., Larrañaga A., Porras-Vázquez J.M., Slater P.R., Arriortua M.I., Characterization of $LaNi_{0.6}Fe_{0.4}O_3$ perovskite synthesized by glycine-nitrate combustion method, *Solid State Ion*. 269 (**2015**) 24-29.

Vidal K., Rodríguez-Martínez L.M., Ortega-San-Martin L., Martínez-Amesti A., Nó M.L., Rojo T., Laresgoiti A., Arriortua M.I., The effect of doping in the electrochemical performance of $(Ln_{1-x}M_x)FeO_{3-\delta}$ SOFC cathodes, *J. Power Sources*. 192 (**2009**) 175-179.

Wain-Martin A., Morán-Ruiz A., Vidal K., Larrañaga A., Laguna-Bercero M.A., Arriortua M.I., Scalable synthetic method for SOFC compounds, *Solid State Ion*. 313 (**2017**) 52-57.

Wang C., Huang S., Xu S., Optimization of girth welded joint in a high-pressure hydrogen storage tank based on residual stress considerations, *Int. J. Hydrog. Energy*. 43 (**2018**) 16154-16168.

Wang F., Yan D., Zhang W., Chi B., Pu J., Jian L., $LaCo_{0.6}Ni_{0.4}O_{3-\delta}$ as cathode contact material for intermediate temperature solid oxide fuel cells, *Int. J. Hydrog. Energy*. 38 (**2013**) 646-651.

Wang J., Lü Z., Chen K., Huang X., Ai N., Hu J., Zhang Y., Su W., Study of slurry spin coating technique parameters for the fabrication of anode-supported YSZ Films for SOFCs, *J. Power Sources*. 164 (**2007**) 17-23.

Wang J., Lü Z., Huang X., Chen K., Ai N., Hu J., Su W., YSZ films fabricated by a spin smoothing technique and its application in solid oxide fuel cell, *J. Power Sources*. 163 (**2007**) 957-959.

Wang L., Li C., Li G., Yang G., Zhang S., Li C., Enhanced sintering behavior of LSGM electrolyte and its performance for solid oxide fuel cells deposited by vacuum cold spray, *J. Eur. Ceram. Soc*. 37 (**2017**) 4751-4761.

Wang W.G., Mogensen M., High-performance lanthanum-ferrite-based cathode for SOFC, *Solid State Ion*. 176 (**2005**) 457-462.

Wang Z., Huang X., Lv Z., Zhang Y., Wei B., Zhu X., Wang Z., Liu Z., Preparation and performance of solid oxide fuel cells with YSZ/SDC bilayer electrolyte, *Ceram. Int*. 41 (**2015**) 4410-4415.

Wincewicz K.C., Cooper J.S., Taxonomies of SOFC material and manufacturing alternatives, *J. Power Sources*. 140 (**2005**) 280-296.

Wilberforce T., Alaswad A., Palumbo A., Dassisti M., Olabi A.G., Advances in stationary and portable fuel cell applications, *Int. J. Hydrog. Energ*. 41 (**2016**) 16509-16522.

Wu X., Tian Y., Zhou X., Kong X., Zhang J., Zuo W., Ye X., High performance yttria-stabilized zirconia based intermediate temperature solid oxide fuel cells with double nano layer composite cathode, *Int. J. Hydrog. Energy*, 42 (**2017**) 1093-1102.

Wulf C., Zapp P., Assessment of system variations for hydrogen transport by liquid organic hydrogen carriers, *Int. J. Hydrog. Energy*. 43 (**2018**) 11884-11895.

Xin X., Liu L., Liu Y., Zhu Q., Novel perovskite-spinel composite conductive ceramics for SOFC cathode contact layer, *Int. J. Hydrog. Energy*. 43 (**2018**) 23036-23040.

Xu X., Ceramics in solid oxide fuel cells for energy generation, Advances in ceramic matrix composites, *Woodhead publishing series in composites science and engineering*, 31 (**2018**) 763-788.

Xu X., Xia C., Huang S., Peng D., YSZ thin films deposited by spin-coating for IT-SOFCs, *Ceram. Int*. 31 (**2005**) 1061-1064.

Yan D., Liang L., Yang J., Zhang T., Pu J., Chi B., Li J., Performance degradation and analysis of 10-cell anode-supported SOFC stack with external manifold structure, *Energy*. 125 (**2017**) 663-670.

Yan K., Kishimoto H., Develos-Bagarinao K., Yamaji K., Horita T., Yokokawa H., Chemical compatibility of doped yttrium chromite and ceria composite materials with YSZ electrolyte, *Solid State Ion*. 288 (**2016**) 88-93.

Yang K., Shen J., Yang K., Hung I.M., Fung K., Wang M., Formation of $La_2Zr_2O_7$ or $SrZrO_3$ on cathode-supported solid oxide fuel cells, *J. Power Sources*. 159 (**2006**) 63-67.

Young R.A. *"The Rietveld method"*. International Union of Crystallography-Oxford Science Publications: Oxford, **1995**.

Zeng K., Zhang D., Recent progress in alkaline water electrolysis for hydrogen production and applications, *Prog. Energy Combust. Sci*. 36 (**2010**) 307-326.

Zhao L., Huang X., Zhu R., Lu Z., Sun W., Zhang Y., Ge X., Liu Z., Su W., Optimization on technical parameters for fabrication of SDC film by screen-printing used as electrolyte in IT-SOFC, *J. Phys. Chem. Solids*. 69 (**2008**) 2019-2024.

Zhong M.M., Yuan H.K., Huang C., Wang G., Electronic properties of porous graphene and its hydrogen storage potentials, *J. Alloy. Compd*. 766 (**2018**) 104-111.

Zhou F., Liu Y., Zhao X., Tang W., Yang S., Zhong S., Wei M., Effects of cerium doping on the performance of LSCF cathodes for intermediate temperature solid oxide fuel cells, *Int. J. Hydrog. Energy*. 43 (**2018**) 18946-18954.

Zhu J.H., Ghezel-Ayagh H., Cathode-side electrical contact and contact materials for solid oxide fuel cell stacking: A review, *Int. J. Hydrog. Energy*. 42 (**2017**) 24278-24300.

Zhuiykov S., Nanostructured semiconductor composites for solid oxide fuel cells (SOFCs), Nanostructured semiconductors, *Woodhead publishing series in electronic and optical materials*, 8 (**2018**) 413-474.

7. Anexo. Técnicas experimentales

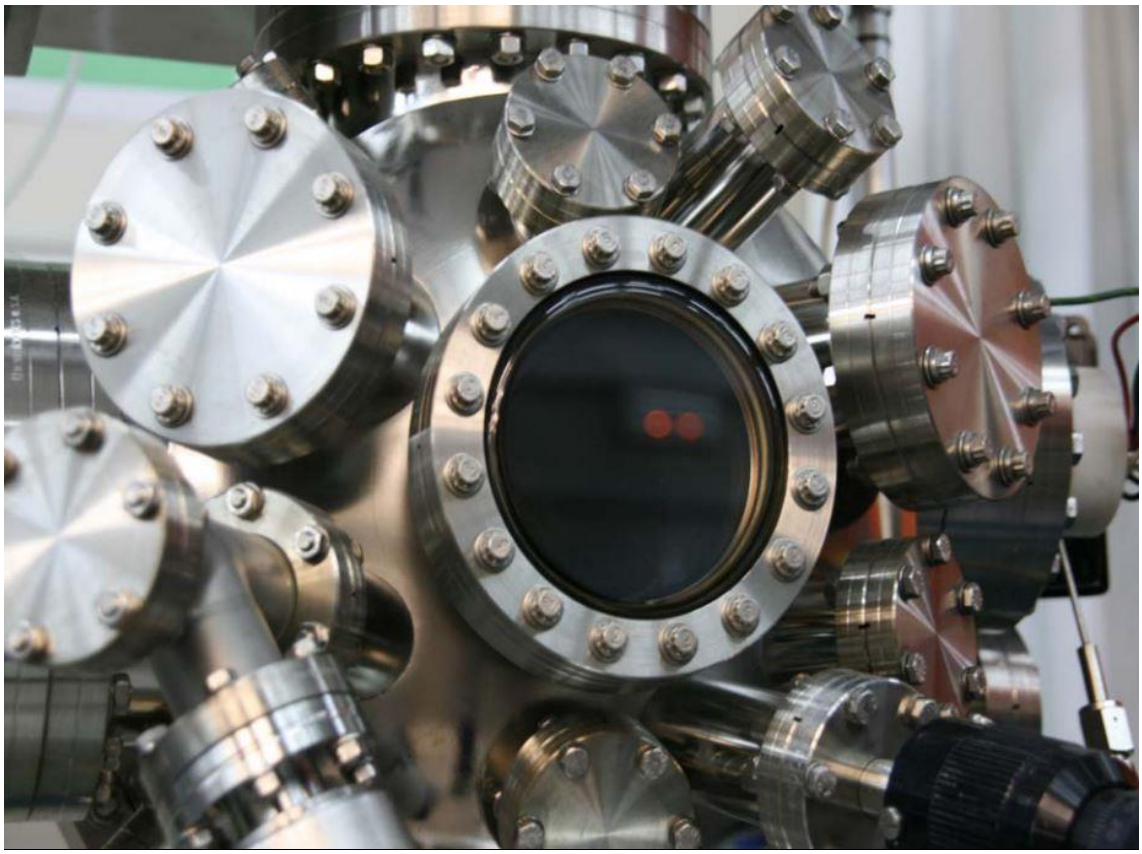

7.1. Técnicas de procesado

7.1.1. Spray manual coloidal

La deposición del electrolito, la barrera química, el cátodo y la capa de contacto se han llevado a cabo sobre un substrato plano mediante spray manual coloidal, utilizando como pistola de pulverización un aerógrafo Iwata eclipse HP-BCS. La deposición de capas mediante el sprayado de polvos húmedos (Wet Powder Spraying, WPS) es una técnica versátil que permite el recubrimiento de superficies tubulares y planares. La calidad del espesor de la capa depositada no solo dependerá de la reología de la suspensión, sino también de la adherencia térmica del componente a recubrir y de la combinación de los siguientes factores: la presión del aire del aerógrafo, la distancia de pulverización, la porosidad del substrato y el ángulo de pulverización, entre otros.

En la preparación de suspensiones para su posterior deposición a través de la técnica de WPS, se ha utilizado un molino de bolas ML007 de Ceremex (Figura 7.1.) para efectuar el ball-milling. El ball-milling es un tipo de molienda comúnmente utilizada para la preparación de pinturas, que funciona según el método de impacto y desgaste. La reducción de tamaño de los polvos se realiza con el impacto de las bolas con la cubierta y entre sí, quedando el polvo entre medias, desgastándose de esta manera. Habitualmente, las bolas utilizadas son cilindros o esferas, normalmente de zirconia o alúmina, pudiendo utilizar diferentes tamaños en función del tamaño final de partícula que se necesite. En este trabajo, para la preparación de las suspensiones, se han mezclado el polvo cerámico a depositar (LNF, LSF, SDC o YSZ) utilizando isopropanol como disolvente.

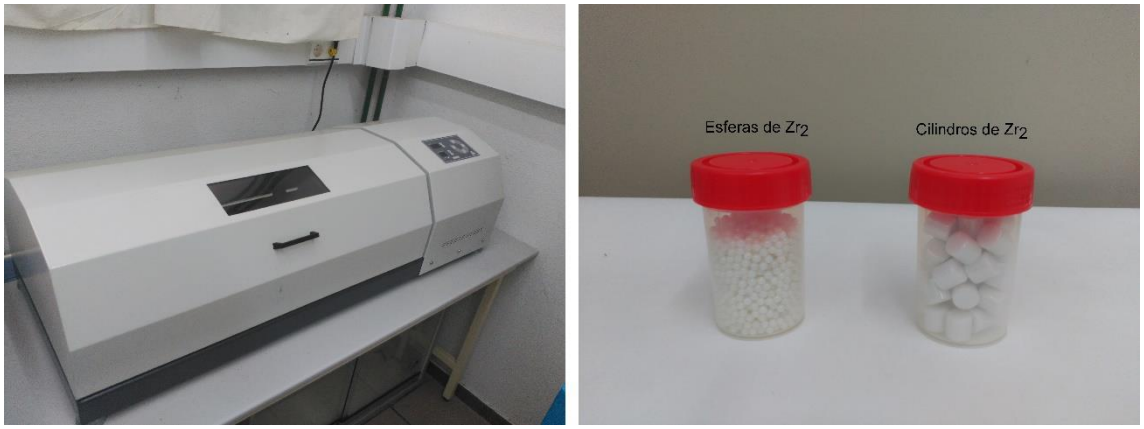

Figura 7.1.- Imagen del molino de bolas ML007.

Para una adecuada homogeneización con el molino de bolas, se han utilizado como medio de dispersión esferas de ZrO_2 de 5 mm de diámetro, sometiéndose el conjunto a una velocidad de 270 r.p.m. durante 24 h.

7.1.2. Prensado

El procesado de los soportes efectuados en el transcurso de la investigación realizada se ha efectuado a través del método de prensado uniaxial. El prensado se realiza colocando el polvo cerámico en un molde de la forma deseada y se somete a la compresión a través de una prensa utilizando una pieza que se ajusta al molde. El molde y los punzones deben ser capaces de resistir múltiples operaciones sin desgastarse ni deformarse, ya que la precisión dimensional es un aspecto fundamental en la tecnología de prensado de polvos; por ello, suelen ser de acero. En esta investigación, se ha utilizado el prensado uniaxial, en el que la presión se aplica en una sola dirección por un ariete. La operación consta de las siguientes partes:

En un primer lugar, se sella la matriz, la cual puede hacerse por volumen o por peso. Posteriormente, se realiza la compactación, hasta llegar a la presión adecuada, permitiendo la salida de gases atrapados entre las partículas a velocidad lenta, para propiciar, el reapilamiento de las partículas. Finalmente, se realiza la expulsión, mediante el punzón inferior, de manera que no se provoquen agrietamientos en el compacto. Este cuerpo compacto, experimentara una recuperación elástica. El resultado final es un cuerpo verde y poroso. Cuanto mayor sea la presión aplicada, mayor es la resistencia y la densidad del cuerpo compactado.

En todo proceso de compactación pueden distinguirse las siguientes etapas, a medida que se aumenta la presión:

- Movimiento de los polvos dirigido a un mayor reapilamiento.
- Una deformación elástica de las partículas.
- Una deformación plástica de las partículas.
- Una rotura de las partículas.
- Una deformación elástica y plástica de cuerpo compactado.

7.1.3. Sinterizado

Para que los materiales cerámicos adquieran una microestructura adecuada y tengan las propiedades requeridas, han de ser tratados por un proceso de sinterizado. La sinterización es un proceso de transporte de materia, activado por la temperatura, en una masa de polvos o en un compuesto poroso, en el que disminuye la superficie especifica por el crecimiento de contacto entre partículas, contrayéndose el volumen de porosidad y cambiando la geometría de los poros. Este contacto entre partículas puede reforzarse mediante la aplicación de presión durante el proceso. También se puede definir como el tratamiento térmico de un polvo a temperatura inferior a la de fusión, con el propósito de aumentar su resistencia a través de la unión de las partículas. Se distinguen tres etapas durante el proceso. En una etapa inicial, crecen los cuellos de enlace entre las partículas, obteniéndose una pérdida significativa del área superficial. Posteriormente, en una etapa intermedia, los granos aumentan su tamaño disminuyendo el tamaño de los poros casi totalmente y produciendo una densificación significativa. Finalmente, los espacios de los poros se cierran lentamente.

A nivel microscópico, la sinterización ocurre mediante la formación de cuellos entre partículas adyacentes, para lo cual son necesarios procesos de transferencia de masa que sustituyan las superficies de contacto sólido/vapor por nuevas superficies de contacto sólido/sólido. La reducción de la entalpía libre del sistema proporciona la fuerza motriz del proceso de sinterización, la cual se debe a: (i) la disminución del área específica debido a la iniciación y/o crecimiento de los contactos, (ii) la reducción del volumen de poros y de su superficie, y (iii) la eliminación de los estados de no equilibrio de la red.

Sin embargo, para lograr el proceso dentro de un tiempo razonable, también se debe considerar la cinética del transporte de materia. Así, la movilidad de las partículas aumenta a altas temperaturas debido al incremento de átomos activos y vacantes disponibles. Los mecanismos de sinterizado describen la trayectoria del flujo de materia. Para la mayoría de los polvos inorgánicos, el mecanismo dominante es la difusión, la cual ocurre a través de la superficie, a través de los bordes de grano o a través de la red cristalina.

Para estos tratamientos de sinterizado de las muestras, se han utilizado los hornos tipo mufla que están ubicados en el laboratorio de Mineralogía y Petrología de la Facultad de Ciencia y Tecnología de la UPV/EHU (Figura 7.2.).

Figura 7.2.- Horno de sinterizado Naverterm 1500 utilizado en los tratamientos de sinterizado de las muestras.

7.2. Técnicas instrumentales

7.2.1. Espectroscopia de emisión por plasma acoplado inductivamente

La determinación cuantitativa de los elementos presentes en los materiales de partida se ha realizado mediante espectroscopia de emisión por plasma acoplado inductivamente (ICP-AES), empleando un espectrómetro Horiba Yobin Yvon Activa (Figura 7.3.), perteneciente al servicio Central de Análisis (SGIker) de la Universidad del País Vasco (UPV/EHU). Este equipo dispone de un sistema de nebulización de vidrio y de teflón y está controlado mediante un ordenador de control con software Activa Analyst 5.4. Para la realización de estas medidas es necesario que el material sea previamente disuelto.

La técnica ICP-AES se basa en la detección de la emisión de energía, en el intervalo de ultravioleta visible, producida por átomos excitados o iones libres cuando éstos son excitados, a temperaturas del orden de 10^4 K.

Las muestras se introducen dentro de un plasma de argón a través de un nebulizador por el que circula un flujo absorbente de este gas. La fuente de plasma de argón (o antorcha) es un tubo de cuarzo rodeado de una bobina de inducción, alimentada por un generador de radiofrecuencias. La ionización de argón se produce, inicialmente, por una chispa y su alta temperatura se mantiene gracias al calentamiento que producen los electrones que atraviesan la bobina de inducción. Los electrones se aceleran por el campo magnético para viajar en órbitas circulares dentro del tubo de cuarzo. Entonces, la energía se transfiere desde los electrones al gas por colisiones, calentándose de esta forma. Las altas temperaturas alcanzadas producen altas concentraciones de átomos excitados e iones.

Los espectros de emisión provienen de las transiciones que se producen entre los electrones de las capas más externas de los átomos. Cuando un átomo excitado vuelve a su estado fundamental, la emisión producida tiene una longitud de onda que es característica de cada elemento, facilitando, de esta manera, su identificación. Además, la intensidad de esta emisión es proporcional a la concentración del elemento en la muestra, por lo que es posible determinar la cantidad presente en la misma.

Una de las grandes ventajas de los equipos de emisión es la posibilidad de analizar docenas de elementos, simultáneamente, debido a que la mayoría de ellos produce buenos espectros de emisión con unas mismas condiciones de excitación. El hecho de que la atomización se produzca en un medio inerte, también permite que sea mayor la vida media del analito y evita que se formen óxidos. En consecuencia, la atomización es más completa y hay menos problemas de interferencias químicas que en la técnica de absorción.

En esta técnica, es necesaria la realización previa de patrones y rectas de calibrado que contengan los elementos a analizar en un intercalo de concentraciones acorde con la sensibilidad de los instrumentos[1,2].

Figura 7.3.- Espectrómetro de emisión atómica con plasma acoplado inductivamente (ICP-AES) *Horiba Yobin Yvon Activa.*

[1] Miller J.C., Miller J.N., *Statistics for Analitical Chemistry*, Ellis Horwood, 2ª Ed., London, **1988**.

[2] Hernandez L., Gonzalez C., *Introducción al Analisis Instrumental*, Editorial Ariel, S.A., Barcelona, **2002**.

7.2.2. Fluorescencia de rayos X

La microfluorescencia de rayos X, se basa en la emisión que se produce en una muestra cuando es irradiada con radiación X. El método más habitual utiliza tubos de rayos X para excitar las muestras, que al absorber el haz primario emiten sus propios rayos X característicos. Este método es uno de los más utilizados para la identificación cualitativa de elementos con números atómicos superiores a 8. También se emplea, a menudo, para el análisis semicuantitativo y cuantitativo. Una de las ventajas importantes de este método es que no es destructivo como la mayoría de las técnicas de análisis elemental.

Un espectro de fluorescencia de rayos X (XRF) utiliza como fuente de radiación un tubo de rayos X para provocar la emisión de rayos X secundarios de una muestra. La radiación emitida por la muestra contiene las líneas de rayos X características de los elementos que la componen. La dispersión de estos rayos X secundarios en un espectro permite identificar los elementos presentes en la muestra. La intensidad de la línea característica de rayos X está relacionada con la concentración del elemento que las produce en la muestra analizada. Esto permite hacer el análisis cuantitativo de la mayoría de los elementos.

Para producir la emisión de rayos X de una muestra es preciso excitarla previamente con radiación X primaria. En el proceso de excitación se crean huecos en las capas más internas del átomo que pasan a ser ocupados por electrones de capas superiores. Las transiciones electrónicas que se producen para ocupar las vacantes creadas conllevan la emisión de rayos X secundarios.

La fuente de radiación primaria más común en XRF es un tubo de rayos X. Los componentes principales de estos tubos son un filamento de wolframio y un ánodo o anticátodo metálico introducidos en un tubo de vidrio a alto vacío. El filamento se calienta mediante el paso de una corriente eléctrica, lo que produce una nube de electrones. Éstos son acelerados mediante un potencial negativo hacía el ánodo. La rápida deceleración de estos electrones al interaccionar con los átomos del ánodo libera energía en forma de rayos X, lo que produce un espectro continuo. El impacto de los electrones puede también ionizar los átomos de ánodo expulsando electrones de las capas más internas. Los electrones de capas más externas tienden a reemplazar las vacantes creadas, emitiendo así rayos X con longitudes de onda características del material del ánodo. El espectro de rayos X generado consiste en un continuo y un conjunto de líneas características (Kα y Kβ). La radiación sale del tubo a través de una ventana, que normalmente es de berilio.

Las medidas de fluorescencia de rayos X sobre los materiales de los componentes se han realizado en un equipo Fischerscope X-ray xdal (Figura 7.4.), utilizando los polvos de partida generados en la investigación realizada.

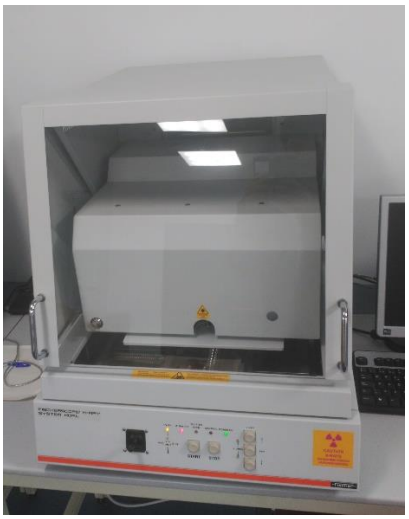

Figura 7.4.- Espectrómetro de fluorescencia de rayos X.

7.2.3. Análisis granulométrico

El tamaño de las partículas que constituyen un material tiene relación directa con sus propiedades, por lo que el conocimiento de éste puede aportar bastante información. Dentro de la variedad de analizadores de distribución de tamaño de partícula, los de Malvern Sizer están basados en el fenómeno de la dispersión láser, es decir, se basa en el principio físico de que las partículas dispersan la luz en todas las direcciones, con un patrón de intensidad que depende del tamaño de la partícula. Estos sistemas no se enmarcan en la categoría de sistemas ópticos de proyección de imagen, debido al hecho de que el resultado se logra sin formar una imagen de la partícula sobre el detector. Al hacer pasar un haz láser monocromático a través de una muestra en suspensión, la luz se dispersa y se produce una figura de dispersión de simetría radial en el plano focal de la lente. El MasterSizerX emplea dos formas de configuración óptica para proporcionar los resultados. El primero es un método óptico bien conocido, llamado óptica convencional de Fourier, mientras que el segundo es una configuración óptica llamada óptica de Fourier inversa, la cual permite alcanzar a medir el intervalo de tamaños de 0.1 μm.

El experimento de dispersión láser consiste en un proceso de dos fases dirigido a medir la dispersión de bajo ángulo característica de las partículas de la muestra. Las medidas se dividen en dos etapas con objeto de eliminar la dispersión generada por otras fuentes de luz. La realización de una medida previa permite, por lo tanto, restar la dispersión recogida del conjunto analizado.

Para una configuración cualquiera, una gran cantidad de partículas está simultáneamente presente en el haz del analizador y la medida de luz dispersada en el detector es la suma de todos los elementos individuales agrupados en el eje central. Así, el sistema intrínsecamente mide la dispersión integral de todas las partículas presentes en el haz. En un experimento típico el número de las partículas necesarias en el haz para obtener una medida adecuada de la dispersión es de 100 a 10.000, dependiendo del tamaño.

El realizar una medida instantánea de la dispersión, por lo tanto, da lugar a una distribución de tamaños (Figura 7.5.) basada solamente en una pequeña sección transversal del material a analizar. Este procedimiento genera problemas de estadística inadecuada y muestreo no representativo del material, que se evita recogiendo la dispersión promedio obtenida al hacer pasar, de forma continua, el material durante un tiempo por el eje del analizador.

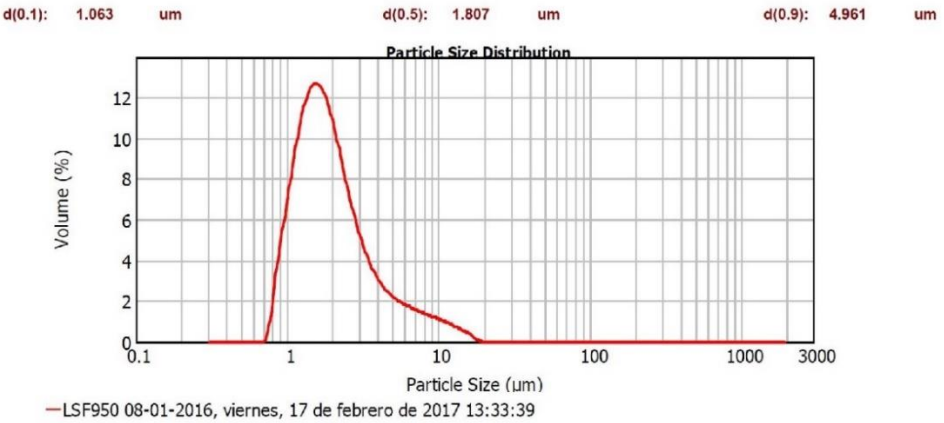

Figura 7.5.- Distribución de tamaños de partícula del Analizador de Tamaño de Partículas.

El material que atraviesa el eje está cambiando de continúo formando una integral de dispersión instantánea del mismo. La elaboración de una gran cantidad de barridos en el detector permite acumular la dispersión de millones de partículas individuales y, dada la rapidez de registro, esta información se obtiene en tiempos de medida de aproximadamente unos segundos.

A la hora de interpretar los resultados de la técnica de difracción láser (Figura 7.6.), hay que tener en cuenta una serie de conceptos fundamentales.

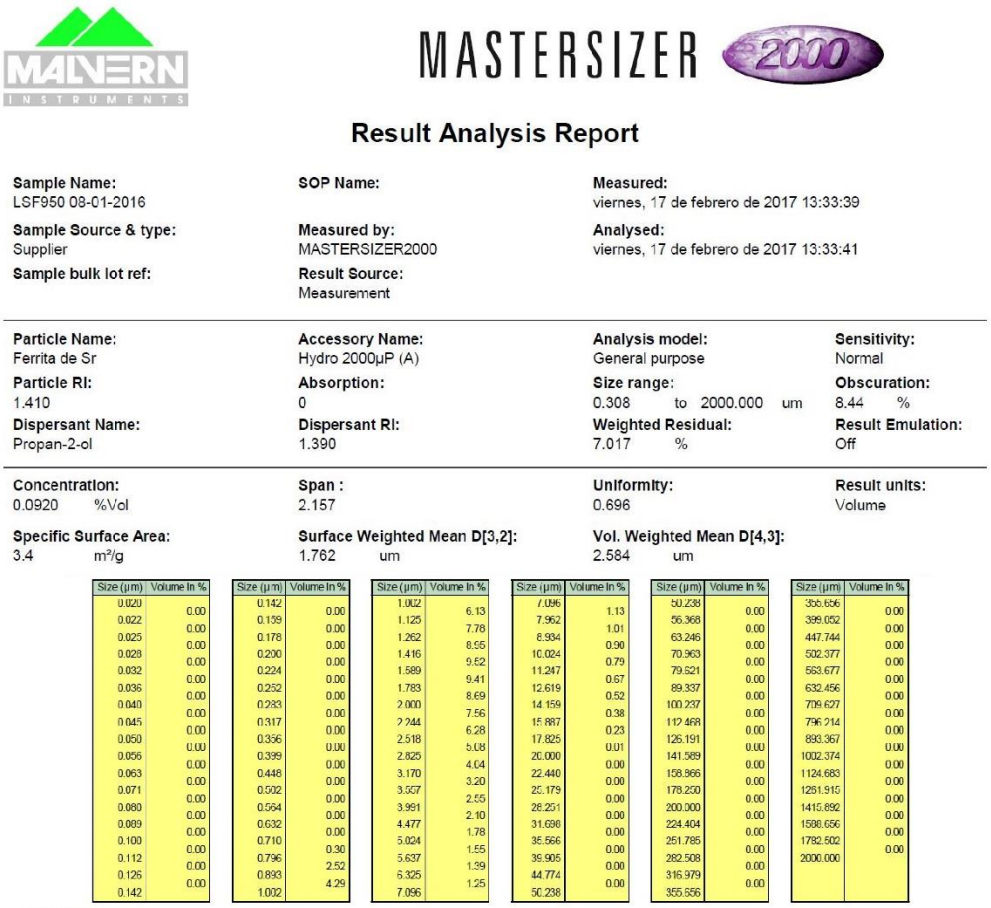

MASTERSIZER 2000

Result Analysis Report

Sample Name: LSF950 08-01-2016	**SOP Name:**	**Measured:** viernes, 17 de febrero de 2017 13:33:39	
Sample Source & type: Supplier	**Measured by:** MASTERSIZER2000	**Analysed:** viernes, 17 de febrero de 2017 13:33:41	
Sample bulk lot ref:	**Result Source:** Measurement		
Particle Name: Ferrita de Sr	**Accessory Name:** Hydro 2000μP (A)	**Analysis model:** General purpose	**Sensitivity:** Normal
Particle RI: 1.410	**Absorption:** 0	**Size range:** 0.308 to 2000.000 um	**Obscuration:** 8.44 %
Dispersant Name: Propan-2-ol	**Dispersant RI:** 1.390	**Weighted Residual:** 7.017 %	**Result Emulation:** Off
Concentration: 0.0920 %Vol	**Span :** 2.157	**Uniformity:** 0.696	**Result units:** Volume
Specific Surface Area: 3.4 m^2/g	**Surface Weighted Mean D[3,2]:** 1.762 um	**Vol. Weighted Mean D[4,3]:** 2.584 um	

Size (μm)	Volume In %	Size (μm)	Volume In %	Size (μm)	Volume In %	Size (μm)	Volume In %	Size (μm)	Volume In %	Size (μm)	Volume In %
0.020	0.00	0.142	0.00	1.002	6.13	7.096	1.13	50.238	0.00	355.656	0.00
0.022	0.00	0.159	0.00	1.125	7.78	7.962	1.01	56.368	0.00	399.052	0.00
0.025	0.00	0.178	0.00	1.262	8.55	8.934	0.90	63.246	0.00	447.744	0.00
0.028	0.00	0.200	0.00	1.416	9.52	10.024	0.79	70.963	0.00	502.377	0.00
0.032	0.00	0.224	0.00	1.589	9.41	11.247	0.67	79.621	0.00	563.677	0.00
0.036	0.00	0.252	0.00	1.783	8.69	12.619	0.52	89.337	0.00	632.456	0.00
0.040	0.00	0.283	0.00	2.000	7.56	14.159	0.38	100.237	0.00	709.627	0.00
0.045	0.00	0.317	0.00	2.244	6.28	15.887	0.23	112.468	0.00	796.214	0.00
0.050	0.00	0.356	0.00	2.518	5.08	17.825	0.01	126.191	0.00	893.367	0.00
0.056	0.00	0.399	0.00	2.825	4.04	20.000	0.00	141.589	0.00	1002.374	0.00
0.063	0.00	0.448	0.00	3.170	3.20	22.440	0.00	158.866	0.00	1124.683	0.00
0.071	0.00	0.502	0.00	3.557	2.55	25.179	0.00	178.250	0.00	1261.915	0.00
0.080	0.00	0.564	0.00	3.991	2.10	28.251	0.00	200.000	0.00	1415.892	0.00
0.089	0.00	0.632	0.00	4.477	1.78	31.698	0.00	224.404	0.00	1588.656	0.00
0.100	0.00	0.710	0.30	5.024	1.55	35.566	0.00	251.785	0.00	1782.502	0.00
0.112	0.00	0.796	2.52	5.637	1.39	39.905	0.00	282.508	0.00	2000.000	
0.126	0.00	0.893	4.29	6.325	1.25	44.774	0.00	316.979	0.00		
0.142		1.002		7.096		50.238		355.656			

Figura 7.6.- Resultados del Analizador de Tamaño de Partículas, Malvern Master SizerX.

El primero, es que la distribución de tamaños obtenidos mediante la técnica de dispersión láser está basada en el volumen. Esto implica que cuando en la lista de resultados, por ejemplo, el 11% de la distribución de tamaños está entre 6.97-7.75 μm, significa que el volumen total de todas las partículas con diámetros en este intervalo representa el 11% del volumen total de todas las partículas en la distribución.

El segundo punto a considerar, es que la distribución se expresa en términos de volúmenes de esferas equivalentes. Considerando una partícula cilíndrica de diámetro 20 μm y longitud 60 μm, la esfera de volumen equivalente tendría un diámetro de 33 μm.

Si se desea correlacionar los resultados de la dispersión láser con valores de una cierta técnica es posible aplicar una corrección de forma usando un procedimiento para la modificación de los resultados.

El tercer punto es que las distribuciones analizadas están expresadas aplicando un sistema de clasificación de tamaño que se optimiza para una mejor resolución, acoplando la geometría del detector y la configuración óptica. Todos los parámetros se derivan de esta distribución fundamental. Los diámetros derivados D[M,N] se calculan a partir de la distribución fundamental usando la adición de las contribuciones de cada intervalo de tamaños.

El empleo de distintos tiempos de medida, genera la formación de agregados por efectos de tensión superficial. Para tamaños de partícula inferiores a 1 μm, estos efectos se observan de forma sistemática en todas las medidas siendo la relevancia diferente en función del medio de dispersión, el tamaño de las partículas, etc.

Para preparaciones en las que, tanto el medio como la muestra no se han modificado, es posible observar la formación de partículas agregadas e incluso la disgregación de parte de las mismas a tiempos largos de medida. Como norma general se consideran válidos resultados con tiempos breves de medida y distribuciones de tamaños de partícula nunca superiores a las distribuciones iniciales obtenidas. Cabe suponer que tamaños de partícula grandes, no observados en tiempos de medida cortos, no son representativos de la muestra original, sino que corresponden a la cohesión de las partículas en el medio empleado.

Una de las variables más significativas a la hora de realizar las medidas de tamaño de partícula empleando un analizador Malvern MasterSizerX es el medio de dispersión. En el caso de esta investigación, en las tintas utilizadas para depositar las capas encima de los soportes, el medio liquido utilizado era isopropanol.

Una cuarta variable es el empleo de un sistema de ultrasonidos incorporado al equipo. El efecto de los ultrasonidos en las muestras se traduce en una disgregación de los aglomerados de partículas. No obstante, a largos tiempos de medida se puede provocar la formación de agregados de partícula de tamaño 4-10 μm.

El proceso de decantación permite realizar una separación mecánica de tamaños, por lo que se debería observar una gradación de tamaños para cada preparación.

Los análisis de tamaño de las partículas de los diferentes materiales a emplear como componentes de pilas SOFC (NiO-YSZ, YSZ, SDC, LSF, LNF y MCF) se han realizado en un analizador de tamaño de partículas “Malvern MasterSizerX 2000E” (Figura 7.7.), ubicado en los Servicios Generales de Investigación (SGIker), de la UPV/EHU.

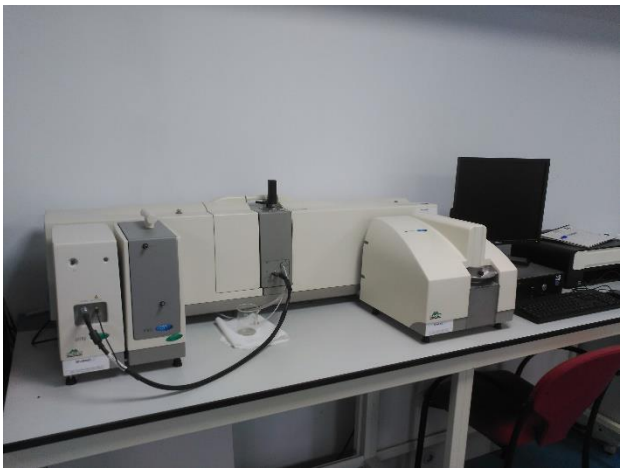

Figura 7.7.- Analizador de distribución de partícula “Malvern MasterSizerX”.

El equipo dispone de un software de adquisición y tratamiento de datos “MasterSizer 2000”. Todas las medidas se han realizado empleando como medio de dispersión isopropanol, utilizando ultrasonidos para deshacer los aglomerados que se forman en los materiales.

7.2.4. Conductividad eléctrica total y Espectroscopia de impedancia compleja

Las medidas de conductividad en bulk (barras rectangulares) se han realizado mediante el método de cuatro puntos (Figura 7.8.) haciendo uso de la ecuación de Ohm.

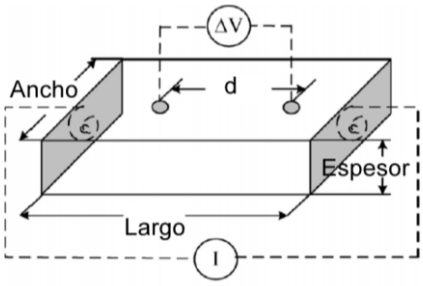

Figura 7.8.- Sistema de cuatro puntos utilizado para las medidas de conductividad eléctrica para los compuestos en bulk.

Por lo tanto, la conductividad (σ) se ha determinado a partir de los valores V-I, según la siguiente ecuación 7.1:

$$\sigma = \frac{1}{\rho} = \frac{d}{A \cdot R} \qquad (7.1)$$

donde σ es la conductividad eléctrica ($S \cdot cm^{-1}$) (inversa de la resistividad, ρ), d es la distancia entre las conexiones (cm), A es el área de la sección transversal (cm^2) y R es la resistencia ($\Omega \cdot cm^{-2}$).

La conductividad total media consta de dos componentes: la conductividad electrónica debida a un movimiento de electrones entre los portadores de carga y la conductividad iónica que resulta del movimiento de iones oxígeno. Sin embargo, la conductividad iónica observada para los compuestos medidos es de aproximadamente dos órdenes de magnitud inferior a la electrónica[3-5]. Como consecuencia de ello, suele considerarse que los valores de conductividad que se obtienen siguiendo este método se atribuyen casi exclusivamente a la conductividad electrónica.

El mecanismo de conducción, de alguno de los materiales analizados, se produce a través del modelo conocido como "small polaron hopping". Este mecanismo se activa térmicamente, existiendo una dependencia de la movilidad de los portadores de carga y, por consiguiente, de la conductividad con la temperatura, que viene dada por la ecuación 7.2 de Arrhenius:

$$\sigma = \left(\frac{C}{T}\right) exp\left(-\frac{Ea}{K \cdot T}\right) \qquad (7.2)$$

---

[3] Ivers-Tiffée E., Weber A., Schichlein H., in Handbook of Fuel cells. vol. 2 (eds. Vielstich W., Gasteiger H.A., Lamm A.), John Wiley & Sons, Chichester, **2003**.

[4] Carter S., Seluck A., Charter R.J., Kajda J., Kilner J.A., Steele B.C.H. Oxygen transport in selected nonstoichiometric perovskite-structure oxides. *Solid State Ionics* 53-56 (**1992**) 597-605.

[5] Bahteeva J.A., Leonidov I.A., Patrakeev M.V., Mitberg E.B., Kozhevnokov V.L., Poeppelmeier K.R. High-temperature ion transport in $La_{1-x}Sr_xFeO_{3-\delta}$. *J. Solid State Electr.* 8 (**2004**) 578-584.

donde T es la temperatura absoluta, Ea es la energía de activación, K es la constante de Boltzmann y C es un factor pre-exponencial relacionado con la movilidad de las cargas. Para cada composición, el valor de Ea se ha calculado a partir de la pendiente de la recta correspondiente (ecuación 7.3) entre las temperaturas en las que se cumple el modelo de Arrhenius.

$$Ln(\sigma \cdot T) = lnC - \frac{Ea}{K \cdot T} \qquad (7.3)$$

Los términos resistencia e impedancia denotan una oposición al flujo o corriente de electrones. En circuitos de corriente continua (dc), únicamente es el resistor el que ofrece este efecto. Sin embargo, en los de corriente alterna (ac), son el condensador e inductor los que se oponen al paso de electrones. La impedancia se puede expresar mediante un número complejo, donde la resistencia es la componente real y la combinación de capacitancia e inductancia es la componente imaginaria.

La espectroscopia de impedancia electroquímica (EIS) muestra un papel importante en el desarrollo y comprensión de los factores que afectan a las celdas de combustible. La mayor ventaja de esta técnica es la capacidad de separar (en campos de frecuencias) las contribuciones individuales de los factores de transporte óhmico, cinético y de masa, que determinan las pérdidas totales de la potencia de la celda de combustible.

Todos los métodos de impedancia aplican una pequeña señal sinusoidal al sistema en estudio, y miden la respuesta de éste en términos de corriente, voltaje, y alguna otra señal de interés. La Figura 7.9. muestra una curva V-I no lineal correspondiente a un sistema electroquímico teórico.

Se sobrepone una onda de baja amplitud de una frecuencia, $\Delta E \sin(\omega t)$, sobre un voltaje DC de polarización E_0. Como respuesta, también lo hace una corriente $\Delta I \sin(\omega t + \varphi)$ sobre la corriente DC I_0. Esta corriente está desplazada con respecto al potencial aplicado. La impedancia del sistema en estudio, por lo tanto, puede calcularse mediante la ley de Ohm, representada mediante la siguiente expresión en la ecuación 7.4;

$$Z(\omega) = \frac{\Delta E(\omega)}{\Delta I(\omega)} = Z(\omega) = \frac{\Delta E(\omega)}{\Delta I(w)} = |Z|(v)e^{\phi(\omega)} = Z_r(\omega) + jZ_j(\omega) \qquad (7.4)$$

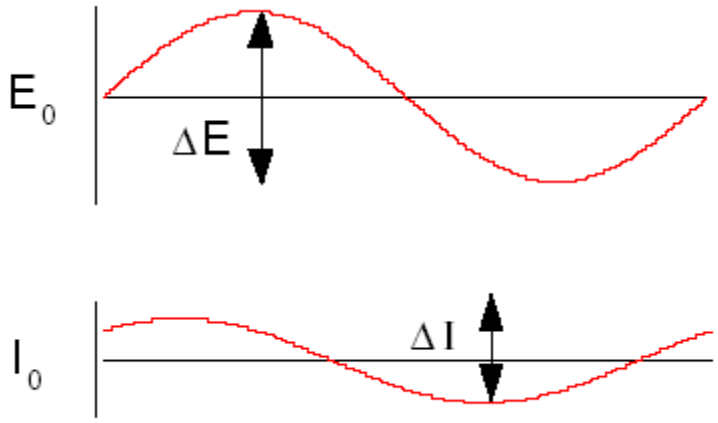

Figura 7.9.- Curva V-I no lineal para un sistema electroquímico hipotético.

La impedancia, Z, es una cantidad compleja cuya magnitud y desfase dependen de la frecuencia de la señal aplicada, ω. Variando ésta, se puede medir la impedancia del sistema en función de la frecuencia. Normalmente, en electroquímica, para este tipo de sistemas, se aplica un intervalo de frecuencias entre 100KHz y 0.1Hz. En la ecuación anterior, la impedancia, Z(ω), viene expresada en coordenada polares y cartesianas, respectivamente[6].

El espectro de impedancia puede representarse de dos formas; mediante la representación de Nyquist (Figura 7.10a), donde se muestra la parte imaginaria negativa, Z´´, frente a la parte real, Z´, o mediante la representación de Bode (Figura 7.10b), donde la impedancia absoluta, |Z|, y el desfase, φ, se muestran frente a la frecuencia angular, ω. Esta última representación puede ser ventajosa cuando la impedancia depende fuertemente de la frecuencia, como en el caso de un condensador.

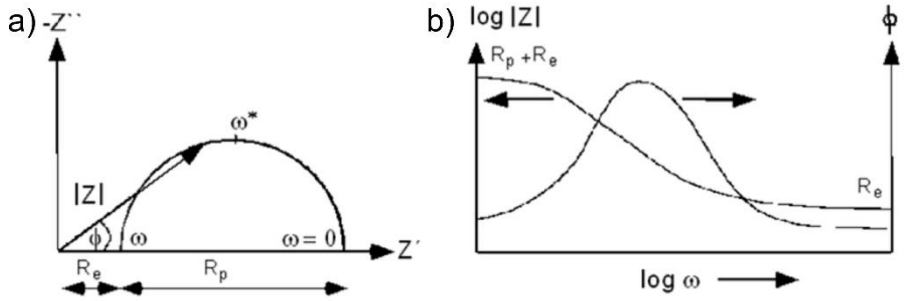

Figura 7.10.- Esquema de la representación de impedancia mediante (a) Nyquist y (b) Bode.

La resistencia de polarización, R_p, corresponde a la resistencia de polarización del electrodo. Ésta puede ser lograda a partir de las dos representaciones.

La resistencia óhmica, R_S, en el caso de las celdas de combustible, corresponde principalmente a la resistencia del electrolito. Ésta puede ser obtenida a partir de la representación de Nyquist de la intersección con el eje real, Z´, en la región de altas frecuencias.

La resistencia superficial específica, ASR, corresponde a la suma de estas dos resistencias (R_p y R_S), y se refiere a la resistencia transversal al paso de corriente.

Y la frecuencia de relajación, ω, se define como el mayor valor de frecuencia alcanzado en la parte imaginaria, obtenido a partir de la representación de Nyquist.

El espectro de impedancia se analiza frecuentemente representando los datos en un circuito equivalente constituido por resistencias, capacitancias (C) e inductancias[7]. En la Figura 7.11 se muestra un circuito RC simple.

---

[6] "The Fuel Cell Review". *Institute of Physics Publishing*, United Kingdom, **2005**.

[7] Macdonald, J.R. *"Impedance Spectroscopy"*. John Wiley & Sons. New York. USA. **1987**.

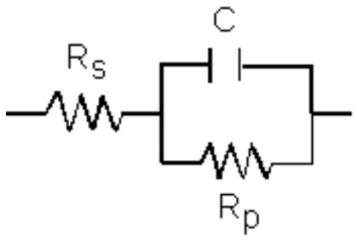

Figura 7.11.- Esquema de un circuito equivalente simple para un electrodo.

Para poder realizar las medidas eléctricas a alta temperatura se ha requerido de un sistema de soporte de muestras Probostat. Este sistema se utiliza para mediciones de propiedades eléctricas, parámetros eléctricos, cinética de materiales, interfases solido/gas y electrodos bajo atmosferas controladas a altas temperaturas. A lo largo de esta tesis se utilizaron dos configuraciones. En la primera de ellas, para las celdas simétricas, no ha hecho falta una distribución de gases por lo que se utiliza la configuración representada en la figura 7.12a. En la segunda, que ha sido utilizada para medir celdas de combustible tipo SOFC, hay que separar la atmósfera reductora de la oxidante, por lo que se ha utilizado la configuración representada en la Figura 7.12b., utilizando el cemento para altas temperaturas Omegabond 700 (Figura 7.12c.).

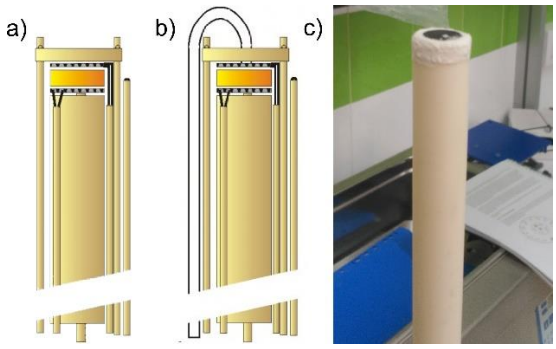

Figura 7.12.- a) Configuración del soporte de mediciones SOFC Probostat; sin flujo de gases, b) con flujo de gases y c) celda tras aplicarle el sellante.

Estos estudios se han llevado a cabo empleando cuatro equipos:

Se ha utilizado una fuente de corriente continua (DC), controlada por un ordenador PC mediante el sistema Lab Windows/CVI, perteneciente al Instituto de Ciencia de Materiales de Aragón (ICMA) de la Universidad de Zaragoza.

Se ha empleado una estación de trabajo Zhanher Zennium (ZHANER- elektrik GmbH &Co. KG, Germany) y un sistema de soporte de muestras Probostat (NorEcs, Norway) (Figura 7.13a.), ubicado en el Instituto de Ciencia de Materiales de Aragón (ICMA) de la Universidad de Zaragoza. Este dispositivo suministra a la celda tanto intensidad de corriente como potencial. En este caso, el dispositivo actúa como una carga electrónica, permitiendo registrar la caída de potencial en la celda para cada valor de intensidad extraída.

Se ha dispuesto un sistema compuesto por los instrumentos Thurlby Thandar Instruments 1604 Digital Mutimeter, que mide la diferencia de potencial al aplicar una corriente mediante Thurlby Thandar Instruments PL300. Estos equipos se encuentran en la "School of Chemistry", de la Universidad de Birmingham, UK (Figura 7.13b).

Se ha empleado una estación de Potentiostat/Galvanostat VMP3 (Biologic) y un sistema de soporte de muestras Probostat (NorEcs, Norway) ubicado en el Centro Nacional del Hidrógeno (CNH2) en Puertollano (Figura 7.13c).

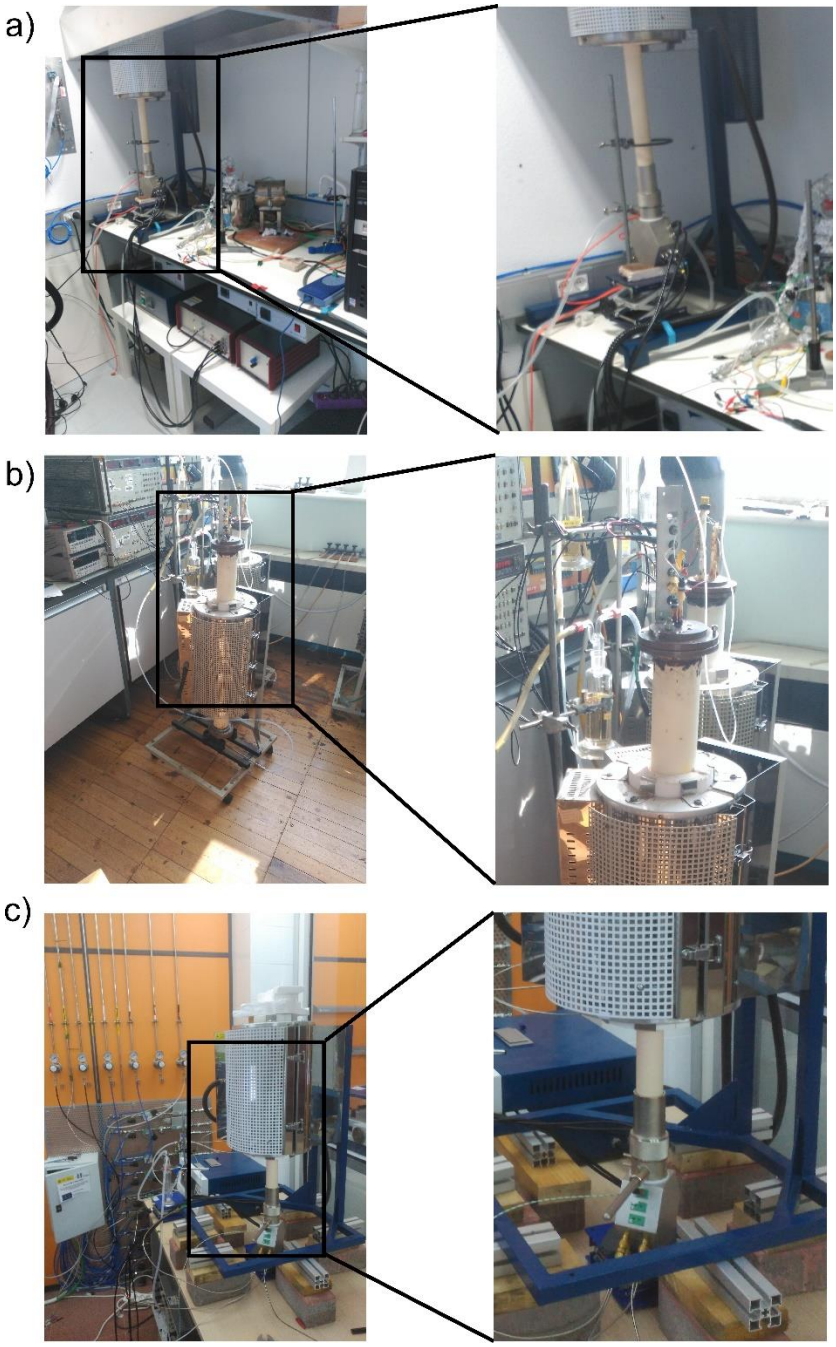

Figura 7.13.- Montajes para llevar a cabo la caracterización electroquímica: a) estación de trabajo Zhanher Zennium con un sistema de soporte de muestras Probostat, b) sistema Thurlby Thandar Instruments 1604 Digital Mutimeter y Thurlby Thandar Instruments PL300 y c) una estación de Potentiostat/Galvanostat VMP3 (Biologic) con un soporte de muestras Probostat.

7.2.5. Difracción de rayos X sobre muestra policristalina

En 1895, el físico alemán Wilhelm Conrad Röntgen (1845-1923) descubrió una radiación (entonces desconocida y de ahí su nombre de rayos X) que tenía la propiedad de penetrar los cuerpos opacos. Esta radiación se genera en un tubo de vacío, en el cual se produce una diferencia de potencial (~ 40 kV) entre un filamento incandescente que actúa como cátodo y una placa metálica que actúa como ánodo. Por el filamento, se hace circular una gran cantidad de corriente que produce que se caliente, creando una nube de electrones a su alrededor. La nube de electrones se ve atraída al lado positivo, saliendo disparados a gran velocidad e impactando contra el lado metálico que actúa como ánodo. En el choque se producen los rayos X, característicos del elemento metálico que constituye el ánodo[8].

Los rayos X son una radiación electromagnética con una longitud de onda λ del mismo orden de magnitud que los parámetros de celda de los cristales, haciendo que las sustancias cristalinas sean capaces de difractarlos. Cuando esta radiación incide sobre la nube electrónica de los átomos de una red cristalina, éstos se convierten en emisores puntuales de esa misma radiación. La radiación emitida por cada átomo se expande en forma de onda esférica e interfiere con la creada por los átomos del entorno. Esta interferencia puede ser destructiva o constructiva. Cuando las direcciones en las interferencias son constructivas, quedan recogidas en la Ley de Bragg (ecuación 7.5):

$$\lambda = 2\, d_{hkl} \operatorname{sen} \theta \qquad (7.5)$$

donde θ es el ángulo de incidencia de la radiación y dhkl (Å) es la distancia entre dos planos consecutivos definidos por un vector de componentes hkl[9].

La difracción de rayos X sobre muestra policristalina se ha utilizado para el análisis cualitativo y cuantitativos de las fases presentadas en la esta memoria. Estos experimentos han sido útiles tanto para la identificación de las fases como para la determinación de su pureza química, ya que todos los sólidos cristalinos tienen un difractograma característico como si fuese su huella dactilar[10].

Los materiales policristalinos están formados por un gran número de cristales diminutos dispuestos al azar los unos respecto a otros. En una muestra de estas características, al ser irradiada con un haz de rayos X, presentará un determinado número de cristales que satisfagan la ley de Bragg y los difractómetros permiten determinar con precisión la dirección en la que se produce la difracción. La geometría que poseen los difractómetros utilizados en esta investigación, la cual es la más habitual, se denomina Bragg-Brentano. En este tipo de geometría, el goniómetro incorpora dos giros coaxiales, uno para la muestra y otro para el detector. Estos giros están acoplados, de tal forma que si la muestra se desplaza en un ángulo θ, el detector recorre al mismo tiempo un ángulo 2θ. El difractograma sería la representación de la intensidad de la radiación X que llega al detector con respecto al ángulo de giro 2θ.

---

8 http://www.xtal.iqfr.csic.es/Cristalografia/parte_02.html.

9 Klein C., Hurlbut J.C.S., *"Manual de Mineralogía"*, 4ª Ed., Ed. Reverté S.A., Barcelona, **1996**.

10 Amorós. J.L. "El Cristal. Morfología, Estructura y Propiedades Físicas". Ed. Atlas, p. 1-33, 201-217, **1990**.

Los difractogramas realizados con el fin de caracterizar las muestras presentadas en esta memoria se han registrado en un difractómetro Philips X´Pert PRO, equipado con anticátodo de cobre (λ=1.5418 Å), con una geometría tipo Bragg-Brentano y con un detector ultrarrápido PIXcel (Figura 7.14a). Además, para una mayor resolución del difractograma se ha utilizado el difractómetro Bruker D8 Advance Vario dotado de un monocromador primario (Cu-$K_{\alpha 1}$) y un detector sólido SolX con una ventana de discriminación de energías optimizada para la radicación $K_{\alpha 1}$ del cobre (Figura 7.14b).

Todos los difractómetros empleados en esta investigación pertenecen a los Servicios Generales de Investigación (SGIker), de la Universidad del País Vasco/Euskal Herriko Unibertsitatea (UPV/EHU) (Figura 7.14.).

(a) (b)

Figura 7.14.- (a) Difractómetro Philips X'Pert PRO, (b) difractómetro Bruker D8 Advance Vario.

Para obtener información de los difractogramas es preciso hacer un análisis de los mismos, en el que se deben tener en cuenta la posición de los máximos de difracción, su perfil y su intensidad. Las fases presentadas en esta memoria se han identificado utilizando el programa X´Pert HighScore[11] a través de la base de datos Power Diffraction File (PDF)[12] y las tablas cristalográficas[13]. El ajuste de los diagramas de difracción se ha realizado mediante el afinamiento de perfil completo sin/o con modelo estructural, método Rietveld[14] mediante el programa informático Fullprof.

---

11 PANalytical, Almelo B.V., Versión 1.0e, The Netherlands, **2003**.

12 ICDD, "Powder Diffraction File-Inorganic and Organic", Pennsylvania, USA, **1995**.

13 Hahn Th., "International tables for crystallography, Volume A: Space-group symmetry", D. Reidel Publishing Company, Boston, USA, **1983**.

14 Rietveld H.M. A profile refinement method for nuclear and magnetic structure. *J. Appl. Crystallogr.* 2 (**1969**) 65-71.

El método de Rietveld fue desarrollado a principio de los años sesenta, un ajuste teórico con el fin de afinar estructuras cristalinas a partir de datos de difracción de neutrones con longitud de onda constante[15]. Posteriormente, su utilización se ha extendido a la difracción de rayos X[16,17].

El método de Rietveld permite el afinamiento de estructuras cristalinas de moderada complejidad ajustando, mediante mínimos cuadrados, el perfil completo del diagrama de difracción a un perfil calculado para un modelo estructural (que depende de los parámetros a afinar). No existe un paso intermedio para extraer los factores de estructura de las reflexiones individuales a partir de las intensidades medidas para cada posición 2θ del difractograma.

El método de Rietveld se basa en la minimización de la función residuo 7.6:

$$\chi^2 = \sum_{i=1}^{n} w_i \left\{ y_i - y_{i,c} \right\}^2 \qquad (7.6)$$

siendo:

n Número total de posiciones $2\theta_i$.

w_i Factor de pesada (peso estadístico de cada reflexión).

y_i Número de cuentas observadas para cada ángulo $2\theta_i$.

$y_{i,c}$ Número de cuentas calculado para cada ángulo $2\theta_i$ a partir de la expresión:

$$y_{i,c} = S \cdot \sum_{k=0}^{k} L_k \cdot |F_k|^2 \cdot W \cdot (2\theta_i - 2\theta_k) \cdot T_k \cdot P_k \cdot + y_{ib} \qquad (7.7)$$

k Número de reflexiones que contribuyen a y_i en una posición $2\theta_i$.

S Factor de escala.

L_k Factores de Lorentz, polarización y multiplicidad de la reflexión k.

F_k Factor de estructura de la reflexión k.

W Función de perfil de la reflexión k.

T_k Factor de transmisión.

P_k Función de orientación preferente de la muestra.

y_{ib} Intensidad del fondo continuo en la posición $2\theta_i$.

---

15 Rietveld H.M. Line profiles of neutron powder diffraction peaks for structure refinement. *Acta Cryst.* 22 (**1967**) 151-152.

16 Young R.A. *"The Rietveld method"*. International Union of Crystallography-Oxford Science Publications: Oxford, **1995**.

17 Rodríguez-Carvajal J. Fullprof program: Rietveld pattern matching analysis of powder patterns, Grenoble, **2011**.

La minimización de la ecuación (7.6) conduce al afinamiento de dos tipos de parámetros, los estructurales y los de perfil, destacando:

- Parámetros estructurales:
  - Coordenadas reducidas de cada átomo: x_i, y_i, z_i.
  - Factores de ocupación: n_i.
  - Parámetros de agitación térmica (isotrópicos o anisotrópicos).
- Parámetros de perfil:
  - Factor de escala: S.
  - Parámetros U, V, W, que determinan la evolución angular de la anchura a media altura de la reflexión k, según la expresión: $FWHM^2 = U\ tg^2\ \theta_k + V\ tg\ \theta_k + W$.
  - Posición del cero del detector: $2\theta_o$.
  - Parámetros de celda: a, b, c, α, β, γ.
  - Parámetro del fondo continuo: m_i.
  - Parámetro de asimetría: P.
  - Parámetros de orientación preferente: G_1, G_2.

La bondad de los afinamientos se expresa mediante los factores de acuerdo R_P, R_{WP}, R_B, R_E, y χ^2, definidos por las expresiones:

Perfil $\quad R_P = 100\ \Sigma\ |y_i - y_{ic}| / \Sigma\ |y_i|$

Perfil ponderado $\quad R_{WP} = 100\ \Sigma\ [w_i\ |y_i - y_{ic}|^{\ 2} / \Sigma\ w_i\ |y_i|^{\ 2}]^{\ 1/2}$

Bragg $\quad R_B = 100\ \Sigma\ |A_{.vii} - A_{.viic}| / \Sigma\ |A_{.vii}|$

Esperado $\quad R_E = 100\ [\ (N-P+C) / \Sigma\ w_i y_i^2]^{1/2}$

Índice de bondad del ajuste $\quad \chi^2 = (R_{WP}/R_E)^2$

siendo:

w_i Factor de pesada (peso estadístico de cada reflexión).

y_i Número de cuentas observadas para cada ángulo $2\theta_i$.

y_{ic} Número de cuentas calculado para cada ángulo $2\theta_i$.

A_{vii} Intensidad integrada para cada ángulo $2\theta_i$.

A_{viic} Intensidad integrada calculada para cada ángulo $2\theta_i$.

(N-P+C) Número de grados de libertad.

El factor de acuerdo más representativo es R_{WP}. El índice de bondad del ajuste, χ^2, que debiera ser próximo a la unidad, está sujeto a errores sistemáticos, fundamentalmente derivados de la representación deficiente de la función de perfil. El factor de acuerdo R_B está relacionado con el área de los máximos de difracción y refleja la calidad del modelo estructural.

Unos valores adecuados de los factores de acuerdo no siempre son condición necesaria para considerar un afinamiento como correcto: este criterio debe acompañarse con el examen de la diferencia entre el difractograma observado y el calculado, con el fin de detectar posibles errores sistemáticos. La bondad del afinamiento final dependerá de varios factores, entre los que destacan: la calidad del difractograma experimental (y de la muestra), el tipo de radiación utilizado (neutrones, rayos X, radiación sincrotrón, etc.), y la presencia de impurezas y errores sistemáticos durante el proceso de afinamiento.

7.2.6. Dilatometría

Los dilatómetros se utilizan para medir la expansión o contracción de los sólidos a diferentes temperaturas.

La obtención de la expansión térmica lineal de una muestra, viene dada por la siguiente expresión:

$$\frac{\Delta L}{L_0} = \frac{L_T - L_0}{L_0} \qquad (7.8)$$

donde:

L_0 Longitud de la muestra a la temperatura de referencia.

L_T Longitud de la muestra a una temperatura T.

En realidad, el valor de ΔL/L0 viene dado por:

$$\frac{\Delta L}{L_0} = \frac{\Delta L_\alpha}{L_0} + \frac{\Delta L_s}{L_0} \qquad (7.9)$$

donde:

$\Delta L_a/L_0$ Es el cambio aparente en la longitud de la muestra.

$\Delta Ls/L_0$ Es el cambio en la longitud del sistema de medición (dilatómetro).

Normalmente, esta corrección se ajusta automáticamente en el software del equipo. El valor resultante de $\Delta L/L_0$ se expresa habitualmente en partes por millón ($\cdot 10^{-6}$) o bien en µm/m.

La expansión lineal de la muestra se puede expresar en porcentaje de expansión, para lo cual se utiliza la siguiente ecuación:

$$\frac{\Delta L}{L_0} \cdot 100 = Coef\% \qquad (7.10)$$

El coeficiente medio de expansión térmica lineal ($\alpha_m \equiv$ TEC) es el coeficiente promedio de la expansión térmica lineal en el intervalo de temperatura, desde $T_{ambiente}$ a T, y viene dado por la expresión:

$$\alpha_m = \frac{1}{L_0}\frac{1}{L_0} \cdot \frac{\Delta L}{\Delta T} = \frac{1}{L_0} \cdot \frac{L_T - L_0}{T - T_a} \qquad (7.11)$$

El α_m se expresa como parte por millón por grado centígrado:

$$\text{TEC}\alpha_m = \frac{10^{-6}}{°C} = \frac{\mu m}{m\ °C} \qquad (7.12)$$

Con objeto de registrar cambios de dimensión asociados a procesos de expansión/contracción de los materiales en bulk recogidos en esta memoria, se han llevado a cabo ensayos de dilatometría, utilizando un dilatómetro Unitherm™ Model 1161 (Figura 7.15., ubicado en Servicios Generales de Investigación (SGIker) de la UPV/EHU). Así, se ha obtenido una idea del efecto de adición de los componentes de las celdas SOFC.

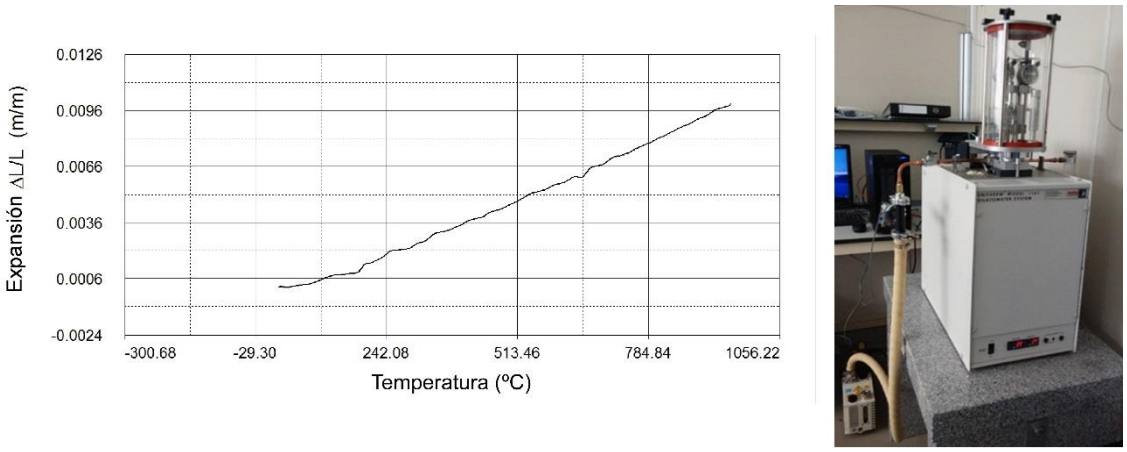

Figura 7.15.- Dilatómetro Unitherm™ Model 1161.

7.2.7. Microscopia electrónica de barrido

Las diferentes técnicas de microscopía electrónica se basan en el análisis de los efectos que se producen de la interacción electrones-muestra, en la que se generan diferentes procesos de absorción y emisión (Figura 7.16a.). Adecuados sistemas de detección para cada uno de los procesos, permiten obtener información sobre la muestra irradiada.

El microscopio electrónico funciona con un haz de electrones generados por un cañón electrónico, acelerados por un alto voltaje y focalizados por medio de lentes magnéticas, todo ello en alto vacío. Los electrones interaccionan con la muestra y la amplificación se produce por un conjunto de lentes magnéticas, que forman una imagen sobre una placa fotográfica o sobre una pantalla sensible al impacto de los electrones que transfiere la imagen formada a la pantalla de un ordenador. Además, estos aparatos suelen combinar la posibilidad de obtener imágenes de gran resolución con el análisis químico de pequeñas áreas del material.

Desde el punto de vista de la Microscopía Electrónica de Barrido (SEM) interesa analizar los electrones secundarios y los retrodispersados. El origen de estos electrones se muestra en la Figura 7.16b.: los retrodispersados son electrones del haz que han sido dispersados elásticamente al colisionar con núcleos y los electrones de los átomos; estos electrones proporcionan imágenes con información composicional.

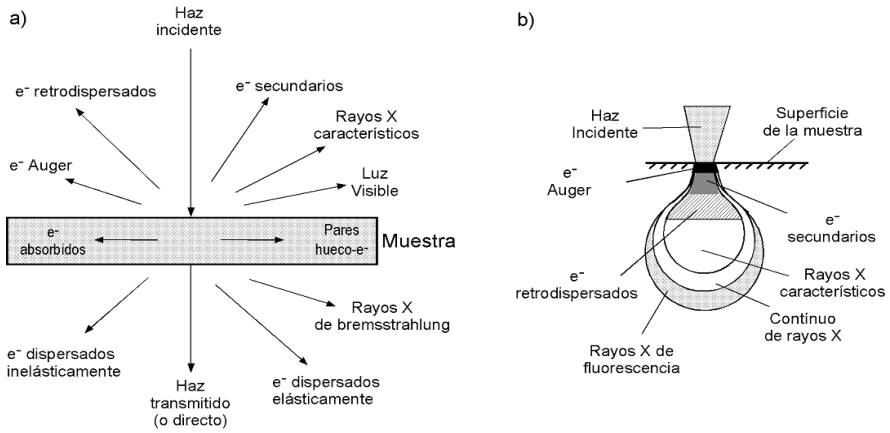

Figura 7.16.- (a) Efectos producidos en una muestra cuando ésta es irradiada con un haz de electrones; (b) Origen de los electrones analizados en un microscopio SEM cuando el haz incide sobre una muestra.

El número de electrones retrodispersados varía con el número atómico promedio (<Z>) de la muestra, de tal manera que cuanto mayor es Z, mayor es la probabilidad de choque y mayor es la cantidad de electrones retrodispersados. Por lo tanto, las imágenes con menor número atómico promedio aparecerán más oscuras que las de mayor (<Z>). Además, estos electrones pueden aportar información topográfica de la muestra, en función del modo de trabajo del detector y son sensibles a la orientación cristalina. Los electrones secundarios son electrones arrancados de las capas más externas de los átomos y proporcionan imágenes de la topografía superficial de la muestra. La cantidad de electrones secundarios dispersados depende de la energía del haz incidente, de la densidad y de la topografía de la superficie de la muestra.

Otra emisión importante que resulta de la interacción del haz de electrones con los átomos de las muestras, son los rayos X, con energía y longitud de onda característicos de los elementos que constituyen la muestra. Esta radiación es recogida por un detector adecuado para obtener el microanálisis del material. El detector utilizado en los microanálisis mostrados en esta memoria es un espectrómetro de dispersión de energía (EDX), que analiza de forma simultánea las energías de los fotones de rayos X, en todo el intervalo desde el boro hasta el uranio. Cuando un haz electrónico suficientemente acelerado, incide en la superficie de un sólido, se produce, entre otros fenómenos, la ionización de los átomos presentes en el mismo; esto es, la pérdida de electrones internos. Cuando un átomo se encuentra en este estado, otro electrón de la capa más externa salta a la capa deficitaria, y rellena el hueco producido. Este salto implica la liberación de energía, cuyo valor es igual a la diferencia entre las energías que tenía cada electrón en su orbital correspondiente. Dicha energía se manifiesta de dos formas: mediante emisión de una radiación electromagnética (rayos X) o por emisión de otro electrón de un orbital exterior (electrón Auger). La probabilidad de que tenga lugar una u otra emisión queda determinada por el rendimiento de fluorescencia[18,19].

[18] Robards A.W., Wilson A.J. Procedures in electron microscopy, John Wiley & Sons, Chichester, UK, **1993**.

[19] Dunlap M., Adaskaveg J.E. Introduction to the scanning electron microscope, Cambridge, p. 3-33, **1997**.

Los análisis morfológicos, microestructurales y composicionales de las muestras se han realizado en dos microscopios electrónicos de barrido (SEM), un S 3400 N (Figura 7.17a.) y un JEOL JSM-7000F (Figura 7.17b.). La configuración de estos microscopios incluye un analizador de energía dispersada de rayos X, Oxford Inca Pentafet X3 (EDX), provisto de un software de adquisición de datos INCA Energy 350. Estos equipos están instalados en los Servicios Generales de Investigación (SGIker), de la UPV/EHU.

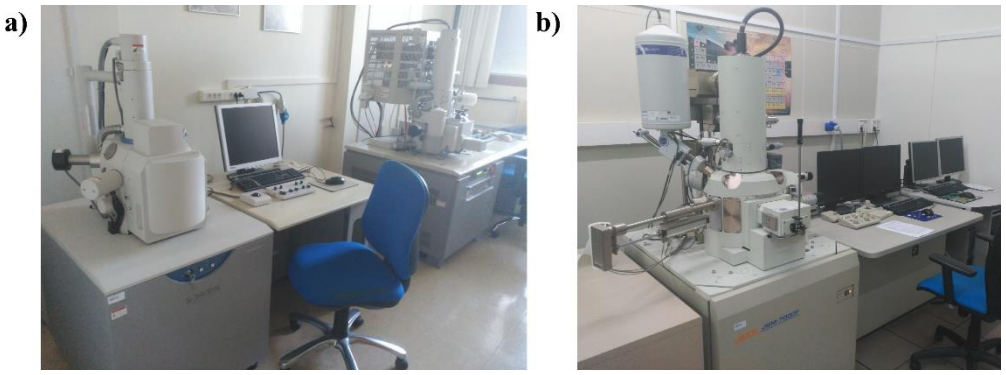

Figura 7.17. Microscopios Electrónicos de Barrido (SEM), a) S-3400 N y b) JEOL JSM-7000F.

El objetivo principal en la preparación de muestra, para observar su sección transversal por SEM, es preparar una pastilla de resina que contenga las partes de interés que se desean analizar. Esta pastilla debe estar pulida de forma que la parte superior de las muestras se encuentre libre de resina y no se haya alterado la microestructura durante el proceso de pulido.

Procedimiento:

A. Colocar las muestras en un molde. Depositar la muestra en un molde y fijar la zona de interés.

B. Activación de la resina. Mezcla de la resina epoxi con el catalizador para que se inicie la polimerización.

C. Infiltración. Se han utilizado dos procesos: (i) añadir la resina al molde hasta cubrir la muestra, y (ii) se cubre la muestra con resina, y se hace vacío hasta que la resina esté en estado de ebullición; posteriormente se elimina el vacío, facilitando la penetración de la resina en los poros. Este proceso permite que la pastilla no presente burbujas.

D. Endurecimiento. Una vez con la resina en el molde se deja en reposo hasta que la reacción de polimerización finalice (24 h).

E. Corte y Pulido. El corte por abrasión de las muestras embebidas en resina, se lleva a cabo mediante un disco de diamante con un equipo Secotom 10 de la marca Struers (Figura 7.18a). Una vez cortada la probeta, es necesario llevar a cabo el pulido de la misma con el fin de que la muestra que se quiere observar quede en la superficie de la probeta. Para ello se llevan a cabo una serie de etapas de pulido con lijas de mayor a menor tamaño de partícula (Figura 7.18b). Si se han llevado a cabo todos los pasos de forma adecuada, tras esta operación, la probeta no debería presentar ninguna imperfección al observarse con un microscopio óptico. El proceso de pulido se realiza utilizando una pulidora automática TegraPol-31 (Struers) (Figura 7.18c). La pulidora consiste en una placa giratoria donde se colocan los discos con el material abrasivo. También dispone de un cabezal automático para la sujeción de la muestra y que faculta ejercer una presión controlada sobre los discos con el material abrasivo. Estos equipos pertenecen al Departamento de Mineralogía y Petrología de la Facultad de Ciencia y Tecnología de la UPV/EHU.

Finalmente, se utiliza un equipo Sputter Coater (Quorum Q150T) que permite recubrir la muestra con carbono y así convertirla en conductora de electrones para poder ser observada en el SEM (Figura 7.18d).

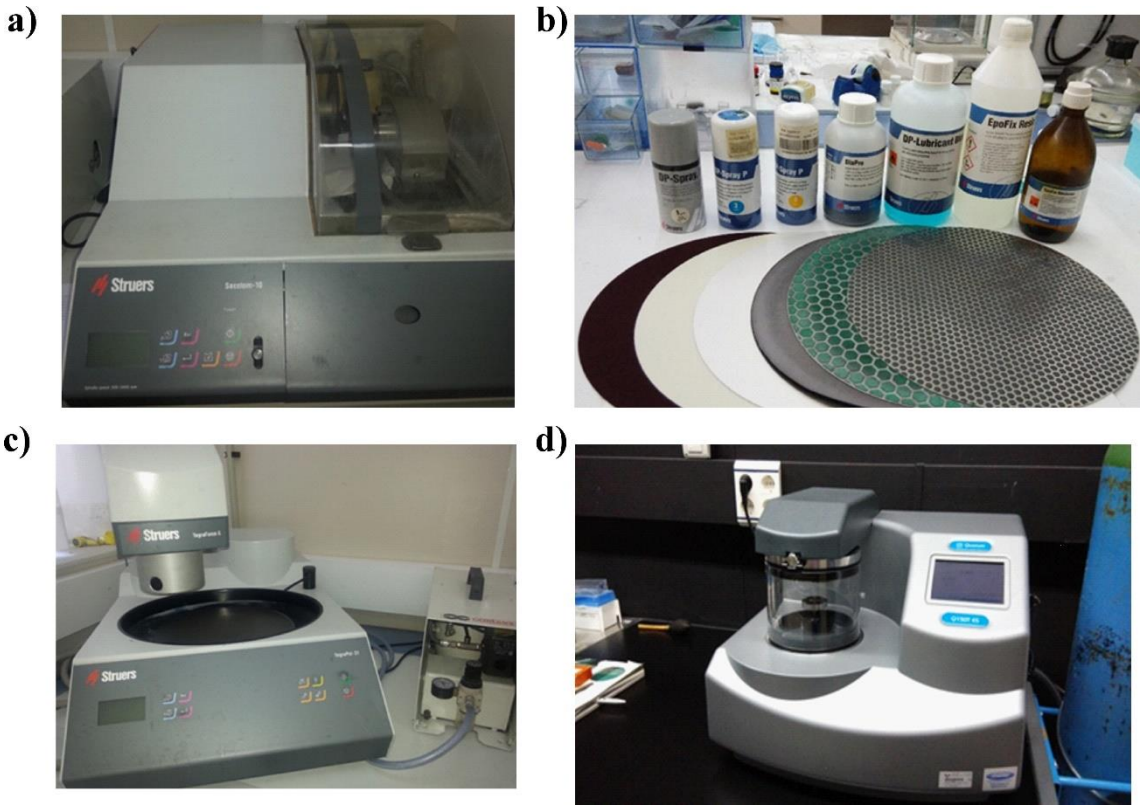

Figura 7.18. (a) Cortadora Secotom 10 de Struers, (b) discos y material abrasivo necesarios para llevar a cabo el pulido, (c) pulidora TegraPol-31 de Struers y (d) equipo Sputter Coater (Quorum Q150T).

Este último equipo pertenece a los Servicios Generales de Investigación (SGIker), de la UPV/EHU.

8. DIFUSIÓN DE RESULTADOS

8.1. Resultados vinculados al trabajo de investigación

Publicaciones

1.- **Aritza Wain-Martin**, Aroa Morán-Ruiz, Karmele Vidal, Aitor Larrañaga, Miguel Angel Laguna-Bercero, Maria Isabel Arriortua, Scalable synthetic method for SOFCs compounds, *Solid State Ion*. 131 (**2017**) 52-57. [Q2, Impact factor: 2.751].

2.- **Aritza Wain-Martin**, Aroa Morán Ruiz, Miguel Angel Laguna-Bercero, Roberto Campana, Aitor Larrañaga, Peter Raimond Slater, Maria Isabel Arriortua, SOFC cathodic layers using wet powder spraying technique with self sunthesized nanopowders, *Int. J. Hydrog. Energy*. 44 (**2019**) 7555-7563. [Q1, Impact factor: 4.229]

3.- **Aritza Wain-Martin**, Aroa Morán-Ruiz, Roberto Campana, Jesus Rodriguez, Aitor Larrañaga, Maria Isabel Arriortua, SOFC cell fabrication procedure with self made nanopowders, *Int. J. Hydrog. Energy*. XX (**2019**) XXX. [Q1, Impact factor: 4.229]

Contribuciones a congresos

1.- XXXV Reunión Bienal RSEQ. A Coruña, 19-23 de Julio de 2015.
Autores: Aritza Wain-Martin, Aroa Morán-Ruiz, Karmele Vidal, Aitor Larrañaga, Maria Isabel Arriortua.
Título: Materiales para su aplicación en celdas SOFCs.
Presentación: Póster

2.- XIV Congreso Nacional de Materiales. Gijón, 8-10 de Junio de 2016.
Autores: Aritza Wain-Martin, Aroa Morán-Ruiz, Karmele Vidal, Aitor Larrañaga, Miguel Angel Laguna-Bercero, Maria Isabel Arriortua.
Título: Celdas de pilas de óxido sólido. Avance en el procesado de materiales.
Presentación: Póster

3.- 12th European SOFC & SOE Forum 2016. Lucerna, 5-8 de Julio de 2016.
Autores: Aritza Wain-Martin, Aroa Morán-Ruiz, Karmele Vidal, Aitor Larrañaga, Maria Isabel Arriortua.
Título: Scalable synthetic method for IT-SOFCs compounds.
Presentación: Póster

4.- The energy & Materials Research Conference- EMR2017. Lisboa, 5-7 de Abril de 2017.
Autores: Aritza Wain-Martin, Aroa Morán-Ruiz, Karmele Vidal, Aitor Larrañaga, Jesus Rodriguez, Miguel Angel Laguna-Bercero, Roberto Campana, Maria Isabel Arriortua.
Título: Electrochemical and degradation behavior study of different SOFC compounds.
Presentación: Oral

5.- I jornada de jóvenes investigadores de cerámica y vidrio en el ICMA. Zaragoza, 20 de Marzo de 2018.
Autores: Aritza Wain-Martin, Aroa Morán-Ruiz, Aitor Larrañaga, Miguel Angel Laguna-Bercero, Roberto Campana, Maria Isabel Arriortua.
Título: procesado y caracterización de celdas de soporte electrolito de pilas de combustible de óxido sólido (SOFC).
Presentación: Oral

6.- 13th European SOFC & SOE Forum 2018. Bilbao, 3-6 de Julio de 2018.
Autores: Aritza Wain-Martin, Roberto Campana, Aroa Morán-Ruiz, Jesus Rodriguez, Aitor Larrañaga, Maria Isabel Arriortua.
Título: Development of a SOFC cell with self-made nanopowders.
Presentación: Póster

Solid State Ionics 313 (2017) 52–57

Contents lists available at ScienceDirect

Solid State Ionics

journal homepage: www.elsevier.com/locate/ssi

Scalable synthetic method for SOFC compounds

A. Wain-Martin[a,*], A. Morán-Ruiz[a], K. Vidal[a], A. Larrañaga[a], M.A. Laguna-Bercero[b], M.I. Arriortua[a,c,**]

[a] Universidad del País Vasco (UPV/EHU), Facultad de Ciencia y Tecnología, Barrio Sarriena S/N, 48940 Leioa, Vizcaya, Spain
[b] CSIC-Universidad de Zaragoza, Instituto de Ciencia de Materiales de Aragón (ICMA), Pedro Cerbuna 12, 50009 Zaragoza, Spain
[c] BCMaterials, Parque Tecnológico de Zamudio, Ibaizabal Bidea, Edificio 500-Planta 1, 48160 Derio, Spain

ARTICLE INFO

Keywords:
SOFC
Synthetic routes
Large scale
Combustion

ABSTRACT

Although economically competitive SOFC systems seems to be ready for commercialization, a broad inventory of key starting materials and fabrication processes are needed to enhance systems and reduce costs. These necessities are raised by the demands for large scale SOFC industrial production. Taking into account these reasons, we have synthesized the mean components of a fuel cell, on a large scale, by the glycine nitrate combustion method.

The synthesized different components of SOFC have been the interconnector protective coating ($MnCo_{1.9}Fe_{0.1}O_4$), contact layer ($LaNi_{0.6}Fe_{0.4}O_3$), cathode ($La_{0.6}Sr_{0.4}FeO_3$), interlayer ($Sm_{0.2}Ce_{0.8}O_{1.9}$), electrolyte $(ZrO_2)_{0.92}(Y_2O_3)_{0.08}$ and anode $(Ni_{0.3}O\text{-}(ZrO_2)_{0.92}(Y_2O_3)_{0.08})$ material, obtaining reproducible pure samples and amounts up to 12 g for each batch, being able to increase easily this amount to lots of hundred of grams.

The obtained materials have been characterized by inductively coupled plasma atomic emission spectroscopy (ICP-AES) and X-ray fluorescence (XRF), X-ray diffraction (XRD), dilatometry, scanning electron microscopy (SEM), particle size distribution and conductivity measurements.

1. Introduction

New kind of necessities arises from the development of technologies used in synthesis of SOFC materials. These necessities are originated from the demands for appropriate industrial production procedure of SOFC materials, and the respective final products. Therefore, Combustion Synthesis (CS) is an important method for advanced SOFC component fabrication, because is economical and energy efficient method [1].

CS methods can be classified into three categories, on the basis of the physical nature of reaction mixture itself: (i) flame synthesis or gas phase combustion, (ii) heterogeneous condensed phase combustion synthesis and (iii) solution combustion synthesis (SCS) [2]. Focusing in the SCS route, it consists of using an oxidizer (generally metal nitrates) and a suitable organic fuel (urea, citric acid, glycine, etc.) [3,4]. In this sense, SCS represents an exothermic method, which can provide enough energy to evaporate volatile impurities as well as, for the complete calcination of the products, producing, by a single step, pure nanostructured and homogeneous oxide powders with appropriate microstructural properties [5,6].

The major parameters such as fuel mixture and fuel/oxidizer ratio can play a significant role on phase formation of different compounds [7]. The choice of organic fuel (usually glycine, urea, sucrose, citric acid or alanine) is important because different fuels have different properties such as decomposition temperature, heat of combustion and reducing valency [8]. In general, a good fuel should react non violently, producing non toxic gases, an reacting as a complexant for metal cations [9]. As consequence, glycine was selected as the fuel since it is more cost-effective, has demonstrate that can be conveniently employed to prepare ceramic powders and its combustion heat ($-3.24\ kcal\ g^{-1}$) is greater than that of urea ($-2.98\ kcal\ g^{-1}$) or citric acid ($-2.76\ kcal\ g^{-1}$), being more stronger complexing agent and forming stable gels in nitrate solution [9–12]. The advantages of the glycine nitrate combustion process are relatively low cost, fast heating rates, short reaction times, high composition homogeneity and high energy efficiency [13].

The commonly used materials for fuel cell devices are porous cermets of metallic NiO-$(ZrO_2)_{0.92}$ $(Y_2O_3)_{0.08}$ (NiO-YSZ) as an anode and dense $(ZrO_2)_{0.92}$ $(Y_2O_3)_{0.08}$ (YSZ) layers as electrolyte [14–16]. According to other authors and to our previous studies, $La_{0.6}Sr_{0.4}FeO_3$ (LSF40) has demonstrated to be a practical cathode using $Sm_{0.2}Ce_{0.8}O_{1.9}$ (SDC) as barrier between cathode and electrolyte,

* Corresponding author.
** Corresponding author at: Universidad del País Vasco (UPV/EHU), Facultad de Ciencia y Tecnología, Barrio Sarriena S/N, 48940 Leioa, Vizcaya, Spain.
E-mail addresses: aritza.wain@ehu.es (A. Wain-Martin), maribel.arriortua@ehu.es (M.I. Arriortua).

http://dx.doi.org/10.1016/j.ssi.2017.08.021
Received 28 June 2017; Received in revised form 4 August 2017; Accepted 29 August 2017
Available online 08 September 2017

avoiding poorly conducting secondary phases which increases contact resistance of the system [17–20]. Earlier studies have concluded that the use of $LaNi_{0.6}Fe_{0.4}O_3$ (LNF60) cathode contact layers improves electrons transfer through the contact interface from interconnect to active cathode layer [21,22]. Also, $MnCo_{1.9}Fe_{0.1}O_4$ (MCF10) can be used as an interconnect protective coating to avoid the Cr poisoning to the cathode [23,24].

The present work presents the adaptation of an existing lab-scale cell components production method to an industrially ready and easily scalable method using glycine-nitrate combustion synthesis. After the synthesis optimization, up to 12 g of sample have been obtained in each batch. The synthesized components were: anodes, electrolytes, interlayers, cathodes, contact layers and interconnect protective coatings. Therefore, results of a complete characterization study have been reported including compositional identification of phases, crystal structure, electrical and ionic conductivity, thermal expansion and morphological structure, showing a good reproducibility in all the cases.

2. Experimental

2.1. Powder preparation

All the SOFC component powders were prepared by a glycine nitrate process (GNP). Stoichiometric amounts of the corresponding metal nitrates, which were chosen because their low price under 2.90 € per gram, were dissolved in deionized water (see Table 1), to yield 36 g of the final oxide powders.

For all compositions glycine was then added into the nitrate aqueous solution while stirring. In all the cases a glycine nitrate molar ratio of 1 was used. The effect of different glycine nitrate ratio was previously analyzed for these kind of compounds in the research group [5]. The resulting viscous liquid was auto-ignited by heating up to approximately 455 °C. The obtained powders were calcined between 600 and 800 °C for 5 h to remove carbon residues. In the case of LSF40, LNF60 and MCF10, the resulting powders were pelletized and calcined in air at 950 °C for 8 h, which after several test, demonstrated to be the most economical treatment conditions to obtain pure samples.

2.2. Characterization techniques

Compositional analysis was performed for all the prepared samples to confirm that the expected elemental composition was achieved. The metal contents of Mn, Co, Fe, Sr, Ni and La, were determined by inductively coupled plasma atomic emission spectroscopy (ICP-AES) on a Horiba Yobin Yvon Activa spectrophotometer. Because their difficulty to dissolve, the analysis of Sm, Ce, Zr and Y contents were carried out with X-ray fluorescence (XRF) on a Fischercope X-ray XDAL.

Room-temperature X-ray diffraction (XRD) data were recorded using an integration time of 10s/0.026° step in the $5 < 2\sigma < 70°$ range with a Philips X'Pert-PRO X-ray diffractometer equipped with a secondary beam graphite monochromated and Cu-Kα radiation.

The morphologies of the powder samples were observed using a scanning electron microscope (JEOL JSM-7000F). Secondary electron images were taken at 20 kV and $1 \cdot 10^{-11}$ A, using a working distance of 8 mm. Particle size distribution of the powders was carried out using a Mastersizer particle size analyzer (Malvern Instruments). All the measurements were done using isopropanol as dispersion medium and using ultrasounds to break up the agglomerates that are formed.

To measure bulk conductivity and thermal expansion coefficient (TEC), pellets of the powders were sintered between 1050 and 1350 °C, and then, cut in 1 × 3 × 7 mm bars. The bulk density of each sample was calculated by measuring the mass and the dimensions of the bars. The samples had a density of around 75% of the theoretical (X-ray) density.

DC conductivity measurements were performed in air by the four-point DC method using a VSP potentiostat controlled by PC using Lab Windows/CVI field point system.

Electrical contacts were made using Pt wires and Pt paste placed over whole end faces ensuring a homogeneous current flow. Voltage contacts were made as small as possible to avoid any disturbance of the contacts on the current flow. Measurements were performed from 450 to 950 °C. The conductivity (σ) was determined from a set of V-I values by taking $\sigma = 1/\rho = L/A \times dI/dV$, where L is the distance between voltage contacts and A is the sample cross section. Finally, TEC measurements were carried out from room temperature to 950 °C in air with a heating rate of 5 °C/min by using a Unitherm Model 1161 dilatometer system (Anter Corporation PA 15235).

3. Results and discussion

3.1. Elemental composition

In order to be able to study the reproducibility of large-scale synthesis of used compounds, three different synthesis have been perform for each compound, labeling as batch the 12 g of product gained in each synthesis. The nominal composition of the samples and the results from the ICP-AES analysis are shown in Table 2.

Within the experimental errors for all the samples, the experimental compositional values match the nominal composition.

Because the difficulties to dissolve SDC, NiO-YSZ and YSZ samples, the compositional measurements of these samples has been performed by XRF technique. The results are shown in the Table 3.

The results obtained by XRF analysis (Table 3) were close to the nominal values for all the studied samples. In all the cases, the difference between the relative amounts of the elements in different batches was not significant. Thus, the synthesis procedure shows an adequate chemical reproducibility.

3.2. Structural study

The purity of the samples was studied by X-ray diffraction. All the materials (LSF40, LNF60, MCF10, SDC, NiO-YSZ and YSZ) prepared through the glycine nitrate (GN) combustion route present the desired final phases. For the LNF60 compound, the appearance of extra shoulders in the experimental profile indicates a possible phase segregation to give two perovskite phases with different Ni/Fe ratio. In the NiO-YSZ case, the diffractogram presents peaks relative to the phases of NiO and YSZ (cubic structure), which evidences that the materials did

Table 1
Summary of used starting materials.

Compound	Starting materials[a]
$La_{0.6}Sr_{0.4}FeO_3$ (LSF40)	$La(NO_3)_3 6H_2O$ (> 99%), $Sr(NO_3)_2$ (> 99%) and $Fe(NO_3)_3 9H_2O$ (> 98%)
$LaNi_{0.6}Fe_{0.4}O_3$ (LNF60)	$La(NO_3)_3 6H_2O$ (> 99%), $Ni(NO_3)_2 6H_2O$ (> 98.5%) and $Fe(NO_3)_3 9H_2O$ (> 98%)
$MnCo_{1.9}Fe_{0.1}O_4$ (MCF10)	$Mn(NO_3)_2 xH_2O$ (> 98%), $Co(NO_3)_2 6H_2O$ (> 98%) and $Fe(NO_3)_3 9H_2O$ (> 98%)
$Sm_{0.2}Ce_{0.8}O_{1.9}$ (SDC)	$Sm(NO_3)_3 6H_2O$ (> 99.9%) and $Ce(NO_3)_3 6H_2O$ (> 99%)
$Ni_{0.5}O$-$(ZrO_2)_{0.92}(Y_2O_3)_{0.08}$ (NiO-YSZ)	$Y(NO_3)_3 6H_2O$ (> 99.9%), $ZrO(NO_3)_2 xH_2O$ (> 99%) and $Ni(NO_3)_2 6H_2O$ (> 98.5%)
$(ZrO_2)_{0.92}(Y_2O_3)_{0.08}$ (YSZ)	$Y(NO_3)_3 6H_2O$ (> 99.9%) and $ZrO(NO_3)_2 xH_2O$ (> 99%)

[a] All the starting materials used were from Sigma-Aldrich.

Table 2
Summary ICP results for LSF40 (La, Sr, Fe), LNF60 (La, Ni, Fe) and MCF10 (Mn, Co, Fe).

	Sr	La	Fe	Ni	Mn	Co
LSF40 (Batch 1)	0.41 (1)	0.58 (2)	1.02 (3)	–	–	–
LSF40 (Batch 2)	0.40 (1)	0.58 (2)	1.01 (3)	–	–	–
LSF40 (Batch 3)	0.41 (1)	0.58 (2)	1.02 (3)	–	–	–
LNF60 (Batch 1)	–	0.98 (9)	0.41 (6)	0.61 (8)	–	–
LNF60 (Batch 2)	–	0.97 (9)	0.41 (6)	0.60 (8)	–	–
LNF60 (Batch 3)	–	1.02 (9)	0.45 (6)	0.65 (8)	–	–
MCF10 (Batch 1)	–	–	0.10 (1)	–	0.99 (4)	1.86 (5)
MCF10 (Batch 2)	–	–	0.10 (1)	–	1.02 (4)	1.90 (5)
MCF10 (Batch 3)	–	–	0.10 (1)	–	0.98 (4)	1.93 (5)

Table 3
Summary XRF results for SDC (Sm, Ce), NiO-YSZ (Ni, Y, Zr) and YSZ (Y, Zr).

	Zr	Y	Ni	Sm	Ce
SDC (Batch 1)	–	–	–	0.8 (1)	0.3 (2)
SDC (Batch 2)	–	–	–	0.8 (1)	0.3 (2)
SDC (Batch 3)	–	–	–	0.8 (1)	0.3 (2)
NiO-YSZ (Batch 1)	0.8 (3)	0.2 (1)	0.3 (4)	–	–
NiO-YSZ (Batch 2)	0.8 (3)	0.2 (1)	0.3 (4)	–	–
NiO-YSZ (Batch 3)	0.8 (3)	0.2 (1)	0.3 (4)	–	–
YSZ (Batch 1)	0.8 (9)	0.2 (3)	–	–	–
YSZ (Batch 2)	0.8 (9)	0.2 (3)	–	–	–
YSZ (Batch 3)	0.8 (9)	0.2 (3)	–	–	–

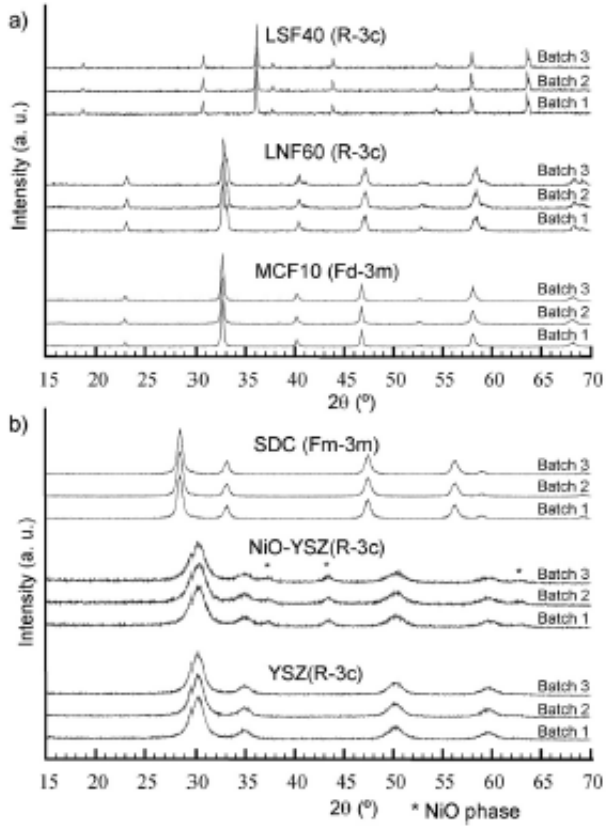

Fig. 1. X-ray diffraction patterns measured of (a) LSF40, LNF60, MCF10, (b) SDC, NiO-YSZ and YSZ.

not react at these temperatures. The signal identification for all XRD patterns is in good agreement with the Power Diffraction File database (PDF) [25]. All the syntheses are reproducible and pure as can be observed in Fig. 1 for different batches.

Table 4
Crystallite sizes of the synthesized compounds.

Batch	Compound (h,k,l)	Crystallite size (nm)	FWHM	Compound (h,k,l)	Crystallite size (nm)	FWHM
1	YSZ (1,1,1)	6 (2)	1.52	LSF40	46 (2)	0.28
2		6 (2)	1.53	(1,0,4)	45 (2)	0.28
3		6 (2)	1.55		45 (2)	0.28
1	SDC (1,1,1)	15 (1)	0.65	LNF60	16 (1)	0.60
2		15 (1)	0.64	(1,0,4)	17 (1)	0.59
3		14 (1)	0.67		16 (1)	0.60
1	NiO-YSZ	5 (1)	1.70	MCF10	182 (5)	0.14
2	(1,1,1)	5 (1)	1.70	(3,1,1)	186 (5)	0.14
3		5 (1)	1.70		189 (5)	0.14
1	NiO (2,2,0)	10 (1)	1.00			
2		11 (1)	0.87			
3		10 (1)	0.99			

The used synthetic temperatures indicate an absence of reactivity or decomposition of the starting materials under SOFC operating conditions (800 °C).

In order to obtain information about the crystal size of the synthesized powders, the Scherrer formula has been used (Table 4). The Scherrer equation relates the width of a powder diffraction peak to the average dimensions of crystallites in a polycrystalline powder (the used instrumental contribution is of 0.1 and the shape factor of 0.9).

As it can be seen, crystallite sizes are homogeneous between different batches of the same compound, showing crystal grown reproducibility.

3.3. Microstructure

Fig. 2 represents the SEM images for all the synthesized powders. In the case of LSF40, LNF60, MCF10 and SDC, well-necked morphologies of the powders synthesized by the combustion method and sintered at 950 °C are shown (a, b, c and d, respectively), which are composed of nanosized particles and agglomerations of grains of small number of micrometers.

The micrographs of the obtained samples of NiO-YSZ and YSZ are shown in Fig. 2 (e and f, respectively). Nano-sized particles are obtained, morphologically homogeneous and uniformly porous. In these cases, because of a large amount of the outcoming gases as-prepared samples are rather voluminous and very fragile. The particles are bound together into agglomerates of different shapes and sizes of a few micrometers.

In all the cases, the agglomerates formed during the combustion reaction are usually soft and easy to break due to the higher escaping gases for these samples [5]. In addition, comparing the same compound between different batches, it can be shown that the particle sizes and shapes are homogeneous. In addition, they are very microstructurally suitable starting materials to be used in the manufacture of SOFCs.

Particle size distribution of these materials has been measured for their manufacturing in SOFCs since this parameter influences the rheological properties for their deposition by wet colloidal spraying, after a ball milling with isopropanol.

As it is shown in Fig. 3, the aggregate sizes are homogeneous between different batches demonstrating that the synthesis is reproducible concerning the final processing sizes. Table 5 summarizes the details.

3.4. Electrical conductivity

The electronic conductivity of LSF40 and Ni-YSZ, can be described by the thermally activated small polaron mechanism [26,27] which is generally expressed as (Eq. (1)):

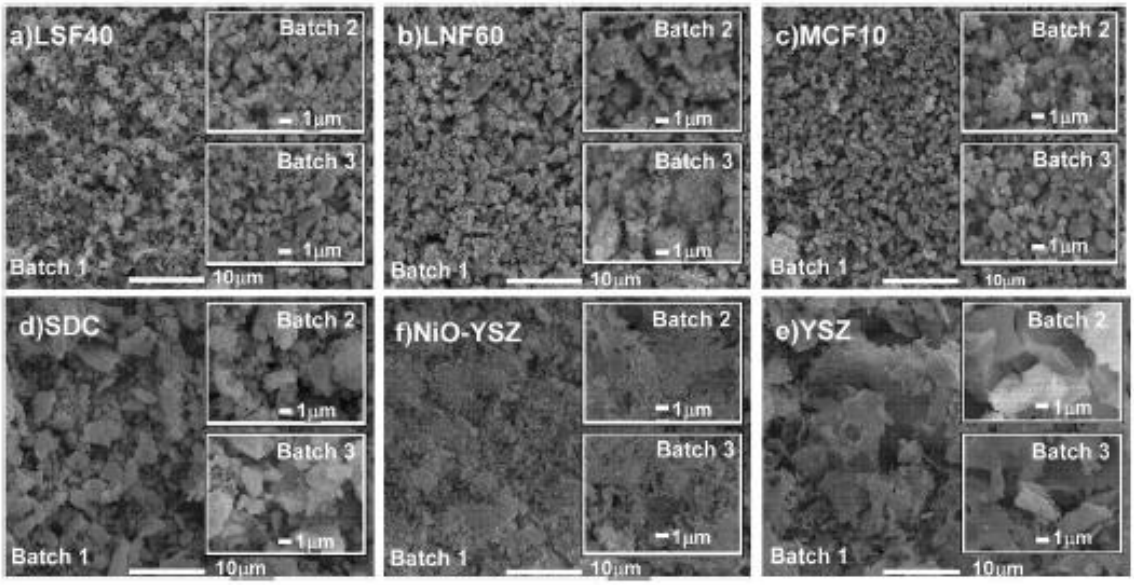

Fig. 2. SEM micrographs of the powder samples of a) LSF40, b) LNF60, c) MCF10, d) SDC, e) NiO-YSZ and f) YSZ.

$$\sigma = A/T \exp(-Ea/kT) \quad (1)$$

In which E_a is the activation energy for small polaron hopping conduction, k is the Boltzmann constant, T is the absolute temperature and A is a pre-exponential factor independent of the temperature.

Taking into account the obtained relative density values, the porosity of the samples has to be considered in further analysis of the electric conductivity. So, for the two-phase systems (electrically conductive and nonconductive (porosity) phases), the corrected electrical conductivity was calculated using Eqs. (2) and (3) [18]:

$$\sigma_{corrected} = \sigma_{measured}(1 + (P_{hvol}/1 - (p_{hvol})^{2/3})) \quad (2)$$

$$P_{hvol} = 1 - (\rho_{exp}/\rho_{theor}) \quad (3)$$

where ρ_{exp} is the experimental geometric density of a pelletised sample and ρ_{theor} the theoretical density from XRD measurements. Note that the relative density, $(\rho_{exp}/\rho_{theor})$, could be slightly underestimated because the formula weight used in the ρ_{theor} calculation ignores oxygen vacancies.

In the case of LSF40, the conductivity increases with increasing temperature up to a maximum and then decreases due to the lattice

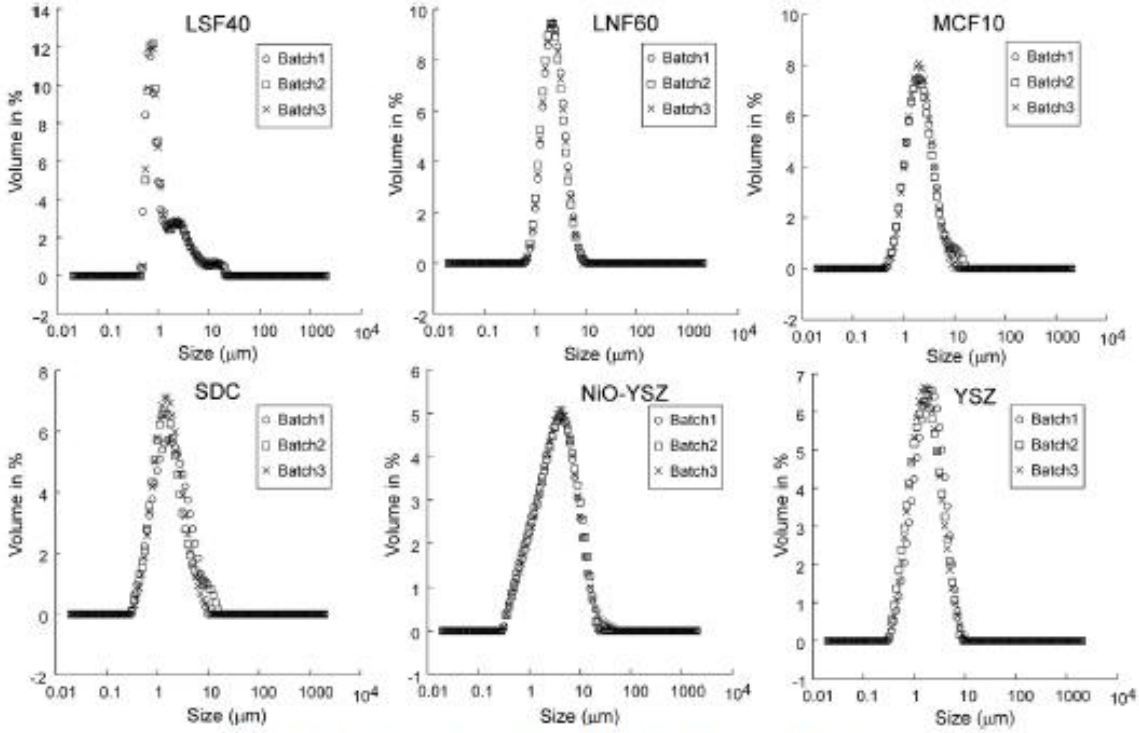

Fig. 3. Particle size distribution curves for LSF40, LNF60 MCF10, SDC, NiO-YSZ and YSZ powders.

Table 5
Summary results of powders particle size distribution tests.

Compound	d (0.5 μm)	Compound	d (0.5 μm)
LSF40 (Batch 1)	0.903	SDC (Batch 1)	1.506
LSF40 (Batch 2)	0.902	SDC (Batch 2)	1.495
LSF40 (Batch 3)	0.960	SDC (Batch 3)	1.665
LNF60 (Batch 1)	2.161	NiO-YSZ (Batch 1)	3.293
LNF60 (Batch 2)	2.025	NiO-YSZ (Batch 2)	3.262
LNF60 (Batch 3)	2.063	NiO-YSZ (Batch 3)	3.260
MCF10 (Batch 1)	1.905	YSZ (Batch 1)	1.551
MCF10 (Batch 2)	1.913	YSZ (Batch 2)	1.371
MCF10 (Batch 3)	1.914	YSZ (Batch 3)	1.828

Table 6
Electrical conductivity values at different temperatures and activation energy.

Compound	NiO-YSZ	LSF40	LNF60	MCF10
σ (600 °C) (S/cm^{-1})	670	89	93	126
σ (700 °C) (S/cm^{-1})	617	74	87	168
σ (800 °C) (S/cm^{-1})	573	63	82	184
Ea (eV)	–	0.03	0.02	0.28

oxygen loss, implying a small semiconductor behavior [22]. The electrical conductivity of MCF10 increases with increasing temperature. For the Ni-YSZ and LNF60 material, however, the conductivity decreases continuously with increasing temperature, implying a metallic behavior in the measured temperature range.

For comparison, electrical conductivities at different temperatures and activation energies for the oxygen ion transport of the different compounds have been represented in the Table 6.

The conductivity values obtained for the compounds are not comparable with the literature conductivity data ([22,24,28]), because these results are obtained on samples prepared using different chemical routes and/or calcined at different temperatures from ours, which may influence the size of the powder particles and the resultant grain size in sintered body [29,30].

Table 7
Average TEC values of the obtained materials.

Component	Average TEC (200–800 °C) (1.10^{-6} °C^{-1})
Crofer 22APU	11.8 [22]
MCF10	14.6 (1)
LNF60	14.8 (0)
LSF40	15.8 (0)
SDC	14.4 (2)
YSZ	13.1 (2)
NiO-YSZ	13.3 (2)

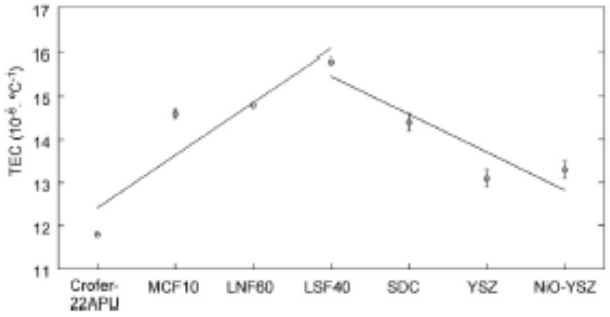

Fig. 5. TEC values obtained over the temperature range of 200-800 °C for all components.

3.5. Thermal expansion study

Thermal expansion coefficients are an important parameter for SOFCs. High temperature fuel cell stacks must meet the critical requirement that all layers have to retain good electrical contact, although large temperature changes occur at assembly and operating temperatures. In an ideal case, all materials would have the same thermal expansion coefficient (TEC), but in real configurations, differences will emerge that can cause thermo-mechanical stress. A further problem can occur because of the differences in the TECs of the different materials which result to a different change in thickness of the various layers and reduction of the system lifetime [31].

Fig. 4 presents dilatometric curves of samples recorded between 200

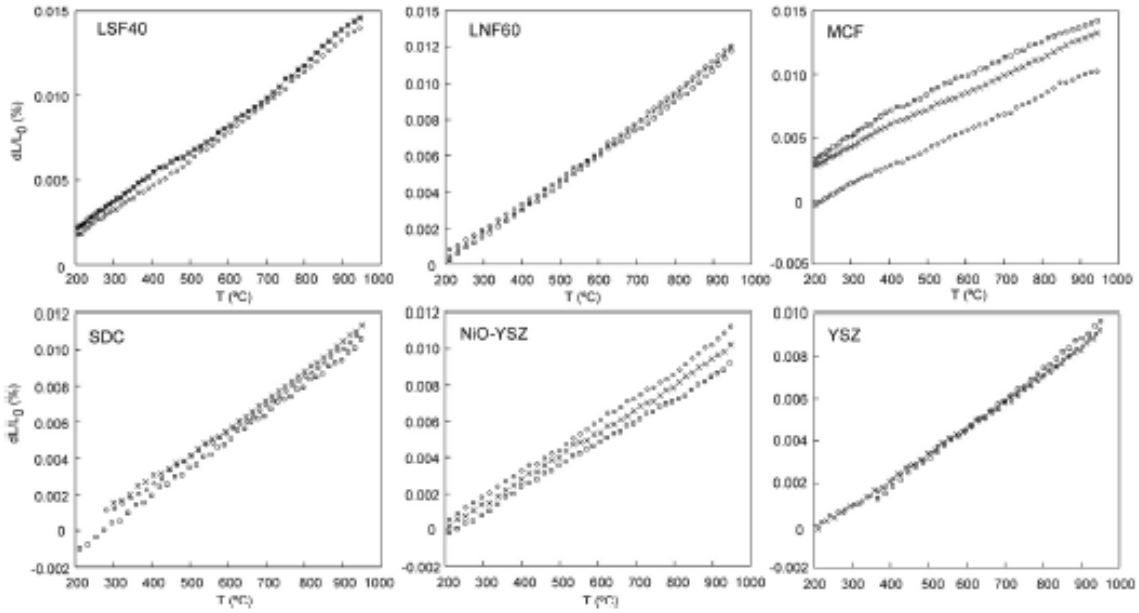

Fig. 4. Thermal expansion behavior of components prepared by the combustion method.

and 950 °C in air that are almost linearly dependent on temperature. The value of the average lineal thermal expansion coefficients (TEC) of the compounds obtained over the temperature range of 200–800 °C are shown in Table 7.

The change in the thermal expansion coefficient between the different components is shown in Fig. 5.

As can be observed, the introduction of the corresponding layers between the electrolyte and cathode, and between the cathode and interconnector, minimizes the difference between their TEC values giving rise to similar values that are indicative of thermal compatibility, a factor which prevents failure due to stresses in SOFCs at high temperatures caused by thermal mismatches. Crofer-22APU interconnector has been included for a better TEC comparison between the adjacent compounds of MCF10 and NiO-YSZ. This material is the one that was analyzed as interconnect material for this kind of SOFC synthesis by the research group [21,23].

4. Conclusions

An increase in the synthesized amount of compounds has been performed without complications, maintaining a suitable microstructure and purity for all studied materials.

Six different fuel cell compounds have been synthesized in big amounts by glycine-nitrate method with stoichiometric fuel/oxidizer ratio, obtaining high quality materials whose microstructural properties can be modified.

The achieved compounds have similar microstructures which limits the long time degradation for these kinds of multilayer systems.

The synthetic times are short, demonstrating to be compositionally and morphologically reproducible in different batches. Therefore, it can be concluded that the glycine-nitrate process, with an optimal G/N ratio of 1.0, is an appropriate technique for preparing big quantities of different compounds for SOFC fabrication.

Acknowledgements

This research has been funded by the Ministerio de Economía, Industria y Competitividad (MAT2016-76739-R) (AEI/FEDER, UE) and (MAT2015-2015-86078-R) and Dpto. Educación of the Basque Government (IT-630-13). The authors thanks the support received by the European Regional Development Fund (ERDF). SGIker of UPV/EHU technical support is gratefully acknowledged. A. Wain-Martin thanks Ministerio de Economía y Competitividad for funding his work (BES-2014-068433).

References

[1] A. Kumar, A. Cross, K. Manukyan, R.R. Bhosale, L.J.P. van den Broeke, J.T. Miller, A.S. Mukasyan, E.E. Wolf, Combustion synthesis of copper–nickel catalysts for hydrogen production from ethanol, Chem. Eng. J. 278 (2015) 46–54.
[2] T. Wilberforce, A. Alaswad, A. Palumbo, M. Dassisti, A.G. Olabi, Advances in stationary and portable fuel cell applications, Int. J. Hydrog. Energy 41 (2016) 16509–16522.
[3] A. Kumar, A.S. Mukasyan, E.E. Wolf, Combustion synthesis of Ni, Fe and Cu multicomponent catalysts for hydrogen production from ethanol reforming, Appl. Catal. A Gen. 401 (2011) 20–28.
[4] A. Ecija, K. Vidal, A. Larrañaga, L. Ortega-San-Martin, M.I. Arriortua, Synthetic methods for perovskite materials. structure and morphology, in: Yitzhak Mastai (Ed.), Advances in Crystallization Processes, 19 2012, pp. 493-514 ISBN:978-953-51-0581-7.
[5] K. Vidal, A. Morán-Ruiz, A. Larrañaga, J.M. Porras-Vázquez, P.R. Slater, M.I. Arriortua, Characterization of $LaNi_{0.6}Fe_{0.4}O_3$ perovskite synthesized by glycine-nitrate combustion method, Solid State Ionics 269 (2015) 24–29.
[6] S.L. González-Cortés, F.E. Imbert, Fundamentals, properties and applications of solid catalysts prepared by solution combustion synthesis (SCS), Appl. Catal. A Gen. 452 (2013) 117–131.
[7] S. Rasouli, S.J. Moeen, Combustion synthesis of Co-doped zinc oxide nanoparticles using mixture of citric acid-glycine fuels, J. Alloys Compd. 509 (2011) 1915–1919.
[8] S. Singh, D. Singh, $LaSrFeO_4$ nanopowders synthesized by different combustion methods: effect of fuel/particle size, Ceram. Int. 42 (2016) 15725–15731.
[9] S. Hajarpour, K. Gheisari, A. Honarbakhsh Raouf, Characterization of nanocrystalline $Mg_{0.6}Zn_{0.4}Fe_2O_4$ soft ferrites synthesized by glycine-nitrate combustion process, J. Magn. Magn. Mater. 329 (2013) 165–169.
[10] K. Boobalan, A. Varun, R. Vijayaraghavan, K. Chidambaram, U.K. Mudali, Facile, scalable synthesis of nanocrystalline calcium zirconate by the solution combustion method, Ceram. Int. 40 (2014) 5781–5786.
[11] C.A. da Silva, N.F.P. Ribeiro, M.M.V.M. Souza, Effect of the fuel type on the synthesis of yttria stabilized zirconia by combustion method, Ceram. Int. 35 (2009) 3441–3446.
[12] R.K. Lenka, T. Mahata, P.K. Sinha, A.K. Tyagi, Combustion synthesis of gadolinia-doped ceria using glycine and urea fuels, J. Alloys Compd. 466 (2008) 326–329.
[13] W. Tuichai, P. Thongbai, V. Amornkitbamrung, T. Yamwong, S. Maensiri, $Na_{0.5}Bi_{0.5}Ca_2Ti_4O_{12}$ nanocrystalline powders prepared by a glycine–nitrate process: preparation, characterization, and their dielectric properties, Microelectron. Eng. 126 (2014) 118–123.
[14] H. Monzón, M.A. Laguna-Bercero, A. Larrea, B.I. Arias, A. Várez, B. Levenfeld, Design of industrially scalable microtubular solid oxide fuel cells based on an extruded support, Int. J. Hydrog. Energy 39 (2014) 5470–5476.
[15] R. Fernández-González, T. Molina, S. Savvin, R. Moreno, A. Makradi, P. Núñez, Fabrication and electrical characterization of several YSZ tapes for SOFC applications, Ceram. Int. 40 (2014) 14253–14259.
[16] Z. Wang, X. Huang, Z. Lv, Y. Zhang, B. Wei, X. Zhu, Z. Wang, Z. Liu, Preparation and performance of solid oxide fuel cells with YSZ/SDC bilayer electrolyte, Ceram. Int. 41 (2015) 4410–4415.
[17] A. Arregui, L.M. Rodriguez-Martinez, S. Modena, M. Bertoldi, J. van Herle, V.M. Sglavo, Stability of ferritic perovskite cathodes in anode-supported solid oxide fuel cells under different processing and operation parameters, Electrochim. Acta 58 (2011) 312–321.
[18] M. Tarko, M. Mosiałek, M. Dudek, P. Nowak, A. Kędra, E. Bielańska, Composite cathode materials $Sm_{0.5}Sr_{0.5}CoO_3$–$La_{0.6}Sr_{0.4}FeO_3$ for solid oxide fuel cells, Solid State Ionics 271 (2015) 103–108.
[19] K. Vidal, A. Larrañaga, A. Morán-Ruiz, A.T. Aguayo, M.A. Laguna-Bercero, M.P. Yeste, J.J. Calvino, M.I. Arriortua, Effect of synthesis conditions on electrical and catalytical properties of perovskites with high value of A-site cation size mismatch, Int. J. Hydrog. Energy 41 (2016) 19810–19818.
[20] K. Shimura, H. Nishino, K. Kakinuma, M.E. Brito, H. Uchida, Effect of samaria-doped ceria (SDC) interlayer on the performance of $La_{0.6}Sr_{0.4}Co_{0.2}Fe_{0.8}O_{3-\delta}$/SDC composite oxygen electrode for reversible solid oxide fuel cells, Electrochim. Acta 225 (2017) 114–120.
[21] A. Morán-Ruiz, K. Vidal, M.Á. Laguna-Bercero, A. Larrañaga, M.I. Arriortua, Effects of using $(La_{0.9}Sr_{0.2})_{0.95}Fe_{0.6}Mn_{0.3}Co_{0.1}O_3$ (LSFMC), $LaNi_{0.6}Fe_{0.4}O_{3-\delta}$ (INF) and $LaNi_{0.6}Co_{0.4}O_{3-\delta}$ (LNC) as contact materials on solid oxide fuel cells, J. Power Sources 248 (2014) 1067–1076.
[22] M.K. Stodolny, B.A. Boukamp, D.H.A. Blank, F.P.F. van Berkel, Impact of Cr poisoning on the conductivity of different $LaNi_{0.6}Fe_{0.4}O_3$ cathode microstructures, Solid State Ionics 225 (2012) 136–140.
[23] V. Miguel-Pérez, A. Martínez-Amesti, M.L. Nó, A. Larrañaga, M.I. Arriortua, The effect of doping $(Mn,B)_3O_4$ materials as protective layers in different metallic interconnects for solid oxide fuel cells, J. Power Sources 243 (2013) 419–430.
[24] X. Montero, F. Tietz, D. Sebold, H.P. Buchkremer, A. Ringuede, M. Cassir, A. Laresgoiti, I. Villarreal, $MnCo_{1.9}Fe_{0.1}O_4$ spinel protection layer on commercial ferritic steels for interconnect applications in solid oxide fuel cells, J. Power Sources 184 (2008) 172–179.
[25] ICCD, Powder Diffraction File—Inorganic and Organic, Pennsylvania, USA, (1995).
[26] X. Pan, Z. Wang, B. He, S. Wang, X. Wu, C. Xia, Effect of Co doping on the electrochemical properties of $Sr_2Fe_{1.5}Mo_{0.5}O_6$ electrode for solid oxide fuel cell, Int. J. Hydrog. Energy 38 (2013) 4108–4115.
[27] M. Lubini, E. Chinarro, B. Moreno, V.C. de Sousa, A.K. Alves, C.P. Bergmann, Electrical properties of $La_{0.6}Sr_{0.4}Co_{1-y}Fe_yO_3$ (y = 0.2–1.0) fibers obtained by electrospinning, J. Phys. Chem. C 120 (2016) 64–69.
[28] D.A. Osinkin, D.I. Bronin, S.M. Beresnev, N.M. Bogdanovich, V.D. Zhuravlev, G.K. Vdovin, T.A. Demyanenko, Thermal expansion, gas permeability, and conductivity of Ni-YSZ anodes produced by different techniques, J. Solid State Electrochem. 18 (2013) 149–156.
[29] Y. Ren, R. Küngas, R.J. Gorte, C. Deng, The effect of A-site cation (Ln = La, Pr, Sm) on the crystal structure, conductivity and oxygen reduction properties of Sr-doped ferrite perovskites, Solid State Ionics 212 (2012) 47–54.
[30] R.N. Basu, F. Tietz, E. Wessel, H.P. Buchkremer, D. Stöver, Microstructure and electrical conductivity of $LaNi_{0.6}Fe_{0.4}O_3$ prepared by combustion synthesis routes, Mater. Res. Bull. 39 (2004) 1335–1345.
[31] L. Blum, An analysis of contact problems in solid oxide fuel cell stacks arising from differences in thermal expansion coefficients, Electrochim. Acta 223 (2017) 100–108.

INTERNATIONAL JOURNAL OF HYDROGEN ENERGY 44 (2019) 7555–7563

Available online at www.sciencedirect.com

ScienceDirect

journal homepage: www.elsevier.com/locate/he

SOFC cathodic layers using wet powder spraying technique with self synthesized nanopowders

Aritza Wain-Martin [a], Aroa Morán-Ruiz [a], Miguel Angel Laguna-Bercero [b], Roberto Campana [c], Aitor Larrañaga [a], Peter Raimond Slater [d], María Isabel Arriortua [a,e,*]

[a] Universidad del País Vasco (UPV/EHU), Facultad de Ciencia y Tecnología, Barrio Sarriena S/N, 48940, Leioa, Spain
[b] CSIC-Universidad de Zaragoza, Instituto de Ciencia de Materiales de Aragón (ICMA), Pedro Cerbuna 12, 50009, Zaragoza, Spain
[c] Centro Nacional del Hidrógeno, Prolongación Fernando el Santo s/n, Puertollano, 13500, Ciudad Real, Spain
[d] School of Chemistry, University of Birmingham, Birmingham, B15 2TT, UK
[e] BCMaterials, Basque Center for Materials, Applications and Nanostructures, BLD. Martina Casiano, 3rd. Floor UPV/EHU Science Park, Barrio Sarriena s/n, 48940, Leioa, Spain

ARTICLE INFO

Artide history:
Received 6 December 2018
Received in revised form
18 January 2019
Accepted 24 January 2019
Available online 16 February 2019

Keywords:
SOFC
Wet powder spray
Cathode
Active layers
Ball milling

ABSTRACTS

In this work, a wet powder spraying method has been investigated as a facile low cost route to deposit electrode layer on SOFC electrolyte support. A particular focus has been examining the interfacial stability of the deposited layers, and determining the influence of the thickness of the different layers, as well as the ball milling regime used to produce the electrode inks.

The developed system consist of an yttria stabilized zirconia electrolyte support, a $La_{0.6}Sr_{0.4}FeO_3$ (LSF) cathode, a $Sm_{0.2}Ce_{0.8}O_{1.9}$ (SDC) barrier layer between the electrolyte and the cathode, and $LaNi_{0.6}Fe_{0.4}O_3$ (LNF) as a contact layer, for a future integration with the SOFC interconnector. The electrolyte supports (300 μm thickness and 9 mm diameter) supports were prepared by uniaxial pressing, while the deposition of thin barrier layers, cathode and contact layer were carried out by manual spray coating.

Introduction

Fuel cells are energy conversion devices that directly convert the chemical energy of a fuel into electrical power and heat. Among the fuel cell types, solid oxide fuel cells (SOFC) have attracted much attention due to their advantages such as higher electrical conversion efficiency, long-term stability, fuel flexibility and environmental friendliness [1–5].

The two main configurations of SOFCs are tubular and planar [6–11]. Among the different configurations, this study is focused in planar SOFCs, which have a much simpler manufacturing process and lower fabrication cost than those of their tubular counterparts [12–14]. Regarding planar configuration, two types are preferred: electrode (mainly at anode) supported cells and electrolyte supported cells [3,15,16]. Although electrolyte supported cells may exhibit

* Corresponding author. Universidad del País Vasco (UPV/EHU), Facultad de Ciencia y Tecnología, Departamento de Mineralogía y Petrología, Barrio Sarriena S/N, 48940, Leioa, Vizcaya, Spain.
E-mail address: maribel.arriortua@ehu.eus (M.I. Arriortua).
https://doi.org/10.1016/j.ijhydene.2019.01.220
0360-3199/

higher ohmic losses, they are more robust and have demonstrated much better stability during the reduction-oxidation processes and thermal cycles [17,18].

The main drawbacks for the industrial implementation of SOFCs are their manufacturing cost and high degradation rate [14,19–21]. The aim is to replace the expensive and complex processing for the cell manufacturing with cheaper, simpler and industrially scalable techniques. Within these techniques, spray coating is a cost effective deposition method for electrode layers, showing good quality and thickness control. In particular, this method present a highly reproducible process for covering planar surfaces [22–25].

In the development of a planar SOFC stack, each repeating unit is composed of an anode, electrolyte, cathode and interconnect [26,27]. Among the typical material choices, yttria stabilized zirconia (YSZ) is the most commonly used electrolyte for SOFCs because of its low cost, high ionic transference number in oxidizing and reducing atmospheres, and good chemical and mechanical properties [28–30]. The mechanical properties of the YSZ allow it to withstand the residual stresses from cell fabrication processes as well as the stresses from the operational conditions. Samarium doped ceria (SDC) or gadolinium doped ceria (GDC) can also be used as electrolytes [31–33], or as a protective barrier between the YSZ electrolyte and commonly used cathode materials, preventing the formation of poorly conducting secondary phases, such as $La_2Zr_2O_7$ or $SrZrO_3$, which are deleterious for as cathode performance [34–38]. Iron containing perovskites such as $La_{0.6}Sr_{0.4}FeO_3$ (LSF) or $La_{0.6}Sr_{0.4}Co_{0.2}Fe_{0.8}O_3$ (LSCF) are good candidates as SOFC cathodes showing high mixed conductivity and good catalytic activity for the oxygen reduction reaction (ORR) [39–42]. The use of cathode contact layers such as $LaNi_{0.6}Fe_{0.4}O_3$ (LNF) and $LaNi_{0.6}Co_{0.4}O_3$ (LNC) have been demonstrated to improve the electron transfer through the contact interface from interconnect to the cathode layer. In addition, it means that the ORR of the TPB in the cathode receives more electrons from the interconnector, increasing the performance of the cell [43–45].

In this research, the deposition of the cathode side components (SDC as protective layer, LSF as cathode and LNF as contact layer) by wet powder spraying (WPS) deposition has been studied with the aim of optimizing the fabrication process using self-made materials, using a cheap, simple and scalable technique. Furthermore, special attention has been paid to the influence of the ball milling process and the layer thickness in determining the morphology and stability of the layers. The systems were characterized by X-ray diffraction (XRD) Scanning Electron Microscopy (SEM) with Energy Dispersive X-ray Spectroscopy (EDX). Electrochemical impedance spectroscopy (EIS) measurements were performed in a button cell test rig (NorECs) and a Zanher Zennium workstation, in air at 700 and 800 °C.

Experimental

Synthesis and system fabrication

All the SOFC component powders were prepared by a glycine nitrate (GN) process. Stoichiometric amounts of the corresponding metal nitrates were dissolved in deionized water. For all compositions, glycine was then added into the nitrate aqueous solution (Glycine-nitrate 1:1) under continuous stirring. The resulting viscous liquid was auto-ignited by heating up to approximately 455 °C and the obtained powders were calcined around 600 °C for 5 h to remove carbon residues. In the case of LSF and LNF, the resulting powders were pelletized and calcined in air at 950 °C for 8 h to obtain pure single phase samples. The properties (composition, morphologies, TEC and conductivities) of the primary materials used in the present study could be consulted in previous works [46].

Various configurations of the symmetrical systems were performed and investigated in this paper, which are described in Table 1. During the first experiments, four cells made out of cathodic and barrier layers, were created with different thicknesses and using inks ball milled at 270 rpm speed. In the second set of samples, with the aim of studying the effect of the ball milling speed in the layers, the cathode powders were ball milled at different speeds maintaining the thicknesses constant. Finally, taking into account previous results, symmetric systems were fabricated adding LNF contact layers.

To prepare the YSZ supports by uniaxial pressing, with 13 mm of diameter and 300 μm of thickness, the synthesized powders were ball milled with zirconia balls in zirconia cylinders for 24 h using 2-propanol as solvent. After being pressed, the supports were sintered at 1425 °C for 2 h. For the deposition of the layers, the starting powders were ground through wet ball milling, by adding the appropriate amount of solvent (2-propanol) and dispersant, for 24 h. The deposition was carried out at room temperature, using an airbrush (Iwata eclipse HP-BCS) operated at an angle of 90° with respect to the supporting plane. The distance between the nozzle and the support was varied between 2 and 10 cm. SDC, LSF and LNF layers were sintered separately at a temperature of 1150, 950 and 950 °C, respectively, for 2 h. The schematic structure of the electrolyte-supported system is shown in Fig. 1.

Morphological characterization

Room-temperature X-ray diffraction (XRD) data were recorded using an integration time of 10 s/0.026° step in the $5 < 2\theta < 70°$ range with a Philips X'Pert-PRO X-ray diffractometer equipped with a secondary beam graphite monochromator and Cu-Kα radiation. Full-profile Rietveld refinements https://www.sciencedirect.com/topics/materials-science/rietveld-refinement were performed using the FullProf program to confirm the structural parameters of the identified phases [47].

Cross sections of the samples were analyzed using SEM/EDX system (JEOL JSM-7000F). Composition analysis was performed using back-scattered electrons (BSE) at 20 kV accelerating voltage and 5×10^{-9} A of current. Moreover, EDX mapping was carried out using 70 ms/pixel. The data processing was performed using Oxford INCA software. The characteristic emission lines used for the analysis were L_α for La and Ce, K_α for Ni and Fe, and $L\beta_1$ for Sr.

Electrochemical measurements

Symmetric systems were used to study the electrochemical performance of the compounds using electrochemical

Table 1 – Details of the investigated samples.

Sample name	Composition	Layer thickness	Ball milling speed(rpm) for 24 h
T1	SDC-LSF	1 μm SDC and 1 μm LSF	270
T3	SDC-LSF	3 μm SDC and 3 μm LSF	270
T10	SDC-LSF	10 μm SDC and 10 μm LSF	270
T30	SDC-LSF	3 μm SDC and 30 μm LSF	270
Effect of Ball Milling			
T3BM130	SDC-LSF	3 μm SDC and 3 μm LSF	130
T10BM130	SDC-LSF	10 μm SDC and 10 μm LSF	130
T3BM270	SDC-LSF	3 μm SDC and 3 μm LSF	270
T10BM270	SDC-LSF	10 μm SDC and 10 μm LSF	270
Complete system			
MCT3	SDC-LSF-LNF	3 μm SDC, 3 μm LSF and 3 μm LNF	270
MCT10	SDC-LSF-LNF	3 μm SDC, 10 μm LSF and 10 μm LNF	270

impedance spectroscopy (EIS). The layers, with a geometrical area of 0.51 cm^2, were deposited onto both sides of the electrolyte. Impedance measurements of symmetric systems were performed in air at 700 and 800 °C. Samples were painted with Au paste to improve current collection and mounted on a button-cell test rig (model Probostat from NorEcs, Norway) for electrochemical testing.

A Zanher Zennium workstation (ZAHNER-elektrik GmbH & Co. KG, Germany) was used to obtain the electrochemical measurements. The frequency was varied between $5{\cdot}10^5$ and 0.01 Hz with an alternating (AC) signal amplitude of 10 mV, at temperatures of 700 and 800 °C. Data were analyzed with the ZPlot 3.5b software, using the equivalent circuit depicted in Fig. 2, where L is an inductance, R_s, R_H and R_L are resistances and CPE_H-CPE_L are constant phase elements.

The capacitance and relaxation frequency of each contribution have been calculated according to Eqs. (1) and (2), respectively [48].

$$C = \left(R^{1-n}Q\right)^{1/n} \tag{1}$$

$$f_0 = \frac{(RQ)^{-1/n}}{2\pi} \tag{2}$$

The ASR was calculated from the ASR = R_p·S/2 formula, where S is the surface area of the sample and Rp is the polarization resistance (the sum of the resistance given by the semicircles at high and low frequencies in the niquist plots). Then, all is divided by 2 to take into account the symmetrical geometry of the half systems.

Results and discussion

Initial structural study of the compounds

The purity of the samples was analyzed by X-ray diffraction. All the materials (YSZ, SDC and LSF) prepared through the GN combustion route show the desired final phases. The signal identification for all XRD patterns was in good agreement with the Powder Diffraction File database (PDF). All the samples were pure as can be observed in Fig. 3 for different batches. For the LNF compound, the appearance of extra shoulders in the experimental profile indicated a possible phase segregation to give two perovskite phase with different Ni/Fe ratio, as confirmed by Rietveld fitting analysis.

Fig. 4 shows the micrographs of the electrolytes supports sintered at 1425 °C for 2 h in air. The heating rate from room temperature to 1425 °C was 3 °C/min and an alumina plate was placed on top to add weight to ensure the production of a flat electrolyte support without bending and/or cracking. After sintering, the diameter of the electrolytes was reduced from 13 to 9 mm (30% of contraction). As can be seen in the micrographs, although there were 1 μm pores, it is possible that those pores were not connected, giving the required density to

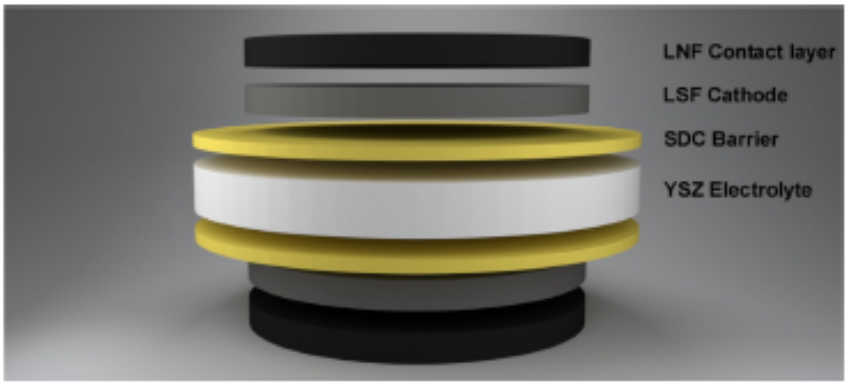

Fig. 1 – Schematic for an electrolyte supported SOFC design.

Fig. 2 – Equivalent circuit used to analyze impedance data.

avoid the gas leakage through the electrolyte. No pinhole or cracks were observed, indicating a good sintering with grains of about 0.5–2.5 μm.

Influence of the layer thickness on the microstructure

In order to determine the effect of the cathode thickness on the interface stability, a series of symmetrical systems were prepared with different cathode thicknesses. Fig. 5 shows the typical cross-section micrographs of the systems a) T1 b) T3 c) T10 and d) T30. The study indicated that the microstructure of the layers were similar, with similar grain size, pore size and overall porosity. One can notice that in the case of sample T1 (Fig. 5a), the interface was not uniform, probably due to an insufficient amount of deposited material to cover the entire surface. In the other cases, although the layers were uniform, in the case of the sample T30 (Fig. 5d) the increase of cathode thickness seemed to detrimentally affect the layer quality, as poor adhesion between the SDC and LSF layers were observed with the appearance of cracks leading to delaminations. As previously reported, the thickness of the layer had an influence on the residual stress distribution, resulting in a poor adhesion between layers [49]. On the other hand, T3 and T10 samples, presented good adhesion and continuous contact between the interfaces.

Taking into account the obtained results, we concluded that the layers with better microstructure were the ones with 3 and 10 μm thickness.

Influence of the ball milling effect

With the aim of studying the influence of the ball milling process on the microstructure, different ball milling speeds have been used to prepare the inks. In Fig. 6, the micrographs taken from the cross-section of the systems are shown. Obvious morphological differences between the two different treatments were observed. As can be seen, the systems deposited with previously ball milled ink at 270 rpm for 24 h, T3BM270 and T10BM270, presented more homogeneous layers, better contact and less fissures. In contrast, the results for the T3BM130 and T10BM130 samples show that, the powders were agglomerated and had bigger particle sizes, with broad size distribution, which leads to coarsening at high temperatures.

The particle sizes results are presented in Table 2. As can be seen in the table, although there was no significant change on the LSF powders rate of microstructural refinement, in the case of SDC there was significant particle size decrease with increasing ball milling speed. This decrease in size may be the cause of the enhanced microstructure of T3BM270 and T10BM270 samples.

Evaluation of a multilayered symmetric system

Taking into account the studies detailed above, SDC, LSF and LNF layers have been deposited onto the electrolyte support. The thickness of the SDC layer was also reduced by taking into account the fact that it has to be thin to minimize the additional contribution to the ohmic resistance of the system, and that an overly thick buffer layer can cause delamination in the cathode [50,51]. To show the characterization of each layer and determine any segregation of elements, EDX micrographs were examined (Fig. 7). The identified elements were, Ni from LNF in green, Sr from LSF in red and Ce from SDC in blue. From

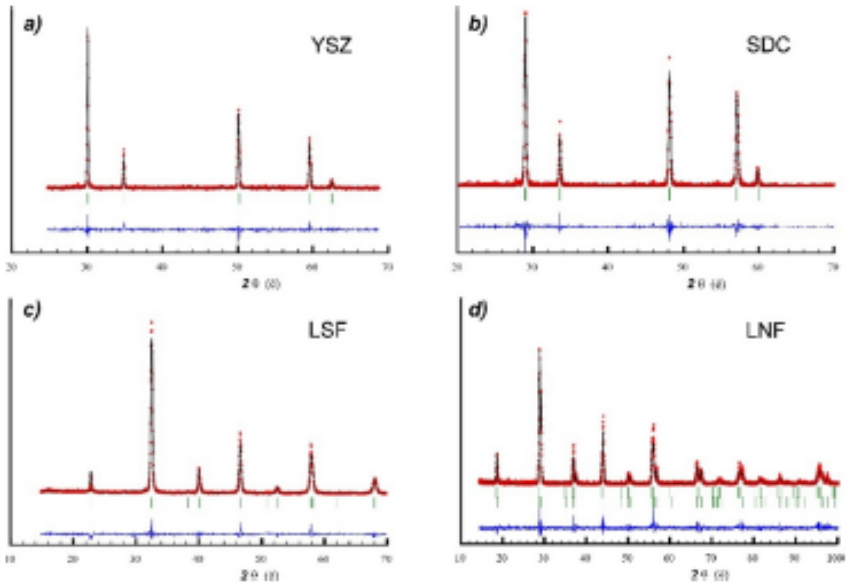

Fig. 3 – X-ray diffraction pattern refinements results obtained for a) YSZ, b) SDC, c) LSF and d) LNF.

INTERNATIONAL JOURNAL OF HYDROGEN ENERGY 44 (2019) 7555–7563

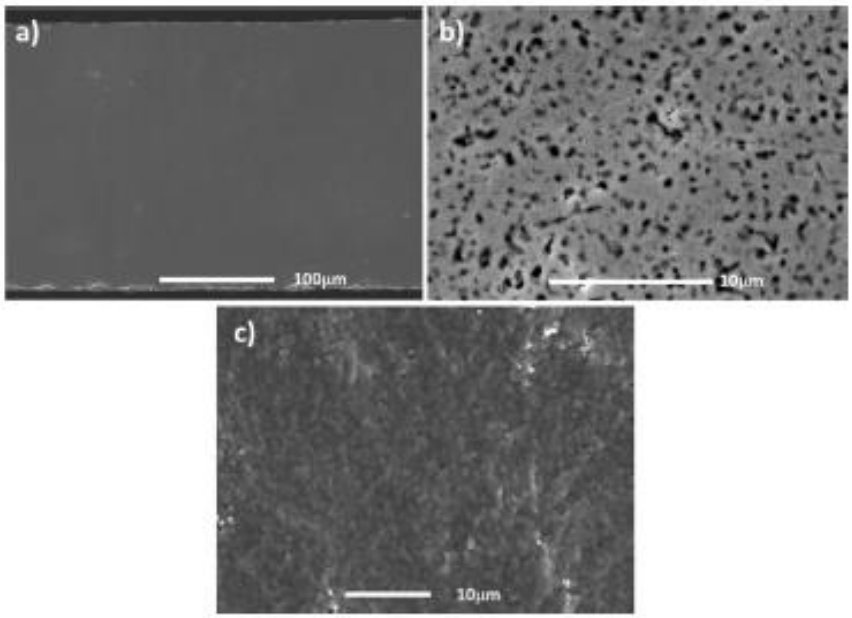

Fig. 4 – SEM cross-sectional images of a) YSZ electrolyte support, b) higher magnification image and c) surface view.

Fig. 7, it can be seen that there has been no diffusion between layers and that the adherence between the layers was good. Thus, by taking into account the systematic previous studies, it has been possible to avoid the creation of cracks and delaminations that could be seen in the other systems.

Fig. 8 shows the typical electrochemical impedance spectra measured at 700 and 800 °C for the MCT3 and MCT10 samples. The high frequency intercept of the impedance arcs with the x axis corresponds to the ohmic resistance (R_s), which is generally attributed to the electrolyte and the contact resistance [52]. In the present case, R_s were in different ranges due to the electrolyte thickness variability. The Nyquist plots at both temperatures were composed of two semicircles at high frequency (HF) and low frequency (LF) range, which corresponds to R_H and R_L electrode polarization resistances, respectively. The total cathode polarization resistance (R_p) is the sum of both (R_H and R_L). All the results from the simulations are listed in Table 3.

For MIEC perovskite electrodes, the HF arc is usually associated with charge transfer processes and the LF arc is usually attributed to oxygen reduction reaction at the cathode surface (adsorption and/or diffusion) [53]. This is consistent

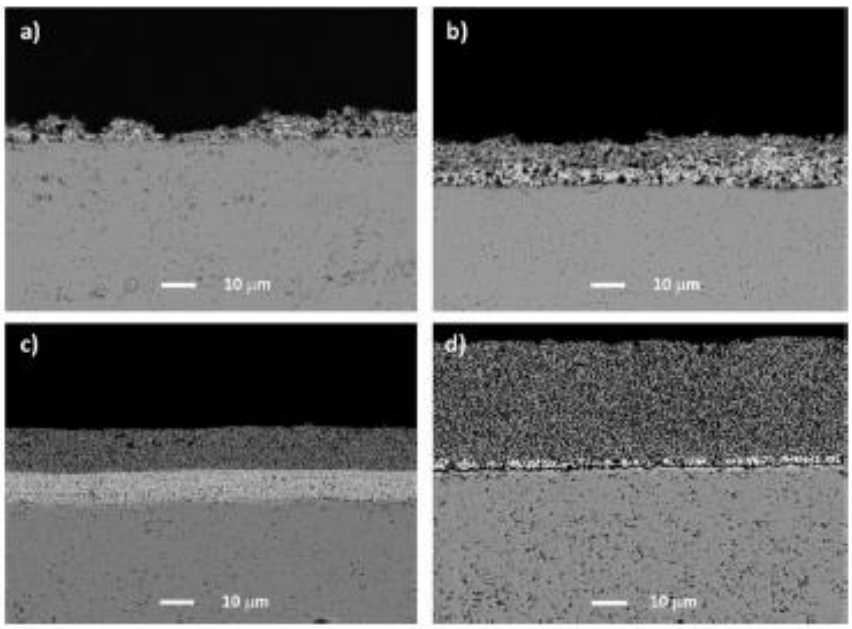

Fig. 5 – SEM secondary electron cross-sectional images of YSZ-SDC-LSF with the thicknesses of samples a) T1, b) T3, c) T10 and d) T30.

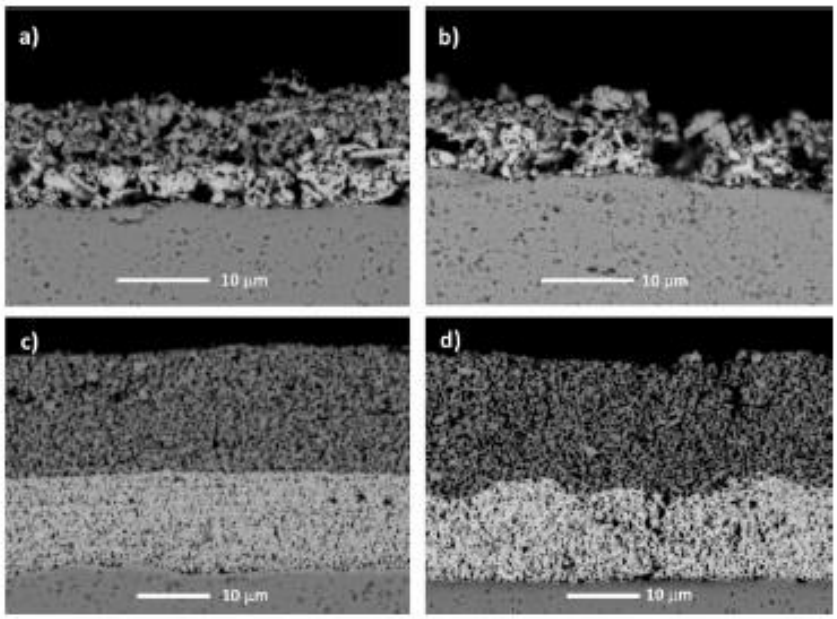

Fig. 6 – SEM cross-section images of YSZ-SDC-LSF systems with different thicknesses and ball milling processes. The samples are a) T3BM270, b) T3BM130, c) T10BM270 and d) T10BM130.

Table 2 – The particle size milled at different speeds.

Compound	d (μm)	Before ball milling	Milling speed 130 rpm	Milling speed 270 rpm
SDC	d_{10}	0.691	0.414	0.109
	d_{50}	1.506	1.032	0.572
	d_{90}	3.582	2.083	2.824
LSF	d_{10}	0.598	0.069	0.069
	d_{50}	0.903	0.136	0.137
	d_{90}	4.213	0.595	0.607

Table 3 – Resistances, capacitances and relaxation frequencies obtained by modelling impedance diagrams of the systems after being optimized.

T (°C)	Name		Contribution no. 1			Contribution no. 2			
		R_s (Ω cm^2)	R_H (Ω cm^2)	C_H (F cm^{-2})	F_H (kHz)	R_L (Ω cm^2)	C_L (F cm^{-2})	F_L (kHz)	R_p (Ω cm^2)
800	MCT3	1.31	0.13	1.18×10^{-4}	10.1	0.53	1.93×10^{-3}	0.16	0.66
	MCT10	1.52	0.07	2.41×10^{-4}	9.62	0.43	2.71×10^{-3}	0.14	0.50
700	MCT3	2.48	1.88	2.68×10^{-7}	315	5.65	1.39×10^{-3}	0.02	7.53
	MCT10	3.10	0.96	9.36×10^{-6}	17.7	4.31	2.75×10^{-3}	0.01	5.26

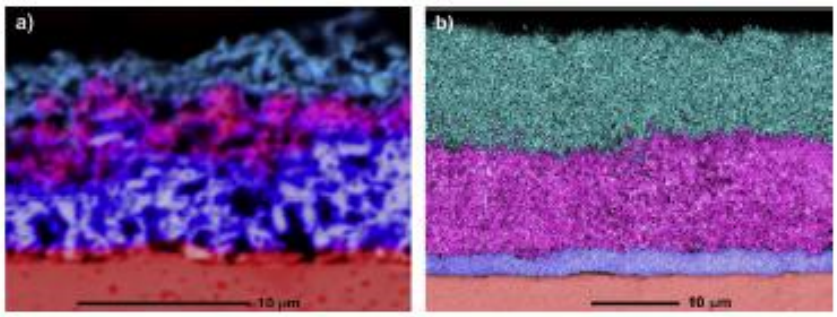

Fig. 7 – EDX mapping of the cross section of the samples a) MCT3 and b) MCT10 after being optimized.

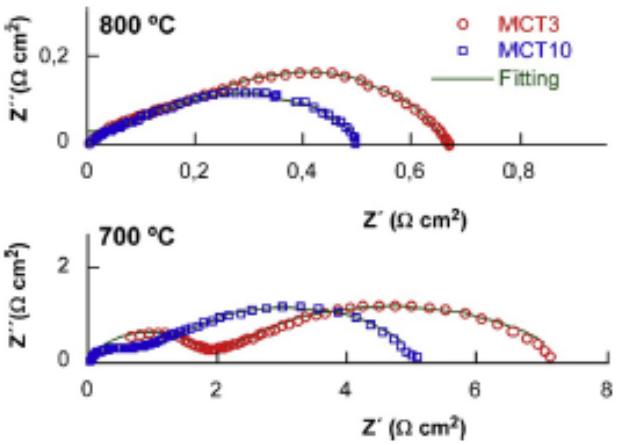

Fig. 8 – Impedance spectra of YSZ-SDC-LSF-LNF systems at 700 and 800 °C.

with the results listed in Table 3, and also with previous LSF systems reported in the literature [54–56]. As expected, the total polarization resistances of the systems decrease when increasing the operating temperature, from 7.53 to 0.66 Ω cm^2 and from 5.26 to 0.66 Ω cm^2, for MCT3 and MCT10 samples, respectively. This decrease is a consequence of the higher oxygen diffusion and surface exchange kinetics of the LSF cathode and LNF contact layer, at higher temperatures. It is also evident that increasing the thickness of the cathode layers from 3 to 10 μm reduces the polarization resistance associated to both charge transfer and surface processes. In any case, these systems have adequate polarization resistances, 0.50 and 0.66 Ω cm^2 at 800 °C for MCT10 and MCT3 samples, respectively, as shown in Fig. 8 in the impedance spectra of the systems.

Conclusions

Uniform and well-adhered coatings of LSF, SDC and LNF have been deposited by wet powder spraying onto an YSZ electrolyte support, with self-synthesized materials. The microstructure of the system has been shown to be unstable at thicknesses greater than 10 μm due to stresses caused by different TECs, while layers below 3 μm thickness lacked homogeneity. The best results have been obtained with the inks ball milled at 270 rpm, avoiding the appearance of coarsening in the layers after sintering. In addition, reducing the thickness of the SDC layer, together with the use of an LNF layer, has produced systems with satisfactory electrochemistry. To evaluate the systems, electrochemical impedance spectroscopy was performed, and a decrease in ASR was achieved with the thicker cathode layer (sample MCT10). The lowest polarization resistances of 0.5 Ω cm^2 at 800 °C corresponds to a symmetrical system consisting of a 3 μm SDC layer, 10 μm LSF layer and 10 μm LNF layer, with the ink used having been milled at a speed of 270 rpm. Thus the results show that, despite being a very simple and cheap process, the wet powder spraying technique is an effective method for the deposition of the fuel cell layers, through suitable control of the layer thickness and ink milling regimes employed.

Acknowledgements

This research has been funded by the Ministerio de Economía, Industria y Competitividad [MAT2016-76739-R and MAT2015-68078-R] [AEI/FEDER, UE] and Dpto. Educación of the Basque Government [IT-630-13]. The authors thanks the support received by the European Regional Development Fund (ERDF). The technical support of SGIker of UPV/EHU is gratefully acknowledged. A. Wain-Martin thanks Ministerio de Economía y Competitividad for funding his work [BES-2014-068433].

REFERENCES

[1] Ramadhani F, Hussain MA, Mokhlis H, Hajimolana S. Optimization strategies for solid oxide fuel cell (SOFC) application: a literature survey. Renew Sustain Energy Rev 2017;76:460–84. https://doi.org/10.1016/j.rser.2017.03.052.

[2] Jin C, Mao Y, Zhang N, Sun K. Fabrication and characterization of Ni-SSZ gradient anodes/SSZ electrolyte for anode-supported SOFCs by tape casting and co-sintering technique. Int J Hydrog Energy 2015;40:8433–41. https://doi.org/10.1016/j.ijhydene.2015.04.088.

[3] Chelmehsara ME, Mahmoudimehr J. Techno-economic comparison of anode-supported, cathode-supported, and electrolyte-supported SOFCs. Int J Hydrog Energy 2018;43:15521–30. https://doi.org/10.1016/j.ijhydene.2018.06.114.

[4] Fernandes MD, de P Andrade ST, Bistritzki VN, Fonseca RM, Zacarias LG, Gonçalves HNC, de Castro AF, Domingues RZ, Matencio T. SOFC-APU systems for aircraft: a review. Int J Hydrog Energy 2018;43:16311–33. https://doi.org/10.1016/j.ijhydene.2018.07.004.

[5] De Marco V, Iannaci A, Rashid S, Sglavo VM. Effect of anode thickness and Cu content on consolidation and performance of planar copper-based anode-supported SOFC. Int J Hydrog Energy 2017;42:12543–50. https://doi.org/10.1016/j.ijhydene.2017.03.221.

[6] Gil V, Gurauskis J, Campana R, Merino RI, Larrea A, Orera VM. Anode-supported microtubular cells fabricated with gadolinia-doped ceria nanopowders. J Power Sources 2011;196:1184–90. https://doi.org/10.1016/j.jpowsour.2010.08.093.

[7] Stoeckl B, Subotić V, Reichholf D, Schroettner H, Hochenauer C. Extensive analysis of large planar SOFC: operation with humidified methane and carbon monoxide to examine carbon deposition based degradation. Electrochim Acta 2017;256:325–36. https://doi.org/10.1016/j.electacta.2017.09.026.

[8]] Kong W, Zhang W, Zhang S, Zhang Q, Su S. Residual stress analysis of a micro-tubular solid oxide fuel cell. Int J Hydrog Energy 2016;41:16173–80. https://doi.org/10.1016/j.ijhydene.2016.05.256.

[9] Menzler NH, Tietz F, Uhlenbruck S, Buchkremer HP, Stoever D. Materials and manufacturing technologies for solid oxide fuel cells. J Mater Sci 2010;45:3109–35. https://doi.org/10.1007/s10853-010-4279-9.

[10] Orera VM, Laguna-Bercero MA, Larrea A. Fabrication methods and performance in fuel cell and steam electrolysis operation modes of small tubular solid oxide fuel cells: a review. Front Energy Res 2014;2:1–13. https://doi.org/10.3389/fenrg.2014.00022.

[11] Duan N, Yan D, Chi B, Pu J, Jian L. High performance anode-supported tubular solid oxide fuel cells fabricated by a novel

slurry-casting method. Sci Rep 2015;5:8174. https://doi.org/10.1038/srep08174.
[12] Yan D, Liang L, Yang J, Zhang T, Pu J, Chi B, Li J. Performance degradation and analysis of 10-cell anode-supported SOFC stack with external manifold structure. Energy 2017;125:663–70. https://doi.org/10.1016/j.energy.2016.12.107.
[13] Aydın Ö, Ochiai T, Nakajima H, Kitahara T, Ito K, Ogura Y, Shimano J. Mass transport limitation in inlet periphery of fuel cells: studied on a planar solid oxide fuel cell. Int J Hydrog Energy 2018;43:17420–30. https://doi.org/10.1016/j.ijhydene.2018.07.030.
[14] Myung J, Ko HJ, Park H, Hwan M, Hyun S. Fabrication and characterization of planar-type SOFC unit cells using the tape-casting/lamination/co-firing method. Int J Hydrog Energy 2012;37:498–504. https://doi.org/10.1016/j.ijhydene.2011.09.011.
[15] Shy SS, Hsieh YD, Huang CM, Chan YH. Comparison of electrochemical impedance measurements between pressurized anode-supported and electrolyte-supported planar solid oxide fuel cells. J Electrochem Soc 2015;162:F172–7. https://doi.org/10.1149/2.0041503jes.
[16] Lin Q, Lin J, Liu T, Xia C, Chen C. Solid oxide fuel cells supported on cathodes with large straight open pores and catalyst-decorated surfaces. Solid State Ionics 2018;323:130–5. https://doi.org/10.1016/j.ssi.2018.05.028.
[17] Preininger M, Subotić V, Stoeckl B, Schauperl R, Reichholf D, Megel S, Kusnezoff M, Hochenauer C. Electrochemical characterization of a CFY-stack with planar electrolyte-supported solid oxide cells in rSOC operation. Int J Hydrog Energy 2018;43:12398–412. https://doi.org/10.1016/j.ijhydene.2018.04.230.
[18] Patcharavorachot Y, Arpornwichanop A, Chuachuensuk A. Electrochemical study of a planar solid oxide fuel cell: role of support structures. J Power Sources 2008;177:254–61. https://doi.org/10.1016/j.jpowsour.2007.11.079.
[19] Scataglini R, Wei M, Mayyas A, Chan SH, Lipman T, Santarelli M. A direct manufacturing cost model for solid-oxide fuel cell stacks. Fuel Cells 2017;17:825–42. https://doi.org/10.1002/fuce.201700012.
[20] Kupecki J, Kluczowski R, Papurello D, Lanzini A, Kawalec M, Krauz M, Santarelli M. Characterization of a circular 80 mm anode supported solid oxide fuel cell (AS-SOFC) with anode support produced using high-pressure injection molding (HPIM). Int J Hydrog Energy 2018. In press, https://doi.org/10.1016/j.ijhydene.2018.02.143.
[21] Lee S, Lee K, Jang Y, Bae J. Fabrication of solid oxide fuel cells (SOFCs) by solvent-controlled co-tape casting technique. Int J Hydrog Energy 2017;42:1648–60. https://doi.org/10.1016/j.ijhydene.2016.07.066.
[22] Morales M, Navarro ME, Capdevila XG, Roa JJ, Segarra M. Processing of graded anode-supported micro-tubular SOFCs based on samaria-doped ceria via gel-casting and spray-coating. Ceram Int 2012;38:3713–22. https://doi.org/10.1016/j.ceramint.2012.01.015.
[23] Carpanese MP, Barbucci A, Canu G, Viviani M. BaCe0.85Y0.15O2.925 dense layer by wet powder spraying as electrolyte for SOFC/SOEC applications. Solid State Ionics 2015;269:80–5. https://doi.org/10.1016/j.ssi.2014.11.014.
[24] Taillades G, Pers P, Mao V, Taillades M. High performance anode-supported proton ceramic fuel cell elaborated by wet powder spraying. Int J Hydrog Energy 2016;41:12330–6. https://doi.org/10.1016/j.ijhydene.2016.05.094.
[25] Liu P, Luo Z, Kong J, Yang X, Liu Q, Xu H. Ba0.5Sr0.5Co0.8Fe0.2O3-delta-based dual-gradient cathodes for solid oxide fuel cells. Ceram Int 2018;44:4516–9. https://doi.org/10.1016/j.ceramint.2017.12.034.
[26] Zhu JH, Ghezel-Ayagh H. Cathode-side electrical contact and contact materials for solid oxide fuel cell stacking: a review. Int J Hydrog Energy 2017;42:24278–300. https://doi.org/10.1016/j.ijhydene.2017.08.005.
[27] Li X, Shi W, Han M. Optimization of interconnect flow channels width in a planar solid oxide fuel cell. Int J Hydrog Energy 2018;43:21524–34. https://doi.org/10.1016/j.ijhydene.2018.09.061.
[28] Setevich CF, Mogni LV, Caneiro A, Prado FD. Optimum cathode configuration for IT-SOFC using La0.4Ba0.6CoO3−δ and Ce0.9Gd0.1O1.95. Int J Hydrog Energy 2012;37:14895–901. https://doi.org/10.1016/j.ijhydene.2012.01.155.
[29] Saebea D, Authayanun S, Patcharavorachot Y, Chatrattanawet N, Arpornwichanop A. Electrochemical performance assessment of low-temperature solid oxide fuel cell with YSZ-based and SDC-based electrolytes. Int J Hydrog Energy 2018;43:921–31.
[30] Yamaji K, Yokokawa H. Oxygen ionic. In: Sorrell CC, Sugihara S, Nowotny J, editors. Conductor materials for energy conversion devices; 2005. p. 212–34. https://doi.org/10.1533/9781845690915.2.212.
[31] Sun H, Rainwater BH, Xiong X, Chen Y, Wei T, Zhang Q, Yang Z, Li C, Liu M. Interfacial effects on electrical conductivity in ultrafine-grained Sm0.2Ce0.8O2−δ electrolytes fabricated by a two-step sintering process. Int J Hydrog Energy 2017;42:11823–9. https://doi.org/10.1016/j.ijhydene.2017.03.151.
[32] Jamil SM, Othman MHD, Rahman MA, Jaafar J, Ismail AF. Anode supported micro-tubular SOFC fabricated with mixed particle size electrolyte via phase-inversion technique. Int J Hydrog Energy 2017;42:9188–201. https://doi.org/10.1016/j.ijhydene.2016.05.016.
[33] Sar J, Dessemond L, Djurado E. Electrochemical properties of graded and homogeneous Ce0.9Gd0.1O2−δ–La0.6Sr0.4Co0.2Fe0.8O3−δ composite electrodes for intermediate-temperature solid oxide fuel cells. Int J Hydrog Energy 2016;41:17037–43. https://doi.org/10.1016/j.ijhydene.2016.07.236.
[34] Martínez-Amesti A, Larrañaga A, Rodríguez-Martínez LM, Nó ML, Pizarro JL, Laresgoiti A, Arriortua MI. Chemical compatibility between YSZ and SDC sintered at different atmospheres for SOFC applications. J Power Sources 2009;192:151–7. https://doi.org/10.1016/j.jpowsour.2009.02.011.
[35] Medisetti S, Ahn J, Patil S, Goel A, Bangaru Y, Sabhahit GV, Babu GUB, Lee J, Dasari HP. Synthesis of GDC electrolyte material for IT-SOFCs using glucose & fructose and its characterization. Nano-Struct Nano-Objects 2017;11:7–12. https://doi.org/10.1016/j.nanoso.2017.05.009.
[36] Dai Y, Lou Z, Wang Z, Qiao J, Sun W, Sun K. Electrochemical and chemical stability performance improvement of Ba0.5Sr0.5Fe0.91Al0.09O3−δ cathode for IT-SOFC through the introduction of a GDC interlayer. Int J Hydrog Energy 2015;40:5939–46. https://doi.org/10.1016/j.ijhydene.2015.02.131.
[37] Yang K, Shen J, Yang K, Hung IM, Fung K, Wang M. Formation of La2Zr2O7 or SrZrO3 on cathode-supported solid oxide fuel cells. J Power Sources 2006;159:63–7. https://doi.org/10.1016/j.jpowsour.2006.04.049.
[38] De Vero JC, Develos-Bagarinao K, Ishiyama T, Kishimoto H, Yamaji K, Horita T, Yokokawa H. Effect of SrZrO3 formation at LSCF-cathode/GDC-interlayer interfaces on the electrochemical properties of solid oxide fuel cells. ECS Trans 2017;75(42):75–81. https://doi.org/0.1149/07542.0075ecst.
[39] Vidal K, Rodríguez-Martínez LM, Ortega-San-Martin L, Martínez-Amesti A, Nó ML, Rojo T, Laresgoiti A, Arriortua MI. The effect of doping in the electrochemical performance of (Ln1−xMx)FeO3−δ SOFC cathodes. J Power Sources 2009;192:175–9. https://doi.org/10.1016/j.jpowsour.2008.12.034.

[40] Shen F, Lu K. Perovskite-type La0.6Sr0.4Co0.2Fe0.8O3, Ba0.5Sr0.5Co0.2Fe0.8O3, and Sm0.5Sr0.5Co0.2Fe0.8O3 cathode materials and their chromium poisoning for solid oxide fuel cells. Electrochim Acta 2016;211:445–52. https://doi.org/10.1016/j.electacta.2016.06.070.

[41] Pan Z, Liu Q, Ni M, Lyu R, Li P, Chan SH. Activation and failure mechanism of La0.6Sr0.4Co0.2Fe0.8O3−δ air electrode in solid oxide electrolyzer cells under high-current electrolysis. Int J Hydrog Energy 2018;43:5437–50. https://doi.org/10.1016/j.ijhydene.2018.01.181.

[42] Wu X, Tian Y, Zhou X, Kong X, Zhang J, Zuo W, Ye X. High performance yttria-stabilized zirconia based intermediate temperature solid oxide fuel cells with double nano layer composite cathode. Int J Hydrog Energy 2017;42:1093–102. https://doi.org/10.1016/j.ijhydene.2016.09.057.

[43] Morán-Ruiz A, Vidal K, Laguna-Bercero MÁ, Larrañaga A, Arriortua MI. Effects of using (La0.8Sr0.2)0.95Fe0.6Mn0.3Co0.1O3 (LSFMC), LaNi0.6Fe0.4O3−δ (LNF) and LaNi0.6Co0.4O3−δ (LNC) as contact materials on solid oxide fuel cells. J Power Sources 2014;248:1067–76. https://doi.org/10.1016/j.jpowsour.2013.10.031.

[44] Guan WB, Zhai HJ, Jin L, Li TS, Wang WG. Effect of contact between electrode and interconnect on performance of SOFC stacks. Fuel Cells 2011;11:445–50. https://doi.org/10.1002/fuce.201000176.

[45] Xin X, Liu L, Liu Y, Zhu Q. Novel perovskite-spinel composite conductive ceramics for SOFC cathode contact layer. Int J Hydrog Energy 2018;43:23036–40. https://doi.org/10.1016/j.ijhydene.2018.10.159.

[46] Wain-Martin A, Morán-Ruiz A, Vidal K, Larrañaga A, Laguna-Bercero MA, Arriortua MI. Scalable synthetic method for SOFC compounds. Solid State Ionics 2017;313:52–7. https://doi.org/10.1016/j.ssi.2017.08.021.

[47] Rodríguez-Carvajal J. FULLPROF rietveld pattern matching analysis of powder patterns. 2011. Grenoble.

[48] Rieu M, Sayers R, Laguna-Bercero MA, Skinner SJ, Lenormand P, Ansart F. Investigation of graded La2NiO4+delta cathodes to improve SOFC electrochemical performance. J Electrochem Soc 2010;157(4):B477–80. https://doi.org/10.1149/1.3298439.

[49] Su S, Zhang W, Wu J, Zhou C. Effect of component thickness and anode composition on the residual stress of micro-tubular solid oxide fuel cell. Int J Electrochem Sci 2017;12:9121–30. https://doi.org/10.20964/2017.10.50.

[50] Kim Y, Kim-Lohsoontorn P, Bae J. Effect of unsintered gadolinium-doped ceria buffer layer on performance of metal-supported solid oxide fuel cells using unsintered barium strontium cobalt ferrite cathode. J Power Sources 2010;195:6420–7. https://doi.org/10.1016/j.jpowsour.2010.03.095.

[51] Endler-Schuck C, Weber A, Ivers-Tiffee E, Guntow U, Ernst J, Ruska J. Nanoscale Gd-doped CeO2 buffer layer for a high performance solid oxide fuel cell. J Fuel Cell Sci Technol 2011;8, 041001. https://doi.org/10.1115/1.4003016.

[52] Ecija A, Vidal K, Larrañaga A, Martínez-Amesti A, Ortega-San-Martín L, Arriortua MI. Structure and properties of perovskites for SOFC cathodes as a function of the A-site cation size disorder. Solid State Ionics 2013;235:14–21. https://doi.org/10.1016/j.ssi.2013.01.010.

[53] Adler S. Factors governing oxygen reduction in solid oxide fuel cell cathodes. Chem Rev 2004;104:4791–843. https://doi.org/10.1021/cr0207240.

[54] Li M, Wang Y, Wang Y, Chen F, Xia C. Bismuth Doped Lanthanum Ferrite Perovskites as novel cathodes for intermediate-temperature solid oxide fuel cells. ACS Appl Mater Interfaces 2014;6:11286–94. https://doi.org/10.1021/am5017045.

[55] Martínez-Amesti A, Larrañaga A, Rodríguez-Martínez LM, Aguayo AT, Pizarro JL, Nó ML, Laresgoiti A, Arriortua MI. Reactivity between La(Sr)FeO3 cathode, doped CeO2 interlayer and yttria-stabilized zirconia electrolyte for solid oxide fuel cell applications. J Power Sources 2008;185:401–10. https://doi.org/10.1016/j.jpowsour.2008.06.049.

[56] Kuengas R, Yu AS, Levine J, Vohs JM, Gorte RJ. An investigation of oxygen reduction kinetics in LSF electrodes. J Electrochem Soc 2013;160:F205–11. https://doi.org/10.1149/2.011303jes.

Libro de Resúmenes

XXXV Reunión Bienal RSEQ

A Coruña
19 a 23 Julio 2015

RSEQ
Real Sociedad Española de Química

UNIVERSIDADE DA CORUÑA
1989 2014

www.bienal2015.cienciasudc.es/es/

S9-PP-40 XXXV Bienal RSEQ

S9: *Síntesis, Caracterización y Propiedades de Materiales Emergentes*

MATERIALES PARA SU APLICACIÓN EN CELDAS SOFCs

A. Wain, A. Moran, K. Vidal, A. Larrañaga, M. Arriortua

Universidad del País Vasco/ Euskal Herriko Unibertsitatea (UPV/EHU). Facultad de Ciencia y Tecnología. Apdo. 644, E-48080 Bilbao, Spain, aritza.wain@ehu.eus

Palabras Clave: *componentes SOFC, métodos de síntesis, caracterización de materiales.*

El desarrollo de nuevos materiales, al igual que las técnicas de fabricación de componentes SOFC (celdas de combustible de óxido sólido) avanzados (Figura 1), es clave para conseguir reducir la temperatura de operación, y con ello, el coste, de estos sistemas de generación de energía [1]. Los métodos de combustión, se proponen como una de las vías de síntesis más prometedoras para la preparación de materiales a emplear en esta tecnología [2].

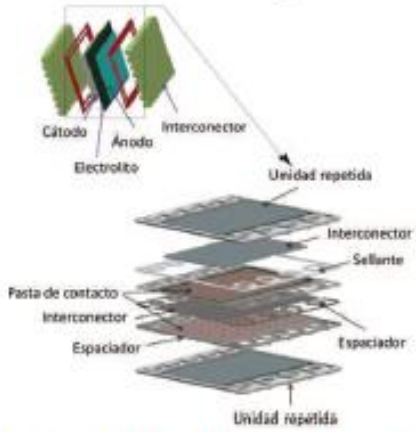

Figura 1. Componentes de una celda SOFC planar.

En este contexto, se han preparado diferentes componentes SOFC mediante el método de combustión con glicina-nitrato. Los materiales obtenidos, se han caracterizado mediante las técnicas de difracción de rayos X (DRX) sobre muestra policristalina, microscopía electrónica de barrido (MEB) y dilatometría (TEC), entre otras.

Agradecimientos: Esta investigación ha sido financiada por el Ministerio de Economía y Competitividad (MAT2013-42092-R) y el Dpto. de Educación, Política Lingüística y Cultura del Gobierno Vasco (IT-630-13). Los autores agradecen a SGIker por el apoyo técnico (UPV/EHU). A. Wain agradece al Ministerio de Ciencia e Innovación por la beca concedida (BES-2014-068433).

Referencias

[1] Z. Shao, W. Zhou, Z. Zhu, *Prog. Mater. Sci.*, **2012**, 57, 804-874.
[2] C. Zhu, A. Nobuta, I. Nakatsugawa, T. Akiyama, *Int. J. Hydrogen Energ.*, **2013**, 38, 13238-13248.

Materiales para su aplicación en celdas SOFCs

A. Wain, A. Morán-Ruiz, K. Vidal, A. Larrañaga y M. I. Arriortua.

Universidad del País Vasco/Euskal Herriko Unibertsitatea (UPV/EHU). Facultad de Ciencia y Tecnología. Apdo. 644, E-48080 Bilbao, España, aritza.wain@ehu.eus

RESUMEN

Se han sintetizado cinco compuestos ($La_{0.4}Sr_{0.6}FeO_3$, $LaNi_{0.6}Fe_{0.4}O_3$, $Zr_{0.8}Y_{0.2}O_{1.9}$, $Sm_{0.2}Ce_{0.8}O_{1.9}$ y $MnCo_{1.9}Fe_{0.1}O_4$) mediante la técnica de combustión glicina - nitrato (G/N = 1) [1], para su utilización como cátodo, electrolito, barrera, capas de contacto y protectoras, en celdas de combustible de óxido sólido de temperatura intermedia (IT-SOFC). Las muestras se han caracterizado mediante difracción de rayos X (DRX) y microscopía electrónica de barrido (MEB), técnicas que han permitido analizar las estructuras y la morfología de los diferentes compuestos. La difracción de rayos X sobre muestra policristalina ha permitido identificar tanto el sistema cristalino de los compuestos como su grupo espacial. Microestructuralmente todos los materiales presentan un tamaño de grano pequeño y superficies homogéneas y porosas.

SÍNTESIS

Proceso de combustión glicina - nitrato (G/N = 1) para la preparación de las muestras.

1 Capa Protectora (MCF10)

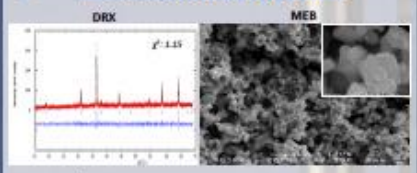

La difracción de rayos X en muestra policristalina [2] indica un sistema cúbico y una única fase pura para el compuesto $MnCo_{1.9}Fe_{0.1}O_4$ (MCF10) tras efectuar un sinterizado a 950ºC durante 8 horas. Las micrografías MEB de la superficie de las muestras en polvo, muestran partículas poco aglomeradas de unos tamaños nanométricos heterogéneos.

Fase	G.E.	a(Å)	V(Å³)
$MnCo_{1.9}Fe_{0.1}O_4$	Fd-3m	8.232(1)	557.80(7)

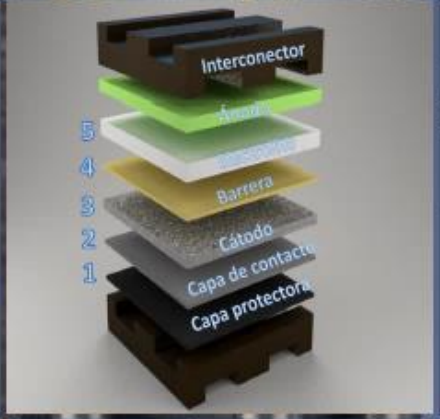

2 Capa de Contacto (LNF60)

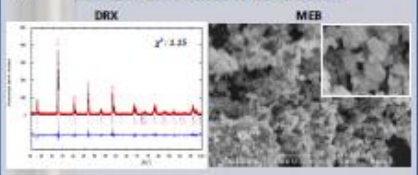

Las medidas de difracción de rayos X en muestra policristalina se han ajustado a un sistema romboédrico con dos estequiometrías para el compuesto $LaNi_{0.6}Fe_{0.4}O_3$ (LNF60), una más rica en níquel y otra más rica en hierro, consecuencia de una segregación de fases por efecto de la temperatura. El estudio de las micrografías de MEB, muestran partículas poco aglomeradas y de diferentes tamaños a escala nanométrica.

Fase	G.E.	a(Å)/c(Å)	V(Å³)	Fracción(%)
$LaNi_{0.6}Fe_{0.4}O_3$	R-3c	5.513(1)/13.399(5)	352.78(9)	21.26
$LaNi_xFe_{1-x}O_3$	R-3c	5.496(1)/13.251(1)	346.62(1)	78.74

3 Cátodo (LSF40)

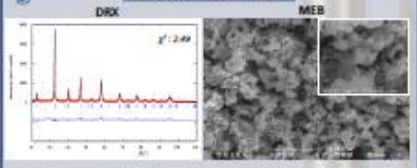

En el caso del cátodo, se ha tenido que disminuir la cantidad de muestra por síntesis con objeto de reducir la aparición de la fase $SrFeLaO_4$ como impureza. El análisis mediante DRX en muestra policristalina, muestra una fase romboédrica para el compuesto $La_{0.6}Sr_{0.4}FeO_3$ (LSF40) [3]. La caracterización morfológica realizada mediante microscopía muestra partículas distribuidas en pequeños aglomerados y de tamaños nanométricos heterogéneos.

Fase	G.E.	a(Å)/c(Å)	V(Å³)
$La_{0.6}Sr_{0.4}FeO_3$	R-3c	5.527(1)/13.451(2)	355.83(9)

4 Barrera (SDC)

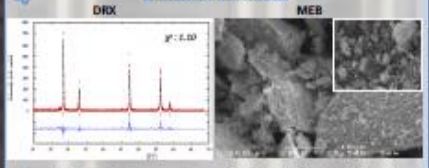

El análisis de DRX en muestra policristalina indica una única fase pura que cristaliza en sistema cúbico. Para la optimización de la síntesis de $Sm_{0.2}Ce_{0.8}O_{1.9}$ (SDC) [4], se ha reducido la relación de G/N debido a las pérdidas de material ocasionadas en la combustión, consecuencia del menor tamaño de partícula como se puede apreciar en las micrografías de MEB. En la figura se observan partículas nanométricas de tamaño homogéneo distribuidas en aglomerados.

Fase	G.E.	a(Å)	V(Å³)
$Sm_{0.2}Ce_{0.8}O_{1.9}$	Fm-3m	5.432(1)	160.26(4)

5 Electrolito(YSZ)

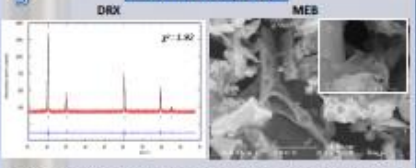

Se han obtenido lotes de 10gr de compuesto por cada síntesis de $Zr_{0.8}Y_{0.2}O_{1.9}$ (YSZ). La difracción de rayos X muestra un sistema cúbico con ausencia de impurezas. Para obtener una mayor densidad del compuesto, se ha elevado la temperatura de sinterización a 1400ºC, obteniéndose, tal y como muestran las micrografías, unas partículas sinterizadas en tamaños micrométricos heterogéneos.

Fase	G.E.	a(Å)	V(Å³)
$Zr_{0.8}Y_{0.2}O_{1.9}$	Fm-3m	5.146(1)	136.27(1)

CONCLUSIONES

- Se han sintetizado los compuestos $La_{0.6}Sr_{0.4}FeO_3$, $LaNi_{0.6}Fe_{0.4}O_3$, $Zr_{0.8}Y_{0.2}O_{1.9}$, $Sm_{0.2}Ce_{0.8}O_{1.9}$ y $MnCo_{1.9}Fe_{0.1}O_4$, manteniendo la temperatura de síntesis en 950ºC y la relación combustible/oxidante (Glicina/Nitrato = 1), con el fin de obtener fases con altos grados de pureza con el menor gasto energético posible.
- Las purezas, morfologías y los tamaños de la partícula han mostrado ser apropiados para la integración de cada componente en la fabricación de una celda SOFC.

AGRADECIMIENTOS

Esta investigación ha sido financiada por el Ministerio de Economía y Competitividad (MAT2013-42092-R) y el Dpto. de Educación, Política Lingüística y Cultura del Gobierno Vasco (IT-630-13). Los autores agradecen la ayuda recibida del Fondo Europeo de Desarrollo Regional (FEDER) y a SGIker por el apoyo técnico (UPV/EHU). A. Wain agradece al Ministerio de Economía y Competitividad por la beca concedida (BES-2014-068433).

REFERENCIAS

[1] K. Vidal, A. Morán-Ruiz, A. Larrañaga, J. M. Porras- Vazquez, P. R. Slater, M. I. Arriortua, *Solid State Ionics*, 269 (2015) 24-29.
[2] J. Rodríguez-Carvajal, Fullprof Program: Rietveld Pattern Matching Analysis of Powder Patterns, Grenoble, 2009.
[3] A. Morán-Ruiz, K. Vidal, M.A. Laguna-Bercero, A. Larrañaga, M.I. Arriortua, *J. Power Sources*, 248 (2014) 1067-1076.
[4] Z. Wang, X. Huang, Z. Lv, Y. Zhang, B. Wei, X. Zhu, Z. Wang, Z. Liu , *Ceramics International*, 41 (2015) 4410-4415.

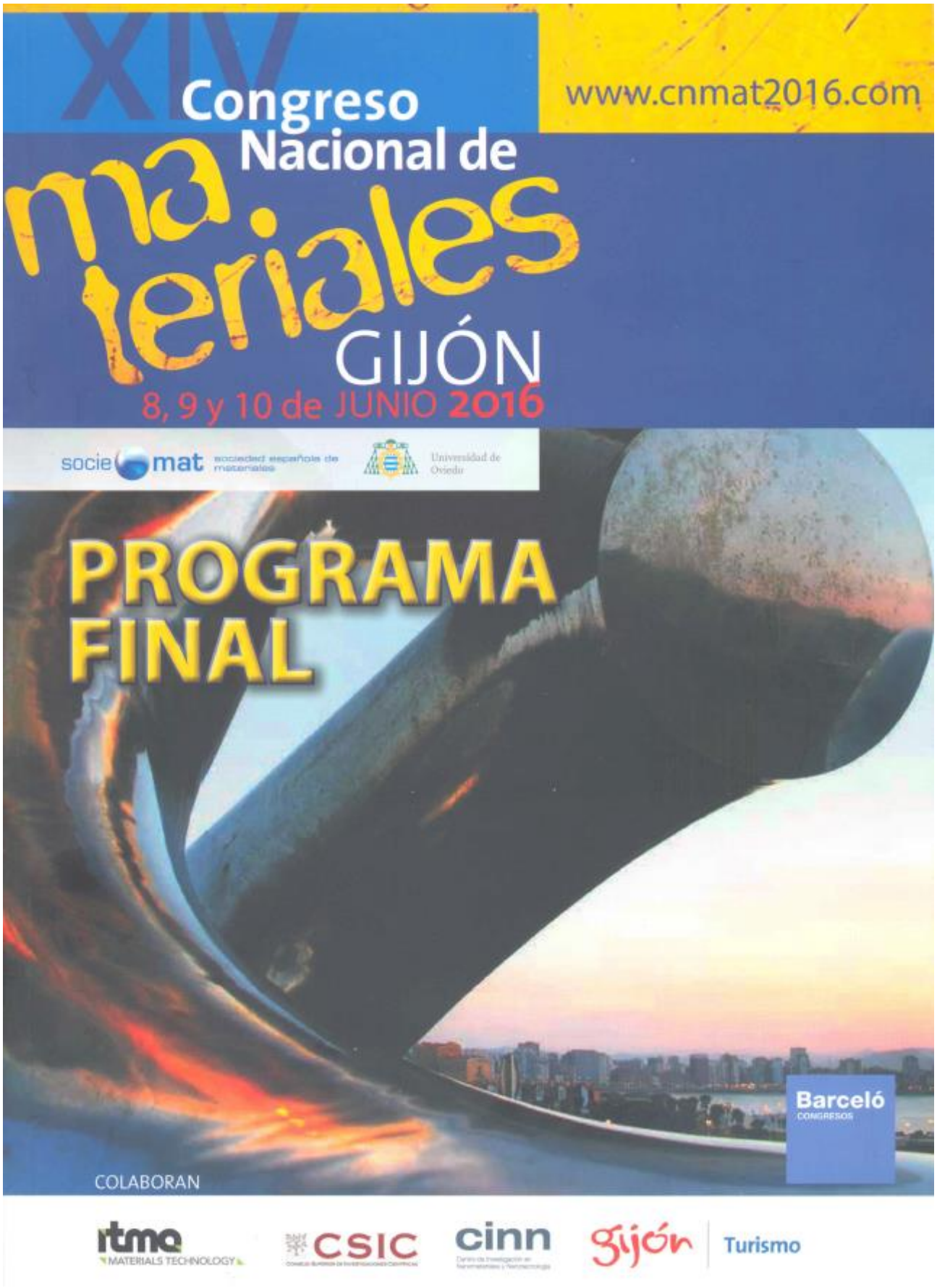
XIV
Congreso
Nacional de
materiales
GIJÓN
www.cnmat2016.com
8, 9 y 10 de JUNIO 2016
sociemat sociedad española de materiales
Universidad de Oviedo
PROGRAMA
FINAL
Barceló
CONGRESOS
COLABORAN
rtma MATERIALS TECHNOLOGY
CSIC
cinn
gijón Turismo

CELDAS DE PILAS DE OXIDÓ SÓLIDO. AVANCE EN EL PROCESADO DE MATERIALES

A. Wain(1), A. Morán-Ruiz(1) , K. Vidal(1), A. Larrañaga(1), M. A. Laguna-Bercero(2) y M. I. Arriortua(1)

(1) Universidad del País Vasco/ Euskal Herriko Unibertsitatea (UPV/EHU). Facultad de Ciencia y Tecnología. Apdo. 644, E-48080 Bilbao, Spain

(2) Instituto de Ciencia de Materiales de Aragón, ICMA, CSIC-Universidad de Zaragoza, Pedro Cerbuna 12, 50009 Zaragoza, Spain

Tel.: +34-94-601-5984
Fax: +34-94-601-3500
aritza.wain@ehu.es

Abstract

Este trabajo está enfocado a la síntesis y al procesado de los componentes de las pilas de combustible de óxido sólido (SOFC). La configuración empleada consiste en celdas (ánodo/electrolito/cátodo) soportadas por el electrolito. Se han sintetizado los compuestos, $NiO\text{-}(ZrO_2)_{0.92}(Y_2O_3)_{0.08}$, $(ZrO_2)_{0.92}(Y_2O_3)_{0.08}$ y $La_{0.6}Sr_{0.4}FeO_3$ como ánodo, electrolito y cátodo, respectivamente. Con objeto de disminuir la reactividad electrolito-cátodo, se ha empleado una barrera $Ce_{0.8}Sm_{0.2}O_{1.9}$ entre ambos componentes. En buen acuerdo con K. Vidal y col. [1] se ha utilizado la técnica de combustión por glicina-nitrato para la síntesis de los compuestos. La evaluación de la pureza, morfología y conductividad se ha llevado a cabo mediante difracción de rayos X (XRD) (método Rietveld), microscopía electrónica de barrido (MEB) y medidas de conductividad en *bulk* a través del método de cuatro puntos.

Para el procesado del electrolito se ha empleado una prensa hidráulica, obteniéndose pastillas de 20 mm de diámetro y 500µm de espesor. Éstas se han sinterizado a 1450 ºC durante 4 h en aire, con objeto de alcanzar las propiedades físico-químicas adecuadas. La deposición del ánodo, cátodo y barrera se ha realizado por spray manual coloidal, empleándose una solución en base orgánica. Para analizar el comportamiento electroquímico de la estructura multicapa, se han realizado medidas de impedancia a 800 ºC durante 100 h. La degradación de los sistemas se ha estudiado a partir de análisis por energía dispersiva de rayos X (EDX) mediante el análisis de las micrografías de las secciones transversales.

Agradecimientos: Esta investigación ha sido financiada por el Dpto. Educación, Política Lingüística y Cultura del Gobierno Vasco (IT-630-13) y al Ministerio de Economía y Competitividad (MAT2013-42092-R). Los autores agradecen a SGIker por el apoyo técnico (UPV/EHU, MEC, GV/EJ and European Social Fund) y a la ayuda recibida del Fondo Europeo de Desarrollo Regional (FEDER).

---

[1] K. Vidal, A. Moran-Ruiz, A. Larrañaga, J.M. Porras-Vázquez, P.R. Slater, M. I. Arriortua, *Solid State Ionics,* 269 (2015) 24–29.

Celdas de combustible de oxido sólido, avance en el procesado de materiales.

A. Wain [1], A. Morán-Ruiz [1], K. Vidal [1], A.Larrañaga [1], M.A. Laguna-Bercero [2] y M.I. Arriortua [1,3]

[1] Universidad del País Vasco (UPV/EHU), Facultad de Ciencia y Tecnología, Departamento de Mineralogía y Petrología, B. Sarriena S/N, 48940 Leioa, Vizcaya, España
[2] CSIC-Universidad de Zaragoza, Instituto de Ciencia de Materiales de Aragón (ICMA), Pedro Cerbuna 12, 50009 Zaragoza, España
[3] BCMaterials, Parque Tecnológico de Zamudio, Ibaizabal Bidea, Edificio 500-Planta 1, 48160 Derio, Vizcaya, España

Introdución

Las pilas de combustible de óxido sólido (SOFCs) son una de las tecnologías de interés para la obtención de energía limpia con alta eficiencia para la conversión directa de energía química en eléctrica. Para la implementación de estos sistemas en el mercado y conseguir que sean económicamente competitivos, se requiere la mejora constante de materiales y procesos de fabricación. Por ello, es necesaria la producción industrial a gran escala de materiales SOFC, siendo la síntesis de combustión un método simple y reproducible para obtener varios tipos de óxidos cerámicos empleados en estos sistemas.

Objetivos

Se han sintetizado lotes de más de 10g de cuatro compuestos, $La_{0.4}Sr_{0.6}FeO_3$ (LSF40), $Sm_{0.2}Ce_{0.8}O_{1.9}$ (SDC), $(ZrO_2)_{0.92}(Y_2O_3)_{0.08}$ (YSZ) y $NiO-(ZrO_2)_{0.92}(Y_2O_3)_{0.08}$ (NIO-YSZ), mediante la técnica de combustión glicina - nitrato (G/N = 1) [1], para su utilización como cátodo, barrera, electrolito y ánodo respectivamente, en celdas de combustible de óxido sólido de Tª intermedia (IT-SOFC). Las muestras se han caracterizado mediante difracción de rayos X (DRX), microscopía electrónica de barrido (MEB) y medidas de conductividad eléctrica, técnicas que han permitido el análisis de las estructuras, la morfología y la electroquímica de los diferentes compuestos.

Síntesis

Se han disuelto en agua los nitratos (cantidades estequiométricas) en un vaso de precipitados.

Se ha homogenizado la disolución en un agitador magnético y se ha añadido el combustible (glicina) en una relación G/N=1.

Se ha aumentado la temperatura hasta 455ºC con el objetivo de inducir la autocombustión (explosión violenta).

Se ha obtenido un polvo de grano muy fino y muy voluminoso.

Se ha molido el polvo en un mortero.

Se han efectuado dos tratamientos térmicos, uno a 600 ºC para todos los compuestos y otro a 950 ºC en el caso de $La_{0.4}Sr_{0.6}FeO_3$. El tratamiento se ha efectuado en un horno mufla.

DRX

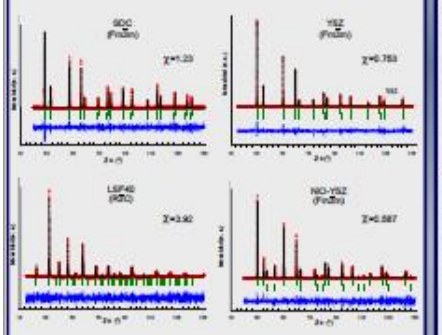

Los afinamientos a partir de los datos de rayos X se han analizado mediante el método Rietveld [2] utilizando el programa FullProf [3].
En los casos de los compuestos YSZ y SDC se puede observar un segregación de fases.

MEB

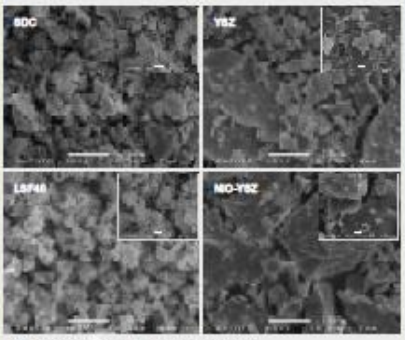

Imágenes MEB para las muestras disgregadas

Las partículas están unidas entre sí formando aglomerados de diferentes formas y tamaños de unas pocas micras. Éstas muestran límites de grano bien definidos a causa de los gases que se escapan a lo largo de la reacción de combustión [4].

Conductividad electrica

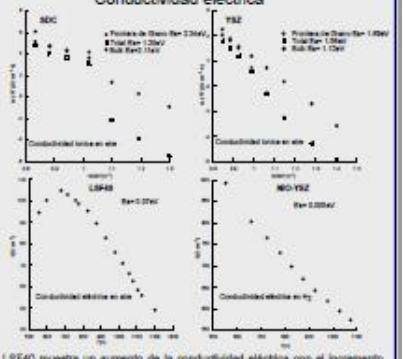

El LSF40 muestra un aumento de la conductividad eléctrica con el incremento de la temperatura, llegando a un máximo en torno a 400ºC, temperatura tras la cual disminuye (conductividad tipo p) [5].
En el caso del NIO-YSZ, la conductividad aumenta con la temperatura, en buen acuerdo con lo observado para contenidos de Ni + 0.3 [6].
En referencia al YSZ y SDC, las energías de activación de la conductividad de frontera de grano son mayores que las del bulk, debido a la mayor resistencia al movimiento de iones oxígeno que presenta la frontera de grano [7].

Procesado

Se han prensado los materiales de YSZ aplicando 7 Tn en un molde de 31 mm de diámetro.

Se ha efectuado un tratamiento térmico a 1400 ºC durante 5 horas a los discos de YSZ conseguidos anteriormente.

En uno de los laterales de los discos se ha depositado, mediante spray manual coloidal, una capa de SDC para luego ser recubierta por LSF. Por el otro lateral se ha depositado una capa de Ni-YSZ.

Tras aplicar cada capa se ha efectuado un tratamiento térmico con el fin de cosinterizar las capas entre sí.

Se han obtenido celdas de 25 mm de diametro y 450 µm de espesor.

Conclusiones

- Se han sintetizado lotes de los compuestos LSF40, SDC, YSZ y NIO-YSZ manteniendo el mismo proceso de síntesis y la misma relación combustible/oxidante (Glicina/Nitrato=1), con el fin de obtener fases puras con el menor gasto energético posible.
- Las medidas electroquímicas realizadas muestran unos valores de conductividad en buen acuerdo con los valores encontrados en la bibliografía.
- Las purezas, morfologías y los tamaños de la partícula de los compuestos han mostrado ser apropiados para su uso en la integración de cada componente en procesado de una celda SOFC.

Agradecimientos

Esta investigación ha sido financiada por el Dpto. Educación, Política Lingüística y Cultura del Gobierno Vasco (IT-630-13) y por el Ministerio de Economía y Competitividad (MAT2013-42092-R). Los autores agradecen a los SGIker por el apoyo técnico (UPV/EHU) y a la ayuda recibida del Fondo Europeo de Desarrollo Regional (FEDER). A. Wain agradece al Ministerio de Economía y Competitividad por la beca concedida (BES-2014-068433).

Referencias

[1] K. Vidal, A. Moran-Ruiz, A. Larrañaga, J.M. Porras-Vázquez, P.R. Slater, M. I. Arriortua, Solid State Ionics, 269 (2015) 24–29.
[2] R. A. Young, The Rietveld method. International Union of Crystallography-Oxford Science Publications:Oxford, 1995.
[3] J. Rodríguez-Carvajal, Fullprof Program: Rietveld Pattern Matching Analysis of Powder Patterns, Grenoble, 2009.
[4] C. Zhu, A. Nobuta, I. Nakatsugawa, T. Akiyama, Int. J. Hydrogen Energ. 38 (2013) 23238-13248.
[5] A.S. Nesaraj, S. Dheenadayalan, I.A. Raj, R. Pattabiraman, Journal of Ceramic Process. Res., 13 (2012) 601-606.
[6] B. S. Prakash, S. S. Kumar, S.T. Aruna, Renew. Sust. Energ. Rev., 36 (2014) 149-179.
[7] M. Krauz, M. Radecka, M. Rekas, Ceram. Maters., 63 (2011) 157-163.

Proceedings of

12th European SOFC & SOE Forum 2016

Chapter 05 - Session B03

State of the art & novel processing routes

Edited by

Prof. Nigel Brandon (Chair)
Dr. Richard Dawson
Dr. Zeynep Kurban
Dr. Farid Tariq
Dr. Antonio Bertei
Dr. Kristina Kareh
Dr. Mardit Matian
Dr. Enrique Ruiz Trejo
Dr. Paul Boldrin
Dr. Jung-Sik Kim
Dr. Paul Shearing
Dr. Vladimir Yufit

Co-Edited by

Olivier Bucheli
Gabriela Geisser
Fiona Moore
Dr. Michael Spirig

ISBN 978-3-905592-21-4

www.EFCF.com/Lib

12th European SOFC & SOE Forum www.EFCF.com/Lib ISBN 978-3-905592-21-4 5 - 8 July 2016, Lucerne/Switzerland

B0321

Scalable synthetic method for IT-SOFCs compounds

A. Wain, A. Morán-Ruiz, K. Vidal, A. Larrañaga, M. I. Arriortua
Universidad del País Vasco/ Euskal Herriko Unibertsitatea (UPV/EHU). Facultad de Ciencia y Tecnología. Sarriena s/n, E-48940 Leioa, Spain
Tel.: +34-94-601-5984
Fax: +34-94-601-3500
aritza.wain@ehu.es

Abstract

Economically competitive SOFC systems appear ready for commercialization, but widespread market penetration will require a broad inventory of key starting materials and fabrication processes to enhance systems and reduce costs. These requirements are originated from the demands for large scale SOFC industrial production. For these reason, we have synthesized different parts of a fuel cell, on a large scale, by the glycine-nitrate combustion method.

It have been synthesized interconnector protective coatings ($MnCo_{1.9}Fe_{0.1}O_4$), contact layers ($LaNi_{0.6}Fe_{0.4}O_3$), cathodes ($La_{0.6}Sr_{0.4}FeO_3$), interlayers ($Sm_{0.2}Ce_{0.8}O_{1.9}$), electrolytes $(ZrO_2)_{0.92}(Y_2O_3)_{0.08}$ and anode $(Ni_{0.3}O\text{-}(ZrO_2)_{0.92}(Y_2O_3)_{0.08})$ materials, obtaining reproducible pure samples and amounts up to 12 g for each batch, being able to increase easily this amount to lots of hundred of grams.

The obtained materials have been characterized compositionally by inductively coupled plasma atomic emission spectroscopy (ICP-AES) and X-ray fluorescence (XRF), structurally by X-ray diffraction (XRD) and microstructurally by scanning electron microscopy (SEM).

Introduction

Solid Oxide Fuel Cells (SOFC) are one of the most promising technologies for the obtaining of clean energy with high efficiency for direct conversion of chemical energy into power [1]. For the implementation of these systems on the market and make them economically competitive, improving materials and manufacturing processes is constantly required. Therefore, industrial-scale production of SOFC materials is necessary, being combustion synthesis a simple and reproducible method to obtain various types of ceramic oxides used in these systems [2].

Technology development scheme.

Objectives

We describe the adaptation of an existing lab-scale cell components production method to an industrially ready and easily scalable method using glycine-nitrate combustion synthesis. For this, batches up to 12 g of sample have been synthesized, were the synthesized components were: interconnect protective coatings (MCF10), contact layers (LNF60), cathodes (LSF40), interlayers (SDC), electrolytes (YSZ) and anodes (Ni-YSZ). The constituent phases were identified compositionally by inductively coupled plasma atomic emission spectroscopy (ICP-AES) and X-ray fluorescence (XRF), structurally by X-ray diffraction (XRD), while the microstructure was characterized by scanning electron microscopy (SEM).

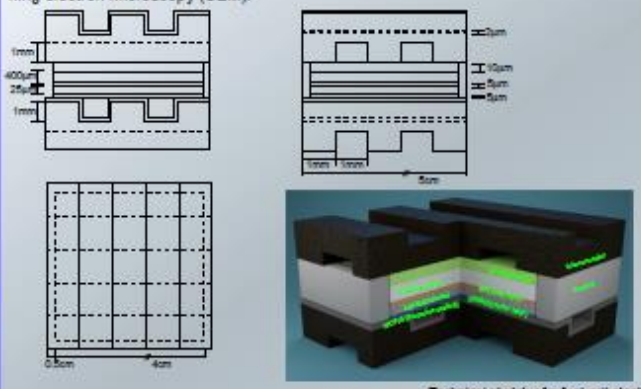

Technical sketch of a fuel cell stack.

Synthesis

Stoichiometric amounts of the corresponding metal nitrates were dissolved in deionized water

The dissolution was homogenized while stirring and glycine was added maintaining glycine to nitrate molar ratio in a unit.

The resulting viscous liquid was autoignited by heating up to approximately to 465 ºC (violent explosion).

Powders with very fine grains and very voluminous have been obtained.

The resulting powders were ball milled.

Powders were calcined between 600 and 800ºC for 5 h to remove carbon residues and in the case of MCF10, LNF60 and LSF40, were pelletized and calcined in air at 950 ºC for 6 h to obtain pure samples.

ICP+XRF

Table 1: Summary ICP results for LSF40 (La, Sr, Fe), LNF60 (La, Ni, Fe) and MCF10 (Mn, Co, Fe).

	Sr	La	Fe	Ni	Mn	Co
LSF40	0.41(1)	0.59(2)	1.02(3)	—	—	—
LSF40	0.40(1)	0.60(2)	1.01(3)	—	—	—
LSF40	0.41(1)	0.59(2)	1.02(3)	—	—	—
LNF60 (Batch 1)	—	0.59(3)	0.41(6)	0.61(6)	—	—
LNF60 (Batch 2)	—	0.61(6)	0.41(6)	0.60(6)	—	—
LNF60 (Batch 3)	—	1.02(3)	0.41(6)	0.61(6)	—	—
MCF10	—	—	0.19(1)	—	0.80(4)	1.99(3)
MCF10	—	—	0.19(1)	—	0.80(4)	1.99(3)
MCF10	—	—	0.19(1)	—	0.80(4)	1.99(3)

Table 2: Summary XRF results for SDC (Sm, Ce), NiO-YSZ (Ni, Y, Zr) and YSZ (Y, Zr).

	Zr	Y	Ni	Sm	Ce
SDC (Batch 1)	—	—	—	0.7(5)	0.2(4)
SDC (Batch 2)	—	—	—	0.7(5)	0.2(4)
SDC (Batch 3)	—	—	—	0.7(5)	0.2(4)
NiO-YSZ (Batch 1)	0.9(3)	0.2(2)	0.3(4)	—	—
NiO-YSZ (Batch 2)	0.9(3)	0.2(2)	0.3(4)	—	—
NiO-YSZ (Batch 3)	0.9(3)	0.2(2)	0.3(4)	—	—
YSZ (Batch 1)	0.8(6)	0.2(2)	—	—	—
YSZ (Batch 2)	0.8(6)	0.2(2)	—	—	—
YSZ (Batch 3)	0.8(6)	0.2(2)	—	—	—

Within the experimental errors for all the samples, the experimental compositional values match the nominal composition. In all the cases, the difference between the relative amounts of the elements in different batches was not significant. Thus, the synthesis procedure shows an adequate chemical reproducibility.

Characterization

XRD

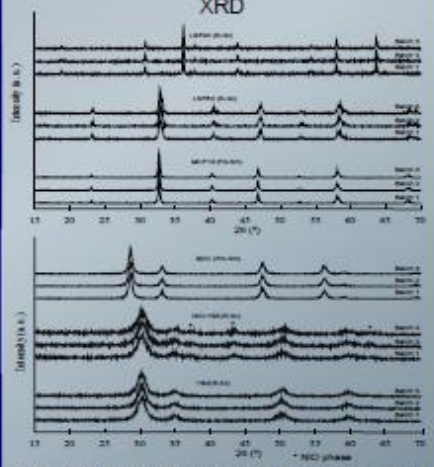

The purity of the samples were studied by X-ray diffraction. All the materials present the desired final phases. For the LNF60 compound, the appearance of extra shoulders in the experimental profile indicates a possible phase segregation to give two perovskite phase with different Ni/Fe ratio.

SEM

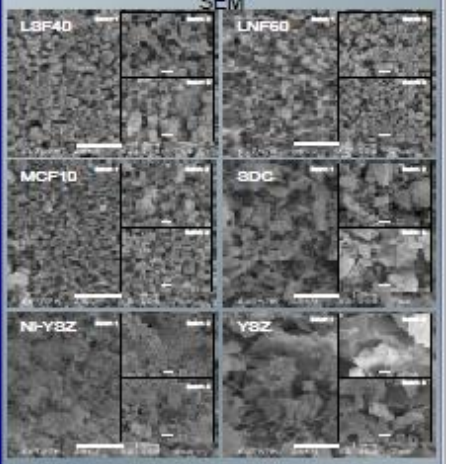

In all the cases, the agglomerates formed during the combustion reaction are usually soft and easy to break due to the higher escaping gases for these samples [3]. In addition, comparing the same compound between different batches, it can be shown that the particle sizes and shapes are homogeneous.

Conclusions

- Six fuel cell different compounds have been easily synthesized in big amounts by glycine-nitrate method with stoichiometric fuel/oxidizer ratio.
- The synthesis has demonstrated to be compositionally and morphologically reproducible in different batches. Therefore, it can be concluded that the glycine-nitrate process, with an optimal G/N ratio of 1.0, is an appropriate technique for preparing big quantities of different compounds for SOFC fabrication.

Acknowledgements

This research has been funded by the Ministerio de Economía y Competitividad (MAT2013-42092-R) and Dpto. Educación, Política Lingüística y Cultura of the Basque Goverment (IT-630-13). The authors thanks the support received by the European Regional Development Fund. (ERDF). SGIker of UPV/EHU technical support is gratefully acknowledged. A. Wain thanks Ministerio de Economía y Competitividad for funding his work (BES-2014-068433).

References

[1] N. Mahato, A. Banerjee, A. Gupta, S. Omar, K. Balani, *Progress in Materials Science*, 72 (2015) 141-337.
[2] D. Pereira, C. de Fraga, V. Caldas, *Powder Technology*, 269 (2015) 481-487.
[3] K. Vidal, A. Moran-Ruiz, A. Larrañaga, J. M. Porras-Vázquez, P. R. Slater, M. I. Arriortua, *Solid State Ionics*, 269 (2015) 24–29.

Book of Abstracts

The Energy and Materials Research Conference - EMR2017

Lisbon (Portugal), 5-7 April 2017

FORMATEX
RESEARCH CENTER

The Energy and Materials Research Conference - EMR2017
Lisbon (Portugal), 5-7 April 2017

Electrochemical and degradation behaviour study of different SOFC compounds

A. Wain-Martin[1], K. Vidal[1], A. Larrañaga[1], J. Rodríguez[2], M.A. Laguna-Bercero[3], R. Campana[2] and M.I. Arriortua[1,4]

[1] Departamento de Mineralogía y Petrología, Universidad del País Vasco (UPV/EHU), Sarriena s/n, 48080 Leioa, Spain
[2] Centro Nacional del Hidrógeno, Prolongación Fernando el Santo, s/n 13500 Puertollano, Spain
[3] Instituto de Ciencia de Materiales de Aragón, ICMA, CSIC-University of Zaragoza, Pedro Cerbuna 12, 50009 Zaragoza, Spain
[4] BCMaterials, Basque Center for Materials, Edificio No.500, Parque Tecnológico de Zamudio, 48160 Derio, Spain

The present work is focused on manufacturing processes of the solid oxide fuel cell (SOFC) components with previously self-synthesized materials by combustion method [1-2]. The configuration used consists of planar electrolyte-supported symmetric cells, with dense yttria-stabilized zirconia (YSZ) membranes about 20mm diameter and a thickness near 300µm.

Ni-yttria-stabilized zirconia cermet (Ni-YSZ) [3] and $La_{0.6}Sr_{0.4}FeO_3$ (LSF40) [4] layers were deposited on the surfaces of the electrolyte as anode and cathode, respectively. In order to decrease the interlayer reactivity and improve the contact between them, $Ce_{0.8}Sm_{0.2}O_{1.9}$ (SDC), $LaNi_{0.6}Fe_{0.4}O_3$ (LNF60) and $MnCo_{1.9}Fe_{0.1}O_4$ (MCF10) were added in different combinations as protection barrier [5], contact layer [6] and protective layer [7] material, respectively.

The deposition of the different compounds has been carried out by manual colloidal spraying, using an organic base solution, or by screen printing. Cross section SEM images have been done to study morphologically the different starting layers. In order to study the degradation of the samples after 500h of exposure time at a temperature of 800 ºC, the energy-dispersive X-ray spectroscopy analysis of the cross sectional micrographs has been evaluated. Electrochemical impedance spectroscopy was used to characterize the electrochemical properties of the different components and multilayer structures.

Keywords: SOFC; YSZ; anode cermet Ni-YSZ; cathode LSF40; SDC; LNF60; MCF10

References

[1] K. Vidal, A. Larrañaga, A. Morán Ruiz, A.T. Aguayo, M.A. Laguna-Bercero, M.P. Yeste, J.J. Calvino, M.I. Arriortua, International Journal of Hydrogen Energy, 41 (2016) 19810-19818.
[2] R.B. Nuernberg, M.R. Morelli, Ceramics International, 42 (2016) 4204-4211.
[3] T. Kawashima, S. Miyoshi, Y. Shibuta, S. Yamaguchi, Journal of Power Sources, 234 (2013) 147-153.
[4] A. Morán-Ruiz, K. Vidal, M.A. Laguna-Bercero, A. Larrañaga, M.I. Arriortua, Journal of Power Sources, 248 (2014) 1067-1076.
[5] Z. Wang, X. Huang, Z. Lv, Y. Zhang, B. Wei, X. Zhu, Z. Wang, Z. Liu , Ceramics International, 41 (2015) 4410-4415.
[6] M. Perz, E. Bucher, W. Sitte, T. Griesser, Solid State Ionics, 273 (2015) 30-34.
[7] X. Montero, F. Tietz, D. Sebold, H.P. Buchkremer, A. Ringuede, M. Cassir, A. Laresgoiti, I. Villarreal, Journal of Power Sources, 184 (2014) 172-179.

I Jornada de Jóvenes Investigadores de Cerámica y Vidrio en el ICMA

En colaboración con la
Sociedad Española de Cerámica y Vidrio

20 de Marzo de 2018

Universidad de Zaragoza
Facultad de Ciencias
Zaragoza - España

icma
Instituto de Ciencia de Materiales de Aragón

CSIC
Consejo Superior de Investigaciones Científicas

Universidad Zaragoza

CIENCIAS ZARAGOZA

SOCIEDAD ESPAÑOLA DE CERAMICA Y VIDRIO

http://www.unizar.es/icma/depart/laser/JJI/

SOCIEDAD ESPAÑOLA DE CERAMICA Y VIDRIO

I Jornada de Jóvenes Investigadores de Cerámica y Vidrio en el ICMA

"Procesado y caracterización de celdas de soporte electrolito de Pilas de Combustible de Oxido Solido(SOFC)"

A. Wain-Martin[1*], A. Morán-Ruiz[1], A. Larrañaga[1], M.Á. Laguna-Bercero[2], R. Campana[3], M.I. Arriortua[1,4]

[1]*Facultad de Ciencia y Tecnología,Universidad del País Vasco/Euskal Herriko Unibertsitatea (UPV/EHU), Sarriena s/n, 48940 Leioa, España*

[2]*CSIC-Universidad de Zaragoza, Instituto de Ciencia de Materiales de Aragón (ICMA), Pedro Cerbuna 12, 50009 Zaragoza, España*

[3]*Centro Nacional del Hidrógeno, Prolongación Fernando el Santo, s/n 13500 Puertollano, España 4 BCMaterials,Edif. Martina Casiano, 3. Planta., Parque científico UPV/EHU, Barrio Sarriena s/n, 48940 Leioa, España*

*aritza.wain@ehu.eus

Las pilas de combustible son sistemas que, mediante un proceso electroquímico, convierten de manera continúa la energía química en electricidad y calor mientras haya suministro de combustible y un agente oxidante. Este trabajo está enfocado en el procesado de componentes de pilas de combustible de óxido sólido (SOFC) sintetizados previamente [1], las cuales se caracterizan por poseer electrolito y electrodos cerámicos y por presentar temperaturas de operación elevadas (600-1000°C)[2]. La configuración empleada consiste en celdas planares (ánodo/electrolito/cátodo) soportadas por el electrolito (Figura 1). Para el procesado del electrolito se ha empleado una prensa hidráulica, obteniéndose pastillas de 20 mm de diámetro y 300µm de espesor. Éstas se han sinterizado a 1450 °C durante 5 h en aire, con objeto de alcanzar las propiedades físico-químicas adecuadas. La deposición de los componentes se ha realizado por espray manual coloidal. Para analizar el comportamiento electroquímico de la estructura multicapa, se han llevado a cabo medidas de impedancia a 800 °C. La morfología de los sistemas se ha estudiado a partir de análisis por energía dispersiva de rayos X (EDX) mediante las micrografías de las secciones transversales.

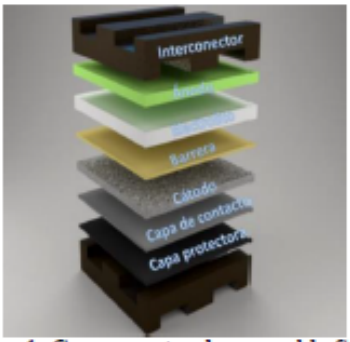

Figura 1: Componentes de una celda SOFC

Referencias:

[1]A. Wain-Martin et al. *Solid State Ion.* 313 (2017) 52-57.

[2]L.S. Mahmud et al. *Renew. Sust. Energ. Rev.* 72 (2017) 105-116.

Agradecimientos: Esta investigación ha sido financiada por el Ministerio de Economía y Competitividad (MAT2016- 76739-R)(AEI/FEDER, UE) y el Dpto. Educación del Gobierno Vasco (IT-630-13). Los autores agradecen a los SGIker por el apoyo técnico (UPV/EHU). A. Wain-Martin agradece al Ministerio de Economía y Competitividad la financiación de su trabajo (BES-2014-068433).

Universidad del País Vasco Euskal Herriko Unibertsitatea

Proceedings of

13th European SOFC & SOE Forum 2018

Chapter 07 - Session A15

Cell and Stack Design & Characterisation

Edited by

Prof. Ellen Ivers-Tiffée (Chair)
Dr. André Weber (Chair)
Dr. Laura Almar
Prof. Ludger Blum
Dr. Cornelia Endler-Schuck
Mr. Andreas Häffelin
Mr. Dino Klotz
Dr. Mihails Kusnezoff
Mr. André Leonide
Mr. Jean-Claude Njodzefon
Ms. Annika Utz
Dr. Stefan Wagner

Co-Edited by

Olivier Bucheli
Gabriela Geisser
Fiona Moore
Dr. Michael Spirig

ISBN 978-3-905592-23-8

www.EFCF.com/Lib

13th European SOFC & SOE Forum www.EFCF.com/Lib ISBN 978-3-905592-23-8 3 - 6 July 2018, Lucerne/Switzerland

A1511 (Published elsewhere)

Development of a SOFC cell with self-made nanopowders

Aritza Wain-Martin (1), Roberto Campana (2), Aroa Morán-Ruiz (1), Jesus Rodríguez (2), Aitor Larrañaga (1), Maria Isabel Arriortua (1,3)
(1) Universidad del País Vasco/ Euskal Herriko Unibertsitatea (UPV/EHU). Facultad de Ciencia y Tecnología. Barrio Sarriena s/n, 48940 Leioa, Spain
(2) Centro Nacional del Hidrógeno, Prolongación Fernando el Santo s/n, 13500 Puertollano (Ciudad Real), Spain
(3) BCMaterials, Basque Center for Materials, Applications and Nanostructures, Bld. Martina Casiano, 3rd. Floor UPV/EHU Science Park, Barrio Sarriena s/n, 48940 Leioa, Spain
Tel.: +34-94-601-5984
Fax: +34-94-601-3500
aritza.wain@ehu.eus

Abstract

The fabrication methods for planar SOFCs have been found to be simple and inexpensive. The selection of a suitable fabrication method for each component of planar SOFCs usually depends on the cell structures and whether the SOFCs are electrolyte-supported or electrode-supported [1].

This work describes the manufacture and characterization of anode supported planar SOFCs for high temperature operation using self-made materials [2]. The developed cells consist of a Ni–YSZ anode support (800 µm thickness and 18 mm diameter), a 15–20 µm thickness YSZ electrolyte and a 10 µm $La_{0.6}Sr_{0.4}FeO_3$ (LSF40) cathode. 5 µm $Sm_{0.2}Ce_{0.8}O_{1.9}$ (SDC) as barrier has been added between the electrolyte and the cathode. The anode supports were prepared by uniaxial pressing and the deposition of thin layers of electrolyte, barrier, cathode and contact layer were made by manual spray coating. The cells were characterized by Scanning Electron Microscopy (SEM) with Energy Dispersive X-ray Spectroscopy (EDX).

The cells were also electrochemically characterized in a button cell test rig (NorECs). The polarization curves and Electrochemical Impedance Spectroscopy (EIS) measurements were performed by a multichannel Potentiostat/Galvanostat VMP3 (Biologic), using 100% of H_2 humidified at 3% as reactant gas in the anodic compartment and air in the cathodic one at temperatures between 750 and 900 C.

Introduction

Solid Oxide Fuel Cells (SOFC) are one of the most promising technologies for the obtaining of clean energy with high efficiency for direct conversion of chemical energy into power [1]. For the implementation of these systems on the market and make them economically competitive, improving materials and manufacturing processes is constantly required. Therefore, the expensive and complex processing steps for anode-supported electrolyte tapes could be replaced by cheaper, simpler and continuous techniques.

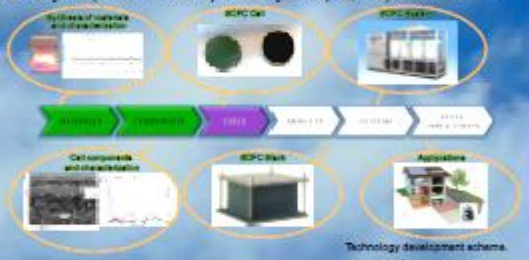

Technology development scheme.

Objectives

The current work describes the fabrication process with previously self synthesized components [2] (Ni-YSZ, YSZ, SDC and LSF) which were developed and applied for the creation of a fuel cell. Anode support was carried out via uniaxial pressing and the deposition of thin layers of electrolyte, barrier and cathode was made by manual spray coating. The microstructure was characterized by Scanning Electron Microscopy (SEM) and Energy Dispersive X-ray Spectroscopy (EDX). The electrochemical response of this assembly was studied using Current-voltage (I-V) and current-power (I-P) curves and electrochemical impedance spectroscopy (EIS).

Experimental procedure

High scale synthesis of the components of the cell has been done through glycine-nitrate combustion method.

The supporting anodes were done by uniaxial pressing after adding starch.

The starting powders were grinded through wet ball-milling, by adding the appropriate amount of solvent (2-propanol), at 180 rpm for 24 h.

The deposition of the layers was carried out at room temperature, through an airbrush.

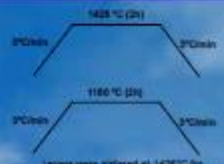

Layers were sintered at 1425°C for 2 h in the case of Ni-YSZ/YSZ tapes and at at 1150°C for 2 h in the case of LSF, LSF-SDC and SDC layers.

Characterization

SEM-EDX

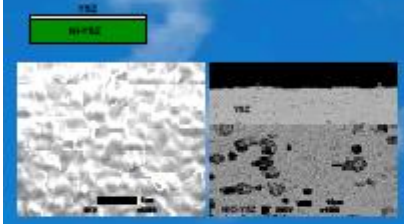

It can be seen from the images that the YSZ layer is well sintered, with closed pores and enough dense electrolyte to avoid fuel leakage. The contact between the layers is also correct after the measurement.

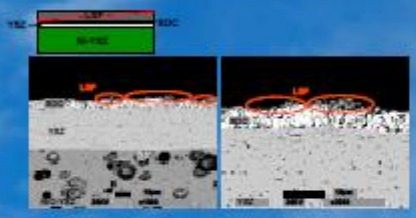

The group tried to spray directly the LSF on top of SDC barrier layer but thermal expansion coefficient (TEC) mismatch between the layers resulted in contact loses and the delaminations of the top layer.

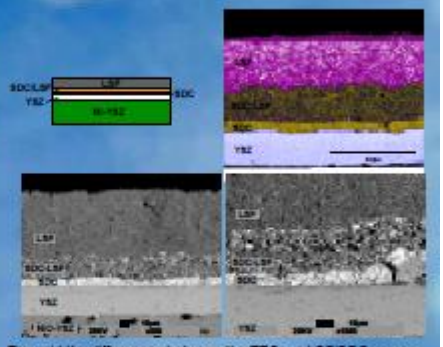

To avoid the differences between the TECs, a LSF/SDC composite layer was deposited between SDC and LSF layers improving the contact between them. As can be seen, no cracking or delamination are observed in the LSF layer. The composite with thickness of 20 µm has been found to show a good adherence with LSF and SDC layers. The electrodes show the typical porous microstructure and the layers are continuous.

Electrochemical characterization

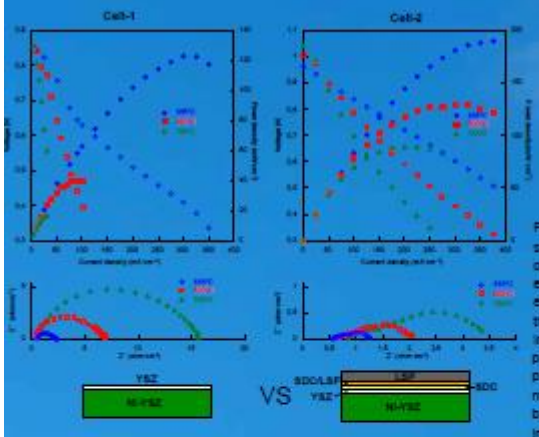

Cell	T (°C)	R_0 (Ωcm²)	R_1 (Ωcm²)	C_1 (Fcm⁻²)	$f_{0,1}$ (Hz)	R_2 (Ωcm²)	C_2 (Fcm⁻²)	$f_{0,2}$ (Hz)	R_{Total} (Ωcm²)
Nº1	750	0.363	5.487	$1.9*10^{-3}$	1472	10.0	$3.9*10^{-6}$	410	15.860
	800	0.330	3.542	$1.2*10^{-3}$	3800	3.12	$1.1*10^{-4}$	480	6.992
	865	0.217	1.617	$4.8*10^{-3}$	2017	1.34	$7.6*10^{-5}$	1560	3.172
Nº2	750	0.819	0.447	$2.9*10^{-4}$	1237	2.33	$4.1*10^{-2}$	1.68	3.599
	800	0.550	0.458	$5.1*10^{-4}$	683	1.10	$6.2*10^{-2}$	2.34	2.104
	865	0.517	0.407	$4.3*10^{-3}$	90	0.34	$4.4*10^{-1}$	1.04	1.270

For the electrochemical characterization two cells have been measured. The cell 1 has only the YSZ layer on top of the anode support, using a platinum paste as cathode. The cell-2 has Ni-YSZ/YSZ/SDC/SDC-LSF/LSF configuration. The obtained open circuit voltage (OCV) in cell 1 and cell 2 reach 0.912 V and 1.066 V at 865ºC, respectively. This, proves that the YSZ electrolyte layer was dense enough without gas cross over, and that the performance of the sealing components was excellent [3]. As might be seen comparing the two cells, the OCV and the maximum power densities of the cell 1 are lower than the cell-2. In the case of cell 1 can be though that the bigger contributor to the Ro is the YSZ electrolyte. The benefit of introducing the cathode side was clearly demonstrated by the R_{Total} reduction observed for the cell-2. The increment in peak power densities and the reduction in total interfacial polarization resistance must derive from the enhanced electrochemical performance associated with the cathode, since the anode and the electrolyte are the same in the two cells. This improvement, correspond to a better adhesion between the porous cathode and the current collector (the platinum paste) and because the cathode enhance the oxygen reduction reaction, increasing number of contact points at electrode-electrolyte interface.

Conclusions

- The simultaneous production of supporting anode and electrolyte have been prepared by sintering the two compounds together.
- Manual spray coating has demonstrated to be an adequate technique in order to create dense YSZ layers and porous SDC, SDC/LSF and LSF layers.
- The incorporation of SDC/LSF layer between the SDC barrier and LSF cathode has improve the contact, avoiding delamination and cracks of the cathode.
- To evaluate the cathode side of the cell, electrochemical impedance spectroscopy and current-voltage (I-V) and current-power (I-P) curves were performed, and a significant decrease in the ASR was achieved in the Ni-YSZ/YSZ/SDC/SDC-LSF/LSF configuration. The lowest ASR or 0.752 Ω cm² at 865ºC corresponds to the cell-2.

Acknowledgments

This research has been funded by the Ministerio de Economía, Industria y Competitividad (MAT2016-76739-R (AEI, FEDER,UE)) and Dpto. Educación of the Basque Goverment (IT-630-13). SGIker of UPV/EHU technical support is gratefully acknowledged. A. Wain-Martin thanks Ministerio de Economía, Industria y Competitividad for funding his work (BES-2014-068433).

References

[1] V. Gil, J. Gurauskis, R. Campana, R.I. Merino, A. Larrea, V.M. Orera, Journal of Power Sources, 196 (2011) 1184-1190.
[2] A. Wain-Martin, A. Morán-Ruiz, K. Vidal, A. Larrañaga, M.A. Laguna-Bercero, M.I. Arriortua, Solid State Ionics, 313 (2017) 52-57.
[3] D. Yan, L. Liang, J. Yang, T. Zhang, J. Pu, B. Chi, J. Li, Energy, 125 (2017) 663-670.

8.2. Resultados vinculados a trabajos del grupo

Publicaciones

1.- Luis-Ortega-San-Martin, Aroa Morán-Ruiz, **Aritza Wain-Martin,** Karmele Vidal, Aitor Larrañaga, Maria Isabel Arriortua, Combustion synthesis and characterization of $Ln_{1-x}M_xCr_{0.9}Ni_{0.1}O_3$ (Ln= La and/or Nd; M=Sr and/or Ca; $x \leq 0.25$) perovskites for SOFCs, *Ceram. Int*. 44 (**2018**) 2240-8. [Q1, Impact factor: 3.057]

2.- Aroa Morán-Ruiz, **Aritza Wain-Martin,** Alodia Orera, Maria Luisa SanJuan, Aitor Larrañaga, Peter Raimond Slater, Maria Isabel Arriortua, Synthesis of new $Ln_4(Al_2O_6F_2)O_2$ (Ln = Sm, Eu, Gd) phases with a cuspidine-related structure, *IUCRJ*, 6 (**2019**) 128-135. [Q1, Impact factor: 6.544]

Congresos

1.- World Hydrogen Energy Conference. Zaragoza, 13-16 de Junio de 2016.
Autores: Aroa Morán-Ruiz, Aritza Wain-Martin, Karmele Vidal, Aitor Larrañaga, Miguel Angel Laguna-Bercero, Maria Isabel Arriortua.
Título: Degradation study of ceramic vs metallic half-cells for SOFCs.
Presentación: Póster

2.- World Hydrogen Energy Conference. Zaragoza, 13-16 de Junio de 2016.
Autores: Iñigo Perez-Fernandez, Aritza Wain-Martin, Aroa Morán-Ruiz, Karmele Vidal, Aitor Larrañaga, Maria Isabel Arriortua.
Título: Optimization of the large scale synthesis of LSF-20 cathode material for SOFCs.
Presentación: Póster

3.- International discussion on hydrogen energy and applications. Nantes, 2-4 de Noviembre de 2016.
Autores: Luis Ortega-San-Martín, Aritza Wain-Martin, Aroa Morán-Ruiz, Karmele Vidal, Aitor Larrañaga, Maria Isabel Arriortua.
Título: Effect of doping level x in $Ln_{1-x}M_xCr_{0.9}Ni_{0.1}O_3$ SOFC anodes.
Presentación: Oral

4.- VI symposium on Hydrogen, Fuel Cells and Advanced Batteries. Oporto, 19-23 de Junio de 2017.
Autores: Luis Ortega-San-Martín, Aritza Wain-Martin, Aroa Morán-Ruiz, Karmele Vidal, Aitor Larrañaga, Miguel Angel Laguna-Bercero, Maria Isabel Arriortua.
Título: Effect of doping level x and fuel on glycine-nitrate combustion synthesis of $(La,Nd)_{1-x}(Sr,Ca)_x\ Cr_{0.9}Ni_{0.1}O_3$ ($x \leq 0.25$) perovskites as anode materials for SOFCs.
Presentación: Oral

5.- 4th International symposium on the catalysis for clean energy and sustainable chemistry. Bilbao, 9-11 de Julio de 2018.
Autores: Roberto Campana, Aritza Wain-Martin, Jonas Gurauskis, Aitor Larrañaga, Maria Isabel Arriortua.
Título: SOFC development at CNH_2.
Presentación: Oral

Ceramics International 44 (2018) 2240–2248

Contents lists available at ScienceDirect

Ceramics International

journal homepage: www.elsevier.com/locate/ceramint

Combustion synthesis and characterization of $Ln_{1-x}M_xCr_{0.9}Ni_{0.1}O_3$ (Ln = La and/or Nd; M = Sr and/or Ca; $x \leq 0.25$) perovskites for SOFCs anodes

L. Ortega-San-Martín[a,*], A. Morán-Ruiz[b], A. Wain-Martin[b], K. Vidal[b,*], A. Larrañaga[b], M.A. Laguna-Bercero[c], M.I. Arriortua[b,d,**]

[a] Departamento de Ciencias, Sección Química, Pontificia Universidad Católica del Perú (PUCP), Av. Universitaria 1801, Lima 32, Peru
[b] Facultad de Ciencia y Tecnología, Universidad del País Vasco/Euskal Herriko Unibertsitatea (UPV/EHU), Sarriena s/n, 48940 Leioa, Spain
[c] CSIC-Universidad de Zaragoza, Instituto de Ciencia de Materiales de Aragón (ICMA), Pedro Cerbuna 12, 50009 Zaragoza, Spain
[d] BCMaterials, Parque Tecnológico de Zamudio, Ibaizabal Bidea, Edificio 500- Planta 1, 48160 Derio, Spain

ARTICLE INFO

Keywords:
Chemical synthesis
Electrical conductivity
SOFC
Anode
A-site

ABSTRACT

A series of chromite perovskites with the general formula $Ln_{1-x}M_xCr_{0.9}Ni_{0.1}O_3$ (Ln = La and/or Nd; M = Sr and/or Ca; $x \leq 0.25$) has been prepared by three combustion synthesis routes using a different combustible substance each time: glycine, urea and sucrose. In order to isolate the effect of divalent dopant concentration from the A cation steric effects, the whole group has a fixed mean A cation radius, $< r_A > \approx 1.22$ Å, and cation size disorder, $\sigma^2(r_A) \approx 0.0001$ Å^2, but variable doping x. Their crystal structure, microstructure, electrical properties and expansion coefficients have been investigated on the basis of their possible use as anode materials for intermediate temperature solid oxide fuel cells (SOFC). Cell parameters, grain sizes, expansion coefficients and conductivities all are found to be dependent on x and the combustible substance used. The most interesting relationship is the negative dependence of the conductivity with x under H_2 atmosphere: conductivity decreases with doping which is the opposite to the expected behavior for a p-type doped perovskites and has not been reported before.

1. Introduction

The research to find new or to improve the most commonly used materials in solid oxide fuel cells (SOFC) is still a important field in materials science [1]. In particular, one of the most active area is the study of SOFC anodes because the operation of commercial SOFC devices is strongly dependent on the behavior of this electrode, which is in contact with the fuel (and all its impurities) [2]. The number of materials studied as possible anodes is huge and, among them, perovskites have also gained attraction due to their good catalytic properties, high ionic and electrical conductivities, and their chemical and thermal stabilities at high temperatures.

The main concern for current nickel-yttria stabilized zirconia cermet anodes is that they are unable to work efficiently with hydrocarbon fuels at intermediate operating temperature range (600–800 °C) due to their sulfur content and also as a consequence of carbon deposition [3]. Hence, there is still a demand for the development of alternate anode materials with improved tolerance towards carbon deposition and sulfur poisoning to improve the fuel flexibility and efficiency of SOFCs.

Oxide-perovskites have been widely studied as possible cathode electrodes for a long time due to their mixed ionic and electronic conductivity (MIEC), high catalytic activity and good stability under oxidizing conditions [1,4]. To be used as anodes, however, perovskites need to be stable under reducing conditions. Among the oxide perovskites that have good catalytic properties and appropriate MIEC, only chromites are reasonably stable in reducing atmospheres and this is why they have been thoroughly investigated as SOFC-interconnectors [5] and also proposed as possible anodes [6–11]. From the thermodynamic point of view, chromites are expected to react with the common YSZ electrolyte but in practice, this only occurs to a great extent at temperatures above the operation ones (that is, higher than 1000 °C) [12].

When a material is evaluated as a SOFC component, it is also important to consider its preparation costs. Perovskites are usually prepared at high temperatures so another important field of research is aimed at reducing energy consumption of the synthesis [13]. Combustion synthesis routes, which involve low cost materials, short processing time and produce large amount of gases that inhibit particle size

* Corresponding authors.
** Corresponding author at: Facultad de Ciencia y Tecnología, Universidad del País Vasco/Euskal Herriko Unibertsitatea (UPV/EHU), Sarriena s/n, 48940 Leioa, Spain.
E-mail addresses: lortegas@pucp.edu.pe (L. Ortega-San-Martín), karmele.vidal@ehu.es (K. Vidal), maribel.arriortua@ehu.es (M.I. Arriortua).

http://dx.doi.org/10.1016/j.ceramint.2017.10.182
Received 30 August 2017; Received in revised form 23 October 2017; Accepted 25 October 2017
Available online 31 October 2017

Table 1
Nominal stoichiometries, mean radii and A-site disorder values of the $Ln_{1-x}M_xCr_{0.9}Ni_{0.1}O_3$ perovskites.

x	$Ln_{1-x}M_xCr_{0.9}Ni_{0.1}O_3$	$< r_A >$ (Å)	$\sigma^2(r_A)$ (Å^2)*
0.10	$La_{0.80}Nd_{0.05}Sr_{0.10}Cr_{0.90}Ni_{0.10}O_3$	1.22	0.00010
0.15	$La_{0.80}Nd_{0.05}Sr_{0.10}Ca_{0.05}Cr_{0.90}Ni_{0.10}O_3$	1.22	0.00011
0.20	$La_{0.80}Sr_{0.10}Ca_{0.10}Cr_{0.90}Ni_{0.10}O_3$	1.22	0.00011
0.25	$La_{0.75}Sr_{0.10}Ca_{0.15}Cr_{0.90}Ni_{0.10}O_3$	1.22	0.00011

* Cation size disorder has been calculated using the equation $\sigma^2(r_A) = < r_A^2 > - < r_A >^2$ and ninefold coordination radii for the A-site cations (see text).

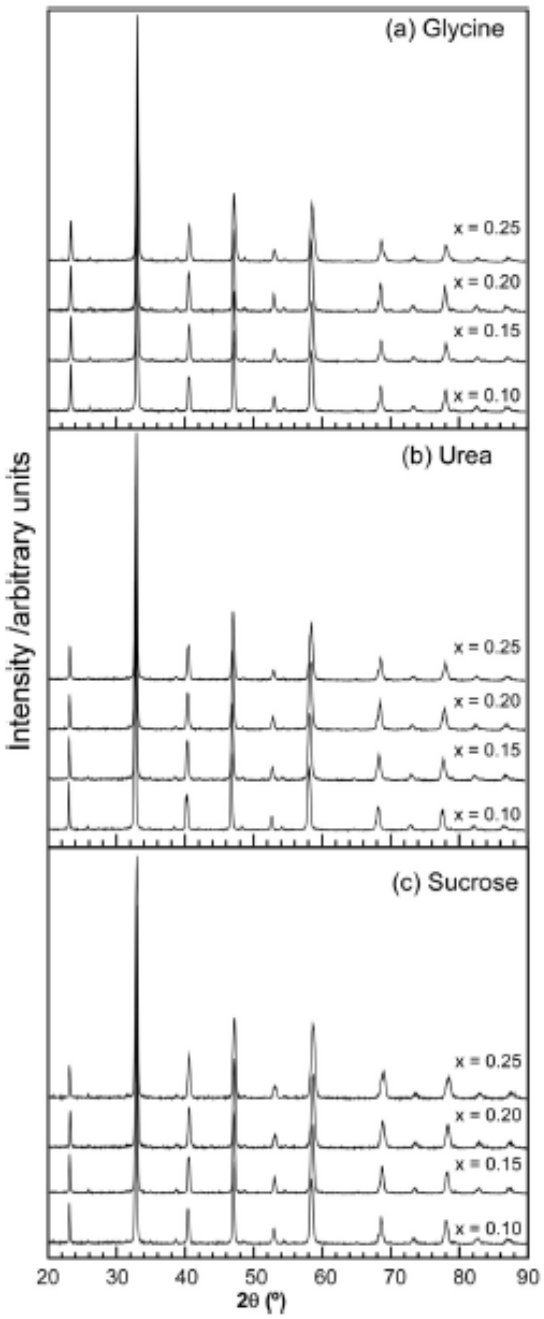

Fig. 1. X-ray diffraction patterns for the series $Ln_{1-x}M_xCr_{0.9}Ni_{0.1}O_3$ (Ln = La and/or Nd; M = Sr and/or Ca; x ≤ 0.25) prepared using (a) glycine, (b) urea and (c) sucrose as combustible agents.

Table 2
Summary of the ICP results for the $Ln_{1-x}M_xCr_{0.9}Ni_{0.1}O_3$ perovskites.

x	Fuel	$Ln_{1-x}M_xCr_{0.9}Ni_{0.1}O_3$
0.10	Glycine	$La_{0.86(1)}Nd_{0.04(1)}Sr_{0.11(1)}Cr_{0.90(2)}Ni_{0.10(1)}$
	Urea	$La_{0.87(1)}Nd_{0.05(1)}Sr_{0.10(1)}Cr_{0.90(2)}Ni_{0.11(1)}$
	Sucrose	$La_{0.85(1)}Nd_{0.05(1)}Sr_{0.11(1)}Cr_{0.90(2)}Ni_{0.11(1)}$
0.15	Glycine	$La_{0.76(1)}Nd_{0.04(1)}Sr_{0.11(1)}Ca_{0.07(1)}Cr_{0.90(1)}Ni_{0.10(1)}$
	Urea	$La_{0.79(1)}Nd_{0.05(1)}Sr_{0.10(1)}Ca_{0.05(1)}Cr_{0.90(1)}Ni_{0.10(1)}$
	Sucrose	$La_{0.81(1)}Nd_{0.06(1)}Sr_{0.10(1)}Ca_{0.06(1)}Cr_{0.90(1)}Ni_{0.10(1)}$
0.20	Glycine	$La_{0.82(1)}Sr_{0.10(1)}Ca_{0.09(1)}Cr_{0.90(2)}Ni_{0.10(1)}$
	Urea	$La_{0.80(1)}Sr_{0.10(1)}Ca_{0.11(1)}Cr_{0.90(2)}Ni_{0.10(1)}$
	Sucrose	$La_{0.81(1)}Sr_{0.11(1)}Ca_{0.10(1)}Cr_{0.90(2)}Ni_{0.11(1)}$
0.25	Glycine	$La_{0.74(1)}Sr_{0.08(2)}Ca_{0.16(1)}Cr_{0.90(2)}Ni_{0.11(1)}$
	Urea	$La_{0.75(1)}Sr_{0.09(2)}Ca_{0.15(1)}Cr_{0.90(2)}Ni_{0.10(1)}$
	Sucrose	$La_{0.75(1)}Sr_{0.11(1)}Ca_{0.13(1)}Cr_{0.89(2)}Ni_{0.10(1)}$

growth, are of great interest in synthesizing nano-size powders with high specific surface area [14]. In this type of synthesis, the combustion velocity, the choice of the combustible substance and its amount are very important factors that influence the final properties of the obtained powder [15]. The effect of the type of combustible substance on the electrochemical properties of SOFC materials has not been investigated in detail and, consequently, its role is unclear [16].

In this study, we investigate two effects: (i) the variation of the doping level x and (ii) the use of different combustible substances (glycine, urea and sucrose) during the synthesis by the combustion method in the structure and electrical properties of a series of new chromite perovskites with the formula $Ln_{1-x}M_xCr_{0.9}Ni_{0.1}O_3$ (Ln = La and/or Nd; M = Sr and/or Ca; x ≤ 0.25). To avoid the interplay of different A-site variables in their properties the mean ionic radius $< r_A >$ (1.22 Å) and the cation size disorder $\sigma^2(r_A)$ (0.0001 Å^2) have been kept constant. To meet these requirements up to four different A cations were used in the same oxide. Low disorder has been selected from previous studies which showed that the higher the disorder the lower the performance of the oxides irrespective their field of application [17–21]. On the other hand, the chemical compositions have been selected bearing in mind the maximum solubility of calcium and strontium in chromites (x < 0.3 for both of them) and considering that they had to contain strontium as its presence improves the stability of the perovskite under low oxygen partial pressures [12]. X-ray powder diffraction (XRD), scanning electron microscopy (SEM), electrical measurements and thermal expansion studies have been also carried out.

2. Experimental

2.1. Powder preparation

$Ln_{1-x}M_xCr_{0.9}Ni_{0.1}O_3$ samples were prepared by combustion synthesis using $La(NO_3)_3 6H_2O$ (> 99%), $Nd(NO_3)_3 6H_2O$ (99.9%), $Sr(NO_3)_2$ (99.99%), $Ca(NO_3)_2 H_2O$ (99.997%), $Ni(NO_3)_2 6H_2O$ (99.999%) and $Cr(NO_3)_3$ (> 99%) as metal precursors and glycine, urea and sucrose (all from Aldrich, > 99%) as combustible substances. The prepared compositions, together with their mean ionic radius, $< r_A >$, and A cation size disorder, $\sigma^2(r_A)$, are summarised in Table 1. It is to note that disorder (quantified as $\sigma^2(r_A) = < r_A^2 > - < r_A >^2$) has been calculated using ninefold coordination radii for the A site cations [22] in order to be consistent with previous literature data and because this is the expected coordination for an orthorhombic perovskite [23] such as the parent $LaCrO_3$ [24].

The metal nitrates were dissolved in distilled water. The solutions (dissolved metal nitrates) were mixed in a glass beaker, which was placed on a hot plate at 100 °C to evaporate excess water under constant stirring. Then, the glycine, urea or sucrose was added to obtain a molar ratio of 1 with the oxidizer. The resulting viscous liquid started autoignition just after placing the glass beaker directly onto a preheated

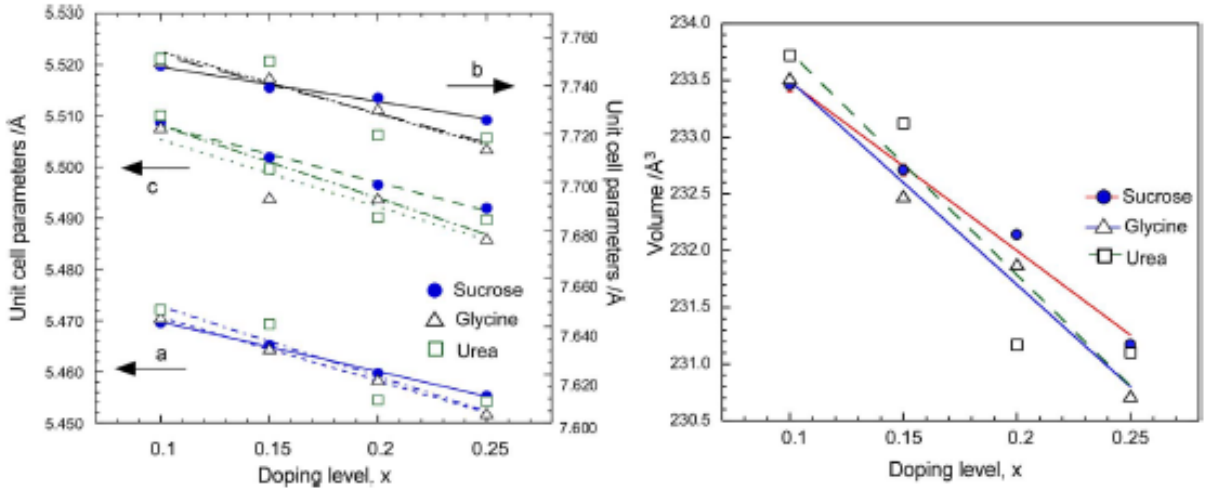

Fig. 2. Variation of the unit cell parameters and volume with doping for the samples obtained using different fuels. Lines are linear fits in all cases.

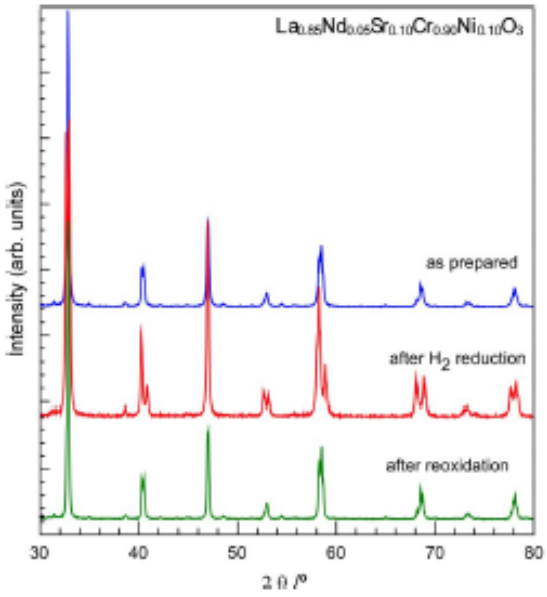

Fig. 3. Comparison of the XRD data taken for x = 0.1 phase under different atmosphere conditions: as –synthesised, after H_2-conductivity test and after reoxidation in air.

plate (at 350 °C). The obtained powders were calcined at 800 °C for 2 h to remove the carbon residues and, after that, these samples were pressed at 45 MPa to form 13 mm diameter pellets by a manual hydraulic press. Pellets were calcined in air for 10 h at temperatures up to 1200 °C until pure samples were obtained. This was achieved after two or three repetitions, the samples being ground and pelletised again for each calcination step.

2.2. Characterization techniques

The structural analysis was performed using laboratory X-ray diffraction (XRD). XRD data were collected from 15 to 90° in 2θ with an integration time of 500 s/0.026° step using a Philips X'Pert-PRO X-ray diffractometer using copper Kα radiation without Ni-filter and a PIXcel solid state detector (active length in 2θ 3.347°). A fixed divergence and antiscattering slit giving a constant volume of sample illumination were used. The crystal structure was refined by the Rietveld method using the GSAS software package [25] and EXPGUI interface [26].

All metal contents were determined by inductively coupled plasma atomic emission spectroscopy (ICP-AES) on a Horiba Yobin Yvon Activa spectrophotometer. For this purpose, samples were dissolved using a mixture of HNO_3 and HCl for two days to obtain a clear and measurable solution.

Prior to bulk conductivity and dilatometry measurements pellets of the as-synthesised powders were sintered at 1350 °C for 10 h and, subsequently, cut into rectangular bars. The bulk density of each sample was estimated by measuring the mass and the dimensions of the bars using a digital micrometer (Mitutoyo, Japan). DC conductivity measurements were performed under pure H_2 by the four-point DC method from 800 to 400 °C using a VSP potentiostat controlled by PC using Lab Windows/CVI field point system. Electrical contacts were made using Pt wires and Pt paste placed over whole end faces ensuring a homogeneous current flow. Prior to the start of the measurements, each oxide was kept at 800 °C for 12 h under flowing H_2 at a rate of 120 ml/min (oxygen partial pressure nearly 10^{-21} atm). Conductivity data were corrected considering the experimental density values (all around 85% of the theoretical (X-ray) density).

Thermal expansion coefficients were measured from room temperature to 950 °C under air with a heating rate of 5 °C min^{-1} using a Unitherm Model 1161 dilatometer. Morphologies of the as-synthesised powder samples and the sintered pellets were observed using a scanning electron microscope (JEOL JSM-7000F). Secondary electron images were taken at 20 kV and 1.1.10^{-11} A.

3. Results and discussion

3.1. Structural study

Room temperature X-ray diffraction patterns of all as-synthesised oxide perovskites are shown in Fig. 1. The patterns reveal that all the samples are single-phase and no impurities are detected within the resolution limits of the used technique.

Results from chemical analyses, presented in Table 2, show a good agreement between the analysed chemical compositions of the prepared powders and the nominal compositions.

Rietveld fits to the powder X-ray diffraction data were carried out using the orthorhombic (*Pnma*) space group, the same observed for the parent $LaCrO_3$ phase at room temperature [24], considering the nominal composition in the different sites of the crystal structure. Only three independent thermal parameters were used in the refinements (one for the A-site cations, another for the B-site ones and a final one for all the oxygen atoms). Graphs of the Rietveld fits to all the oxides

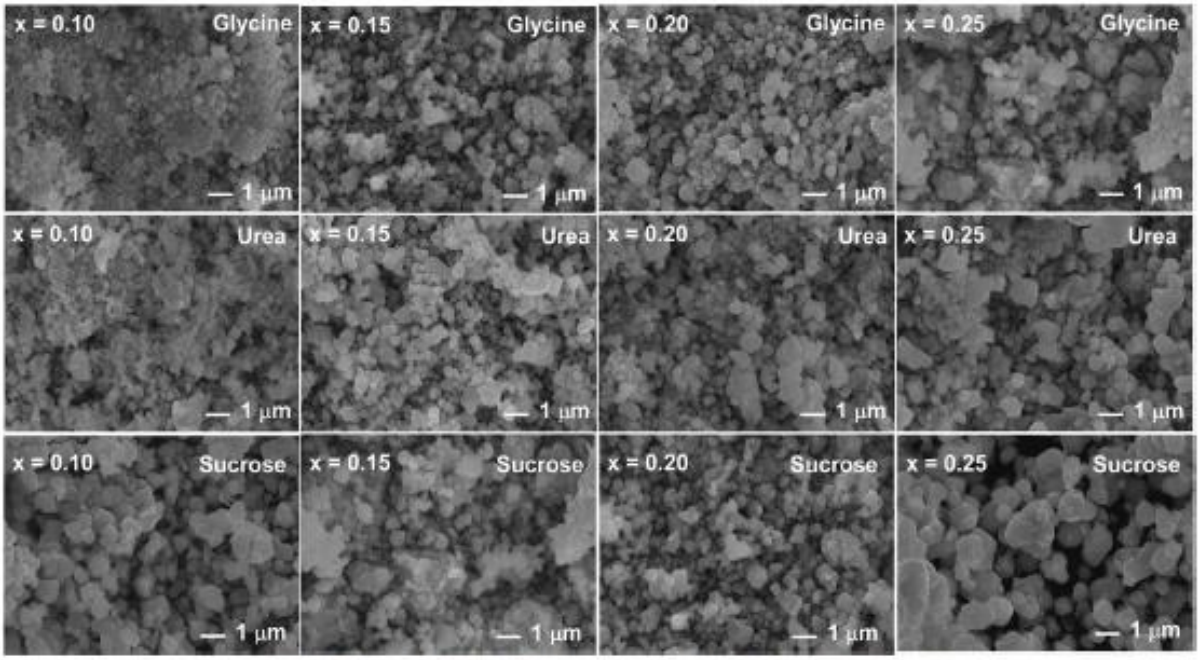

Fig. 4. SEM micrographs of $La_{1-x}M_xCo_{0.9}Ni_{0.1}O_3$ perovskites calcined between 1100 and 1200 °C.

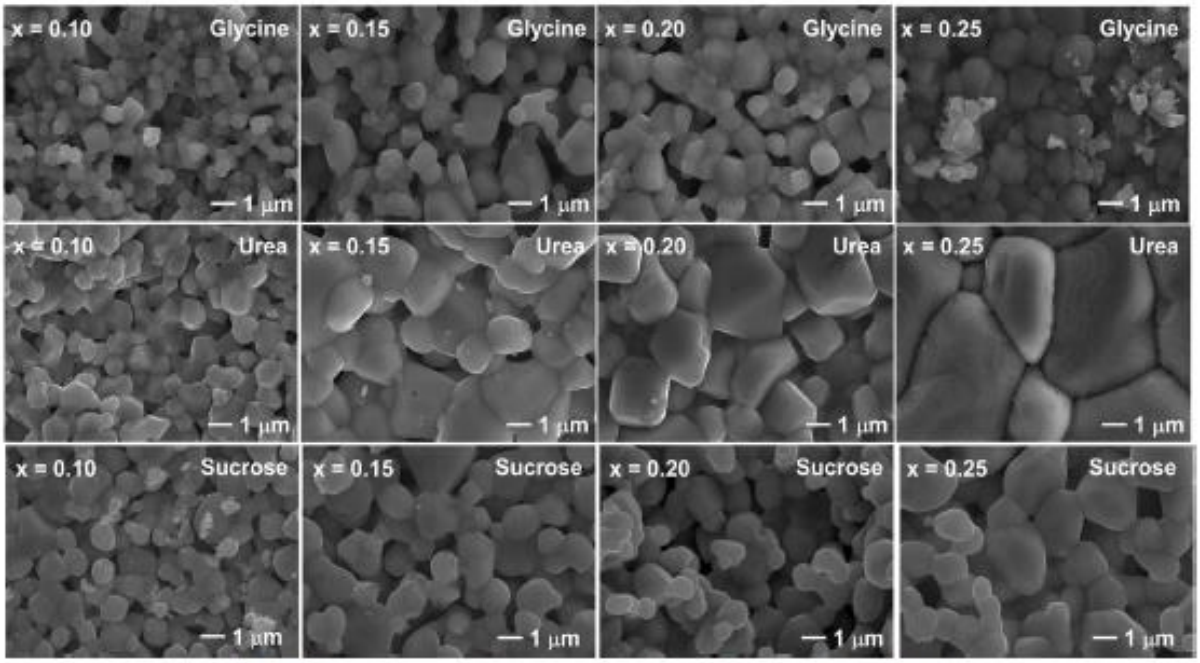

Fig. 5. SEM micrographs taken on the surface of the pellets sintered at 1350 °C in air for 10 h.

prepared are shown in supplementary Figs. S1–S3.

The variation of the unit cell parameters and cell volume with doping (x) is shown in Fig. 2. As it can be observed, there is a systematic decrease in volume with increasing divalent dopant content. This behavior cannot be associated with changes in the A position because the variables that influence lattice volume, such as the A-site mean ionic radius $< r_A >$ and the A-site disorder [27], have been kept constant throughout the series. Therefore, the observed decrease of the lattice parameters can be only associated with the reduction of the B-site (chromium and nickel) mean ionic radii ($< r_B >$) as a consequence of their oxidation with the increase of the doping level x (the ionic radii in octahedral coordination of Cr and Ni decrease from $r_{(Cr3+)} = 0.615$ Å and $r_{(Ni2+)} = 0.69$ Å to $r_{(Cr4+)} = 0.55$ Å, and $r_{(Ni3+)} = 0.56$ Å, respectively) [22].

The structural parameters, atomic distances and R factors obtained by Rietveld refinement to the X-ray data of all the compounds obtained using the different combustible substances are displayed in Tables S1–S3 of the supplementary information. According to our data, there are not many structural variations along the series with doping apart from the compression of the unit cell, as expected.

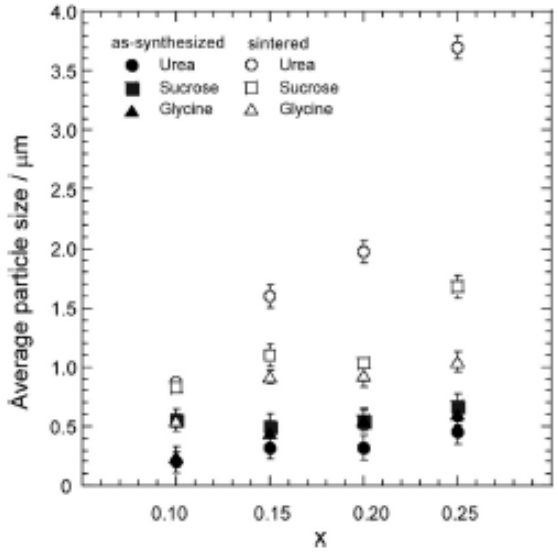

Fig. 6. Doping and fuel dependence of the average particle sizes calculated from SEM images.

The crystal structure of the oxides was also studied after the conductivity measurements that were carried out under hydrogen atmosphere in order to establish the stability of the samples. It is interesting to note that the room temperature XRD data showed that none of the samples degraded and all were single phase after the treatment but with a different crystal structure: data were fitted to a *R*-3*c* distorted perovskite. This indicates that the oxides retain the high temperature phase of the parent $LaCrO_3$ which experiments a *Pnma* → *R*-3*c* phase transition above 250 °C [24]. This higher symmetry structure is probably a result of the rearrangement of the atoms that resulted from the oxygen loss at temperatures between 400–800 °C. Nevertheless, the initial crystal structure is fully recovered after the oxides are heated again in air at 800 °C. Fig. 3 shows the x = 0.1 oxide prepared using sucrose as a representative example. No impurities are observed after this cycle which further supports that these oxides are thermally stable as expected for anode perovskites.

3.2. Morphological study

Representative SEM micrographs of the powder samples obtained by the combustion method using glycine, urea and sucrose after final calcination (as-synthesised powders) are shown in Fig. 4.

These powders are composed of agglomerates formed by very small size particles. The average size of the grains calculated by direct SEM observation ranges from 200 to 250 nm observed for the x = 0.10 oxide prepared using glycine to 550–600 nm observed for the x = 0.25 phase prepared using sucrose. It is interesting to note that the average particle size slightly increases with x irrespective of the synthesis method, being the x = 0.25 oxides the ones that show the biggest grain sizes.

Usually, smaller crystallite sizes are formed when the combustion temperature is not very high and, specially, when a large volume of gases is evolved because this further enhances the dissipation of heat and limits the inter-particle contact, preventing grain growth. The comparison of combustible substances in the literature [15,28,29], however, are not definitive regarding to which one results in smaller particles mainly because each author uses different combustible to oxidizer ratios, which has a strong influence on the combustion temperature [30], so those results are not easily comparable. In the present case, our results indicate that glycine and urea combustion yield smaller particles than sucrose probably because non-nitrogen containing combustibles are not as efficient dissipating the combustion temperature

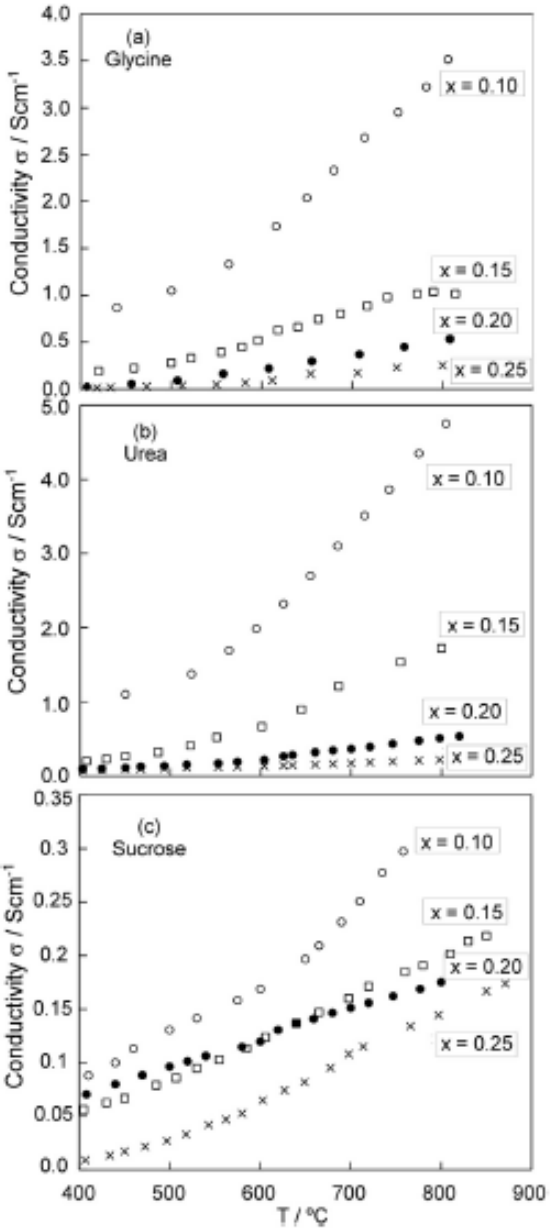

Fig. 7. Conductivity dependence upon temperature as a function of x measured in H_2 for the oxides prepared using (a) glycine, (b) urea and (c) sucrose as combustible agents.

than the nitrogen ones.

On the other hand, the increase of grain size with x can be related to the calcium content in the phases. Several studies have shown that the addition of calcium to $LaCrO_3$ allows the formation of a transient liquid phase due to the formation of $CaCrO_4$, specially above 1150 °C, resulting in sintered microstructures with bigger particle sizes and denser ceramics [31,32].

After sintering at 1350 °C in air for 10 h the trends in particle sizes are maintained, as observed in the SEM images shown in Fig. 5: the higher the x (calcium content) the biggest the particle sizes. As expected, this also resulted in denser materials with x: from the lowest to the highest doping, the relative densities increased from 60% to 88%, from 76% to 95% and from 70% to 92% of the theoretical XRD-values for the perovskites synthesised using glycine, urea and sucrose, respectively.

Fig. 5 also shows that, after sintering, all oxides present bigger

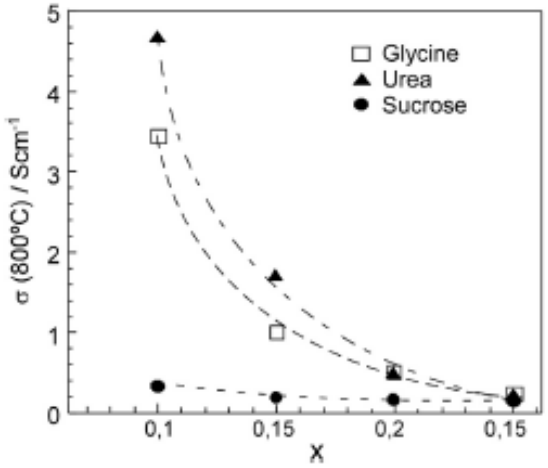

Fig. 8. Doping dependence of the conductivity at 800 °C measured under reducing conditions. Lines are guides for the eyes.

particle sizes compared to the as-synthesised powders, which is an expected result, but the increase is dependent on the synthesis method, being the samples prepared by the urea combustion process the ones that show the biggest increase (near tenfold for the x = 0.25 oxide). Fig. 6 summarises the observed tendencies. This difference in the sintering behavior is probably a result of the different agglomeration that results from the combustion. According to the literature [33], this seems to indicate that the as-synthesised urea powders presented softer agglomerates which could be broken during cold-pressing to enhance number of contact points. A more detailed study of the sintering behavior (using different firing temperatures, for example) would be necessary, however, to know if this behavior is maintained in all cases, but this is beyond the scope of this work.

3.3. Electrical conductivity study

The total electrical conductivity, σ, measured under H_2 atmosphere of all the sintered $Ln_{1-x}M_xCr_{0.9}Ni_{0.1}O_3$ perovskites as function of doping level x from 400 to 800 °C is shown in Fig. 7. A summary of the data at 800 °C for all the studied compounds appears in Fig. 8.

It can be clearly seen that the conductivity is strongly dependent on both the preparation route and the doping level. In all cases the oxides prepared by the urea combustion route show higher conductivity values than the glycine and sucrose oxides. It is interesting to note that the maximum conductivity values of the glycine and urea samples with x = 0.1 and 0.15 are above the minimum of 1 S cm^{-1} expected for an oxide anode [34] and higher than many of the previously reported values of similar $Ln_{1-x}A'_xCr_{1-y}M_yO_{3-d}$ compounds at low oxygen partial pressures [35–39]. The sucrose samples, however, show conductivity values that are roughly an order of magnitude smaller and below those expected for anode applications.

The most important feature of the electrical behavior of these samples is, however, the conductivity dependence on the doping value x. As observed, it follows the opposite trend that would be expected for these oxides: the conductivity decreases as the doping increases and this occurs irrespective of the synthesis process followed. This is interesting because, under air, this type of oxides show a p-type conductivity mainly based on the hoping process between Cr^{4+} and Cr^{3+} (together with some Ni^{2+} – Ni^{3+} exchange, in this case). The conducting mechanism when x increases is well known: as the alkaline-earth ions are introduced in the A-site to substitute the rare earth ions the concentration of electronic holes (mainly Cr^{4+}, but also some Ni^{3+} in the present case) increases to compensate for the smaller oxidation state of the new ions and, as a consequence, the same occurs to the p-type conductivity [40]. Under low oxygen partial pressures the formation of oxygen vacancies overrides this compensation mechanism and causes a strong reduction on the amount of holes (two Cr^{4+} ions reduce to Cr^{3+} in order to compensate for every O^{2-} ion that leaves the lattice) and this is why, in this type of oxides, conductivity under reducing conditions is always smaller than under oxidizing conditions [35–37,39–44].

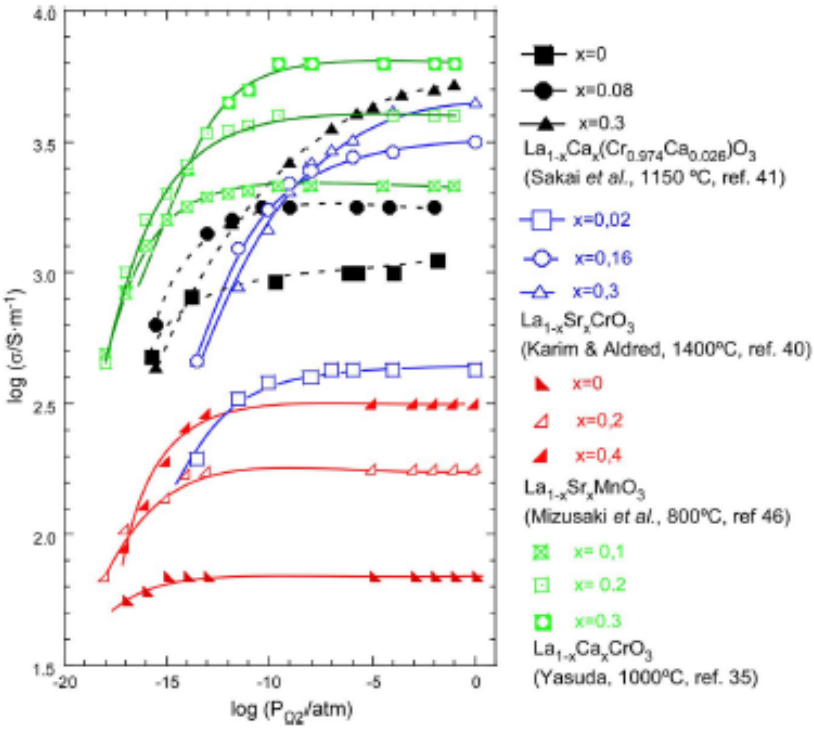

Fig. 9. Oxygen partial pressure dependence of the electrical conductivity in several doped oxides. Data taken from the literature cited. Lines are guides for the eyes. Fits are to be found in the original literature.

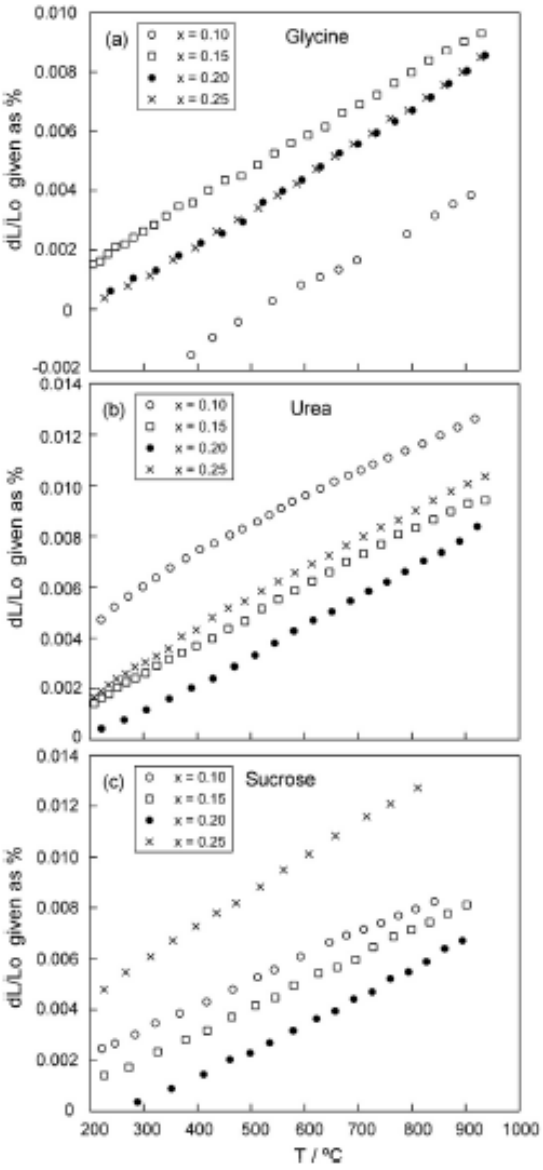

Fig. 10. Thermal expansion behavior of the $La_{1-x}M_xCr_{0.9}Ni_{0.1}O_3$ perovskites obtained using (a) glycine, (b) urea and (c) sucrose as fuels.

Nevertheless, if the conductivity of these oxides remained as p-type the same trend (increase of electrical conductivity) should be observed with increasing x (or y) as it has been reported in many of the previous studies of $A_{1-x}A'_xCr_{1-y}M_yO_3$ chromites [36,37,41,43,45]. However, we observe exactly the opposite behavior in all our cases irrespective of the synthesis process which indicates that this behavior is an intrinsic characteristic of the present oxides.

A thorough search of similar chromites in the literature has revealed that this behavior could also be intrinsic to other doped chromites if sufficiently low oxygen pressures are used [35,40–42]. Although, to our surprise, this negative correlation between doping and conductivity has not been noted by previous authors, data taken from their works and shown together in Fig. 9 indicate that this inversion would occur in all cases at low oxygen partial pressures. As it is observed, this behavior also occurs in doped manganites such as $La_{1-x}Sr_xMnO_3$ [46] and similar effects are encountered in $La_{1-x}Sr_xCoO_3$ cobaltites (not included in Fig. 9) [47]. All previous works coincide in two observations when

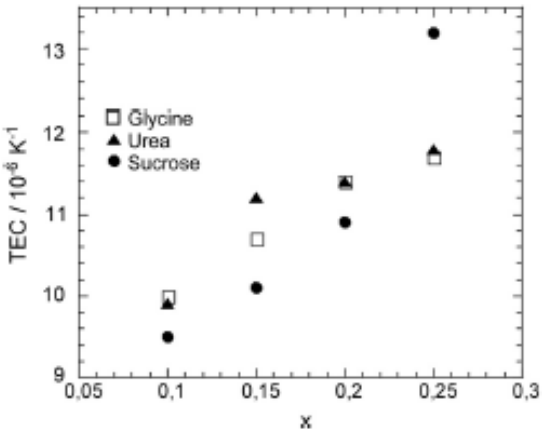

Fig. 11. Doping dependence of the thermal expansion coefficients for all samples.

these oxides are studied at low pO_2: the amount of oxygen vacancies increases more rapidly as x increases and the electric conductivity decreases in the same way [35,47,48]. The increase of oxygen vacancies is also correlated with a higher lattice expansion as pO_2 reduces [49].

Nevertheless, we have not found in the literature an explanation of why the formation of vacancies increases much faster on heavily doped oxide perovskites although this is important for the final electrical behavior. We have to rule out lattice effects coming from A-site mean ionic radii or the A-site disorder because this occurs either with them fixed (present case) and when they are left to change for every x-value (all other examples). The synthesis method seems not to be an option either because all show the same behavior (present case and in the literature). There is a correlation with the reduction of the lattice volume but it is difficult to find cause-effect relationship in this case considering that the lattice expansion, bigger for higher x, seems to override this effect at low pO_2 as indicated before [49]. What is common in all cases, including the present, is the reduction of the mean electronegativity of the A-site cations, which is systematically reduced as calcium or strontium ions substitute the more electronegative rare earths [50]. The lowering of the average electronegativity of the A-site with x might facilitate the creation of oxygen vacancies and, as a result, the reduction of conductivity is bigger in the most heavily doped oxides. At sufficiently low oxygen partial pressure this greater reduction for samples with higher x leads to an inversion of the tendency with doping: conductivity reduces with doping instead of increasing.

We consider that this is an interesting and important finding because most studies are focused, including this one, on finding the highest conductivity of a group of oxide perovskites by increasing the doping but if the conductivity is not tested at sufficiently low oxygen partial pressures (present case is $\sim 10^{-21}$ atm), the observed results might not be representative of the final behavior under SOFC operation conditions as this study shows.

3.4. Thermal expansion study

Thermal expansion measurements on rectangular bars carried out in air atmosphere upon heating from 200 to 950 °C are shown in Fig. 10a-c. The average linear thermal expansion coefficient obtained from this figure for each sample is shown in Fig. 11.

It can be seen that, although the thermal expansion coefficients (TEC) of all phases are all very similar and also agree with those of similar chromite perovskites [51], there is a small increase in TECs with increasing the doping level x in the three families of perovskites prepared.

This increase may be attributed to the formation of oxygen vacancies and the concomitant reduction of Cr^{4+} and Ni^{3+} ions with increasing x as both processes will result in lattice expansion. It is

interesting to note that the TEC values obtained for the samples with low amount of dopant are very close to those of YSZ electrolyte ($TEC_{(8mol\%YSZ;300-1000\,^{\circ}C)} = 10.0–10.8 \times 10^{-6}\,K^{-1}$) [52], and those are also the phases with higher conductivity, which is quite important if these oxides were to be used as anodes. The higher expansion of the most heavily doped phases agrees with all the literature data: either under air or under low pO_2 atmosphere it is always observed that lattice expansion increases with temperature due to the increase of oxygen vacancies and, as indicated previously, given that the amount of vacancies formed increases with x, the same is expected to occur with the thermal expansion coefficients.

4. Conclusions

A series of perovskites with the general formula $Ln_{1-x}M_xCr_{0.9}Ni_{0.1}O_3$ (Ln = La and/or Nd; M = Sr and/or Ca; $x \leq 0.25$) has been prepared by the combustion method using glycine, urea and sucrose as combustible substances. The effect of doping x has been isolated from other lattice effects by fixing $< r_A >$ to 1.22 Å and $\sigma^2(r_A)$ to 0.0001 $Å^2$. At room temperature, all compounds show orthorhombic symmetry (S.G: *Pnma*) and the unit cell compresses as x increases. There is also a systematic increase in grain growth with doping, which is consistent with the introduction of increasing amounts of alkaline-earth cation, specially Ca, which is believe to form low temperature melting intermediate species that promote sintering.

The electrical conductivity measured in H_2 shows important dependences with x and with the synthetic method. Irrespective of x, conductivity is always higher in the following order: urea, glycine and sucrose. An interesting observation is that, upon doping, the electronic conductivity measured under hydrogen atmosphere decreases contrary to common expectations for a p-type doping of the oxide perovskites. This effect has not been reported before although there were some evidences that this could occur under reducing conditions at sufficiently low oxygen partial pressures. Moreover, this behavior is consistent with all literature works that report the increase of oxygen vacancy formation with x, which could be attributed to the lower charge density of the doping cations. As a consequence, only samples with lower doping values have conductivity values that are reasonable for a SOFC anode. Thermal expansion coefficients are also closer to that of the most common SOFC electrolyte (YSZ) for samples with lower x, which indicates that less doped phases are the only ones that reasonably meet the basic needs as anodes.

Acknowledgements

This research has been funded by the Ministerio de Economía y Competitividad (MAT2016-76739-R), the Feder program of the European Union and Dpto. Educación, Política Lingüística y Cultura of the Basque Government (IT-630-13). The authors thank for technical and human support provided by SGIker of UPV/EHU. L.Ortega-San-Martin acknowledges Departamento de Ciencias, PUCP (Peru), for funding two shorts stays at UPV/EHU.

Appendix A. Supporting information

Supplementary data associated with this article can be found in the online version at http://dx.doi.org/10.1016/j.ceramint.2017.10.182.

References

[1] N. Mahato, A. Banerjee, A. Gupta, S. Omar, K. Balani, Progress in material selection for solid oxide fuel cell technology: a review, Prog. Mater. Sci. 72 (2015) 141–337, http://dx.doi.org/10.1016/j.pmatsci.2015.01.001.

[2] W.-H. Kan, V. Thangadurai, Challenges and prospects of anodes for solid oxide fuel cells (SOFCs), Ion. 21 (2014) 301–318, http://dx.doi.org/10.1007/s11581-014-1334-6.

[3] D.K. Niakolas, Sulfur poisoning of Ni-based anodes for solid oxide fuel cells in H/C-based fuels, Appl. Catal. A Gen. 486 (2014) 123–142, http://dx.doi.org/10.1016/j.apcata.2014.08.015.

[4] J. Sunarso, S.S. Hashim, N. Zhu, W. Zhou, Perovskite oxides applications in high temperature oxygen separation, solid oxide fuel cell and membrane reactor: a review, Prog. Energy Combust. Sci. 61 (2017) 57–77, http://dx.doi.org/10.1016/j.pecs.2017.03.003.

[5] H. Teruhisa, LaCrO3-Based perovskite for SOFC interconnects, Perovskite Oxide Solid Oxide Fuel Cells (2009) 285–296, http://dx.doi.org/10.1007/978-0-387-77708-5.

[6] J.T.S. Irvine, Perovskite oxide anodes for SOFCs, in: T. Ishihara (Ed.), Perovskite Oxide Solid Oxide Fuel Cells, Springer Science, 2009, pp. 167–182, , http://dx.doi.org/10.1007/978-0-387-77708-5.

[7] S. Tao, J.T.S. Irvine, Discovery and characterization of novel oxide anodes for solid oxide fuel cells, Chem. Rec. 4 (2004) 83–95, http://dx.doi.org/10.1002/tcr.20003.

[8] N.P. Brandon, S. Skinner, B.C.H. Steele, Recent advances in materials for fuel cells, Annu. Rev. Mater. Res. 33 (2003) 183–213, http://dx.doi.org/10.1146/annurev.matsci.33.022802.094122.

[9] S. Gupta, H. Sabarou, Y. Zhong, P. Singh, Phase evolution and electrochemical performance of iron doped lanthanum strontium chromite in oxidizing and reducing atmosphere, Int. J. Hydrog. Energy 42 (2017) 6262–6271, http://dx.doi.org/10.1016/j.ijhydene.2016.11.141.

[10] T. Zhu, D.E. Fowler, K.R. Poeppelmeier, M. Han, S.A. Barnett, Hydrogen oxidation mechanisms on perovskite solid oxide fuel cell anodes, J. Electrochem. Soc. 163 (2016) F952–F961, http://dx.doi.org/10.1149/2.1321608jes.

[11] V.Y. Zenou, D.E. Fowler, R. Gautier, S.A. Barnett, K.R. Poeppelmeier, L.D. Marks, Redox and phase behavior of Pd-substituted (La,Sr)CrO3 perovskite solid oxide fuel cell anodes, Solid State Ion. 296 (2016) 90–105, http://dx.doi.org/10.1016/j.ssi.2016.09.006.

[12] J. Sfeir, LaCrO3-based anodes: stability considerations, J. Power Sources 118 (2003) 276–285, http://dx.doi.org/10.1016/S0378-7753(03)00099-5.

[13] O.V. Komova, V.I. Simagina, S.A. Mukha, O.V. Netskina, G.V. Odegova, O.A. Bulavchenko, A.V. Ishchenko, A.A. Pochtar, A modified glycine-nitrate combustion method for one-step synthesis of LaFeO3, Adv. Powder Technol. 27 (2016) 496–503, http://dx.doi.org/10.1016/j.apt.2016.01.030.

[14] S. Singh, D. Singh, LaSrFeO4 nanopowders synthesized by different combustion methods: effect of fuel/particle size, Ceram. Int. 42 (2016) 15725–15731, http://dx.doi.org/10.1016/j.ceramint.2016.07.032.

[15] D.P. Tarragó, C. de, F. Malfatti, V.C. de Sousa, Influence of fuel on morphology of LSM powders obtained by solution combustion synthesis, Powder Technol. 269 (2015) 481–487, http://dx.doi.org/10.1016/j.powtec.2014.09.037.

[16] F. Deganello, L.F. Liotta, G. Marcì, E. Fabbri, E. Traversa, Strontium and iron-doped barium cobaltite prepared by solution combustion synthesis: exploring a mixed-fuel approach for tailored intermediate temperature solid oxide fuel cell cathode materials, Mater. Renew. Sustain. Energy 2 (2013) 8, http://dx.doi.org/10.1007/s40243-013-0008-z.

[17] L.M. Rodriguez-Martinez, J.P. Attfield, Cation disorder and size effects in magnetoresistive manganese oxide perovskites, Phys. Rev. B 54 (1996) R15622–R15625.

[18] A.K. Kundu, M.M. Seikh, K. Ramesha, C.N.R. Rao, Novel effects of size disorder on the electronic and magnetic properties of rare earth manganates of the type La 0.7−xLnxBa0.3MnO3 (Ln = Pr,Nd, Gd or Dy) with large average radius of the A-site cations, J. Phys. Condens. Matter 17 (2005) 4171–4180, http://dx.doi.org/10.1088/0953-8984/17/26/015.

[19] K. Vidal, A. Larrañaga, A. Morán-Ruiz, A.T. Aguayo, M.A. Laguna-Bercero, M.P. Yeste, J.J. Calvino, M.I. Arriortua, Effect of synthesis conditions on electrical and catalytical properties of perovskites with high value of A-site cation size mismatch, Int. J. Hydrog. Energy 41 (2016) 19810–19818, http://dx.doi.org/10.1016/j.ijhydene.2016.02.088.

[20] J.-G. Cheng, J.-S. Zhou, J.B. Goodenough, Lattice effects on ferromagnetism in perovskite ruthenates, Proc. Natl. Acad. Sci. USA 110 (2013) 13312–13315, http://dx.doi.org/10.1073/pnas.1311871110.

[21] A. Ecija, K. Vidal, A. Larrañaga, A. Martinez-Amesti, L. Ortega-San-Martin, M.I. Arriortua, Structure and properties of perovskites for SOFC cathodes as a function of the A-site cation size disorder, Solid State Ion. 235 (2013) 14–21, http://dx.doi.org/10.1016/j.ssi.2013.01.010.

[22] R.D. Shannon, Revised effective ionic radii and systematic studies of interatomic distances in halides and chalcogenides, Acta Cryst. A32 (1976) 751–767, http://dx.doi.org/10.1107/S0567739476001551.

[23] P.M. Woodward, Octahedral tilting in perovskites. I. Geometrical considerations, Acta Crystallogr. Sect. B Struct. Sci. 53 (1997) 32–43, http://dx.doi.org/10.1107/S0108768196010713.

[24] K. Oikawa, T. Kamiyama, T. Hashimoto, Y. Shimojyo, Y. Morii, Structural phase transition of orthorhombic laCrO3 studied by neutron powder diffraction, J. Solid State Chem. 154 (2000) 524–529, http://dx.doi.org/10.1006/jssc.2000.8873.

[25] A.C. Larson, R.B. Von Dreele, General structure analysis system (GSAS), Los Alamos Lab. Rep. LAUR 86–74 (2004).

[26] B.H. Toby, EXPGUI, a graphical user interface for GSAS, J. Appl. Crystallogr. 34 (2001) 210–213, http://dx.doi.org/10.1107/S0021889801002242.

[27] L. Ortega-San-Martin, K. Vidal, B. Roldán-Pozo, Y. Coello, A. Larrañaga, M.I. Arriortua, Synthesis method dependence of the lattice effects in Ln0.5M0.5FeO3 perovskites (Ln = La and (Nd or Gd); M = Ba and (Ca or Sr)), Mater. Res. Express 3 (2016) 56302, http://dx.doi.org/10.1088/2053-1591/3/5/056302.

[28] A.L.A. Da Silva, G.G.G. Castro, M.M.V.M. Souza, Synthesis of Sr-doped LaCrO 3 powders by combustion method: influence of the fuel agent, J. Therm. Anal. Calorim. 109 (2012) 33–38, http://dx.doi.org/10.1007/s10973-011-1527-4.

[29] B.S. Barros, J. Kulesza, D.M. De. Araújo Melo, A. Kiennemand, Nickel-based catalyst

precursor prepared via microwave-induced combustion method: thermodynamics of synthesis and performance in dry reforming of CH4, Mater. Res. 18 (2015) 732–739, http://dx.doi.org/10.1590/1516-1439.018115.
[30] A.S. Mukasyan, C. Costello, K.P. Sherlock, D. Lafarga, A. Varma, Perovskite membranes by aqueous combustion synthesis: synthesis and properties, Sep. Purif. Technol. 25 (2001) 117–126, http://dx.doi.org/10.1016/S1383-5866(01)00096-X.
[31] S. Simner, J. Hardy, J. Stevenson, T. Armstrong, Sintering mechanisms in strontium doped lanthanum chromite, J. Mater. Sci. 34 (1999) 5721–5732, http://dx.doi.org/10.1023/A:1006733414271.
[32] S.W. Paulik, S. Baskaran, T.R. Armstrong, Mechanical properties of calcium- and strontium- substituted lanthanum chromite, J. Mater. Sci. 3 (1998) 2397–2404.
[33] S.R. Nair, R.D. Purohit, A.K. Tyagi, P.K. Sinha, B.P. Sharma, Role of glycine-to-nitrate ratio in influencing the powder characteristics of La(Ca)CrO3, Mater. Res. Bull. 43 (2008) 1573–1582, http://dx.doi.org/10.1016/j.materresbull.2007.06.021.
[34] J.T.S. Irvine, P. Connor, Alternative materials for SOFCs, opportunities and limitations, in: J.T.S. Irvine, P. Connor (Eds.), Solid Oxide Fuels Cells Facts Figures Past, Present Future Perspectives SOFC Technologies, Springer-Verlag, London, 2013, pp. 163–180, , http://dx.doi.org/10.1007/978-1-4471-4456-4_7.
[35] I. Yasuda, T. Hikita, Electrical conductivity and defect structure of calcium-doped lanthanum chromites, J. Electrochem. Soc. 140 (1993) 1699, http://dx.doi.org/10.1149/1.2221626.
[36] I. Yasuda, M. Hishinuma, Electrical conductivity and chemical diffusion coefficient of Sr-doped lanthanum chromites, Solid State Ion. 80 (1995) 141–150, http://dx.doi.org/10.1016/0167-2738(95)00136-T.
[37] S. Tao, J.T.S. Irvine, Structural and electrochemical properties of the perovskite oxide Pr0.7Sr0.3Cr0.9Ni0.1O3−δ, Solid State Ion. 179 (2008) 725–731, http://dx.doi.org/10.1016/j.ssi.2008.04.027.
[38] S. Tao, J.T.S. Irvine, Phase transition in perovskite oxide La0.75Sr0.25Cr0.5Mn0.5O3-δ observed by in situ high-temperature neutron powder diffraction, Chem. Mater. 18 (2006) 5453–5460, http://dx.doi.org/10.1021/cm061413n.
[39] S.P. Jiang, L. Liu, K.P. Ong, P. Wu, J. Li, J. Pu, Electrical conductivity and performance of doped LaCrO3 perovskite oxides for solid oxide fuel cells, J. Power Sources 176 (2008) 82–89, http://dx.doi.org/10.1016/j.jpowsour.2007.10.053.
[40] D.P. Karim, A.T. Aldred, Localized level hopping transport in La(Sr)CrO3, Phys. Rev. B 20 (1979) 2255–2263, http://dx.doi.org/10.1103/PhysRevB.20.2255.
[41] N. Sakai, T. Kawada, H. Yokokawa, M. Dokiya, T. Iwata, Sinterability and electrical conductivity of calcium-doped lanthanum chromites, J. Mater. Sci. 25 (1990) 4531–4534, http://dx.doi.org/10.1007/BF00581119.
[42] L. Manxi, C. Xiangfeng, Z. Weichang, D. Yongping, C. Tongyun, Preparation and performance of Sm1-xCaxCrO3-δ as new interconnect materials for IT-SOFC, Rare Met. Mater. Eng. 43 (2014) 1337–1341, http://dx.doi.org/10.1016/S1875-5372(14)60119-3.
[43] K.J. Yoon, C.N. Cramer, E.C. Thomsen, C.A. Coyle, G.W. Coffey, O.A. Marina, Calcium- and cobalt-doped yttrium chromites as an interconnect material for solid oxide fuel cells, J. Electrochem. Soc. 157 (2010) B856–B861, http://dx.doi.org/10.1149/1.3337156.
[44] X.-M. Ge, S.-H. Chan, Q.-L. Liu, Q. Sun, Solid oxide fuel cell anode materials for direct hydrocarbon utilization, Adv. Energy Mater. 2 (2012) 1156–1181, http://dx.doi.org/10.1002/aenm.201200342.
[45] N. Sakai, H. Yokokawa, T. Horita, K. Yamaji, Lanthanum chromite-based interconnects as key materials for SOFC stack development, Int. J. Appl. Ceram. Technol. 1 (2004) 23–30, http://dx.doi.org/10.1111/j.1744-7402.2004.tb00151.x.
[46] J. Mizusaki, Y. Yonemura, H. Kamata, K. Ohyama, N. Mori, H. Takai, H. Tagawa, M. Dokiya, K. Naraya, T. Sasamoto, H. Inaba, T. Hashimoto, Electronic conductivity, seebeck coefficient, defect and electronic structure of nonstoichiometric La1−xSrxMnO3, Solid State Ion. 132 (2000) 167–180, http://dx.doi.org/10.1016/S0167-2738(00)00662-7.
[47] J. Mizusaki, J. Tabuchi, T. Matsuura, S. Yamauchi, K. Fueki, Electrical conductivity and seebeck coefficient of nonstoichiometric La1−xSrxCoO3−δ, J. Electrochem. Soc. 136 (1989) 2082–2088, http://dx.doi.org/10.1149/1.2097187.
[48] J. Mizusaki, S. Yamauchi, K. Fueki, A. Ishikawa, Nonstoichiometry of the perovskite-type oxide La1−xSrxCrO3−δ, Solid State Ion. 12 (1984) 119–124, http://dx.doi.org/10.1016/0167-2738(84)90138-3.
[49] F. Boroomand, E. Wessel, H. Bausinger, K. Hilpert, Correlation between defect chemistry and expansion during reduction of doped LaCrO3 interconnects for SOFCs, Solid State Ion. 129 (2000) 251–258, http://dx.doi.org/10.1016/S0167-2738(99)00330-6.
[50] J.E. Huheey, E.A. Keiter, R.L. Keiter, Inorganic Chemistry: Principles of Structure and Reactivity, 4th ed., Harper Collins College Publishers, New York, 1993.
[51] M.K. Rath, K.T. Lee, Investigation of aliovalent transition metal doped La0.7Ca0.3Cr0.8 × 0.2O3-δ (X = Ti, Mn, Fe, Co, and Ni) as electrode materials for symmetric solid oxide fuel cells, Ceram. Int. 41 (2015) 10878–10890, http://dx.doi.org/10.1016/j.ceramint.2015.05.029.
[52] V.V. Kharton, F.M.B. Marques, A. Atkinson, Transport properties of solid oxide electrolyte ceramics: a brief review, Solid State Ion. 174 (2004) 135–149, http://dx.doi.org/10.1016/j.ssi.2004.06.015.

research papers

IUCrJ
ISSN 2052-2525
CHEMISTRY | CRYSTENG

Synthesis of new $Ln_4(Al_2O_6F_2)O_2$ (Ln = Sm, Eu, Gd) phases with a cuspidine-related structure

Aroa Morán-Ruiz,[a]* Aritza Wain-Martin,[a] Alodia Orera,[b] María Luisa Sanjuán,[b] Aitor Larrañaga,[a] Peter R. Slater[c] and Maribel Arriortua[a,d]*

[a]Universidad del País Vasco (UPV/EHU), Facultad de Ciencia y Tecnología, Barrio Sarriena S/N, Leioa, Vizcaya 48940, Spain, [b]Instituto de Ciencia de Materiales de Aragón (CSIC - Universidad de Zaragoza), C/ Pedro Cerbuna 12, Zaragoza 50009, Spain, [c]University of Birmingham, School of Chemistry, Birmingham B15 2TT, UK, and [d]BCMaterials (Basque Centre for Materials, Applications and Nanostructures), Bld. Martina Casiano, 3rd. Floor, UPV/EHU Science Park, Barrio Sarriena S/N, Leioa, Vizcaya 48940, Spain. *Correspondence e-mail: aroa.moran@ehu.eus, maribel.arriortua@ehu.eus

Received 28 August 2018
Accepted 10 December 2018

Edited by C.-Y. Su, Sun Yat-Sen University, China

Keywords: cuspidine-type rare-earth aluminates; fluorination; X-ray diffraction; poly(vinylidene difluoride); Raman spectroscopy.

CCDC references: 1886577; 1886578

Supporting information: this article has supporting information at www.iucrj.org

The first fluorination of the cuspidine-related phases of $Ln_4(Al_2O_7\square)O_2$ (where Ln = Sm, Eu, Gd) is reported. A low-temperature reaction with poly(vinylidene difluoride) lead to the fluorine being substituted in place of oxygen and inserted into the vacant position between the dialuminate groups. X-ray photoelectron spectroscopy shows the presence of the F 1*s* photoelectron together with an increase in Al 2*p* and rare-earth 4*d* binding energies supporting F incorporation. Energy-dispersive X-ray spectroscopy analyses are consistent with the formula $Ln_4(Al_2O_6F_2)O_2$, confirming that substitution of one oxygen by two fluoride atoms has been achieved. Rietveld refinements show an expansion in the cell upon fluorination and confirm that the incorporation of fluoride in the $Ln_4(Al_2O_7\square)O_2$ structure results in changes in Al coordination from four to five. Thus, the isolated tetrahedral dialuminate Al_2O_7 groups are converted to chains of distorted square-based pyramids. These structural results are also discussed based on Raman spectra.

1. Introduction

Minerals belonging to the cuspidine group have the general stoichiometry $M_4(Si_2O_7)X_2$ (M = divalent cation; X = OH, F, O), with $Ca_4(Si_2O_7)(OH,F)_2$ being the archetype compound. The cuspidine structure can be described as built up of chains of edge-sharing MO_7/MO_8 polyhedra running parallel to the *a* axis (in the $P2_1/c$ space group); the tetrahedral disilicate groups (Si_2O_7) interconnect with these ribbons through the vertices. The structural formula of cuspidine is better described as $Ca_4(Si_2O_7\square)(OH,F)_2$ to directly show the vacant position between the disilicate groups. The filling of that position may convert the isolated pyrogroups into infinite chains of distorted trigonal bipyramids (Martín-Sedeño *et al.*, 2004).

Other systems also adopt this structural type, including the $Ln_4(Al/Ga)_2O_9$ (Ln = rare-earth) type phases, which have attracted attention because of their ionic conductivity and thermal stability (Ghosh, 2015; Zhou *et al.*, 2014; Martín-Sedeño *et al.*, 2006; Morán-Ruiz *et al.*, 2018). In more recent years, the preparation and characterization of inorganic oxyfluorides have attracted significant interest. Thus, low-temperature fluorination methods can alter chemistry of the precursor oxide in different ways by charge compensation effects (Clemens & Slater, 2013). In particular, polymer reagents such as poly(vinylidine fluoride) and poly(tetra-fluoroethylene) have been proven to be successful low-temperature fluorinating reagents, following the early work by

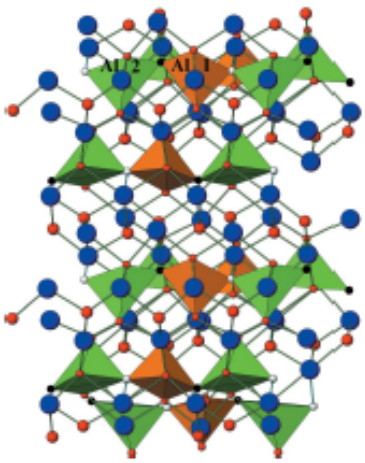

OPEN ACCESS

Slater (2002) which illustrates the use of PVDF to prepare $Ca_2CuO_2F_2$ and $Sr_2TiO_3F_2$. Since then, a wide range of perovskite and related phases have been successfully fluorinated using this polymer route (Clemens *et al.*, 2014; Hancock *et al.*, 2012; Berry *et al.*, 2008; Heap *et al.*, 2007), and the method has been shown to be equally applicable to the fluorination of thin films (Kawahara *et al.*, 2017; Katayama *et al.*, 2016; Moon *et al.*, 2015). This earlier research has mainly focused on the fluorination of transition-metal containing materials, and so here we investigate the potential use for the fluorination of oxide systems that do not contain transition metals. In particular, given the recent studies on oxide ion/proton conductivity in $La_4(Ga_{2-x}Ti_xO_{7+x/2})O_2$, which illustrate the ability of the cuspidine structure to accommodate extra anions (Martín-Sedeño *et al.*, 2005), this would appear to be an ideal structure to examine the possible incorporation of fluoride. We have therefore investigated the fluorination of $Ln_4(Al_2O_7\square)O_2$ to give new $Ln_4Al_2O_{9-x}F_{2x}$ (Ln = Sm, Eu, Gd) ($0 \leq x \leq 1$) phases. Here we report the results of these first low-temperature fluorination reactions of a range of rare-earth aluminate cuspidine-related phases. The introduction of fluorine ($2\,F^-$ replacing O^{2-}) was achieved through a reaction with poly(vinylidene fluoride) (PVDF) as the fluorinating agent. We investigate the success and effects of fluorination on the starting structure by X-ray diffraction (XRD), X-ray photoelectron spectroscopy (XPS), ^{27}Al solid-state nuclear magnetic resonance (NMR), Raman spectroscopy, scanning electron microscopy (SEM) and energy dispersive X-ray spectroscopy (EDX). The thermal stability of these samples after fluorination was evaluated in air through thermogravimetric analysis (TGA).

2. Experimental

2.1. Powder preparation

Starting precursor oxides of $Ln_4(Al_2O_7\square)O_2$ (Ln = Sm, Eu, Gd) were prepared by the glycine nitrate combustion route using the appropriate quantities of metals and combustible substance as previously reported by Morán-Ruiz *et al.* (2018). The introduction of fluorine ($2\,F^-$ replacing O^{7-}) into the $Ln_4(Al_2O_7\square)O_2$ structure was achieved through a low-temperature (400°C) reaction with PVDF (Slater, 2002) as the fluorinating agent. Thus, fluorination was achieved by mixing the rare-earth aluminate phase with PVDF in a 1:1 mol ratio (precursor oxide: CH_2CF_2 monomer unit) and heating (80°C h^{-1}) the mixture at 400°C for 12 h in air.

Since poly(tetrafluoroethylene) (PTFE) has also been shown to be a very good fluorinating reagent, we investigated the possibility of fluorination of $Eu_4(Al_2O_7\square)O_2$ with PTFE under the same conditions. This gave similar results to the reaction with PVDF, with an observed expansion in the unit cell consistent with F incorporation.

2.2. Characterization techniques

X-ray powder diffraction patterns were recorded with a Philips X'Pert-Pro diffractometer using graphite-monochromated Cu $K\alpha_{1,2}$ radiation (λ_1 = 1.5406 Å; λ_2 = 1.5443 Å). The compounds were scanned between 15 and 90° (2θ) in 0.026° steps, counting 380 s per step. In addition, a Bruker D8 Advance Vário diffractometer, equipped with a primary monochromator and a solid SolX detector, with energy discrimination optimized for such radiation (Cu $K\alpha_1$, λ_1 = 1.5406 Å), were also used to improve the quality of the XRD data for structure refinement. The overall measuring time was ~120 h per pattern to have good statistics over the 2θ angular range of 5–100° with a 0.02° step size. The fitting of the measured and calculated pattern structure refinement was carried out using the program *FullProf* (Rodríguez-Carvajal, 2011). Moreover, *Atoms62* software (Shape Software, 2005) was also used to illustrate the structure.

X-ray photoelectron spectroscopy (XPS) measurements were performed using an XPS spectrometer (SPECS). All XPS spectra were acquired using a monochromatic X-ray source producing Al $K\alpha$ radiation ($h\nu$ = 1486.6 eV) and recorded using a Specs Phoibos 150 analyser. An initial analysis of the elements present in the sample was carried out (wide scan: step energy 1 eV, dwell time 0.1 s, pass energy 80 eV) and individual high-resolution spectra were obtained (detail scan: step energy 0.1 eV, dwell time 0.1 s, pass energy 30 eV) with an electron take-off angle of 90°. The binding energies (BEs) were calibrated using the C 1*s* peak (BE = 284.6 eV) as an internal standard. The spectra were fitted by *CasaXPS* 2.3.16 software, modelling the properly weighted sum of Gaussian and Lorentzian component curves, after background subtraction according to Shirley.

The ^{27}Al solid-state NMR spectra were recorded on a Bruker Avance III, at 9.4 T under magic angle (MAS) at 14 kHz using a Bruker probe head 4 mm MAS DVT X/Y/H. The ^{27}Al MAS NMR were recorded at 104.27 MHz using a single-pulse sequence with a 4 µs rf pulse ($\pi/2$); the relaxation delay was 0.5 s and a total of 20000 scans were accumulated. The ^{27}Al chemical shifts were calibrated indirectly with $Al(NO_3)_3$.

For Raman scattering measurements a DILOR XY spectrometer with a CCD detector and 2 cm^{-1} of spectral resolution was used. The 514.5 nm line of an Ar^+-ion laser was used as the excitation source, and the power output was kept below 20 mW after verifying that no changes were induced in the samples. A 50× microscope objective lens was used both for excitation and dispersed light collection. Some spectra were also collected in a WITEC Alpha 300M+ spectrometer working with 633 nm excitation. For each material, at least 3–4 representative spectra of different sample zones were recorded.

Thermogravimetric analyses were performed for all compositions on a TA Instruments SDT 2960 simultaneous DSC–TGA balance. The temperature was varied from room temperature up to 900°C at a heating rate of 3°C min^{-1} in air.

Compositional analysis was performed using an analytical scanning electron microscope (SEM, JEOL JSM-7000 F) with an electron microanalysis probe EDX (Oxford Pentafet energy dispersive X-ray analyzer). Samples were coated with a coal graphite layer (10 nm) deposited by evaporation

(Quorum Q150T Sputter Coater) to provide electrical conductivity. Back-scattered electrons were measured at a 20 kV accelerating voltage and 5×10^{-9} A current. A measurement time of 100 s per point was established for data acquisition. EDX system calibration was performed by measuring the beam current on $Ln_4(Al_2O_7\square)O_2$ and AlF_3 as standards, to allow quantitative elemental analyses. The data processing was performed using Oxford *Inca* software. The characteristic emission lines used for the analysis were *Kα* for Al and F, and *Mα* for Sm, Eu and Gd. The morphologies of the powders were observed using secondary electrons at an accelerating voltage of 20 kV, a current of 1.1×10^{-11} A and a working distance of 9 mm. These samples were metallized by gold sputtering for better image definition.

3. Results and discussion

The X-ray powder diffraction patterns recorded from $Ln_4(Al_2O_7\square)O_2$ (Ln = Sm, Eu, Gd) and their new fluorinated derivatives are shown in Fig. 1. The XRD patterns show that all the samples consist of a single phase without impurities. Moreover, the fluorination induces a shift in peak position to lower angles corresponding to an increase in unit-cell sizes as the total anion content increases.

The volumes recorded from the pure oxides and their fluorinated derivatives are graphically represented in Fig. 2. From the data in the graphic it can be seen that the fluorination leads to a significant increase in unit-cell parameters. The volume difference between the starting oxide and fluorinated oxides becomes more noticeable as the rare earth size decreases. Moreover, the cell parameters change in good agreement with the variation of the ionic radii of the rare-earth cations, with the largest cell volume observed for the Sm system and the smallest for the Gd system (Morán-Ruiz *et al.*, 2018) [Gd^{3+} (coordination number VII): 1.00 Å; Gd^{3+} (VIII): 1.05 Å; Eu^{3+} (VII): 1.01 Å; Eu^{3+} (VIII): 1.07 Å; Sm^{3+} (VII): 1.02 Å; Sm^{3+} (VIII): 1.08 Å].

Representative SEM micrographs of the powder samples (as prepared and after fluorination at 400°C) are shown in Fig. 3. As observed, no significant differences can be seen in the morphology or the average particle size of the different samples in these images. All samples are composed of agglomerated sub-micrometre particles.

The chemical compositions of the obtained fluorinated oxides were analysed using SEM–EDX. The measured values of the elements were checked on different points to obtain the average composition. The atomic percentage concentrations of detected elements are listed in Table 1. For comparison, data were also collected for $Eu_4(Al_2O_7\square)O_2$ fluorinated with half the molar equivalents of PVDF, in order to illustrate that F content can be controlled by the amount of polymer added.

These results indicate that the substitution of two fluorine atoms for one oxygen is satisfactorily achieved to obtain new

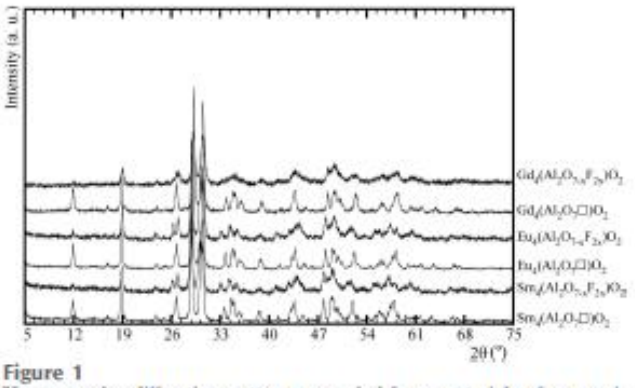

Figure 1
X-ray powder diffraction patterns recorded from materials of composition $Ln_4(Al_2O_7\square)O_2$ (Ln = Sm, Eu, Gd) and their fluorinated derivatives.

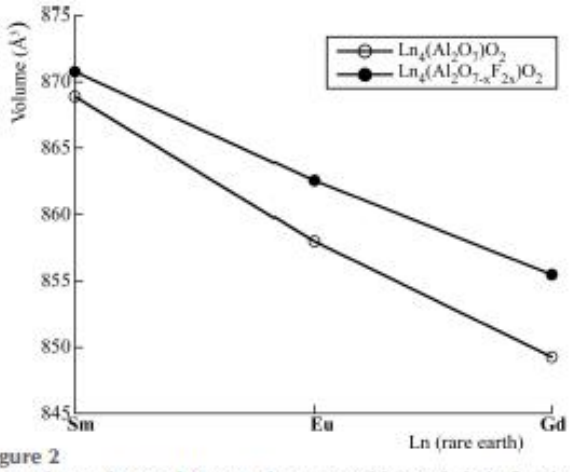

Figure 2
The volume changes between the pure oxides and their fluorinated derivatives.

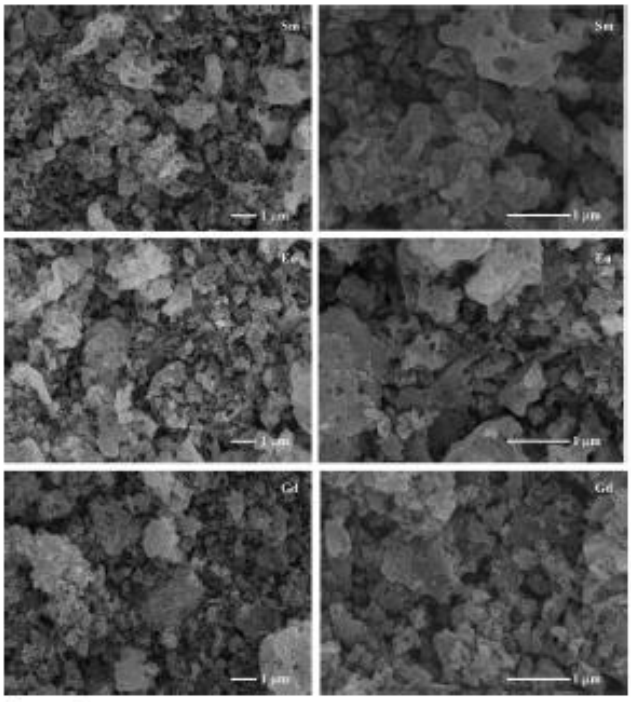

Figure 3
Micrographs of $Sm_4(Al_2O_6F_2)O_2$, $Eu_4(Al_2O_6F_2)O_2$ and $Gd_4(Al_2O_6F_2)O_2$ phases prepared using a low-temperature fluorination route.

Table 1
Chemical compositions (at.%) of fluorinated oxides obtained under various synthetic conditions.

The use of plasma-cleaning could reduce the fluorine content near to 12.5 at.%.

Sample	Ln†	Al	F
$Sm_4(Al_2O_{7-x}F_{2x})O_2$	24.0 (2)	12.2 (2)	13.4 (3)
$Eu_4(Al_2O_{7-x}F_{2x})O_2$	25.0 (4)	12.2 (3)	13.1 (1)
$Gd_4(Al_2O_{7-x}F_{2x})O_2$	25.6 (2)	12.6 (3)	13.6 (2)
$Eu_4(Al_2O_{7-x}F_{2x})O_2$‡	23.2 (1)	12.0 (2)	6.9 (1)
$Eu_4(Al_2O_{7-x}F_{2x})O_2$§	22.7 (2)	11.5 (1)	12.7 (2)
$Eu_4(Al_2O_{7-x}F_{2x})O_2$¶	23.0 (1)	11.5 (1)	12.3 (1)
Theoretical $Ln_4(Al_2O_6F_2)O_2$	25	12.5	12.5

† Ln = Sm, Eu, Gd. ‡ Fluorination reaction using $\frac{1}{2}$ PVDF [equivalent to 1 F (x = 0.5) incorporation]. § Fluorination reaction using poly(tetrafluoroethylene) (PTFE). ¶ - Fluorination reaction using $\frac{1}{2}$ PTFE.

$Ln_4Al_2O_8F_2$ (Ln = Sm, Eu, Gd) compositions. Examination of the fluorination with higher levels of PVDF led to no further increase in cell volume, illustrating the maximum F content had been reached. From these results it can be concluded that these cuspidine phases permit a maximum of two fluorine atoms per formula.

The samples were heated in a thermogravimetric analyzer in air at 900°C. The thermograms of all oxyfluorides are shown in Fig. 4. A decrease in mass with increasing temperature occurs between 550 and 900°C, which is associated with the loss of fluorine content due to the reaction with moisture in the air, leading to loss of HF and replacement by oxygen to reform the simple oxide system.

For all compositions, a gravimetric mass loss of ~3% is observed. From these results the $(O/F)_\varepsilon$ relation is calculated (Table 2).

From the TGA data it can be concluded that the mass loss is not complete due to the low kinetic decomposition of these compounds. Preliminary studies show that the stabilization of the mass requires a long heating time (~6 h) at 1000°C (see supporting information, Fig. S1). In order to obtain the total

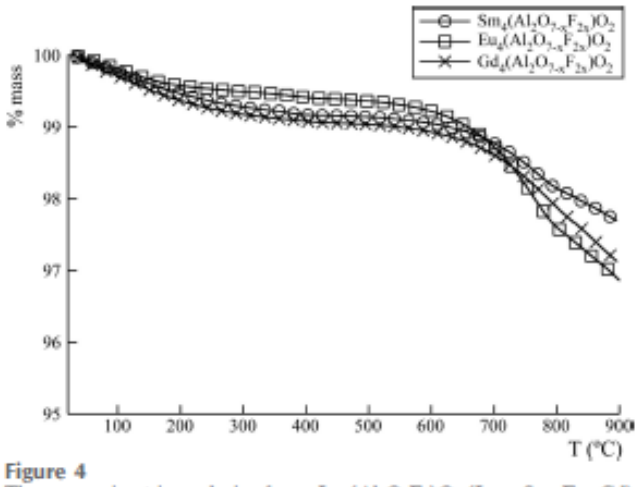

Figure 4
Thermogravimetric analysis of new $Ln_4(Al_2O_6F_2)O_2$ (Ln = Sm, Eu, Gd) phases.

Table 2
Fluorine content loss calculated from the gravimetric mass loss (550–900°C).

Sample	x
$Sm_4(Al_2O_{7-x}F_{2x})O_2$	0.52
$Eu_4(Al_2O_{7-x}F_{2x})O_2$	0.93
$Gd_4(Al_2O_{7-x}F_{2x})O_2$	0.72

Table 3
Chemical compositions (at.%) of the TGA residues of fluorinated oxides.

Residue	Ln† (at.%)	Al (at.%)	F (at.%)
$Sm_4(Al_2O_{7-x}F_{2x})O_2$	24.8 (3)	12.6 (3)	6.6 (3)
$Eu_4(Al_2O_{7-x}F_{2x})O_2$	26.9 (1)	12.7 (1)	1.0 (1)
$Gd_4(Al_2O_{7-x}F_{2x})O_2$	27.4 (3)	11.5 (3)	2.8 (6)

† Ln = Sm, Eu, Gd.

Table 4
XPS analysis results of detected elements for the surface of the obtained $Ln_4(Al_2O_{7-x}F_{2x})O_2$ compositions.

Sample	Ln 4*d*† (BE, eV)	Al 2*p* (BE, eV)	F 1*s* (BE, eV)
$Sm_4(Al_2O_7)O_2$	131.7	73.1	–
$Sm_4(Al_2O_{7-x}F_{2x})O_2$	133.1	74.3	685.0
$Eu_4(Al_2O_7)O_2$	135.5	73.1	–
$Eu_4(Al_2O_{7-x}F_{2x})O_2$	137.0	74.3	686.5
$Gd_4(Al_2O_7)O_2$	141.9	73.1	–
$Gd_4(Al_2O_{7-x}F_{2x})O_2$	142.8	74.3	685.3

† Ln = Sm, Eu, Gd.

fluorine content remaining in each sample after treatment at 900°C, the residues were analyzed by EDX. The atomic percentage concentrations of detected elements are summarized in Table 3. The obtained data coincide with the calculated fluorine content loss.

The success of the fluorination of rare-earth aluminates is also confirmed by XPS. A clear peak is observed in the analysed areas of the fluorinated oxides using a wide scan up to 1380 eV, attributable to an F 1*s* photoelectron (Fig. 5).

The resultant peak BEs before and after fluorination are presented in Table 4. In particular, we observe that fluorine incorporation induces an increase of the BEs of Al 2*p* and Ln 4*d* due to fluorine having a higher electronegativity than oxide.

This indicates greater electron transfer to fluorine, causing a decrease in the electron density at the cation and resulting in higher binding energy of the electrons from the core level of the cation (Dae-Min *et al.*, 2011). These peak-position shifts are observed in the high-resolution spectra of the Al 2*p* and Ln 4*d* spectral regions (Fig. 6).

The ^{27}Al NMR spectra of the fluorinated samples and $Ln_4(Al_2O_7)O_2$ (Ln = Sm, Eu, Gd) are provided as supporting information (Fig. S2). It seems that the shape of the $Ln_4(Al_2O_6F_2)O_2$ spectra changes compared with the $Ln_4(Al_2O_7)O_2$ spectra, which could be due to a modification of the coordination environment of Al^{3+} in the fluorinated derivatives. However, the obtained ^{27}Al NMR data are not conclusive due to the paramagnetism of Sm, Eu and Gd rare-earth metals.

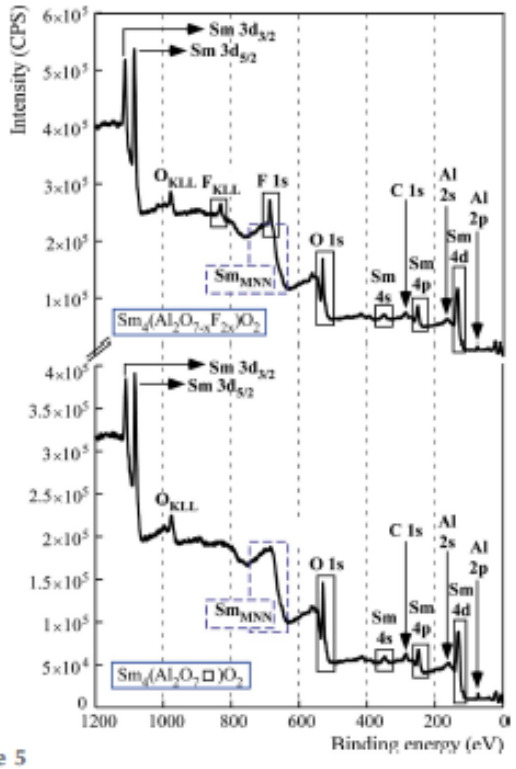

Figure 5
As an example, XPS survey spectra of the surface composition $Sm_4(Al_2O_7\square)O_2$ and their new fluorinated derivative.

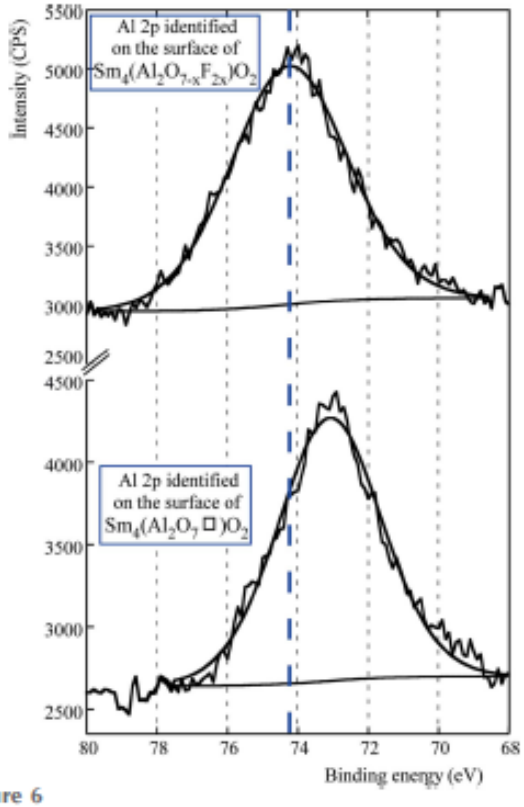

Figure 6
As an example, Al 2*p* spectral regions of the surface of $Sm_4(Al_2O_7\square)O_2$ and their new fluorinated derivative showing a shift to higher binding energy upon fluorination.

Full structural refinements of XRD data for $Sm_4Al_2O_{9-x}F_{2x}$ and $Eu_4Al_2O_{9-x}F_{2x}$ were carried out in the space group $P2_1/c$ by using the $Sm_4(Al_2O_7)O_2$ and $Eu_4(Al_2O_7)O_2$ structures as starting models, respectively. Refined cell and positional parameters, obtained bond distances and angles, and the bond valences are summarized in Tables S1–S11. The Rietveld fittings of the X-ray data are displayed in Fig. 7.

After the convergence of the overall parameters, the occupation of the bridge oxygen site O(5) was replaced by F(1) (Kendrick *et al.*, 2008) and an extra fluorine position, F(2) (Martín-Sedeño *et al.*, 2006), was added in the vacant anion site between two Al_2O_7 units, in order to account for the increase in anion content, and then refined. In both refinements, bond-length constraints were applied. The quality factors of the refinements are given in Table 5. It should be noted that distinguishing O and F by either X-ray or neutron diffraction is very difficult because of the nearly identical scattering factors. Therefore, the respective positions are commonly inferred by bond valence sum (BVS) calculations from the determined bond distances. In this respect, neutron diffraction data would lead to more accurate O/F positions and hence bond distances. However, Gd, Sm and Eu all show very strong neutron absorption, which makes such studies impractical. Therefore we have used BVS calculations based on the structures determined from the X-ray diffraction data.

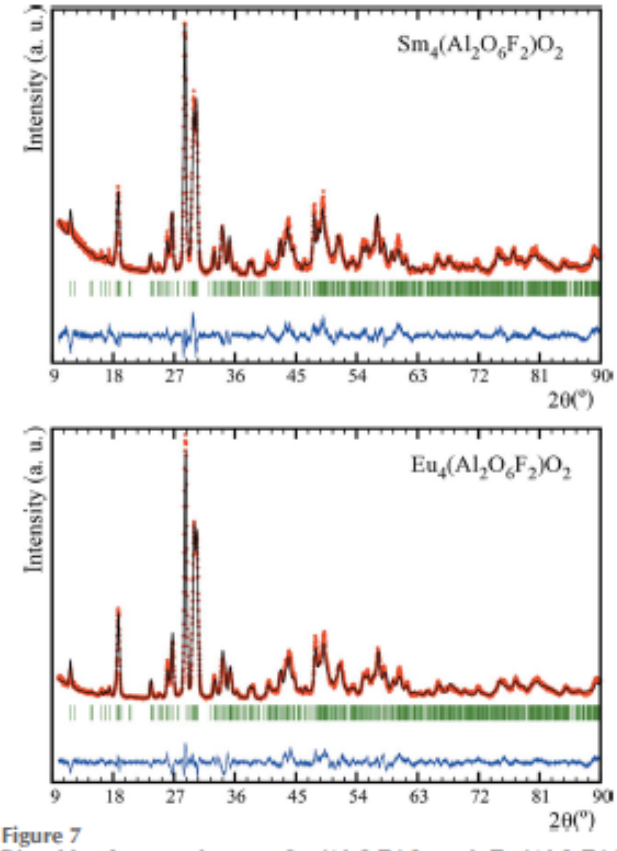

Figure 7
Rietveld refinement for new $Sm_4(Al_2O_6F_2)O_2$ and $Eu_4(Al_2O_6F_2)O_2$ cuspidine-related materials.

Table 5
The quality of refinements performed on new fluorinated oxides.

Samples	$Sm_4Al_2O_{9-x}F_{2x}$	$Eu_4Al_2O_{9-x}F_{2x}$
χ^2	3.7	5.7
R_{Bragg}	12.8	11.7
R_f	10.6	9.2
R_p	10.9	10.2
R_{wp}	13.6	12.8
R_{exp}	7.06	5.39

These calculations are in agreement with the assignment of the F positions proposed, which is further supported by the Raman results (see later). In addition, the BVS values that are calculated for the F(1) and F(2) sites, assuming O is present, show a critical deficit of valence charge in the oxygen atoms. These results add further weight to the conclusion that F occupies these sites.

The introduction of fluorine leads to the conversion of isolated $M_2O_7\square$ groups into infinite chains of distorted square-based pyramids along the *a* axis, as observed for $La_4(Ti_2O_8)O_2$.

It is interesting to compare the present results with those of Si cuspidines of the $M_4(Si_2O_7)F_2$ type (Achary *et al.*, 2017), where the Si_2O_7 units are preserved and fluorine occupies the O(8) and O(9) sites instead of filling the anionic vacancies and substituting for bridge oxygen ions along the AlO_4 chains. The different behaviour can be attributed to the larger size of Al cations compared with Si, and its higher ability to accommodate coordination numbers greater than four.

In summary, the structures of $Ln_4(Al_2O_6F_2)O_2$ (Ln = Sm, Eu) are monoclinic ($P2_1/c$) with two sites for fluorine between the aluminate groups. Thus, as observed from Figs. 8 and 9, the aluminium coordination changes from four to five. Because of low crystallinity, the $Gd_4(Al_2O_{7-x}F_2)O_2$ diffractogram produces a poor signal, which limits its Rietveld refinement. This lower crystallinity is probably related to the fact that Gd is the smallest rare-earth metal and also the large volume change upon fluorination, which may have reduced the particle size/crystallinity. Considering $Ln_4(Al_2O_6F_2)O_2$ (Ln = Sm, Eu) as representative structures of the obtained $Ln_4(Al_2O_6F_2)O_2$ (Ln = Sm, Gd) compositions, similar results could be expected for the gadolinium sample.

These structural assumptions have been further discussed based on Raman results. Raman spectra are shown in Fig. 10 for samples $Ln_4(Al_2O_7\square)O_2$ (bottom set) and $Ln_4(Al_2O_{7-x}F_{2x})O_2$ (top set) (Ln = Sm, Eu, Gd). The relatively low intensity of all the spectra could be a priori attributed to the method of synthesis, where a low preparation temperature was used and thus low crystallinity was expected. The Raman spectra of the starting $Ln_4(Al_2O_7\square)O_2$ materials are quite similar, since they are structurally akin, and are in good agreement with the bibliography (Hasdinor-Bin-Hassan, 2010). An evaluation of the whole spectra is beyond the scope of this work due to the complexity of the structure, so only the high-frequency region will be treated in detail. The as-prepared samples show four well defined bands between 700 and 800 cm^{-1} that can be unambiguously ascribed to Al—O

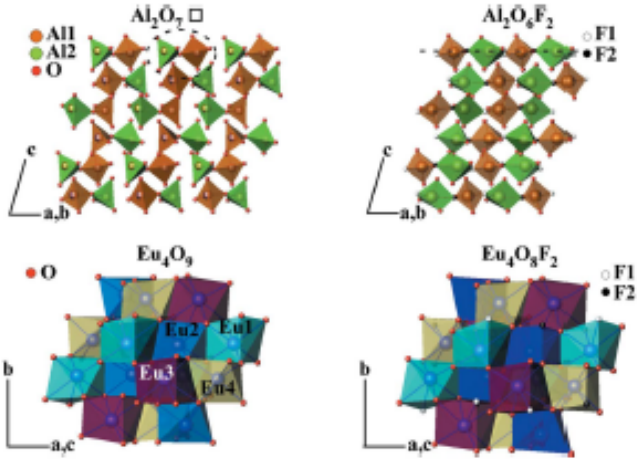

Figure 8
As an example, a polyhedral view of the $Eu_4(Al_2O_7\square)O_2$ and $Eu_4(Al_2O_6F_2)O_2$ phases obtained from the Rietveld refinement structural data using *Atoms62* software.

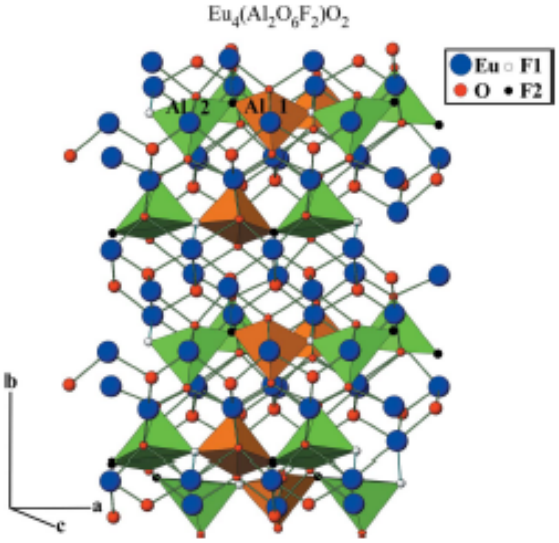

Figure 9
As an example, a simplified representation of the new $Eu_4(Al_2O_6F_2)O_2$ phase structure obtained from the Rietveld refinement structural data using *Atoms62* software.

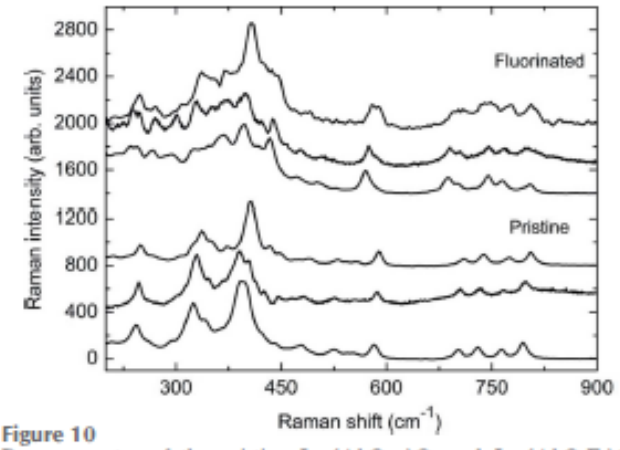

Figure 10
Raman spectra of the pristine $Ln_4(Al_2O_7\square)O_2$ and $Ln_4(Al_2O_6F_2)O_2$ samples. Bottom to top: Ln = Sm, Eu, Gd.

stretching modes, since these have shorter bond distances than Ln—O. In the cuspidine structure, the existence of pyroaluminate units of $[Al_2O_7]$ type suggests that it is appropriate to separate the expected modes into internal pyrogroup modes and lattice modes, although the covalent degree of the Al—O bond is lower than that of Si—O or P—O bonds in $[Si_2O_7]$ or $[P_2O_7]$ groups. Moreover, since these units are disconnected within the structure, correlation effects can be dismissed.

Following this approach, and taking into consideration the crystallographic results, the $[Al_2O_7]$ units can be considered as consisting of two AlO_3 pyramids connected by a bridging oxygen O′ [O(5) in Tables S2 and S3] in the form O_3—Al—O′—Al—O_3. Within this model, the expected modes can be divided into vibrational modes of the AlO_3 pyramids and those of the Al—O′—Al bridge.

A regular pyramid with $C3v$ symmetry would give two stretching modes in the region of study, one A_1 mode and one E mode, consisting mainly of the vibration of the three oxygens of the pyramid along the Al—O bonds. However, since Al is located in a 4*e* site with very low local symmetry ($C1$), the pyramids must be considered as irregular, giving three A modes. On the other hand, the Al—O′—Al bridge is expected to give two stretching modes: one symmetric mode coming mainly from the vibration of Al atoms and one antisymmetric mode involving Al and O vibrations. The energy of the former will obviously depend on the cation and is found between 520–560 cm^{-1} in the case of $[Ge_2O_7]$ (Saez-Puche *et al.*, 1992; Hanuza *et al.*, 2011) and $[Ga_2O_7]$ (Kaminskii *et al.*, 2014) and 620–700 cm^{-1} for $[Si_2O_7]$ (Achary *et al.*, 2017; Lecleach & Gillet, 1990), $[P_2O_7]$ and $[S_2O_7]$ (Kazuo, 2009). In our case, the Al vibration was expected to be around 600 cm^{-1} and could be tentatively ascribed to the intense band at 590 cm^{-1}. Therefore, the only mode from the bridge in the high frequency region would be the antisymmetric mode. Although some authors have considered in analogous systems that the O′ is located in an inversion centre, thus yielding a Raman forbidden or very weak antisymmetric mode (Saez-Puche *et al.*, 1992), the approximation needs the angle of X—O′—X to be close to 180° and both X—O′ distances to be alike. These assumptions seem to be far from our case, where the X—O′—X angle is around 140°.

Since only four modes are observed in the high-frequency region of the $Ln_4(Al_2O_7\square)O_2$ sample, the model that best fits our data is that of two irregular but similar pyramids, which would give three stretching modes, connected by an Al—O′—Al bridge whose antisymmetric mode would supply the required fourth mode.

The model of the isolated $[Al_2O_7]$ units is not valid anymore for the fluorinated samples, where F is proposed to be located in the interstitial positions between these units as well as substituting for the O′ in the bridge. Thus, AlO_3F_2 quasi-square pyramids sharing F vertices form infinite chains along the *a* axis (see Fig. 10). By applying the point group $C2v$ symmetry operations to the constituent atoms of the pyramid (two F and two O atoms in the base and one apical O_{ap}), five stretching modes are expected in the high frequency region, considering that all the pyramids are equivalent: three A_1 (Al + O_{ap}, F, O), one B_1 (Al + F) and one B_2 (Al + O). This number of modes is in good agreement with what we observe in the spectra of the fluorinated samples, where five modes are found in the 650–820 cm^{-1} region. The agreement with the experimental observation suggests that correlation effects, if present, result in almost degenerate modes that remain unresolved because of the spectral broadening. Regarding the symmetrical mode of the Al—O′—Al bridge in the pristine samples, its position shifts from 590 to 570 cm^{-1} upon fluorination, which would agree with the substitution of the O′ bridge by F, supporting the assumption from the structural studies that F is located in this site.

Therefore, the Raman measurements are consistent with the crystallographic model proposed for fluorinated $Ln_4(Al_2O_6F_2)O_2$ cuspidines.

4. Conclusions

In summary, new $Ln_4(Al_2O_6F_2)O_2$ (Ln = Sm, Eu, Gd) phases with a cuspidine-related structure have been synthesized using a low-temperature fluorination route, a technique that uses $Ln_4(Al_2O_7)O_2$ as the oxide precursor and poly(vinylidene difluoride) as the fluorination agent. The results illustrate the versatility of this fluorination route for the synthesis of new oxide–fluoride systems. The Raman measurements are consistent with the crystallographic model proposed for new fluorinated $Ln_4(Al_2O_6F_2)O_2$ cuspidines: the incorporation of fluorine in the $Ln_4(Al_2O_7\square)O_2$ structure results in Al coordination changes from four to five, which allows the conversion of isolated $Al_2O_7\square$ groups into infinite chains of distorted square-based pyramids.

Funding information

This research was funded by the Ministerio de Economía, Industria y Competitividad (MAT2016-76739-R) (AEI/FEDER, UE), and Departamento de Educación of the Basque Government (IT-630–13). The authors thank SGIker of UPV/EHU for technical and personnel support. A. Morán-Ruiz thanks UPV/EHU for funding.

References

Achary, S. N., Tyagi, A. K., Gupta, M. K., Mittal, R., Bhattacharya, K. & Rao, R. (2017). *J. Alloys Compd.* **702**, 573–584.
Berry, F. J., Heap, R., Helgason, Ö., Moore, E. A., Shim, S., Slater, P. R. & Thomas, M. F. (2008). *J. Phys. Condens. Matter*, **20**, 215207–215213.
Clemens, O., Kruk, R., Patterson, E., Loho, C., Reitz, C., Wright, A. J., Knight, K. S., Hahn, H. & Slater, P. R. (2014). *Inorg. Chem.* **53**, 12572–12583.
Clemens, O. & Slater, P. R. (2013). *Rev. Inorg. Chem.* **33**, 105–117.
Dae-Min, K., Sang-Ho, L., William, B. A., Kyeong-Beom, K., Yoon-Suk, O. & Sung-Min, L. (2011). *J. Am. Ceram. Soc.* **94**, 3455–3459.
Ghosh, S. (2015). *Advanced Ceramic Processing*, edited by A. Mohamed, pp. 111–138. London: InTech.
Hancock, C. A., Herranz, T., Marco, J. F., Berry, F. J. & Slater, P. R. (2012). *J. Solid State Chem.* **186**, 195–203.

Hanuza, J., Maczka, M., Ptak, M., Lorenc, J., Hermanowicz, K., Becker, P., Bohatý, L. & Kaminskii, A. A. (2011). *J. Raman Spectrosc.* **42**, 782–789.
Hasdinor-Bin-Hassan, O. (2010). *Oxides with Polyatomic Anions Considered as New Electrolyte Materials for Solid Oxide Fuel Cells*, pp. 48–53. Jülich: Forschungszentrums Jülich GmbH.
Heap, R., Slater, P. R., Berry, F. J., Helgason, O. & Wright, A. J. (2007). *Solid State Commun.* **141**, 467–470.
Kaminskii, A. A., Yu, H. H., Wang, J. Y., Zhang, Y. Y., Zhang, H. J., Lux, O., Rhee, H., Eichler, H. J., Hanuza, J., Yoneda, H. & Shirakawa, A. (2014). *Laser Phys.* **24**, 085803–085810.
Katayama, T., Chikamatsu, A., Kamisaka, H., Kumigashira, H. & Hasegawa, T. (2016). *Appl. Phys. Expr.* **9**, 025801–025804.
Kawahara, K., Chikamatsu, A., Katayama, T., Onozuka, T., Ogawa, D., Morikawa, K., Ikenaga, E., Hirose, Y., Harayama, I., Sekiba, D., Fukumura, T. & Hasegawa, T. (2017). *CrystEngComm*, **19**, 313–317.
Kazuo, N. (2009). Editor. *Infrared and Raman Spectra of Inorganic and Coordination Compounds, Part A: Theory and Applications in Inorganic Chemistry*. Hoboken, New Jersey: John Wiley & Sons.
Kendrick, E., Russ, M. & Slater, P. R. (2008). *Solid State Ionics*, **179**, 819–822.
Le Cléach, A. & Gillet, P. (1990). *Eur. J. Mineral.* **2**, 43–54.
Martín-Sedeño, M. C., Losilla, E. R., León-Reina, L., Bruque, S., Marrero-López, D., Núñez, P. & Aranda, M. A. G. (2004). *Chem. Mater.* **16**, 4960–4968.
Martín-Sedeño, M. C., Marrero-López, D., Losilla, E. R., Bruque, S., Núñez, P. & Aranda, M. A. G. (2006). *J. Solid State Chem.* **179**, 3445–3455.
Martín-Sedeño, M. C., Marrero-López, D., Losilla, E. R., León-Reina, L., Bruque, S., Núñez, P. & Aranda, M. A. G. (2005). *Chem. Mater.* **17**, 5989–5998.
Moon, E. J., Choquette, A. K., Huon, A., Kulesa, S. Z., Barbash, D. & May, S. J. (2015). *APL Mater.* **3**, 062511–062517.
Morán-Ruiz, A., Vidal, K., Larrañaga, A. & Arriortua, M. I. (2018). *Ceram. Int.* **44**, 8761–8767.
Rodriguez-Carvajal, J. (2010). *FULLPROF*. Version 4.80. ILL, Grenoble, France.
Saez-Puche, R., Bijkerk, M., Fernández, F., Baran, E. J. & Botto, I. L. (1992). *J. Alloys Compd.* **184**, 25–34.
Shape Software (2005). *ATOMS*, version 6.2. Shape Software, Kingsport, Tennessee, USA.
Slater, P. R. (2002). *J. Fluor. Chem.* **117**, 43–45.
Zhou, X., Xu, Z., Fan, X., Zhao, S., Cao, X. & He, L. (2014). *Mater. Lett.* **134**, 146–148.

whec 21st 2016 Zaragoza Spain

World Hydrogen Energy Conference 2016

PROCEEDINGS

Organiser: AeH2 Asociación Española del Hidrógeno

Under the auspices of: hia2

Collaborators: Ha Foundation for the Development of New Hydrogen Technologies in Aragon; Gobierno de Aragón, Departamento de Economía, Industria y Empleo

21st World Hydrogen Energy Conference 2016. Zaragoza, Spain. 13-16th June, 2016

Optimization of the large scale synthesis of the LSF-20 cathode material for SOFCs

I. Perez-Fernandez[1*], A. Wain[1], A. Morán-Ruiz[1], K. Vidal[1], A. Larrañaga[1] and M.I. Arriortua[1]

[1]Universidad del País Vasco (UPV/EHU), Facultad de Ciencia y Tecnología, Barrio Sarriena S/N, 48940 Leioa, Vizcaya, Spain

(*) iperez089@ikasle.ehu.eus

Solid oxide fuel cells (SOFCs) have the potential to be one of the cleanest and most efficient energy technologies for direct conversion of chemical fuels to electricity. Economically competitive SOFC systems appear poised for commercialization, but widespread market penetration will require continuous innovation of materials and fabrication processes to enhance system lifetime and reduce cost. Additional requirements arise for the technologies for synthesis of SOFC materials. These requirements originate from the demands for large scale SOFC industrial production. In this sense, solution combustion synthesis (SCS) is a simple and reproducible method used to obtain several types of ceramic oxides for a variety of applications. A typical SCS procedure utilizes a self-sustained exothermic reaction among well-mixed reactants to achieve the rapid and economical synthesis of particulate products. Up to 2008, SCS method has been adopted to fabricate more than 1000 kinds of oxide powders over more than 65 countries [1]. The properties of the resulting powders (crystalline structure, amorphous structure, crystallite size, purity, specific surface area and particle agglomeration) depend heavily on the adopted processing parameters [2,3].

The objective of this work is to obtain, on a large scale, the perovskite-type oxide $La_{0.8}Sr_{0.2}FeO_3$ that shows promising properties as cathode for SOFC applications. In this study, the optimization of the large scale synthesis has been realized by the glycine-nitrate combustion method (**Figure 1**). In this sense, first of all, the effect of some parameters such as temperature, glycine/nitrate ratio and times and cooling rates used in the temperature treatments, that play a key role in the final properties of the obtained materials, has been analyzed. The characterization has been realized by ICP (inductively coupled plasma atomic emission spectroscopy) XRD (X Ray diffraction), SEM (scanning electron microscopy) and dilatometry.

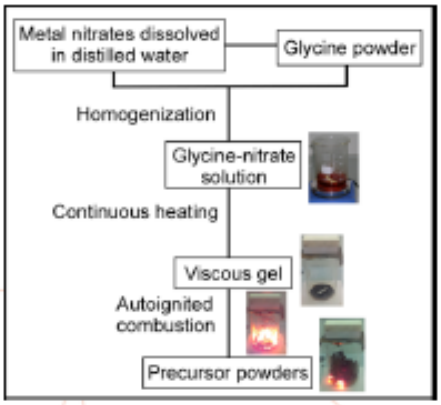

Figure 1. Scheme of glycine nitrate combustion synthesis.

References

[1] W. Wen, and J-M. Wu, RSC Adv. 4 (2014) 58090-58100.
[2] D. Pereira, C. de Fraga, V. Caldas, Powder Technol. 269 (2015) 481-487.
[3] K. Vidal, A. Morán-Ruiz, A. Larrañaga, J.M. Porras-Vázquez, P.R. Slater, M.I. Arriortua, Solid State Ionics 269 (2015) 24-29.

Acknowledgments

This research has been funded by the Ministerio de Economía y Competitividad (MAT2013-42092-R) with co-financing FEDER-EU) and Dpto. Educación, Política Lingüística y Cultura of the Basque Goverment (IT-630-13). The authors thank SGIker (UPV/EHU) technical support.

21st World Hydrogen Energy Conference 2016. Zaragoza, Spain. 13-16th June, 2016

Degradation study of ceramic vs metallic half-cells for SOFCs

A. Morán-Ruiz[1*], A. Wain[1], K. Vidal[1], A. Larrañaga[1], M.A. Laguna-Bercero[2], M.I. Arriortua[1]

[1]Universidad del País Vasco (UPV/EHU), Facultad de Ciencia y Tecnología, Barrio Sarriena S/N, 48940 Leioa, Vizcaya, Spain
[2]Instituto de Ciencia de Materiales de Aragón, ICMA, CSIC-Universidad de Zaragoza, Pedro Cerbuna 12, 50009 Zaragoza, Spain

(*) aroa.moran@ehu.eus

The development of new electrolytes, electrodes and interconnect materials for solid oxide fuel cells (SOFCs) is associated with the increase of the long-term stability [1, 2]. There is now considerable effort directed towards the development of new materials and structures with better performance for cathode-interconnect electrical contact [3].

The cathode contact materials must have adequate conductivity, appropriate thermal expansion coefficient, be chemically compatible with adjacent components and stable in air [4, 5]. In this work, femtosecond laser machined holes are produced in a composite based on a Fe-22Cr mesh dipped into $LaNi_{0.6}Co_{0.4}O_{3-\delta}$ (LNC) ceramic slurry as a possible gas permeable contact layer for SOFCs. The contact composite has been studied with respect to its contact with Crofer22APU channeled metallic interconnect and $La_{0.6}Sr_{0.4}FeO_3$ (LSF) ceramic cathode. The electrical performance of the half-cell {LSF/ablated mesh-LNC/Crofer22APU} was examined at 800 °C in air. The obtained results showed that the overall area specific resistance (ASR) values were stable over time (1000 h). The calculated ASR average value was 0.12(1) ohm·cm² (Figure 1).

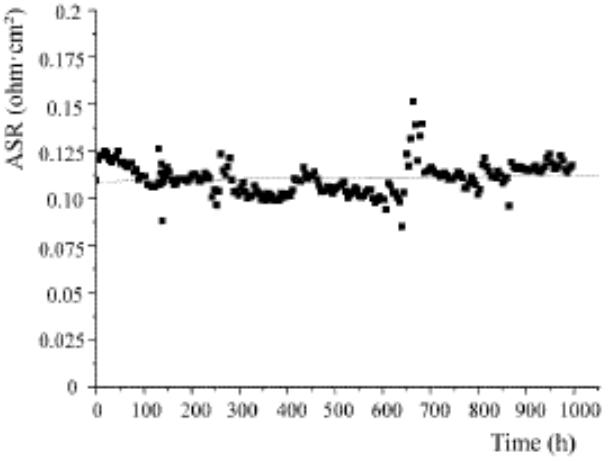

Figure 1. ASR measurements of half-cell {LSF/ablated mesh-LNC/Crofer22APU} as a function of time.

For post-test degradation studies, the samples are characterized by X-ray diffraction (XRD). Moreover, the microstructure, compositional analysis and phase distribution of samples are examined by scanning electron microscopy (SEM) equipped with an energy dispersive X-ray analyzer (EDX) technique.

References

[1] N. Schrödl, E. Bucher, A. Egger, P. Kreiml, C. Teichert, T. Höschen, W. Sittle, Solid State Ionics **276** (2015) 62-71.
[2] S.K. Skinner, M.A. Laguna-Bercero, in: Energy Materials, D.W. Bruce, D. O´Hare, R.I. Walton. (Ed.), John Wiley & Sons, 2011, pp. 33-95.
[3] A. Morán-Ruiz, K. Vidal, A. Larrañaga, J.M. Porras-Vázquez, P.R. Slater, M.I. Arriortua, Int. J. Hydrogen Energ. **40(26)** (2015) 8407-8418.
[4] F. Wang, D. Yan, W. Zhang, B. Chi, J. Pu, L. Jian, Int. J. Hydrogen Energ. **38** (2013) 646-651.
[5] A. Morán-Ruiz. Desarrollo de capas de contacto para su aplicación en SOFC/ Development of contact coatings for SOFC. Ph.D. thesis, UPV/EHU, 2015.

Acknowledgments

This research has been funded by the Ministerio de Economía y Competitividad (MAT2013-42092-R) with co-financing FEDER-EU and Dpto. Educación, Política Lingüística y Cultura of the Basque Goverment (IT-630-13). The authors thank SGIker (UPV/EHU) technical support.

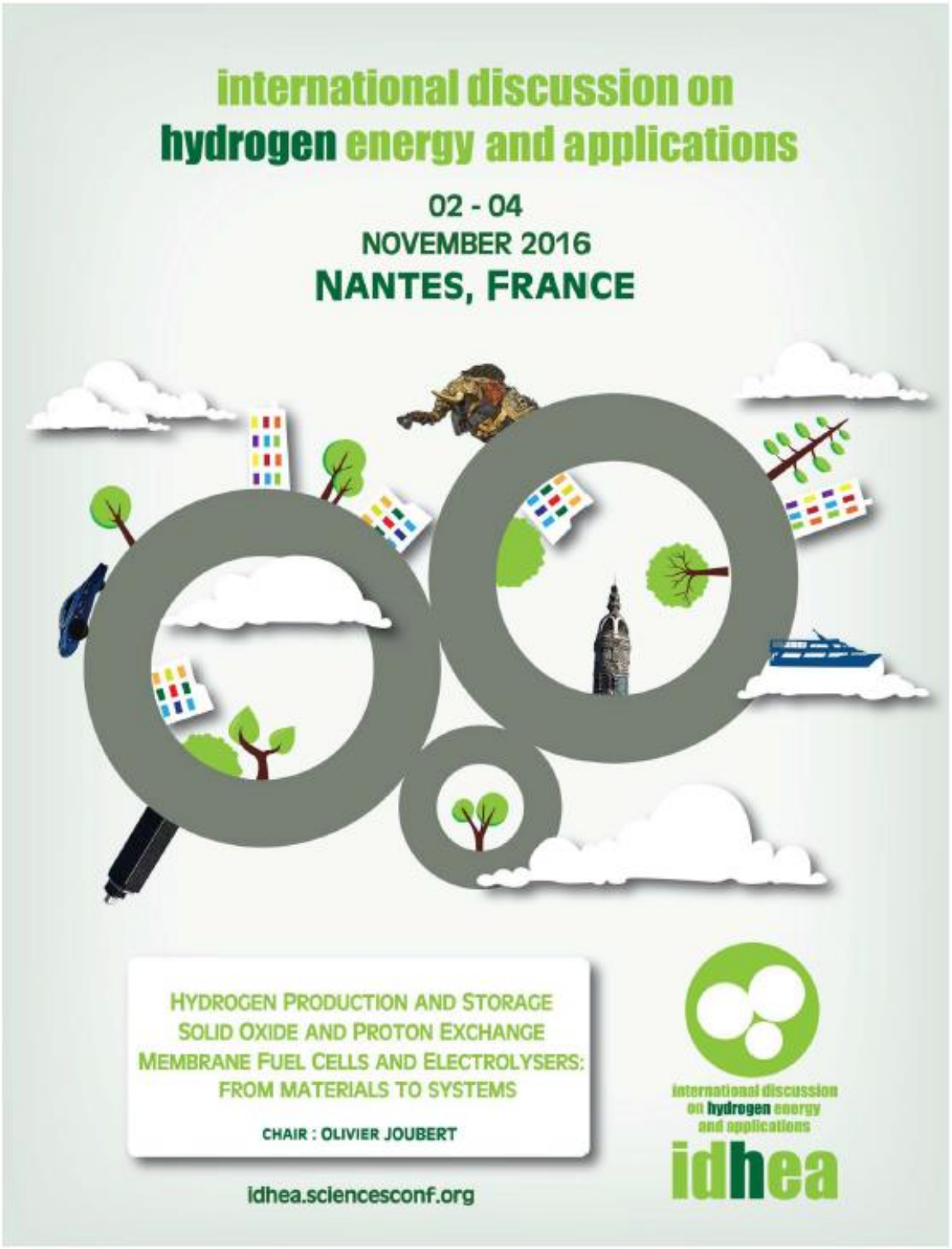
international discussion on
hydrogen energy and applications
02 - 04
NOVEMBER 2016
NANTES, FRANCE
HYDROGEN PRODUCTION AND STORAGE
SOLID OXIDE AND PROTON EXCHANGE
MEMBRANE FUEL CELLS AND ELECTROLYSERS:
FROM MATERIALS TO SYSTEMS
CHAIR : OLIVIER JOUBERT
idhea.sciencesconf.org
international discussion
on hydrogen energy
and applications
idhea

PROGRAM

ORAL O32:

Effect of doping level x in $Ln_{1-x}M_xCr_{0.9}Ni_{0.1}O_3$ SOFC anodes

Aroa Morán[a], Aritza Wain[a], Karmele Vidal[a], Aitor Larrañaga[a], Miguel Laguna[b], María I. Arriortua[a]

[a] *Facultad de Ciencia y Tecnología,Universidad del País Vasco/Euskal Herriko Unibertsitatea (UPV/EHU), Sarriena s/n, 48940 Leioa, Spain.*

[b] *CSIC-Universidad de Zaragoza, Instituto de Ciencia de Materiales de Aragón (ICMA), Pedro Cerbuna 12, 50009 Zaragoza, Spain*

[c] *Basque Centre for Materials, Applications & Nanostructures (BC Materials), 48160 Derio, Spain*

email address of the presenting author: aritza.wain@ehu.eus

There is an increasing demand for the development of alternate anode materials with improved tolerance towards carbon deposition and sulfur poisoning to improve the fuel flexibility and efficiency of Solid Oxide Fuel Cells (SOFCs) [1]. In this sense, perovskites have gained attraction as electrode materials for SOFCs due to their catalytic, ionic and electrical conductivities, chemical and thermal stabilities at higher temperatures [2,3].

Several studies based on perovskites have shown that changes in physical properties are related to changing doping level x of the A-site. However, these physical properties can vary even at a constant value of x [4], being very sensitive to changes not only in the doping level (x), but also in the average size of the A cations ($\langle r_A \rangle$), and in the effects of A cation size disorder ($\sigma^2(r_A)$) quantified as $\sigma^2(r_A) = \langle r_A^2 \rangle - \langle r_A \rangle^2$ [5-7].

In this study, we investigate the variation of the doping level x in the structure and electrical properties of a series of $Ln_{1-x}M_xCr_{0.9}Ni_{0.1}O_3$ (Ln = La y/o Nd; M = Sr y/o Ca; $x \leq 0.25$) perovskites. This has been achieved by keeping the mean ionic radius $\langle r_A \rangle$ (1.22 Å) and the cation size disorder $\sigma^2(r_A)$ (0.0001 $Å^2$) constant throughout the whole series of compositions prepared.

The samples are prepared using the urea combustion method. X-ray powder diffraction (XRD) shows that all of the compounds have orthorhombic symmetry (space group: Pnma). The structural, morphological and electrical properties are highly dependent on x; a systematic decrease in unit cell volume, increase in grain growth and decrease in electrical conductivity (in reducing atmosphere) is observed with increasing doping level.

Acknowledgements: This research has been funded by the Ministerio de Economía y Competitividad (MAT2013-42092-R) and Dpto. Educación, Política Lingüística y Cultura of the Basque Goverment (IT-630-13). The authors thanks the support received by the European Regional Development Fund. (ERDF). SGIker of UPV/EHU technical support is gratefully acknowledged. A. Wain thanks Ministerio de Economía y Competitividad for funding his work (BES-2014-068433).

[1] K. Zheng, K. Swierczek, Solid State Ion. 288 (2016) 124-129.

[2] W.H. Kan, V. Thangadurai, Ionics 21(2) (2015) 301-318.

[3] I.Z. Rahman, M.A. Raza, M.A. Rahman, Adv. Mater. Res. 445 (2012) 497-502.

[4] K. Vidal, L.M. Rodríguez-Martínez, L. Ortega San-Martín, A. Martínez-Amesti, M.L. Nó, T. Rojo, A. Laresgoiti, M.I. Arriortua, J. Power Sources 192 (2009) 175-179.

[5] M. Rodríguez-Martínez, J.P. Attfield, Phys. Rev. B 54 (1996) R15622–R15625.

[6] A. Ecija, K. Vidal, A. Larrañaga, A. Martínez-Amesti, L. Ortega San-Martín, M.I. Arriortua, Solid State Ion. 235 (2013) 14-21.

[7] K. Vidal, A. Larrañaga, A. Morán-Ruiz, A.T. Aguayo, M.A. Laguna-Bercero, M.P. Yeste, J.J. Calvino, M. I. Arriortua, Int. J. Hydrogen Energ. In Press. DOI: 10.1016/j.ijhydene.2016.02.088.

HYCELTEC 2017

VI Symposium on Hydrogen, Fuel Cells and Advanced Batteries

Porto, Portugal, 19-23 June 2017

Book of Abstracts

HYCELTEC 2017
VI Symposium on Hydrogen, Fuel Cells and Advanced Batteries
Porto, Portugal, 19-23 June 2017

6th Symposium on Hydrogen, Fuel Cells and Advanced Batteries, Porto, June 19th-23rd 2017

Effect of doping level x and fuel on glycine-nitrate combustion synthesis of $(La,Nd)_{1-x}(Sr,Ca)_xCr_{0.9}Ni_{0.1}O_3$ ($x \leq 0.25$) perovskites as anode materials for SOFCs.

A. Wain-Martin[1*], L. Ortega-San-Martín[2], A. Morán-Ruiz[1], K. Vidal[1], A. Larrañaga[1], M.A. Laguna-Bercero[3], M.I. Arriortua[1**]

[1] Facultad de Ciencia y Tecnología,Universidad del País Vasco/Euskal Herriko Unibertsitatea, (UPV/EHU), Sarriena s/n, 48940 Leioa, Spain
[2] Departamento de Ciencias, Sección Químicas, Pontificia Universidad Católica del Perú (PUCP), Av. Universitaria 1801, Lima 32, Perú
[3] CSIC-Universidad de Zaragoza, Instituto de Ciencia de Materiales de Aragón (ICMA), Pedro Cerbuna 12, 50009 Zaragoza, Spain

(*) Pres. author: aritza.wain@ehu.eus (**) Corresp. author: maribel.arriortua@ehu.es

Keywords: SOFCs, Lanthanum chromite, Anode, Electrical conductivity

1. Introduction

The application of mixed ionic-electronic conductors (MIEC) in SOFC anodes is considered to be highly beneficial, as it allows for the electrode reaction to occur on the whole surface on the electrode material, improving electrochemical properties. Perovskite based materials have oxygen ion vacancies depending on composition, temperature, and surrounding crystalline environment that impart mixed ionic and electronic conductivities to them. Since perovskites can accommodate almost all the elements in the periodic table they can offer excellent catalytic properties [1].

Another important field of research aimed at reducing energy consumption of the perovskite synthesis [2]. To synthesize nano-size powders with high specific surface area, combustion methods are of great importance [3]. The effect of the combustion fuel on the electrochemical properties of SOFC materials has been investigated recently, for both single fuels and fuel mixtures [4].

On the other hand, several studies based on perovskites have shown that changes in physical properties are related to changing doping level (x) of the A-site. However, these physical properties can vary even at a constant value of x, being very sensitive to changes not only in the doping level, but also in the average size of the A cations ($\langle r_A \rangle$), and in the effects of A cation size disorder ($\sigma^2(r_A)$) quantified as $\sigma^2(r_A) = \langle r_A^2 \rangle - \langle r_A \rangle^2$ [5].

In this study, we investigate two effects: (i) the variation of the doping level x and (ii) the use of different fuels (glycine and urea) during the combustion synthetic method in the structure and electrical properties of a series of $Ln_{1-x}M_xCr_{0.9}Ni_{0.1}O_3$ (Ln = La and/or Nd; M = Sr and/or Ca; $x \leq 0.25$) perovskites. This has been achieved by keeping the mean ionic radius $\langle r_A \rangle$ (1.22 Å) and the cation size disorder $\sigma^2(r_A)$ (1.10^{-5} Å^2) constant throughout the whole series of compositions prepared. These compounds have been characterized by X-ray powder diffraction (XRD), scanning electron microscopy (SEM), thermal expansion coefficient (TEC) and electrical conductivity measurements.

2. Experimental

2.1 Powder preparation

$Ln_{1-x}M_xCr_{0.9}Ni_{0.1}O_3$ samples were prepared by combustion synthesis using the metal-nitrates as metal precursors and as combustion fuels: (1) glycine and (2) urea (all from Aldrich). The prepared compositions, together with their mean ionic radius, $\langle r_A \rangle$, and A cation size disorder, $\sigma^2(r_A)$, are summarised in Table 1.

Table 1. Nominal stoichiometries of $Ln_{1-x}M_xCr_{0.9}Ni_{0.1}O_3$ perovskites whit $\langle r_A \rangle$ = 1.22 Å and $\sigma^2(r_A)$ = 1. 10^{-5} Å^2.

x	$Ln_{1-x}M_xCr_{0.9}Ni_{0.1}O_3$
0.10	$La_{0.85}Nd_{0.05}Sr_{0.10}Cr_{0.90}Ni_{0.10}O_3$
0.15	$La_{0.80}Nd_{0.05}Sr_{0.10}Ca_{0.05}Cr_{0.90}Ni_{0.10}O_3$
0.20	$La_{0.80}Sr_{0.10}Ca_{0.10}Cr_{0.90}Ni_{0.10}O_3$
0.25	$La_{0.75}Sr_{0.10}Ca_{0.15}Cr_{0.90}Ni_{0.10}O_3$

The metal nitrates were dissolved in distilled water. Then, the glycine or urea was added to obtain a fuel/oxidizer molar ratio of 1. The resulting viscous liquid started autoignition just after placing the glass beaker directly onto a preheated plate (at 350°C). The obtained powders were calcined at 800°C for 2 h to remove the carbon residues, and after that, these samples were pressed into pellets and calcined in air between 1100 and 1200°C for 10 hours at each temperature until pure samples were obtained.

2.2 Characterization techniques

The structural analysis was performed using X-ray diffraction technique (XRD). XRD data were collected on a Bruker D8 Advance diffractometer equipped with a Cu tube, a Ge (111) incident beam monochromator (λ=1.5406 Å) and a Sol-X energy dispersive detector. Data were collected at room temperature (r.t.) from 18 to 90° in 2θ and a step size of 0.02° (time per step=10 s). The crystal structure was refined by the Rietveld method using the GSAS software package [6] and EXPGUI interface [7].

HYCELTEC 2017
VI Symposium on Hydrogen, Fuel Cells and Advanced Batteries
Porto, Portugal, 19-23 June 2017

6th Symposium on Hydrogen, Fuel Cells and Advanced Batteries, Porto, June 19th-23rd 2017

All metal contents were determined by inductively coupled plasma atomic emission spectroscopy (ICP-AES) on a Horiba Yobin Yvon Activa spectrophotometer. For bulk conductivity and dilatometry measurements, pellets of the as-synthesised powders were sintered at 1350°C for 10 hours and, subsequently, cut into bars. DC conductivity measurements were performed under H_2 by the four-point DC method from 800 to 400°C using a VSP potenciostat controlled by PC using Lab Windows/CVI field point system. The bulk density of each sample was estimated by measuring the mass and the dimensions of the bars. Conductivity data were corrected considering the experimental density values (all around 85% of the theoretical (X-ray) density). Thermal expansion coefficients were measured from room temperature to 950°C under air with a heating rate of 5ºC.min^{-1} by using a Unitherm Model 1161 dilatometer.

Morphologies of the powder samples and the sintered pellets were observed using a scanning electron microscope (JEOL JSM-7000F). Secondary electron images were taken at 20 kV and 1.1.10^{-11} A.

3. Results and Discussion

3.1 Structural study

The X-ray diffraction patterns of all prepared compositions are shown in Figure 1. The patterns reveal that all the samples are single-phased and no impurity phases are detected within the resolution limits of the technique.

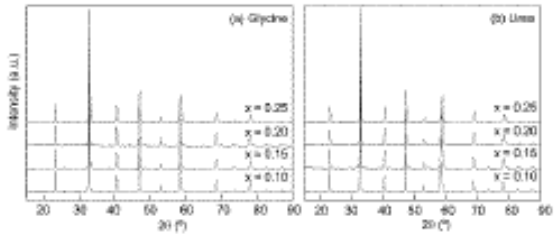

Fig. 1. X-ray diffraction patterns for all samples.

Results from chemical analyses, presented in Table 2, show a good agreement between the analysed chemical compositions of the prepared powders and the nominal compositions.

Table 2. Summary of the ICP analyses for the perovskites $Ln_{1-x}M_xCr_{0.9}Ni_{0.1}O_3$ nominal composition.

x	Fuel	$Ln_{1-x}M_xCr_{0.9}Ni_{0.1}O_3$
0.10	Glycine	$La_{0.86(1)}Nd_{0.04(1)}Sr_{0.11(1)}Cr_{0.90(2)}Ni_{0.10(1)}$
	Urea	$La_{0.87(1)}Nd_{0.05(1)}Sr_{0.10(1)}Cr_{0.90(2)}Ni_{0.11(1)}$
0.15	Glycine	$La_{0.76(1)}Nd_{0.04(1)}Sr_{0.11(1)}Ca_{0.07(1)}Cr_{0.90(1)}Ni_{0.10(1)}$
	Urea	$La_{0.78(1)}Nd_{0.05(1)}Sr_{0.10(1)}Ca_{0.05(1)}Cr_{0.90(1)}Ni_{0.10(1)}$
0.20	Glycine	$La_{0.82(1)}Sr_{0.10(1)}Ca_{0.09(1)}Cr_{0.90(2)}Ni_{0.10(1)}$
	Urea	$La_{0.80(1)}Sr_{0.10(1)}Ca_{0.11(1)}Cr_{0.90(2)}Ni_{0.10(1)}$
0.25	Glycine	$La_{0.74(1)}Sr_{0.08(2)}Ca_{0.16(1)}Cr_{0.90(2)}Ni_{0.11(1)}$
	Urea	$La_{0.75(1)}Sr_{0.09(2)}Ca_{0.15(1)}Cr_{0.90(2)}Ni_{0.10(1)}$

The analysis of the X-ray Diffraction (XRD) data indicated that all samples crystalised as single phase in the orthorhombic space group Pnma. Rietveld fits for the samples obtained with glycine are represented in Figure 2.

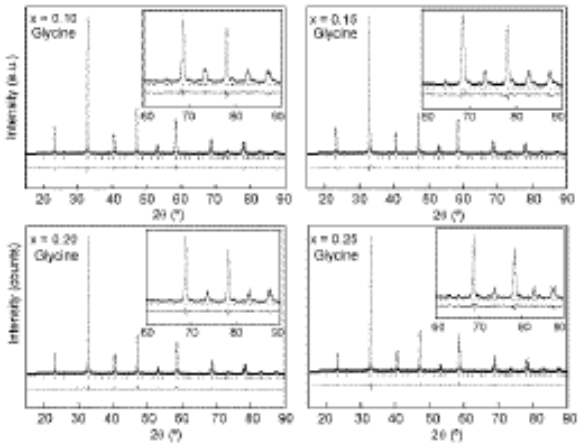

Fig. 2. Rietveld fits of the XRD data for the samples using orthorhombic Pnma space group for the compounds obtained using glycine as fuel.

The variation of the cell parameters and cell volume with doping x is shown in Figures 3 and 4. A systematic decrease in volume is observed with increasing divalent dopant content.

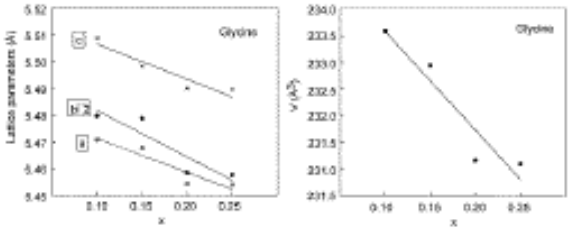

Fig. 3. Variation of the unit cell parameters and volume per formula unit with doping for the samples obtained using glycine as fuel.

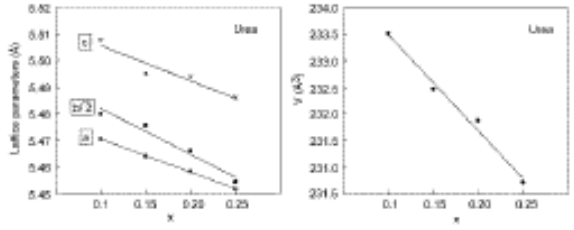

Fig. 4. Variation of the unit cell parameters and volume per formula unit with doping for the samples obtained using urea as fuel.

In the system studied, the A-site mean ionic radius <r_A> has been kept constant. Therefore, the observed decrease of the lattice parameters can be associated exclusively to a reduction of the B-site mean ionic radius (<r_B>) as the doping level x increases. The ionic radii of Ni and Cr decrease when they are oxidized from a higher oxidation state [rVI(Cr^{3+}) = 0.615 Å; rVI(Ni^{2+}) = 0.69 Å] to a smaller oxidation state [rVI(Cr^{4+}) = 0.55 Å; rVI(Ni^{3+}) = 0.56 Å] [8].

3.2 Structural study

According to the literature, smaller crystallite sizes of the initial materials are formed when using urea because in this case the combustion is lower and the large volume of gases envolved enhances dissipation of heat and limits the inter-particle contact [9,10].

Representative SEM micrographs of the powder samples obtained by the combustion method using glycine and urea as fuel after calcination are shown in Figure 5. These powders are composed of agglomerates formed by fine size particles slightly linked. In the case of the sample with x = 0.10 obtained with urea as fuel, the average size of the grains determined by direct SEM observation is about 370 nm and for the obtained with glycine about 200 nm. As have been observed in other works [11] the change of fuel promotes the increase in the size of particles. For the case of using urea, when the combustion is more gradual, the porosity rises when increasing the amount of released gas and smaller crystallite sizes are formed, favouring the sinterability of the sample.

In this sense, the average size of the grains increased from 200 to 550 nm and from 370 to 730 nm when increasing Ca^{2+} content, for the samples obtained using glycine and urea as fuel, respectively. As has been reported [12], the density of the calcium doped lanthanum chromite samples increases with increasing acceptor content.

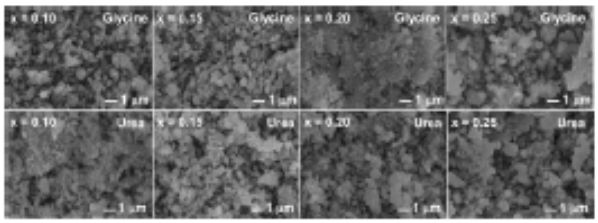

Fig. 5. Micrographs of $Ln_{1-x}M_xCr_{0.9}Ni_{0.1}O_3$ perovskites calcined between 1100 and 1200°C.

SEM images of the sintered pellets at 1350°C in air for 10 h are shown in Figure 6. The most important feature of the samples is that there is an evident effect of doping level x as well as the fuel used in the combustion synthesis in the particle size.

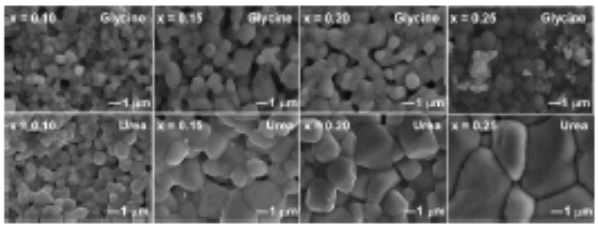

Fig. 6. SEM micrographs taken on the surface of the pellets sintered at 1350°C in air for 10 h.

The average size of the grains increases with x from 0.60 (x = 0.10) up to 1.05 µm (x = 0.25) and from 0.90 (x = 0.10) up to 3.65 µm (x= 0.25) for the samples prepared using glycine and urea, respectively.

On the other hand, the difference in the sintering behavior for the samples is due to the relative difference in their nature of agglomeration. The better sinterability of the powder obtained using urea as fuel is due to the presence of softer agglomerates, which could be broken during cold-pressing to enhance number of contact points [13].

3.3 Electrical conductivity study

The total electrical conductivity, σ, after porosity correction [14], of $Ln_{1-x}M_xCr_{0.9}Ni_{0.1}O_3$ perovskites synthesized with glycine and sintered at 1350°C for 10h as function of doping level x in the temperature range from 400 to 800ºC is shown in Figure 7 (a).

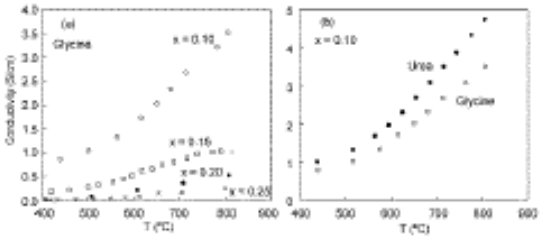

Fig. 7. Conductivity dependence in H_2 upon temperature as a function of (a) x and (b) used fuel.

The preparation route has an important influence on the electrical properties of the obtained materials. For the samples with x = 0.10, the sample obtained with urea shows slightly higher values of conductivity, as can be observed in the Figure 7(b). This result can be explained by the morphological analysis previously, indicating that this material seems better sintered than the obtained using glycine.

3.4 Thermal expansion study

Figure 8 shows the thermal expansion curves of some samples obtained upon heating from 200 to 950°C.

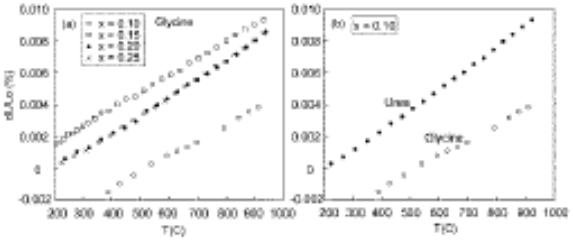

Fig. 8. Thermal expansion behaviour of sintered samples using glycine and (b) x = 0.10 using glycine and urea.

The average linear thermal expansion coefficient (TECs) values are $10.0x10^{-6}$ K^{-1}, $10.7x10^{-6}$ K^{-1}, $11.4x10^{-6}$ K^{-1} and $11.7x10^{-6}$ K^{-1}, for samples with x = 0.10, 0.15, 0.20 and 0.25, respectively, using glycine as fuel. The obtained for the sample with x = 0.10 usin urea is $13.0x10^{-6}$ K^{-1}.

It can be seen that TEC values increase when increasing the doping amount of Ca^{2+}. The obtained TEC values are in reasonable agreement with the literature data for this type of perovskites [15]. In particular, as it can be observed, the

obtained TEC values for the samples with low amounts of dopant are very close to those for the YSZ electrolyte (TEC(8YSZ;300-1000°C) = 10.0-10.8x10^{-6} K^{-1}) [16].

4. Conclusions

A series of perovskites with the general formula $Ln_{1-x}M_xCr_{0.9}Ni_{0.1}O_3$ (Ln=La y/o Nd; M=Sr y/o Ca; x≤0.25) have been prepared by the combustion method using glycine and urea as fuels.

The effects of fuel and doping x have been successfully studied on the series by fixing $\langle r_A \rangle$ to 1.22 Å and $\sigma^2(r_A)$ to 1.10^{-5} Å^2.

At room temperature, all compounds show orthorhombic symmetry (S.G: Pnma). However, cell parameters and unit cell volume, decrease when increasing x.

There is also a systematic increase of grain growth with doping, which is consistent with the introduction of increasing amounts of alkaline-earth cation. This phenomenon is greater for the sample obtained with urea.

The electrical conductivity measured in H_2 is lower for the samples with higher x due to an increase of the oxygen vacancy concentration, being higher for the specimen obtained with urea as fuel.

The obtained TEC values for the samples with low x and using glycine as fuel are more similar to those of YSZ electrolyte.

These results confirm that the sample with low doping level and using urea as fuel, shows good behaviour as anode for SOFC. Nevertheless, its electrochemical behaviour as electrode in a symmetrical or single cell must be studied.

5. Acknowledgements

This research has been funded by the Ministerio de Economía y Competitividad (MAT2016-76739-R and MAT2015-68078-R) (AEI/FEDER, UE) and Dpto. Educación, Política Lingüística y Cultura of the Basque Goverment (IT-630-13). The authors thank for technical and human support provided by SGIker of UPV/EHU. A. Wain-Martin thanks Ministerio de Economía y Competitividad for funding his work (BES-2014-068433).

6. References

[1] F. Zurlo, I.N. Sora, V. Felice, I. Luisetto, C. D'Ottavi, S. Licoccia, E. Di Bartolomeo, Copper-doped lanthanum ferrites for symmetric SOFCs, Acta Materiala, 115(15) (2016) 77-83.

[2] O.V. Komova, V.I. Simagina, S.A. Mukha, O.V. Netskina, G.V. Odegova, O.A. Bulavchenko, A.V. Ishchenko, A.A. Pochtar, A modified glycine–nitrate combustion method for one-step synthesis of $LaFeO_3$, Advanced Powder Technology, 27(2) (2016) 496-503.

[3] D. Pereira, C. de Fraga, V. Caldas de Sousa, Influence of fuel on morphology of LSM powders obtained by solution combustion synthesis, Powder Technology, 269 (2015) 481-487.

[4] F. Deganello, L. F. Liotta, G. Marcı, E. Fabbri, E. Traversa, Strontium and iron-doped barium cobaltite prepared by solution combustion synthesis: exploring a mixed-fuel approach for tailored intermediate temperature solid oxide fuel cell cathode materials, Materials for Renewable Sustainable Energy, 2(8) (2013) 1-14.

[5] M. Rodríguez-Martínez, J.P. Attfield, Cation disorder and size effects in magnetoresistive manganese oxide perovskites, Physical Review B, 54 (1996) R15622–R15625.

[6] A.C. Larson, R.B. Von Dreele, GSAS: General Structure Analysis System, Los Alamos National Laboratory, LAUR 86-748, 2004.

[7] B.H.Toby, EXPGUI, a graphical user interface for GSAS, Journal of Applied Crystallography, 34 (2001) 210-221.

[8] R. D. Shannon, Revised effective ionic radii and systematic studies of interatomic distances in halides and chalcogenides, Acta Crystallographica Section A, 32 (1976) 751-767.

[9] A.L.A. da Silva, G.G.G. Castro, M.M.V.M. Souza, Synthesis of Sr-doped $LaCrO_3$ powders by combustión method. Influence of agent, Journal of Thermal Analysis and Calorimetry, 109 (2012) 33-38.

[10] D. Pereira, C. de Fraga, V. Caldas, Influence of fuel on morphology of LSM powders obtained by solution combustion synthesis, Powder Technology, 269 (2015) 481-487.

[11] B. Silva, J. Kulesza, D.M. de Araújo, A. Kienneman, Nickel-based precursor prepared via microwave-induced combustion method: thermodynamics of synthesis and performance in dry reforming of CH_4, Materials Research, 18(4) (2015) 732-739.

[12] A. Heidarpour, M.H. Abbasi, A. Saidi, Synthesis and sintering of Sr- and Ca-doped lanthanum chromite ultrafine powder for SOFC interconnect, Journal of Materials Science, 48 (2013) 1401-1406.

[13] R.N. Sathi, R.D. Purohita, A.K. Tyagib, P.K. Sinhaa, B.P. Sharmaa. Role of glycine-to-nitrate ratio in influencing the powder characteristics of $La(Ca)CrO_3$, Materials Research Bulletin, 43(6) (2008) 1573-1582.

[14] A.K. Tripathi, H.B. Lal, Electrical transport in light rare-earth orthochromites, Journal of Materials Science, 17 (1982) 1595-1609.

[15] M.K. Rath, K.T. Lee, Investigation of aliovalent transition metal doped $La_{0.7}Ca_{0.3}Cr_{0.8}X_{0.2}O_{3-\delta}$ (X= Ti, Mn, Fe, Co, and Ni) as electrode materials for symmetric solid oxide fuel cells, Ceramics International, in press.

[16] V.V. Kharton, F.M.B. Marques, A. Atkinson, Transport properties of solid oxide electrolyte ceramics: a brief review, Solid State Ionics, 174 (2004) 135-149.

SOFC development at CNH_2

Campana R [1], Wain A [2], Gabriel I [1], Gurauskis J [3], Larrañaga A [2], Arriortua MI [2,4], Rodriguez J [1]

(1) CNH2, Prolongación Fernando el Santo s/n, 13500 Puertollano (Ciudad Real), Spain
(2) UPV/EHU, Facultad de Ciencia y Tecnología. Apdo. 644, E-48080 Bilbao, Spain
(3) ARAID researcher in ICMA CSIC-UZ, C/ Pedro Cerbuna 12. 50009 Zaragoza Spain
(4) BCMaterials, Parque Tecnológico de Zamudio, Ibaizabal Bidea, Edificio 500-Planta 1, 48160 Derio, Spain

Introduction:

Solid oxide fuel cells (SOFC´s) are devices that convert chemical energy from reactants into heat and electricity with high efficiency. Usually, these systems operate at high temperatures (600-1000ºC) and are able to run with different fuels [1, 2]. Here we present the current activities that are being carried out at the Solid Oxide laboratory of the Hydrogen National Centre in Spain, which is focused on the development and electrochemical characterization of SOFC materials and devices.

Results and Discussion:

The fabrication methods for planar SOFCs have been found to be simple and inexpensive. In this work we describe the manufacture and characterization of both electrolyte and anode supported planar SOFCs for high temperature operation using either commercial or self-made materials.

On one hand, the electrolyte supported cells consist of $Gd_{0.2}Ce_{0.8}O_{1.9}$ (CGO) electrolyte of 200µm thickness and thin films (20-50µm thickness) of anode (Ni-CGO) and cathode $La_{0.6}Sr_{0.4}FeO_3$ (LSF). On the other hand, anode supported cells consist of a Ni–YSZ anode support of 800 µm thickness and 18 mm diameter, a 15–20 µm thickness YSZ electrolyte and a LSF cathode. $Sm_{0.2}Ce_{0.8}O_{1.9}$ (SDC) as barrier has been added between the electrolyte and the cathode.

In electrolyte supported cells, the electrolytes were prepared by tape casting and the deposition of thin layers of anodes and cathodes were made by manual spray coating. While in the case of anode supported cells, the anodes were made by uniaxial pressing and the deposition of thin layers of electrolyte, barrier, and cathode were made by manual spray coating.

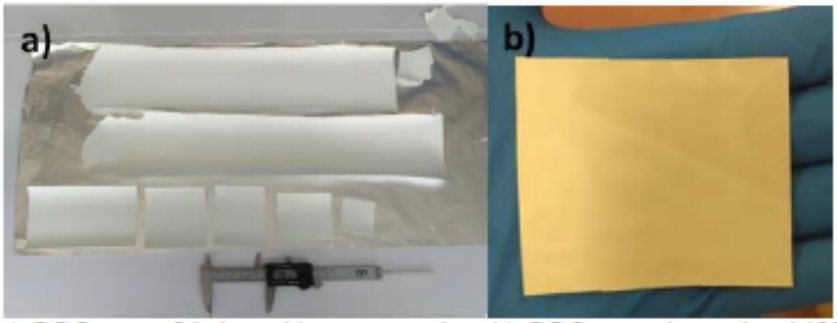

Figure 1. a) CGO tapes fabricated by tape casting. b) CGO tape sintered at 1400ºC.

Figure 1 shows CGO tapes fabricated by tape casting which are the electrolytes in electrolyte supported planar cells. Fig 1a) as prepared tapes. Fig 1b) tapes after the sinterization process. It is noteworthy that those tapes are flexible and easily processable using low-power laser techniques before the sinterization process. After that, the anode and the cathode layers were deposited in order to manufacture the cells.

Both types of cells were characterized by Scanning Electron Microscopy (SEM) with Energy Dispersive X-ray Spectroscopy (EDX). The cells were also electrochemically characterized in a button cell test rig (NorECs). The polarization curves and electrochemical impedance spectroscopy (EIS) measurements were performed by a multichannel Potentiostat/Galvanostat VMP3 (Biologic) using 100% of H_2 humidified at 3% as reactant gas in the anodic compartment and air in the cathodic one at temperatures between 750 and 900 °C.

Figure 2 shows the I-V and I-P curves obtained for the anode supported cells in the temperature range of 750-865ºC. As it can be seen, the open circuit voltages (OCV) are high enough to ensure an efficient sealing and to prove that the YSZ electrolyte layer was tight enough without gas cross over. The power density of the cell reaches values close to 200mW·cm^{-2} at 865ºC:

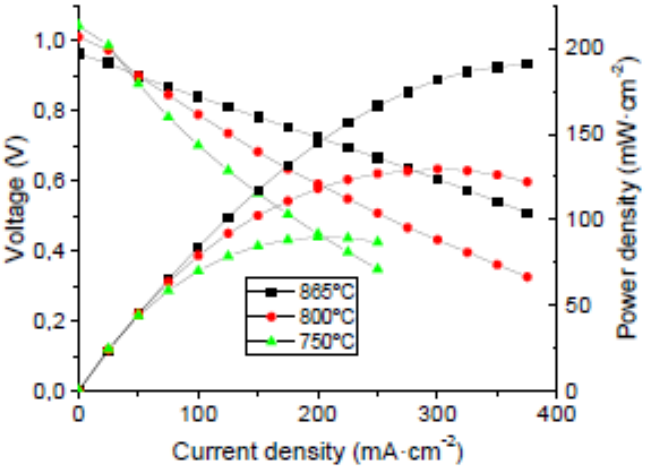

Figure 2. I-V and I-P curves for anode supported cells fabricated at CNH_2.

References:

[1] Singhal S. C, Kendall K.,"High Temperature Solid Oxide Fuel Cells: Fundamentals, Design and Applications". Oxford: Elsevier Advanced Technology, 2002.

[2] Larminie J., "Fuel Cell Systems Explained". 2nd edition, John Wiley & Sons, 2003.